Volume 134 Numbers 1–4(1992)

FEROA8 134(1–4) 1–376 (1992)
ISSN: 0015-0193

1

FERROELECTRICS

GORDON AND BREACH SCIENCE PUBLISHERS
SWITZERLAND • AUSTRALIA • BELGIUM • FRANCE • GERMANY • GREAT BRITAIN
INDIA • JAPAN • MALAYSIA • NETHERLANDS • RUSSIA • SINGAPORE • USA

FERROELECTRICS
and related materials

GENERAL INFORMATION

Aims and Scope *Ferroelectrics* is designed to provide a forum for people working in ferroelectrics and related materials such as ferroelastics, ferroelectric-ferromagnetics, electrooptics, piezoelectrics, pyroelectrics, nonlinear dielectrics, and liquid crystals. *Ferroelectrics* publishes experimental and theoretical papers aimed at the understanding of ferroelectricity and associated phenomena and applied papers dealing with the utilization of these materials in devices and systems. An important aspect of *Ferroelectrics* is to provide a vehicle for the publication of interdisciplinary papers involving ferroelectricity.

The editor invites original papers and short communications on the theory, fabrication, properties, and applications of ferroelectrics and related materials. In addition to research papers, *Ferroelectrics* publishes appropriate and timely review articles. There are no charges to authors or to institutions.

Notes for contributors can be found at the back of the journal.

Please see inside back cover for information on subscription rates and ordering information.

Distributed for Gordon and Breach Science Publishers S.A. by STBS Ltd., P.O. Box 90, Reading, Berkshire RG1 8JL, Great Britain. Printed in the United States of America.

FERROELECTRICS, ISSN 0015-0193, is published monthly for U.S. $298.00 per volume by Gordon and Breach Science Publishers S.A., Y-Parc, Chemin de la Sallaz, 1400 Yverdon, Switzerland. Second-class postage paid at New York, NY and additional mailing offices. POSTMASTER: Send address changes to FERROELECTRICS, % Gordon and Breach Science Publishers S.A., P.O. Box 786, Cooper Station, New York, NY 10276.

SEPTEMBER 1992

PROCEEDINGS OF

THE SECOND EUROPEAN CONFERENCE ON THE APPLICATION OF POLAR DIELECTRICS

TO CELEBRATE

The 25th Anniversary of the Dielectric Society

Incorporating

1st International Workshop on Integrated Ferroelectrics

Part II of II Parts

12–15 April 1992
London, United Kingdom

Guest Editors

J. M. Herbert
R. W. Whatmore

FERROELECTRICS
Volume 134 (1992)

CONTENTS—PART II

Note on Pagination, Author Index and Table of Contents

*The Proceedings of The Second European Conference on the Application of Polar Dielectrics are being published in two volumes of **Ferroelectrics** (Volumes 133 and 134). To facilitate indexing and referring to these Proceedings, the page numbers of Volume 134 run continuously from the end of Volume 133. The complete Table of Contents and an Author Index appear in both Volumes 133 and 134.*

Section III. CONTRIBUTED PAPERS
IIIf. Piezoelectric Devices and Materials

Section 3. CONTRIBUTED PAPERS
IIIg. Pyroelectrics

FERROELECTRICS
Volume 133 (1992)

CONTENTS—PART I

Note on Pagination, Author Index and Table of Contents

The Proceedings of The Second European Conference on the Application of Polar Dielectrics are being published in two volumes of Ferroelectrics (Volumes 133 and 134). To facilitate indexing and referring to these Proceedings, the page numbers of Volume 134 run continuously from the end of Volume 133. The complete Table of Contents and an Author Index appear in both Volumes 133 and 134.

THE SECOND EUROPEAN CONFERENCE ON THE APPLICATION OF POLAR DIELECTRICS

12–15 April 1992
London, United Kingdom

ORGANIZING COMMITTEE

F. W. Ainger	Conference Chair and Treasurer of the Dielectric Society
R. W. Whatmore	Programme Chair
K. J. Humphrey	Secretary
R. C. Twiney	Exhibition
P. Groves	Programme
A. J. Bell	European Co-ordinator
R. Freer	University Liaison
J. H. Calderwood	Chairman of the Dielectric Society
R. M. Hill	*The Dielectric Society*
B. C. H. Steele	Local Representative
G. W. Taylor	Editor *Ferroelectrics*
S. B. Lang	Associate Editor *Ferroelectrics*

IWIF-1

R. Panholzer	Chairman
J. Alexander	Programme
J. F. Scott	Representing ISIF
C. A. P. Araujo	Representing ISIF
F. W. Ainger	Co-ordinator

J. M. Herbert, Guest Editor

The Organizers wish to thank the following for their generous support:

Defence Advanced Research Projects Agency, DARPA, ONREUR, Gordon and Breach Science Publishers, The Dielectric Society, Cooksons Plc, and GEC-Marconi Materials Technology Group.

Ferroelectrics, 1992, Vol. 134, pp. xix–xxi
Reprints available directly from the publisher
Photocopying permitted by license only

LIST OF PARTICIPANTS

AUSTRALIA
CHAN, H. L. W.

BRAZIL
MOREIRO, R. L.

CANADA
MUKHERJEE, B. K.

CHINA
FANG, C. S.

CZECHOSLOVAKIA
KAMBA, S.
PETZELT, J.

DENMARK
MILLAR, C. E.

FINLAND
JANTUNEN, H.
TURUNEN, A.

FRANCE
ACHARD, H.
AILLERIE, M.
FONTANA, M.
GARABEDIAN, C.
GAUCHER, P.
GONNARD, P.
HADNI, A.
KUGEL, G. E.
LE BIHAN, R.
LE MOËL, A.
LEWINER, J.
RICHARD, C.
TROCCAZ, M.

GERMANY
BALZER, G.
BÖTTGER, U.
BRUCHHAUS, R.
HOFMANN, G.
KLEE, M.
KLIEM, H.
KOBIALKA, T.
KUNTZ, M.
LUBITZ, K.
NEUMANN, N.
QUAD, R.
ROBELS, U.
SCHÖNER, H. P.
SIMON, M.
WASER, R.

INDIA
BHANUMATHI, A.
PILLAI, P. K. C.
RAMANA MURTY, K. V.

IRELAND
McGETTRICK, B. P.
SESHADRI, A. T.

ISRAEL
LANG, S. B.
ROSENMAN, G.

ITALY
WATTS, B.

JAPAN
FUJIMOTO, S.
HAMAJI, Y.
HIRAKATA, K.
HIRAKATA, M.
ITOU, Y.
KANNO, M.
KATO, T.
KAWAMURA, Y.
MOCHIZUKI, S.
SAKASHITA, Y.
SEGAWA, H.
SUGIHARA, S.
TAKENAKA, T.
TOMIYASU, H.

UESU, Y.

KOREA
CHO, S. H.
SOO, K. E.
YOON, K. H.

LATVIA
STERNBERG, A.

LITHUANIA
BANYS, J.

MOROCCO
ELAMMARI, L.
OUCHETTO, M.

POLAND
POPRAWSKI, R.

PORTUGAL
FERREIRA, V. M.
MARAT-MANDES, J. N.
RAPOSO, M.
RIBEIRO, P. A.

RUSSIA
FRIDKIN, V.
LEMANOV, V. V.
PARINOV, I. A.
SHUVALOV, L. A.
SIGOV, A. S.
VERKHOVSKAYA, K. A.

SLOVENIA
LAVRENCIC, B. B.

SPAIN
BENADERO, A.
JIMENEZ, B.
SAN EMETERIO PRIETO, J. L.
ZALDO, C.

SWITZERLAND
BELL, A. J.
BICHSTEL, R.
COLLA, E. L.
DAMJANOVIC, D.
FORSTER, M.
GÜNTER, P.
GUTMANN, R.
HUANG, Y.
VAN DER KLINK, J.
LUTHIER, R.
REANEY, I. M.
ROLAND, G.
SREENIVAS, K.
STURZENEGGER, M.
ZURMUHLEN, R.

THE NETHERLANDS
FEINER, L. F.
LARSEN, P. K.

TAIWAN
LEE, W. Y.
WANG, H. M.

UNITED KINGDOM
AINGER, F. W.
ANIS, M. K.
AZOUGH, F.
BUTCHER, S.
CALDERWOOD, J. H.
CALZADA, M. L.
CANNELL, D. S.
CHILTON, J.
CLOSE, J. A.
DAS-GUPTA, D. K.
DEXTER, K. F.
FOTHERGILL, J.
FREER, R.
GARNER, G.
GLEESON, H.
GROVES, P.
HALL, D. A.
HERBERT, J.
HUMPHREY, K. J.
KINSMAN, B.
LEWIS, T. J.
LLEWELLYN, I. P.
MAGILL, J. H.
MURPHY, C. E.
MURRAY, S.

OSBOND, P.
PATEL, A.
SALLOWAY, A. J.
SHORROCKS, N. M.
SIMPSON, J. A.
SIRISOON-THORN, S.
SMITH, C. W.
TILLEY, D.
TODD, M.
TONTRAKOON, J.
TOSSELL, D.
TWINEY, R. C.
WANG, H. W.
WATTON, R.
WHATMORE, R.
WILLIAMS, M.

UKRAINE
POPLAVKO, Y. M.

USA
ALEXANDER, J.
BECKER, R.
CROSS, L. E.
DEY, S. K.
GRABOWSKI, J.
HUFFMAN, M.
KINGON, A. I.
LAMPE, D. R.
McMILLAN, L.
PAN, W.
PANHOLZER, R.
RANDALL, C. A.
ROSETTI, JR., G. A.
SCOTT, J.
SMITH, W. A.
SMYTH, D. M.
TAYLOR, G. W.
THAKOOR, S.

GUEST EDITORIAL

The Second European Meeting on the Applications of Polar Dielectrics was held in April 1992 to celebrate the 25th Anniversary of the Dielectric Society. Recognising the rising importance of thin films of ferroelectrics for a wide range of applications, the meeting also incorporated the 1st International Workshop on Integrated Ferroelectrics. To facilitate international participation the meeting was held at Imperial College, London.

Over 150 delegates registered for the meeting from 27 countries. Unfortunately, attendance from Eastern Europe was limited by the present economic and political problems. However, the generous financial support provided by our sponsors enabled the organisers to assist the attendance of many from this region and to provide reduced attendance costs for students.

Reflecting the current extent of interest in dielectric materials, 175 abstracts were submitted. Topics ranged from stable ceramics for microwave applications to organic crystals and polymers with high non-linear electro-optical coefficients. About one sixth of the contributions were concerned with the preparation and properties of thin films, particularly those involving ferroelectric materials. A wide range of sol-gel and vapour phase methods are still under development for piezoelectric, pyroelectric, electro-optic and information storage devices.

In the case of thin films for electro-mechanical applications, processes are sought which will yield multilayer structures that give large movements for small applied voltages. For information storage, it is already possible to deposit high permittivity layers on silicon, but it is proving more difficult to produce materials exhibiting switchable polar states that retain this property after prolonged exposure to the large variety of switching pulse sequences that may be experienced in storage systems. The great improvements already achieved promise eventual success.

For electro-optical applications, the possibilities of non-linear behaviour have been expanded by the use of organic compounds for which the Langmuir Blodgett technique remains an important means of obtaining large areas of oriented molecules.

The uses of ferroelectric ceramics in electro-mechanical transducers continue to expand with, for instance, the possibility of efficient small motors based on surface waves. New compositions offering improved electrostrictive and piezoelectric properties are being developed. The behaviour of domain walls underlying such phenomena as the poling of ceramics and the changes in dielectric properties with time are under scrutiny. Models explaining the interaction of lattice defects with walls are increasingly successful. High permittivity dielectric ceramics that can be sintered with base-metal electrodes *in situ* are being further improved by combining donor with acceptor substituents so as to minimise the concentration of vacant oxygen sites and thereby prolong life at high temperatures under high fields. High stability dielectrics continue to be studied for microwave applications and thin organic polymer films as constituents of silicon circuits.

The main objective of such occasions is the interchange of ideas between individuals and the encouragement of a feeling of common purpose among scientists

and engineers. This was enhanced by the informal atmosphere at the poster sessions, the introductory buffet and banquet.

The organisers would particularly like to thank the financial sponsors (DARPA, ONR Europe and Gordon and Breach Science Publishers) for their support and the Dielectric Society for sponsoring and underwriting the conference, and allowing the occasion of their 25th anniversary to be used for ECAPD-2.

Grateful thanks are also due to all those who gave their time in the organisation and execution of the meeting and to their partners for patient forebearance and, in many cases, active assistance on registration desks, poster assembly, etc.

Finally, the programme chair would like to add a personal word of thanks to his friends and colleagues who assisted with the production of the abstract book and spent much time refereeing and commenting upon manuscripts.

We all look forward to ECAPD-3, to be held in Germany in 1996.

J. M. Herbert
R. W. Whatmore

SECTION III
CONTRIBUTED PAPERS
IIId. Electro-Optics/Other Optical

Ferroelectrics, 1992, Vol. 134, pp. 1–6
Reprints available directly from the publisher
Photocopying permitted by license only

EoC21

STRONGLY TEMPERATURE DEPENDENT ELECTRO-OPTIC COEFFICIENTS IN $BaTiO_3$

F. ABDI, M.D. FONTANA, M. AILLERIE
Groupe Matériaux Optiques à Propriétés Spécifiques-C.L.O.E.S., Université de Metz et Supelec, 2 rue E. Belin, 57078 Metz Cedex 3, France
G. GODEFROY
Laboratoire de Physique des Solides-UA CNRS 785, Université de Bourgogne, B.P. 138, 21004 Dijon Cedex, France

Abstract : By means of a Sénarmont set up and a very sensitive method, electro-optic coefficients in $BaTiO_3$ are accurately determined from the phase measurement of the retardation Γ due to the electric field induced birefringence of the crystal. Electro-optic properties are investigated as a function of temperature around room temperature. A very large value of the coefficient r_{42} is found, in agreement with previous investigations. In addition, this coefficient is shown to be very sensitive to temperature even for a very small change. The importance of both the thermo-optic effect and the thermal variation of electro-optic properties is pointed out for device applications of $BaTiO_3$.

INTRODUCTION

Perovskite oxide crystals are well known materials with large non-linear optical and electro-optical (EO) coefficients[1]. Among this family, $BaTiO_3$ exhibits the largest EO coefficient which has been detected[1]. It leads this compound to be promising for various optical applications. In particular, it can be favourably used for photorefractive applications such as light diffraction, two- or four- wave mixing, phase conjugating mirror[2], or for EO applications, such as bulk or waveguide modulators or switches[3,4].

EO properties are known to be strongly affected by impurities specially iron doping[4,5] or oxygen vacancies[6]. The accurate determination of the EO coefficients is needed for the various reasons as follows i) the knowledge of the figures of merit and switching voltage[4] ii) the relative contribution of electrons and holes in the photorefractive properties[7] iii) the influence of the nature and concentration of defects[7]. We have recently shown that the thermal variation of the refractive index via the thermo-optic effect has to be accounted for in order to obtain correct values of the EO coefficients[8]. Therefore the results previously reported[9,10] in $BaTiO_3$ may

be questionable. Further the potential applications of $BaTiO_3$ require that the coefficients have to be independent of temperature.

Our study therefore concerns the accurate determination of the EO coefficients in $BaTiO_3$ and their temperature dependence with a new and very sensitive method.

ELECTRO-OPTICAL EFFECT IN $BaTiO_3$

Electro-optic properties in $BaTiO_3$ (C_{4v} point group) can be described by the three components r_{13}, r_{33} and r_{42} of the EO tensor.

With the applied electric field $E=(E_1,E_2,E_3)$ the optical indicatrix is given in the principal axis system of the crystal without field by :

$$\left(\frac{1}{n_o^2}+r_{13}E_3\right)x^2+\left(\frac{1}{n_o^2}+r_{13}E_3\right)y^2+\left(\frac{1}{n_e^2}+r_{33}E_3\right)z^2 + 2r_{42}xzE_1+2r_{42}yzE_2=1 \tag{1}$$

where n_o and n_e are respectively the ordinary and extraordinary refractive indices.

The EO r_{42} coefficient is determined in the transverse configuration when the electric field is along the x axis and the light propagation along the y axis.

With $E=(E,O,O)$, eq 1 becomes :

$$\frac{x^2}{n_o^2}+\frac{y^2}{n_o^2}+\frac{z^2}{n_e^2}+2r_{42}xzE=1 \tag{2}$$

The indicatrix can be expressed in a new axis system (primed axes) by a rotation through an angle θ around the y axis :

$$\begin{aligned}&X'^2\left(\cos^2(\theta)/n_o^2+\sin^2(\theta)/n_e^2+2r_{42}E\cos(\theta)\sin(\theta)\right)+Y'^2/n_o^2+\\&Z'^2\left(\sin^2(\theta)/n_o^2+\cos^2(\theta)/n_e^2-2r_{42}E\cos(\theta)\sin(\theta)\right)+\\&2X'Z'\left(\cos(\theta)\sin(\theta)\left(1/n_e^2-1/n_o^2\right)+r_{42}E\left(\cos^2(\theta)-\sin^2(\theta)\right)\right)=1\end{aligned} \tag{3}$$

where the axis X',Y' and Z' are the principal axes of the indicatrix if the last term of the right member of equation 3 is equal to zero, or if :

$$\tan(2\theta)=\frac{2r_{42}E}{\frac{1}{n_e^2}-\frac{1}{n_o^2}} \tag{4}$$

Introducing the condition eq 4 into eq 3, we obtain :

$$\left[\frac{1}{n_o^2}+r_{42}E\tan(\theta)\right]X'^2+\frac{Y'^2}{n_o^2}+\left[\frac{1}{n_e^2}-r_{42}E\tan(\theta)\right]Z'^2=1 \tag{5}$$

Since the rotation angle is necessarily very small, the change in the refractive indices can be therefore written :

$$\delta n_x(E)=\frac{n_o^3 r_{42}^2 E^2}{2\left(\frac{1}{n_o^2}-\frac{1}{n_e^2}\right)}\ ,\ \delta n_y(E)=0\ ,\ \delta n_z(E)=\frac{n_e^3 r_{42}^2 E^2}{2\left(\frac{1}{n_o^2}-\frac{1}{n_e^2}\right)} \tag{6}$$

Consequently, the phase shift between the x and z light polarization components is :

$$\Gamma_{zx}(E)=\frac{2\pi L_y}{\lambda}\Delta n_{zx}(E)=\frac{\pi L_y}{\lambda}\frac{n_e^3+n_o^3}{\left(\frac{1}{n_o^2}-\frac{1}{n_e^2}\right)}r_{42}^2E^2 \tag{7}$$

where L_y is the crystal length along the laser propagation direction and λ is the laser wavelength. The phase shift induced by the external electric field is thus a function which is quadratic in field magnitude. The r_{42} coefficient is determined from the measurement of Γ_{zx} (E) as function of DC applied voltage V=Ed, where d is the electrode spacing.

EXPERIMENTAL

The $BaTiO_3$ crystals used for this study were grown by the Czochralski method. Particular attention was paid in order to obtain single domain crystals with good optical quality by the application of appropriate electric field and thermal gradient during the cooling process through the cubic tetragonal phase transition. A nominally pure sample of 4.15x2.96x2.07mm^3 size and a 0.135% iron-doped sample of 4.87x3.92x2.85mm^3 size were used. They were cut normal to the principal axes, polished and electroded with evaporated gold.

EO coefficients were determined with a new method described elsewhere[11] which is based upon the Sénarmont compensating set-up. The optical transmission of such a system follows the general law : $I = I_0 \sin^2(\Gamma/2-\beta+\pi/4)$ if the optical absorption is neglected. In this equation I_0 and I are respectively the input and output laser intensity and Γ the phase shift introduced by the sample. Γ can be caused by the natural birefringence and/or by its variation due to a change of the temperature, electric field or strain applied to the sample. The method consists of adding an AC

voltage with a frequency f to the DC voltage and to measure the angle β_{2f} of the analyser corresponding to the detection of the output signal with the frequency 2f.

RESULTS

The EO r_c and r_{42} coefficients are determined in the "pure" and the iron-doped samples for various modulation frequencies. Complete results are presented and discussed elsewhere. Here we focus our attention on the r_{42} coefficient obtained in the "pure" crystal as a function of temperature for a modulation frequency f=1kHz and a laser wavelength λ=633nm.

Figure 1 exhibits the value of the angle $\beta_{2f}(E)=\Gamma(E)/2$ as function of the DC voltage amplitude V=Ed. Data obtained for increasing and decreasing V are similar, which is indicative that no memory effect or optical damage is induced by the field. Fit of the data to eq 7 yields the value of the r_{42} coefficient for a given temperature. The values of the indices n_e and n_o are taken in Ref. 12. At 19.1°C, we find the value r_{42}= 1776 pmV^{-1}.

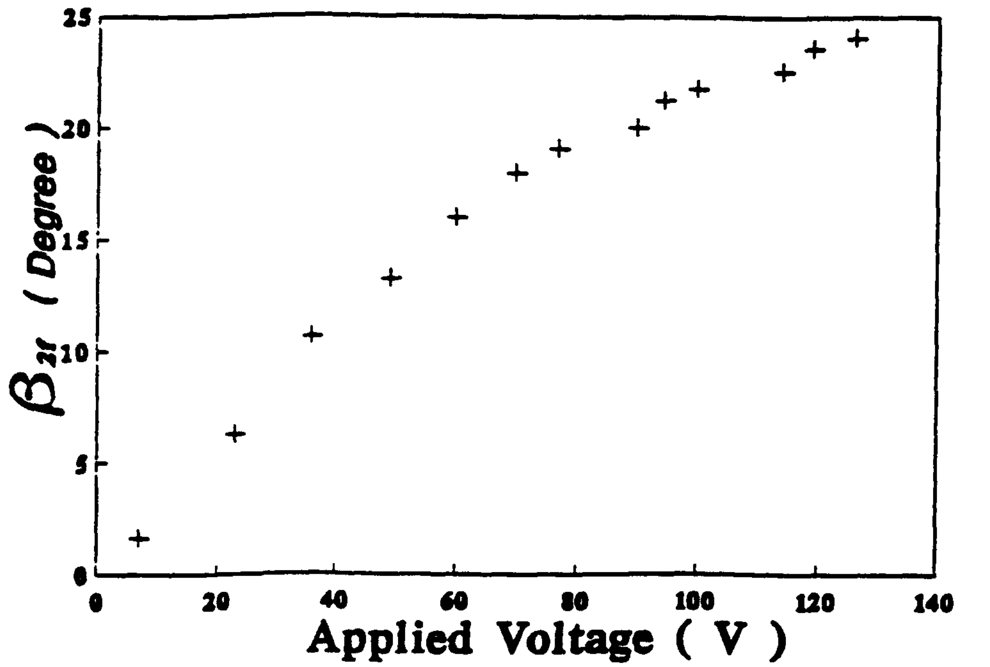

FIGURE 1 Variation of the retardation angle β_{2f} due to the applied DC voltage

To obtain the temperature dependence of the r_{42} coefficient, we repeat the same measurements around room temperature. This requires a perfect stabilization of the temperature for each data. Indeed the measured phase shift Γ includes the value $\Gamma(O)$ wich is due to the natural birefringence together with the value $\Gamma(E)$ which is induced by the field via the EO effect. It is necessary to discriminate between both

these contributions during the measurements of $\Gamma = 2\beta_{2f}$, particularly if each one depends on the temperature. For the first contribution we find $\delta\beta_{2f}(0)/\delta T=167$ degrees$^{\circ}C^{-1}$, which corresponds to a thermal dependence of the natural birefringence of $\delta\Delta n_{zx}(0)/\delta T=1.42 \cdot 10^{-4} {}^{\circ}C^{-1}$. This very large dependence determined from our modulation technique is in good agreement with the results previously measured by other techniques[13]. This shows that the determination of the r_{42} coefficient versus T requires, for each temperature, the measurement of the difference between $\delta\beta_{2f}$ and $\delta\beta_{2f}(0)$., or the measurement of $\beta_{2f}(E)$ after a perfect temperature stabilization. In our data, the temperature is assumed to be constant within a 0.01°C shift. The temperature dependence of the r_{42} coefficient is illustrated in figure 2. A very large variation of the value of r_{42} is pointed out, even for a very small temperature shift. A change of 1°C can thus lead to a multiplication of the value of r_{42} by two. A smaller dependence was reported in Refs 14 and 15, when a wide temperature range was considered. The understanding of such dicrepancies is actually in progress and involves various elasto-optic, thermo-optic effects.

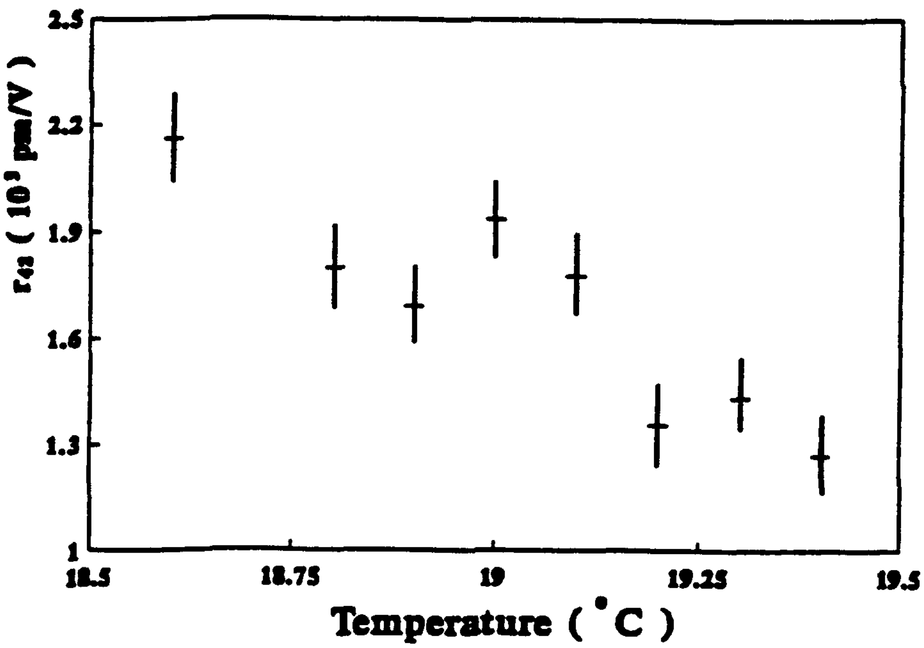

FIGURE 2 Temperature dependence of the r_{42} EO coefficient of pure $BaTiO_3$

DISCUSSION

The extremely large dependence on the temperature of both the natural birefringence $\Delta n_{zx}(0)$ and the electric-field induced birefringence $\Delta n_{zx}(E)$ constitutes the main results pointed out in our investigations. The first consequence concerns the necessity to insure a perfect temperature stabilization for a determination of EO coefficients as

well as for the use of $BaTiO_3$ in optical devices. Concerning the thermo-optic effect, it could be compensated by associating with a first crystal of $BaTiO_3$, a second one with the same dimensions but the axes crossed relative to the axes of the first crystal[16]. In fact, this possibility is doubtful from a practical point of view since a temperature shift of 0.1°C between both crystals should be sufficient to lead a change in the birefringence of $1.4 * 10^{-5}$ while the same variation in Δn can be caused by an applied electric field of 47.2 kV/m. The variation of temperature can be due to the laser beam itself. Thus one needs to wait a sufficient time to obtain a temperature stabilization after application of the laser. This was previously mentioned for 2 or 4 wave mixing experiments[17], where only the thermo-optic effect was considered. In fact, we have shown that the thermal dependence of the electro-optical effect causes an additional problem. The determination of precise values of figures of merit of $BaTiO_3$, for instance the driving voltage required in a switcher or modulator is very delicate. This limits the use of $BaTiO_3$ crystals for various applications in optical devices.

REFERENCES

1- P.Günter , Ferroelectrics 24, 35 (1980).
2- M.B.Klein and R.N.Schwartz, J.Opt Soc. Am B,3 , 293(1986).
3- I.P.Kaminow, Appl. Phys Lett 7, 123 (1965).
4- M.B.Klein and G.C.Valley, SPIE Proceedings 567,116(1985).
5- G.Godefroy, G.Ormancey, P.Jullien, W.Ousi Benomar and Y.Semanou. Proc of 6th conf IEEE, 12. (1986).
6- S.Ducharme and J.Feinberg, J.Opt Soc. Am B,3 (2), 283(1986).
7- M.B.Klein , in " Electrooptic and Photorefractive Materials ". Ed by P.Günter,Springer, Berlin, p266 (1986).
8- M.Aillerie, M.D.Fontana. F.Abdi, C.Carrabatos-Nedelec, N.Theophanous and G.Alexakis, J.Appl.Phys. 65, 2406(1989).
9- S.Ducharme, J.Feinberg and R.R.Neurgaonkar,.IEEE J Quant Elect, QE 23; 12, 2116(1987).
10- P.Jullien,A.Maillard,G.Ormancey and A.Lahlafi, Ferroelectrics 94 ,81(1989).
11- M.Aillerie, M.D.Fontana. F.Abdi, C.Carabatos-Nedelec and N.Theophanous,SPIE, 1018,94(1988).
12- S.H.Wemple, M.Didomenico and I.Camlibel, J.Phys Chem Solids, 29, 1797(1968).
13- N.N.Kristoffel and A.V.Gulbis, Opt Spectrosc , 49, 175.(1980).
14- A.R.Johnston and J.M.Weingart, J.Opt.Soc.Am, 55(7), 828(1965).
15- P.Jullien, Y.Abid and G.Godefroy, Private Communication.
16- P.Günter, in "Electrooptic and Photorefractive Materials". ref.7, p2 (1986).
17- D.W.Rush, B.M.Dugan, and G.L.Burdge, CLEO, Baltimore 1991.

Ferroelectrics, 1992, Vol. 134, pp. 7-15
Reprints available directly from the publisher
Photocopying permitted by license only

EoC21a

PHOTOCONDUCTING FERRCELECTRIC POLYMERS

K.A.Verkhovskaya, V.M.Fridkin, A.V.Bune

Institute of Crystallography of the Academy of Sciences of Russia, 117333 Moscow, Russia

J.F.Legrand

Institute Laue-Langevin, B.P. 156X, 38042 Grenoble Cedex, France

Abstract The new photoconducting ferroelectric polymer is prepared by means of dye sensitization of ferroelectric vinylidene fluoride-trifluoroethylene copolymers P(VDF-TrFE). The photoconductivity, the bulk photovoltaic effect and photochromic effect have been observed in the spectral bands connected with dye molecules absorption. The new photoconducting ferroelectric polymer may be used as the photorefractive material. By means of the photochromic effect in the ferroelectric copolymer doped by indolynospiropyran the transmission gratings were received. At the ferroelectric phase transition the sharp changes of the dye energy level and oscillator strength are revealed.

INTRODUCTION

Photoferroelectrics have been studied for the past 30 years.[1] One of the most remarkable phenomena in this field is the bulk photovoltaic effect, that is a characteristic of photoconductive crystals without the center of symmetry.[2]

The other important phenomenon is the photorefractive effect.[3]

The investigations of ferroelectric polymers lead us to design new materials - the photoconducting ferroelectric polymers. This idea was performed in 1990 by means of optical sensitization of the ferroelectric vinylidene fluoride-trifluoroethylene copolymers (VDF/TrFE).[4] Thus, all known photoferroelectric phenomena, including the bulk photovoltaic and photorefractive effects, may be observed

in the photoconducting ferroelectric polymers. In[5] we had really observed the bulk photovoltaic effect in VDF/TrFE, doped by rhodamine dyes. Some recent papers[6-8] show the possibility of the photorefractive films production by means of photoconducting piezoelectric polymers.

This paper describes the properties of the polymer photoferroelectrics, namely optically sensitized ferroelectric vinylidene fluoride-trifluoroethylene copolymers. In contrast to the homopolymer PVDF copolymers VDF/TrFE show the ferroelectric phase transition below the melting point. That makes it possible to study the influence of the phase transition on the dye electronic absorption spectra and to prove the effect of optical sensitization for ferroelectric polymers.

EXPERIMENTAL

This paper reports results on two copolymers VDF/TrFE (70/30 and 60/40 mol.%), which structure and ferroelectric phase transition have been widely investigated[9,10]. The raw material of copolymer was donated by Atochem Company, France. The sensitized copolymer films 20-30 μm thick were prepared from the solution of copolymer and dye in acetone. Subsequent annealing was performed at 400 K in oder to eliminate possible remaining solvent. The dye concentration in copolymer is equal to 1 wt.%. The optical absorption spectra and their temperature dependences were measured by means of spectrophotometer Specord UV-VIS in unpolarized light. The accurancy of the measurements of the band shift $\Delta\nu \simeq 5\cdot10^{-4}$ eV and optical density $\Delta D \simeq 2\cdot10^{-3}$.

The photoconductivity was measured by usual technique. A two-electrode sandwich sample was used to determine the dc conductivity change resulting from illumination with a 500-W Xe lamp or an Ar-laser ($\lambda = 514\,nm$).

Semitransparent gold electrodes were evaporated on the film surfaces. The spectral distribution of the photoconductivity was measured by means of a monochromator and

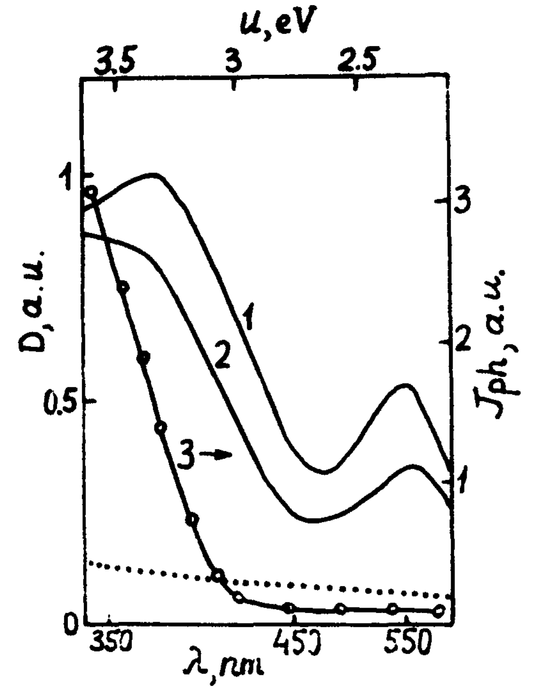

FIGURE 1
Absorption spectra of VDF/TrFE (70/30) copolymer, undoped (dotted line), doped by spiropyran (1,2).
Curve 3 - the spectral distribution of photoconductivity. 1,3,T = 300 K; 2,400K.

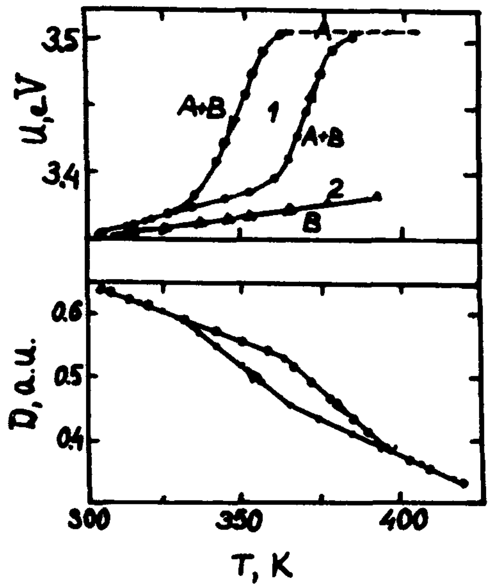

FIGURE 2
The temperature dependence of SP dye optical transition energy ($\lambda = 370$ nm) in VDF/TrFE (70/30) copolymer (1) and in PMMA (2)(a); the temperature dependence of the optical density D of SP absorption band at $\lambda =$ = 550 nm in VDF/TrFE (b).

and modulated light.

OPTICAL ABSORPTION AND PHOTOCONDUCTIVITY

The spectral sensitization and structural chromic effect were performed for VDF/TrFE (70/30) films, doped by 3',3'-dimethyl-1'-(β -hydroxyethyl)-6-nitrospiro (2H-1-benzopyran-2,2' indoline)(SP). SP is the photochromic compound, which exists in two forms A and B.[11] The correlation between A and B form concentrations changes under illumination and depends on the polarity of medium. The curve 1 on Fig.1 shows the SP spectral absorption in the ferroelectric phase of copolymer at T = 300 K. The absorption curve consists of two bands at 370 and 550 nm, which correspond to the B form of SP. At the transition to the paraelectric phase the dye form B transforms to form A (curve 2, Fig.1). The absorption band at λ = 370 nm disappears and the intensity of the optical band at λ = = 550 nm decreases. At the same time the film is observed to change color. The purple color of the film appears again when the reversal transition to the ferroelectric phase occurs. The observed structural chromic effect in the VDF/TrFE films, doped by SP, follows the temperature hysteresis (Fig.2a). It is seen that B and A dyes correspond to the ferro- and paraelectric phases of polymer. At the ferroelectric phase transition there is the temperature hysteresis loop, where A and B forms coexist. The analogous temperature hysteresis in the region of the phase transition is observed for the intensity of the absorption band at λ = 550 nm and connected with the transition B to A (Fig.2b). This hysteresis correlates with the temperature hysteresis of the dielectric constant[10] and confirms the existence of the first-order phase transition.

The curve 2 on Fig. 2a shows the temperature dependence of the SP dye spectrum in polar polymethylmethacrylate (PMMA), which does not show the phase transitions. In con-

trast to the ferroelectric polymer the temperature dependence of the optical absorption spectrum is linear and corresponds to form B.

The ferroelectric copolymer VDF/TrFE doped by SP reveals the photoconductivity. Fig.1 (curve 3) shows the spectral distribution of photocurrent. The photoconductive sensitivity $J_{ph}/I \simeq 1,7 \cdot 10^{-8}$ A/W for $\lambda = 370$ nm. The spectral absorption of the nonsensitized copolymers is shown by the dotted line (Fig.1). Accordingly there is no photoconductivity in the copolymer in absence of the optical sensitization.

PHOTOCHROMIC GRATINGS

By means of the photochromic effect in the ferroelectric copolymer doped by SP the transmission gratings were received. Two coherent beams at $\lambda = 514$ nm with equal intensities of 5 $mW \cdot cm^{-2}$ were intersected in the sample, thus producing interference bands with spacing $\Lambda \simeq 15$ μm. The grating is caused by the photochromic effect in SP. The light exposure time was ~ 30 min. The life time of the photochromic grating was not less than 10^2 hours.

The diffraction was observed from the grating. The application of the external electric field to the semitransparent electrodes leads to the change of Λ due to the electrostriction in the ferroelectric copolymer. This change is determined by the component of the piezoelectric tensor $e_{31} \simeq 1 \cdot 10^{-9}$ mV^{-1} and appears to be small.

These results show that optically sensitized ferroelectric copolymers may be used for the optical processing and optical storage.

THE INFLUENCE OF PHASE TRANSITION ON THE SPECTRA OF MEROCYANINES

The copolymers VDF/TrFE (60/40) were doped by merocyanines with different number of conjugated double bonds.[12]

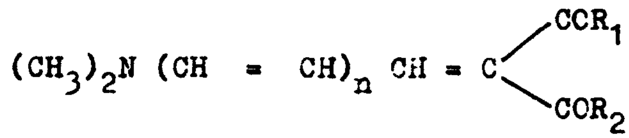

n = 1	R_1 = OCH_3	R_2 = OCH_3	(MC1)
n = 2	R_1 = OCH_3	R_2 = OCH_3	(MC2)
n = 3	R_1 = OCH_3	R_2 = OCH_3	(MC3)
n = 2	R_1 = OCH_3	R_2 = CH_3	(MC4)

It is known, that the merocyanines molecules exist in two mesomeric forms, nonpolar I and bipolar II. In general, in polar medium merocyanines exist in form II, its absorption band is red-shifted with respect to the form I.

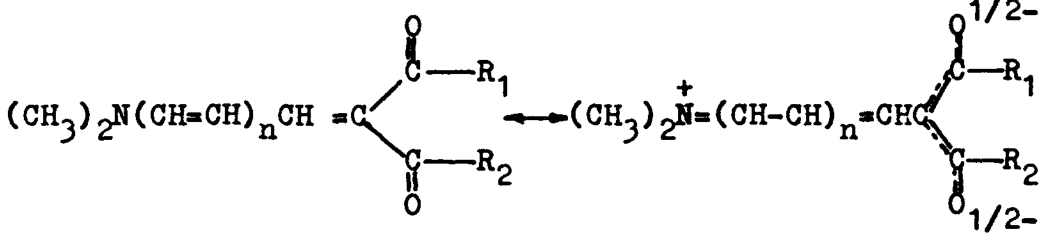

I II

The copolymer films with merocyanines show the absorption bands in UV and visible regions. The absorption maximum changes with n and medium polarity (Table).

TABLE λ_{max} of merocyanines absorption bands, nm

Solvent, Material	MC1	MC2	MC3	MC4
Toluene (ε = 2,24)	367	421	462	446
Acetone (ε = 21,5)	367	433	471	458,476
Ethanol (ε = 27,8)	376	456	493	490
Copolymer VDF/TrFE (60/40) (ε = 15)	370	450	507	476
Polymethylmetacrylate (ε = 3,5)	367	433	471	458

For example, for MC4 the bathochromic shift of λ_{max} from 446 to 490 nm is observed in different solvents (toluene → acetone → ethanol). This effect is connected with the fact that the ground state of MC in nonpolar medium

exists in structure I, but polar medium leads to the intermolecular displacement of charges and to the bipolar structure II respectively. The absorption maximum of MC4 in acetone split in two, one is of shorter and the other of longer wavelengths (see Table). This can be explained by putting form I spectrum on the spectrum of form II.

Fig.3a shows the optical absorption spectra of copolymer film doped by MC4 at different temperatures. At room temperature the spectrum shows an absorption maximum at 476 nm and a shoulder in the 450-460 nm region, connected with bipolar form II and nonpolar form I correspondingly. For VDF/TrFE (60/40) the region of phase transition from ferroelectric (polar) phase to paraelectric (nonpolar) $\Delta T \simeq 345 \div 365$ K and temperature hysteresis is $\sim 10^{\circ}$. As seen from Fig.3a the transition from polar phase to nonpolar in copolymer is accompanied by the redistribution of band intensities in spectra. We explain this as being due to the increasing of form I and to the decreasing of form II contributions, and therefore the absorption intensity of longer wavelengths region changes.

Fig.3b shows the optical absorption spectra of form II at different temperatures which are received by graphic subtracting of the form I spectrum (curve 7, Fig.3a) from the total spectrum. It is seen, that the intensity of band absorption of bipolar form II changes with temperature. Fig.4 shows the temperature dependence of oscillator strength f of absorption of molecular bipolar form at the phase transition. This dependence reveals the temperature hysteresis.

Thus, the essential difference of merocyanine absorption spectra in polar and nonpolar phases of copolymer is determined by the collective influence of the surrounding molecules on the dye molecules. Unlike[4,5] in the case of dopping of VDF/TrFE by merocyanines the structural optic effect appears as the change of oscillator strength f at the phase transition in copolymer.

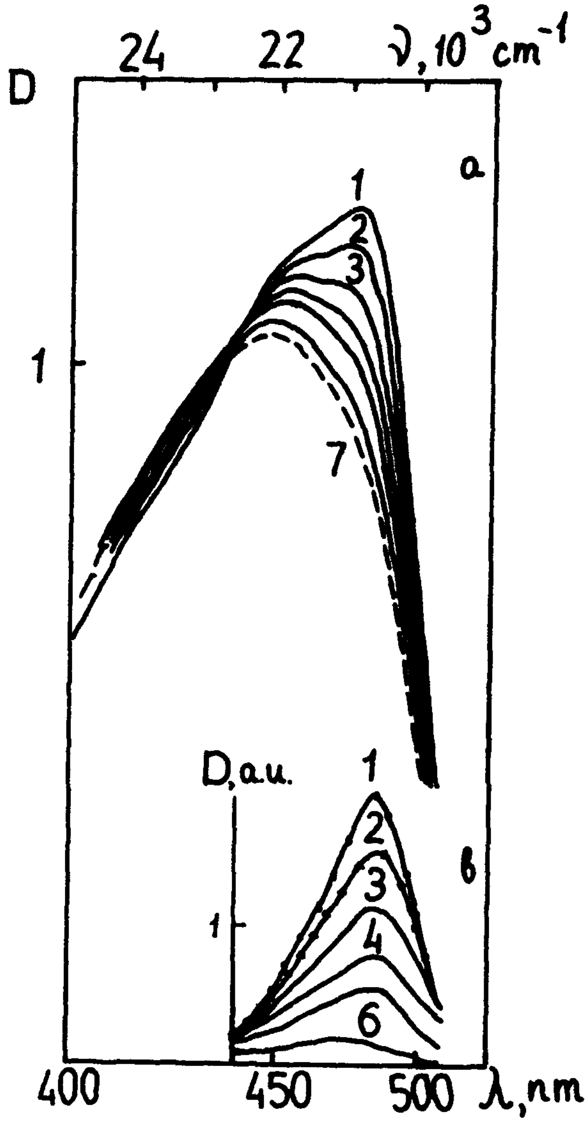

FIGURE 3

The optical absorption spectra of VDF/TrFE (60/40) doped by MC4 (a) and absorption spectra, corresponding to bipolar form (b).
1 - 296; 2 - 309; 3 - 326; 4 - 339; 5 - 349; 6 - 364; 7 - 371 K.

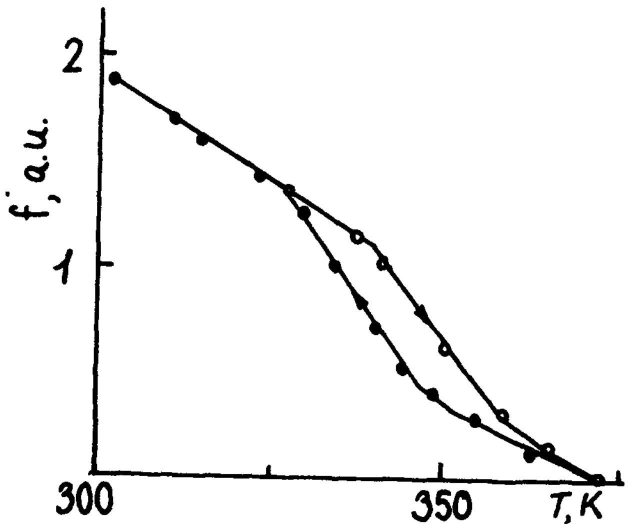

FIGURE 4

The temperature dependence of oscillator strength f of absorption of MC molecular bipolar form at the phase transition in copolymer VDF/TrFE (60/40).

The ferroelectric copolymers VDF/TrFE doped by merocyanines reveal the photoconductivity, which spectral distribution coincides with the dye absorption band. The photoconductive sensitivity (J_{ph}/intensity) changes with n. $J_{ph}/I = 2{,}5\cdot10^{-5}$; $8\cdot10^{-8}$; $2\cdot10^{-11}$ A/W for VDF/TrFE, doped by MC1 (n = 1), MC2 (n = 2) and MC3 (n = 3) correspondingly. We observe the decrease of photocurrent by several orders of magnitude with increasing n from 1 to 3, e.g. with lengthening conjugated system of MC molecule.

The optical sensitization is confirmed by the creation of new absorption bands and photoconductivity ones. The optically sensitized ferroelectric VDF/TrFE is the new perspective photoconducting material and may be used for creation of new photorefractive films and photovoltaic elements.

REFERENCES

1. V.M.Fridkin, Photoferroelectrics (Springer Verlag, Berlin, Heidelberg, New York, 1979).
2. B.I.Sturman, V.M.Fridkin, The Photovoltaic and Photorefractive Effects (Gordon and Breach,London,1992).
3. Photorefractive Materials and Their Applications I and II,edited by P.Günter and J.-P.Huignard (Springer Verlag, Berlin, 1988, 9).
4. K.A.Verkhovskaya, A.V.Bune, V.M.Fridkin, J.F.Legrand, Appl. Phys. Lett., 57, 2532 (1990).
5. A.V.Bune, V.M.Fridkin, K.A.Verkhovskaya, J.F.Legrand Ferroelectrics Letters, 12, 103 (1991).
6. J.S.Schildkraut, Appl. Phys. Lett., 58, 340 (1991).
7. S.Ducharme, J.C.Scott, R.J.Twieg and W.E.Moerner, Phys. Rev. Lett., 66, 1846 (1991).
8. W.E.Moerner, C.Walsh, J.C.Scott, S.Ducharme, D.M.Burland, G.C.Bjorklund and R.J.Twieg, SPIE Vol. 1560, Nonlinear Optical Properties of Organic Materials IV (1991).
9. The Applications of Ferroelectric Polymers, edited by T.T.Wang, T.M.Herbert and A.M.Glass (Blackie, Glasgow and London, 1988).
10. J.F.Legrand, Ferroelectrics, 91, 303 (1989).
11. Techniques of Chemistry, Vol.III, Photochromism, edited by G.H.Brown (Wiley, London, 1971).
12. E.P.Prokof'ev, Zh.A.Krasnaya and V.F.Kucherov, Organic Magnetic Resonance, 6, 240 (1974).

Ferroelectrics, 1992, Vol. 134, pp. 17–22
Reprints available directly from the publisher
Photocopying permitted by license only

EoP202

SPATIAL RESOLUTION OF A PHASE-CONJUGATE RING-RESONATOR

GERHARD BALZER, TORSTEN KOBIALKA AND THEO TSCHUDI

Institut für Angewandte Physik, Licht- und Teilchenoptik, Hochschulstraße 6, 6100 Darmstadt, Germany

Abstract We describe our study of the spatial resolution of a phase-conjugating ring-resonator (PCR) consisting of a Sagnac interferometer and a phase-conjugating mirror (PCM) based on four-wave mixing in photorefractive $BaTiO_3$. The use of optical image processing systems depends on the amount of information channels and the nonlinear coupling between the channels. We examined the contrast function of a set of incoming signals which depends on the gain of the PCR and the feedback ratio of the whole system. We obtained about 10^5 independent channels within our system. Additionally, we tried to investigate the transfer function of the system by comparing the power spectrum of the incoming signal and the output signal. By changing the geometrical setup of the system it should be possible to observe a higher resolution. On the other hand it is possible to control the coupling strength by varying the linear feedback part of the PCR.

INTRODUCTION

For any application of an image processing system, the spatial resolution is one of the most important informations to characterize the system. There exist many applications of feedback systems for optical image processing or optical computing.[1, 2, 3, 4] The advantage of an active feedback system is the possibility to exceed the losses of the feedback path. Moreover, with a nonlinear feedback system like the PCR we are able to use the nonlinearity for optical processing and we can vary it by changing the feedback ratio.

EXPERIMENTAL SETUP

We investigate a phase-conjugate ring resonator consisting of a PCM and a Sagnac interferometer. The PCM is realized by four-wave mixing in a photorefractive $BaTiO_3$ crystal, which provides phase conjugation and a high, nonlinear amplification. The signal is focused into the crystal with lens L_1 (Figure 1). The distance between the

crystal and the lens is approximately the focal length of the lens, so that the crystal is working in the Fourier plane of the signal. With perfect alignment of the resonator each pixel of the signal is imaged into itself. In this way, the phase conjugate ring resonator is an active feedback system with a large image plane and high resolution.

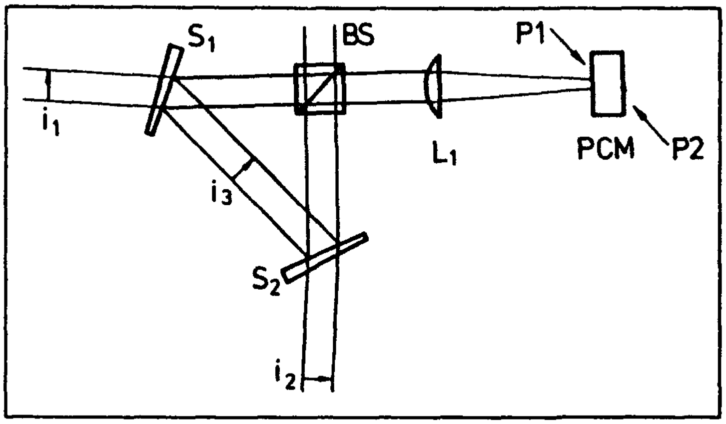

FIGURE 1: Experimental setup of the PCR with input i_1, output i_2, round propagating image i_3, mirrors S_1 and S_2, and beam splitter BS. L_1, lens.

All experiments were performed using a TEM_{00} single-mode argon ion laser at a wavelength of 514.5 nm. The stabilized output power was approximately 150 mW. The reflectivity of the resonator was $R_{Res} = 0.86$; therefore an amplification of the PCM of $R_{PCM} \geq 1.2$ compensates for resonator losses. In the experiments the amplification for small signals was up to 10.

THRESHOLD OF SELF-OSCILLATION

The reflectivity of the phase-conjugating mirror (PCM) is given by [5]:

$$\frac{1}{R_{PCM}} = \frac{|p_1|^2}{|p_2|^2(1-\epsilon)^2} + \frac{|s_1|^2(1+\epsilon^2)}{|p_2|^2(1-\epsilon)^2}$$

with

$$\epsilon = exp(\frac{\gamma l}{I_0}(|p_1|^2 + |s_1|^2))$$

R_{PCM}= Reflectivity of the crystal

$|p_1|^2, |p_2|^2$= Intensity of the pump waves

$|s_1|^2$= Intensity of the signal wave

γl= Coupling coefficient of the crystal

Without an external signal and the PCM gain high enough to compensate the resonator losses, the effect of self-oscillation occurs and a pattern arises. It starts from self-induced gratings in the crystal formed by scattered light from pump beams P_1 and P_2. The threshold of self-oscillation [5] is given by

$$R_{PCM}(|s_1|^2 \rightarrow 0) = \frac{1}{R_{Res}}$$ R_{Res}= Reflectivity of the resonator

which leads to

$$R_{Res} = \frac{|p_1|^2}{|p_2|^2(1-exp(\gamma l \frac{|p_1|^2}{I_0}))^2}$$

The self-oscillation pattern dominates in the resonator and destroys any information given by an external signal. That means, for image processing the system has to be under the threshold of self-oscillation. On the other hand, the amplification has to be as high as possible. By varying the reflectivity of the Sagnac interferometer, it becomes possible to use a large range of amplification of the PCM. So, we are able to change the nonlinear characteristic of the PCR in a wide range.

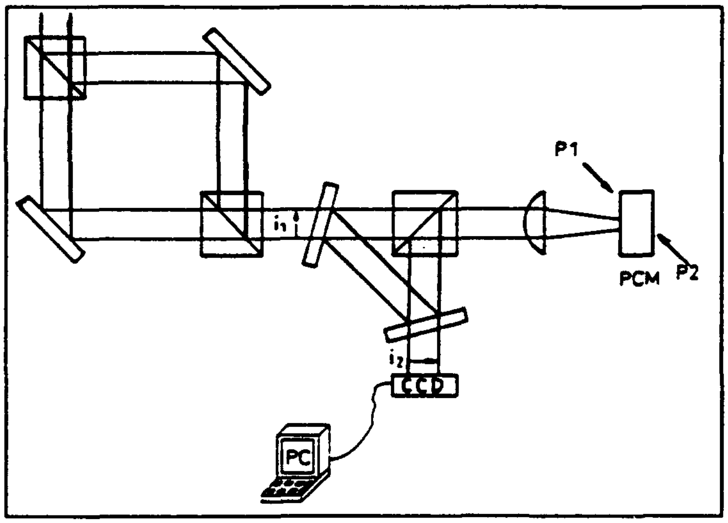

FIGURE 2: Experimental setup of the PCR with the interferometer to produce the phase grating.

To measure the spatial resolution of the PCR, we produce a variable phase grating by the interference of two plane waves (Figure 2). First we estimate the smallest structure which can be transfered by the system. The incoming signal is Fourier transformed by the lens. The active region in the crystal is limited by the crystal dimensions and the diameter of the pump waves [6]. Because of the high Fresnel-number of our Sagnac interferometer (the smallest aperture is about 25 mm wide), the limiting component is the interaction region of the $BaTiO_3$-crystal. From the Fourier transfomation we obtain:

$$\Lambda = \frac{x_f}{\lambda f}$$

f: focal length

λ: wavelength of laser

Λ: wavelength of the signal structure (grating)

x_f: position of the spatial frequency in the Fourier plane

With the data of our setup: f = 180 mm, x_f = 1.2 mm (diameter of pump waves), λ = 514 nm we get $\Lambda \approx 13\ \frac{\text{lines}}{\text{mm}}$. That means, we are able to transfer about 10^5 channels within our system.

EXPERIMENTAL RESULTS

The output signal of the PCR (i_2 in Figure 2) was detected by a linear CCD array. The camera consists of a CCD-line with 3456 elements and a distance of 10.7 μm between each diode. The output was recorded by a PC. The amplification of the PCM during all measurements was just under the threshold. The two pump waves had an intensity of approximately 5 mW each, and the intensity of the signal beam was about 0.7 μW.

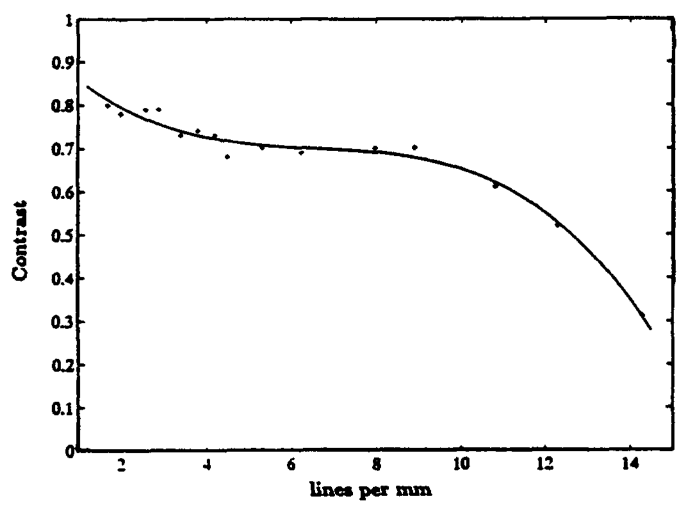

FIGURE 3: Contrast function of the output signal of the PCR over the spatial frequency of the grating of the input signal. The gain of the PCM was constant.

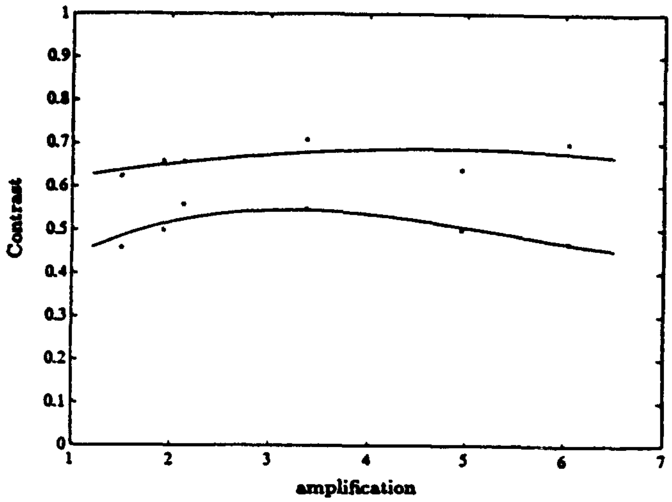

FIGURE 4: Contrast function of the output signal of the PCR over the amplification of the PCM. The input signal was in the first case a phase grating with a period of 8.4 $\frac{lines}{mm}$ (the upper graph) and in the second case a grating with 12.4 $\frac{lines}{mm}$ (the lower graph).

The contrast function is defined by $K = \frac{\overline{s_{max}} - \overline{s_{min}}}{\overline{s_{max}} + \overline{s_{min}}}$.
The contrast function of the PCR with constant amplification (Figure 3) shows that the limit of the resolution is in the range between 12 and 14 $\frac{lines}{mm}$. Up to about 10 $\frac{lines}{mm}$ *the contrast* is nearly constant. The system is not able to amplify structures that are smaller than approximately 12 $\frac{lines}{mm}$. Additionally to the contrast function, the Fourier transform of the output signal is a good proof for the spatial resolution. In Figure 5 we see the powerspectrum of an output signal with 4.5 $\frac{lines}{mm}$. There can be clearly seen a peak at that value. In contrast the powerspectrum with 14 $\frac{lines}{mm}$ in Figure 6 shows a wide range of spatial frequencies, only a small part of the power is contained in the peak of the signal frequency.

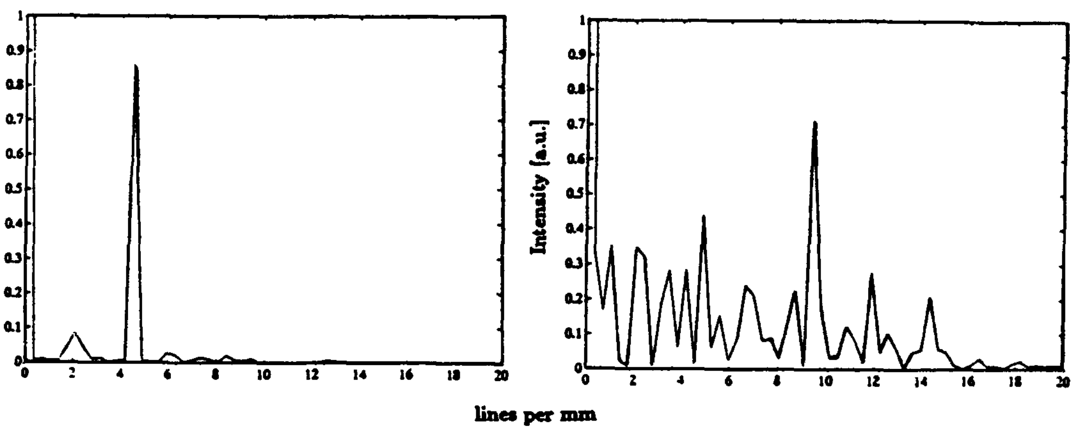

FIGURE 5: Powerspectrum of the output of the PCR for a signal of 4.5 $\frac{lines}{mm}$

FIGURE 6: Powerspectrum of the output of the PCR for a signal of 14 $\frac{lines}{mm}$

CONCLUSION

We have shown that the spatial resolution of the PCR with our setup is about 13 $\frac{\text{lines}}{\text{mm}}$, which corresponds exactly to the calculated value. As a result we can see, that the resolution is not limited by the crystal, but by the experimental setup at the moment. On the other hand, it is not clear up to now, whether the calculated 10^5 channels are independent and how strong the coupling of the pixels is [7].

REFERENCES

1. J. Cederquist, S. H. Lee: Coherent optical feedback for the analog solution of partial differential equations, J.Opt.Soc.Am. **70/8** (1980) 944-953
2. D. P. Jablonowski, S. H. Lee: A coherent optical feedback system for optical information processing, Appl.Phys. **8/1** (1975) 51-58
3. A. Herden, H. Klumb, F. Laeri, T. Tschudi, J. Albers: Analog optical computing, Proc. SPIE 700 IOCC (1986) 178-83
4. J. O. White, A. Yariv: Real-time image processing via four-wave mixing in a photorefractive medium, Appl.Phys.Lett. **37/1** (Jul 80) 5-7
5. T. Kobialka: Diploma thesis, IAP TH Darmstadt (1988)
6. S. Odulov, M. Goulkov: Private communications, (1991)
7. T. Kobialka, R. Blumrich, G. Balzer: Interpretation of the variation of the correlation dimension D_2 in the self-oscillation pattern, Annual Report 89/90 IAP TH Darmstadt (1990) 34-35. ISSN 0990-7168

Ferroelectrics, 1992, Vol. 134, pp. 23–28
Reprints available directly from the publisher
Photocopying permitted by license only

EoP203

CIRCULAR PHOTOGALVANIC EFFECT OF SOME OPTICALLY ACTIVE CRYSTALS

H. TOMIYASU, Y. FUKUSHIMA and Y.UESU
Department of Physics, Waseda University,
3-4-1, Okubo, Shinjuku-ku, Tokyo 169, Japan
S.TOYODA
Electronic Materials Laboratory, NGK Insulators, Ltd.,
2-5-6, Sudacho, Mizuho-ku, Nagoya 467, Japan

Abstract The circular photogalvanic (CPG) effect was investigated on three kinds of optically active crystals $Bi_{12}SiO_{20}$, $Bi_{12}GeO_{20}$ and $Pb_5Ge_3O_{11}$. For this purpose, we constructed an apparatus which detects the CPG current synchronously with the phase modulation of the incident light. The magnitude and direction of the current were observed to vary depending on the polarization state of the incident light. $Bi_{12}SiO_{20}$ and $Bi_{12}GeO_{20}$ produced the CPG current with opposite sense although their chirality was same. In $Pb_5Ge_3O_{11}$, the sense of the CPG current could be reversed by the external electric field.

1.INTRODUCTION

When light enters a crystal, an electric current is induced inside the crystal depending on the polarization state of the incident light.[1] The current density J is expressed by the following expression.

$$J_i = \{\beta_{ijk}\, e_j\, e_k^* + i\, \gamma_{il}\, (e \times e^*)_l\, \}I_0 \qquad (1)$$

Here e denotes the unit vector of the electric field of the incident light, i, j, k and l suffix representing the cartesian coordinate, I_0 the intensity of the incident light. The first term represents the linear photogalvanic effect and the coefficient β is the third-rank polar tensor, while the second term is

called the circular photogalvanic (CPG) effect and is characterized by the coefficient γ which is the second-rank axial tensor. According to the symmetry of the coefficient γ, the CPG effect is allowed only in gyrotropic (optically active) crystals. According to Eq.(1), right-handed and left-handed polarized light generate currents with opposite sense, while linearly polarized light induces no current This phenomenon is promising especially in the application to new phase-detectors of the light in opto-electronics. Although measurements have been made on the CPG effect by using several kinds of chiral crystals,[2,3] it seems to us that experimental conditions,i.e., the power density of the incident light, magnitude of the CPG current, wavelength dependence, etc., have not been precisely reported. The main reason for the ambiguity of reports can be attributed to the smallness of the effect; the usual photocurrent has a magnitude which is 10^4 times larger than that of the CPG effect. Then special apparatus which can discriminate the extremely weak CPG current from the ordinary photocurrent is necessary in the study of the CPG effect.

In the present study, we constructed an apparatus which realizes accurate measurements of the CPG effect by modulating the phase of the incident light and applied it to 3 kinds of optically active crystals; $Bi_{12}SiO_{20}$ (BSO), $Bi_{12}GeO_{20}$ (BGO) and ferroelectric $Pb_5Ge_3O_{11}$ (5P3G).

2. EXPERIMENTAL METHOD

The block diagram of apparatus for measuring the CPG effect is shown in Fig.1. The polarization state of the incident light from Ar ion laser (λ=

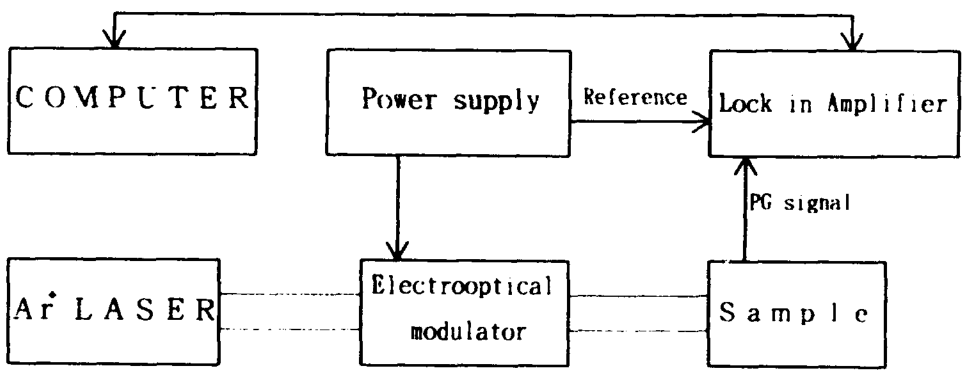

Fig.1 Block diagram of the apparatus for measuring the circular photogalvanic effect.

488 nm, maximum power 60mW) was modulated with a frequency of 70Hz by exploiting the electrooptic effect of $LiNbO_3$:MgO crystal. Then the CPG current was detected synchronously with the polarization state of the incident light by a lock-in amplifier as a function of the phase shift of the lock-in amplifier. An examination was made whether this phase shift really corresponds to the change in polarization state of the incident light, by inserting a Babinet-Soleil compensator between the phase modulator and the crystal: the additional phase shift of 180° produced by the compensator changed the sign of the CPG current without change in its magnitude. We also measured the circular dichroism (CD) of each crystal in the wavelength region from 370 nm to 570 nm to clarify the relation between the chirality of the crystals and relative sign of the CPG current.

The dimension and orientation of the specimens are illustrated in Fig.2. Transparent electrodes of In_2O_3 were sputtered on the surfaces of the specimens.

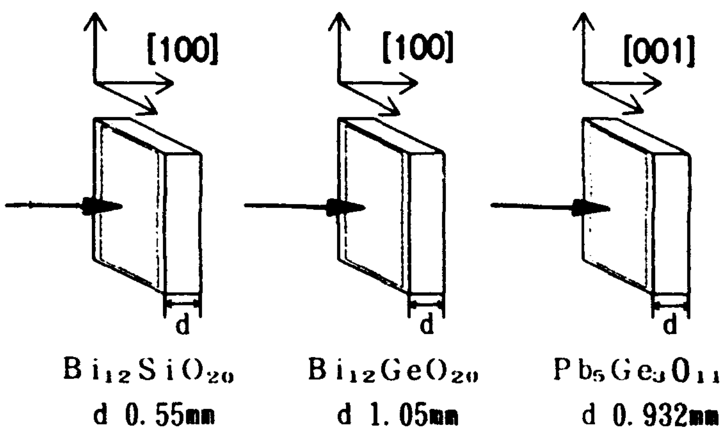

Fig.2 Dimension and orientation of the specimens used in the present experiment.

3.EXPERIMENTAL RESULTS AND DISCUSSIONS

3.1. BSO and BGO

BSO and BGO belong to the same point group T-23 and have one independent γ tensor component γ_{11}, which can be determined by measuring the CPG signal along the [100] with the light incident along the [100] direction. Results of the CD and the CPG effect are shown in Fig.3 and Fig.4, respectively. The CD spectra indicate that BSO and BGO used in the present experiment were both laevo-rotatory. The CPG current was

measured with an incident light power density of 400mW/cm^2. Fig.4 clearly shows that the CPG signal induced by the incident light varies depending on the polarization state of the incident light. It should be noted that the sense of the CPG signal was opposite in BSO and BGO, although the chirality of these crystals was same. The origin of the different sign of the γ tensor of these crystal is an open question at present.

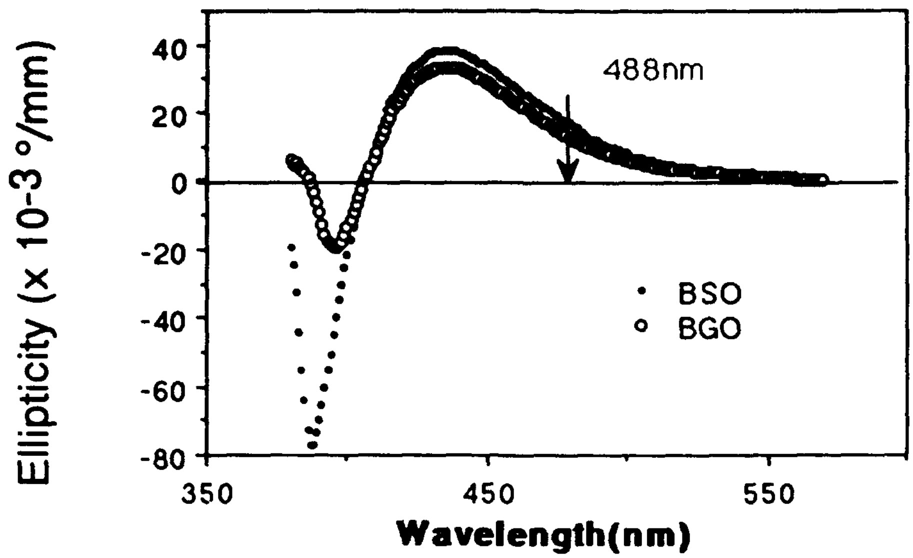

Fig.3 The circular dichroic spectra of BSO and BGO crystals.

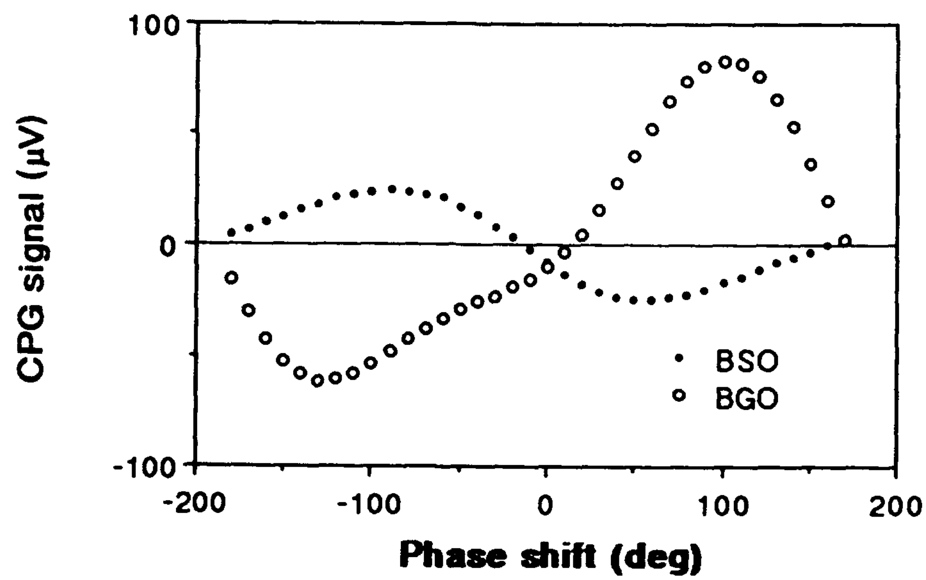

Fig.4 The circular photogalvanic effect observed in BSO and BGO crystals.

3.2. Ferroelectric 5P3G

5P3G belongs to the point group C_3-3 and exhibits ferroelectricity at room temperature. We measured the CPG effect related to the γ_{33} component with the incident light along [001] direction and the CPG current along [001] direction. The chirality of 5P3G can be changed by the application of an external electric field as shown in the CD spectra(Fig.5), and it is also expected that the sense of the CPG current can change its sense by accompanying the transformation of the enantiomorphic state by the electric field. This phenomenon really occurred and the result is indicated in Fig.6. We could reverse the sense of the CPG current under an electric field of above 750V/cm. On the other hand, the virgin specimen did not show the CPG effect, as it contained almost equal number of regions with opposite chirality. This fact indicates that the CPG effect can be used as a sensitive tool for discriminating the enantiomorphic state of crystals.

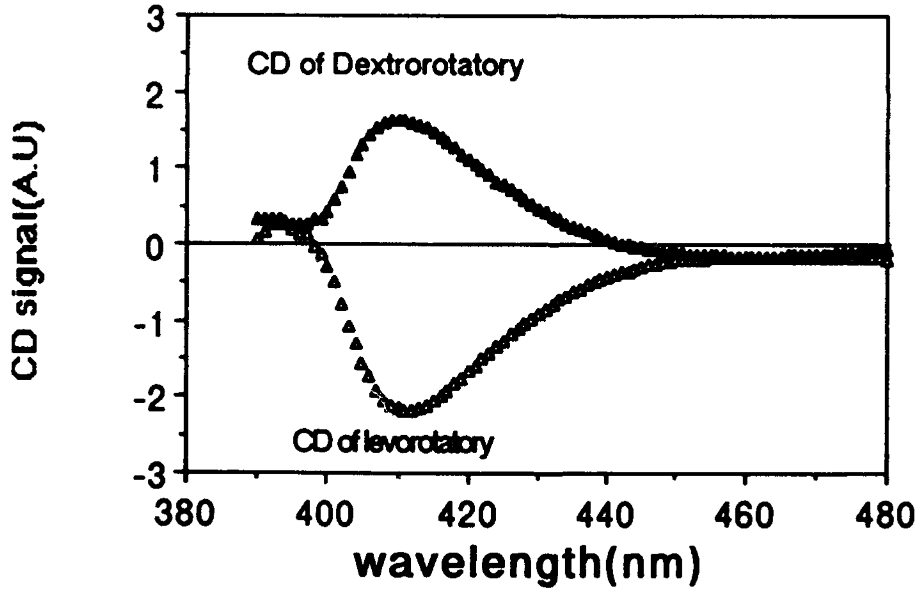

Fig.5 Circular dichroic spectra of ferroelectric 5P3G measured in the room temperature. Sign of the CD spectra can be changed by the application of the electric field.

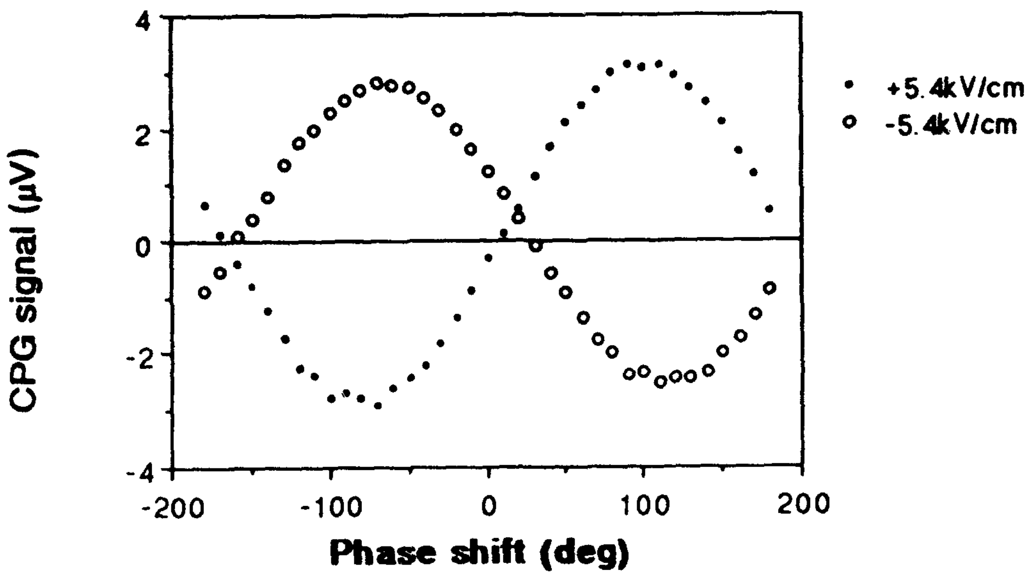

Fig.6 The circular photogalvanic effect observed in ferroelectric 5P3G. The CPG current can be reversed by the application of the electric field.

ACKNOWLEDGEMENT

We wish to thank Prof.B.A.Strukov, Moscow Univ., for providing an excellent crystal of 5P3G.

REFERENCES

1. B.L.Ivchenko and G.N.Pikus, JETP Lett., 27, 604(1978).
2. M.P.Petrov and A.I.Grachev, JETP Lett., 30, 16(1979).
3. V.V.Lemanov, S.Kh.Esayan, A.Yu.Maksimov and V.T.Gabrielyan, JETP Lett., 34, 423(1981).

Ferroelectrics, 1992, Vol. 134, pp. 29–34
Reprints available directly from the publisher
Photocopying permitted by license only

EoP250

RECENT ADVANCES IN TRANSPARENT FERROELECTRIC CERAMICS RESEARCH AND APPLICATIONS

ANDRIS STERNBERG
Institute of Solid State Physics, University of Latvia, Riga, Latvia

Abstract. *The studies of field-induced lattice rearrangement and field-induced phase transition (PT), laser beam effects in transparent ferroelectric ceramics (TFC), dopant and radiation effects in PLZT, Kerr effect demonstration and application of an intracavity matrix-addressed spatial-time modulator are discussed.*

INTRODUCTION

Most of TFC, being typical relaxor materials have offered opportunities for new methods (optical, electrooptical, non-linear optical) in studies of ferroelectricity, providing as results essential for understanding the nature of PT[1,2].

STRUCTURE, PROPERTIES AND PHASE TRANSITIONS

A complex X-ray study of the crystallographic characteristics of PLZT with respect to temperature, applied field and kinetics are considered from a common viewpoint on the 9/65/35 compound as a test material[3]. Thus, the X-ray data confirm a complete reversibility of the induced polar phase at 22°C (Figure 1) and so the unpolarized state at 22°C (from kinetic studies of the induced polar phase) is essentially permanent.

Kinetics of the field induced PT has been studied (with 8,5/65/35 compounds [4]). Variation of the average size and volume concentration of polarized submicroregions with the field is obtained by two independent methods - IR

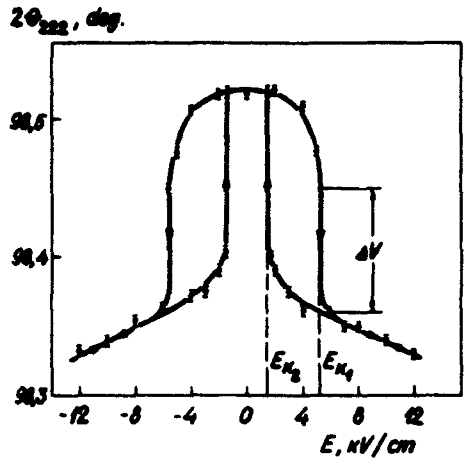

FIGURE 1. The change of the 222 maximum position at cycling of the applied field for PLZT 9/75/35; $T=22^{o}C$.

birefringence and scattering studies (CO laser; $\lambda=5.56$ μm). Appearance of quasi-single domain FE clusters is suggested near the critical field.

To explain the memory effects observed [5,6] in PLZT ceramics and its display in the behaviour of $\varepsilon^{*}(\omega,\tau)$ the distribution of relaxation times in the region of diffused PT is assumed to follow the Vogel-Fulcher law

$$\tau_{cut-off}=\tau_{o}\ \exp\frac{E}{T-T_{g}}\ ,$$

the interaction with ultra-slow defects resulting in gradual freezing of relaxators at $\tau>\tau_{lim}$ (Fig.2)[7]. The approach has allowed to do without proposed anomalies of structure and static properties not observed in the region of diffused PT and to explain the change of P(E) at PT in PLZT X/65/35 ceramics with X>8 at.%.

The temperature vs.time rise profiles in the bulk have been calculated (numerical simulation)[8] (Figure 3) from the results of thermal self-focusing, self-deflection of laser beams and induced transparency in PLZT ceramics[9]; the thermooptical constant has a rather high value in PLZT ($\sim10^{-5}$ cm^{2}/W). A laser beam thermally induced PT from strongly to weak scattering state (in coarse-grained PLZT 8/65/35) followed by drastic increase of sample transparency has been achieved by Ar- and CO- lasers.

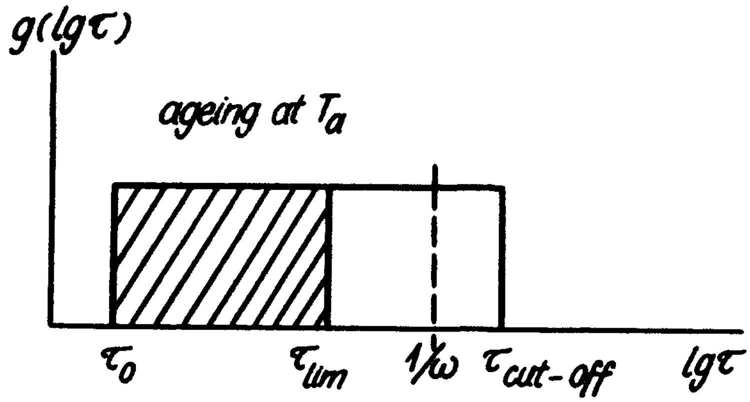

FIGURE 2. Distribution function of relaxation times $g(\tau)$ at ageing at $T \leq T_m$ (E=0).

DOPING AND DEFECTS

Essential specific changes of structure and properties (dielectric, optical, elastic) of the PLZT 8/65/35 ceramics doped by 3d elements[10] have suggested to undertake more comprehensive examination of the materials to reveal the micromechanism of dopant effects - ESM[11], Raman scattering (RS)[12] and EPR[13] studies were provided.

The most essential contribution to the change of RS is due to Jahn-Teller, i.e., d^4 of Mn^{2+} configurations. Appearance of new bands about 660 and 960 cm^{-1} is related to localized defects like Mn^{5+}-Ti^{3+}, Mn^{2+}-V_0, Mn^{3+}-La^{3+} a.o.

We identify the absorption in the region of $0.1 \leq B \leq 0.2$ T as the spin transition $-3/2 \rightarrow -1/2$ of Mn^{4+} (d^3) ions, and that in the region of $0,25 \leq B \leq 0,40$ - as the spin transition $-1/2 \rightarrow 1/2$ of Mn^{2+} (d^5) ions (Fig.4). It is reasonable to assume the presence, along with Mn^{2+} and Mn^{4+}, of Mn^{3+} (d^4) not detectable by EPR, particularly responsible for the evident shift of T_m to a higher temperature [10] and changes in RS.

We have detected significant alterations in the optical and dielectric properties of PLZT X/65/35 and PSN

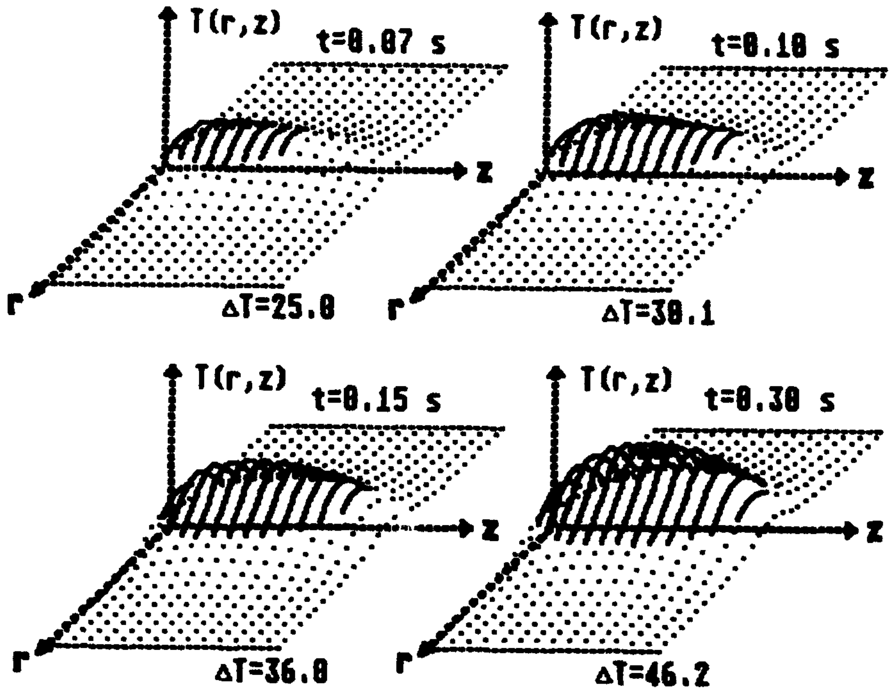

FIGURE 3. Temperature rise profiles in the bulk of PLZT 8/65/35 sample. Ar-laser beam intensity - 1 kW/cm^2; e^{-1} radius - 0,2 mm. Solid lines - transparent state; dotted lines -strongly scattering state.

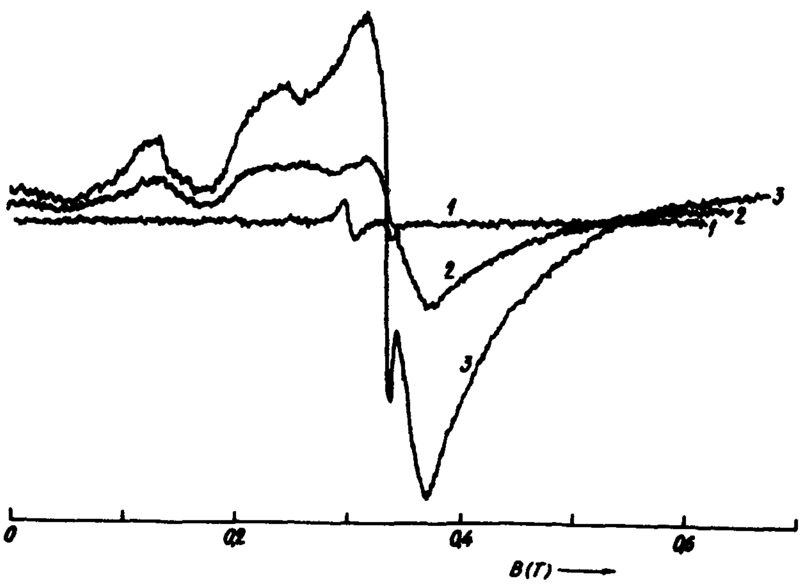

FIGURE 4. EPR spectra of Mn in PLZT 8/65/35+ X wt.%Mn. 1 - X=0; 2 - X=0.1; 3 - X=0.3; λ=3 cm; T=20^{o}C.

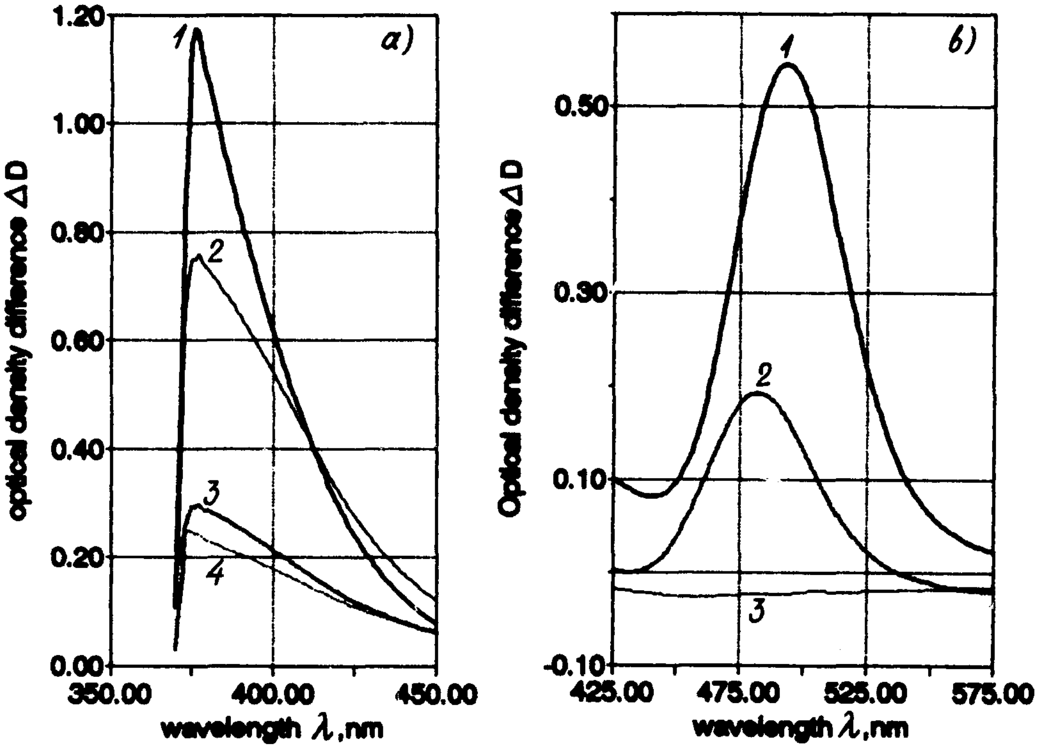

FIGURE 5. Optical density difference ΔD vs. wavelength:

a) of PLZT 10/65/35 irradiated by: 1 - neutrons ($2\cdot10^{18}$ n/cm^2); 2 - electrons ($8,4\cdot10^{17}$ electr./cm^2); 3 - γ-rays and neutrons ($5\cdot10^9$ rad; $2\cdot10^{16}$ n/cm^2); 4 - γ-rays ($9\cdot10^8$ rad);

b) PSN: 1 - electron irradiated (fluence $8\cdot4\cdot10^{17}$ electr/cm^2); 2- annealed up to 150°C (2 deg/min.); 3 - annealed up to 250°C.

ceramics, following irradiation by neutrons, electrons and gamma-rays [14,15]. The change in optical properties of PLZT 8-11/65/35 ceramics is mainly observed near absorption edge - a characteristic maximum in the absorption difference ΔD (prior to and after irradiation) at wavelength of 380-390 nm is estimated, irrespective of the type of radiation employed (Figure 5,a). Intensity of coloring (the value of ΔD) depends on the type of irradiation and fluence. Defects can be annealed at temperatures between 400-600°C.

In the case of electron-irradiated PSN ceramics (fluence $8{,}4\cdot10^{17}$ electr./cm^2) - ΔD maximum is observed at ~490 nm, however completely annealed at temperatures about 230°C (Fig. 5,b).

APPLICATION

PLZT frequency stifter (20 kHz) as well as a voltage-controlled PLZT $\lambda/4$ phase plate have been introduced in the laser heterodyne interterometer for an automatic displacement measurements with the accurancy ±10 nm [16]. A low voltage PLZT ceramics Kerr cell and computer controlled DC and AC voltage sources are developed for didactic use and classroom demonstration, for transfer of information by laser beams [17].

An intracavity matrix addressed (30x30 programmable scanning elements) PLZT spatial-time modulator is demonstrated with a pulse YAG:Nd laser [18]. Difraction limited beam quality and 10 μs direction exchange time have been achieved.

REFERENCES

1. A.Sternberg, Ferroelectrics, 91, 53 (1989).
2. A.Sternberg, Ferroelectrics, to be published.
3. L.A.Shebanov, Ferroelectrics, 90, 65 (1989).
4. M.Knite, A.Kapenieks and A.Sternberg, Acta Universitatis Latviensis, 559 (Riga, 1991), p.44.
5. A.V.Shilnikov, A.I.Burkhanov and E.H.Birks, Soviet Solid State Physics, 29, 809 (1987)(in Russian).
6. L.E.Cross, Ferroelectrics, 76, 241 (1987).
7. A.Spule and E.Birks, Ferroelectrics, to be published.
8. V.Zauls, doctor theses.
9. G.B.Altshuler et al., Ferroelectrics, 69, 67 (1986); M.Knite et al., Ferroelectrics, 80, 255 (1988).
10. V.I.Dimza et al., Ferroelectrics, 90, 45 (1989).
11. V.Dimza, A.Plaude et al., Ferroelectrics, to be published.
12. V.Dimza, P.Paulins et al., Ferroelectrics, to be published.
13. V.Dimza, Jing Tong-Zheng et al. Phys.Stat.Sol., to be published.
14. A.Sternberg et al. Acta Universitatis Latviensis, 559 (Riga, 1991), p.88.
15. A.Sternberg et al., Ferroelectrics, to be published.
16. E.Klotins, P.Kreicbergs, J.Kotleris and A.Kapenieks, Sensors and Actuators, A, 25-27, 271 (1991).
17. A.Krumins et al., Ferroelectrics, to be published.
18. V.Alekseev et al., Ferroelectrics, to be published.

Ferroelectrics, 1992, Vol. 134, pp. 35–40
Reprints available directly from the publisher
Photocopying permitted by license only

EoP254

THE ANALYSIS OF ELECTRIC FIELD FOR A PERIODIC ELECTRODE WITH A DIELECTRIC BUFFER–LAYER

GEN–SIN LIN†, JANG–JENG LIANG*, WEI–YU LEE†
PING–OU CHEN* AND CHI–CHIEN CHEN*
† Dept. of Elec. Eng., Tatung Institute of Technology, Taipei, Taiwan
* Chunghwa Picture Tubes, Ltd.

ABSTRACT Several types of integrated optical modulating and switching devices are based on the change of the refractive index while applying a voltage between electrodes fabricated on the crystal. Many solutions of the electric field are proposed. However, most of them focus on the single pair of electrode. In this paper, we analyze the periodic electrode with a dielectric buffer–layer and successfully solve the potential's equation by DFT (discrete Fourier transform). The DFT is a correct and simple technique for dealing with the problem of periodic pattern. On the other hand, the method is efficient for solving the differential equation directly. We present the results of estimation for the electric field of periodic electrodes with a buffer–layer (SiO_2) evaporated on z–cut $LiNbO_3$ and suggest some considerations of design for electrodes.

INTRODUCTION

For the z–cut $LiNbO_3$ waveguides, we tend to use the largest electro–optic coefficients, r_{33}, so the electrodes are evaporated on the wave guides directly. However, the metal–clad waveguide may lead to large attenuations [1]. In order to reduce the attenuation, a dielectric buffer–layer is added between the waveguides and electrodes, shown in fig.1. We can easily apply the conformal mapping method to analyze the electric fields of the structure without buffer layers, but can't apply that method to solve the fields distribution of the configuration with buffer layers[1]. Another solution was proposed by means of Fourier transform[2] but it also resulted in some difficulty : requiring guessing the potential on the electrodes surface in advance and repeating an iterative procedure to approach the exact answer. Recently, a few authors analyze the electrode on the dielectric waveguides by the method of line[3,4]. However, they are also unable

to deal with a periodical electrode pattern such as spectrum analyzer[5,6], tunable polarization converter[7,8], wavelength filter[9] etc..

In this paper, we make use of DFT to calculate the electric field distribution directly through a series of matrix operations. Comparing the results of periodic electrodes with that of a single pair obtained by conformal mapping method, we show that the electric field intensity of the former is a little larger than the latter. This is owing to the influence of periodicity and the simulation results also meet our prediction. Frequently, we must trade off several factors such as the width of a gap, the thickness of the dielectric buffer and the problem of fabrication etc. So, we analyze the two most important parameters, the gap between electrodes and the thickness of a buffer-layer and then suggest some considerations for the optimum design of periodic electrodes.

ANALYZING THE ELECTRIC FIELD BY DFT

The electrodes are assumed to be infinitely thin compared to the width of gap, 2a. One electrode is at zero potential while the other has applied an voltage , U, and the z-cut orientation of the $LiNbO_3$ crystal and TM mode propagating wave are assumed, shown in fig.1. The changes of dielectric constants which are introduced by the Ti-diffusion are small and can be neglected in the computations. The electrostatic potential ψ is a solution of the differential equations[2,6]

$$\frac{\partial^2 \psi}{\partial x^2} + \frac{\partial^2 \psi}{\partial y^2} = 0 \qquad \text{for } y < 0 \tag{1a}$$

$$\epsilon_x \frac{\partial^2 \psi}{\partial x^2} + \epsilon_y \frac{\partial^2 \psi}{\partial y^2} = 0 \qquad \text{for } y > 0 \tag{1b}$$

According to our assumptions above, the ϵ_x and ϵ_y are the ordinary and extraordinary dielectric constants respectively. Now, we transfer the problem to another domain by DFT. First, we define the discrete Fourier transform as

$$\Phi_i(\nu,y) = \sum_x \psi_i(x,y)\cdot \exp\left(\frac{-j2\pi\nu x}{N}\right) \tag{2}$$

where N is the period of electrode and ν ,x = − N/2...N/2−1. The index 'i' represents the region '1' , '0' or '−1'. The Φ denotes the DFT of the electric potential ϕ along the x−coordinate at y. Then, applying the boundary conditions of Ex and Dy at the interfaces, we derive the potential in the substrate as below

$$\phi_1(x,y) = \sum_{\nu} \Phi_1(\nu,d) \cdot \exp\left(\frac{j2\pi\nu x}{N} \right) \cdot \exp\left(\frac{-2\pi}{N} |\nu| \cdot (y-d) \cdot \sqrt{\frac{\epsilon_e}{\epsilon_o}} \right) \quad (3)$$

and

$$\Phi_0(\nu,0) = \Phi_1(\nu,d) \cdot \left\{ \cosh\left(\frac{2\pi d}{N} |\nu|\right) + \left(\frac{\sqrt{\epsilon_e/\epsilon_o}}{\epsilon_b}\right) \cdot \sinh\left(\frac{2\pi d}{N} |\nu|\right) \right\} \quad (4)$$

If $\Phi_0(\nu,0)$ can be found, $\Phi_1(\nu,d)$ is easily calculated. So we must calculate $\Phi_0(\nu,0)$ in advance. Another boundary condition between air and buffer yields

$$\sum_{\nu} |\nu| \cdot \Phi_0(\nu,0) \cdot H(\nu) \cdot \exp\left(\frac{j2\pi\nu x}{N} \right) = 0 \quad (5)$$

where

$$H(\nu) = \epsilon_b \cdot \frac{\sinh\left(\frac{2\pi d}{N} |\nu|\right) + \alpha \cdot \cosh\left(\frac{2\pi d}{N} |\nu|\right)}{\cosh\left(\frac{2\pi d}{N} |\nu|\right) + \alpha \cdot \sinh\left(\frac{2\pi d}{N} |\nu|\right)} + \epsilon_a \quad (6)$$

and

$$\alpha = \frac{\sqrt{\epsilon_e/\epsilon_o}}{\epsilon_b}$$

Once $\Phi_0(\nu,0)$ is found and then we use eq.(3) and eq.(4), the electric field in the waveguide can be calculated.

SIMULATION RESULTS AND SUGGESTIONS

In this section, we simulate different conditions for z−cut $LiNbO_3$ substrate with dielectric constants ϵ_e=28 ,ϵ_o=43. The wavelength λ=0.6328 μm, N=80μm and the electrode width 20μm are assumed. The conformal mapping method is used to to calculate the electric field of a single pair of electrode and is regarded as a precise method[1,2]. For the periodic electrodes, we may predict that the electric field is larger than that of a single pair of electrodes because of the influence of the neighboring pattern. In fig.2(a) and (b), we calculate the electric fields of the

electrodes separating from each other by 8 μm at the depth $y=1.5$ μm and it is found that the electric field calculated by DFT is always a little larger than that by conformal mapping method. It fits our prediction. So the DFT method is also reliable.

For design considerations, we tend to place the strongest electric field on the waveguides in order to obtain the best modulation effect. There are many facts influencing the intensity of electric fields. It is easy to understand that the waveguides near the electrodes edges have larger electric fields. The separation of electrodes is one important fact decreasing the lateral and vertical electric fields. It is obvious at the inner edges of electrodes. In order to get stronger electric fields, the narrower gaps are suggested but it may result in the difficulty of fabrication.

Another dominant fact is the thickness of the dielectric buffer–layer which may considerately attenuate the electric fields. The distributions of Ex and Ey electric fields are presented in fig.3 at the depth of 1.5 μm with different thicknesses of buffer layers (d=0.05, 0.3 and 0.8 μm). The attenuation is obvious at the electrodes gap, shown in fig.3(a). The changed effective propagation constant $\delta\beta$ according to the electric field is

$$\delta\beta = \frac{1}{2} k_0 \cdot r_{33} \cdot n_e^3 \cdot Ey \tag{7}$$

The decrease of $\delta\beta$ with increasing the widths of gaps and the thicknesses of buffer layers at $y=2\mu m$ are shown in fig.4. This is a useful reference figure when we design the electrodes. Because, frequently we need to trade off between the higher electric fields for modulation and the thicker buffer to decrease the power attenuations. If the thickness is larger than 0.4 μm, the $\delta\beta$ is smaller than $3.5 \cdot 10^{-4}$ rad/cm. Then, a period of phase variation requires about a centimeter when we apply 10V. The smaller gap between electrodes tends to give a larger electric field but is more difficult in manufacture. The optimum thickness of gap we suggest is about $4\mu m$ because of easy performance and larger electric field.

CONCLUSIONS

In this paper, we have analyzed the periodical electrode pattern having a buffer–layer and directly calculated the electric field by DFT. From our simulation results, there are two important facts influencing the modulation effects

— the width of gap and the thickness of the buffer layer. Some references of design are suggested in this paper. Now, we are interesting in the attenuations of the planar and channel optical waveguides for the metal/buffer/guide/substrate four–layer structure which are generally used in integrated optics.

REFERENCES

1 O.G. Ramer, IEEE. J. Quantum Electronics, QE–18, pp.386–392 (1982)
2 Lars Tylen and Per Granestrand, J. Opt. Comm., 6 pp.11–14 (1986)
3 A.G.Keen, M.J.Wale, M.I.Sobhy and A.J.Holden, J. of Lightwave Tech., 8 pp.42–50 (1990)
4 J.Gerdes, K.H.Helf and R.Pregla, J. of Lightwave Tech., 9 pp.461–467 (1991)
5 Gunnar Arvidsson and Lars Thylen, Appl. Opt., 21 pp.797–803 (1982)
6 L. Thylen and L.Stensland, Appl. Opt., 20 pp.1825–1832 (1981)
7 F. Heismann, IEEE. J. Quantum Electronics, QE–25 pp.1898–1906 (1989)
8 F.Hesimann and R.C.Alferness, IEEE J. Quantum Electronics, QE–24 pp.83–93 (1988)
9 F.Heismann, L.L.Buhi and R.C.Alferness, Electronics Letter, 23 pp.572–574 (1987)

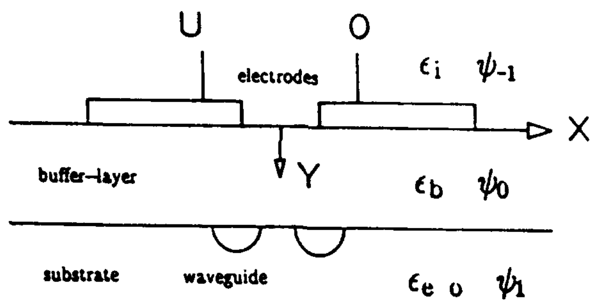

FIGURE 1 The structure of electrodes for one period and waveguides

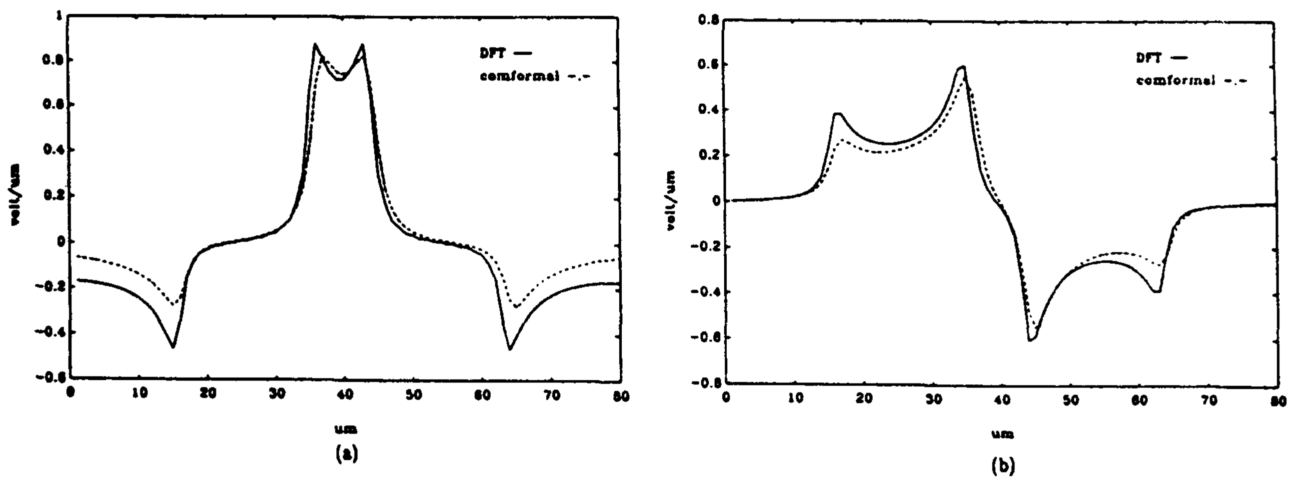

FIGURE 2 The electric fields are calculated by DFT and conformal mapping method where y=1.5 μm, gap=8 μm and electrode width=20 μm. (a) Ex component (b) Ey component

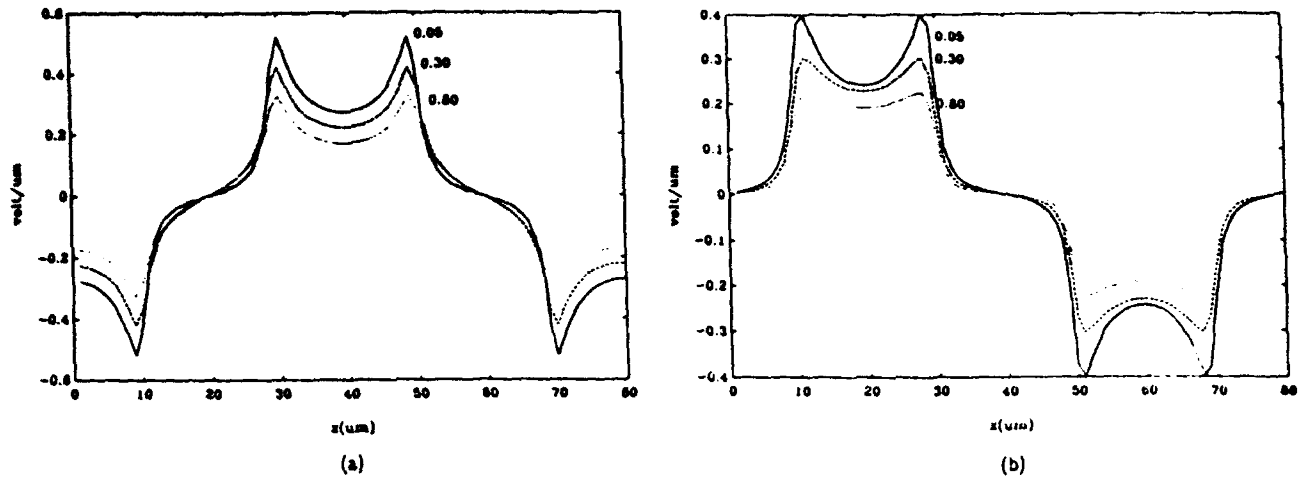

FIGURE 3 The electric field distribute for different thicknesses of buffer layers at the depth of 1.5 μm. (a) Ex component (b) Ey component

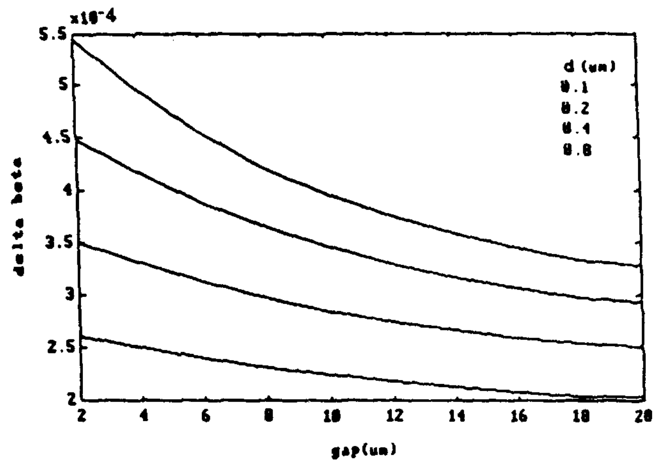

FIGURE 4 We show the variations of $\delta\beta$ V.S. the widths of gaps at y=2μm.

Ferroelectrics, 1992, Vol. 134, pp. 41–46
Reprints available directly from the publisher
Photocopying permitted by license only

EoP261

A NUMERICAL TECHNIQUE FOR ANALYSIS OF ARBITRARILY SHAPED INHOMOGENEOUS OPTICAL WAVEGUIDES

HUEY–MIN WANG†, WEI–YU LEE†, JANG–JENG LIANG*
AND SHUG–JUNE HWANG†

† Dept. of Elec. Eng., Tatung Institute of Technology, Taipei, Taiwan, R.O.C.
* Chunghwa Picture Tubes, Ltd.

Abstract A simple and efficient procedure for determining the propagation characteristics of arbitrarily shaped inhomogeneous waveguide is described. This procedure was mainly based on effective–index method[1] and Ritz–Galerkin method.[2] Our procedure can be easily implemented on a small personal computer. We compared the results with those obtained by other method.[3] It was shown that the results obtained for mode spectra and field distributions are also accurate even in the case closed to the cutoff region.

INTRODUCTION

Dielectric waveguides are useful components for realizing integrated optical devices. In order to properly design and use an optical channel waveguide link, the propagation characteristics and field distributions of the guided modes must be known.

Except for a few special refractive index profile shapes that allow explicit analytic solution of this scalar wave equation (step index and parabolic index fibers[4,5]), the guided modes capable of propagating along the fiber must be determined by approximation. However, due to fabrication techniques and other applications, the methods which can cope with both the problem of arbitrary index profile and arbitrary cross–sectional shape of the waveguide are required. We mentioned here the finite element[6] and finite difference[7] methods and effective–index method[1].

In this paper, we adopt Ritz–Galerkin formalism to extend Chiang's model for arbitrarily shaped inhomogeneously optical waveguides. The results of our procedure are accurate both in the low frequency and high frequency region. Even for the fundamental mode with frequency very near to the cutoff value, the mode still can be followed by our method.

THEORY

The mode field of the fiber satisfies the 2–D scalar wave equation:

$$\frac{\partial^2\phi}{\partial x^2} + \frac{\partial^2\phi}{\partial y^2} + [\ n^2(x,y)\kappa^2 - \beta^2\ ]\ \phi = 0, \tag{1}$$

where ϕ is the field, κ is the wave number, β is the propagation constant, and $n(x,y)$ is the refractive index distribution. For weakly guiding fiber, the field can be expressed as:

$$\phi(x,y) = \phi_x(x)\cdot \phi_{xy}(x,y) \tag{2}$$

while $\phi_{xy}(x,y)$ is assumed to be a slowly varying function of x.

Substite Eq. (2) into Eq. (1), neglect some terms reasonably in the process of derivation, and define an effective index profile $n_{eff}(x)$, we can obtain the followed two 1–D scalar wave equations:

$$\frac{\partial^2\phi_{xy}}{\partial y^2} + [n^2(x,y)\kappa^2 - n_{eff}^2(x)\kappa^2]\phi_{xy} = 0, \tag{3}$$

$$\frac{d^2\phi_x}{dx^2} + [\ n_{eff}^2(x)\kappa^2 - \beta^2\ ]\phi_x = 0, \tag{4}$$

Eq. (4) is just the scalar wave equation for an inhomogeneous slab waveguide with index profile $n_{eff}(x)$. This means that once the effective index profile $n_{eff}(x)$ has been determined, the propagation constant β in the original two dimensional waveguide can be obtained from a one dimensional waveguide with index profile $n_{eff}(x)$. Then the original 2–D problem is converted into 1–D problem. The effective index profile $n_{eff}(x)$ can be obtained by calculated propagation constant $\beta' = n_{eff}(x_i)\kappa$ at each point x_i.

For arbitrarily shaped inhomogeneous optical waveguides, the effective index profile $n_{eff}(x)$ must be pointwise determined. We used Ritz–Galerkin formalism[2] to solve the problem of one dimensional waveguide with inhomogeneous refractive index profile. The schematic representation of our method is shown in Fig. 1.

By Ritz–Galerkin method, the mode field $\Psi_m(x)$ was expanded by a suitable finite set of known basis functions $\{\ \Psi_{0,u}\ \}$:

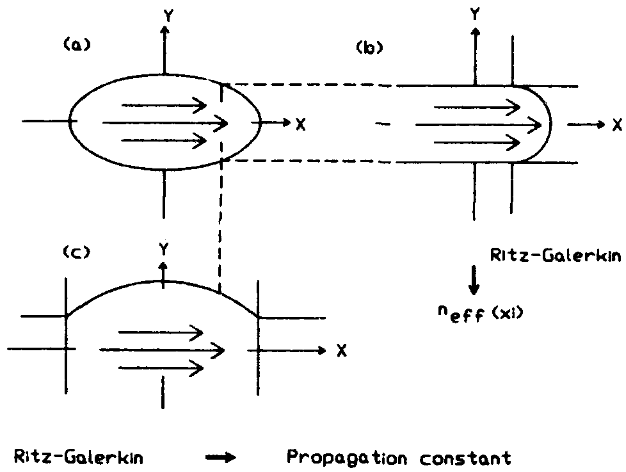

FIGURE 1 The schematic representation of our method

$$\Psi_m(x) = \sum_{u=0}^{N} C_u \, \Psi_{0,u}(x) \tag{5}$$

where C_u are coefficients which are initially undetermined. The eigenvalue β_m was refered to the propagation constant for the mth order mode, C_u is the corresponding eigenvector. Since the β_m and the C_u can be obtained simultaneously, the field distributions can be easily generated by Eq. (5). Therefore we can obtain both the propagation constant β and the field distributions for the original two dimensional waveguide.

Because the effective index method is derived in the Cartesian coordinate system, it can only be applied to waveguide modes which can be designated as E^x_{ij} (or E^y_{ij}) modes. For these E^x_{ij} and E^y_{ij} modes, the field configuration in each coordinate axis is well discussed in Ref. 8. The general symbolic formula[3] for each 1D process can be given as followed:

$$\beta(E^x_{mn}) = \left\{ TE_{n-1}\left[\begin{matrix} n2 \\ \hline n1 \\ \hline n2 \end{matrix}\right], \; TM_{m-1}(\, n2|neff|n2 \,) \right\} \tag{6}$$

$$\beta(E^y_{mn}) = \left\{ TM_{n-1}(\, n2|n1|n2 \,), \; TE_{m-1}\left[\begin{matrix} n2 \\ \hline n_{eff} \\ \hline n2 \end{matrix}\right] \right\} \tag{7}$$

For a weakly waveguide, E^x_{mn} and E^y_{mn} modes are approximately degenerate, the waveguide modes can be denoted as E^{xy}_{mn} and the general notation then

becomes:

$$\beta(E^{x,y}_{mn}) = \left\{ TE_{n-1}\left\{\begin{matrix} n2 \\ \overline{n1} \\ \overline{n2} \end{matrix}\right\} , TE_{m-1}(n2|neff|n2) \right\} \tag{8}$$

<u>Numerical Results</u>

In order to show the accuracy of the results of our method, we consider the circular graded index waveguide with refractive index profile given as followed:

$$\begin{aligned} n^2(r) &= n^2_{co} \{ 1 - 2 \cdot \Delta \cdot f(r/r_o) \}, \quad r \leq r_o \\ &= n^2_{cl}, \quad r \geq r_o \\ \Delta &= \frac{n^2_{co} - n^2_{cl}}{2n^2_{co}} \end{aligned} \tag{9}$$

where n_{co} and n_{cl} are the refractive indices at the axis and in the cladding respectively, and r_o is the radius of the waveguide, for the waveguide of this kind index profile possesses exact solutions for the propagation constant β of the guided modes.[9] We use:

$$V = \kappa_0\, r_o\, (n^2_{co} - n^2_{cl})^{1/2}, \ \delta = \beta/\kappa_0$$
$$n_{co} = 1.4516$$
$$n_{cl} = 1.4473$$
$$r_o = 5 \times 10^{-6} \text{ m.}$$

The following notations will be used:

δ_{th} Theoretical value of δ. This is the exact analytical solution for this geometrical shape and refractive index profile.[9]

δEVM Value of δ obtained by Velde et al.[3]

δERG Value of δ obtained by the present method.

The propagation constants of E^y_{11} mode and E^y_{12} mode for various V–number are displayed in Table I and in Table II. In the Table, the error is called procentual error[3] and is defined as followed:

$$\text{percent error} \qquad = 100 \times (\delta_{th} - \delta_{approximated}) / \delta_{th} \tag{10}$$

TABLE I Comparison of the propagation constant δ for E^y_{11} mode

V	δth	δERG	δEVM	E—4% ERG	ERROR EVM
1.25	1.447355	1.447309	1.447455	32	70
4.00	1.449482	1.449488	1.449393	3	60
6.00	1.450170	1.450170	1.450037	ex	90

ex : the result is equal to the theoretical value of δ.

TABLE II Comparison of the propagation constant δ for E^y_{12} mode

V	δth	δERG	δEVM	. E—4% ERG	ERROR EVM
3.50	co	co	1.447385		
3.518	1.447300	1.447352	1.447392	35	64
4.00	1.447578	1.447619	1.447615	27	25
6.00	1.448757	1.448763	1.448760	3	2

co : the mode is found to be in cut off.

$\delta_{\text{approximated}}$ $= \delta$EVM for Velde et al. method

$= \delta$ERG for our present method

Discussion and Conclusion

The effective index method itself has limitations and restrictions. Most of these have already been mentioned by Chiang[1], and some of the important restrictions are emphasized by Velde et al.[3]. One of them should be especially noted is the intrinsic restriction which is due to the central assumption that ϕ_{xy} is a slowly varying function of x in the average sense. It implies that the mode field spreads over the entire cross section of the fiber should let $\partial\phi_{xy}/\partial x$ and $\partial^2\phi_{xy}/\partial x^2$ become negligible in comparison with $d^2\phi_x/dx^2$ and $\partial^2\phi_{xy}/\partial y^2$. Therefore for higer order modes this assumption would lead to a decrease in the accuracy. If we choose one frequency (from V = 4.00, 6.00) and check the error of the results for E^y_{11} mode and E^y_{12} mode, we could find that our results meet the expected result of this intrinsic restriction, however the results from Ref. 3. did not meet.

From Table I and Table II we could find that in the low frequency region our results are better than those of Ref. 3., even in the region very near to cutoff (V <

1.5), this cannot be done by any other procedure. Also we found that as the frequency is away from the cutoff value, the error of our results will become smaller gradually. This means that in the high frequency region the accuracy of the results can also be obtained by our procedure, but this can not be obtained by Ref. 3.. Moreover we has led to an procedure to find the field distribution for guided modes. Therefore our procedure is reasonable and powerful.

REFERENCES

1. K.S. Chiang, Applied Optics, 25, pp. 348–354 (1986).
2. J.P. Meunier, J. Pigeon, J.N. Massot, Opt. Quant. Elect., 15, pp. 77–85 (1983).
3. K.V.D. Velde, H. Thienpont, and R.V. Geen, IEEE Journal of Lightwave Technology, 6, pp. 1153–1159 (1988).
4. A.W. Synder, IEEE Trans. Microwave Theory Tech., 17, pp. 1130–1139 (1969).
5. M.S. Sodha and A.K. Ghatak, Inhomogeneous Optical Waveguides (Plenum, New York, 1977).
6. C. Yeh, S.B. Dong, and W. Oliver, J. Appl. Phys., 46, pp.2125–2129 (1975).
7. E. Schweig and W.B. Bridges, IEEE Trans. Microwave Theory Tech., 32, pp. 531–541 (1984).
8. M.J. Adams, An Introduction to optical waveguides (Wiley, New York, 1981).
9. A.W. Synder and R.A. Sammut, J. Opt. Soc. Amer., 69, pp. 1663–1671 (1979).

Ferroelectrics, 1992, Vol. 134, pp. 47-51
Reprints available directly from the publisher
Photocopying permitted by license only

EoP264

LATTICE SITE OF TRANSITION METAL AND RARE-EARTH IMPURITIES IN $LiNbO_3$ SINGLE CRYSTALS. AN EXAFS STUDY

C. Zaldo and C. Prieto

Instituto de Ciencia de Materiales de Madrid. C.S.I.C.
Campus Universitario de Cantoblanco. C-IV. 28049 Madrid. Spain.

Abstract: Extended X-ray Absorption Fine Structure (EXAFS) spectroscopy has been used to study the lattice site of impurities in lithium niobate single crystals. The determination of the distances from the impurity to the first oxygen coordination sphere and to the niobium neighbours gives the lattice site of the impurity and its displacement along the c-axis of the lattice. In this way, it has been determined the position of transition metal (Ni^{2+}, Fe^{3+}, Ti^{4+}, Hf^{4+} and Ta^{5+}) and rare-earth (Er^{3+}, Nd^{3+}) impurities.

INTRODUCTION

Lithium niobate single crystals have found application in the optoelectronic area as waveguide subtrates, photorefractive devices and solid state laser matrices. These applications are related to the properties of the impurities introduced. Waveguides are commonly produced by diffusion of Ti in $LiNbO_3$ subtrate[1]. Photorefractive properties are due to the incorporation of Fe and other transition metal ions[2]. Nd and other rare-earth ions have been used to induce laser action in $LiNbO_3$ bulk single crystals[3] and waveguides[4].

In spite of the important roles of the impurities in $LiNbO_3$, their lattice locations have been ignored until very recently. The reason of that fact has been that the first coordination sphere of the three possible lattice locations (Li, Nb or vacancy lattice sites) are rather similar.

EXAFS spectroscopy may provide direct information on the nature, number and distance of the neighbors around of the atoms tested. From this information the lattice site location of the impurity may be inferred and compared with the information given by the other

techniques applied recently to investigate the lattice site of impurities in $LiNbO_3$: Rutherford backscattering (RBS), Proton Induced X-ray Emission (PIXE)/channeling spectroscopies[5] and ENDOR[6].

EXPERIMENTAL TECHNIQUES

Congruent $LiNbO_3$ single crystals have been grown by the Czochralski method with different impurities of transition metals and rare-earth elements. As a general rule, to obtain a signal to noise ratio which allows us the analysis of the spectra a minimum of 0.5% molar concentration of impurity in the crystal was required.

Fluorescence EXAFS spectra were acquired at room temperature at the K-edge of the first series of transition metal and at the L_{III}-edge of the rare-earth and third series of transition metal ions. We used synchrotron radiation emitted by the L.U.R.E. (Orsay) D.C.I. storage ring running at 1.85 GeV, with an average current of 250 mA. X-rays were monochromatized using a Si(311) double-crystal spectrometer. Detection of the total fluorescence yield has been made using a plastic scintillator attached to a photomultiplier.

EXPERIMENTAL RESULTS AND DISCUSSION

The method for the analysis of the experimental data has been described previously[7,8]. The atomic Radial Distribution Function (RDF) is related to the fourier transform of the EXAFS signal, $\chi(k)$, weighted by the third power of the photoelectron momentum, k.

As an example, Fig. 1 shows the RDF around the Fe^{3+} impurities in $LiNbO_3$. Peak I is related to the first oxygen coordination sphere and peaks II and III to the niobium neighbors. The contribution of Li neighbors to the RDF has been ignored because of its low backscattering amplitude. On the other hand the contribution of oxygen shells different from the first one has been found to be minor compared with the contribution of niobium[7,8].

In order to determine the actual distances from Fe^{3+} to oxygen and niobium neighbors we have fitted the experimental data with the well known EXAFS expression[9]:

$$\chi(k) = \sum_j \frac{N_j}{kR_j} \exp(-2k^2\sigma_j^2) \exp(-\Gamma_j R_j/k)\, f_j(k) \sin(2kR_j+\phi_j(k)) \quad [1]$$

where j indicates different coordination shells, N_j is the coordination number, R_j is the neighbor distance, σ_j is the Debye-Waller disorder parameter, f_j is the backscattering amplitude of the neighbors, Γ_j is related to the mean free path of the photoelectron and ϕ_j is the phase shift.

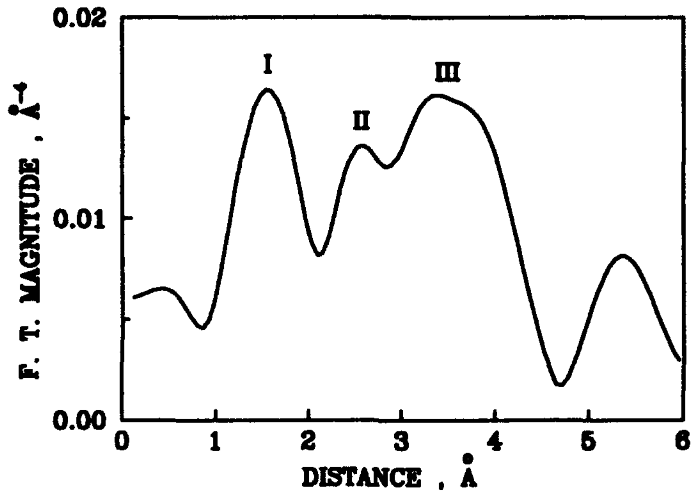

Fig. 1. Fourier Transform of $k^3\chi(k)$ from k=4 to 10 Å^{-1} of the EXAFS signal of Fe^{3+} in $LiNbO_3$.

In the fitting procedure a filtering has been performed in order to fit each peak of the RDF separately. Peak I has been fitted with two different oxygen distances, though in most cases there was a convergence to a unique one, on the other hand peaks II and III have been fit with two different niobium distances. N_j was assumed according to the expected coordination of the $LiNbO_3$ lattice. The values of R_j, σ_j^2 and Γ_j obtained from the best fits are summarized in Table I.

In order to decide the lattice site of the impurity and its shift along the c-axis, the impurity-neighbor distances obtained from the fits of the EXAFS spectra must be compared to those expected from the $LiNbO_3$ lattice. Fig. 2 summarizes the distances from the center of the

TABLE I. Summary of results obtained from the fittings of the the EXAFS spectra using Eq. [1].

Ion	Pair	N	R(Å)	σ^2(Å^2)	Γ(Å^{-2})	δ(Å)	(site/technique)
Ni^{2+}	Ni-O	6	2.01	0.08	1.8	0	(Li/EXAFS)
	Ni-Nb	6	3.1	0.09	1.8		
Fe^{3+}	Fe-O	3	2.041	0.086	1.0	-0.5	(Li/EXAFS,PIXE)
	Fe-O	3	2.298	0.105	1.0		
	Fe-Nb	4	3.199	0.06	1.0		
	Fe-Nb	3	3.398	0.049	1.0		
Ti^{4+}	Ti-O	6	1.97	0.08	1.9	0	(Li/EXAFS)
	Ti-Nb	7	3.18	0.06	1.9		
Hf^{4+}	Hf-O	6	2.065	0.094	2.2	0	(Li/EXAFS,RBS)
	Hf-Nb	1	2.57	0.089	2.2		
	Hf-Nb	6	3.30	0.085	2.2		
Ta^{5+}	Ta-O	3	1.93	0.08	4.75	+0.25	(Nb/EXAFS,RBS)
	Ta-O	3	1.99	0.08	4.75		
	Ta-Nb	6	3.68	0.09	4.75		
Er^{3+}	Er-O	6	2.00	0.067	2.8	0	(Li/EXAFS,RBS)
	Er-Nb	4	3.05	0.105	2.8		
	Er-Nb	3	3.60	0.022	2.8		
Nd^{3+}	Nd-O	6	2.03	0.077	2.0	0	(Nb/EXAFS)
	Nd-Nb	6	3.65	0.082	2.0		(Li and Nb/RBS)

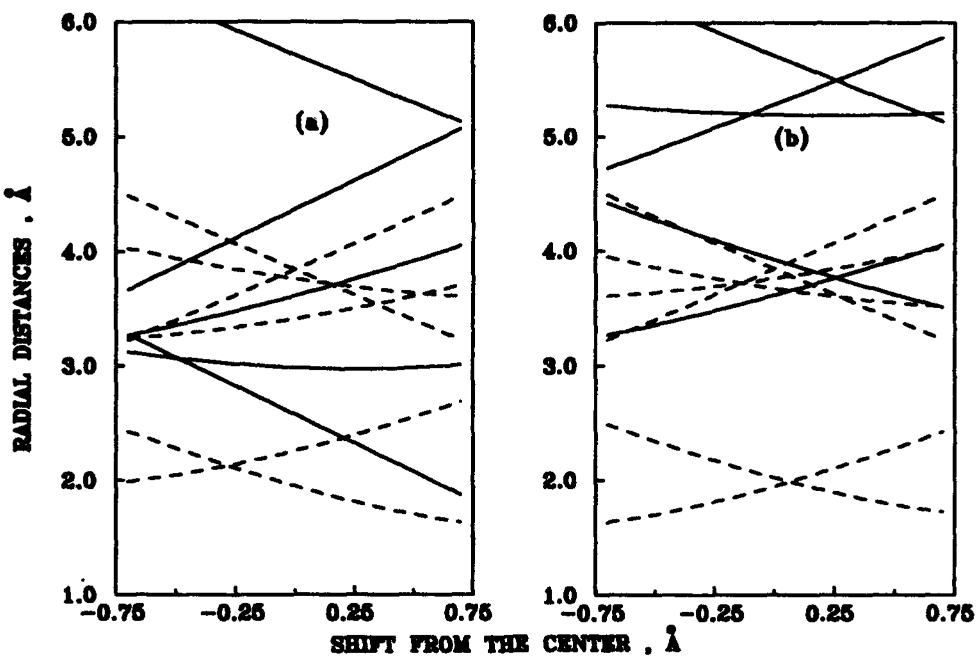

Fig. 2. Impurity host ions radial distances calculated for oxygens (dashed lines) and niobium (continuous lines) in the lithium niobate lattice as a function of the shift, δ, from the centre of the octahedron. a) Li-site. b) Nb-site.

oxygen octahedra to the oxygen and niobium ions. The distances are given as a function of the displacement, δ, from this center.

From the inspection of Table I, it may be observed that the Li site is commonly found for transition metal ions with a valence equal to or less than 4+. Only Ta^{5+} replaces lattice niobium cations.

This experimental conclusion agrees with the theoretical expectation on the incorporation of impurities in $LiNbO_3$[10]. It has been concluded that the incorporation of 2+ and 3+ ions removes the niobiums antisited in Li sites. However the rare-earth impurities do not seem to follow this rule and they are found in Li and Nb sites.

Though our results indicate a well defined lattice site for the impurities reported in Table I, a minor fraction of those impurities in other lattice environments can not be excluded.

CONCLUSIONS

We have shown that EXAFS spectroscopy may determine the lattice location of transition metal and rare-earth ions in $LiNbO_3$ crystals.

For the impurity concentrations considered in this work ($\approx$ 0.5-1% molar) the impurities are found in a well defined lattice site. Transition metal ions with valence $\leq$4+ are found in the Li site, however 3+ rare-earth ions (Er and Nd) are found in Li or Nb sites.

REFERENCES

1. R.V. Schmidt and I.P. Kaminow. Appl. Phys. Lett, 25, 458 (1974).
2. H. Kurz, E. Krätzing, W. Keune, H. Engelmann, U. Gonser, B. Dischler and A. Räuber. Appl. Phys., 12, 355 (1977).
3. L. F. Johnson and A.A. Ballman. J. Appl. Phys., 40, 297 (1969).
4. T.Y. Fan, A. Córdova-Plaza, M.J.F. Digonnet, R.L. Bijer and H.J. Shaw. J. Opt. Soc. Am. B 3, 140 (1986).
5. L. Rebouta, J.C. Soares, M.F. da Silva, J. A. Sanz-García, E. Diéguez and F. Agulló-López. J. Mat. Res., 7, 1 (1992).
6. G. Corradi, H. Söthe, J.M. Spaeth and K. Polgár. J. Phys. Cond. Matter, 2, 6603 (1990).
7. C. Prieto et al. Phys. Rev. B 43, 2594 (1991).
8. C. Zaldo et al. J. Phys.: Condens. Matt. 3, 4135 (1991).
9. B.K. Teo, EXAFS: Basic Principles and Data Analysis. Inorganic Chemistry Concepts (Springer-Verlag, Berlin 1986) vol. 9, Chap. 2.
10. H. Donnerberg, S.M. Tomlinson, C.R.A. Catlow and O. F. Schirmer. Phys. Rev. B, 44, 4877 (1991).

Ferroelectrics, 1992, Vol. 134, pp. 53–57
Reprints available directly from the publisher
Photocopying permitted by license only

PmP154

NEWLY DEVELOPED MULTICOMPONENT PIEZOCERAMIC SYSTEM FOR ALTERNATING PRESSURE SENSORS

S.A. GRIDNEV, N.G. PAVLOVA, V.V. GORBATENKO
Polytechnical Institute, Voronezh 394711, Russia

L.A. SHUVALOV
Institute of Crystallography of Russian Academy of Sciencies, Moscow 117333, Russia

Abstract In multicomponent ferroelectric solid solution system based on $PbZrO_3$ - $(K_{0.5}Bi_{0.5})TiO_3$ with perovskite-type structure, successful results such as high piezoelectric modulus $d_{33} \simeq (120 - 200)\cdot 10^{-12}$ C/N, wide operating temperature (250 - 300°C), suitable dielectric constant (150 - 550) and high piezoelectric modulus ratio $d_{33}/d_{31} \simeq (3.8 - 6.5)$ have been obtained. Piezoceramics were used in diminutive sensors for the measurement of dynamic pressures.

INTRODUCTION

In spite of a number of evident advantages, widely used PZT ceramics [1] have some shortcomings which prevent them from being used in special sensors. Namely, they very associated with small anisotropy of the piezoelectric modulus, low operating temperatures, low temperature stability of piezoelectric modulus and high dielectric permittivity.

The aim of this paper is to show the experimental results of the piezoelectric and dielectric properties of multicomponent system based on $PbZrO_3$ - $(K_{0.5}Bi_{0.5})TiO_3$ and to discuss the use of these materials in the alternating pressure sensors.

1. EXPERIMENTAL PROCEDURES

1.1. Sample Preparation

All the starting oxide powders, in stoichiometric ratio, were mixed in a polyethylene jar with agate balls in distilled water for 16 hours. The mixed reagents were dried and pressed under a pressure of 1000 kg/cm^2. Having been calcined at 850°C for 3 hours in air, the pellets were cru-

shed in a mortar and ball-milled in a jar. After drying and dry-pressing, the samples were finally fired at 1050°C for 1.5 hours in lead oxide atmosphere. The samples were poled at 150°C and d.c. field strength of ≃ 30 kV/cm in polysilicone liquid medium.

1.2. Methods of Dielectric and Piezoelectric Measurements

Dielectric parameters (ε and $tg\delta$) and their temperature dependences were measured using the bridge method at ≃ 1 kHz and measuring field strength ≃ 3 V/cm, and over a temperature range of 20° to 500°C.

Piezoelectric modulus d_{33} was defined using the quasistatic method [1] at ≃ 20 Hz but piezomodulus d_{31}, electromechanical coupling coefficient K_p and mechanical quality factor Q_m were estimated from resonance and antiresonance frequencies.

2. EXPERIMENTAL RESULTS

2.1. Binary Piezoceramic System

The study of the (1 - x) $PbZrO_3$- x $K_{0.5}Bi_{0.5}TiO_3$ solid solutions showed the morphotropic phase transition near the concentration x ≃ 0.3, in the vicinity of which the ceramic materials have good piezoelectric and dielectric properties [2]: $d_{33} \simeq (100 - 200)\cdot10^{-12}$ C/N, $d_{33} \simeq (20 - 50) \times 10^{-12}$ C/N and $\varepsilon_r \simeq 600 - 2100$. Such a combination of good parameters is favourable for the use of the materials in the piezoelectric sensors, since the materials with high ε are usually characterized by the negligible parameter drifts taking place under the influence of great mechanical stress. However the Curie points of this binary system are not high (T_c = 140 - 270°C) that restricts the scope of the piezoelectric sensor.

2.2. Ternary Piezoceramic System

To extend the range of working temperatures and to increase the anisotropy of piezoelectric modulus, keeping the high piezoelectric characteristics of the material practically unchanged, an addition of $PbTiO_3$ was made to binary

ceramic system.

In the $(0.7\ PbZrO_3 + 0.3\ K_{0.5}Bi_{0.5}TiO_3) + x\ PbTiO_3$ system, where $PbTiO_3$ content was changed in the range from 0.25 to 0.30 mol %, a morphotropic phase transition was observed between the composition with the tetragonal structure at $x > 0.30$ mol % and rhombohedral one at $x < 0.25$ mol %. The experimental results showed the effect of the third component doping on the increase of T_c up to 270 - - 410°C, the decrease of ε down to 157, the increase of d_{33}/ε ratio up to $(4.56 - 11.95)\cdot 10^{-12}$ C/N and d_{33}/d_{31} ratio up to 3 - 4. So, new piezoceramic materials of ternary system are of a considerable interest for dynamic pressure sensors.

2.3. Piezoelectric-Polymer Composites Based on Ternary System

To be used in broadband electromechanical transducers and in piezoelectric sensors with narrow beam, the piezoactive materials must have high anisotropy of piezoelectric moduli, low values of ε, high hydrostatic piezomodulus $d_v = d_{33} + 2d_{31}$ and high piezoelectric sensitivity to the volume strain $g_v = d_v/\varepsilon_r$.

To improve the material characteristics mentioned above, piezoelectric-polymer composites with connectivity 1 - - 3 were developed.Such composites are based on the ternary ceramic system $(0.7\ PbZrO_3 + 0.3\ K_{0.5}Bi_{0.5}TiO_3) + 0.6\ PbTiO_3$ and the epoxy resin as a binder. Table 1 shows the dielectric and piezoelectric properties of the composites obtained.

Table 1 Properties of 1 - 3 piezoelectric-polymer composites

Volume fraction (%)	ε_r	d_{33} ($\times 10^{-12}$, C/N)	d_{31} ($\times 10^{-12}$, C/N)	d_v ($\times 10^{-12}$, C/N)	g_v ($\times 10^{-12}$, C/N)
40	74	46	-5	36	0.49
55	160	57	-7	43	0.27
90	240	85	-11	63	0.25

As seen, the piezoelectric properties of the composite materials, such as d_v, d_{33}/d_{31} and g_v, were much higher than that of the piezoelectric bulk ceramic. Because their characteristics are better than that of PZT and epoxy resin composites ($\varepsilon_r \simeq 300$, $g_v \simeq 0.05 \cdot 10^{-12}$ C/N, $d_v \simeq 17 \cdot 10^{-12}$ C/N), therefore the developed materials are very useful for the different applications.

2.4. Four-component Piezoelectric Ceramic System

With a view to developing a new material, the influence of $PbNb_{2/3}Zn_{1/3}O_3$ doping on the electrophysical properties of ternary $PbZrO_3$ - $K_{0.5}Bi_{0.5}TiO_3$ - $PbTiO_3$ system has been studied. The main parameters of the ceramic system studied are given in Table 2.

Table 2 Dielectric and piezoelectric properties of four-component ceramics

Dope (wt.%)	T_c (°K)	ε_r	d_{33} ($\times 10^{-12}$, C/N)	d_{31} ($\times 10^{-12}$, C/N)	d_v ($\times 10^{-12}$, C/N)	$\frac{d_{33}}{d_{31}}$
1	650	460	154	30	7,6	5,1
5	630	370	169	26	8,1	6,5
10	600	470	169	37	7,7	4,6
20	570	630	185	43	7,6	4,3
40	530	850	195	46	6,5	4,2

Note that the materials obtained are characterised by large values of ratio $d_{33}/d_{31} \simeq 3.8 - 6.5$, high values of piezomoduli $d_{33} \simeq (125 - 200) \cdot 10^{-12}$ C/N, $d_{31} \simeq (30 - 47) \cdot 10^{-12}$ C/N and $d_{33}/\sqrt{\varepsilon} \simeq (6 - 8) \cdot 10^{-12}$ C/N.

3. DIMINUTIVE PIEZOELECTRIC SENSOR FOR ALTERNATING PRESSURE

On the basis of new piezoelectric materials mentioned above, a diminutive sensor (diameter 3.5 mm, length 10 mm) has been worked out for the dynamic pressure measurements (from 10^{-2} to 2.5 MPa) in suction and compression chambers of compressors of refrigeration plants with operating frequency $(5 - 20) \cdot 10^3$ Hz.

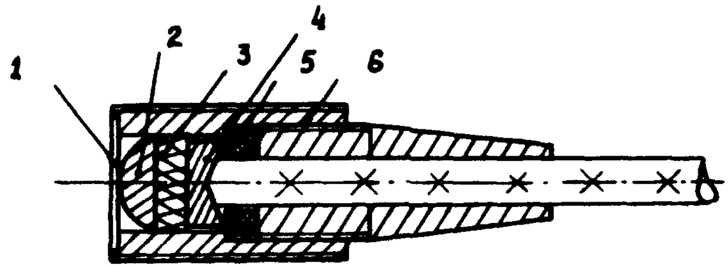

FIGURE 1 The construction of the sensor for alternating pressure

The construction of the sensor is shown in Figure 1. A measuring pressure is acting on the thin membrane (thickness 0.1 mm) 1 and hemisphere element 2 which transfer an alternating load to the piezoceramic disk 3. The hemisphere 2 provides the uniform distribution of forces all over the whole plate of the piezoelement. Piezoelectric charge, proportional to the pressure applied, is removed from the silver electrodes by a contact 4, separated from the body 6 by the insulator 5 (6 is the second contact). The signal obtained is subjected to some analysis by the measuring apparatus.

Tests show that the temperature error at a temperature change up to 600 K and a time error of piezoceramic alternating pressure sensor is not more than 1 %.

ACKNOWLEDGEMENT

The authors deeply acknowledge Mr. P.C. Osbond for his help in improvement of the English of this manuscript.

REFERENCES

1. B. Jaffe, W.R. Cook, H. Jaffe, Piezoelectric Ceramics, (Acad. Press., London and New York, 1971).
2. S.A. Gridnev, N.G. Pavlova et al., USSR Pat. № 939425.

SECTION III
CONTRIBUTED PAPERS
IIIe. Piezoelectric Composites

Ferroelectrics, 1992, Vol. 134, pp. 59–64
Reprints available directly from the publisher
Photocopying permitted by license only

PcC2

1.3.1 PZT-POLYMER COMPOSITES FOR HIGH PRESSURE HYDROPHONE APPLICATION

C. RICHARD, P. EYRAUD, L. EYRAUD, Ms. M. RICHARD[1], G. GRANGE
INSA - Laboratoire de G.E et Ferroelectricite,
69621 VILLEURBANNE Cedex - FRANCE
[1]GERDSM - DCAN - Le Brusc - 83140 SIX FOURS LES PLAGES - FRANCE

Abstract 1.3.1 piezolectric-polymer composites are made on the basis of non-mechanical contact between the polymer matrix and the PZT rods within the transverse directions. The gh.dh hydrostatic figures of merit lie between 10.10^{-12} Pa^{-1} and $27.10^{-12}Pa^{-1}$. A gh.dh of $19.10^{-12}Pa^{-1}$ is obtained with variations lower than 1dB from the room pressure to 10 MPa. The great influence of the uniaxial stress-dependence of the PZT longitudinal figure of merit is analysed and is considered as the basis of the optimalisation of the piezocomposite.

INTRODUCTION - 1.3.1 PIEZOCOMPOSITES

The low hydrostatic coupling efficiency of PZT is a well-known problem. Lead titanates, modified lead titanates or lead metaniobates are interesting solutions because of their high hydrostatic figures of merit and their large pressure stabilities. Piezocomposite materials, despite their difficult elaboration, are even more interesting because they reach very high hydrostatic figures of merit with a reasonable pressure stability. The highest figures of merit have been obtained by Newnham and co-workers on the 1.3 piezocomposite basis[1].

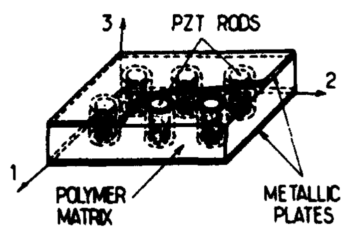

FIGURE 1 : A 1.3.1 composite device

Hydrostatic figures of merit up to $100.10^{-12}Pa^{-1}$have been reached with complex 1.3 composite devices. Foamed polyurethane matrices[2], matrices with a single large void [3] or fiber reinforced matrices[4] are some technical solutions to reach high hydrostatic figures of merit, but all the previous realizations are based on needle shaped PZT rods. This fine rod shape, of which the fabrication is delicate, is the solution for an accurate stress-transfer from the compliant phase to the stiffer one. In order to make a 1.3 composite with a more common PZT rod shape, a transducer was designed with the rod shape not so much involved in the stress-transfer accuracy . This device presents the general properties of a 1.3 piezocomposite but without lateral contact between the polymer matrix and the PZT rods.No charges are then generated by the lateral coupling of the PZT. The stress transfer

between the PZTand the polymer is carried out by two metallic armature plates also used as electrodes. A 1.3.1 composite transducer is drawn on Figure 1. The second number "1" in the "1.3.1" connectivity designation stands for the air surrounding the PZT rod.

EXPERIMENTAL

Three shapes of sample have been tested :

- 30x30 mm square, 5mm thick with 4 to 25 rods, each rod is inserted in a 4 mm diameter hole (perforated matrix type).
- 30x30 mm square, 5mm thick with a single 22x22 mm square large void where the rods are inserted in (shell matrix type).
- 10mm in diameter, 5mm thick cylindrical sample with only one PZT rod.

The polymer matrix is made with epoxy resin (Araldite D + HY956 from Ciba-Geigy) or polyurethane resin (Flexcomet 80 or 94 SA). The matrix is cut to the desired size, the holes are then drilled as numerous as it is necessary to get the right volume ratio.
The armature plates are cut in sheet steel of various thicknesses.
The piezoelectric rods, 2.7mm in diameter and 5mm high are used. This is the smallest size industrially manufactured in quantities for impact high voltage ignitors. It is a Navy I type PZT : TDK FM91e .

PZT-Epoxy composite realizations

Figure 2 shows the variations of the gh.dh figure of merit as a function of the PZT volume fraction. These results are obtained with square shaped samples for various plate thicknesses. The ratio of the hole radius to the rod radius is constant and equal to 1.5 . Figure 3 shows the variations of the gh.dh figure of merit as a function of the matrix hole diameter. The rod diameter is held constant and equal to 2.7 mm. These results are obtained with cylindrical samples for various plate thicknesses. Very low pressure-dependences have been measured on these samples presenting too low hydrostatic figures of merit. Some variations have been observed caused by assembling defects.

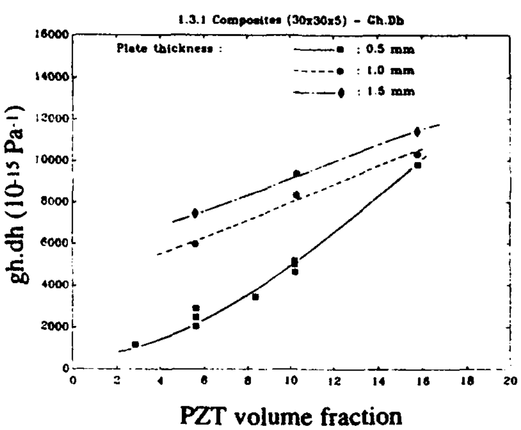

FIGURE 2 Square samples

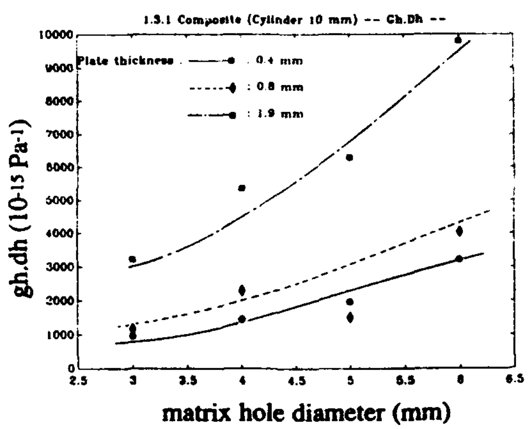

FIGURE 3 Cylindrical samples

PZT-Polyurethane composite realizations

In order to increase the figure of merit, it is necessary to increase the matrix hole diameter or to increase the polymer compliance. As it is rather difficult to bond correctly the armature plates on a small area of epoxy , we experimented with polyurethane resins. The results obtained with the perforated type matrices are reported on table 1. β is the stress amplification ratio defined afterwards.

TABLE 1 PZT-polyurethane composite with a perforated matrix

sample number	PU type	PZT volume %	numb of rods	hole Φ (mm)	gh.dh TPa^{-1}	β	Δ(gh.dh) to 10MPa	Δ(gh.dh) to 15MPa	Δ(gh.dh) 35 cycles to 10MPa	Δ(gh.dh) 35 cycles to 15MPa
3129	94SA	15.9	25	4	16.7	3.4	+0.75dB	/	/	/
3150	80SA	15.9	25	4	24.0	4	+0.35dB	-0.8dB	/	/
3155	80SA	15.9	25	4	25.5	4.2	+0.41dB	-0.9dB	/	/
3192	94SA	10.2	16	6	27	5.4	+0.0dB	-3 dB	-1.7dB	/
3193	94SA	15.9	25	4	15	3.3	+0.7dB	+0.0dB	-0.1dB	/
3202	80SA	15.9	25	4	19.3	3.7	+0.6dB	-0.2dB	-0.1dB	-1.2dB

The results obtained with the shell type matrices are reported on table 2. As the bonding of steel on a polyurethane matrix is less homogeneous than on epoxy, it was necessary to embed completely the device in polyurethane resin to avoid oil penetration between the matrix and the plates. The first samples, not embeded, have been filled up with oil during the first pressure testing cycles. Hydrostatic figures of merit up to $27.10^{-12}Pa^{-1}$ have been reached.

TABLE 2 PZT-polyurethane composite with a shell type matrix

sample number	PU type	PZT volume %	numb of rods	gh.dh TPa^{-1}	β	Δ(gh.dh) to 10MPa	Δ(gh.dh) to 15MPa	Δ(gh.dh) 35 cycles to 10MPa	Δ(gh.dh) 35 cycles to 15MPa
3156	94SA	10.2	16	18.2	4.3	-1.9dB	/	/	/
3157	94SA	15.9	25	15.3	3.1	+0.4dB	-1.3dB	/	/
3158	94SA	22.9	36	10.9	2.3	+0.5dB	+0.2dB	/	/

Figure of merit variations with the hydrostatic pressure

The composite pressure stability is evaluated as follows. At first, a measurement under atmospheric pressure is made. The hydrostatic pressure is slowly increased at a 7.5MPa/h speed until 10MPa . It is then symetrically decreased until the atmospheric pressure. Gh.dh measurements are made continuously during this cycle. Another pressure cycle until a 15MPa hydrostatic pressure is similarly driven. Then 35 cycles, 20 minutes long, are applied until 10 MPa followed by 35 cycles until 15 MPa. During these two tests the gh.dh measurements are made on the highest and lowest pressure steps. These 4 tests are separated by at least a 24 hours recovering period under atmospheric pressure.The gh.dh under pressure are reported on tables 1 and 2 and are expressed in dB relatively to the first gh.dh measurement without pressure. Figure 4 shows typical variations for dh and εr as a function of the hydrostatic pressure for a 1.3.1 piezocomposite.

PZT LONGITUDINAL CHARACTERISTICS DEPENDENCE ON UNIAXIAL STRESS

As a result of the stress transfer, the longitudinal stress applied to the PZT rods can be several times the hydrostatic pressure applied to the composite. For the sample number 3192 under a 15MPa hydrostatic pressure, a 81MPa uniaxial stress is applied to the rods along the polarization direction. Then, the stress dependence of the PZT $g_{33}.d_{33}$ figure of merit is the keystone of the composite hydrophone design.

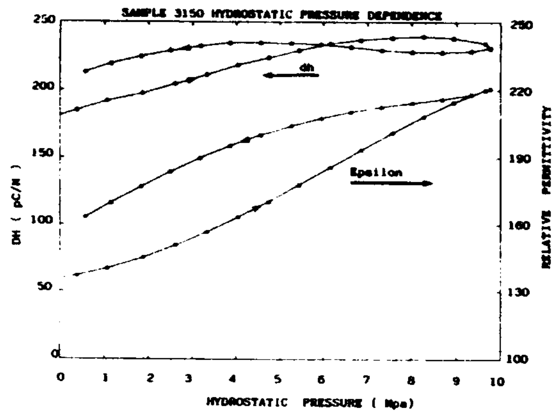

FIGURE 4 pressure dependence of the piezocomposite.

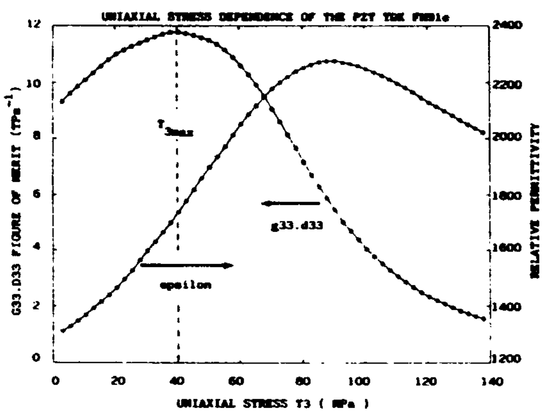

FIGURE 5 Uniaxial stress dependence of the PZT.

This stress dependence has been evaluated by Krueger[5] for PZT-4, PZT-5 and PZT-8 materials. A special device allowing d_{33} and ϵ_{33}^{T} measurements under high uniaxial stress is built and used to characterize the PZT TDK FM91e. The $g_{33}.d_{33}$ changes are evaluated with a slowly applied stress until 140MPa. The $g_{33}.d_{33}$ figure of merit and ϵ_{33}^{T} versus the uniaxial stress T_3 are plotted on figure 5. The PZT figure of merit is also measured during multiple stress cycles up to 40, 60, 80 and 100MPa. These repeated stress cycles proved that even if the PZT shows a rather weak $g_{33}.d_{33}$ decrease during the first slow stress cycle (corresponding to Figure 5), multiple stress cycles are able at long duration to decrease it more significantly. Figure 6 is a plot extrapolated from stress cycle measurements presenting the $g_{33}d_{33}$ changes versus the stress cycle amplitude. The continuous curve corresponds to measurements made on the lowest stress steps (1 MPa) and the dotted curve to measurements made on the highest stress steps (40,60,80 or 100 MPa depending on the stress cycle amplitude). It is noticed that the main decrease begins near 40MPa, the same stress corresponding to the maximum of the $g_{33}.d_{33}$ versus stress plot. The PZT material will then be considered as stable only until the stress corresponding to this maximum, noted T_{3max}, here equal to 40MPa.

PIEZOCOMPOSITE OPTIMALIZATION WITH PZT TDK FM91e

Theoretical model for 1.3.1 piezocomposites

The theoretical model is based on the following assumptions:

* No transverse stress applied to the piezoelectric rods
* Cylindrical geometry of the assembly.
* Uniform strain of the polymer matrix.
* Stress transfer assumed by the rigid plates.
* Cylindrical symetric flexure strain of the plates.
* The matrix-plate and rod-plate bondings are perfect.

The stress transfer is calculated for only one elementary cell: a rod in a matrix hole. To simulate the hydrostatic properties of a multi-rod composite, we formulated the assumption that an assembly made with many cells presents the same behavior as one cell. The model allows to calculate an amplification coefficient β which is the uniaxial stress to the hydrostatic pressure ratio. As no transverse stress is applied to the rods, the expression of the resulting gh.dh can be summarized as follows:

$$gh.dh = \beta^2 \cdot g_{33} \cdot d_{33} \cdot v$$

where g_{33} and d_{33} are the PZT piezoelectric coefficients and v is the PZT volume fraction.

Partitioning the plane defined by gh.dh and the PZT volume fraction

Now the β constant locus in the plane defined by gh.dh and the PZT volume fraction is considered. It is a straight line. Its slope is proportional to β^2. According to the PZT stability criterion defined previously, a maximum useful hydrostatic pressure allows to calculate a β_{limit} value equal to T_{3max} divided by this maximum pressure (for PZT TDK FM91e T_{3max}= 40MPa). By this way, the upper straight line on Figure 7 corresponds to a maximum hydrostatic pressure equal to 10MPa while the lower one is representative of a 15MPa limit. Above the line, the composite transducer is unstable. Also plotted on Figure 7 are some of the experimental PZT-Polyurethane composite representative points .

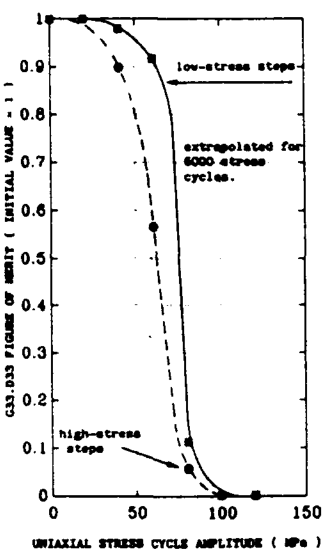

FIGURE 6 PZT $g_{33}.d_{33}$ variations

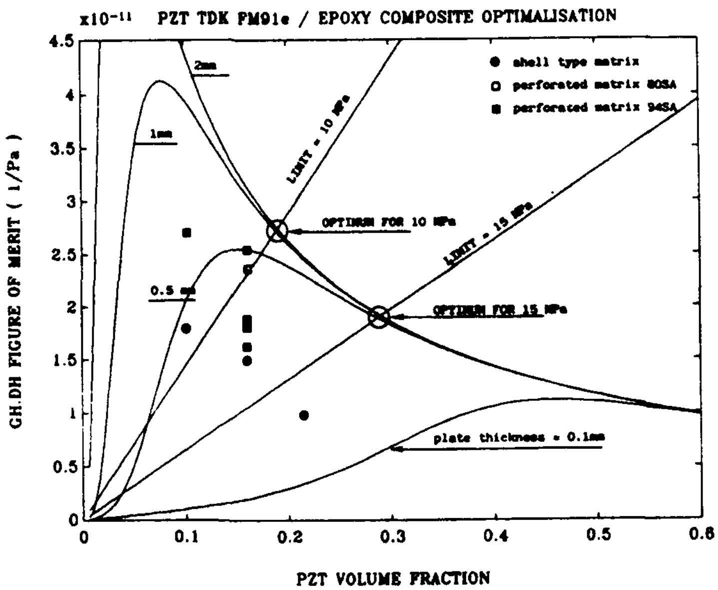

FIGURE 7 1.3.1 piezocomposite optimalisation

1.3.1 PZT-epoxy composite pressure-dependence optimalisation

Finally, the theoretical gh.dh versus the PZT volume fraction curves given by our model are superimposed on figure 7. Those curves are calculated for idealized 1.3.1 composites (the matrix holes, the largest possible, are tangent to each other in a square arrangement) and give an upper limit for various plate thicknesses. The maximum gh.dh for high pressure applications are established near $25.10^{-12}Pa^{-1}$ for a 10 MPa use and near 19.10^{-12} Pa^{-1} for a 15 MPa use by the intersections between the theoretical curves and the straight lines. These optimums are obtained for a 1mm thick armature plates and with 18% and 29% PZT volume fractions. Note that only theoretical plots for PZT-epoxy composites are proposed because difficulties were encountered to caracterize accurately the polyurethane resin. Slight changes of these limits could occur when using polyurethane .

CONCLUSION

It is experimentally and theoretically shown that no lateral contact between the PZT rod and the matrix allows high hydrostatic figures of merit without using very small diameter PZT rods. Industrial PZT rod shapes permit a gh.dh equal to $19.10^{-12}Pa^{-1}$ under a 15 MPa hydrostatic pressure with a good stability. It is pointed out that the pressure-dependence of those composites is directly connected with the longitudinal stress dependence of the PZT. A characterization of the PZT TDK FM91e rods under high stress established that a maximum uniaxial stress equal to 40MPa must not be overtaken in order to conserve a good stability along stress cycles. According to that limit, the highest figure of merit with PZT TDK FM91e-epoxy composites are 25.10^{-12} Pa^{-1}under a 10 MPa hydrostatic pressure and $19.10^{-12}Pa^{-1}$ under a 15MPa pressure. This simple 1.3.1 piezocomposite application allows to approach the optimized figures of merit.
A similar calculation based on Navy III type PZT coefficients dependence on the uniaxial stress showed the possibility to reach higher figures of merit to an even higher hydrostatic pressure. Further experiments are in progress to verify that point.

ACKNOWLEDGEMENT

This work is sponsored by the GERDSM department of the DCN Toulon and by the DRET. The authors thank Roger Vignat for his help in the fabrication of the composite parts and David Audigier for his help in the PZT characterization under uniaxial stress.

REFERENCES

1 . R.E NEWNHAM, L.J. BOWEN, K.A. KLICKER and L.E. CROSS . Material in Engineering , 2 , 93 (December 1980)
2 . K.A. KLICKER, W.A. SCHULZE, J.V. BIGGERS . J. Am. Ceram. Soc. , 65 , C-208 (Dec. 1982)
3 . M.J. HAUN, R.E. NEWNHAM . Ferroelectrics , 68 , 123 (1986)
4 . M.J. HAUN, P. MOSES, T.R. GURURAJA, W.A. SCHULZE and R.E. NEWNHAM. Ferroelectrics , 49 , 259 (1983)
5 . H.H.A. KRUEGER . J. Acoust. Soc. Am. , 42 [3] , 636 (1967)

Ferroelectrics, 1992, Vol. 134, pp. 65–69
Reprints available directly from the publisher
Photocopying permitted by license only

PcC3

0 – 3 PIEZOELECTRIC – GLASS COMPOSITES

S. SHERRIT, H.D. WIEDERICK, B.K. MUKHERJEE
Royal Military College of Canada, Kingston, Ont., Canada K7K 5L0

S.E. PRASAD
Sensor Technology Ltd.(B.M. Hi-Tech Division), P.O.Box 97,
Collingwood, Ont., Canada L9Y 3Z4

Abstract Piezoelectric 0–3 ceramic–glass composites have been developed by firing a mixture of modified Lead Zirconate Titanate (PZT) and a lead based glass powder. Composites with 58 to 92 volume percent PZT were fabricated and their dielectric, piezoelectric and hydrostatic properties have been determined. The hydrostatic properties were pressure independent and the material showed good mechanical stability. The measured properties of the composites suggest that they could be useful in hydrophones and also as acoustic backing material.

INTRODUCTION

Electroceramic composites are today being increasingly used as transducer materials. By a suitable choice of the phases and connectivities, the properties of the composites can often be tailored to meet design requirements[1]. The preparation and properties of a large variety of piezoelectric ceramic–polymer composites have been reported[2]. However, the use of a polymer matrix restricts the use of these composites to relatively low temperatures. Grain–oriented glass–ceramics, based on fresnoite, have been developed for piezoelectric applications[3], but they show poor mechanical integrity and their fabrication requires temperature gradient crystallisation which is inconvenient. Conventional glass–ceramic processing has also been used to fabricate piezoelectric glass–ceramics based on Lead Titanate[4]. We have used similar techniques to fabricate piezoelectric glass–ceramic composites using a mixture of Lead Zirconate Titanate and lead based glass powders and, in this paper, we report on the dielectric, piezoelectric and hydrostatic properties of these composites.

MATERIAL FABRICATION

The piezoelectric material chosen was a Navy Type V modified Lead Zirconate Titanate (PZT) composition marketed by Sensor Technology Ltd. as BM 532 material. This material has a high dielectric constant (~3250) and good piezoelectric properties (d_{33} ~ 580 pC/N). The glass used in our composites is a proprietary lead based composition

developed by Sensor Technology Ltd. (BM1000) for the production of polarisable glasses. This glass has a relatively low softening temperature, which makes for easier processing; it is chemically compatible with the ceramic particle and it has good electrical insulation properties which makes poling easier.

The PZT and glass powders had a particle size of 2 to 4 μm. The powders were mixed in the desired composition and the mixture was milled in methanol for two hours and pan dried. A 5% solution of poly-vinyl-alcohol (Air Products 107) was added to the powder as a binder and discs, 25 mm in diameter and 2.5 mm thick, were pressed at a pressure of 20 MPa. The binder was burnt out by heating at 500°C and the discs were fired at temperatures of between 550 to 600°C. These sintering temperatures were sufficiently low that no additional precautions were taken regarding the atmosphere during sintering; however, the firing was carried out in covered alumina crucibles. The fired discs were ground to produce uniform dimensions and a silver composition, with a low firing temperature, was applied to form the electrodes. The discs were poled for 30 minutes with an electric field of 5 KV/mm at a temperature of 120°C.

Since the properties of 0-3 composites are known to be a function of their composition, a total of 6 compositions were fabricated with their PZT content in the range of 58 - 92 volume percent.

MATERIAL PROPERTIES

The dielectric constant and the dissipation of our samples were measured at room temperature and at a frequency of 1 KHz. Their values are shown, as a function of PZT content, in Figure 1. The dielectric constant is found to be much lower than the value for the bulk PZT (~ 3250) while the dissipation also is somewhat reduced when compared with bulk PZT value (~ 0.02).

The piezoelectric d_{33} coefficients of the discs were determined by using a Berlincourt type d_{33} Meter. As shown in Figure 2(a), the d_{33} values of the composites show a roughly linear increase as a

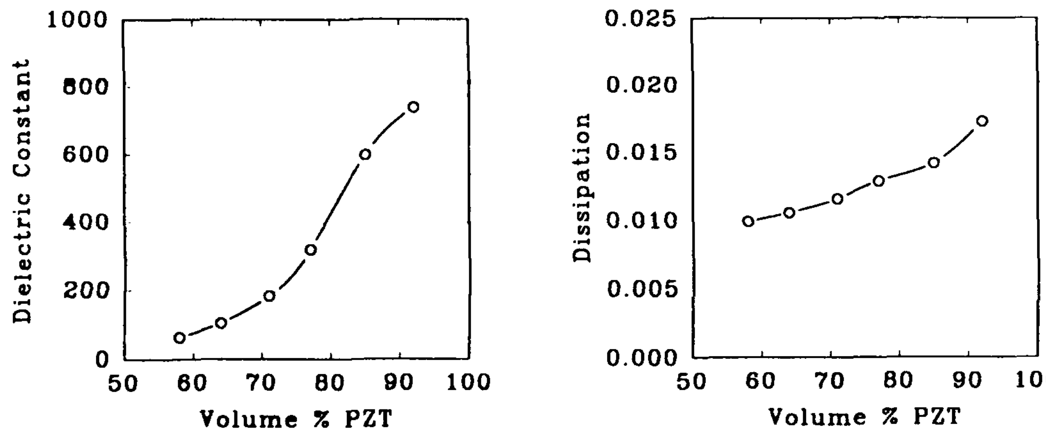

FIGURE 1. The dielectric constant and the dissipation of the composites as a function of PZT volume percent.

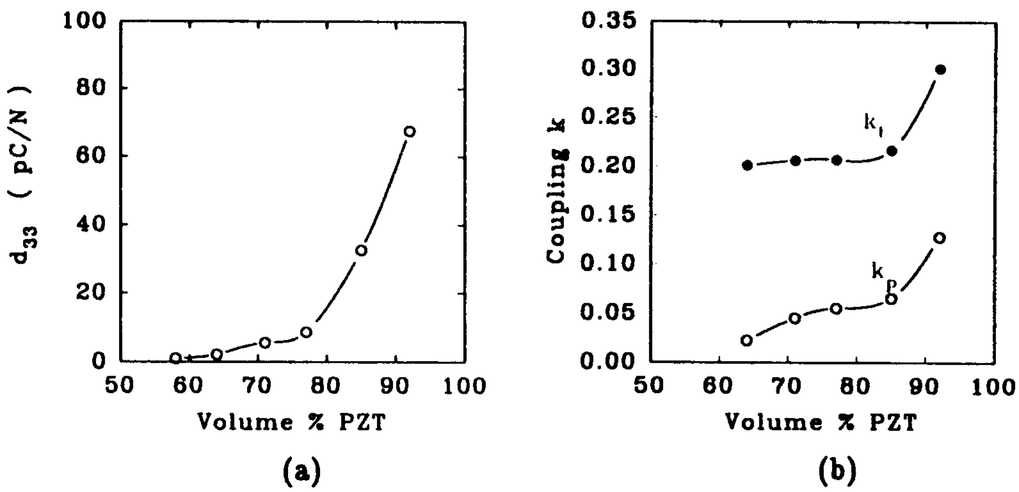

FIGURE 2. The piezoelectric d_{33} coefficient and the coupling constants of the composites as a function of PZT content.

function of the PZT content until the latter reaches about 80%; but for higher PZT content the d_{33} values increase much more sharply to reach a maximum of about 68 pC/N for the specimen with 92 volume percent of PZT.

The thickness mode electromechanical coupling constant, k_t, and the planar coupling constant, k_p, of the composites were determined from resonance measurements, and the values are shown in Figure 2(b).

A technique similar to that developed by Sims and Henriquez[5] has been used to measure the hydrostatic voltage coefficient, g_h, of our

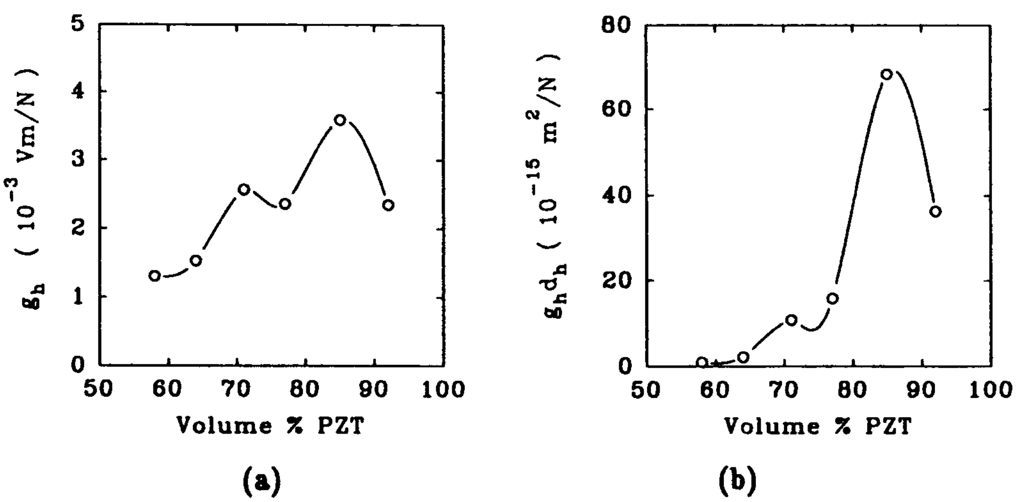

FIGURE 3. The hydrostatic voltage coefficient, g_h, and the figure of merit, g_hd_h, of our composites as a function of PZT content.

composites, at a pressure of 2 MPa, and the variation of g_h as a function of PZT content in the composites is shown in Figure 3(a). The product of the hydrostatic voltage coefficient and the hydrostatic charge coefficient, $g_h d_h$, is commonly used as a figure of merit for hydrophone materials and has been determined for our specimens. As shown in Figure 3(b), the best figure of merit has been obtained for the sample with 85 volume percent PZT, for which $g_h d_h$ is 68 x 10^{-15} m^2/N. g_h has been measured as a function of hydrostatic pressure and, for pressures up to 14 MPa, g_h has been found to be independent of pressure to within experimental uncertainty.

The acoustic velocity and attenuation of the composites were measured using standard transmission techniques. The discs were precision lapped to provide good contact with the transducers and a standard metal plate was used to calibrate the system. The results are shown in Table 1 which provides a summary of the properties of the PZT-glass composites; for purposes of comparison, the table also gives published data on a few other types of composites and polar glass ceramics.

TABLE I Characteristics of the PZT-glass composites.

Vol % PZT	Diel. Const.	d_{33} 10^{-12}C/N	g_h 10^{-3}Vm/N	$g_h d_h$ $10^{-15}m^2/N$	Acoustic Velocity m/sec	Attenuation dB/cm
58	62	1.00	1.3	0.9		
64	104	2.11	1.5	2.0	3395	26
71	183	5.5	2.6	10	3490	26
77	319	8.6	2.4	15	3520	27
85	598	33	3.6	68	3215	30
92	738	68	2.4	36	3340	30
0-3 ceramic-glass comp. with 49 vol. % $PbTiO_3$.[4]	52	8				
Polar Glass Ceramics.[6]	~10	~8-10	83	747	~5000	
0-3 $PbTiO_3$ - rubber composite.[7]	54	60	47	1000		

CONCLUSIONS

Piezoelectric 0–3 ceramic–glass composites have been fabricated by the conventional firing of a mixture of powders of PZT and a lead based glass. The best d_{33} values obtained were comparable to those of some 0–3 ceramic–polymer composites and were an improvement over the d_{33} of similar composites made with Lead Titanate and those of polar glass ceramics. The hydrostatic properties of the composites were pressure independent and they showed good mechanical stability. This type of ceramic–glass composite is easier to fabricate than polar glass ceramics, their dielectric dispersion is less than that of polymer based composites. They can also be used over a much wider temperature range than polymer based composites since the elastic properties of glasses are much less temperature dependent than those of polymers. In addition to their possible use in transducers, the relatively large acoustic attenuation of these materials suggests their possible use as acoustic backing material.

ACKNOWLEDGEMENT

The authors thankfully acknowledge financial support from the Defence Research Establishment Atlantic of the Department of National Defence, Canada.

REFERENCES

1 R.E. Newnham, D.P. Skinner and L.E. Cross, Mat. Res. Bull., 13, 525 (1978).

2 R.E. Newnham, A. Safari, J. Giniewicz and B.H. Fox, Ferroelectrics, 60, 15 (1984).

3 A. Halliyal, A. Safari, A.S. Bhalla and R.E. Newnham, Ferroelectrics, 50, 45 (1983).

4 G.S. Lee, S. Kim and T.R. Shrout, Sensors and Materials, 2, 1, 7 (1990).

5 C.C. Sims and T.A. Henriquez, J. Acoust. Soc. Am., 36, 1704 (1964).

6 A. Halliyal, A. Safari, A.S. Bhalla, R.E. Newnham and L.E. Cross, J. Am. Cer. Soc., 67, 331 (1984).

7 H. Banno, Ferroelectrics, 50, 3 (1983).

Ferroelectrics, 1992, Vol. 134, pp. 71–76
Reprints available directly from the publisher
Photocopying permitted by license only

PcC15b

NON-POLAR POLYMER/FERRO AND ANTIFERROELECTRIC CERAMIC COMPOSITE FILMS FOR HIGH ENERGY STORAGE CAPACITORS

D.K. DAS-GUPTA School of Electronic Engineering Science, University of Wales, Bangor Dean Street, Bangor, Gwynedd LL57 1UT U.K.

ZHANG SHUREN Department of Materials, University of Electronic Science & Technology of China, Chengdu, 61005, P.R. CHINA

Abstract Five different composite films of Polypropylene-Ceramic (both ferro- and antiferroelectric) materials were prepared by introducing fine grain ceramic powder in the matrix of polypropylene. The dielectric and charge storage properties of these composites were studied. The results show that an introduction of fine powder of appropriately modified ferroelectric ceramics in a polymer-ceramic composite enhances its charge storage properties.

INTRODUCTION

The use of polymer-ceramic composites which combine the superior mechanical and electrical strength of the insulating polymer with the advanced dielectric properties of suitable ceramics is considered to be a possible approach to the high energy storage capacitors. The manufacturing flexibility of the composite makes it possible to produce thin film capacitors with high capability of energy storage while this is difficult to achieve with the multilayer ceramic capacitors due to the complicated fabrication process and their inevitable structural defects.

In the present work, several ferro and anti-ferroelectric ceramic materials were introduced into matrix of polypropylene. An

investigation of the influence of the ceramics on the dielectric and the charge storage properties of the composites were made.

EXPERIMENTS

Three ferroelectric and two antiferroelectric ceramic materials were prepared (Table 1). BT and BST were produced by liquid phase coprecipitation technique, while the other three by the traditional ceramic preparation process. The ceramics were quenched from the firing temperature and then milled with absolute alcohol for 72 hours. The ceramic powder of fine particle size was obtained by a floating segregation method. The particle size of BT and BST were 0.05-0.5μm, and that of the others was around 1μm.

TABLE 1 The Ceramic Materials for Composites

Code	Specifications
BT	$BaTiO_3$ doped by Nb_2O_5, Sb_2O_3
BST	$(Ba,Sr)TiO_3$ system
PMN	Modified $Pb(Mg,Nb)O_3$ system
PZSTN	$Pb(Zr,Sn,Ti)O_3$ doped by Nb_2O_5
PZSTL	$Pb(Zr,Sn,Ti)O_3$ doped by La_2O_3

The composites were prepared on a hot roller machine by mixing the ceramic powder with prolypropylene (PP) polymer pellets at 400K and then pressing into films of approximately 50 μm thickness in a temperature controlled hydraulic press as described in the previous work.[1,2] The fraction of ceramics in the composites was 30 percent by volume. After depositing an aluminum electrode on each surface of the films, the samples were cured at 343K for 12 hours to release the strain and electric charges accumulated in the process of their fabrication.

The dielectric data were obtained in an evacuated measurement chamber using a General Radio Bridge (Type 1621 with a 1238 detector

and a 1316 oscillator) or using a Solartron Frequency Response Analyser (Model 1250)

RESULTS AND DISCUSSION

In order to observe the effects of ceramics on the composites, both high and low permittivity ceramic materials were selected for the present work. Figure 1 shows the temperature dependence of permittivities of the ceramics. BT is modified by Niobium Pentoxide and Antimony Oxide. PZSTN and PZSTL have the same antiferroelectric composition $Pb(Zr,Sn,Ti)O_3$ but doped by Nb^{+5} and La^{+3} ions respectively. In the test temperature range, they behave like linear materials only showing a slight increase of permittivity with the increase of temperature. PMN shows a higher permittivity and a larger variation with temperature, while BST gives a moderate permittivity and limited variation with the temperature.

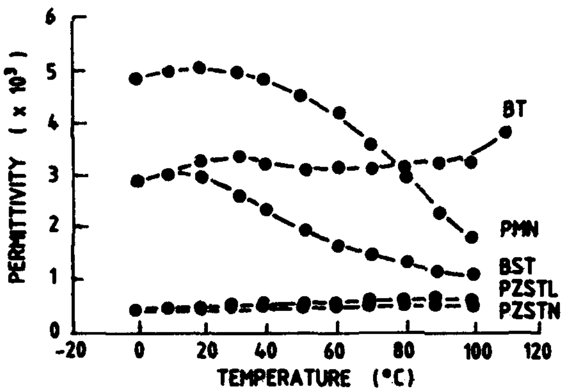

Fig.1 Temperature dependence of permittivities of ceramics f=1,000(Hz), V=1(V)

Figures 2 and 3 show the nature of permittivities and dissipation factors respectively of the composites as a function of the temperature. It is noticeable that the composite PP-PMN shows highest loss factor (figure 3) but not the highest permittivity (figure 2) as expected although PMN possesses highest permittivity within the materials selected.

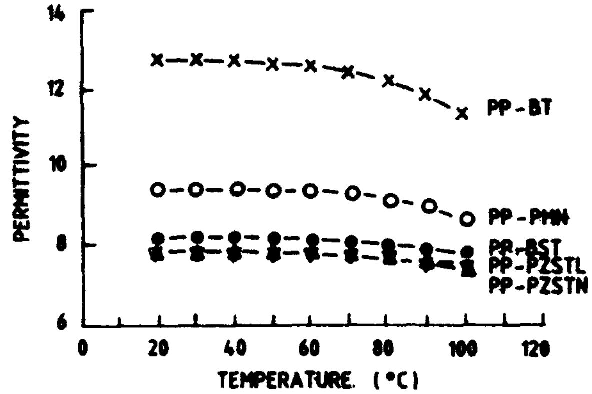

Fig.2 Temperature dependence of permittivity of the composites, Volume fraction of ceramics: 30% f=1,000(Hz), V=1(V)

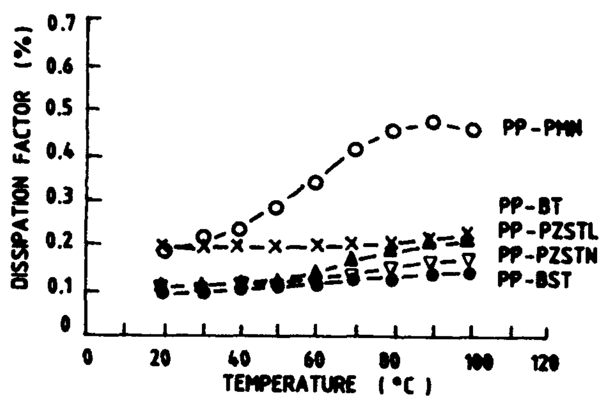

Fig.3 Temperature dependence of dissipation factors f=1,000(Hz), V=1(V), Volume fraction of ceramics: 30%

Figure 4 shows the AC measuring field dependence of dielectric properties of the three composites. The dielectric properties of the composite PP-PZSTN is observed to be constant with the AC field. In contrast, the composite PP-PMN shows a significant increase of the dissipation factor with the increase of the AC field. It should be noted that PMN has stronger ferroelectric characteristics compared with other selected ceramics[3], whereas PZSTN behaves practically like a paraelectric dielectric within the measuring range.

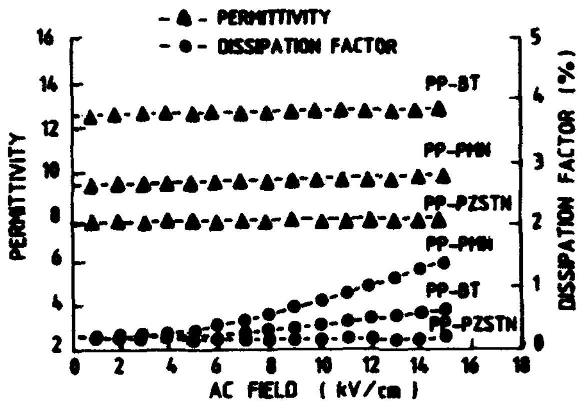

Fig.4 Measuring field dependence of dielectric properties f=1,000(Hz), V=1(V), Volume fraction of ceramics: 30%

The dielectric strengths of the composites are given in Table 2.

TABLE 2 The Dielectric Strengths of Composites

Composite	Dielectric Strength(KV/cm)
PP-BT	800
PP-BST	750
PP-PMN	700
PP-PZSTN	650
PP-PZSTL	400

The composites containing BT and BST which were produced by coprecipitation method and possessing ultra-fine particle size, appear to have the higher dielectric strength than the other composites.

The density of energy stored in a linear material J is given by,

$$J = 1/2\varepsilon_0\varepsilon_r E^2 \qquad .....(1)$$

where ε_0 is the permittivity of the vacuum, ε_r the relative permittivity and E is the electric field. whereas in a non-linear material it is expressed by,

$$J = \int \varepsilon_0 \varepsilon_r E \, dE \qquad \ldots\ldots (2)$$

Figure 5 shows the calculated energy storage densities of the composites as a function of the electric field, using equation 2. The efficiency of energy storage in the composites appears to be higher than that of Polypropylene.

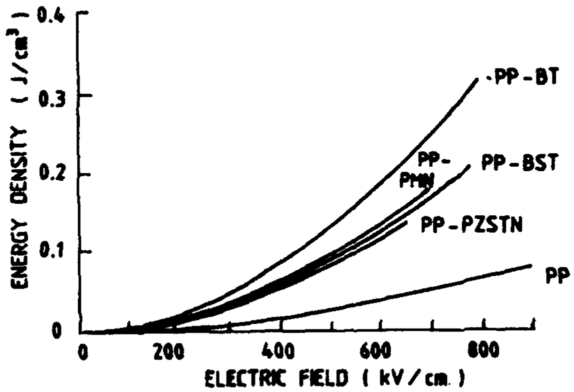

Fig.5 The properties of energy storage vs, electric field Volume fraction of ceramics: 30%, T=20°C

The present results indicate that the ferroelectric ceramics are more effective than the antiferroelectric ceramics to enhance the energy storage capabilities of the PP-ceramic composites. However, appropriately modified ferroelectric ceramics should have fine particle size to serve this purpose.

ACKNOWLEDGEMENT

One of the authors (S. Zhang) acknowledges the award of a maintenance grant by SINO-BRITISH FRIENDSHIP SCHOLARSHIP SCHEME (SBFSS) during the course of this study.

REFERENCES

1. D.K. Das-Gupta & M.J. Abdullah J.Mat.Sci.Letters., 7, 167, (1988)
2. M.J. Abdullah & D.K.Das-Gupta IEEE Trans. Electric. Insulation, 25, No.3, 605, (1990)
3. S.L.Swarts IEEE Trans. on Electric Insulator, 25 No.5 935, (1990)

Ferroelectrics, 1992, Vol. 134, pp. 77–82
Reprints available directly from the publisher
Photocopying permitted by license only

PcP123

MICROSTRUCTURAL DEPENDENCE OF PIEZOELECTRIC PROPERTIES OF CERAMIC-GLASS COMPOSITES

L. Pardo, F. Carmona, C. Alemany and B. Jimenez.
Instituto de Ciencia de Materiales (Sede A). C.S.I.C.
Serrano, 144. 28006 - MADRID (SPAIN).

ABSTRACT

Glass matrix composites of different connectivities have been prepared from Ca-modified lead titanate ceramics and boron-lead glasses. Microstructural characterization reveals that the processing methods minimize the chemical interaction between the phases. Different microstructures are obtained by using diverse processing methods, giving rise to related electromechanical properties through the influence of the microstructure on the polarizability of the materials.

I. INTRODUCTION

The enhancement of the strength characteristics with respect to the ceramics has been one of the reasons used to justify glass matrix piezoelectric composites [1,2]. Also, the authors found recently that inorganic glass matrix composites are potencially attractive as ultrasonic transducers at higher temperatures than their polymer counterparts, since both types of composites have similar advantages over ceramics [3].

The preparation of composites from boron-lead glass and Ca-modified lead titanate ceramic was analyzed in a previous paper paying attention to the influence of the crystalline anisotropy of the ceramic on the thermomechanical matching of the composite phases [3]. Here a microstructural analysis is carried out on these composites to explain the differences observed in their piezoelectric behaviour for the different processing methods, which give place to diverse composite connectivities, i.e., number of dimensions in which each composite phase is self-connected [4,5].

II. EXPERIMENTAL PROCEDURES

The piezoelectrically active phase of the composite is a Ca-modified lead titanate ceramic with a ratio Ca/Pb=35/65 (PTC35) prepared by a reactive process [6] and the matrix is a boron-lead glass(B_2O_3-PbO-Na 48/50/2 weight %).

Composites of 1-3 connectivity, according to the extensively used Newnham's nomenclature [4,5], where the first digit refers to the piezoceramic, were prepared. Deep groves were cut into the ceramic in two perpendicular directions to obtain a regular structure of square pillars. This ceramic structure was dipped into the melted glass (750°C), that fills the groves, and quenched to room temperature to avoid the reactions between the phases. Details of the method are given elsewhere [3]. Ceramics with different densification were used in this process.

Composites were prepared from ceramic particles [7] by mixing with finely

powdered glass, uniaxial press moulding and further thermal treatments: a) hot pressing and b) heating to melt the glass. 0-3 and mixed 0-3/1-3 connectivities were prepared by changing the ratio G/t between the average particle size (G=1-2 mm) and the composite thickness, t [8]. When G/t<1 particles are not self-connected between the composite surfaces (0-3 connectivity), whereas when G/t>1 only a fraction of the particles is self-connected between the electroded surfaces of the composite due to the random distribution of the particles in the glass matrix (0-3/1-3 mixed connectivity).

Considered as 3-3 connnectivity composites, glass bonded ceramics of PTC26 were also obtained by adding a 4% by weight of finely powdered glass to the precursor ceramic powder, moulding and sintering.

SEM and compositional analysis by EDX were carried out on the composites obtained. Cutting, lapping and polishing of the materials allowed the preparation of composite disks of, typically, 10mm diameter and 0.5mm thickness, onto which Ag vacuum evaporated electrodes were deposited. The composites were poled at 30-40 KV/cm -120°C , cooling down to room temperature with the electric field applied to the sample. Permittivity at 1 KHz, K_{33}^{T}, was determined. Thickness electromechanical coupling factor, K_t, frequency number, N_t, mechanical quality factor, Q_m and acoustic impedance, Z_a, were measured at room temperature by the resonance method [9].

III. EXPERIMENTAL RESULTS

Composites of 1-3 connectivity, prepared from PTC35 ceramics characterized by their density and diameter contraction during sintering, which will be refered to as dense and less dense ceramic, were analyzed. Microstructures of these two types of ceramics are shown in Figures 1 (density = ρ = 6.18 g.cm^{-3} - contraction = 15.2%) and 2(ρ = 6.10 g.cm^{-3} - contraction = 11.5%).

Figure 1

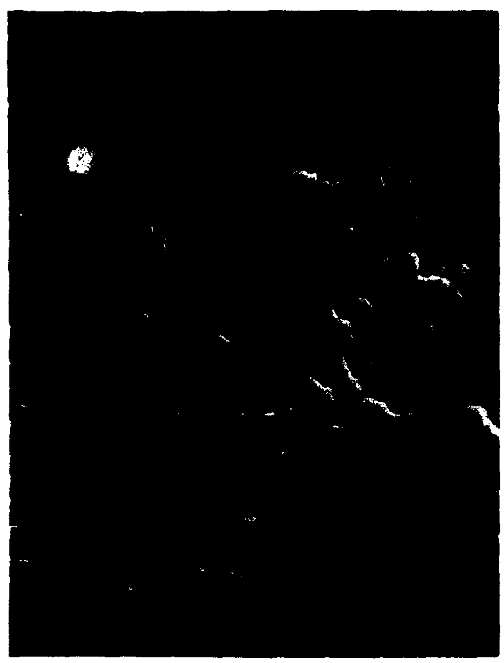

Figure 2

The formation of intermediate zones has been observed only when forming composites from less dense ceramics. These zones are due to diffusion of glass in the ceramic through the open porosity (Figure 3). A common fact in composites prepared from the two types of ceramics is the appearance of a thin ($<<1\,\mu m$) interphase between the ceramic and the glass (Figure 4). EDX analysis of the ceramic and the glass in the intermediate zone as well as the interphase is shown in Table I. The dielectric and piezoelectric parameters of the composites in comparison with those of the ceramics are shown in Table II, where n_{cer} is the volumetric fraction of ceramic in the composite and the rest of the symbols have the ususal meaning, which has been explained in the text.

Figure 3

Figure 4

0-3 and mixed connectivity composites present different microstructures when prepared by hot-pressing (15MPa-550°C) of the moulded mixture (Figure 5) or by heating at 600°C. Less dense structures and crystallization of the matrix is observed (Figure 6) when the second method is used. The results of the characterization of these composites are shown in Table II.

The 3-3 composites present the peculiar structure shown in Figure 7, which is constituted by cubic shape grains surrounded by a continuous glass phase. Dielectric and piezoelectric parameters of this material are shown in Table II.

IV. DISCUSSION AND CONCLUSIONS

The results of the EDX analysis carried out on the 1-3 connectivity composites (Table I) show that the glass diffusion into the porosity of the less dense ceramic occurs during the composite preparation without a chemical reaction between the two phases, and, therefore, leaves unchanged the composition of the ceramic in the intermediate zone with respect to that found inside the piezoelement of the composite.

Figure 5

Figure 6

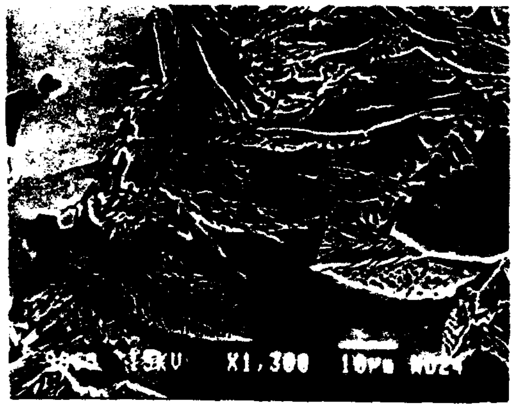

TABLE I

atom %	Pb	Ca	Ti	W	Co	Mn	Na	light elements (O,B,..)
1-3 COMPOSITES FROM LESS DENSE PTC35 CERAMIC								
CERAMIC inside piezoelement	10.47	5.58	16.27	0.41	–	0.31	–	66.96
CERAMIC intermediate zone	10.86	6.08	17.49	0.19	–	0.26	–	65.08
GLASS intermediate zone	5.76	0.14	0.255	–	–	–	2.05	91.79
INTERPHASE	3.12	0.83	15.43	0.18	–	0.38	–	80.07
1-3 COMPOSITES FROM DENSE PTC35 CERAMIC								
CERAMIC inside piezoelement	10.39	5.95	16.61	0.45	0.24	0.36	–	65.98
INTERPHASE	2.07	0.95	18.28	–	–	0.55	–	78.15

Figure 7

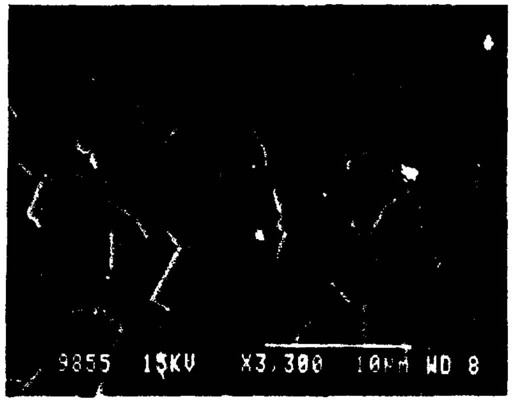

TABLE II

Contr (%)	ρ cer g/cm^3	PRESENCE OF INTERMEDIATE ZONE	n_{cer} (%)	ρ comp g/cm^3	K_{33}^T	K_t (%)	N_t KHz.mm	Q_m	Z_a (x10^6 Rayls)
		DENSE	CERAMIC	PTC35					
15.79	6.27	—	—	—	468	54.3	2079	36	13.02
	1-3	COMPOSITES							
15.70	6.02	NO	24.69	4.91	152	21.7	2094	29	10.28
16.00	6.19	NO	25.77	4.97	152	10.5	2180	115	10.83
17.68	6.27	NO	28.47	5.04	154	28.4	2160	18	10.88
15.79	6.18	NO	35.00	5.12	161	11.3	2049	105	10.49
		LESS DENSE	CERAMIC	PTC35					
12.53	6.29	—	—	—	432	55.3	1906	17	11.99
	1-3	COMPOSITES							
11.23	6.26	YES	18.63	4.87	78	28.8	2402	23	11.68
11.23	6.23	YES	23.27	4.94	92	30.3	2359	23	11.65
11.23	6.36	YES	31.11	5.11	117	24.8	1970	35	10.07
12.4	6.39	YES	38.09	5.25	151	34.0	1920	9	10.06
12.4	6.29	YES	41.76	5.27	175	36.5	1858	41	9.79

TYPE OF COMPOSITE	ρ(g.cm^{-3})	K_{33}^T	K_t(%)	N_t(KHz.mm)
3-3 connectivity PTC26 + 4% glass	5.0	130	--	--
PTC26 ceramic	6.7	197	46.5	2158
0-3 connectivity PTC35 hot-pressed	4.2	40	3.1	1971
0-3/1-3 mixed (G/t=2.3-3.7) PTC35 hot-pressed	4.1	56	15.8	1908
0-3/1-3 mixed (G/t=1.2-1.8) PTC35 simply heated	3.9	51	14.7	1940

These results (Table I) show also that composites prepared from both types of PTC35 ceramics have present only a very thin interphase, whose composition presents a deficiency of Pb and Ca with respect to Ti. The preparation process, therefore, minimizes the chemical interaction between the ceramic and the glass providing, in the case of the less dense ceramics, a stronger adhesion between phases through the formation of a intermediate zone.

As shown in Table II all the composites present lower density, and, consequently, lower acoustical impedance, Z_a, and permittivity, K_{33}^T, than the corresponding ceramics.

It is interesting that 1-3 composites prepared from the less dense PTC35 ceramics present higher K_t values. Polarizability of this ceramic is higher [10], because their remanent porosity reduces intergranular stresses arising on poling, allowing easier 90° domain orientations. The intergranular clamping effect that appears in dense ceramics of high crystalline anisotropy is enhanced in the composite, because the piezoelements of ceramic are surrounded by a stiffer glass matrix (Young's Modulus =E (ceramic) = 100-150 GPa ;E (glass) = 50 GPa).

The decrease of the properties when the connectivity changes from mixed 0-3/1-3 to 0-3 by changing the ratio G/t [8] is clearly shown for the particle composites prepared by hot-pressing from results in Table II.

Similar K_t values were found (Table II) for the mixed 0-3/1-3 composites prepared by hot pressing and simple heating. Since the ratio G/t is higher in hot-pressed composites, higher K_t values could be expected. This leads to the conclusion that composites obtained by heating are more polarizable. A similar reasoning than the one used in 1-3 composites could explain that the less dense structure, and, consequently, less clamped, that is found in mixed connectivity composites prepared by simple heating, results more polarizable.

AKNOWLEDGEMENTS

Authors wish to thank C. Fandiño and F. Díaz for their collaboration in the material preparation, D. Gomez (Centro Nacional de Microelectrónica. CSIC) and Dra. P. Adeva and A. Requibatiz (Centro Nacional de Investigaciones Metalurgicas. CSIC) for the SEM and EDX analysis. This work has been carried out under project MAT88-0164 of the Spanish CICYT.

REFERENCES

(1) S.O. Kramarov, A.V. Beliaev, A.A. Grekov and L.M. Katsnelson. Ferroelectrics 68, 45 (1986).
(2) E. Freidenfeld, E.M. Pachenko, R.Z. Kleine and V.A. Zagorniko. Ferroelectrics 68, 141 (1986).
(3) L. Pardo, B. Jimenez, L. Calzada, C. Alemany and F. Carmona. Ferroelectrics 127, 179-184 (1992).
(4) R.E. Newnham, D.P. Skinner and L.E. Cross. Mat. Res. Bull. 13, 525 (1978).
(5) D.S. MacLachlan, M. Blaszkiewicz and R.E. Newnham. J. Am. Ceram. Soc. 73 (8), 2187-2203 (1990).
(6) L. del Olmo, C. Fandiño, J.I. Pina, C. Alemany, J. Mendiola, B. Jimenez, L. Pardo y E. Maurer. Patente Española de Invención nº 555469.
(7) L. Calzada and L. del Olmo. Cer. Acta 2(3), 21-26 (1990).
(8) L. Pardo, J. Mendiola and C. Alemany. J. Appl. Phys. 64 (10), 5092 (1988).
(9) "IEEE Standard on Piezoelectricity". ANSI/IEEE Std. 176 (1987).
(10) J. Mendiola, L. Pardo, F. Carmona and A.M. Gonzalez. Ferroelectrics 109, 83-88 (1990).

SECTION III
CONTRIBUTED PAPERS

IIIf. Piezoelectric Devices and Materials

Ferroelectrics, 1992, Vol. 134, pp. 83-88
Reprints available directly from the publisher
Photocopying permitted by license only

PdCl

PIEZOELECTRIC MICRO-MOTOR

Munekazu KANNO, Hiroshi OKABE and Susumu SAKANO
College of Engineering, Nihon University
1 Nakagawara, Tokusada, Koriyama-shi, Fukushima 963, Japan

Abstract This paper describes a new piezoelectric micro-motor based on a piezo - resonator and explains the mechanism of motion and the motor's basic characteristics.

INTRODUCTION

Piezoelectric elements are expected to become increasingly popular and to be used as actuators in fields such as medicine, precision instruments and mechatronics. There are many kinds of actuator elements[1-3], using thermal strain, magnetic strain and electropneumatic power etc. However, they have some problems with size, precision and motion response.

Recently, many studies[4] have been carried out on ultrasonic motors. These are better than electro - magnetic motors for some applications in mechatronics. An ultrasonic motor is driven by the friction between the rotor and stator. Conventional ultrasonic motors use an ultrasonic wave of 20-50 kHz . Piezoelectric elements have many possible applications for small actuators and micro - actuator . Many studies[5,6] on piezoelectric elements have carried out for actuators , but there have been no studies on piezoelectric motors.

We have developed a new type of piezoelectric micro-motor. It can be rotated clockwise or counter-clockwise by the piezoelectric element. This is one of its main features. The principle of the motion is different from the usual ultrasonic motor. The driving frequency of the piezo - electric motor ranges from 130 Hz to 1500 Hz, and it can rotate smoothly at low speeds.

This paper describes the new piezoelectric motor and explains its mechanism of the motion, and gives experimental results for its dynamic response characteristics and efficiency.

MECHANISM OF THE MOTOR

Principle of Motion

Figure 1 shows the basic structure of the piezoelectric motor. It consists of a piezoelectric reed, a trembler and a rotor. The piezo - electric reed is made of a bimorph piezoelectric element. It is clamped at one end and free at the other. The trembler is fixed to the free end of the reed, and touches the rotor. Voltage from the power supply causes the reed to vibrate. Vibration of the reed and trembler cause the rotor to rotate.

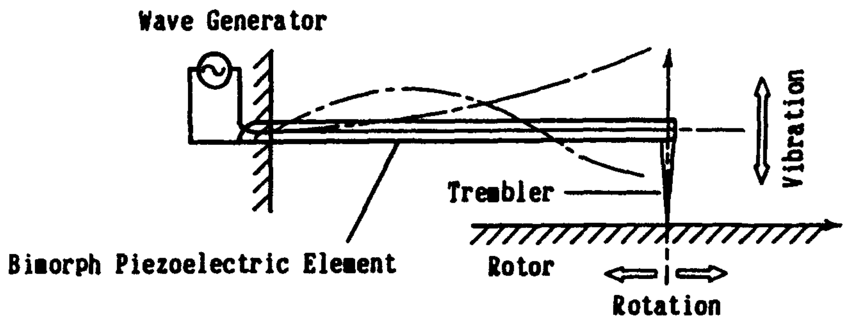

FIGURE 1 Basic structure of motor

Figure 2 shows the principle of motion. For example , if the rotor rotates clockwise at the first resonance mode of the reed , then it will rotate counter- clockwise at the second mode of vibration. The rotor can be rotated clockwise or counter - clockwise by selecting the vibration resonance mode.

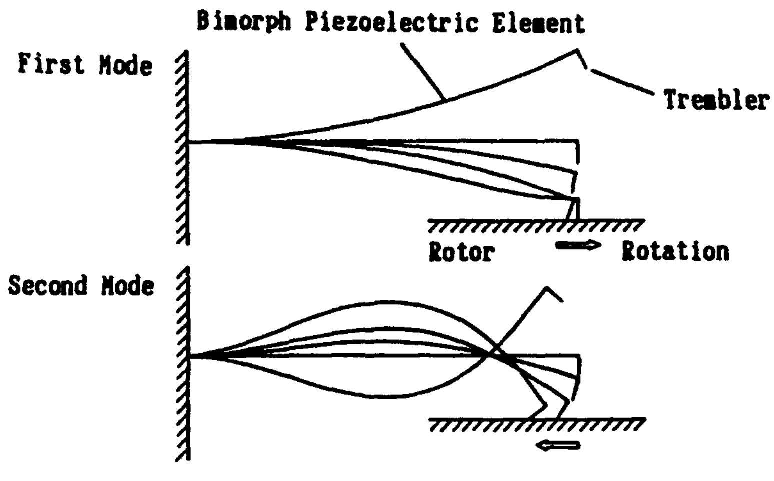

FIGURE 2 Resonance modes of piezoelectric reed

Characteristics of Piezoelectric Element

The piezoelectric element is a bimorph PZT 28 mm long x 10 mm wide x 0.5 mm thick. Figure 3 shows its piezoelectric properties. A driving voltage of 200 v produces 970 μm of displacement and 55 g of power.

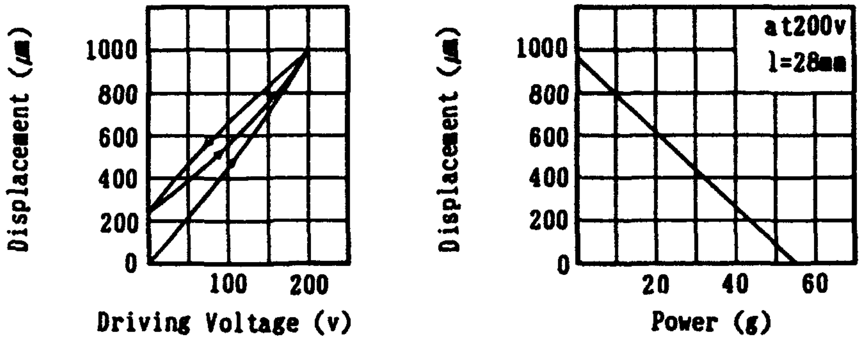

FIGURE 3 Piezoelectric properties of element

PROTOTYPE PIEZOELECTRIC MOTOR

Figure 4 schematically shows a prototype of the piezoelectric motor. The piezoelectric reed is supported by two sheets of acrylic resin plate, and they are fixed by screws to the holder . The holder can move along the x, y and z axes.

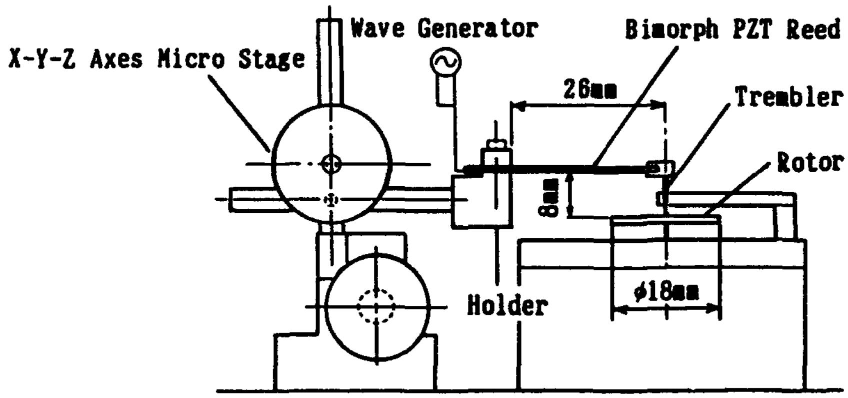

FIGURE 4 Prototype of piezoelectric motor

The trmbler is bonded onto the free end of the piezoelectric reed. It is a steel needle with a diameter of 1 mm. The rotor is designed to be small and light and require little driving force. The rotor is supported with steel ball bearings to reduce friction as much as possible . The rotor face is made of plastic, and is 18 mm in diameter.

Figure 5 shows the driving, control and measuring equipment. Three types of driving voltage waves were used in this experiment , sine , triangle and square waves. The wave generator has ranges of 0-15 V, 0-200 mA and 0 - 20,000 Hz. The driving voltage of the piezoelectric reed is amplified by a booster amplifier.

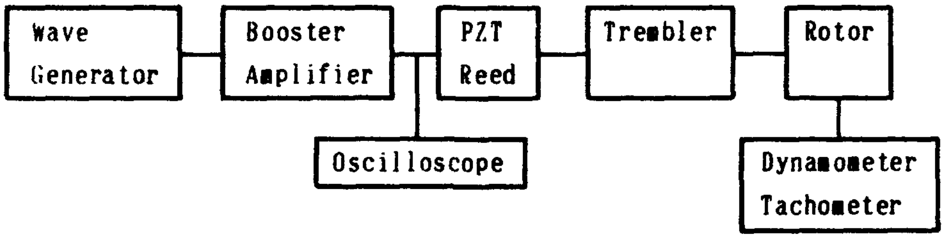

FIGURE 5 Block diagram of driving test

EXPERIMENTAL RESULTS

Rotational Speed

The rotational speed of the piezoelectric motor was measured with a noncontact tachometer. Figure 6 shows one example of the rotational speed when driven at 40 V and in the frequency range 0-300 Hz. The rotor rotated counter-clockwise at 133 Hz and clockwise at 1333 Hz, corresponding to the first and second resonance modes of the PZT reed , respectively. The maximum rotational speed was 1700 rpm clockwise and 500 rpm counter-clockwise , and the shape of the driving wave , i.e., sine , triangle or square wave, had little effect on the rotational speed.

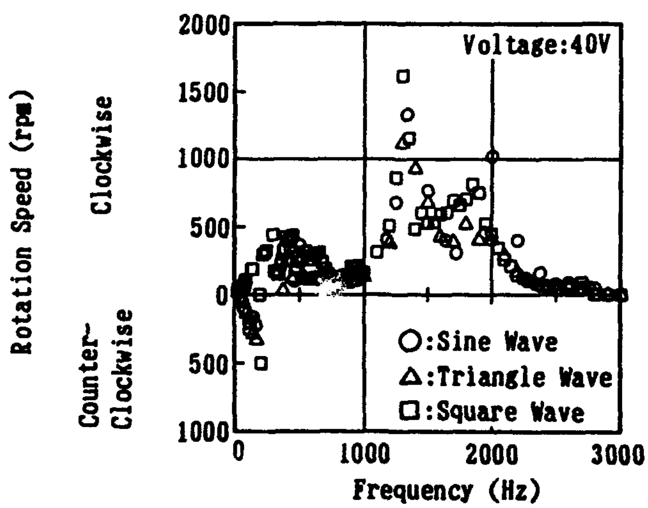

FIGURE 6 Speed of motor

Torque, Output Power and Efficiency

The output power was measured from the torque applied by the piezo-electric motor to a weight hanging from a string attached to the motor shaft. As shown in Figure 7 , there are differences in torque , output power and efficiency between counter - clockwise (133 Hz) rotation and clockwise (1333 Hz) rotation . This difference is drives from the number of the contacts per second between the trembler and the rotor of the motor. The maximum efficiency was about 18 % for clockwise rotation.

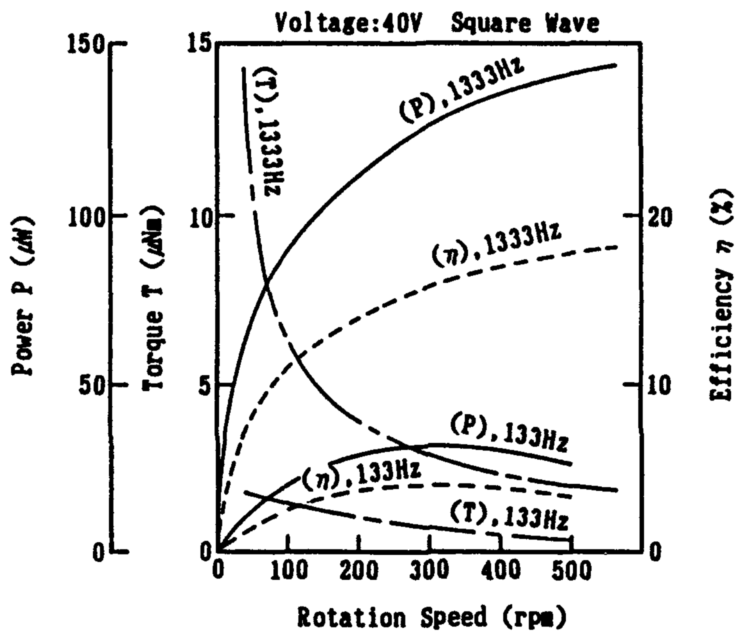

FIGURE 7 Performances of motor

Motion of The Trembler and The Rotor

The motion of the trembler and rotor was studied with an ultra- high speed video camera (Figure 8). The trembler touches the rotor and pushes its surface in the rotational direction. This motion can rotate the piezoelectric motor steadily and its rotational speed smoothly.

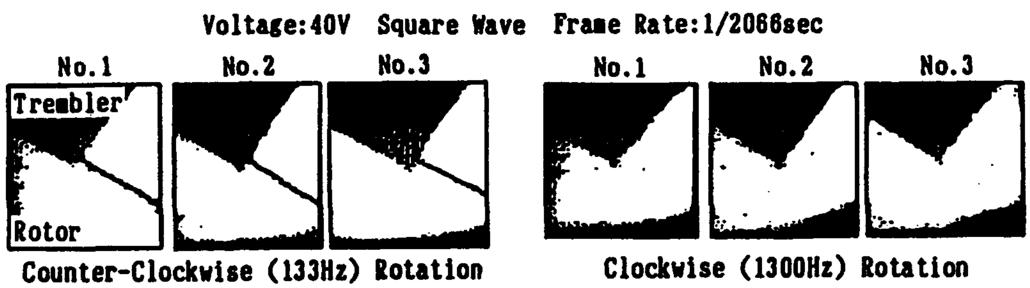

FIGURE 8 Motion of oscillating trembler

Figure 9 shows a magnified view of the motion of the trembler tip . The tip moves counter - clockwise at 133 Hz and clockwise at 1333 Hz, corresponding to the rotational directions of the piezoelectric motor.

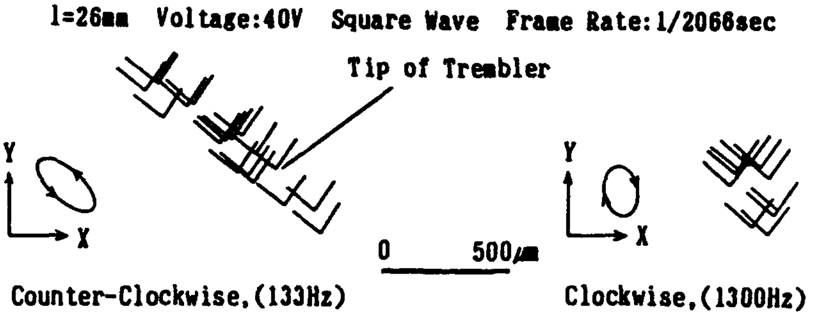

FIGURE 9 Tip motion of trembler

CONCLUSIONS

A piezoelectric micro-motor has been developed. The rotor is driven by a bimorph PZT reed with a trembler , which pushes the surface of the rotor toward the direction of rotation . The motor can be made to rotate clockwise or counter-clockwise ; the first resonance mode of the PZT reed gives clockwise rotation and the second resonance mode counter-clockwise. Rotation is smooth and steady. This micro-motor, which is small, is suitable for movable devices , such as a micro-mobile robot , a micro-robot hand or a manipulator , which cannot use conventional electro - magnetic motors. It shoud also be useful in micromachines where space is limited.

REFERENCES

1. I. Hayashi , N. Iwatsuki and M. Kawai, A Piezoelectric Cycloid Motor and Its Fundamental Characteristics, Second International Symposium on Micro-Machines and Human Science, pp.73-77, (1991).
2. H.S. Tzou , A Piezoelectric Dynamic Actuator for Micro - Isolation and Control, ibid., pp.17-27, (1991).
3. R. Matsuda, R. Kaneko , Micro - Step X Y - Stage Using Piezoelrctric Tube Actuator, MEMS, pp.137-141, (1991).
4. K. Uchino, Ultrasonic Motors, Journal of JSPE, 55-3(1989), 485.
5. K. Uchino, Piezoelectric and Electro - strictive Actuators, (1988), Morikita Publishing Corp., Tokyo.
6. F. Scire, C. Teague, Piezodriven 50 μm Range Stage with Subnanometer Resolution, Rev. of Sci. Instr., 49-12(1978), 1735.

Ferroelectrics, 1992, Vol. 134, pp. 89–91
Reprints available directly from the publisher
Photocopying permitted by license only

PdC4a

THE ACTIVE CONTROL OF SOUND REFLECTION/TRANSMISSION COEFFICIENTS USING PIEZOELECTRIC COMPOSITE MATERIALS

A J Salloway, R C Twiney, R W Whatmore and R Lane*, GEC-Marconi Materials Technology Ltd, Caswell, Towcester, Northants, NN12 8EQ, UK
*DRA Maritime Division, Holton Heath, Poole, Dorset, BH16 6JU, UK

Abstract An active noise control device has been fabricated using a 0-3 piezo-composite sensor and actuator. This device has been used with a fast feedback electronic system. The reflection and transmission coefficients have been measured in a pulse tube. The energy was reduced by up to 0.5 in active noise reduction mode and increased by up to 0.17 in active noise enhancement mode from 1.5 to 8.5kHz. With an air backed noise control device, the echo reduction was increased by up to 12dB from 1 to 8kHz.

INTRODUCTION

The principles of active noise control (ANC) have been known for many years (ref Olson), but their practical application in-air was largely limited by the available transducers and drive electronics. Major advances have been made in signal processing electronics which combined with new transducer technologies has led to the current emergence of a number of useable systems such as ear defenders using the principles of ANC. In water acoustics, the application of the principles of ANR has had similar problems. Relatively fast signal processing chips are now available, but large area transducers suitable for conformally coating a surface have been lacking. Advances in piezoelectric materials have opened up the possibility of active control of sound on relatively large area interfaces.

TRANSDUCER MATERIALS

For the sensor, a material is required which will respond to the sound pressure wave. Thus, a material with a high hydrostatic voltage coefficient (g_h) is a fundamental requirement. Further, a material which will give an output only to a hydrostatic pressure and not to other vibrational modes is important. 0-3 piezoelectric composite materials are a good choice as their hydrostatic voltage coefficient is high and so well suited to use with a head amplifier and their output due to flexure is low.

SYSTEM OVERVIEW

It is envisaged that the outside of underwater structures could be covered with the noise control system to control the degree of reflection or transmission of sound. This would require the structures to be conformally coated with the transducers. The underwater sound would be detected by the sensors which would cause the actuator to be driven. The system acts to modify the acoustic impedance mismatch at the water/material interface and can work to either reduce or enhance reflected or transmitted sound at the interface.

SENSOR TRANSDUCER

The sensor was manufactured from 2 pieces of 0-3 piezocomposite material. A bilayer sensor was formed with the poling directions opposed. The output has been measured in water to be broadband with an output level of -201.5dB re 1V μPa^{-1} at 400Hz.

ACTUATOR TRANSDUCER

The actuator was manufactured with the same material and in the same way as described for the sensor. The output in water has been found to increase with frequency with an output level of 100dB re $1\mu PaV^{-1}$ at 2.5kHz.

NOISE CONTROL SYSTEM

A noise control system has been constructed by connecting the sensor to analogue electronics which provides a phase invertion, gain and stabilising electronics. The phase of the system may be switched to allow either in phase or out of phase operation.

NOISE CONTROL MEASUREMENTS

Pulse Tube Measurements

The noise control system has been measured in a 7.6m long pulse tube with a diameter of 70mm. The sample was positioned half way up the pulse tube. A sound pulse was generated at the bottom of the tube and this wave travelled towards the sample. The reflected pulse was compared with the incident pulse to obtain the reflection coefficient. Similarly, the transmitted pulse was compared with the incident pulse to obtain the transmission coefficient. The reflection coefficient was measured with the system off and operating in both phases. With the system operating in either phase, the reflection coefficient was increased by up to 0.06 from 1.5 to 4.5kHz. Above 4.5kHz, the coefficient was reduced in ANR mode by up to 0.22 and increased in ANE mode by up to 0.05.

The changes in the transmission coefficient were larger than those for the reflection coefficient. From 1.5 to 9kHz, the transmission coefficient was reduced by up to 0.42 in ANR mode and increased in ANE mode by up to 0.22.

The energy, represented by the square of the transmission and reflection coefficients, can be seen to be reduced by the noise control device in active noise reduction (ANR) mode between ~1.5 and 8.5kHz and increased in active noise enhancement (ANE) mode over the same bandwidth as compared to the off state. These results are presented in Figure 1.

The noise control device was backed with a closed cell foam so that virtually all the sound would be reflected from the noise control device. Figure 2 presents the changes in echo reduction achieved with the system off and in both ANE and ANR modes. An active noise reduction between 4 and 12dB was observed from 1.5 to 8kHz and an enhancement of up to 4dB between 2 and 9.75kHz.

The time responses showing the incident and reflected signals with the system off and in ANR mode are presented in Figure 3. The reflected pulse can be observed to be reduced by more than 6dB with the system operating.

CONCLUSIONS

A noise control device has been manufactured using 0-3 piezocomposite material as both the sensor and the actuator. Noise control has been demonstrated in both the tank and the pulse tube. The echo reduction has been increased by up to 12dB from 1.5 to 8kHz in ANR mode in the pulse tube.

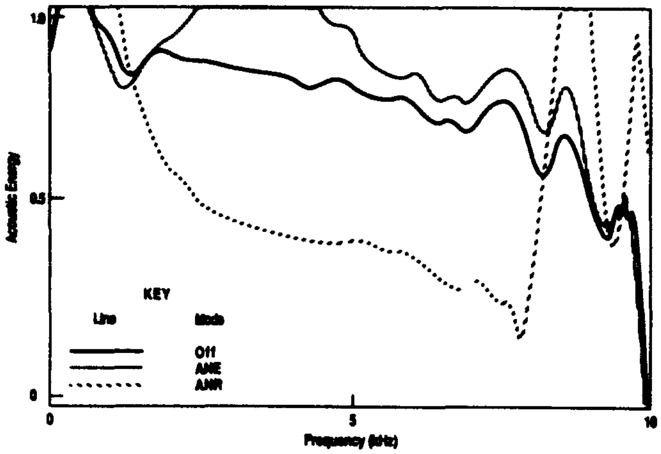

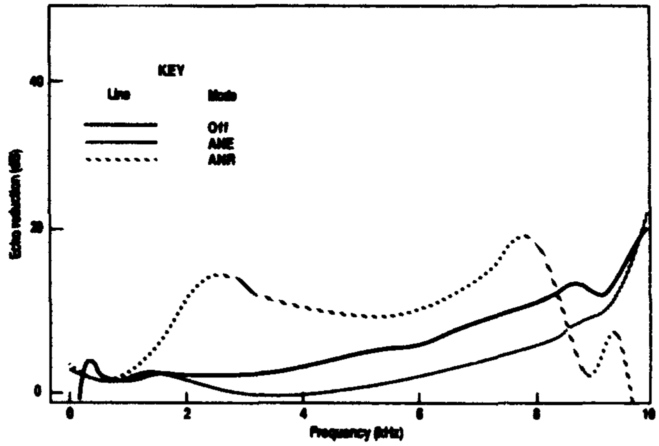

Fig 1 Energy versus frequency with the system off and operating in both phases

Fig 2 Echo reduction versus frequency with system off and operating in both phases

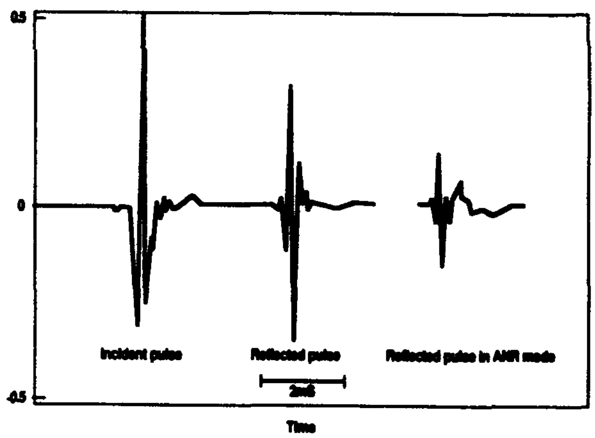

Fig 3 Time traces of incident and reflected waves with the noise control device off and operating in ANR mode with the device backed with Evazote

ACKNOWLEDGEMENTS

GEC-Marconi wishes to thank D Townend at DRA, Maritime Division, Holton Heath, for the pulse tube measurements during this work programme. This work was supported by the UK Defence Research Agency through the Holton Heath Establishment.

REFERENCE

1. Electronic Sound Absorbers, Olsen & May, JASA, pp1130-6, (1953).

Ferroelectrics, 1992, Vol. 134, pp. 93–98
Reprints available directly from the publisher
Photocopying permitted by license only

PdC13

INVESTIGATIONS INTO PIEZOELECTRIC SPARK GENERATORS

P. GONNARD, C. GARABEDIAN, H. OHANESSIAN, L. EYRAUD
Laboratoire de Génie Electrique et Ferroélectricité, INSA
20, avenue A. Einstein, 69621 VILLEURBANNE FRANCE

Abstract : The theoretical energy conversion under uniaxial stress is studied. A theoretical model is based on an electrical equivalent circuit of the whole system. The experimental results are compared to the simulated ones which show anomalously high electromechanical values (d_{33} , ε^T_{33} , s^E_{33}) and losses ($tg\delta$) during the impact.

I - INTRODUCTION

Physical phenomena occuring during a mechanoelectrical conversion are complex due to the simultaneous occurence of high stresses, high electric fields and resonant phenomena in the case of dynamic compression. The purpose of this paper is to present the modeling of a piezoelectric spark generator using classical mechanoelectrical analogies. Some fundamental aspects of a dynamic compression (pulsed stress generated by impact) are analysed. Experimental results are compared to the modeling and discussed.

II - ANALOG MODELS AND FIGURES OF MERIT

II-1 Equivalent circuit for length expander bar with parallel mechanical stress

The piezoelectric element (area A=5.72.10^{-6} m^2, length ℓ=5 mm) is assumed to be excited only on a longitudinal mode (L>>Diameter). One face of the bar is in contact with a base having an infinite stiffness and mass and the mechanical force is applied to the other face (Fig.1a).

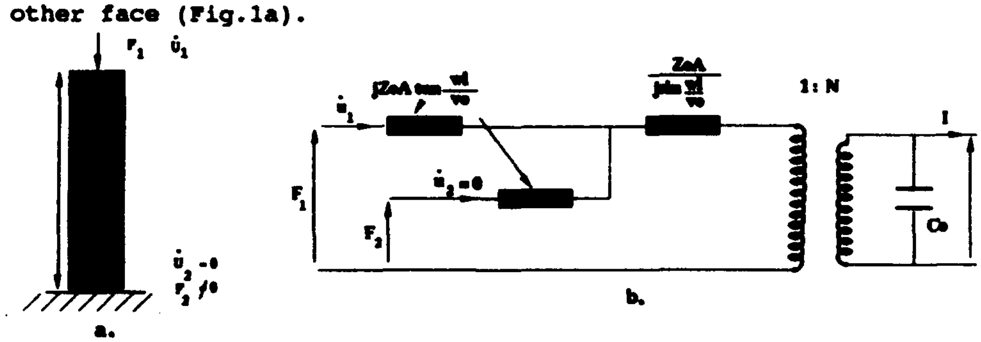

FIGURE 1 : The piezoelectric bar and its equivalent circuit.

The equivalent circuit for the bar is developed using the motionnal equation and the piezoelectric equation [1], [2] with the hypothesis of a constant electric field in the bar (Fig.1b)

F_1, F_2 and $\dot{u}_1, \dot{u}_2$ are respectively the forces and particle velocities on each face,

$$N = \frac{\text{Mechanical force (F)}}{\text{Electric voltage (V)}} = \frac{\text{Electric current (I)}}{\text{Face velocity } (\dot{u})}$$ is the

transformer ratio. All these terms can be expressed as a function of the usual piezoelectric and mechanical coefficients [1] :

$$C_o = \frac{\varepsilon^S_{33} A}{\ell} \qquad v_o = (\rho\ s^E_{33})^{-1/2} \qquad Z_o = \rho\ v_o \qquad N = \frac{A}{\ell}\frac{d_{33}}{s^E_{33}}$$

Both terms of the mechanical section can be further simplified near the fundamental resonance corresponding to $\ell = \frac{\lambda}{4}$ (vibration node on face 2). They are equivalent to first order with lumped circuit values given by :

$$C_1 = \frac{8}{\pi^2}\frac{\ell}{A} s^E_{33} \qquad\qquad L_1 = \frac{\rho A \ell}{2} = \frac{\text{Mass}}{2} .$$

The equivalent network of the piezoelectric bar working as a mechanoelectrical converter is given in Figs.2a and 2b after transforming the mechanical elements L_1 and C_1 across the electrical side.

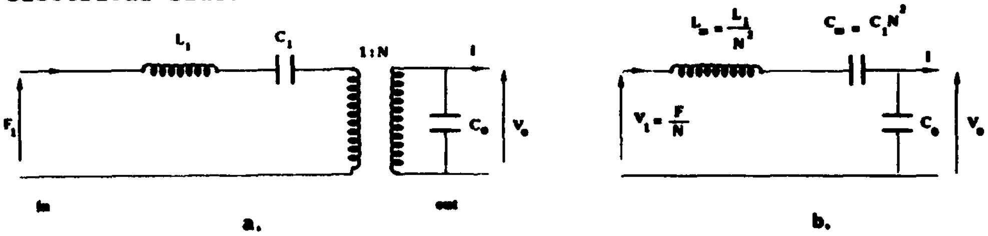

FIGURE 2 : Equivalent networks a) with and b) without the electromechanical transformer.

The low frequency capacitance is $C_{LF} = C_m + C_o$ with $C_m = k^2\ C_{LF}$ where k is the dynamic coupling factor.

II-2 Figures of merit in short and open circuit

The dynamic compression is generally achieved by the impact of a mass. So the resulting frequency of the stress will be the whole system resonance frequency.

Under short circuit conditions the electric charges are limited only by the mechanical resistance R_m in series in the motionnal branch and under open circuit conditions, the voltage is controlled by both of the mechanical resistance R_m and the electrical resistance R_o (Fig.3).

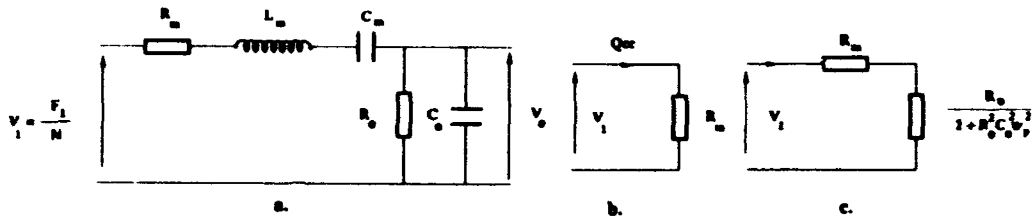

FIGURE 3 : Equivalent circuits for : a) General case ; b) Short circuit at f_s ; c) Open circuit at f_p

At the resonance frequency f_s ($L_m C_m \omega_s^2 = 1$) the electric charges in short circuit are given by : $Q_{cc} = Q_s d_{33} F_1$.

The classical figure of merit d_{33} is multiplied by the mechanical quality factor $Q_s = L_m \omega_s / R_m$

At the resonance frequency f_p the output voltage Vo is given by :

$$E_o = \frac{V_o}{\ell} = \frac{\sqrt{1 + tg^2\,\delta}}{k^2\, tg\delta + (1+tg^2\,\delta) Q_p^{-1}}\, g_{33}\, T_1$$

where $tg\delta = (R_o\, C_o\, \omega_p)^{-1}$, $Q_p = L_m\, \omega_p / R_m$

The classical figure of merit g_{33} is multiplied by an expression depending on the loss tangent tgδ and the mechanical quality factor Q_p .

II - 3 ELECTRICAL EQUIVALENT CIRCUIT EXTENDED TO THE WHOLE SYSTEM

In industrial applications, the piezoelectric ceramic is inserted into mechanical environments in order to hold it correctly on one hand and to produce the impact on it on the other hand.

The mechanical pulse is achieved by a spring loaded hammer or a falling steel ball striking an anvil located at the top of the ceramic, the bottom being clamped (Fig.4a). Taking into account these new mechanical parts constituting the high voltage generator a complete equivalent circuit is established corresponding to the mechanical equations at the two interfaces (Fig.4b) [3].

Anvil-falling ball interface : $F = m_1 \ddot{x} = -k_H (x-y)$

Anvil-ceramic interface : $F_1 = F_H - k_H (x-y) = M\ddot{x} - k_H (x-y)$

The initial conditions are given by the initial velocity $V_o = \dot{x}_o$ of the mass m_1 which transfers its kinetic energy to the system.

$$x(o) = y(o) = 0,\ \dot{x}(o) = V_o\ ,\ \ddot{x}\,(o) = 0$$

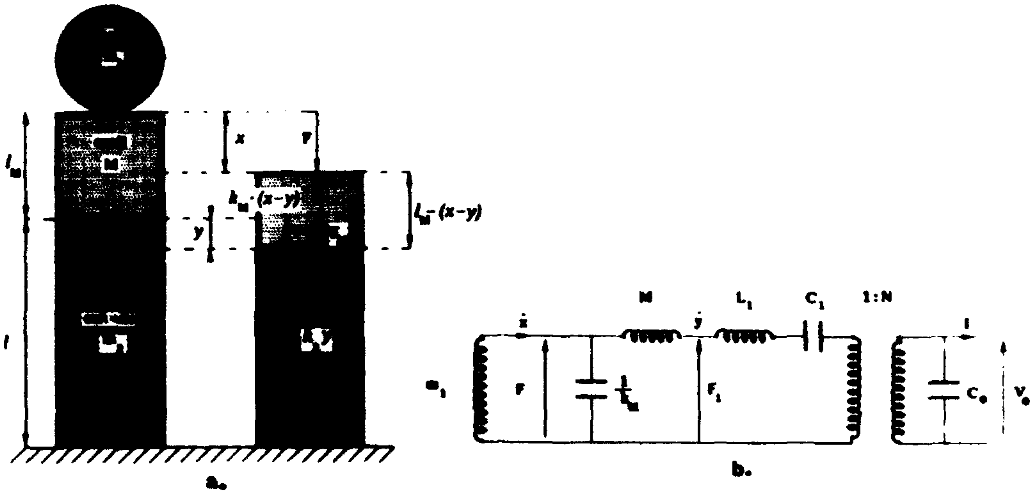

FIGURE 4 : Equivalent circuit of the spark generator

Finally, the equivalent electrical circuit of Fig.4b is given in Fig.5 in which the losses are introduced.

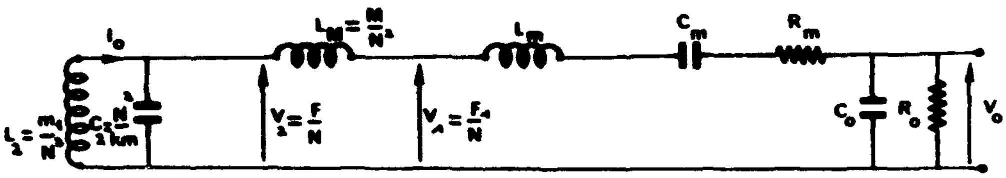

FIGURE 5 : Electrical equivalent circuit of the whole generator

III - THEORETICAL MODELING

III - 1 GENERAL METHODS

Usual networks resolution methods yield a differential equation of n^{th} order in the general case (here n = 9) describing the evolution of the S signal with the time at the ends of the piezo bar

$$\sum_{i=1}^{n} a_i \frac{d^i S(t)}{dt^i} = 0 \qquad (1)$$

where a_i are a function of network parts.

Laplace transforms have been largely used in order to solve the differential equation (1). A computer program solving an n^{th} order s-polynomial expression has been performed using the mathematical tools supplied by the MATLAB environments. The final solution S(t) then can be written as a finite sum of exponential terms (2).

$$S(t) = \sum_{i=1}^{n} A_i \exp(\tau_i \cdot t) \qquad (2)$$

where A_i are the i^{th} rank coefficients of the exponential
A_i are a function of network parts and initial conditions
τ_i are the i^{th} rank roots.

III - 2 PARTICULAR TIMES t_1 AND t_2

The description of pulsed stress phenomena can be split into three distinct time intervals.

a- from $t=0$ to $t=t_1$, the hammer applies a force onto both anvil and ceramic. The electrical equivalent scheme is given Figure 5.

The force applied by the hammer to the anvil reaches a maximum value then decreases until 0 at $t=t_1$. The solution S_1 (t) is given by (2).

b- From $t=t_1$ to $t=t_2$, no force is now applied to the anvil but the piezobar keeps on being stressed by the anvil within a decreasing force. (Fig.6b). At $t=t_2$ this force F_c equals zero. In this time interval, the solution S(t) has the same expression as relation (2) where only the indices are changed.

c- At $t>t_2$, as hypothesis we take into account the fact that no tensile forces can be applied to the piezo bar. This yields a third electrical equivalent scheme given Fig.6c.

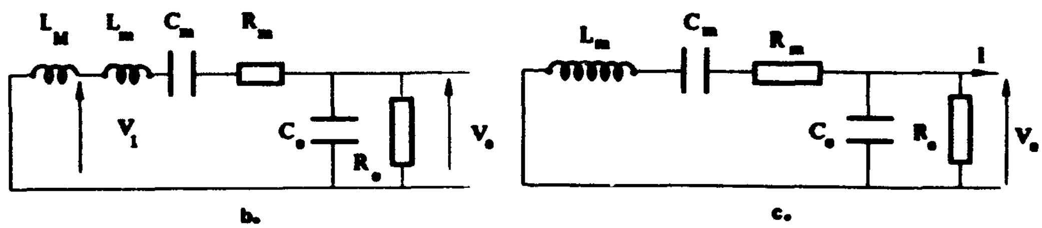

FIGURE 6 : Equivalent schemes at : b) $t_1<t<t_2$ c) $t>t_2$

The solution S(t) is expressed by (2) where only the indices are changed again.

Note : Both open circuit and short circuit conditions can be simulated, short circuit conditions just being the limit case of open circuit conditions when $R_o \to 0$.

IV - EXPERIMENTAL RESULTS AND DISCUSSION

The pulsed stress is performed by a 21.6 g steel ball falling from a 33 cm height on the anvil . The open and short circuit characteristics are recorded by a digitizing oscilloscope and loaded by the computer. The fine adjustment of time and amplitude parameters constituting the equivalent electrical scheme yields both experimental characteristics. Fig.7 shows the accuracy of the simulation.

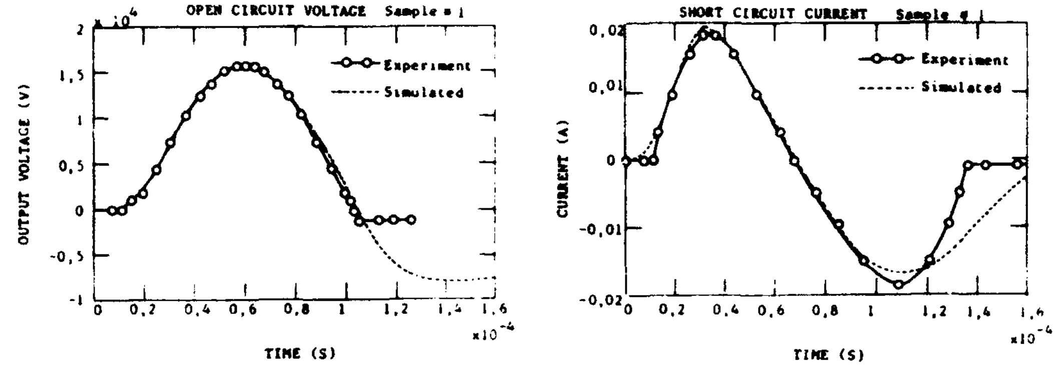

FIGURE 7 : Experimental and simulated characteristics

The mechanical and piezoelectric coefficients values measured at low level (LL) following the IEEE standards [4] are compared to those obtained by the simulation (HL). For samples # 1 and # 2, the results are given in table 1. It shows that the real part of ε^T_{33} is largely increased as well as the loss tangent tgδ. Moreover the ratio $d_{33}(HL)/d_{33}(LL)$ may be greater than 2 and non linearities on the s^E_{33} coefficient are observed. By the same time, the increase of the coupling factor is less in the case of sample # 1.

In terms of open circuit voltage Vo, available total charges Q and energy W, it seems that large non linearities would yield larger values of Q and W. However the voltage Vo is limited by the large increase of the loss tangent.

d_{33} : pC/N s^E_{33} : $10^{-12}m^2/N$	d_{33} LL	d_{33} HL	$\varepsilon^T_{33_r}$ LL	$\varepsilon^T_{33_r}$ HL	k_{33} LL	k_{33} HL	tgδ % LL	tgδ % HL	s^E_{33} LL	s^E_{33} HL
Sample #1	245	410	930	2418	0.67	0.69	0.7	16.6	16.1	16
Sample #2	210	550	714	1928	0.67	0.83	0.65	9.47	15.6	29.6

TABLE 1 : Mechanical and piezoelectric coefficients at low and high levels

CONCLUSION :

Using an analog model the experimental behaviour of a piezoceramic subjected to a resonant uniaxial stress is fully described. It is confirmed that both of the mechanical and piezoelectric coefficients and the loss tangent present very high values during the compression.

REFERENCES

1 W.P. MASON, Physical Acoustics, Vol.1, Part A (1964)
2 P. GONNARD, P. CHAMP, L. EYRAUD, Power Sonic and Ultrasonic Transducer Design, 25-40, Springer Verlag (1988)
3 H. OHANESSIAN, Thèse, LYON, France, N°89-ISAL 0020, 1989
4 IEEE Standards on piezoelectricity, ANSI/IEEE Std 176-1978

Ferroelectrics, 1992, Vol. 134, pp. 99–104
Reprints available directly from the publisher
Photocopying permitted by license only

PdP131

LOW SIGNAL ANALYSIS OF PIEZOELECTRIC TRANSFORMERS

R. PÉREZ, L. BENADERO, A. ALBAREDA, M. TRESANCHEZ, J.A. GORRI and J.L. VILLAR
Dept. Fisica Aplicada. E.T.S.E.T. Barcelona . U.P.C.
J. Girona Salgado s/n. 08034 BARCELONA (SPAIN)

Abstract

The transmission matrix, that depends on frequency, has been proved to be useful to characterize piezoelectric transformers behaviour at low signal. It shows at which frequency the device is able to step up the voltage and which parameters describe its behaviour, taking into account not only the voltage but also the output current.

In order to compare their performances, these parameters were measured or computed for ceramic disc-shaped transformers, working in their first or higher modes, and also for plate-shaped ones. Parameters G_o and Z allow an analysis of the suitability of a device for each application, depending on input-output impedance and voltage gain required.

An analysis of the validity boundaries of this model has been made, taking into account that mechanical quality Q falls down when stress and temperature increase.

INTRODUCTION

Some types of the piezoelectric transformer have been proposed[1-5]. The basic aim of them was a higher voltage gain, not taking into account the load current capability.

In this paper we propose the transformer analysis considering equally both aspects. The use of the transmission matrix in order to describe linear behaviour has been proposed in a previous paper [6].

In contrast to resonators, these bi-port devices have four characteristic frequencies for each mode, instead of two. Each coefficient of the transmission matrix becomes equal to zero at a different characteristic frequency.

CHARACTERISTIC PARAMETERS

Maximum gain of the transformer corresponds to the frequency f_A, at which the coefficient A, of the transmission matrix, takes its minimum value, specifically the real part of A is null and the imaginary one is nearly constant. This situation corresponds to resonance when the primary is shorted and the secondary open.

Close to f_A, coefficients B and C are almost purely imaginary and they obey the relationship $B \cdot C = -1$. We define mean impedance Z as the reciprocal of the transadmittance modulus at frequency f_A , $Z = 1/j \cdot C$.

If Z_g is the generator output impedance and Y_l is the load admittance, the voltage gain $G = V_2/\mathcal{E}$, defined as the ratio between the output voltage and the e.m.f. of the generator is:

$$1/G = A + B \cdot Y_l + C \cdot Z_g + D \cdot Z_g \cdot Y_l$$

In the most advantageous case in which $Z_g = 0$ and $Y_l = 0$, we have:

- Maximum gain $G_0 = 1/|Amin|$
- Input impedance $Z_{in} = Z/G_0$
- Output impedance $Z_{out} = Z.G_0$

The bandwidth Δf is the allowed deviation from f_A without losing the gain. Reactive component of Y_l and Z_g can be compensated by properly shifting the frequency.

Coefficient D, reciprocal of the current gain, ought to be small $|D| \ll G_0$ in order to increase the range of load impedances.

In order to decide the best electrode arrangement, all these parameters can be obtained by numeric calculation using a simplified model. Here it is assumed that the device is infinitely thin. The wave function is the superposition of the two functions that we would obtain shorting the primary or the secondary respectively. For both functions, primary and secondary charges are calculated, which furnishes us the admittance matrix.

COMPARATIVE ANALYSIS AMONG DIFFERENT TYPES OF TRANSFORMERS

In order to compare them, we may represent each device as a point in a $\log(G_o)$-$\log(Z)$ plot that also gives us Z_{in} and Z_{out} directly (see Figure 1). The parameters G_o and Z must be related with the kind of transformer, the characteristics of the material it is made with, the sizes and electrode arrangement.

-Material characteristics:

G_o	depends on	Q	(mechanical quality factor)
	and on	k^2	(electromechanical coupling coeficient)
Z	depends on	ε^{-1}	(electrical permitivity)
	and on	$c^{-1/2}$	(elastic coeficient)

-Sizes: (it depends on type of transformer)

For the Rosen-Jaffe transformer[1]:

G_o depends on the ratio L/t (length / thickness)

Z depends on the ratio L/w (length / width)

For a disc-shaped transformer working on its radial mode:

G_o does not depend on size

Z depends on the ratio t/D (thickness / diameter) and on the working mode.

-Electrode arrangement:

Both parameters depends on them, but the relation is not easy. Numerical calculation must be done in order to decide the best arrangement.

Different transformers, with extremes sizes within each type of transformer, are described in the figure 1. Radial modes in disc shaped transformers have been included, working in fundamental, first and second overtones, as will be described later. In all cases PXE41 material has been used, because of its good quality factor.

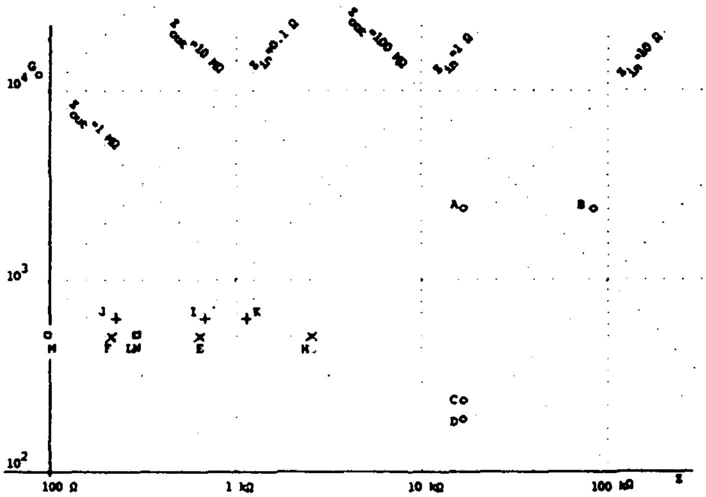

FIGURE 1 : Plot of maximum gain G_o, and main impedance Z for the following devices:

ROSEN-JAFFE :

	t	L	w
A[3]	1mm	50mm	25mm
B[3]	1	50	5
C[3]	10	50	25
D[3]	1	4	2

RADIAL 1st MODE

	t	D
E[1]	3mm	50mm
F[2]	1	50
G[2]	12	50
H[2]	1	4

RADIAL 2on MODE

	t	D
I[1]	3mm	50mm
J[2]	1	50
K[2]	1	10

RADIAL 3rd MODE

	t	D
L[1]	3mm	50mm
M[2]	1	50
N[2]	1	16

1) Measured experimentally

2) Calculated from measures over similar transformers

3) Calculated theoretically from the model.

USING HIGHER MODES IN A DISC TRANSFORMER

Mean impedance Z must be decreased when higher current is required. This can be obtained by increasing diameter/thickness ratio or by using higher overtones, due to their higher working frequencies. The decrease of Z in these cases can be appreciated in the G_o-Z representation (see Figure 1).

Design of electrode arrangement must take into account the presence of nodal lines which are characteristic of the higher overtones. Figure 2 represents stress field as a function of the radius for the second overtone. The primary electrodes must be split in accord with that line, and electric interconnection between the two zones must be inverted.

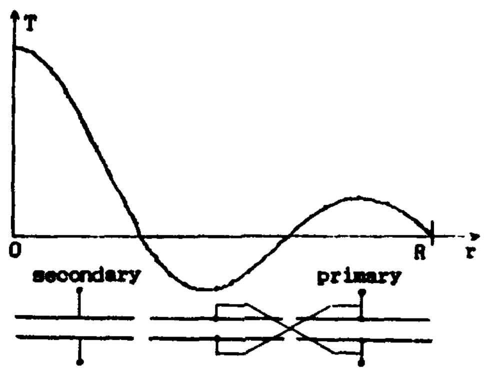

Figure 2: plot of stress T_r+T_θ versus the radius r, and electrode arrangement for the second overtone in a radial transformer.

In the Figure 2 the central zone is completely occupied by the secondary. This assignation is more adequate because stress is higher in that zone. The stress is weaker near the nodal line, so a reduction in secondary electrode extension could be convenient in order to maximize voltage gain. In this case, the rest of the internal zone could be used also as a primary.

The order of the mode is limited by the fact that wavelength must be rather higher than device thickness.

NON LINEAR BEHAVIOUR

In order to obtain a high voltage between secondary electrodes it is intended to have an amplitude of stress T as great as possible. So, it will be strong enough to produce non-linear effects. Then, the behaviour of a transformer can be described by the preceding linear analysis only as a first order approximation .

Moreover, power dissipation can notably increase the temperature of the ceramic. Both facts will decrease the mechanical quality factor Q, decreasing the gain G_o. Furthermore, they modify the elastic constants, shifting the optimum working frequency.

Stress strong enough to depolarize the ceramic must never be applied, but the reasonable limit of T becomes from the stress dependence of Q. Taking into account that E_2 is proportional to $E_1 \cdot Q(T)$, the relation between E_1 ($\propto T/Q(T)$) and E_2 ($\propto T$) can be obtained, as it is shown in Figure 3.

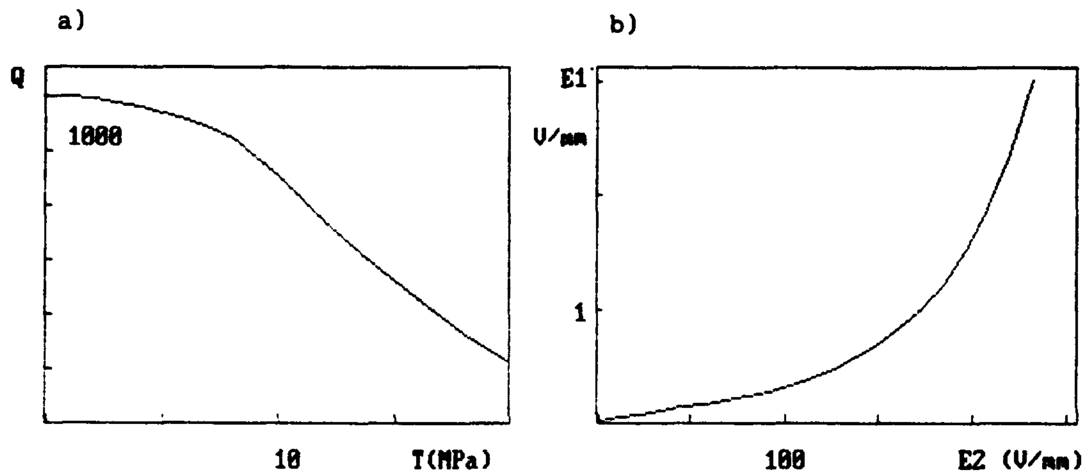

FIGURE 3: a) Stress dependence of mechanical quality factor Q.
b) Dependence between the electric fields in the primary and the secondary, E_1 and E_2.

It can be seen that E_2 cannot be higher than a saturation value E_S in spite of the increase of E_1. If a device must keep a high gain and low dissipation power, the field E_2 must be lower than E_S.

E_S is a characteristic value of the material, so the highest output voltage is proportional to the distance between the secondary electrodes (the thickness for the radial transformer).

The rate of heat generation is proportional to $T^2/Q(T)$, so it can be strongly increased by a rise of stress T. The resulting temperature increase $\Delta\theta$ will produce an additional decrease of Q. Since $\Delta\theta$ depends also on the external thermal conductivity, which is weak due to mechanical uncoupling of the device, the time needed to reach thermal stability is often long (10 minutes for a 3 mm. thickness device).

According to that, two kinds of analysis must be done: the first one can be applied just after turning on the transformer, when only a stress-dependence of Q must be considered, and the second one must be applied at the steady state, when the temperature effect is also important.

The working frequency shifting, due to the dependence c(T), force us to use the transformer also as an oscillator. To serve this function, a third pair of electrodes may be useful to feedback the oscillator circuit. The dependence of the frequency with the amplitude makes unstable the optimum point, leading to a frequency where performances are slightly worse than the optima.

CONCLUSIONS

In the design of a piezoelectric transformer, it must be taken into account the following facts:

The most appropriate working frequency in order to increase voltage, is f_A, which corresponds to the resonant frequency when the primary is shorted and the secondary is open.

Linear behaviour is mainly characterized by the parameters G_o and Z, and also by Δf and D.

Radial transformers are adequate if the required gain is not too high. Output current can be increased using higher overtones.

Linear analysis cannot give the working boundaries of the device. Maximum output voltage depends on the distance between secondary electrodes and on the function Q(T), characteristic of the material.

Heat dissipation must be considered in devices continuously working. It will determine the working temperature and the value of Q.

Acknowledgements:

This work is a part of the project (TIC91-1038) supported by Spanish C.I.C.Y.T.

REFERENCES

1. H.Jaffe, IEEE Trans. on electr. dev., ED-16, (6), p.557 (1969)
2. Li Long Tu et al., Ferroelectrics, 28, p.403 (1980)
3. Y. Kodama et al., Sumimoto Electric Technical Review, 14, p.79 (1970)
4. R.J.Kraszewski et al., J. Acoust. Soc. Am., 90, (5), p.2769 (1991)
5. R.Pérez et al., I Reunión Nacional Electrocerámica, El Escorial (Spain), p.75 (1991)
6. R.Pérez et al., XXIII Reunión Bienal R.S.E. Física, Valladolid (Spain), p.212 (1991)

Ferroelectrics, 1992, Vol. 134, pp. 105–110
Reprints available directly from the publisher
Photocopying permitted by license only

PdP133

ACCURACY OF THE FORMULAS USED FOR THE CHARACTERIZATION OF PIEZOELECTRIC THICKNESS MODE RESONATORS WITH IMPEDANCE ANALYZERS.

J. L. SAN EMETERIO PRIETO
Instituto de Acustica, CSIC. Serrano 144, 28006 Madrid (Spain).

Abstract
The resonance method allows the determination of different elastic, dielectric, and piezoelectric constants of the material using an adequately shaped sample. The accuracy of the relationships between the measured electrical input impedance quantities and the material constants is of capital importance. In the International Standards[1-2] these relations, and consequently the derived formulas, are based either on the exact one-dimensional expression of the input impedance of an ideal lossless resonator, or on the simplified (Butterworth-Van Dyke) equivalent circuit. In this paper, the accuracy of equations frequently used for the measurement of the longitudinal acoustic velocity, v_t^D, the thickness electromechanical coupling coefficient, k_t, and the *mechanical quality factor*, Q_m are analyzed. The exact one-dimensional model of a thickness expander piezoelectric resonator, with a rigorous account of the internal mechanical losses, is taken as a reference.

INTRODUCTION.

Disk shaped piezoelectric ceramics and composite piezoelectric materials play an important role in the development of transducer devices. The material constants of the piezoelectric resonator and the 'effective' material parameters of the composites[3] (considered as a new homogeneous piezoelectric material) are a key in the global performance of the transducers. Some of these relevant constants and parameters, can be obtained from the measurement of the electrical input impedance of a material sample using an impedance analyzer. Formulas relating the measured impedance quantities to the material constants and parameters, are derived from the analytical expression of the electrical input impedance of a vibration mode assuming different approximations.

In this work, the expression of the electrical input impedance of the lossy piezoelectric resonator[4], shown in the Apendix (Eq. (A1)), is

taken as a reference in the analysis of the accuracy of well-known characterization formulas. This expression is exact under the following assumptions: linear theory of piezoelectricity, one-dimensional mode of vibration and negligible dielectric and piezoelectric losses. The complex propagation wave number (γ^{*}/d) and the complex electromechanical coupling coefficient k_t^{*} account for the mechanical losses. In the particular case of tan $\delta_m = 0$, equation (A1) reduces to the well-known expression for the ideal lossless thickness piezoelectric resonator[5] .

The procedure used to analyze the accuracy of some frequently used characterization formula, is as follows:

a) Assumed values of the parameters k_t , Q_m , C_0^S ,and $f_2 = v_t^D / 2d$, are used to generate impedance data using Eq.(A1). These assumed values are the "input" or "exact" parameters.

b) The conventional material characterization formula are applied to the previously generated impedance data in order to calculate the "approximate" values of the parameters.

c) The comparison between the "approximate" and the "input" parameters gives the accuracy of the characterization formula.

d) The percent of the relative error, with respect to the initial "input" parameters is taken as a figure of merit, defined as:

$$\%(\ .) = 100\ (\text{"true" value} - \text{"approximate" value}) / \text{"true" value.}$$

A similar procedure ,for the analysis of the accuracy of some relationships between resonator parameters and impedance quantities, has been previously used by Martin[6] and Shibayama[7], taking as a reference the expression of the input impedance of the simplified (Butterworth-Van Dyke) RLC equivalent circuit. It has also been used to test the accuracy in the determination of radial mode constants[8] .

In the following, an attenuation coefficient directly proportional to the frequency, and consequently a mechanical loss tangent independent of frequency is assumed. The case of small values of k_t and Q_m is specially considered.

MEASUREMENT OF v_t^D AND k_t

In the International Standards[1-2] the equations for the measurement of

the wave velocity v_t^D , and the electromechanical coupling coefficient k_t ,are both derived from the expression of the input impedance of an ideal lossless resonator.

When the dissipative terms are null ($\tan\delta_m = 0$,in Eq. (A1)), there are only two single frequencies of interest around each resonance, which correspond to the admittance and impedance maxima (f_1 and f_2 respectively). The following conventional equations are obtained from $Z_{in}(f_1) = 0$, and $Y_{in}(f_2) = 0$, after the substitution of f_s for f_1 and f_p for f_2

$$v_t^D = 2\, f_p\, d \qquad (1)$$

$$k_t^2 = \frac{\pi f_s}{2 f_p} \tan \frac{\pi (f_p - f_s)}{2 f_p} \qquad (2)$$

being f_p the frequency of the maximum input resistance and f_s the frequency of the maximum input conductance.

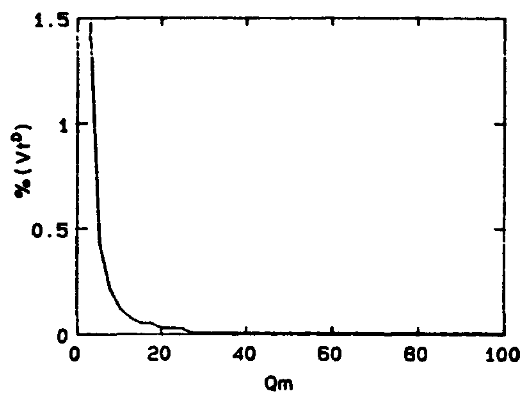

FIGURE 1. Percent error $\%(v_t^D)$ as function of Q_m .

Figure 1 shows the percent error $\%(f_p)$ when using Eq.(1) for the determination of v_t^D . This error depends only on the discrepancy between f_p and f_2 , since the possible inaccuracy in the measurement of the thickness d is not considered in this analysis. The percent error , increasing with the mechanical losses, is less than 1.5% in the extreme case of $Q_m = 3$. In addition the error is independent of k_t.The determination of f_p from high overtone resonances is sometimes recommended [1], being $v_t^D = 2 f_p^{(m)} d / m$, with $m = 3,5,7$ .The percent error in f_p (and therefore in v_t^D) when using the overtone m=5 is

2.5% for $Q_m = 3$ .The good accuracy of Eq. (1) can be noticed.
Figures 2.a and 2.b show the percent error $\%(k_t)$ when using Eq. (2) for the determination of the electromechanical coupling coefficient. The percent error is function of both k_t and Q_m "input" constants. A strong increase of the error in the case of high mechanical losses and low coupling coefficient can be noticed (52% when $k_t = 0.3$ and $Q_m = 3$). However, for a normal PZT ceramic material (i.e., $k_t = 0.5$, $Q_m = 100$) the error is completely negligible (0.038%). In the case of a typical ceramic-polymer composite (i.e., $k_t = 0.7$ and $Q_m = 20$) the error 0.16% ,is also very low.

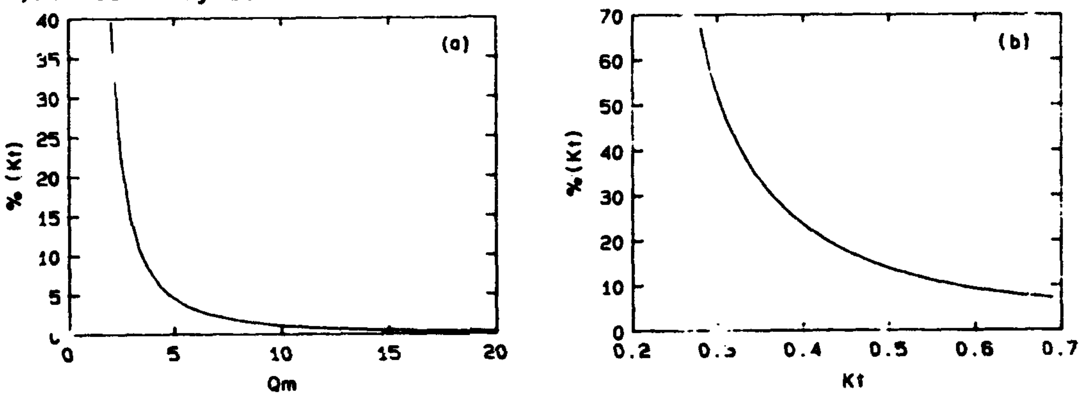

FIGURE 2. Percent error $\%(k_t)$ as function of the input parameters. a) $k_t = 0.5$; b) $Q_m = 3$.

A frequency sweep with 1900 data points, in the frequency interval ($0.7f_2$ - $1.01f_2$) has been used in the computation of the percent errors previously presented. The same frequency sweep will be used in the following.

MEASUREMENT OF Q_m

The mechanical quality factor Q_m is a parameter of key importance for the piezoceramics characterization and, consequently, for the design of ultrasonic transducers.. The accuracy of the following expressions is analyzed in this paper:

$$Q_m = f_p^2 / (2 \pi f_s |Z_m| C_0^T (f_p^2 - f_s^2)) \tag{3}$$

$$Q_m = f_s / \Delta f \tag{4}$$

where $|Z_m|$ is the minimum of the impedance module at the fundamental resonance, C_0^T is the free capacitance, and Δf is the bandwidth at half of the maximum input conductance. Eq. (3) is the expression for Q_m proposed by the (1961) IRE Standards on Piezoelectric Crystals[2]. Eq.(4) corresponds to the ratio of the frequency f_s to the power bandwidth [1,9].

Figures 3.a and 3.b show the percent errors $\%(Q_m)$ in the determination of the mechanical quality factor Q_m when using Eq. (3). C_0^T has been determined from the computed input reactance at 1kHz.Figures 3.c and 3.d show the percent error in the determination of Q_m with Eq. (4). After the determination of f_s ,the frequency intervals $(0.5f_2-f_s)$, and $(f_s-1.5f_2)$,with 1900 data points in each case, have been used for the determination of the half bandwidth frequencies.

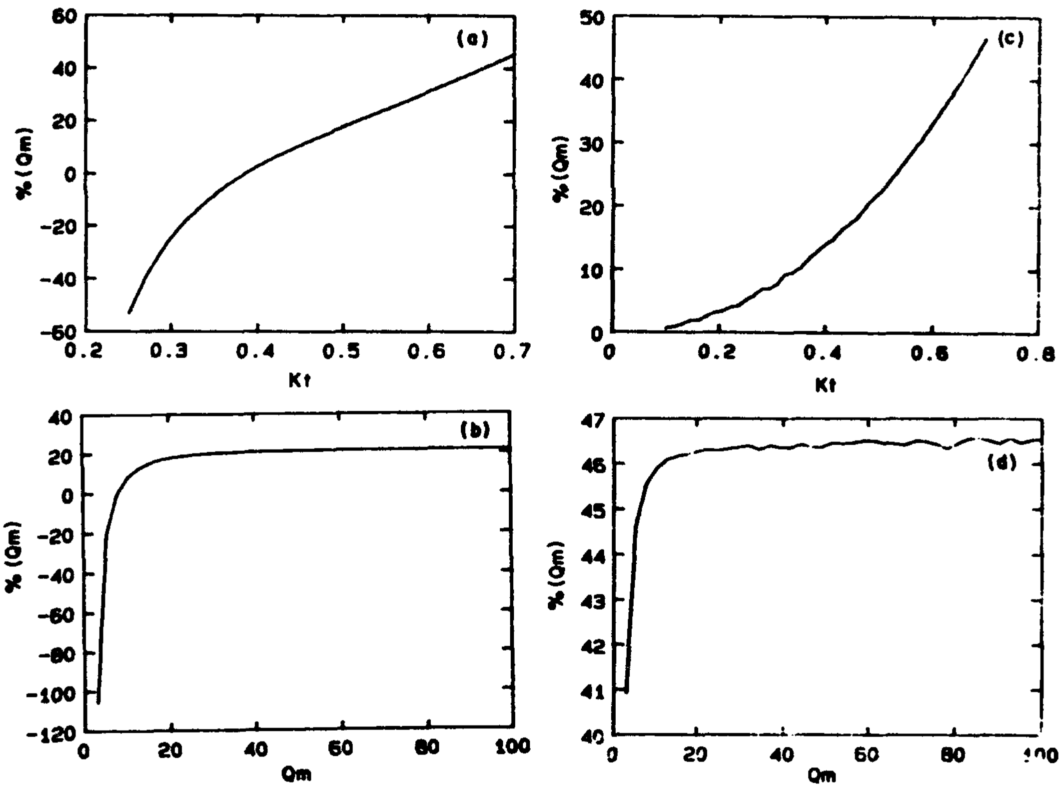

FIGURE 3. Percent error $\%(Q_m)$ as function of the input parameters. ; a) Eq. (3) and $Q_m = 20$; b) Eq.(3) and $k_t = 0.5$; c) Eq. (4) and $Q_m = 100$; d) Eq. (4) and $k_t = 0.7$.

A notable inaccuracy of the two characterization formula can be noticed. In the two cases, the percent error increases strongly for

materials with high electromechanical coupling coefficients. For a typical ceramic-polymer composite (i.e., $k_t = 0.7$ and $Q_m = 20$) the percent error is 45.4% with Eq.(3) and 46.2% with Eq. (4).

APPENDIX.

The electrical input impedance of a thickness extensional piezoelectric resonator, including the internal mechanical losses[4] is given by:

$$Z_{in}(\omega) = \frac{1}{j\,\omega\,C_0^S}\left(1 - (k_t^*)^2\,\frac{\tan(\gamma^*/2)}{(\gamma^*/2)}\right) \qquad \text{(A1)}$$

where:

$$k_t^* = k_t / (1 + j\tan\delta_m)^{1/2} \quad ; \quad \gamma^* = \gamma / (1 + j\tan\delta_m)^{1/2}$$

$$\gamma = \omega\, d / v_t^D \quad ; \quad v_t^D = (\mathrm{Re}(c_{33}^D)^*/\rho)^{1/2}$$

$$\tan\delta_m = 1/Q_m = \mathrm{Im}(c_{33}^D)^* / \mathrm{Re}(c_{33}^D)^*$$

and where C_0^S is the clamped capacitance, d is the thickness of the piezoelectric disk, k_t the electromechanical coupling coefficient, Q_m the mechanical quality factor, v_t^D the sound velocity, $(c_{33}^D)^*$ the complex elastic stiffened constant, and ρ the density of the material.

ACKNOWLEDGMENTS :This work was supported by CICYT Project N^0 ROB91-0723. The author is indebted to Dr. F.R. Montero de Espinosa for valuable comments and suggestions.

REFERENCES

1. IEEE Standard on Piezoelectricity, ANSI/IEEE Std.176 (1987).
2. IRE Standard on Piezoelectric Crystals: Measurements of Piezoelectric Ceramics, Proc. IRE, 49, 1161 (1961).
3. W.A. Smith and B.A. Auld, IEEE Tarns. on Ultras. Ferr. and Freq. Contr., 38, 40 (1991).
4. C. Mequio, R.H. Coursant and J.M. Tellier, Sensors and Actuators, 14, 1 (1988).
5. D.A.Berlincourt, D.R.Curran and H.Jaffe, in Piezoelectric and piezomagnetics materials and their function in transducers, Physical Acoustics, Vol IA (Academic press,New York,1964).
6. G.E.Martin, J. Acoust. Soc. Am. , 26 , 413 (1954).
7. K.Shibayama, J. Acoust. Soc. Am. , 34 ,1883 (1962).
8. S.Sherrit, N.Gauthier, H.D.Wiederick and B.K.Mukherjee, Ferroelectrics, 119, 17 (1991).
9. T.R.Gururaja, Q.C.Xu, A.R.Ramachandran, A.Halliyal, R.E.Newnham, Proc. of the IEEE 1986 Ultras. Symp., 703 (1986).

Ferroelectrics, 1992, Vol. 134, pp. 111–119
Reprints available directly from the publisher
Photocopying permitted by license only

PdP135

NON-ITERATIVE EVALUATION OF THE REAL AND IMAGINARY MATERIAL CONSTANTS OF PIEZOELECTRIC RESONATORS

S. SHERRIT, H.D. WIEDERICK, B.K. MUKHERJEE
Royal Military College of Canada, Kingston, Ont., Canada K7K 5L0

Abstract We describe a new method for determining the real and imaginary parts of the material constants of piezoelectric resonators. Our method is applicable to any of the common resonator geometries, it is non-iterative and its accuracy is comparable to that of other methods which are currently in use.

INTRODUCTION

The recent past has seen the introduction of new lossy piezoelectric materials such as ceramic-polymer composites. The proper calculation of the transducer transfer function of such materials requires the determination of both the real and imaginary components of the material constants. The IEEE standard[1] on Piezoelectricity gives the standard methods for measuring the material constants from the electrical resonance curves, but these methods are of limited value in determining the imaginary parts of the constants. Smits[2] has described an alternative method using an iterative technique to determine the complex material constants. This method is normally very accurate and useful in research work. However, it requires the judicious choice of three admittance or impedance data points and this becomes tedious when a large number of samples need to be evaluated. Besides, around resonance, the low sample impedances may overload the voltage source and distort the impedance data thus reducing the accuracy of the measurement[3]. Holland[4] has shown how the piezoelectric phase angle may be found by analysing the real parts of the material constants obtained by using the methods of the IEEE standard[1] or by applying the results of the gain-bandwidth[5] method to a Taylor's series expansion of the resonance equation. However, once again the data has to be judiciously chosen and a complex equation has to be solved so that the method is rather cumbersome to use.

In this paper we present a simpler technique to determine the complex material constants for a piezoelectric resonator. Our technique is easy to use and it only requires frequency data around resonance and admittance or impedance data away from resonance. Besides, the method only requires data at certain critical frequencies and does not involve the experimenter in making a suitable choice of data points. In an earlier paper we have reported on the application of this method to the particular case of radial mode resonance[6].

METHOD

We illustrate our method by considering the thickness mode resonance of a plate resonator of thickness t and electrode area A. The impedance of the plate is given by[1]

$$Z(\omega) = (t/i\omega\epsilon^s_{33}A)\left[1 - k_t^2 \frac{\tan(\omega/4f_p)}{\omega/4f_p}\right], \tag{1}$$

where ϵ^s_{33} is the clamped permittivity, k_t is the electromechanical coupling constant for the thickness mode and f_p is the parallel resonance frequency. We define the parallel and series resonance frequencies, f_p and f_s, as the frequencies which correspond to maxima in the real parts of $\omega Z(\omega)$ and $Y(\omega)/\omega$ respectively, and not in the real parts of $Z(\omega)$ and $Y(\omega)$ as in the IEEE method. Our definitions are mathematically more correct since f_p, for example, is the frequency at which the expression in square brackets in (1) has a maximum in its real part. The difference between the two definitions is only significant for materials with a low mechanical Q which is defined as the ratio of the real part of the elastic constant to its imaginary part. Land et al[7] have shown that the bandwidth at resonance, defined as the frequency of maximum reactance minus the frequency of minimum reactance, is related to the mechanical Q of a resonator. While the IEEE method uses critical frequencies from the real impedance and admittance data, we have used Land et al's result to define frequencies, with complex arguments, which combine the critical frequencies from both the real and imaginary parts of the impedance and admittance spectra. Thus, the first series, the second series and the first parallel resonance frequencies are respectively defined by

$$\hat{f}^1_p = f^1_p\left[1 - i\,\frac{f^{1p}_{-1/2} - f^{1p}_{+1/2}}{f^1_p}\right]^{-1/2}, \tag{2}$$

$$\hat{f}^1_s = f^1_s\left[1 - i\,\frac{f^1_{-1/2} - f^1_{+1/2}}{f^1_s}\right]^{-1/2}, \tag{3}$$

$$\hat{f}^2_s = f^2_s\left[1 - i\,\frac{f^2_{-1/2} - f^2_{+1/2}}{f^2_s}\right]^{-1/2}, \tag{4}$$

where all the particular frequencies are shown in Figure 1.

The complex elastic stiffness is then given by

$$c^D_{33} = 4\rho(\hat{f}^1_p)^2t^2/n^2, \tag{5}$$

where n has the values 1, 3 or 5 for the first, the second or the third resonance respectively. The complex value of the thickness mode electromechanical coupling constant, k_t, may be evaluated in one of two ways. The first way is to follow the IEEE standard[1] but replace f_p and f_s with $\hat{f}^1_p$ and $\hat{f}^1_s$ respectively, which gives

$$k_t^2 = \frac{\pi}{2}\frac{\hat{f}^1_s}{\hat{f}^1_p}\tan\left[\frac{\pi}{2}\frac{\hat{f}^1_p - \hat{f}^1_s}{\hat{f}^1_p}\right], \tag{6}$$

where the tan function may be evaluated using the identity

$$\tan(a+ib) = (\sin 2a + i\sinh 2b)/(\cos 2a + \cosh 2b).$$

Alternatively, k_t may be determined using the technique suggested by

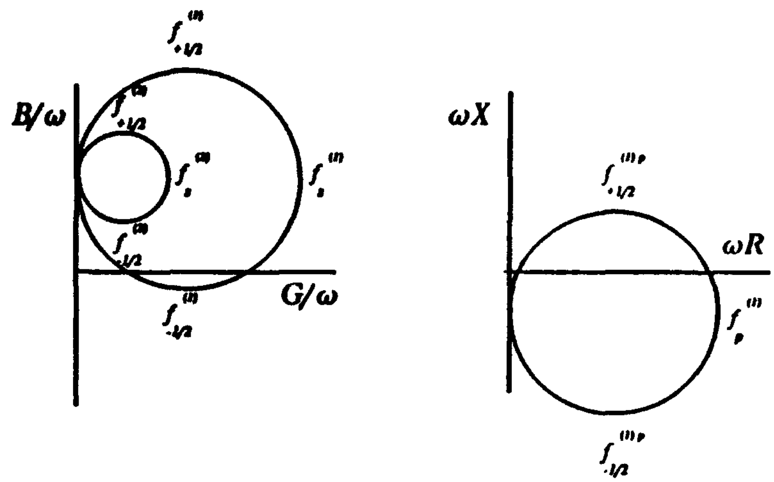

FIGURE 1. The critical frequencies determined from the modified admittance and impedance locus diagrams which are plots of $B(\omega)/\omega$ vs. $G(\omega)/\omega$ and of $\omega X(\omega)$ vs. $\omega R(\omega)$.

Onoe et al[8] who have presented a numerical table of the coupling constant k as a function of the ratio of the second series resonance frequency to the first series resonance frequency. We have used a least squares technique to fit their table to a polynomial of the form

$$k^2 = a_0 + \frac{a_1}{r_s} + \frac{a_2}{r_s^2} + \frac{a_3}{r_s^3} + \frac{a_4}{r_s^4} + \frac{a_5}{r_s^5}$$

$$= \sum_{n=0}^{5} a_n (r_s)^{-n} = \sum_{0}^{5} a_n (r_s)^{-n} \cos(n\theta) - i \sum_{0}^{5} a_n (r_s)^{-n} \sin(n\theta), \qquad (7)$$

where $r_s = \hat{f}_s^m / \hat{f}_s^1$ is a complex series frequency ratio with m representing the order of the resonance. The values of the coefficients are shown in Table I. In the range $0 < k < 0.8$ the polynomial fits are valid to within an average error of 0.014% and the fit has been illustrated in an earlier publication[9]. Onoe et al's method and, hence, the above polynomial are applicable to the length extensional and the thickness shear modes in addition to the thickness extensional mode under discussion here. Table II shows the relationship between the coupling coefficients in each resonance geometry and the k given in Equation (7). In the thickness mode of materials with large k_t, sideband resonances are common and these cause a shift in the critical frequencies which introduces a

TABLE I. Coefficients for the polynomial in equation (7).

a_n	f_s^2/f_s^1	f_s^3/f_s^1	f_s^4/f_s^1
a_0	2.6027556	1.3600551	1.2470973
a_1	–30.879689	–11.956448	–11.627842
a_2	231.71003	140.14918	180.95922
a_3	–925.12604	–1085.1453	–2121.5036
a_4	1800.5885	3674.9833	10130.643
a_5	–1463.0141	–5542.2805	–22071.221

TABLE II. Formulae for calculating the elastic and electromechanical coupling coefficients for the various resonance geometries.

	Thickness Extensional
$c_{33}^D = 4\rho t^2 \hat{f}_p^2$	$k^2 = k_t^2 = \frac{\pi}{2}\frac{\hat{f}_s}{\hat{f}_p}\tan\left[\frac{\pi}{2}\frac{(\hat{f}_p - \hat{f}_s)}{\hat{f}_p}\right]$
	Length Extensional
$s_{33}^D = \frac{1}{4\rho l^2 \hat{f}_p^2}$	$k^2 = k_{33}^2 = \frac{\pi}{2}\frac{\hat{f}_s}{\hat{f}_p}\tan\left[\frac{\pi}{2}\frac{(\hat{f}_p - \hat{f}_s)}{\hat{f}_p}\right]$
	Length Thickness Extensional
$s_{11}^E = \frac{1}{4\rho l^2 \hat{f}_s^2}$	$\frac{k_{31}^2}{1 - k_{31}^2} = \frac{\pi}{2}\frac{\hat{f}_p}{\hat{f}_s}\tan\left[\frac{\pi}{2}\frac{(\hat{f}_p - \hat{f}_s)}{\hat{f}_s}\right]$
	Thickness Shear
$c_{55}^D = 4\rho t^2 \hat{f}_p^2$	$k^2 = k_{15}^2 = \frac{\pi}{2}\frac{\hat{f}_s}{\hat{f}_p}\tan\left[\frac{\pi}{2}\frac{(\hat{f}_p - \hat{f}_s)}{\hat{f}_p}\right]$

significant error in the argument of the tan function in Equation (6) and hence an error in the value of $k = k_t$ obtained by using the IEEE equation, and so in this case the technique of Onoe et al is the more accurate one. For materials with low k_t, the sideband resonances are insignificant and in this case the IEEE equations are adequate when k is small. Onoe et al have found that their method is suitable for the thickness shear mode and the thickness mode provided that the length or diameter of the specimen is at least 10 times its thickness. Table II shows all the equations required to find k by the IEEE method as well as by using Onoe et al's technique.

With k_t and $\hat{f}_p^1$ known, the clamped permittivity ϵ_{33}^s may be found by choosing one impedance data point $Z(\omega)$ and rearranging Equation (1) to give

$$\epsilon_{33}^s = (t/i\omega AZ(\omega))\left[1 - k_t^2\,\frac{\tan(\omega/4\hat{f}_p^1)}{\omega/4\hat{f}_p^1}\right]. \tag{8}$$

While there is no particular criterion for choosing the data point $Z(\omega)$, it is advisable to avoid choosing a point near resonance where small errors can get magnified in the analysis; we suggest choosing the point at a frequency $f = (n+1)f_p$ so that it is between the fundamental and the second resonance and so that the mode coupling between the free and the clamped boundary conditions is complete and the data is that of a clamped resonator.

The piezoelectric constant is given by[1]

$$e_{33} = k_t(c_{33}^D\epsilon_{33}^s)^{1/2}. \tag{9}$$

SPECIAL CASES

For materials which exhibit a strong dielectric dispersion, such as

polyvinylidene difluoride or some ceramic-polymer composites, the value obtained for ϵ^s_{33} at $f = (n+1)f_p$ will be different from the value of ϵ^s_{33} at resonance. To ensure that material constants are evaluated at the same frequency, we suggest that, for these materials, the real part of ϵ^s_{33} derived at $f = (n+1)f_p$ be adjusted to give the best fit to the imaginary data $B(\omega)$ around resonance and that the imaginary part of ϵ^s_{33} be adjusted to give the best fit to $G(\omega)$. Alternatively, equations (6) and (8) can be used to find the clamped complex permittivity $\epsilon^s_{33}(\omega)$ as a function of frequency.

As we have mentioned earlier, Equations (5) and (6) were derived from the piezoelectric-elastic term in brackets in equation (1) and their derivation assumed that ϵ^s_{33} is real, since a complex ϵ^s_{33} shifts the critical frequencies. For materials with low k_t ($k_t < 0.3$), the seperation between the series and parallel resonance frequencies is small and the shifts due to a complex ϵ^s_{33} may introduce significant errors in the calculated values of c^D_{33} and k_t. We have found that if k_t is low, or if the imaginary component of ϵ^s_{33} is large, then a second set of critical frequencies must be determined. The value of ϵ^s_{33}, found from the first set of critical frequencies, is used to offset the shift in critical frequencies by determining the new sets of critical frequencies (f_p, $f^p_{-1/2}$, $f^p_{+1/2}$) from plots of $X'(\omega)$ vs. $R'(\omega)$ and (f_s, $f_{-1/2}$, $f_{+1/2}$) from plots of $B'(\omega)$ vs. $G'(\omega)$ with the new impedance and admittance functions being defined as

$$\begin{aligned}
G'(\omega) &= (G(\omega)\epsilon^{s\prime}_{33} + B(\omega)\epsilon^{s\prime\prime}_{33}) \,/\, \omega((\epsilon^{s\prime}_{33})^2 + (\epsilon^{s\prime\prime}_{33})^2) \,, \\
B'(\omega) &= (G(\omega)\epsilon^{s\prime\prime}_{33} - B(\omega)\epsilon^{s\prime}_{33}) \,/\, \omega((\epsilon^{s\prime}_{33})^2 + (\epsilon^{s\prime\prime}_{33})^2) \,, \\
R'(\omega) &= (R(\omega)\epsilon^{s\prime}_{33} - X(\omega)\epsilon^{s\prime\prime}_{33})\omega \,, \\
X'(\omega) &= (R(\omega)\epsilon^{s\prime\prime}_{33} + X(\omega)\epsilon^{s\prime}_{33})\omega \,, \\
Z'(\omega) &= R'(\omega) + iX'(\omega) \,, \\
Y'(\omega) &= G'(\omega) + iB'(\omega) \,.
\end{aligned} \tag{10}$$

In the above equations, $R(\omega)$, $X(\omega)$, $G(\omega)$ and $B(\omega)$ are the measured resistance, reactance, conductance and susceptance respectively, while $\epsilon^{s\prime}_{33}$ and $\epsilon^{s\prime\prime}_{33}$ are the real and imaginary parts of ϵ^s_{33} which has been determined earlier. The calculation follows the method outlined previously: $\hat{f}^1_p$ is calculated from a plot of $X'(\omega)$ vs. $R'(\omega)$, $\hat{f}^1_s$, and $\hat{f}^2_s$ are calculated from a plot of $B'(\omega)$ vs. $G'(\omega)$ and these lead to new values of c^D_{33}, k_t, ϵ^s_{33} and e_{33}.

Finally, we note that when k_t and Q are both low, the seperation between f_p and f_s is again small while f_p and f_s can only be measured to an accuracy determined by Q. So the larger error in $f_p - f_s$ will produce a larger error in the calculated value of k_t.

EVALUATION OF OUR METHOD

We have evaluated our method as follows. We have used the known material constants of a niobium doped lead zirconate titanate (PZT), taken from Jaffe[10], with the imaginary part of the piezoelectric constant assumed to be $e''_{33} = -0.02\, e'_{33}$, to generate the impedance and admittance spectra and we have then used our technique to determine the material constants from these spectra for final comparison with the original values. We have done this assuming two different sets of values for Q and for k_t to check the accuracy under differing conditions. We have also applied our method to determine the material constants of a 1-3 ceramic-polymer composite and we have compared the results with those obtained by using Smits' technique.

Case 1: Q = 50 and $k_t = 0.4807(1 - 0.02i)$

In this case the dielectric dissipation is low enough and k_t is high enough for the critical frequencies to be found directly from $Y(\omega)/\omega$ and $\omega Z(\omega)$ and we have used the polynomial form of Equation (7) to find k_t. Our results are compared to the input values of the material constants in Table III and we note that the largest error of 0.2% occurs for the piezoelectric constant and the coupling constant.

TABLE III. Comparision between the input material constants and the values derived by our method.

Material Constant	Input Value	Calculated Value from $Y(\omega)/\omega$ and $\omega Z(\omega)$	Error % Real part	Error % Imag part
k_t	0.4807(1-0.02i)	0.4818(1-0.02002i)	0.2	0.2
$c^D_{33}(10^{-11}N/m^2)$	1.47(1+0.02i)	1.469(1+0.02000i)	0.04	0.04
$\epsilon^S_{33}(10^9F/m)$	7.345(1-0.02i)	7.349(1-0.01999i)	0.05	0.01
$e_{33}(C/m^2)$	15.8(1-0.02i)	15.84(1-0.01999i)	0.2	0.2

Case 2: Q = 10 and $k_t = 0.04788(1-0.05990i)$

In this case k_t is low and the small Q implies that ϵ^S_{33} has a significant imaginary component. As explained earlier, this requires the determination of a second set of critical frequencies using the set of Equations (10), and the results obtained by using this method are shown in Table IV. The maximum error of 2.1% is to be found for the imaginary component of the piezoelectric constant e_{33} and it should be noted that, for real materials with such low values of Q and k_t, it is unlikely that the material constants could be determined to such a precision due to the limited accuracies to which the critical

frequencies could be measured. It should also be noted that had the calculations been carried out directly with the first set of critical frequencies, determined from $Y(\omega)/\omega$ and $\omega Z(\omega)$, the errors in the real parts of k_t and e_{33} would be as large as 46% and their imaginary parts would have even larger errors; however such a calculation would have

TABLE IV. Comparision between the input material constants and the values derived by our method.

Material Constant	Input Value	Calculated Value from $Y'(\omega)$ and $Z'(\omega)$	Error % Real part	Error % Imag. part
k_t	0.04788(1-0.05990i)	0.04879(1-0.05934i)	1.9	1.0
$c^D_{33}(10^{-11}N/m^2)$	1.47(1+0.10i)	1.454(1+0.10026i)	1.1	0.8
$\epsilon^s_{33}(10^9F/m)$	7.345(1-0.02i)	7.359(1-0.01981i)	<0.01	0.01
$e_{33}(C/m^2)$	1.58(1-0.02i)	1.601(1-0.01932i)	1.4	2.1

given reasonable values of c^D_{33} and ϵ^s_{33}. Thus our use of the second set of critical frequencies yields much better results.

Case 3: 1-3 ceramic-polymer composite

We have used our technique to determine the material constants of a 1-3 connectivity ceramic-polymer composite with lead zirconate titanate (PZT) as the ceramic material. Table V shows the data

TABLE V. Measured data for the 1-3 PZT-polymer specimen.

Diameter D = 0.03143 m. Thickness t = 0.00203 m.
Density ρ = 4170 kg/m³ Z(3 MHz) = 2.27 + 29.34i ohms

Resonance	f (kHz)	$f_{+1/2}$(kHz)	$f_{-1/2}$(kHz)
First series	698.2	663.1	723.6
First parallel	895.4	878.8	911.3

TABLE VI. Material constants for the 1-3 composite calculated by our method and by Smits' technique.

Material Constant	Our method	Smits' method
k_t	0.6670(1 - 0.03516)	0.6681(1 - 0.08232i)
$c^D_{33}(10^{-10}N/m^2)$	5.49(1 + 0.0363i)	5.503(1 + 0.0370i)
$\epsilon^s_{33}(10^9F/m)$	5.336(1 - 0.0582i)	5.096(1 - 0.163i)
$e_{33}(C/m^2)$	11.4(1 - 0.0455i)	11.2(1 - 0.145i)

measured by us for this specimen. Since the impedance spectrum was clean and since there was no evidence of coupling to the lower modes, we have used Equation (6) to determine k_t. The material constants obtained by the use of our method are shown in Table VI which also gives the values of the same constants obtained by using Smits' technique. Figure 2 shows the fit to the impedance data given by our method as well as by Smits' method; both methods give very good fits and their curves overlap for the most part. However, Smits' method gave different material constants depending on the data points that

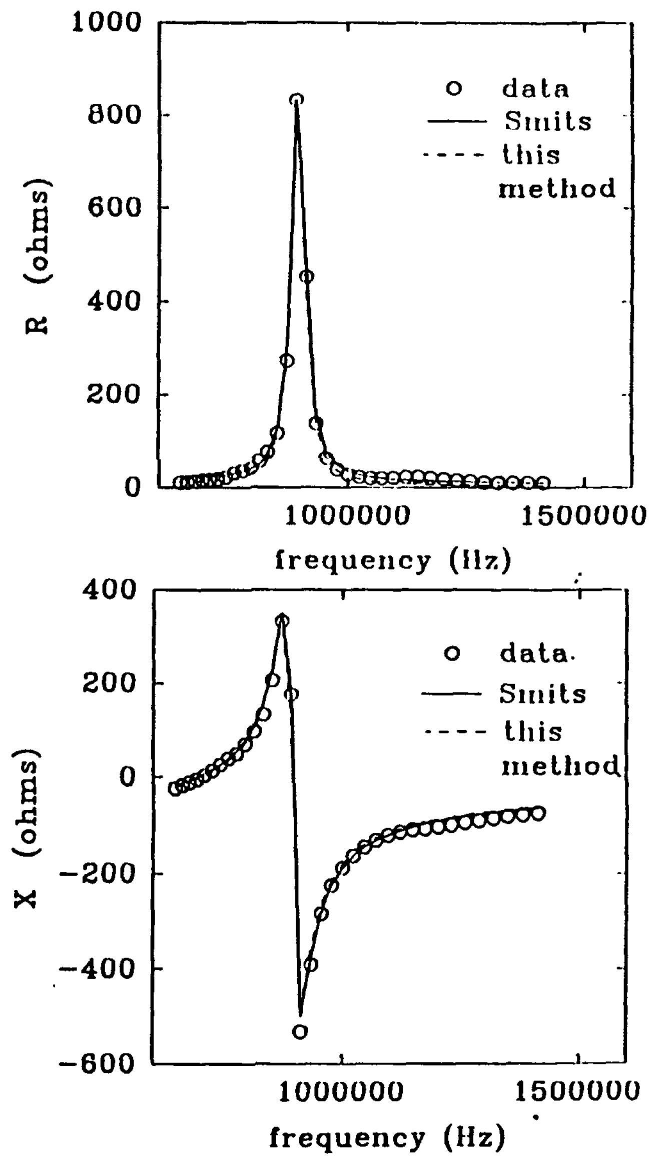

FIGURE 2. Impedance data points for a 1–3 PZT–polymer composite compared with curves derived from the material constants calculated by our method and by Smits' method.

were used in the calculation; in particular, the imaginary parts of k_t, e_{33}, and ϵ^s_{33} changed appreciably depending on the data points used even though the fit remained good.

The three cases which we have evaluated show that our non-iterative method gives unique values of the complex material constants with an accuracy that is comparable to other methods currently in use.

ACKNOWLEDGEMENT

The authors gratefully acknowledge support from the Defence Research Establishment Atlantic of the Department of National Defence, Canada.

REFERENCES

1 IEEE Standard on Piezoelectricity, 176-1987.

2 J.G. Smits, IEEE Transactions on Sonics and Ultrasonics, SU-23, 6 (1976).

3 J.G. Smits, Ferroelectrics, 64, 275 (1985).

4 R. Holland, IEEE Transactions on Sonics and Ultrasonics, SU-17, 2 (1970).

5 R. Holland and E.P. EerNisse, IEEE Transactions on Sonics and Ultrasonics, SU-16, 4 (1969).

6 S. Sherrit, N. Gauthier, H.D. Wiederick and B.K. Mukherjee, Ferroelectrics, 119, 17 (1991).

7 C.E. Land, G.W. Smith and C.R. Westgate, IEEE Trans. on Sonics and Ultrasonics, SU-11, 8 (1964).

8 M. Onoe, H.F. Tiersten and A.H. Meitzler, J. Acoust. Soc. Am., 35, 36 (1963).

9 S. Sherrit, H.D. Wiederick and B.K. Mukherjee, J. Acoust. Soc. Am., 91(3), 1770 (1992).

10 B. Jaffe, W.R. Cook and H. Jaffe, Piezoelectric Ceramics (Academic Press, London, 1971), p 146.

Ferroelectrics, 1992, Vol. 134, pp. 121–126
Reprints available directly from the publisher
Photocopying permitted by license only

PdP136

Application of Piezoelectric Actuator to Burr-Free Blanking

YUKINORI KAWAMURA AND KOZO MATSUMOTO
Fuji Electric Corp. R & D Ltd., 2-2-1, Nagasaka, Yokosuka, Japan
MITSUHARU NONAMI AND FUMISATO NIINO
Fuji Electric Co. Ltd. Fukiage Factory, 1-5-45, Minami, Fukiage-Cho, Kitaadachi-Gun, Saitama Pref., Japan

Abstract A high power, multilayer piezoelectric ceramic actuator has been developed and has been applied to burr-free blanking of thin foil using the reciprocating blanking method. A ternary system, $Pb(Ni_{1/3}Nb_{2/3})O_3-PbZrO_3-PbTiO_3$, was selected for piezoelectric ceramics prepared using the conventional method. The following results were obtained from this study.
(1) The maximum force and displacement of the actuator (D=35mm) induced by an applied voltage of 400V were 2.8×10^4N and 50μm respectively.
(2) It was possible to blank foil 13 - 80μm thick using piezoelectric ceramic actuators with this method, and obtain burr-free edges.
As a result, it was confirmed that burr-free blanking of thin foil can be done with a multilayer piezoelectric ceramic actuator.

INTRODUCTION

The blanking process includes intrinsic problems of shear drop and burrs generated during the shearing process. Many efforts[1-5] have been made particularly to suppress or remove burrs, which have greatly influenced product reliability. Few reports, however, seem to have been made on burr-free blanking or blanking equipment for foil less than 100μm thick.

To achieve burr-free precision blanking of very thin metal foil (100μm or less) with the reciprocating blanking method developed by Maeda[6], the authors have developed a new system of blanking equipment which directly uses the force induced by the electric field of piezoelectric ceramics as a shearing force and controls the punch position with micron-level precision through generated strain.

Reciprocating blanking deforms foil to a certain extent with the first-process punch and die; then does so again in reverse with the second-process punch and die. When the proper penetration depth is obtained with the first-process punch, the shear drop remains on both sides of the sheared surface and no burr is generated. In this process for thin foil, stroke control at the micron level during first-process punch is essential.

This paper introduces the construction of the actuator and this new blanking equipment and reports test results obtained for blanking of 13–80μm stainless steel foil.

CONSTRUCTION OF THE ACTUATOR AND EQUIPMENT

Piezoelectric ceramics

A ternary system, $0.5Pb(Ni_{1/3}Nb_{2/3})O_3$-$0.15PbZrO_3$-$0.35PbTiO_3$ with perovskite structure, was selected for the piezoelectric ceramics, because it generates a fairly large field induced strain. They were prepared using the conventional method[7] in which the microstructure of the ceramics was controlled. The properties of the piezoelectric ceramics are shown in Table I.

Table I Properties of piezoelectric ceramics

Coupling factor		0.60
Relative dielectric const.		5700 (at room temp.)
Mechanical quality factor		70
Piezoelectric const.	$d_{33}(10^{-12}m/V)$	650
	$d_{31}(10^{-12}m/V)$	-280
Young's modulus	$Y_{11}^{E}(10^{10}N/m^2)$	6.8
Poisson's ratio		0.34
Curie temp. (°C)		130
Density $(10^3kg/m^3)$		8.0

Multilayer piezoelectric actuator

The multilayer piezoelectric actuator consists of 101 piezoelectric ceramic disks 0.7mm in thickness and 20 - 60mm in diameter, and internal Ag paste electrodes alternately arranged and insulated by small gaps filled with epoxy resin and electrically connected in parallel with an external electrode. The actuator makes use of strain in the thickness direction induced by an electric field in the piezoelectric ceramics. Figure 2 shows the construction and appearance of the actuators which we have developed.

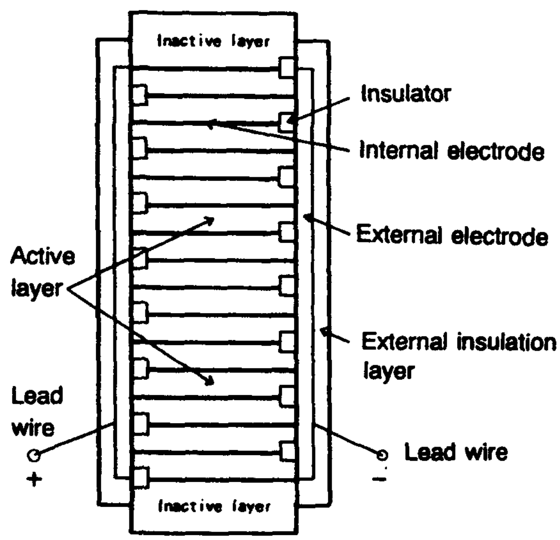

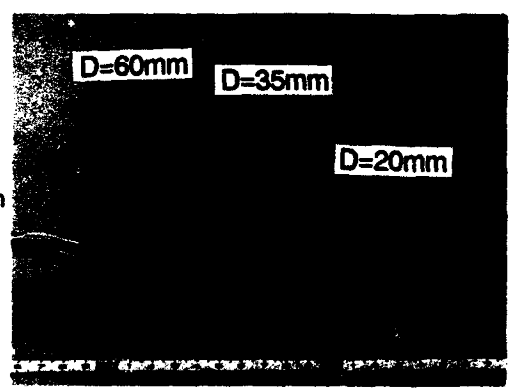

FIGURE 2 Construction and appearance of actuators

Table II shows the properties of the multilayer piezoelectric actuator 35mm in diameter used in this study.

TABLE II Properties of multilayer piezoelectric actuator

Diameter (mm)	35
Length (mm)	90
Max. force (10^4 N)	2.8
Max. displacement (μm)	50
Driving voltage (V)	400
Capacitance (μF)	7.0

Figure 3 shows the relation between the voltage applied to the actuator and displacement. When the actuator is mounted on the equipment, a preloading spring is incorporated to give a compression load to the actuator, but the relation between applied voltage and displacement remains almost the same. Hysteresis, an intrinsic property of piezoelectric ceramics, is a big problem in servo control. However, in the case of repeated digital two-point positioning, it is enough to provide a displacement sensor for the condition setting and punch position monitoring.

Figure 4 shows the relation between the force caused by the voltage applied to the actuator and displacement. When the actuator is mounted on the equipment, it cannot be used in the range near the maximum force corresponding to displacement zero, so it is used at less than half of the maximum force.

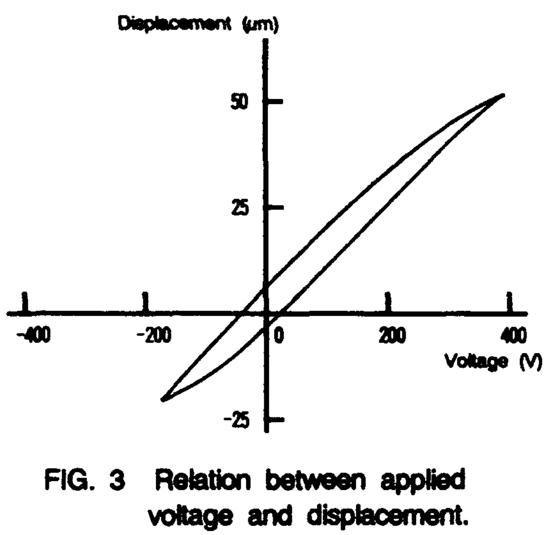

FIG. 3 Relation between applied voltage and displacement.

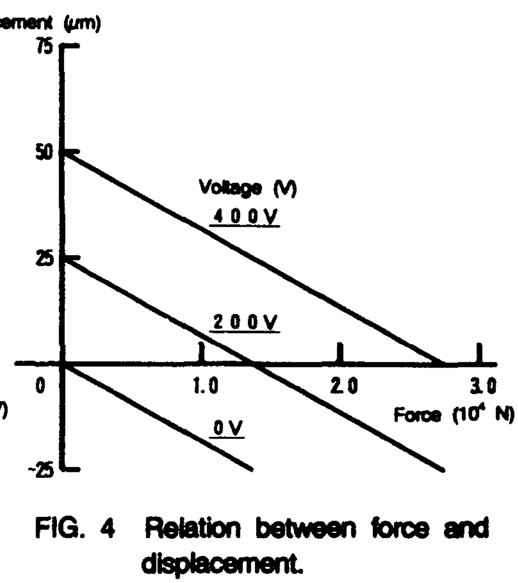

FIG. 4 Relation between force and displacement.

Construction and control of the PIEZOPRESS

The reciprocating blanking system has cylinders incorporating the above mentioned actuator and a preloading spring, which are arranged on the upper and lower sides of the blanking die. The actuator controls punches for the first and second processes when the system is operated. We have named this system a PIEZOPRESS.

Figure 5 shows the construction of the PIEZOPRESS. To increase displacement, two units of the actuator are arranged in series vertically. The stripper in the die is of a movable type using small multilayer piezoelectric actuators, so the electromagnetic noise source can be eliminated, resulting in a quiet, low-noise, high-precision blanking press. Figures 6 and 7 show the appearance of the PIEZOPRESS.

An eddy-current type displacement meter provided in the cylinder is used for monitoring punch displacement. A high-speed control system where a sequencer and power transistors are combined is used to control the voltage applied to the upper and lower actuators and the movable stripper. Figure 8 shows a typical example of the punch action and operation sequence.

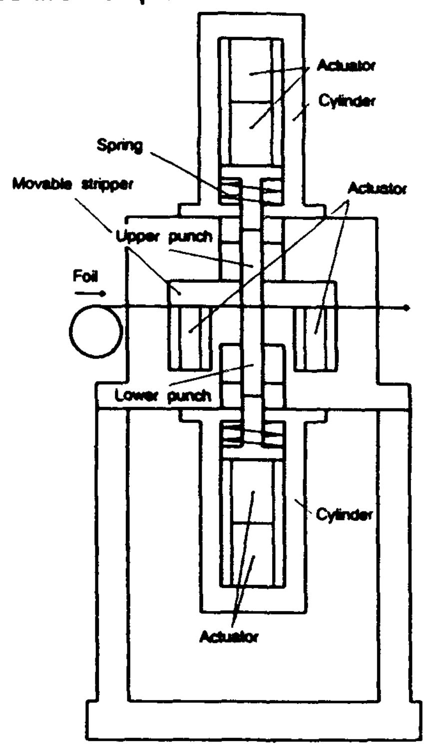

FIGURE. 5 Construction of PIEZOPRESS

FIG. 6 Appearance of the system

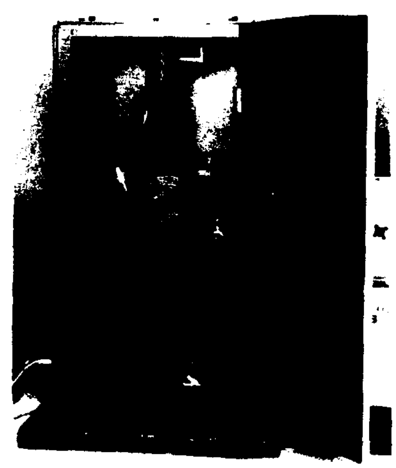

FIG. 7 Inner view of PIEZOPRESS

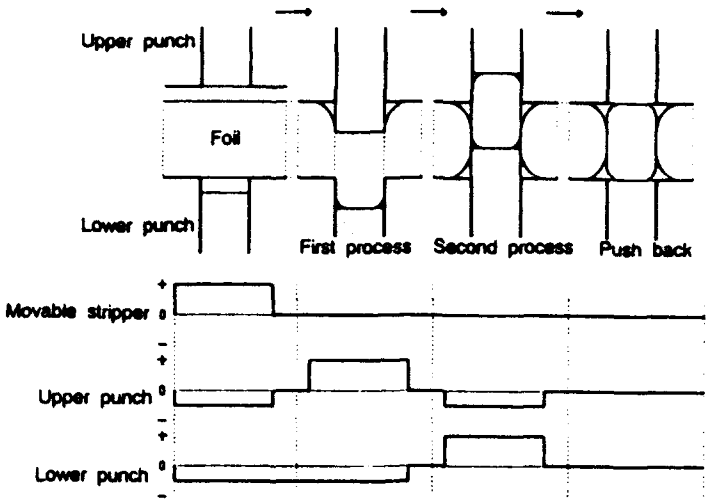

FIGURE 8 Typical punch action and operation sequence

RESULT OF RECIPROCATING BLANKING, AND DISCUSSION

A reciprocating blanking test was carried out using stainless steel foil 13 - 80μm thick and 20mm wide as sample material and a blanking circle with a 10mm diameter. Die clearance was less than 10% of foil thickness for both the upper and lower dies. The number of blanking strokes per minute, depending on foil feed speed, was set at about 60 in this test. Single blanking was carried out under the same conditions for the purpose of comparison.

Figure 9 shows a typical sheared surface obtained with the blanked samples. The single blanking sample(a) shows that only one edge drops smoothly and, therefore, it is probable a burr will be left on the opposite side of the edge. On the other hand, the reciprocating blanking sample(b) shows that both edges drop smoothly and that a burr is prevented from occurring. We obtained the same results on the blanking of other samples 13 - 80μm thick.

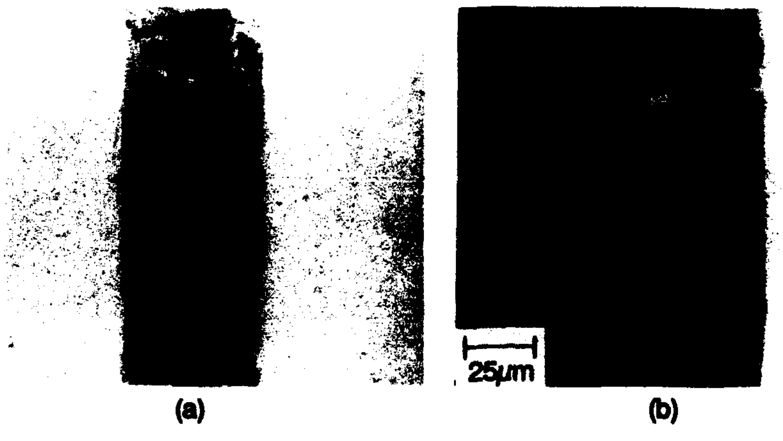

FIGURE 9 Typical sheared surfaces. (Stainless steel foil 50μm thick)
(a): Single blanking (b): Reciprocating blanking

Figure 10 shows a sectional view of a typical half-blanked sample taken out to determine the degree of penetration after the first-process punch. The samples were plated with Ni for the observation.

Figure 11 shows the sheared surface of stainless steel foil 13μm thick. In this case, we used reciprocating blanking with slight vibration, because die clearance became more than 10% of foil thickness. No burr can be observed on either edge.

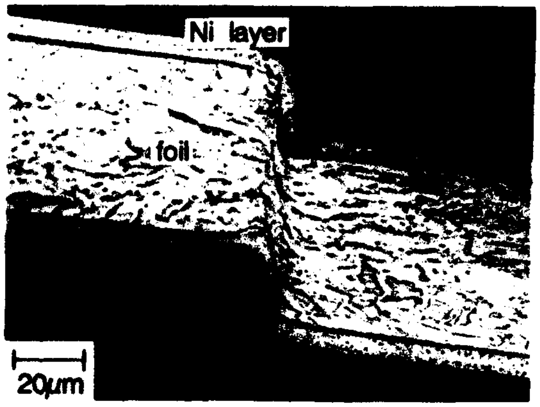

FIG. 10 Sectional view of half-blanked sample. (50μm thick)

FIG. 11 Sheared surface of stainless steel foil. (13μm thick)

CONCLUSION

This paper describes the construction of a piezoelectric actuator and a new type of blanking equipment, PIEZOPRESS. In this system, the reciprocating blanking method is applied to obtain burr-free blanking of thin metal foil. A force induced by the electric field of piezoelectric ceramics is used directly for the shearing force, and micron-level punch position control is obtained with generated strain. A burr-free blanking test with stainless steel foil 13 - 80μm thick confirmed that reciprocating blanking is practicable with this system.

The new equipment is characterized by high precision, small size, and cleanness. Therefore, it can be built in a precision device assembly line. We also expect that new and unconventional uses will be found for this equipment.

From now we will try to improve the actuator and equipment and also investigate the optimum punch stroke for the first process and die clearance matching materials, to enhance the equipment's reliability.

REFERENCES

1. A. Ujihara, Mechanical Engineering, December separate vol., 114 (1988)
2. I. Makino, Press Working, 13-5, 93 (1975)
3. J. Brokhau, et al., Blech. Rohre. Profile, 17-8, 2 (1970)
4. M. Murakawa and T. Maeda, J. Jpn. Soc. Tech. Plas., 20-219, 270 (1979)
5. K. Kondo, Press Working, 8-7, 10 (1970)
6. T. Maeda, Science of Machine, 10-1, 140 (1958)
7. Y. Kawamura, et al., Jpn. J. Appl. Phys. Supple., 28-2, 77-79 (1989)

Ferroelectrics, 1992, Vol. 134, pp. 127–131
Reprints available directly from the publisher
Photocopying permitted by license only

PdP152

THE INFLUENCE OF THE ELECTRIC STIFFENING ON THE RESONANT FREQUENCY TEMPERATURE DEPENDENCE OF QUARTZ RESONATORS

Jiri ZELENKA
Technical University of Liberec, Halkova 6, Liberec
Czechoslovakia

Abstract Holland, Sinha and Tiersten, Lee and Yong proposed a new method for the more precise determination of the temperature dependence of the resonant frequency of quartz resonators in the period from 1976 to 1984. The method is based on the proposition that the small vibrations of the quartz plate are superposed on the large thermally induced deformation. The extension of the Lee and Yong's method is explained in the paper. The piezoelectric properties and the temperature dependence of the piezoelectric constants and permitivities are considered by the description of the modified method.

INTRODUCTION

Lee and Yong presented [1] one set of the first temperature derivatives $C^{(1)}_{pq}$ and one set of the effective second temperature derivatives $C^{(2)}_{pq}$ of quartz. The mentioned sets of the first and second temperature derivatives were calculated from the temperature coefficients of the frequency measured by Bechmann, Ballato and Lukaszek[2]. By the derivation of the temperature derivatives $C^{(n)}_{pq}$ Lee and Yong considered the linear field equations for small vibrations superposed on thermally induced deformations by steady and uniform temperature changes. They derived the deformation caused by the temperature changes from the nonlinear field equations of thermoelasticity in Lagrangian formulation. The inclusion of the nonlinear effects to the expression of the thermally induced deformation makes it possible to describe more precisely the resonant frequency temperature behaviour of the quartz resonators.

When Lee and Yong derived the sets of the temperature derivatives $C^{(n)}_{pq}$ they neglected the influence of the piezoelectric properties of the quartz plates on the resonant frequency. As it was shown by Zelenka and Lee[3] neglecting

the piezoelectric properties of the plates and bars caused in some cases a large difference between the calculated and measured values of the resonant-frequency-temperature characteristic of the quartz resonators. To remove the discrepancy the modification of Lee and Yong's procedure is given in this paper.

INCLUSION OF PIEZOELECTRIC PROPERTIES TO THE EQUATIONS OF MOTION FOR SMALL VIBRATIONS SUPERPOSED ON THERMALLY-INDUCED DEFORMATION

We will consider, similarly as Lee and Yong, three states of crystal:

(1) A natural state when the crystal is at rest, free of stress and strain, has a uniform temperature T_0. Let x_i denotes the position of a generic material point, ρ_0 the mass density, C_{ijkl}, C_{ijklmn}, and $C_{ijklmnpq}$ the second, third, and fourth order elastic stiffness of the crystal.

(2) An initial state when the crystal is now subject to a steady and uniform temperature increase from T_0 to T, and is allowed to expand freely. At this state, the position of a material point is moved, due to the thermal expansion from x_i to y_i ($y_i = x_i + U_i$), where U_i denotes initial displacement.

(3) A final state when small-amplitude vibrations are superposed on thermally induced deformations. The position of the material point is moved from y_i to z_i ($u_i = z_i - y_i$), where u_i is the incremental displacement due to vibrations.

The behaviour of the crystal in the initial state can be described by the same set of equations as in Lee and Yong's paper (Eqs.(1) to (8)). The additional stress appears in the crystal caused, due to its piezoelectric properties by the changing of the thermally-induced deformation. But if the temperature changes very slowly, the additional stress will be very small and in the steady state diminished (the electrical charges which caused the additional stress reach zero).

The governing equations in the final state are given as follows:

$$\bar{U}_i = U_i + u_i = z_i - x_i, \quad \bar{\Phi} = \phi + \varphi,$$

$$
\begin{aligned}
\bar{E}_{ij} &= E_{ij} + e_{ij} = \frac{1}{2}\left(\bar{U}_{j,i} + \bar{U}_{i,j} + \bar{U}_{k,i}\bar{U}_{k,j}\right), \\
\bar{T}_{ij} &= T_{ij} + t_{ij} = C^{\theta}_{ijkl}\bar{E}_{kl} + \frac{1}{2} C^{\theta}_{ijklmn}\bar{E}_{kl}\bar{E}_{mn} + \\
&\quad + \frac{1}{6} C^{\theta}_{ijklmnpq}\bar{E}_{kl}\bar{E}_{mn}\bar{E}_{pq} + e^{\theta}_{rij}\bar{\Phi}_{,r} + \frac{1}{2} e^{\theta}_{rijkl}\bar{\Phi}_{,r}\bar{E}_{kl} - \\
&\quad - \lambda^{\theta}_{ij}, \\
\bar{\Phi}_{,i} &= \Phi_{,i} + \varphi_{,i}, \\
(\bar{T}_{ij} &+ \bar{T}_{ik}\bar{U}_{i,k})_{,j} = \rho_0 \ddot{\bar{U}}_i, \\
\bar{P}_i &= n_j(\bar{T}_{ij} + \bar{U}_{i,k}) \quad \text{on } S, \\
e^{\theta}_{rij}&\bar{E}_{ij,r} + \frac{1}{2} e^{\theta}_{rijkl}\bar{E}_{ij}\bar{E}_{kl,r} + \frac{1}{2} e^{\theta}_{rijkl}\bar{E}_{ij,r}\bar{E}_{kl} - \\
&\quad - \varepsilon^{\theta}_{rj}\bar{\Phi}_{,jr} - \varepsilon^{\theta}_{rjk}\bar{\Phi}_{,j}\bar{\Phi}_{,kr} - \varepsilon^{\theta}_{rjk}\bar{\Phi}_{,jr}\bar{\Phi}_{,k} = 0 \qquad (1)
\end{aligned}
$$

where $\bar{U}_i$, $\bar{E}_{ij}$, $\bar{T}_{ij}$, $\bar{P}_i$ and $\bar{\Phi}$ are total displacement, strain, stress, traction and potential respectively.

The incremantal strain (e_{ij}), stress (t_{ij}), traction (ρ_i) and potential (φ) give the governing equations for incremental fields:

$$
\begin{aligned}
e_{ij} &= \frac{1}{2}\left(u_{j,i} + u_{i,j} + U_{k,j}u_{k,i} + U_{k,i}u_{k,j}\right), \\
t_{ij} &= (C^{\theta}_{ijkl} + C^{\theta}_{ijklmn}E_{mn} + \frac{1}{2} C^{\theta}_{ijklmnpq}E_{mn}E_{pq} + \\
&\quad + \frac{1}{2} e^{\theta}_{rijkl}\Phi_{,r})e_{kl} + (e^{\theta}_{rij} + \frac{1}{2} e^{\theta}_{rijkl}E_{kl})\,\varphi_{,r} + \\
&\quad + e^{\theta}_{rij}\Phi_{,r}, \\
(t_{ij} &+ t_{jk}U_{i,k} + T_{jk}u_{i,k})_{,j} = \rho_0 \ddot{u}_i, \\
\rho_i &= n_j(t_{ij} + t_{jk}U_{i,k} + T_{jk}u_{i,k}) \quad \text{on } S, \\
(e^{\theta}_{rij} &+ e^{\theta}_{rijkl}E_{kl})e_{ij,r} + (e^{\theta}_{rij} + e^{\theta}_{rijkl}e_{kl})E_{ij,r} = \\
&= (\varepsilon^{\theta}_{rj} + 2\varepsilon^{\theta}_{rjk}\Phi_{,k})\varphi_{,jr} + (\varepsilon^{\theta}_{rj} + 2\varepsilon^{\theta}_{rjk}\varphi_{,k})\Phi_{,jr} \qquad (2)
\end{aligned}
$$

The material property-temperature relation can be expressed as follows

$$
\begin{aligned}
C^{\theta}_{ijkl} &= C_{ijkl} + C^{(1)}_{ijkl}\theta + C^{(2)}_{ijkl}\theta^2, \\
C^{\theta}_{ijklmn} &= C_{ijklmn} + C^{(1)}_{ijklmn}\theta, \\
C^{\theta}_{ijklmnpq} &= C_{ijklmnpq}, \\
\alpha^{\theta}_{ij} &= \alpha^{(1)}_{ij}\theta + \alpha^{(2)}_{ij}\theta^2,
\end{aligned}
$$

$$e^{\theta}_{ijk} = e_{ijk} + e^{(1)}_{ijk}\theta,$$

$$e^{\theta}_{ijklm} = e_{ijklm},$$

$$\varepsilon^{\theta}_{ij} = \varepsilon_{ij} + \varepsilon^{(1)}_{ij}\theta,$$

$$\varepsilon^{\theta}_{ijk} = \varepsilon_{ijk} \tag{3}$$

where α^{θ}_{ij} are values of the linear thermal expansion coefficient, e^{θ}_{ijk} and e^{θ}_{ijklm} denote linear and quadratic piezoelectric stress tensor components and $\varepsilon^{\theta}_{ij}$ and $\varepsilon^{\theta}_{ijk}$ are the components of the tensor of linear and quadratic permitivities.

The plate in the initial state is at rest and allowed free expansion, that is

$$U_{j,i} = U_{i,j} = E_{ij} = \alpha^{\theta}_{ij},$$

$$T_{ij} = 0, \quad U_i = 0, \quad \Phi_{,i} = 0. \tag{4}$$

The substitution from relations (4) into (3) gives the incremental strain-displacement relations

$$e_{ij} = \frac{1}{2}\,(u_{j,i} + u_{i,j} + \alpha^{\theta}_{kj}u_{i,j} + \alpha^{\theta}_{ki}u_{j,i}), \tag{5}$$

the stress-strain-temperature relations

$$t_{ij} = (C_{ijkl} + D^{(1)}_{ijkl}\theta + D^{(2)}_{ijkl}\theta^2)e_{kl} + (e_{rij} + F^{(1)}_{rij}\theta)\,\varphi_{,r}, \tag{6}$$

the charge equation of electrostatics

$$(e^{\theta}_{rij} + e^{\theta}_{rijkl}\alpha^{\theta}_{kl})e_{ij,r} - \varepsilon^{\theta}_{rj}\varphi_{,jr} = 0, \tag{7}$$

and stress equations of motion

$$(t_{ij} + \alpha^{\theta}_{ik}t_{jk})_{,j} = \rho_0\ddot{u}_i, \tag{8}$$

$$p_i = n_j(t_{ij} + \alpha^{\theta}_{ik}t_{jk}) \quad \text{on S}, \tag{9}$$

where

$$D^{(1)}_{ijkl} = C^{(1)}_{ijkl} + C_{ijklmn}\alpha^{(1)}_{mn},$$

$$D^{(2)}_{ijkl} = \frac{1}{2}\,\tilde{C}^{(2)}_{ijkl} + C_{ijklmn}\alpha^{(2)}_{mn},$$

$$F^{(1)}_{rij} = e^{(1)}_{rij} + \frac{1}{2}\,e_{rijkl}\alpha^{(1)}_{kl},$$

$$\tilde{C}^{(2)}_{ijkl} = C^{(2)}_{ijkl} + 2C^{(1)}_{ijklmn}\alpha^{(1)}_{mn} + C_{ijklmnpq}\alpha^{(1)}_{mn}\alpha^{(1)}_{pq}, \tag{10}$$

$\varphi_{,jr}$ can be expressed from Eq. (7)

$$\varphi_{,jr} = \beta^{\theta}_{rj}(e^{\theta}_{rij} + e^{\theta}_{rijkl}\alpha^{\theta}_{kl})\, e_{ij,r}. \tag{11}$$

where β^{θ}_{jr} are the components of the tensor of linear impermeability.

By substituting Eqs. (6), (10) and (11) into Eq. (8) we obtained the incremental displacement equations of motion

$$G_{ijkl}u_{k,jl} = \rho_0 \ddot{u}_i, \tag{12}$$

where

$$G_{ijkl} = C_{ijkl} + \beta_{rj}e^2_{rij} + G^{(1)}_{ijkl}\theta + G^{(2)}_{ijkl}\theta^2,$$

$$G^{(1)}_{ijkl} = (C_{sjkl} + \beta_{rj}e^2_{rij})\,\alpha^{(1)}_{is} + C_{ijsl}\alpha^{(1)}_{ks} + D^{(1)}_{ijkl} +$$

$$+ (\beta_{rj}e^2_{rij})^{(1)} + \frac{3}{2}\,\beta_{rj}e_{rij}\,e_{rijkl}\alpha^{(1)}_{kl} \tag{13}$$

and $G^{(2)}_{ijkl}$ is the same as in Lee and Yong's paper.

CONCLUSION

The piezoelectric terms in Eqs. (13) are necessary to be considered only when the guided displacement u_i of the vibrations is coupled to the electric field.

REFERENCES

1. P.C.Y. Lee and Y.K. Yong, J. Appl. Phys., 56, 1514 (1984).
2. R. Bechmann, A.D. Ballato and T.J. Lukaszek, Proc. IRE, 50, 1812 (1962).
3. J. Zelenka and P.C.Y. Lee, IEEE Trans. Son. Ultrason., SU-18, 79 (1971).

Ferroelectrics, 1992, Vol. 134, pp. 133–138
Reprints available directly from the publisher
Photocopying permitted by license only

PmC4

PIEZOELECTRIC PROPERTIES OF $Pb(Zn_{1/3}Nb_{2/3})O_3$-$PbTiO_3$ PREPARED BY HIP

Tadashi TAKENAKA, Ken-ichi MURAMATSU* and Takamitsu FUJIU*

Faculty of Science and Technology, Science University of Tokyo, Noda, Chiba-ken, 278 Japan

* *Opto-electronic Materials Lab., Nikon Corporation, Sagamihara, Kanagawa, 228 Japan*

Abstract Piezoelectric properties of the solid solution, $(1\text{-}x)Pb(Zn_{1/3}Nb_{2/3})O_3 \cdot x \cdot PbTiO_3$ (PZN-PT100x), synthesized by hot isostatic pressing (HIP), are intensively studied from a standpoint of applications to piezoelectric actuator materials. Electromechanical coupling factors and piezoelectric strain constants are reported on the perovskite-type PZN-PT ceramics. For example, coupling factors, k_{33}=0.455 and k_{31}=0.148, are obtained for PZN-PT0 (PZN) ceramics. The data are comparable with those of the single crystal. The value of d_{33} for PZN-PT12 (HIP) is 235×10^{-12} C/N.

INTRODUCTION

Lead niobate relaxor family such as lead magnesium niobate, $Pb(Mg_{1/3}Nb_{2/3})O_3$ (PMN), lead zinc niobate, $Pb(Zn_{1/3}Nb_{2/3})O_3$ (PZN) or lead nickel niobate, $Pb(Ni_{1/3}Nb_{2/3})O_3$ (PNN), give growing attractive interest for electronic applications such as piezoelectric actuators and multilayer ceramic capacitors[1,2]. Among the family, PZN[3,4] is known to form only the pyrochlore structure when sintered as ceramics under atmospheric pressure, though perovskite PZN single crystal with high piezoelectric activities can be synthesized by a PbO flux method[3,4]. Also perovskite-structured PZN-based ceramics can be stabilized by substituting for 6~7 mol % $BaTiO_3$[5] or for 10 mol % $KNbO_3$[6]. Single crystal data on solid solution[7,8] of PZN and lead titanate, $PbTiO_3$ (PT), shows remarkable enhanced dielectric and piezoelectric properties at a morphotropic phase boundary (MPB) with 10~12 mol% PT content. Perovskite PZN-PT ceramics of low PT content including the MPB composition, however, are difficult to obtain by the usual sintering process since the pyrochlore formation is mainly recognized during calcination and sintering under conventional conditions.

Recently, we reported[9,10] a two-step process for fabricating perovskite PZN

ceramics. The first step is to calcine the mixture of component oxides with the pyrochlore structure by the usual conditions. Secondly, the pyrochlore PZN is converted to the perovskite phase by using hot isostatic pressing (HIP) under 200 MPa at 1150 °C for 1 h.

In this paper, we utilize the two-step process[9,10] for fabricating perovskite-type $(1\text{-}x)Pb(Zn_{1/3}Nb_{2/3})O_3\text{-}x{\cdot}PbTiO_3$ [PZN-PT100x] solid solution ceramics. Piezoelectric and related properties of the PZN-PT ceramics are discussed as compared with the results of the single crystal data and the conventional method.

EXPERIMENTAL

Perovskite PZN-PT ceramics were fabricated by means of the two-step process, described in detail elsewhere[9,10]. The first step is the formation of pyrochlore PZN-PT powders under atmospheric pressure with 5 wt% excess PbO by the conventional ceramic technique from reagent-grade starting powders of PbO, ZnO, Nb_2O_5 and TiO_2. The second is the conversion-step of the pyrochlore PZN-PT to the perovskite PZN-PT by applying high pressure (150~200 MPa) at high temperature (1150~1200 °C) using a commercial HIP (Kobe Steel Ltd.). Conventional firing (CF) ceramics were also prepared for comparisons to the HIPped samples.

The characterization of the pyrochlore to perovskite transformation was carried out by X-ray powder diffraction (XRD). The ratio of the perovskite phase to pyrochlore phase present in a specimen was defined as the ratio of the respective intensities, I, of the main peaks in X-ray patterns for both phases as follows.

$$\text{Perovskite content (\%)} = \frac{I\,(110)\ \text{perovskite}}{I\,(110)\ \text{perovskite} + I\,(222)\ \text{pyrochlore}} \times 100$$

Au-sputtering was used as electrodes for the measurements of the dielectric and piezoelectric properties. Temperature dependences of dielectric constant, ε_s, and loss tangent, tanδ, of unpoled samples were measured at 10 kHz, 100 kHz and 1MHz by a multifrequency LCR meter (YHP 4275A). D-E hysteresis loops were observed by a standard Sawyer-Tower circuit at 50 Hz.

Specimens for piezoelectric measurements were poled at 25~50 °C in a stirred silicone oil bath by applying a dc electric field of 3 kV/mm for 5~10 minutes. Piezoelectric properties were measured by the resonance-antiresonance method on the basis of IEEE standards using an impedance analyzer (YHP 4192A). The electromechanical coupling factors, k_{33} and k_{31}, were calculated from the resonance and the antiresonance frequencies using Onoe's formula.

RESULTS AND DISCUSSION

The perovskite phase of the obtained $(1\text{-}x)Pb(Zn_{1/3}Nb_{2/3})O_3\text{-}\ xPbTiO_3$ [PZN-

PT100*x*] system was confirmed by X-ray diffraction patterns. Figure 1 shows X-ray diffraction patterns for (a) perovskite PZN-PT20 with tetragonal symmetry, (b) perovskite PZN-PT10 with rhombohedral symmetry and (c) pyrochlore PZN-PT10, respectively. Figure 2 shows the effects of HIP processing on the perovskite formation in PZN-PT system. The perovskite content of the HIP treated and the normal sintered ceramics are evaluated as a function of PT content where HIP conditions are 1150~1200 °C and 200 MPa for 1 h. Addition of 5 % excess PbO enhanced the perovskite contents of PZN-PT10 ceramics to almost 100 % while the content of the ceramics without excess PbO was 82 %. Excess 5 wt% PbO was used to compensate the loss for the evaporation of PbO during sintering. Figure 3 shows the unit cell parameters of the PZN-PT as a function of PT content. The morphotropic phase boundary (MPB) between the rhombohedral region of PZN side and the tetragonal region of PT side was confirmed to lie around 12~13 mol% PT content. This composition shifts slightly to PT side as compared with that of the single crystal data[7;8]. The lattice constant, $a = 4.06$ Å, of PZN-PT0 (PZN) presents a reasonable agreement with the result of the single crystal[4,7].

Amount of the perovskite present in the PZN ceramics after the post-hip heating[9] changed from 96 % without heating to 95 %, 92 %, 42 % and 2 % under heat treatment at 700, 800, 900 and 1000 °C, respectively. The heating treatment converted the

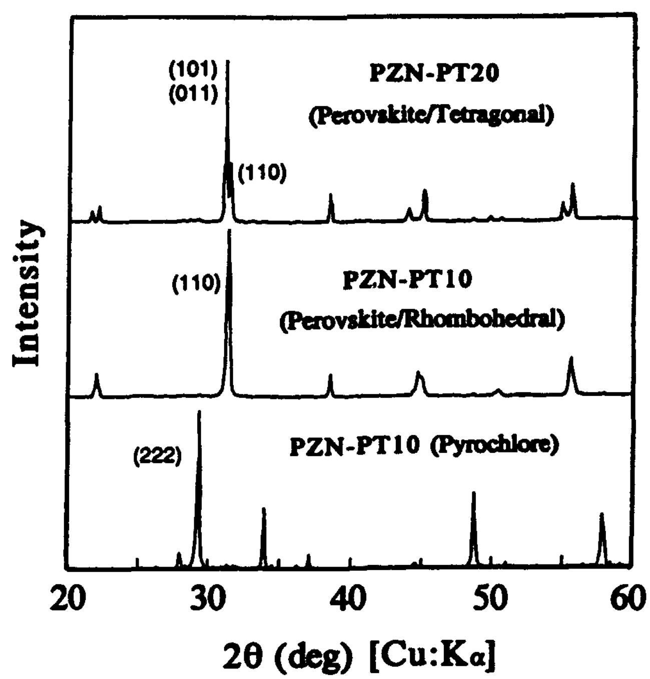

FIGURE 1 X-ray diffraction patterns for (a) PZN-PT20 (perovskite/tetragonal), (b) PZN-PT10 (perovskite/rhombohedral), and (c) PZN-PT10 (pyrochlore) of the $(1\text{-}x)$ $Pb(Zn_{1/3}Nb_{2/3})O_3$ - $x PbTiO_3$ [PZN-PT100x].

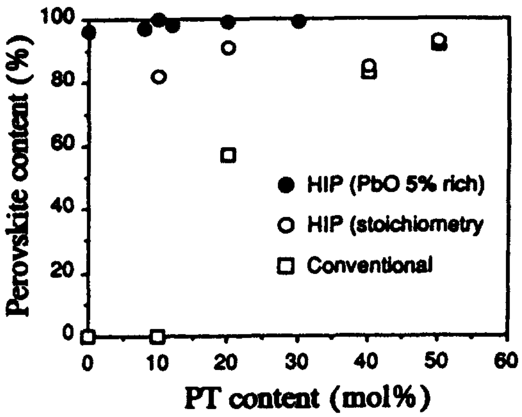

FIGURE 2 Effects of the HIP on the perovskite formation in the PZN-PT system as a function of PT content.

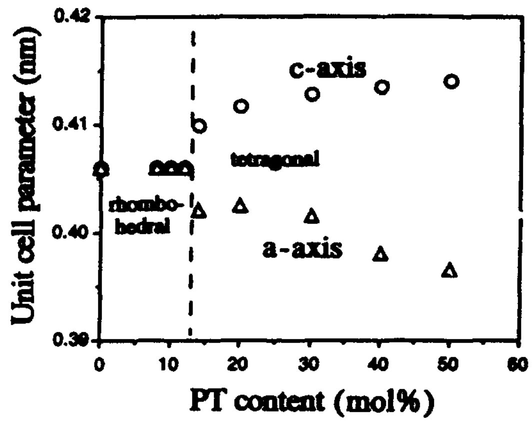

FIGURE 3 Unit cell parameters of the PZN-PT solid solution as a function of PT content.

perovskite phase to the pyrochlore phase. This means that the perovskite phase in PZN ceramics is essentially metastable.

Figure 4 shows temperature dependence of dielectric constant, ε_S, of perovskite-type (a) PZN (HIP) and (b) PZN-PT12 (HIP) and PZN-PT10 +$MnCO_3$ (3 wt%) (CF). The values of ε_S in PZN and PZN-PT12 near the MPB measured at 1 MHz is about 800 and 1420 at room temperature and reach 7110 and 10730 at 175 °C and 222 °C of the respective Curie temperature, T_C. The T_C of conventionally fired PZN-PT10+$MnCO_3$ (3 wt%) with 5 wt% excess PbO (CF) is 173 °C. Single crystal data[3,8] show the T_C of PZN and PZN-PT12 are 140 °C and 192 °C, respectively. On the other hand, the T_C of the high-pressure-synthesized PZN[3,4] was 188 °C owing to Zn-rich ratio of Zn/Nb while it was estimated[3] to be 170 °C for stoichiometric Zn/Nb ratio (=0.5). The higher value of T_C in the high-pressure-synthesized PZN by about 30 °C compared to the single crystals data seems to be caused not only by a slight variation[3,4] in the atomic ratio of Zn/Nb but also by an internal stress. For example[11], a pressure effect on the transition temperature,T_C, for strontium titanate, $SrTiO_3$, indicates that the shift of T_C to higher temperatures is proportional to the magnitude of applied pressure above 150 MPa.

D-E hysteresis loops could be easily observed, as shown in Fig. 5. For example, the loop of PZN-PT12 has a remanent polarization, P_r=16.9 μC/cm^2 and a coercive field, E_c=9.8 kV/cm. Smaller P_r than that of single crystal may be caused by the lower density ratio, ρ_o/ρ_x, to the theoretical density because the loop has no saturation owing to the breakdown.

Table 1 summarizes the results of piezoelectric and related measurements of PZN-PT ceramics prepared by HIPping. The electromechanical coupling factors, k_{33} and

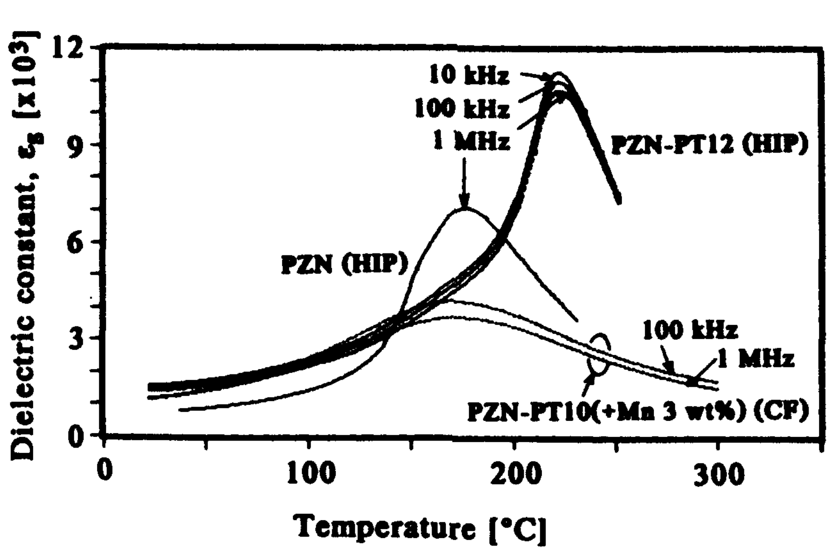

FIGURE 4 Temperature dependence of dielectric constant, ε_s, of the perovskite-type PZN-PT ceramics.

k_{31}, in the longitudinal expansion and the transverse modes, of PZN are 0.455 and 0.148, respectively. The values are almost the same as those of the expected values which are estimated from the single crystal data. Piezoelectric strain constants, d_{33}=155 and d_{31}=49.4 x10^{-12} C/N, can be calculated from the values of a free permittivity, $\varepsilon_{33}{}^T/\varepsilon_0$=690 and the respective coupling factors. Piezoelectric constants, d_{33}=235 and d_{31}=135 x10^{-12} C/N of PZN-PT12 near the MPB were about twice higher than those of CF PZN-PT10+Mn (3 wt%) with excess 5 wt% PbO. However, the values were slightly lower than the expected values from the single crystal data because of the lower coupling factors.

CONCLUSIONS

The two-step pro ss for fabricating the perovskite-type (1-x)$Pb(Zn_{1/3}Nb_{2/3})O_3$-x·$PbTiO_3$ [PZN-PT100x] ceramics was developed by using hot isostatic pressing (HIP) under 150~200MPa at 1150~1200°C for 1 hour. PZN-PT10 ceramics containing 82% perovskite phase were obtained without excess PbO. Addition of 5 % excess PbO enhanced the perovskite contents to almost 100 %. The MPB between PZN and PT solid solution was found to lie the composition between 12 mol% and 14 mol% PT content.

Coupling factors, k_{33}=0.455 and k_{31}=0.148, of the perovskite-type PZN are comparable with those of the single crystal. However, the composition near the MPB, PZN-PT12 gave slightly lower piezoelectric constants, d_{33}=235 and d_{31}=135 x 10^{-12} C/N, than those of the single crystal because of the lower coupling factors.

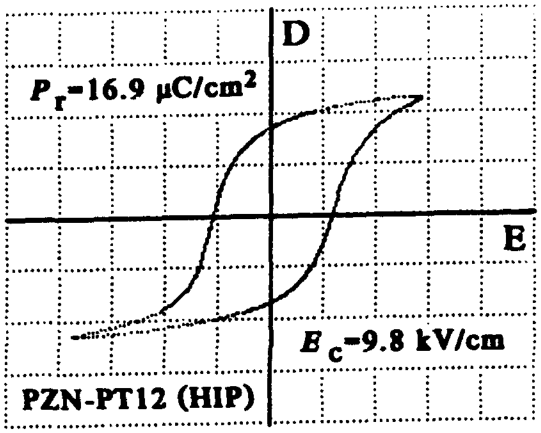

FIGURE 5 D-E hysteresis loop of PZN-PT12 ceramics at 50 Hz.
(X: 8.2 kV/cm/div, Y: 9.5 μC/cm²/div)

TABLE I Piezoelectric properties of the perovskite-type $(1\text{-}x)Pb(Zn_{1/3}Nb_{2/3})O_3 - x \cdot PbTiO_3$ [PZN-PT100*x*] ceramics.

	PZN	PZN-PT12
Curie temperature		
T_C (°C)	175	222
Dielectric constant at 20 °C		
$\varepsilon_{33}^T/\varepsilon_0$	690	1660
Coupling factor		
k_{33} (%)	45.5	48.0
k_{31}	14.8	28.3
Frequency constant		
N_{33} (Hz·m)	1478	1600
N_{31}	1339	1440
Piezoelectric constant		
d_{33} (10^{-12} C/N)	155	235
d_{31}	49.4	135
g_{33} (10^{-3} V·m/N)	25.3	16.0
g_{31}	8.07	9.18
Elastic compliance		
s_{33}^E (10^{-12} m²/N)	18.9	16.3
s_{11}^E	18.3	15.5

Future work is needed to obtain the thermally stable PZN-PT solid solution with the MPB composition. Also, the detailed relation between the Curie temperature, T_C, and the ratio of Zn/Nb to Ti should be investigated.

The authors would like to acknowledge Mr. T. Kanegae and Mr. S. Matsuo for their experimental efforts.

REFERENCES

1. J. M. Herbert: "*Ceramic Dielectric and Capacitors*" (Gordon and Breach, NY, 1985).
2. T. R. Shrout and J. P. Dougherty: "*Ceramic Dielectrics: Composition, Processing and Properties*", (Ceramic Transactions Vol. **8**, The American Ceramic Society, Inc., 1990), p.3.
3. Y. Matsuo, H. Sasaki, S. Hayakawa, F. Kanamaru and M. Koizumi: *J. Phys. Soc. Jpn.* **28**, Suppl., 410 (1970).
4. Y. Matsuo: *Yogyo-Kyokai-Shi* **78** (7), 213 (1970) [*in Japanese*].
5. T. R. Shrout and A. Halliyal: *Am. Ceram. Soc. Bull.* **66** (4), 704 (1987).
6. T. Takenaka, M. Satou, K. Nakata and K. Sakata: *Ferroelectrics* (1992) (in press).
7. S. Nomura, M. Yonezawa, K. Doi, S. Nanamatsu, N. Tsubouchi and M. Takahashi: *NEC Research & Development* **No.29**, 15 (1973).
8. J. Kuwata, K. Uchino and S. Nomura: *Ferroelectrics* **37**, 579 (1981).
9. T. Fujiu, A. Tanaka and T. Takenaka: *Jpn. J. Appl. Phys.* **30** (2B), L298 (1991).
10. T. Fujiu, A. Tanaka, K. Muramatsu and T. Takenaka: "*Ceramic Powder Science IV*" (Ceramic Transactions, Vol.**22**, The American Ceramic Society, Inc., 1991), p.509.
11. H. Fujii, H. Uwe and T. Sakudo: *J. Phys. Soc. Jpn.* **56** (8), 1940 (1987).

Ferroelectrics, 1992, Vol. 134, pp. 139–144
Reprints available directly from the publisher
Photocopying permitted by license only

PmC6

GIANT ELECTROSTRICTION OF FERROELECTRICS WITH DIFFUSE PHASE TRANSITION - PHYSICS AND APPLICATIONS

V.V.Lemanov, N.K.Yushin, E.P.Smirnova, A.V.Sotnikov, E.A.Tarakanov, and A.Yu.Maksimov
Physical-Technical Institute, 194021 St. Petersburg, Russia

Abstract Giant Electrostriction (GE) of disordered ferroelectrics such as Ferroelectrics with Diffuse Phase Transition (FDPT) is noteworthy for application and basic researches. We present experimental data on the electrostrictive strain in FDPT. The description of the peculiarities of the electrostrictive strain is given. Some possible applications of the materials with GE are reviewed.

INTRODUCTION

Electrostriction means the appearence of the strain of the sample under action of an external electric field, the strain being proportional to the field squared. This effect is observed in all solids including centrosymmetric ones in contrast to piezoelectric effect which exists only in noncentrosymmetric crystals, the piezoelectric strain being linear function of the field. For linear dielectrics the electrostrictive strain has value of 10^{-8} for the field E about 10 kV/cm. The electrostrictive strain is described by

$$S = Q \cdot P^2, \qquad (1)$$

where P is the electric polarization of the sample, Q is electrostrictive coefficients. Since $P = \chi E$ (here χ is the dielectric permittivity) the electrostrictive strain S grows due to increasing χ near the ferroelectric phase transition. In FDPT for a wide temperature interval the strain can achieve the value of 0.1 % for the field E

about 10 kV/cm. In addition to the large value the strain in FDPT is characterized by a very slim electromechanical hysteresis loop S(E). Therefore we can speak about GE in such materials. Cross et al[1] have been the first to propose to use the GE for practical devices.

The aim of this report is to present the data on GE strain and to discuss possible technical applications of these materials.

EXPERIMENTS ON THE ELECTROSTRICTION IN FERROELECTRICS WITH DIFFUSE PHASE TRANSITION

The most part of the experiments on the GE was performed for the lead magnesium niobate, $PbMg_{1/3}Nb_{2/3}O_3$ (PMN), and its solid solutions.

The temperature dependences of S(E,T), H(T), and residual strain S_r are shown in Fig.1 for PMN-PSN solid solution (PSN = $PbSc_{1/2}Nb_{1/2}O_3$). Here H is the value of the electromechanical hysteresis introduced by Uchino[2]. One can see the wide temperature interval of coexistence of the large strain S(E) and the small hysteresis H along with the negligible residual strain S_r. When the temperature goes down parameter H becomes as large as in piezoceramics.

It is very important to note that the experimental $S(P^2)$ dependence shows a complicated shape[3], only for small P and high T the strain S being proportional to P^2 (see Fig.2). The S(P) dependence can be described by polynom:

$$S(P) = Q_1P^2+Q_2P^4+Q_3P^6 , \qquad (2)$$

where Q_2 and Q_3 are the forth and the sixth order nonlinear coefficients, respectively. Since S(P) is even function of P (the strain is not changed when the field is inversed), only even powers of P have been taken into account in Eq. (2). It should be noted that the nonlinear

coefficients Q_2 and Q_3 become negligible for the temperatures higher than the mean Curie temperature T_m (T_m = 25 $^\circ$C for this PMN-PSN solid solution)[3]. It means that for these temperatures Eq. (1) is practically valid.

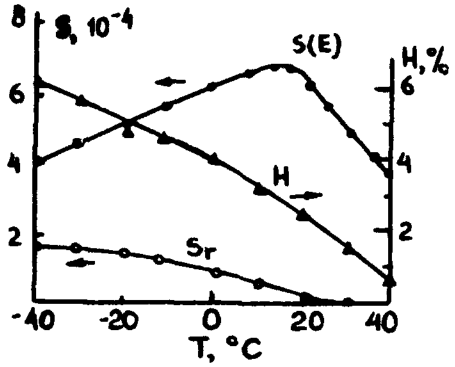

FIGURE 1 S(E), H, and S_r vs T for ceramics 0.55PMN+0.45PSN. E=10kV/cm

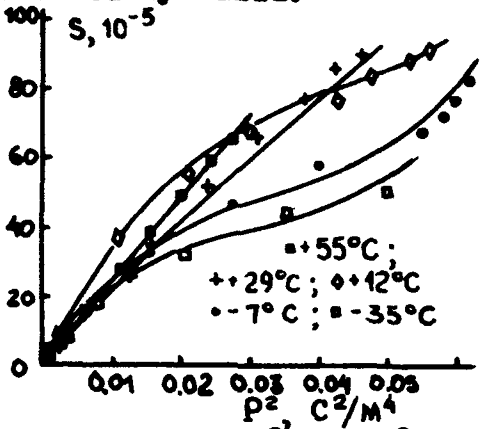

FIGURE 2 $S(P^2)$ vs P^2 for various temperatures shown by numbers[3].

PHYSICAL MODELS OF GIANT ELECTROSTRICTION

FDPT were discovered about thirty years ago[4-6]. Here we omit the discussion of physical models of FDPT to refer to Refs.[4-13].

On the basis of these models we propose that the electrostrictive strain is due to pure electrostriction of the disordered matrix and the structurely ordered microregions [7-10], the reversible changes of polar clusters consisting of groups of strongly correlated polar microregions, the spontaneous strain induced by phase transitions in the ordered microregions, and the rearrangement of ferroelectric domains appearing in homogeniously ferroelectric ordered structure which can be created by field cooling. These types of the strain give various contributions to the total effect for different temperature intervals[13].

As far as the nonlinear dependence $S(P^2)$ is concerned, it could be explained as follows. In the experiment only

values of P averaged over the sample can be measured , but the total strain is the sum of the local strains, each of them being proportional to the local electrostrictive constant by the local polarization squared (according to Eq. 1). It is clear that the total strain $\langle S \rangle$ is not equal to the average electrostrictive coefficient $\langle Q \rangle$ by square of the average polarization $\langle P \rangle$, i.e. $\langle S \rangle = \langle Q \cdot P^2 \rangle \neq \langle Q \rangle \langle P \rangle^2$. It should be pointed that the nonlinear coupling between $\langle P \rangle$ and E is the reason of the nonlinearity of $S(E^2)$ [3].

ELECTROSTRICTIVE DEVICES

The applications of the materials with GE include mainly actuators for deformable mirrors for adaptive optics and lasers, precise displacement micropositioners for scanning microscopy and lithography, linear and rotational motors for machine tools and electric contact systems, impact devices for a printing head matrix, etc.[14]

The electrostrictive actuators are widely used in various devices. We have studied static and dynamic characteristics of different types of actuators. The stack-type actuators provide displacements up to 100 μm under the control voltage 800 V, loads up to 1000 kgf, the hysteresis less than 2 %, a time response shorter than 1 msec, and no residual strain. As far as the thickness of the layers is concerned, the compromise must be found between lowering of the driving voltage and increasing of the electric capacity of the actuators. The bimorphous and multimorphous actuators give chance to obtain displacements to several hundreds μm, but with a noteceable hysteresis, worse time responces, less loads.

The linear motor involves a number of electrostrictive stack actuators which sequential elongations/restorations give a step-by-step motion in accordance with the control electric pulses applied to these actuators. The pass dis-

tance of the motor is to several cm with accuracy of the installation about 1 μm (it is possible to use an additional actuator for precise correction), the step frequency is up to 30 Hz, the loads are up to 100 kgf, the velocity is up to 0.5 mm per min.

The goniometric devices with the electrostrictive actuators were proposed for driving systems and angular measurement systems adopted for coaxial mounting. Absolute accuracy of angular measurements in $0^\circ...360^\circ$ range is defined by the accuracy of the angular sensor, while the minimum linear step is not more than 0.01 μm, the maximum rotation speed is 40 deg. per min. on 30 cm diameter base.

Another valuable application of GE ceramics is in deformable adaptive monolithic mirrors. For such mirrors it is very important to have no residual strain after switch-off the driving voltage because it is difficult to use any feed-back electronics to suppress the hysteresis phenomena. There are two types of these mirrors. In the mirrors with integrated electrodes the mirror surface is changed as a whole. For example the Fig. 3 shows the change of the focus distance R of the mirror with uniform electrodes as a function of the voltage. In the mirror with N separate electrodes one can control the local position of the mirror surface beneath the electrode applying the driving voltage to it. The 52 mm diameter mirror with 97 electrodes has provided the local displacement up to 4 μm for the voltage less than 600 V and no mechanical resonance up to 10 kHz.

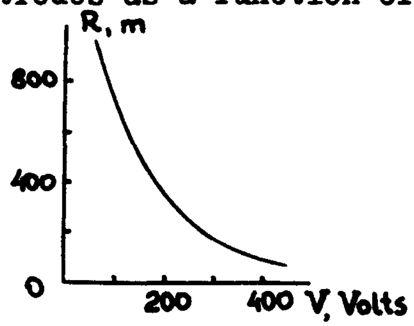

FIGURE 3 The focus R vs voltage V for the 60 mm mirror.

The electrostrictive ceramic precise micromanipulators can be used in the tip of scanning tunneling microscopes.

The hysteresis-free motion of the needle increases the resolution of the devices. We have a success in using PMN-PSN ceramics in the manipulator of the microscope which can resolve the carbon atoms on the graphite surface.

The main advantages of the electrostrictive devices in comparison with piezoceramic ones are smaller electromechanical hysteresis, higher temperature and temporal stabilities and absence of aging. Using materials with GE in all tipes of the microdisplacement devices allowes to shorten response times of the system, to simplify the control electronics, to avoid the deterioration in the characteristics after high-temperature heating and during the operation.

REFERENCES

1. L.E.Cross et al., Ferroelectrics, 23, 187(1980).
2. K. Uchino et al., Jpn. J. Appl. Phys., 4, Suppl. 24-4, 733, (1985).
3. G. A. Smolenskii et al., Pis'ma ZhTF, 13, 44, (1987).
4. G. A. Smolenskii et al., Zh.TF, 27, 1491, (1958).
5. G. A. Smolenskii, J. Phys. Soc. Jpn., Suppl., 28, 26, (1970).
6. V. A. Isupov, Fiz. Tverd. Tela, 5, 187, (1963).
7. E. Husson et al., Mat. Res. Bull., 23, 357, (1988).
8. L.E.Cross, Ferroelectrics, 76, 241, (1987).
9. A.D.Hilton et al., Ferroelectrics, 93, 173, (1989).
10. P. Bunneau et al., Mat. Res. Bull., 24, 201, (1989).
11. S.B.Vakhrushev et al., Physica B, 13, 44, (1989).
12. G.A.Smolenskii et al., Izv. AN SSSR, ser. fiz., 51, 1742, (1987).
13. N.K.Yushin, Mat. Sci. Forum, 62-64, 375, (1990).
14. K. Uchino, Ceram. Bull. 65, 647, (1986).

Ferroelectrics, 1992, Vol. 134, pp. 145–150
Reprints available directly from the publisher
Photocopying permitted by license only

PmC6a

MAXIMAL ELECTROMECHANICAL COUPLING IN PIEZOELECTRIC CERAMICS — ITS EFFECTIVE EXPLOITATION IN ACOUSTIC TRANSDUCERS

WALLACE ARDEN SMITH
Office of Naval Research, Materials Division, Arlington, Virginia 22217
Naval Research Laboratory, Underwater Sound Reference Detachment, Orlando, Florida 32856

Abstract The stress patterns—two shears and one direct stress—that are maximally coupled to the electric field in piezoelectric ceramics are identified. This is achieved by a simplifying initial choice of coordinate axes in the ceramic's thermodynamic phase space and by a subsequent sequence of elementary coordinate changes—rotations and scale changes; simple physical arguments lead to the new coordinates. The utility of this perspective is pointed out in two important applications of piezoceramics in acoustic transducers: naval hydrophone sensors and pulse-echo ultrasonic transducers used in medical diagnostic imaging.

INTRODUCTION

More than three decades ago, Baerwald[1,2] presented an incisive analysis of electromechanical coupling in piezoelectric materials. Baerwald's essential point was that in all piezoelectric materials there are three stress patterns which couple to the electric field—called piezoelectrically 'live'—and three stress combinations which only have an elastic effect—called piezoelectrically 'dead'. Despite the considerable use of piezoelectric ceramics in applications, only modest attention has been paid to this insight,[3] perhaps because the analysis was presented in a mathematical language of symmetry group invariants not commonly spoken by scientists and engineers concerned with practical applications of piezoelectric ceramics. While isolating the maximally coupled stress patterns is quite complex for an arbitrary piezoelectric material of low symmetry, the high symmetry—axial ∞m—of piezoelectric ceramics allows one to proceed using elementary mathematical methods.

In the next section the constitutive matrix for a piezoceramic is explicitly reduced to a standardized form by elementary rotations and coordinate scale changes. This process yields the desired maximally coupled stress patterns. The concluding section presents examples involving the conventional piezoelectric ceramic PZT5H. First we point out what limits its performance in hydrostatic and pulse-echo applications, and then show how structures have been designed using PZT5H which overcome these limitations and provide excellent electromechanical coupling in both naval hydrophone sensors and pulse-echo ultrasonic transducers.

ELECTROMECHANICAL COUPLING IN PIEZOELECTRIC CERAMICS

As formed, piezoelectric ceramics are macroscopically isotropic, nonpolar materials; their microscopic polar regions point in random directions. A macroscopic polarization is produced by applying a strong electric field to orient the microscopic polarizations preferentially along a fixed direction in space—the direction of the poling electric field. Perpendicular to this poling axis, even the poled ceramic is macroscopically isotropic. The piezoceramic's ∞m macroscopic symmetry simplifies considerably cataloging its properties.[4,5] The conventional choice is to align the 'z-axis' or '3-axis' of the coordinate system along the ceramic's polar axis, thereby exploiting the symmetry in physical space to minimize the number of independent material parameters. For the thermodynamic coordinates, the most natural choice is the extensive thermodynamic parameters—the components of the stress, T_I, and electric field, E_i. Using these coordinates, we can expand the internal energy, U, as,

$$U = \frac{1}{2}\sum_{I,J=1,1}^{6,6} s_{IJ}^{E} T_I T_J + \sum_{i,J=1,1}^{3,6} d_{iJ} E_i T_J + \frac{1}{2}\sum_{i,j=1,1}^{3,3} \varepsilon_{ij}^{T} E_i E_j, \tag{1}$$

where s_{IJ}^E is the elastic compliance, d_{iJ} are the piezoelectric coefficients, and ε_{ij}^T is the dielectric permittivity. The abbreviated matrix notation is used to index the six components of the stress tensor with one index. The elastic, dielectric and piezoelectric properties are usually summarized in a 9×9 constitutive matrix shown in Figure 1A. This choice of coordinates—based on the ceramic's symmetry in physical space—yields a constitutive matrix populated mostly by zeros. The thrust of this section is to show how this matrix can be simplified even futher by changes in the coordinates, and thereby provide insight into the fundamental electromechanical coupling. The first step is to rearrange the order of the coordinates to produce the matrix shown in Figure 1B. This makes evident that: first, the shear in the horizontal plane, T_6, has no electrical interaction—it produces no electric response and no electric field can produce such a shear; second, the vertical plane shears, T_4 and T_5, couple to electric fields in the horizontal plane, E_2 and E_1, which lie in the plane of the respective shears; and third, the direct stresses, T_1, T_2, and T_3, couple to a vertical electric field, E_3.

An instructive digression at this point is to rescale the lengths of the coordinates, namely, set $\hat{T}_I = (s_{II}^E)^{1/2} T_I$, and $\hat{E}_i = (\varepsilon_{ii}^T)^{1/2} E_i$, yielding the matrix shown in Figure 1C, containing one's along the diagonals, the Poisson's ratios, $\sigma_{12}^E = -s_{12}^E/s_{11}^E$ and $\sigma_{13}^E = -s_{12}^E/(s_{11}^E s_{33}^E)^{1/2}$, and the electromechanical coupling constants, $k_{31} = d_{31}/(s_{11}^E \varepsilon_{33}^T)^{1/2}$, $k_{33} = d_{33}/(s_{33}^E \varepsilon_{33}^T)^{1/2}$, and $k_{15} = d_{15}/(s_{44}^E \varepsilon_{11}^T)^{1/2}$. Normalizing out the elastic and dielectric response of the medium, reveals that the electromechanical coupling factors measure the true strength of the piezoelectric interaction.

The ceramic's isotropy perpendicular to the polar axis helps us isolate the one direct elastic deformation that couples to E_3. Namely, both the stresses T_1 and T_2 produce the same electric effect, if one has an opposite sign to the other, they just cancel out, producing no electric effect. Thus we choose new axes in the T_1-T_2 plane rotated by 45°, defining, for the uncoupled coordinate, $T_0 = (T_1 - T_2)/2^{1/2}$, and for the coupled planar coordinate, $T_p = (T_1 + T_2)/2^{1/2}$, to yield the constitutive matrix given in Figure 1D. This is *not* a rotation in physical space; E_1 and E_2 do not change; the rotation is carried out in the thermodynamic phase space of the system. The resulting constitutive matrix makes clear that only the isotropic component of the planar stress has an electric effect, the anisotropic component produces an elastic deformation only. Normalizing the coordinates, $\hat{T}_0 = (s_{11}^E - s_{12}^E)^{1/2} T_0$, and $\hat{T}_p = (s_{11}^E + s_{12}^E)^{1/2} T_p$, casts the constitutive matrix into the form shown in Figure 1E. This renormalization brings out two important material parameters: the planar Poisson's ratio, $\sigma_p^E = \sigma_{13}^E \sqrt{2/(1-\sigma_{12}^E)}$, and the planar electromechanical coupling factor, $k_p = k_{31}\sqrt{2/(1-\sigma_{12}^E)}$.

In typical piezoelectric ceramics, the sign of k_p and k_{33} are opposite, so an appropriately weighted sum of an isotropic planar stress, T_p, and axial stress, T_3, will cancel each other out and produce no electric effect. The reverse combination of a planar stress with sign opposite to the axial stress then provides the maximal coupling to E_3. This coordinate change can be done in three steps. First, rotate by 45° in the $\hat{T}_p$-$\hat{T}_3$ plane. This produces a constitutive matrix with a zero in the place of σ_p^E, but changes the diagonal elements from one. Next, renormalize the diagonal elements to one, making a total coordinate change to $\hat{T}_+ = (\hat{T}_p + \hat{T}_3)\sqrt{(1-\sigma_p^E)/2}$, and $\hat{T}_- = (\hat{T}_p - \hat{T}_3)\sqrt{(1+\sigma_p^E)/2}$. Finally, rotate by α, where $\tan\alpha = [(k_p + k_{33})/(k_{33} - k_p)][(1+\sigma_p^E)/(1-\sigma_p^E)]^{1/2}$, and reverse the sense of the maximal axis (to conform to convention), to yield the final axes, $\hat{T}_n = \hat{T}_+\cos\alpha + \hat{T}_-\sin\alpha$, and $\hat{T}_m = \hat{T}_+\sin\alpha - \hat{T}_-\cos\alpha$. This produces the final constitutive matrix shown in Figure 1F, where the maximal coupling factor, $k_{t3} = [(k_p^2 + k_{33}^2 + 2\sigma_p^E k_p k_{33})/(1 - \sigma_p^{E2})]^{1/2}$, links $\hat{T}_m$ and E_3.

Thus, we have an explicit route to construct the three maximal coupling stress patterns in a piezoelectric ceramic. These are the two vertical plane shears, T_4 and T_5, which couple to the horizontal electric fields, E_2 and E_1, respectively, with strength $k_{15} = k_{t1} = k_{t2} = k_{24}$, and $\hat{T}_m = (k_p/k_{t3})\sqrt{s_{11}^E + s_{12}^E}\, T_p + (k_{33}/k_{t3})\sqrt{s_{33}^E}\, T_3$ which couples to the vertical field, E_3, with strength k_{t3}. Other stress patterns, the horizontal shear, T_6, the anisotropic horizontal direct stress, $T_0 = (T_1 - T_2)/2^{1/2}$, and $\hat{T}_n = [(k_{33} + \sigma_p^E k_p)/\sqrt{1-\sigma_p^{E2}}\, k_{t3}]\sqrt{s_{11}^E + s_{12}^E}\, T_p - [(\sigma_p^E k_{33} + k_p)/\sqrt{1-\sigma_p^{E2}}\, k_{t3}]\sqrt{s_{33}^E}\, T_3$ — all these three have an elastic effect only. Any arbitrary stress pattern has an electric effect only to the extent that it overlaps the maximally coupled stresses. Such a general stress will have a lessened electromechanical coupling coefficient to the extent that mechanical energy is wasted in its purely elastic components.

A. CONVENTIONAL FORM

$$\begin{array}{ccccccccc} T_1 & T_2 & T_3 & T_4 & T_5 & T_6 & E_1 & E_2 & E_3 \end{array}$$
$$\begin{bmatrix} s_{11}^E & s_{12}^E & s_{13}^E & \cdot & \cdot & \cdot & \cdot & \cdot & d_{31} \\ s_{12}^E & s_{11}^E & s_{13}^E & \cdot & \cdot & \cdot & \cdot & \cdot & d_{31} \\ s_{13}^E & s_{13}^E & s_{33}^E & \cdot & \cdot & \cdot & \cdot & \cdot & d_{33} \\ \cdot & \cdot & \cdot & s_{44}^E & \cdot & \cdot & \cdot & d_{15} & \cdot \\ \cdot & \cdot & \cdot & \cdot & s_{44}^E & \cdot & d_{15} & \cdot & \cdot \\ \cdot & \cdot & \cdot & \cdot & \cdot & s_{66}^E & \cdot & \cdot & \cdot \\ \cdot & \cdot & \cdot & \cdot & d_{15} & \cdot & \varepsilon_{11}^T & \cdot & \cdot \\ \cdot & \cdot & \cdot & d_{15} & \cdot & \cdot & \cdot & \varepsilon_{11}^T & \cdot \\ d_{31} & d_{31} & d_{33} & \cdot & \cdot & \cdot & \cdot & \cdot & \varepsilon_{33}^T \end{bmatrix}$$

B. REARRANGE COORDINATE ORDER

$$\begin{array}{ccccccccc} T_1 & T_2 & T_3 & E_3 & T_4 & E_2 & T_5 & E_1 & T_6 \end{array}$$
$$\begin{bmatrix} s_{11}^E & s_{12}^E & s_{13}^E & d_{31} & \cdot & \cdot & \cdot & \cdot & \cdot \\ s_{12}^E & s_{11}^E & s_{13}^E & d_{31} & \cdot & \cdot & \cdot & \cdot & \cdot \\ s_{13}^E & s_{13}^E & s_{33}^E & d_{33} & \cdot & \cdot & \cdot & \cdot & \cdot \\ d_{31} & d_{31} & d_{33} & \varepsilon_{33}^T & \cdot & \cdot & \cdot & \cdot & \cdot \\ \cdot & \cdot & \cdot & \cdot & s_{44}^E & d_{15} & \cdot & \cdot & \cdot \\ \cdot & \cdot & \cdot & \cdot & d_{15} & \varepsilon_{11}^T & \cdot & \cdot & \cdot \\ \cdot & \cdot & \cdot & \cdot & \cdot & \cdot & s_{44}^E & d_{15} & \cdot \\ \cdot & \cdot & \cdot & \cdot & \cdot & \cdot & d_{15} & \varepsilon_{11}^T & \cdot \\ \cdot & \cdot & \cdot & \cdot & \cdot & \cdot & \cdot & \cdot & s_{66}^E \end{bmatrix}$$

C. NORMALIZE COORDINATES

$$\begin{array}{ccccccccc} \hat{T}_1 & \hat{T}_2 & \hat{T}_3 & \hat{E}_3 & \hat{T}_4 & \hat{E}_2 & \hat{T}_5 & \hat{E}_1 & \hat{T}_6 \end{array}$$
$$\begin{bmatrix} 1 & -\sigma_{12}^E & -\sigma_{13}^E & k_{31} & \cdot & \cdot & \cdot & \cdot & \cdot \\ -\sigma_{12}^E & 1 & -\sigma_{13}^E & k_{31} & \cdot & \cdot & \cdot & \cdot & \cdot \\ -\sigma_{13}^E & -\sigma_{13}^E & 1 & k_{33} & \cdot & \cdot & \cdot & \cdot & \cdot \\ k_{31} & k_{31} & k_{33} & 1 & \cdot & \cdot & \cdot & \cdot & \cdot \\ \cdot & \cdot & \cdot & \cdot & 1 & k_{15} & \cdot & \cdot & \cdot \\ \cdot & \cdot & \cdot & \cdot & k_{15} & 1 & \cdot & \cdot & \cdot \\ \cdot & \cdot & \cdot & \cdot & \cdot & \cdot & 1 & k_{15} & \cdot \\ \cdot & \cdot & \cdot & \cdot & \cdot & \cdot & k_{15} & 1 & \cdot \\ \cdot & \cdot & \cdot & \cdot & \cdot & \cdot & \cdot & \cdot & 1 \end{bmatrix}$$

D. ROTATE 45° in T_1-T_2 PLANE

$$\begin{array}{ccccccccc} T_0 & T_p & T_3 & E_3 & T_4 & E_2 & T_5 & E_1 & T_6 \end{array}$$
$$\begin{bmatrix} s_{11}^E - s_{12}^E & \cdot & \cdot & \cdot & \cdot & \cdot & \cdot & \cdot & \cdot \\ \cdot & s_{11}^E + s_{12}^E & 2^{1/2} s_{13}^E & 2^{1/2} d_{31} & \cdot & \cdot & \cdot & \cdot & \cdot \\ \cdot & 2^{1/2} s_{13}^E & s_{33}^E & d_{33} & \cdot & \cdot & \cdot & \cdot & \cdot \\ \cdot & 2^{1/2} d_{31} & d_{33} & \varepsilon_{33}^T & \cdot & \cdot & \cdot & \cdot & \cdot \\ \cdot & \cdot & \cdot & \cdot & s_{44}^E & d_{15} & \cdot & \cdot & \cdot \\ \cdot & \cdot & \cdot & \cdot & d_{15} & \varepsilon_{11}^T & \cdot & \cdot & \cdot \\ \cdot & \cdot & \cdot & \cdot & \cdot & \cdot & s_{44}^E & d_{15} & \cdot \\ \cdot & \cdot & \cdot & \cdot & \cdot & \cdot & d_{15} & \varepsilon_{11}^T & \cdot \\ \cdot & \cdot & \cdot & \cdot & \cdot & \cdot & \cdot & \cdot & s_{66}^E \end{bmatrix}$$

E. NORMALIZE ROTATED COORDINATES

$$\begin{array}{ccccccccc} \hat{T}_0 & \hat{T}_p & \hat{T}_3 & \hat{E}_3 & \hat{T}_4 & \hat{E}_2 & \hat{T}_5 & \hat{E}_1 & \hat{T}_6 \end{array}$$
$$\begin{bmatrix} 1 & \cdot & \cdot & \cdot & \cdot & \cdot & \cdot & \cdot & \cdot \\ \cdot & 1 & -\sigma_p^E & k_p & \cdot & \cdot & \cdot & \cdot & \cdot \\ \cdot & -\sigma_p^E & 1 & k_{33} & \cdot & \cdot & \cdot & \cdot & \cdot \\ \cdot & k_p & k_{33} & 1 & \cdot & \cdot & \cdot & \cdot & \cdot \\ \cdot & \cdot & \cdot & \cdot & 1 & k_{15} & \cdot & \cdot & \cdot \\ \cdot & \cdot & \cdot & \cdot & k_{15} & 1 & \cdot & \cdot & \cdot \\ \cdot & \cdot & \cdot & \cdot & \cdot & \cdot & 1 & k_{15} & \cdot \\ \cdot & \cdot & \cdot & \cdot & \cdot & \cdot & k_{15} & 1 & \cdot \\ \cdot & \cdot & \cdot & \cdot & \cdot & \cdot & \cdot & \cdot & 1 \end{bmatrix}$$

F. $\hat{T}_p$-$\hat{T}_3$ TRANSFORM; RENORMALIZE

$$\begin{array}{ccccccccc} \hat{T}_0 & \hat{T}_n & \hat{T}_m & \hat{E}_3 & \hat{T}_4 & \hat{E}_2 & \hat{T}_5 & \hat{E}_1 & \hat{T}_6 \end{array}$$
$$\begin{bmatrix} 1 & \cdot & \cdot & \cdot & \cdot & \cdot & \cdot & \cdot & \cdot \\ \cdot & 1 & \cdot & \cdot & \cdot & \cdot & \cdot & \cdot & \cdot \\ \cdot & \cdot & 1 & k_{t3} & \cdot & \cdot & \cdot & \cdot & \cdot \\ \cdot & \cdot & k_{t3} & 1 & \cdot & \cdot & \cdot & \cdot & \cdot \\ \cdot & \cdot & \cdot & \cdot & 1 & k_{15} & \cdot & \cdot & \cdot \\ \cdot & \cdot & \cdot & \cdot & k_{15} & 1 & \cdot & \cdot & \cdot \\ \cdot & \cdot & \cdot & \cdot & \cdot & \cdot & 1 & k_{15} & \cdot \\ \cdot & \cdot & \cdot & \cdot & \cdot & \cdot & k_{15} & 1 & \cdot \\ \cdot & \cdot & \cdot & \cdot & \cdot & \cdot & \cdot & \cdot & 1 \end{bmatrix}$$

FIGURE 1. Reduction of the constitutive matrix to a standardized form by a succession of coordinate transformations. In each step the coordinates are given as a row vector, then the constitutive matrix; a dot denotes a zero matrix element and $s_{66}^E = 2(s_{11}^E - s_{12}^E)$. (A) The conventional form of the constitutive matrix. (B) Coordinates listed in a new order to make explicit the decoupling of the shear and direct components of stress. (C) Coordinates normalized to show the significance of coupling coefficients. (D) Unnormalized coordinates rotated by 45° in the T_1-T_2 to uncouple the anitsymmetric planar stress from the symmetric planar stress and axial stress that couple to E_3. (E) Normalized rotated coordinates. (F) Transformation to final coordinates and final renormalization: the maximal stress, $\hat{T}_m$, which couples to E_3 is isolated explicitly.

EXAMPLES

To make concrete these rather abstract coordinate changes, this section considers a specific piezoelectric ceramic, Vernitron's PZT5H[6] whose properties are listed in Table I. This material is typical of the lead zirconate titanate ceramics; in particular, all the primary coupling factors have magnitudes greater than 65% and fall in the sequence, $k_{t3} \cong k_{33} > k_{t1} = k_{15} > |k_p|$.

Figure 2 illustrates the final coordinate change in the T_p-T_3 plane to the new axes, $\hat{T}_n$, a stress pattern having no piezoelectric coupling, and $\hat{T}_m$, the stress pattern having the strongest electromechanical coupling factor, k_{t3}, linking it to the electric field along the polar axis, E_3. Both T_3 and T_p have appreciable overlap with T_m and, consequently, have electromechanical coupling factors, k_{33} and k_p, respectively, whose magnitudes are substantial.

A hydrostatic stress pattern, $T_1 = T_2 = T_3$, lies along the axis labeled T_h in Figure 2. This axis is nearly collinear with the uncoupled T_n axis having only a modest overlap with the maximally coupled stress pattern, T_m. This is reflected in the fact that the hydrostatic coupling constant, k_h, in this material is nearly zero; lead zirconate titanate ceramics are, by themselves, not very effective transducers for hydrostatic pressures.

The other direction depicted in Figure 2, labeled T_t, corresponds to the stress pattern in the ceramic in pulse-echo ultrasonic transducers where thin plates are used near their thickness-mode resonance to generate or detect high frequency sound waves. The plate's thickness dimension lies near the acoustic wavelength, while the plate's lateral dimensions are much larger than that wavelength. Because of this large lateral dimension the plate's lateral motion is effectively inertially clamped, namely, in one acoustic cycle the plate simply does not have time to expand or contract laterally. In such transducers, the incoming pressure wave, an applied stress T_3, causes the plate to oscillate in its thickness direction. The lateral inertial clamping results in an oscillating internal stress, T_p, in the plane perpendicular which is in phase with the applied T_3. The ceramic experiences both the applied and internal stress, so T_t has components along both T_3 and T_p. The precise magnitude of the internally generated stresses in the plane of the plate depends on the electrical boundary conditions; in Figure 2, T_t corresponds to the open circuit, $D_3 = 0$, case, in which $T_1 = T_2 = -(s_{13}^E - d_{31}d_{33}/\varepsilon_{33}^T)/(s_{11}^E + s_{12}^E - 2d_{31}^2/\varepsilon_{33}^T)T_3$. The electromechanical coupling factor for the thickness mode oscillation is appreciable, approximately 50%, but still has room for improvement.

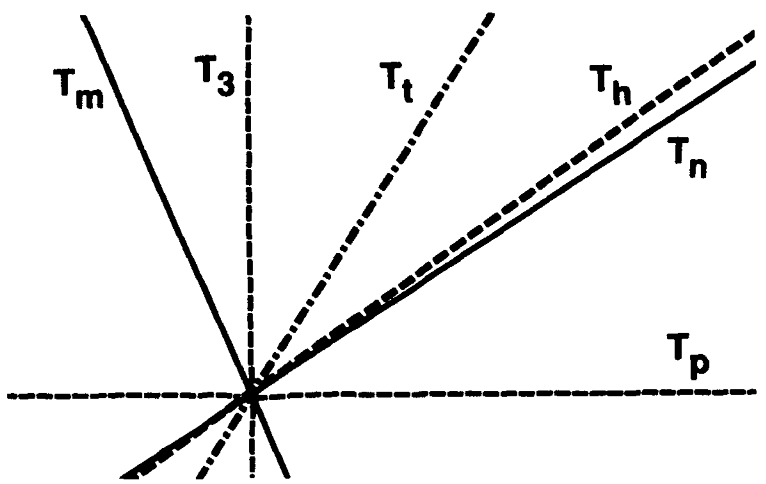

FIGURE 2. The T_p-T_3 plane for PZT5H piezoceramic showing: (a) the T_m axis that represents the stress pattern with maximal electromechanical coupling; (b) the T_n axis that represents a stress pattern with no electromechanical coupling; (c) the T_h axis that corresponds to the hydrostatic stress pattern; and (d) the T_t axis that corresponds to the stress pattern for thickness-mode oscillations in a plate with open circuit electrical boundary conditions.

TABLE I. PZT5H Material Parameters[6]

s^E_{11} $(10^{-12} m^2/N)$	16.5	d_{31} $(10^{-12} C/N)$	-274	k_{31}	-0.389
s^E_{12} $(10^{-12} m^2/N)$	-4.78	d_{33} $(10^{-12} C/N)$	593	k_{33}	0.751
s^E_{13} $(10^{-12} m^2/N)$	-8.45	d_{15} $(10^{-12} C/N)$	741	$k_{15} = k_{i1}$	0.675
s^E_{33} $(10^{-12} m^2/N)$	20.7			k_{i3}	0.761
s^E_{44} $(10^{-12} m^2/N)$	43.5	σ^E_{12}	0.290	k_p	-0.653
$\varepsilon^T_{11}/\varepsilon_0$	3130	σ^E_{13}	0.457	k_h	0.081
$\varepsilon^T_{33}/\varepsilon_0$	3400	σ^E_p	0.767	k_t	0.505

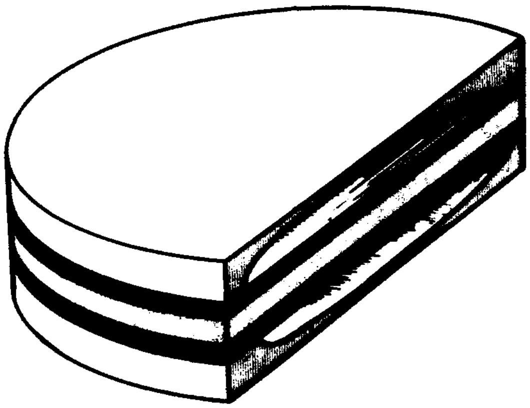

FIGURE 3. Cut away depiction of a miniature composite hydrophone sensor consisting of a piezoceramic disk, electroded on its faces and poled through its thickness, sandwiched between two arched metal disks. When subject to a compressive hydrostatic stress the metal disks not only compress the ceramic where they touch it on its rim, but also push radially outward on the ceramic disk.

To fully exploit lead zirconate titanates ceramics in hydropone transducers, structures have been devised to redirect the hydrostatic stress. Figure 3 illustrates a recent innovation[7-8] that incorporates the principle of macroscopic flextensional transducers—devised for high power actuators—into small hydrophone sensors. In this design, the metal disks transform the vertical, T_3, component of an external hydrostatic compressive stress into an tensile isotropic planar stress that overwhelms the external compressive isotropic planar stress, T_p. The net stress on the piezoceramic disk is then a compressive T_3 transmitted directly to the rim of the disk, plus a tensile T_p acting throughout the disk. Since the coupling factors, k_{33} and k_p, have opposite signs, the electrodes on the disk faces sum in unison the charge from these two opposite stresses—one compressive, the other tensile. Moreover, the electrical response is indeed appreciable since both coupling factors are large in magnitude.

To enhance the performance of lead zirconate titanates in pulse-echo applications, composite materials have been devised which combine the piezoceramic with a passive polymer. Figure 4 illustrates a 1-3 or rod piezocomposite material design that has seen practical commercial application[9-10] in the ultrasonic transducers used in medical diagnostic imaging. In the rod piezocomposite plates the thin rods can expand or contract laterally at the expense of the surrounding softer polymer even though the plate as a whole is laterally clamped. The resulting thickness-mode coupling constant of the composite exceeds that of its constituent ceramic, ranging up to nearly the ceramic's k_{33}. The resulting increased bandwidth and higher sensitivity are important advantages for pulse-echo transducers used in medical diagnostics.

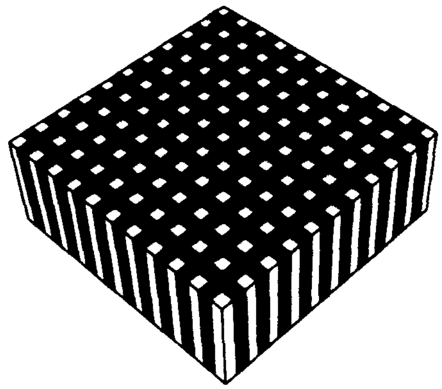

FIGURE 4. Schematic representation of a 1-3 or rod piezoelectric composite plate, consisting of long thin piezoceramic rods, poled along their axis, held parallel to each other and perpendicular to the faces of the plate by a piezoelectrically passive polymer. The soft polymer allows the piezoceramic rods to expand and contract laterally when the plate is used near its thickness-mode resonance, thereby yielding an enhanced thickness-mode electromechanical coupling factor.

CONCLUSIONS

The explicit identification of the stress patterns that provide maximal electromechanical coupling in piezoelectric ceramics provides insights into how these materials have been used effectively in hydrostatic sensors for naval hydrophones and in pulse-echo transducers for medical diagnostic imaging. Moreover, this perspective can guide our thinking in fruitfully exploiting piezoelectric ceramics in future acoustic transducer applications.

REFERENCES

1. H. G. Baerwald, "Eigen Coupling Factors and Principal Components, The Thermodynamic Invariants of Piezoelectricity," *1960 IRE International Convention Record* part 6, pp. 205-211 (1960).

2. H. G. Baerwald, "Invariant Form of Linear Twin-Property Constitutive Equations and Its Application to Piezoelectricity," *IEEE Transactions on Sonics and Ultrasonics*, vol. SU-17, pp. 210-223 (1970).

3. R. Holland and E. P. EerNisse, "Stationary or Eigen Coupling Factors and Loss Tangents," pp. 16-41 in *Design of Resonant Piezoelectric Devices*, Research Monograph No. 56, The M.I.T. Press, Cambridge, Massachusetts, 1969.

4. J. F. Nye, *Physical Properties of Crystals, Their Representation by Tensors and Matrices*, Oxford University Press, Oxford, United Kingdom, 1957.

5. D. A. Berlincourt, D. R. Curran and H. Jaffe, "Piezoelectric and Piezomagnetic Materials and Their Function in Transducers," pp. 169-270 in *Physical Acoustics, Volume 1A*, edited by W. P. Mason, Academic Press, New York, New York, 1964.

6. *Piezoelectric Technology Data for Designers*, Vernitron Piezoelectric Division, Bedford, Ohio (1983).

7. R. E. Newnham, Q. C. Xu, and S. Yoshikawa, "Transformed Stress Direction Acoustic Transducer," U. S. Patent 4,999,819, 12 March 1991.

8. Q. C. Xu, S. Yoshikawa, J. R. Belsick, and R. E. Newnham, "Piezoelectric Composites with High Sensitivity and High Capacitance for Use at High Pressures," IEEE Transactions on Ultrasonics, Ferroelectrics, and Frequency Control, vol. 38, no. 6, pp. 634-639 (1991).

9. W. A. Smith and A. A. Shaulov, " Composite Piezoelectrics: Basic Research to a Practical Device," *Ferroelectrics*, vol. 87, pp. 309-320 (1988).

10. W. A. Smith, "The Role of Piezocomposites in Ultrasonic Transducers," *Proceedings of the 1989 IEEE Ultrasonics Symposium*, pp. 755-766, 1989.

Ferroelectrics, 1992, Vol. 134, pp. 151–156
Reprints available directly from the publisher
Photocopying permitted by license only

PmP111

EFFECTS OF DOPANT Nb^{+5} ON LEAD ZIRCONATE-TITANATE

TERUMASA KATO, NORIAKI YAMADA and ATSUO IMAI
Nagoya Municipal Industrial Research Institute, electrical Division.
Rokuban-3chiome Atsuta-ku, NAGOYA, 456, JAPAN

Abstract Impurity effects of Nb^{+5} dopants were investigated on optimum calcination temperatures and grain growth in sintering process. As the amount of Nb^{+5} dopant increased, optimum calcination temperatures increased. Grain sizes in sintered ceramics decreased in inverse proportion to the amount of Nb^{+5}. Experimental results were expressed in terms of the volume ratio between grain boundary region and grain. Thickness of grain boundary region is estimated to be about 40 A, that corresponds to about 10 lattice layer.

1. INTRODUCTION

Lead Zirconate-Titanate (PZT) with composition near the morphotropic phase boundary are important ferroelectric ceramics, which are widely used for piezoelectric devices.[1)] Defect structures in PZT have been reported upon the effects on electrical properties and sintering kinetics.[2,3)] Several workers reported electrical resistivities for PZT ceramics containing various metal oxides as dopants.[4,5,6,7)] Gerson and Jaffe[8)] proposed that the p-type electrical conduction in PZT resulted from vacancies on the lead sites, which were caused by partial loss of lead during sintering process. In this report, the effects of Nb^{+5} dopant have been investigated on the synthesis of the perovoskite structure during the calcination process and grain growth during the sintering process.

2. EXPERIMENTAL PROCEDURE

The reagent grades of PbO, TiO_2, ZrO_2 and Nb_2O_5 were used as raw materials.

Starting materials, in proper ratios corresponding to the compositions near the morphotopic phase boundary, were mixed in a ball mill with water for 20 hours by using nylon balls as grinding media. The dry powders were press-formed into pellets of about 3 mm thick and 20 mm in diameter at 1 ton per cm^2. After calcining, the samples were milled in water and dried. The dry powders were again press-formed into pellets of about 3 mm thick and 20 mm in diameter at 1 ton per cm^2. All sintering runs were conducted at a constant heating rate of 300°C/h to the sintering temperature of 1280°C. Samples were held for 3 hours at the sintering temperature and were cooled at the natural rate of the furnace. The high vapour pressure of PbO made it necessary to use multiphase pellets, lead zirconate-titanate plus 50 mol% PbO, to keep a PbO atmospheres during the sintering process.[9,10,11]. Samples were always sintered with the multiphase pellets in the container to maintain the PbO vapor pressure for the samples. Grain sizes on the ceramics were observed with Scanning Electron Microscope (SEM).

3. RESULTS AND DISCUSSION

Although it has been discovered that the fabrication process determines the electrical properties,[12] phenomena involved in the process of calcination have not been fully understood. It is necessary to distribute ur'.'.ɔrmly elements of the composition in this process. Figure 1 shows the relation between the calcination time and changes in the rate of the pellet's diameters with Nb^{+5} concentration

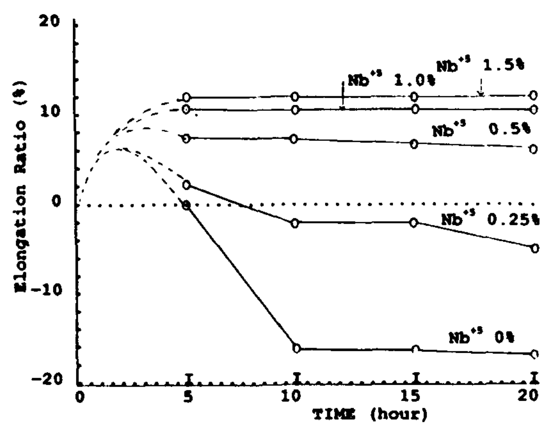

FIGURE 1 Relation between calcination time and changes of pellet's diameters in the case of calcination at 800°C.

in the case of the calcination at 800°C. Diameters changed with amounts of Nb^{+5} dopant, but those did not change so much in the time region over 10 hours. This shows that most of the raw materials are reacted with a short time. Figure 2 shows the X-ray diffraction patterns of powders calcined at 750°C, 780°C and 800°C for 20 hours. Figures 2(a) and (b) show that calcination powders consist of the tetragonal phase ($PbTiO_3$) and the rhombohedral phase (PZT). However, figure 2(c) shows that the sample almost has the single rhombohedral PZT phase.

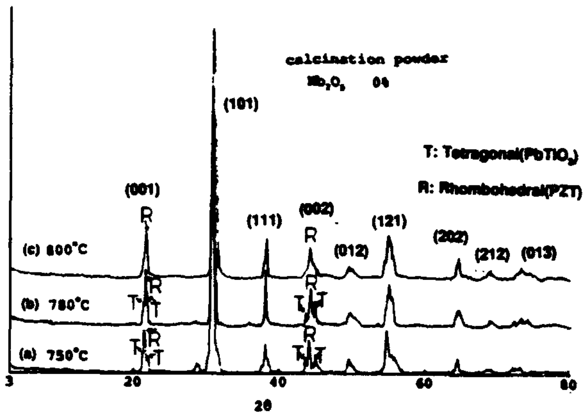

FIGURE 2 X-ray diffraction patterns of intrinsic PZT powders that were calcined at several temperatures (a) 750°C, (b) 780°C, (c) 800°C.

Thus the optimum temperature for calcination of un-doped PZT was determined to be 800°C. Optimum calcination temperatures of Nb^{+5} doped PZT were determined by the same manner as the un-doped PZT's. Figure 3 shows that the

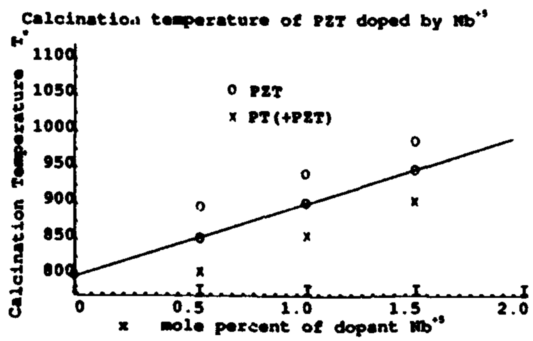

FIGURE 3 Relation of optimum calcination temperature to obtain the PZT single phase and amounts of Nb^{+5} dopant.

optimum calcination temperature increases linearly with amounts of Nb^{+5} dopant. Relation between T_c, the calcination temperature and Xmol% dopant Nb^{+5}, can be formulated as follows;

$$T_c = 800 + 100X. \quad (1)$$

Figure 4 shows the microstructure of ceramics sintered at 1280°C for 3 hours. Grain sizes were measured from Figure 4 and plotted against amounts of Nb^{+5} dopants in Figure 5. Grain sizes were in inverse proportion to the amount of the dopant. It is possible that when the samples were heated to the sintering temperature, the high vapour pressure of PbO created Pb vacancies near the surface of each grain. For compensating the inbalance of the ionic valence, Nb^{+5} ions substituted for Zr^{+4} near the boundary surface of each grain.[13)]

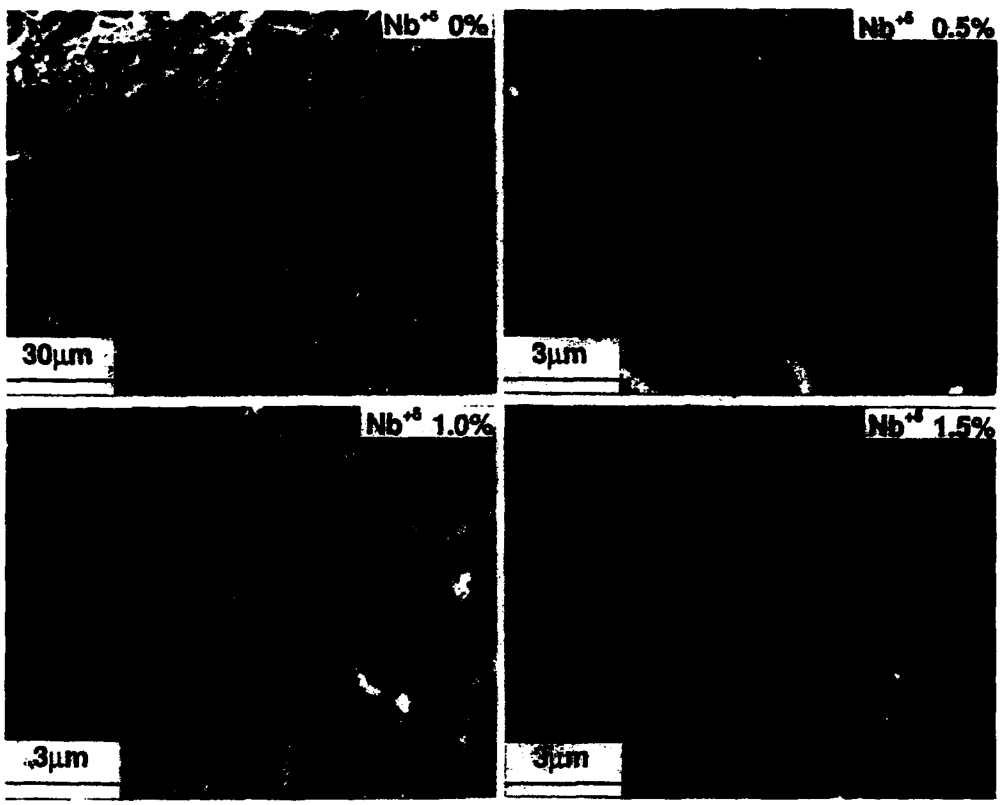

FIGURE 4 Microstructure of PZT ceramics doped Nb^{+5}

Here it is assumed that the diffusion rate of Nb^{+5}, which is substituted for Zr^{+4} in each PZT grain, is low and then Nb^{+5} ions localize at the grain boundary region,

of which the thickness is indicated by δ. If grain boundaries are surrounded with PZT substituted by Nb^{+5} ions, vapour pressures of PbO might be decreased and grain growth should be inhibited. One lead ion vacancy corresponds to two Nb^{+5} ions substituting for Zr^{+4} ions. As a result, $Pb_{(1+x)/2}Nb_{(1-x)}Ti_xO_3$ phase is formed in the surface region, of a sintered PZT grain. If Nb^{+5} ions substitute for all Zr^{+4} in the surface region with thickness δ, the relation X, δ and grain diameter D is expressed as

$$X = 6\times 100\ \delta/D. \qquad (2)$$

In figure 5, the grain size data at each amount of dopant Nb^{+5} was fitted to

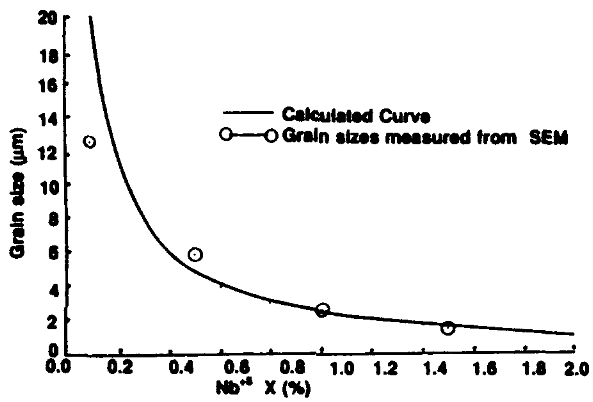

FIGURE 5 Relation of grain sizes and amounts of dopant Nb^{+5}.

equation (2), and grain boundary thickness was determined to be 40 A. That corresponds to 10 unit cell distances. The real thickness of the region containing Nb^{+5} may be larger than δ, because residual Zr^{+4} ions exist even at the grain boundary region.

4. Conclusion

The optimum calcination temperature increases linearly with amounts of Nb^{+5} dopant. Nb^{+5} dopant obstructs the progress of reaction steps. Relation between T_c, the optimum calcination temperature and X mol% amounts of dopant Nb^{+5}, can be formulated as follows;

$$T_c = 800 + 100X.$$

According as the increase of the dopant amounts, grain sizes of sintered ceramics were decreased.

Grain surfaces include lattice defects and lost balances of ionic valence between cation and anion. Amounts of the dopant can be related to ratio of grain boundary volume and grain volume on the assumption of lead vacancy and Nb^{+5} in grain boundary region. Thickness of the grain boundary corresponds about 40 A, that is about 10 lattice layers.

REFERENCES

1. Bernard JAFFE, William R. COOK and Hans JAFFE, PIEZOELECTRIC CERAMIC (Academic Press, LONDON, NEW YORK 1971).
2. R.B.Atkin and R.M.Fulrath, J.Am.Ceram.Soc., 54 (1971) 265.
3. A.H.Webster, T.B.Weston and N.F.H.Bright, J.Am.Ceram.Soc. ,50, 490 (1967).
4. M.Takahashi, Jpn.J.Appl.Phys., 10, 643 (1971).
5. C.V.Stepheson and C.E.Flanagan, J.Chem.Phys., 34 2203 (1961).
6. R.C.Heckman, D.D.Glower and C.R.Hill, Bul.Amer.Phys.Soc., 8 601 (1963).
7. M.Takahashi and S.Takahashi, Jpn.J.Appl.Phys., 9 1006 (1970).
8. R.Gerson and Hans Jaffe, J.Phys.Chem.Solids, 24 979 (1963).
9. R.B.ATKIN, R.L.HOLMAN and R.M.FULRATH , J.Amer.Ceram.Soc., 54 113 (1971).
10. J.J.DIH and R.M.FULRATH; J.Amer.Ceram.Soc., 60 92 (1977).
11. J.J.DIH and R.M.FULRATH; J.Amer.Ceram.Soc., 61 448 (1978).
12. S.S.CHANDRATREYA, R.M.FULRATH and J.A.PASK, J.Amer.Ceram.Soc., 64 422 (1981).
13. T.IKEDA, Y. TANAKA, T. AYAKAWA and H.NOAKE; Jap.J.of Appl.Phys., 3 581 (1964).

Ferroelectrics, 1992, Vol. 134, pp. 157–162
Reprints available directly from the publisher
Photocopying permitted by license only

PmP113

FREQUENCY DEPENDENCE OF THE PIEZOELECTRIC d_{31} COEFFICIENT AS A FUNCTION OF CERAMIC TETRAGONALITY

J.M. VICENTE(*) AND B. JIMENEZ(+)

(*)Dpto de Física. Universidad de Alcalá de Henares. 28801. Madrid. Spain.
(**)Itto. Ciencia de Materiales. Sede A. Serrano 144.28006 Madrid. Spain.

ABSTRACT
Measurements have been made of the complex piezoelectric coefficient (d_{31}), by a quasistatic method, so as to determine its real and imaginary components as a function of frequency (f = 10^{-3} - 10^{3} Hz) and temperature. Results obtained with Ca-modified lead titanate and lead lanthanum titanate-zirconate ceramic samples reveal the existence of relaxations at a very low frequency for the former and at frequencies of tens of hertzs for the latter. Tetragonal distortion and polar microregions could be considered as the respective causes of such relaxation processes.

1.-INTRODUCTION

Some technological applications require piezoelectric materials in which the ratio of electromechanical coupling factors (K_t/K_p) is high. Such is the case, for instance, in echographic imaging, as regards the improvement of resolution.

The direct relation that exists between K_p and the piezoelectric coefficient d_{31} has promoted many studies aimed at understanding the behaviour of d_{31} and its influence on K_p. The materials that have been mainly studied are those with a small K_p, such as samarium-modified lead titanate (PTS) and calcium-modified lead titanate (PTC)[1], and lead-lanthanum titanate-zirconate (PLZT)[2]. In these materials the piezoelectric coefficient, d_{31}, can be written in the form[3]:

$$d^*_{31} = d_{31}' + \Delta d_{31}' - j\, d_{31}'' \qquad (1)$$

where d'_{31} corresponds to values of the coefficient at frequencies well over relaxation, and is the intrinsic contribution of the piezoelectric material. The term $\Delta\, d_{31}'$ is the extrinsic contribution from several types of effects that, in some cases, can be of the same order as d'_{31} and of different sign.

The relaxation character of the extrinsic contributions through the terms $\Delta\, d_{31}' - j\, d_{31}''$ has been confirmed, both in some piezoelectric polymers and in single crystals of Rochelle salt[4] and silver-sodium nitrite[5].

In ceramics, there are no clear results as to the existence of relaxation in some frequency region. In the present work, a study is made of the coefficient d_{31} as a function of frequency between $5*10^{-3}$ and 10^{3} Hz, and as a function of temperature for several frequencies, so as to gather information towards a better understanding of the piezoelectric relaxational processes, and of the extrinsic factors contributing to the final values of d_{31}. The materials that have been studied are lead-calcium titanate and lanthanum-lead titanate-zirconate ceramics.

2.- EXPERIMENTAL METHOD

2.1.- Piezoelectric ceramics

Ceramics of nominal composition

$$Pb_{1-x}Ca_x(Co_{.05}W_{.05}Ti_{.90})O_3 \;+\; MnO(1\%) \qquad (PTC)$$

with x = 0.20 and 0.30 were prepared by a reactive chemical method, as described elsewhere[6].

Ceramics of composition

$$Pb_{.92}La_{.08}(Ti_{.65}Zr_{.35})O_3 \qquad (PLZT\text{-}8)$$

were obtained by coprecipitation from alkoxides, synthesized at 750 °C and afterwards sintered at 1250 °C. From these ceramics pieces of dimensions 13x5x0.5 mm were cut; electroded with silver paint, sintered at 600 °C and polarized to saturation at temperatures 120°C (PTC samples) and 80°C (PLZT samples).

FRECUENCY DEPENDENCE OF THE ...

2.2.- Piezoelectric current

The equivalent circuit of a piezoelectric material subject to a sinusoidal mechanical stress[7] is shown in Fig. 1, with an impedance Z and a phase such that

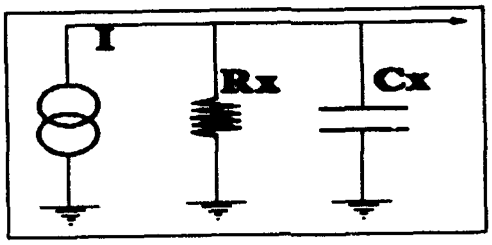

Fig. 1.- Equivalent circuit

$$|Z| = R_x/(1 + \omega^2 C_x^2 R_x^2)^{1/2} \quad \text{tg } \delta = 1/(\omega R_x C_x) \tag{2}$$

The piezoelectric current is given by:

$$i_p = S\,(dD/dt) = d_{31}\,(dT_1/dt) = w\, d_{31}\, T_{10}\, \text{sen}(wt+\theta) = i_o\, \text{sen}(wt+\theta) \tag{3}$$

Between the *piezoelectric current* i_p *and the mechanical stress* T_1 there is a lag θ such that the real and imaginary components of i_p can be written as

$$i_p^{Re} = i_o \cos\theta \quad i_p^{Im} = i_o \sin\theta \tag{4}$$

and, from the relation between i_p and d_{31} ($i_p \propto d_{31}(dT_1/dt)$) we have:

$$d_{31}' \sim i_p^{Re} \qquad d_{31}'' \sim i_p^{Im} \tag{5}$$

Now, the current amplifier also introduces a lag γ, and thus the total lag between T_1 and i_p measured by the osciloscope is $\Phi = \theta + \delta + \gamma$, and must be taken care of by a previous calibration of the system. This calibration has to be done for each sample. The error in the measurement of Φ is of $\pm$ 1°.

Measurements of i_o as a function of temperature were made with the sample in an electric oven up to 150°C. The temperature of the sample was measured with a chromel-alumel thermocouple with an error of $\pm$ 1°C.

3.- RESULTS AND DISCUSSION

In Figs. 2 and 3 we shows the results obtained, for the real and imaginary components of coefficient d_{31}, (or, rather, peak values of i_p/ω , which are proportional to d_{31}) with PTC and PLZT ceramics, as a function of frequency.

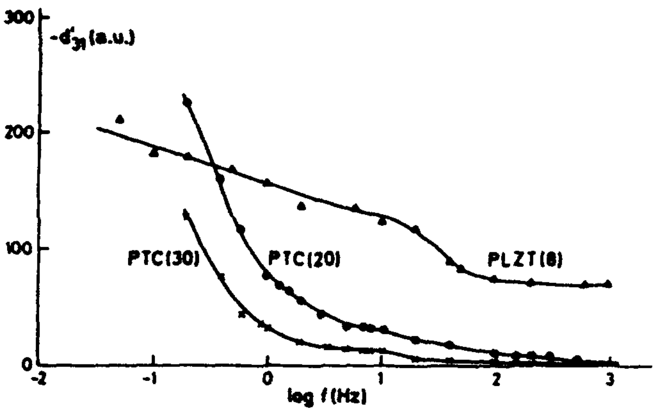

Fig. 2.- Real part of d_{31} vs. frequency. (1a.u.$\approx 3\cdot10^{-13}$C)

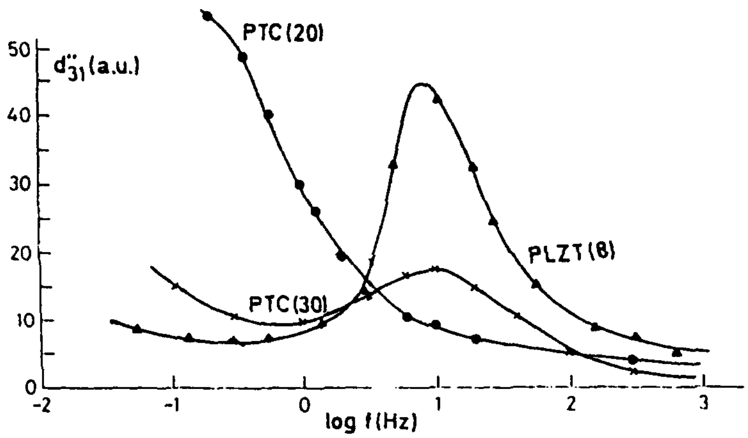

Fig. 3.- Imaginary part of d_{31} vs. frequency. (1a.u.$\approx 3\cdot10^{-13}$C)

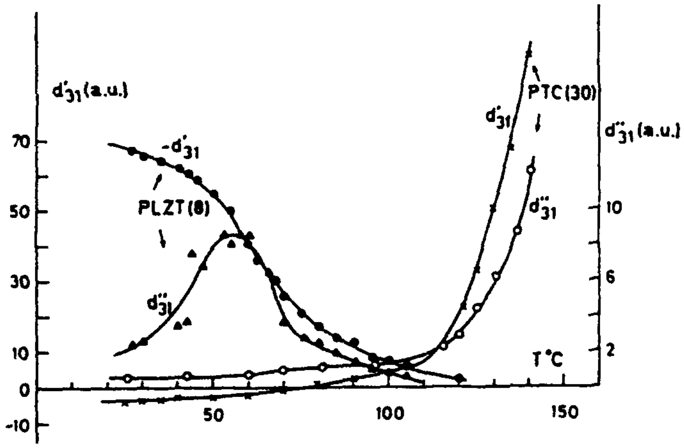

Fig. 4.- Real and imaginary parts of d_{31} vs. temperature. (1a.u.$\approx 3\cdot10^{-13}$C)

A marked increase of d_{31} components is observed, in PTC ceramics, for frequencies under 1 Hz. In turn, PLZT shows a slight and gradual increase, down to the limiting frequency ($5*10^{-3}$ Hz).

Tashiro et al.[8] have studied the transverse mechanical displacement in PTC 24 (c/a=1.039) and in PZT (c/a$\simeq$1.002) as a function of time for different values of an applied DC field. The results of this study show that Ca-modified ceramics behave according to a transverse displacement mechanism, with long relaxation time, that does not exist in PLZT ceramics. The d_{31} coefficient in PTC 24 depends on the amplitude of the AC electric field. The time that PTC 24 ceramics take to reach the equilibrium value is larger than 60 sec. In PZT the equilibrium is reached almost instantaneously.

The results of Figs. 2 and 3 show a behaviour of d_{31} (d_{31}', d_{31}'') in clear agreement with those of Tashiro[8]. The strong increase of these components in PTC -mainly in PTC 20 (c/a=1.045)- in the very low frequency region suggests the existence of a piezoelectric relaxation below 10^{-1} Hz. The behaviour of PLZT-8 is in agreement with that of PZT in ref. (8).

Figures 2 and 3 also show relaxations for PTC-30 and PLZT-8 at frequencies of the order of tens of hertzs. According to the relation $d^* = d_{31}' + \Delta d_{31}' - j d_{31}''$, these relaxations can be ascribed to extrinsic contributions of defects ($\Delta d_{31}' - j d_{31}''$). 90° domain walls have been claimed as being responsible for this contribution[3] but they would probably have a relaxation frequency higher than those obtained in this work.

A possible explanation for the piezoelectric relaxation observed in PLZT-8 (Figs. 2 and 3) could be the contributions to d_{31} of polar microregions[9,10] that exist in ferroelectric materials with a diffuse phase transition (which is the case of PLZT-8). These microregions could also explain the behaviour of the components of PLZT-8 with temperature that is shown in Fig. 4. The temperature for a maximum of piezoelectric losses is lower than that corresponding to the disappearance of the real part of d_{31} (ferroelectric transition temperature). This result is also in agreement with the behaviour of relaxor ferroelectrics as a function of temperature. The apparently anomalous thermal variation of the real component (which decreases with increasing temperature) is very similar to that

of remanent transverse deformation vs. electric field derived from butterfly loops in PLZT ceramics[11]. The variation of the components of d_{31} with temperature for the PTC-30 ceramic (a continuous increase with change of sign of the real component) is similar to that of PTC and PTS ceramics[1,2]. Studies of the components of d_{31} vs. frequency above the temperature where $d'_{31} = 0$ in PTC ceramics are in progress to understand the extrinsic contibutions.

4.- CONCLUSIONS

The relaxational behaviour of the piezoelectric coefficient d_{31} has been determined by quasistatic measurements. The relation between transverse deformation, tetragonal distortion and d_{31} could explain the very low frequency relaxations of PTC ceramics. Polar microregions in PLZT could be responsible for the thermal relaxation behaviour of this ferropiezoelectric ceramic.

AKNOWLEDGMENTS

The authors wish to thank C. Fandiño and F. Díaz for their collaboration in preparing the materials. This work has been carried out under project MAT88-0164 of the Spanish CICYT.

5.- REFERENCES

1.- D.Damjanovic, T.R.Gururaja, S.J.Jang and L.E.Cross. **Mat. Letters, 4**, 414 (1986)
2.- J.G. Smits. **Ferroelectrics, 64**, 275 (1985)
3.- G.Arlt, **Ferroelectrics,40,** 37, (1982)
4.- H.E. Müser and H. Schmitt, **Proc. 2nd EMF,** Dijon 1971
5.- Y.Yamaguchi and K. Hamano. **J. Phys. Soc. Jpn., 18**, 927 (1979)
6.- del Olmo L.,Fandiño C., Pina J.I., Alemany C., Mendiola J., Pardo L., Jiménez B., Maurer E. , **Spanish Patent. Nº 555469** (1986) España
7.- B.Jiménez and J. de Frutos. **Ferroelectrics, 109**, 107, (1990)
8.- S.Tashiro, K. Gotoh and H. Igarashi. **Jap. J. Appl. Phys., 27,** sup. 27-1, 108 (1987).
9.- M.Yokosuka and M.Marutaka. **Jap. J. Appl. Phys., 25,** 981 (1986)
10.- L.E.Cross. **Ferroelectrics, 94**, 241 (1987)
11.- B.Jiménez, L. Pardo and C. Alemany. **Ferroelectrics, 94**, 201 (1989)

Ferroelectrics, 1992, Vol. 134, pp. 163–168
Reprints available directly from the publisher
Photocopying permitted by license only

PmP114

PROPERTIES OF SUBSTITUTED $PbNb_2O_6$ CERAMICS AND MEASUREMENT OF THEIR LOW ELECTROMECHANICAL COEFFICIENTS

ROLAND BRIOT, NEJIB GLISSA, MICHEL TROCCAZ
INSA, Laboratoire de Génie Electrique et Ferroélectricité,
69621, Villeurbanne, FRANCE

Abstract Ceramics of the $PbNb_2O_6$ type with substitutions on Pb and Nb sites are studied. The firing conditions - various cycles of temperature and time - are carefully examined. The main electromechanical coefficients are given. The weak Q and k_p coefficients are calculated from a method perfected in our laboratory.

In the last few years, materials of $PbNb_2O_6$ type have been developed for electroacoustical applications, because these piezoelectric ceramics have the advantage to exhibit a large anisotropy in electromechanical coupling factors between thickness mode k_t and planar mode k_p (the largest possible k_t/k_p ratio with a k_p factor as low as possible) and simultaneously a low mechanical quality factor Q. These compounds seem promising if the relatively difficult manufacturing process can be properly controled. In addition, the measurement of their very low coefficients poses problems.

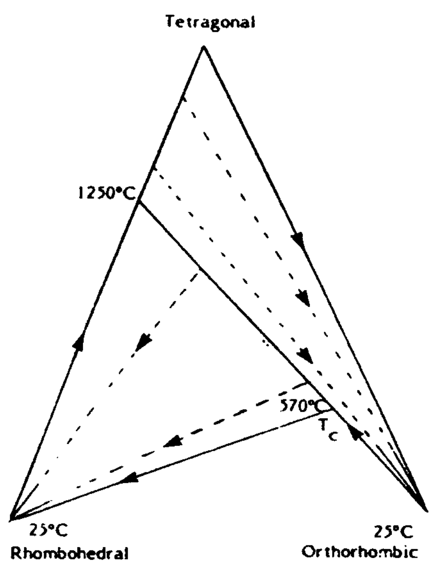

FIGURE 1 Schematic diagram of the $PbNb_2O_6$ transformations

Niobium metaniobate can present two crystallographic forms at room temperature, a rhombohedral one (non ferroelectric), and an orthorhombic one (ferroelectric). In order to obtain polarisable samples, indeed crystallised in the orthorhombic phase, the sintering temperatures must reach at least 1250°C[1]. For the ferroelectric material the structure is tetragonal above the Curie Point (570°C)[2], but the preparation of the polarisable material becomes complicated owing to the reversibility of the transition ferro-non ferroelectric for temperatures not much higher than the Curie temperature.

These transformations are summarized in Figure 1. Apart from this condition on the sintering temperature, the difficulties encountered during the preparation of $PbNb_2O_6$ type ceramics are closely related to the tungsten bronze structure and the weak diffusion of niobium oxide : that is to say the lack of homogeneity, densification and aging.

All the tests have been carried out with a 5 % Sr substitution on the Pb site in order to obtain better piezoelectric characteristics without increasing the Q factor.

PREPARATION OF HOMOGENEOUS SINTERED CERAMICS

As reported by Roth[3], six coumpounds are known to exist in the system $PbO-Nb_2O_5$: P3N, P5N2, P2N, P3N2, with a pyrochlore structure and PN, PN2 with a tungsten bronze structure (P = PbO, N = Nb_2O_5).

However, except for P3N2 and PN, results concerning composition and crystallography of the various compounds are conflicting[4]. For a mixture corresponding to a ratio $PbO/Nb_2O_5 = 1$, the more stable pyrochlore phase formed is P3N2 and rhomboedral $PbNb_2O_6$ would be formed via the process[5] :

$$3\ PbO + 2\ Nb_2O_5 \xrightarrow[\text{fast}]{500\text{-}700°C} 3\ PbO\quad 2\ Nb_2O_5 \tag{1}$$

$$3\ PbO\quad 2\ Nb_2O_5 \xrightarrow[\text{sluggish}]{750\text{-}1000°C} 4\ PbNb_2O_6 \tag{2}$$

According to Yamaguchi[4] PN2 can be formed from 600°C and combines with P3N2

$$3\ PbO\quad 2\ Nb_2O_5 + PbO\quad 2\ Nb_2O_5 \xrightarrow{700\text{-}900°C} 4\ PbNb_2O_6 \tag{3}$$

Another reaction can also occurs if an excess Nb_2O_5 exists :

$$PbNb_2O_6 + Nb_2O_5 \xrightarrow{> 900°C} PbO\quad 2\ Nb_2O_5 \tag{4}$$

X Ray analysis performed on powders fired at 650°C and 1000°C during 10 hours confirms these results (Figure 2)[6,1].

- At 650°C, presence of P3N2 phase according to (1). $PbNb_2O_6$ is already formed, at a lower temperature than that given by reaction (2), perhaps through the reaction (3), although the diffraction lines of PN2 don't appear on the pattern.
- At 1000°C, the pattern corresponds only to the rhombohedral phase $PbNb_2O_6$[1].

Tests carried out at temperatures between 650 and 1000°C show the progressive decrease of the P3N2 phase and never the diffraction lines of the PN2 compound.

So in order to obtain homogeneous sintered ceramics several kinds of firing at 1000°C were performed, summarized on Table 1.

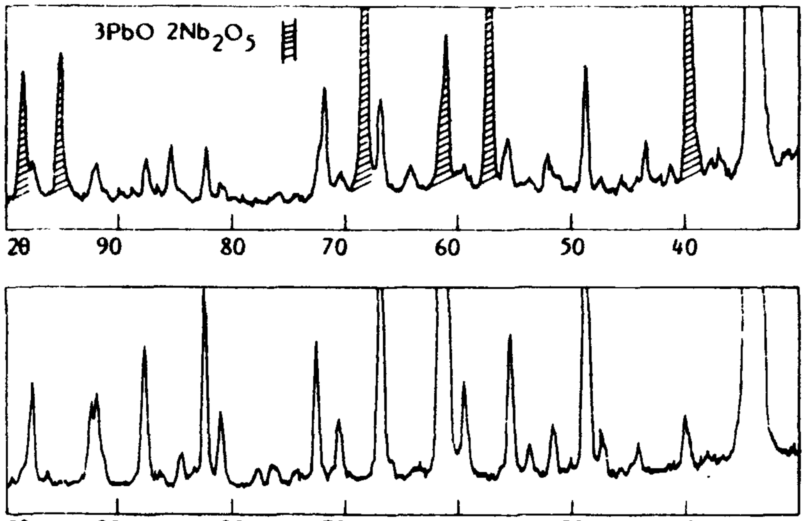

FIGURE 2 X-Ray powder diffraction pattern at various temperatures

TABLE 1 Conditions of firing and resultant characteristics

Firing	1000°C/10 h	1000°C/20 h	1000°C/40 h	2 x (1000°C/10h)
Powder appearance	White yellow traces not compact	White not compact	White not compact	White compact
Sintered sample	inhomogeneous	inhomogeneous	inhomogeneous	homogeneous

It seems that a second rise in temperature at 1000°C finishes the reaction (3) or (2) without going through the reaction (4). A test made with a powder containing 0.01 mole excess Nb_2O_5, which leads to inhomogeneous ceramics, confirms this explanation.

INCREASE OF THE CERAMIC DENSITY - AGING

A notable improvement of the density of the sintered samples is observed when some compounds are added in small amount to the firing powder before grinding, for example MgF_2 or CaF_2. This improvement occurs without changing the piezoelectric characteristics.

Other additives, such as BaF_2, NiO, WO_3, have been tested but the samples recrystallize very easily to form coarse-textured ceramics. Sintering tests with glasses have also been performed. Unfortunately the sintering temperatures are too low, and so the well sintered ceramics obtained are not in the ferroelectric state.

The operations of mixing and grinding the powders have been first carried out in agate jars with ethylic alcohol. It can be observed in

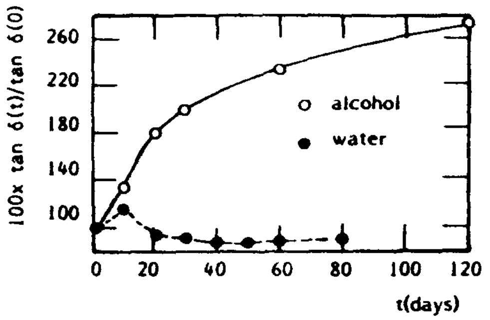

FIGURE 3 Time dependence of tanδ

Figure 3 that the dielectric losses (tanδ) have doubled one month after the ceramic polarization. The other dielectric properties are not modified. On the other hand if the operations are performed with water as the dispersing medium, tanδ remains stable with time (Figure 3).

SUBSTITUTED COMPOSITIONS

Several tests have been performed with various substituting ions on the B site, such as Ni^{2+}, Fe^{3+}, W^{6+} but the piezoelectric coefficients are too weak because of the difficulty in poling these ceramics.

On the other hand it is possible to prepare well sintered ceramics, easy to pole, with a Ti^{4+} ion substitution or an addition of Nb^{5+} ion. The following formulae have been manufactured and their main characteristics measured (Table 2).

A $Pb_{0.95}\ Sr_{0.05}\ Nb_2\ O_6$

B $Pb_{0.95}\ Sr_{0.05}\ (Nb_{1.99}\ Ti_{0.01})\ O_{5.995}$

C $Pb_{0.95}\ Sr_{0.05}\ (Nb_{1.98}\ Ti_{0.02})\ O_{5.99}$

D $Pb_{0.95}\ Sr_{0.05}\ (Nb_{1.97}\ Ti_{0.03})\ O_{5.985}$

E $Pb_{0.95}\ Sr_{0.05}\ Nb_{2.02}\ O_{6.05}$

It can be seen that until a 2 % Ti substitution the electromechanical coefficients are unchanged. Moreover this substitution allows a decrease of the sintering temperature, an easier poling and results are more repetitive.

Ceramics with a Nb excess (E) are quite good, but show some inhomogeneities certainly due to the presence of the PbO 2 Nb_2O_5 compound which is also ferroelectric with a tungsten bronze structure.

TABLE 2 Main characteristics of substituted $PbNb_2O_6$ samples

Sample	Dopant %	ρ	T_s °C	ε_r	tgδ %	d_{33} pC/N	k_p	Q_p	k_t	Q_t
A	0	5.9	1290	242	4.5	72	0.037	10	0.28	8
B	1 Ti	5.6	1270	240	2.6	70	0.048	10	0.27	10
C	2 Ti	5.9	1270	236	2.6	74	0.063	11	0.36	8
D	3 Ti	6.1	1250	345	2.5	72	0.114	24	0.34	23
E	2 Nb	5.7	1270	240	1.8	70	0.069	11	0.33	7

ρ = density ($10^3 Kg.m^{-3}$), T_s = sintering temperature (time = 6 h)

EXPERIMENTAL DETERMINATION OF ELECTROMECHANICAL COEFFICIENTS

The characterization of piezoceramics with low electromechanical coupling coefficient and high mechanical quality factor Q is largely described in IEEE standard on piezoelectricity[7].

The lead metaniobate structure studied in this paper present high mechanical losses with very weak electromechanical coupling especially in radial mode. The experimental method for the determination of electromechanical coefficients derived from G. Martin[8] has been described by R. Briot[9].

A piezoelectric ceramic without dielectric losses can be represented by an equivalent electrical circuit consisting of a series connection (motional resistance R_m, motional capacitance C_m and motional inductance L_m) in parallel with a capacitance at constant strain C_o. The admittance $|Y|$ for this circuit may be written as a function of the normalized frequency $x = f/f_s$ (f_s is defined as the frequency of maximum conductance), the capacitance ratio $r = C_o/C_m$ and the quality factor Q[9].

For each pair (r, Q) selected, it is possible to calculate the ratio $|Y_m|/|Y_n|$ and f_m/f_n where $|Y_m|$ (resp. $|Y_n|$) represents maximum (resp. minimum) of admittance for the frequency f_m (resp. f_n).

The experimental method consists in measuring from a network analyser HP 4194 A, $|Y_m|$, $|Y_n|$, f_m and f_n.

A computer program has been developed in order to calculate r and Q. Then the electromechanical coupling coefficient can be determinated according to the vibration mode :

Radial mode[10] : $$1/k_p^2 = 0,395 \frac{f_s}{f_p - f_s} + 0,574$$

Thickness mode[7] : $$k_t^2 = \frac{\pi}{2}\frac{f_s}{f_p}\left(\tan\frac{\pi}{2}\frac{f_s}{f_p}\right)^{-1}$$

where f_p is defined as the frequency of maximum resistance of piezoelectric ceramic for this vibration mode : $f_p^2 \approx f_s^2\,(1 + 1/r - 1/2\,Q^2)$.

From the network analyser it is also possible to evaluate f_s and f_p and to calculate the electromechanical coupling coefficient, but for lossy material the determination of Q is very difficult.

Figure 4 represents with good accuracy, experimental (points) and simulated electrical (solid line) admittance against frequency.

Experimental and simulated phase curves show the validity of this experimental method which is based only on two experimental points measured from the electrical admittance.

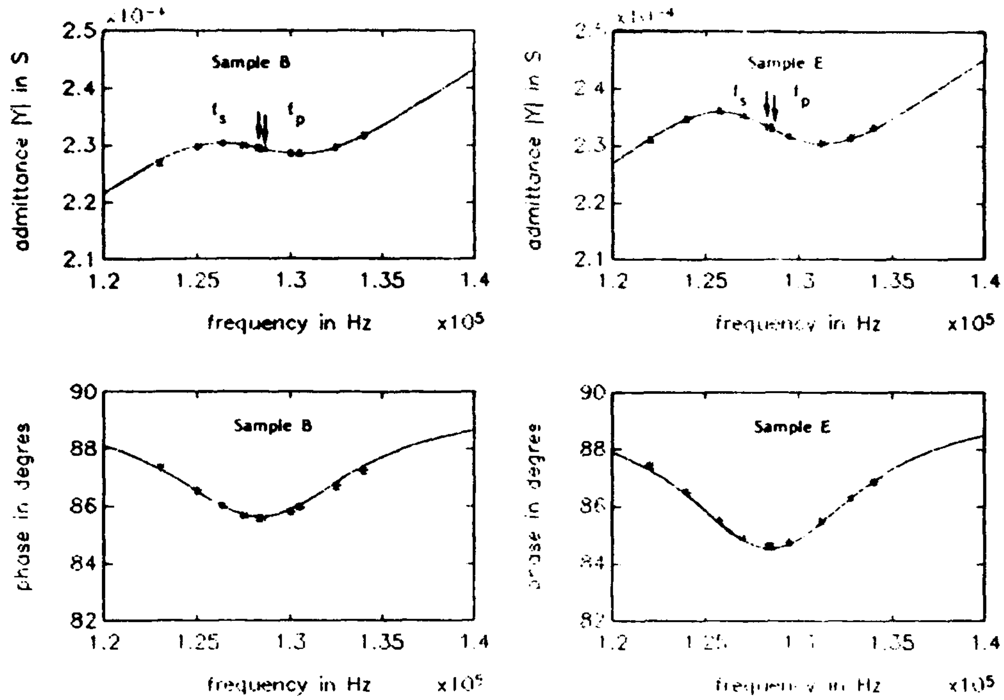

FIGURE 4 Resonance curves - Admittance and phase - versus frequency

CONCLUSION

A manufacturing process of $PbNb_2O_6$ type ceramics has been performed. Samples with 5 % Sr and various amounts of Ti substitutions have been prepared and studied. The main characteristic coefficients are presented, in particular the low electromechanical coefficients Q and k_p measured with a method described in this paper.

REFERENCES

1 H. Francombe, Acta Cryst. 9, 683 (1956)
2 B. Jaffe, W. Cook, H. Jaffe, Piezoelectric Ceram. Academic Press, New-York (1971)
3 R. Roth, J. Res. NBS, 62, 27 (1959)
4 O. Yamaguchi, Y. Mukaida, J. Amer. Ceram. Soc. 73(6), 1705 (1990)
5 V. Prisedskii, L. Gusakova, Russ. J. Inorg. Chem. 21(10) (1976)
6 H. Brusset, H. Gillier-Pandraud, R. Mahé, S.D. Voliotis, Mat. Res. Bull. 6, 413 (1971)
7 IEEE Standard on Piezoelectricity, ANSI/IEEE St 176, (1978), J. Acoust. Soc. Amer. SU31(2) part 2, 1-55 (1984)
8 G. Martin, J. Acoust. Soc. Amer. 46(3), 413-420 (1954)
9 R. Briot, Acoustica 61(1), 28-34 (1986)
10 M. Onoe, H. Tiersten, A. Meitzler, J. Acoust. Soc. Amer. 35(1), 36-42 (1963)

ACKNOWLEDGEMENTS We are grateful to SOCIETE QUARTZ ET SILICE, 77140, Nemours, for having supported this work.

Ferroelectrics, 1992, Vol. 134, pp. 169–174
Reprints available directly from the publisher
Photocopying permitted by license only

PmP116

STUDIES ON FLAWS IN PZT CERAMICS USED IN UNDERWATER DETECTION TRANSDUCERS

MARIE MADELEINE GUILLEMOT-AMADEI, PAUL GONNARD, MICHEL TROCCAZ
INSA, Laboratoire de Génie Electrique et Ferroélectricité,
69621, Villeurbanne, FRANCE

Abstract Experiments on a piezoelectric Tonpilz power transducer show the importance of the quality of the ceramic active material. In order to determine if internal defects appear in PZT ceramics owing to the working of the transducer, two methods of investigation are proposed : an electrical one by measurement of the admittance versus frequency and an ultrasonic one. These two methods lead to identical results for eliminating defective ceramics.

INTRODUCTION

Most of the transducers well suited to underwater detection use the piezoelectric effect to convert an electric signal into an acoustic wave. During the last years many studies have been carried out on sonars in order to lower the working frequencies for an increased detection range and also to increase the radiated power and the working duration. For this purpose we studied a Tonpilz type transducer[1] which has a configuration depicted in Figure 1.

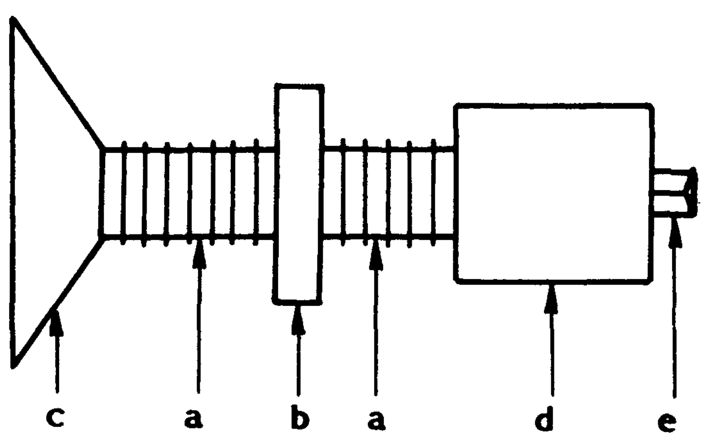

FIGURE 1 : Schematic representation of the studied Tonpilz transducer

It is a longitudinal vibrator consisting of :

- a piezoelectric ceramic stack (a) made of 7 independent pairs (external diameter 50 mm and a 15 mm diameter central hole). In each pair, the piezoceramics are organized with opposed polarities and electrically driven with parallel connection
- a nodal electrode (b)
- a head mass (c) made up of a light material which is in contact with water, the propagation medium
- a tail mass (d) made up of a heavy material in order to absorb the back vibration.

The whole device is glued and held in position by a pre-stressing rod (e) which imposes a 300 bars pre-stress.

The electrical, mechanical and thermal characterization of this transducer has been carried out in air, with the aim to research and identify the different sources of losses and working limitations[2] :

- losses are due to the assembly itself
- but for repetitive tests performed on the same transducer, different results have been obtained. As the only active elements are the piezoceramics, we were induced to study and test these materials.

The ferroelectric compositions used for transducers working under high acoustic load and therefore high electric field are "hard" PZT ceramics. The main characteristics at low level of industrial "hard" PZT ceramics are the following[3] :

$\varepsilon_r = 1200$

$\mathrm{tg}\delta\ (\%) = 0{,}2 - 0{,}4$

$k_{33} = 0{,}62 - 0{,}66$

$d_{33}\ (\mathrm{pC/N}) = 230 - 270$

The study was carried out as follows :

- test of each piezoceramic ring
- assembly in the transducer
- operating (nominal speed 0.16 m/s at 3 kHz in the center of the head mass)
- test again of each ceramic element after the disassembly.

Two methods of investigation are used in order to check the state of the ceramic rings : an electrical and an ultrasonic one.

ELECTRICAL MEASUREMENTS

Using a HP Analyzer 4294 A, the admittance curve of each ceramic is drawn versus frequency under low electric field (1 V/cm). The first resonance in radial mode lies about 35-45 kHz. The typical curve of a good ceramic is given on Figure 2. Figure 3 shows the admittance of two bad ceramics : interfering resonance frequencies appear which can be due to microcracks in the ceramic. These defects are found again on resonances at higher frequencies.

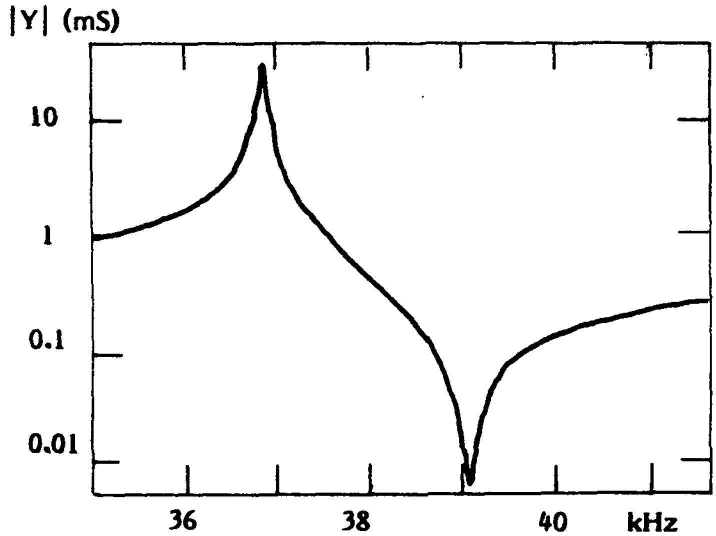

FIGURE 2 : Admittance versus frequency for a good ceramic

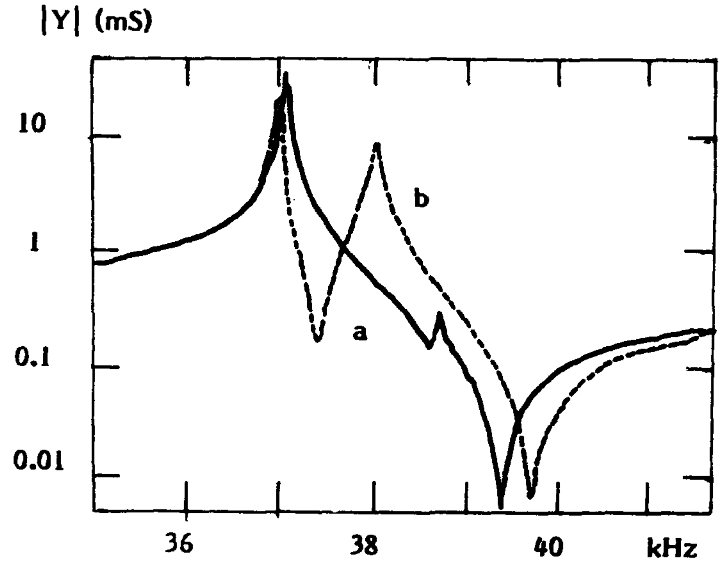

FIGURE 3 : Admittance versus frequency for bad ceramics:
a) small defect
b) important defect

ULTRASONIC ANALYSIS

The principle of the measurement method is the well known immersion technique.

The piezoceramic is placed in a tank filled with water. The ultrasonic beam passes through the ceramic and this beam which has come through the thickness of the ceramic will be representative of its internal state ; for instance if there is an horizontal microcrack the part of the beam which will reach the backwall will be attenuated. For example, using an on-off method to measure the echo amplitude it is seen on Figure 4a that the defects are located :

- n° 1 along a radius and around the central hole
- n° 2 along two radii.

Another method, taking into account a greater number of threshold values, gives the mapping of the ceramics as shown on Figure 4b.

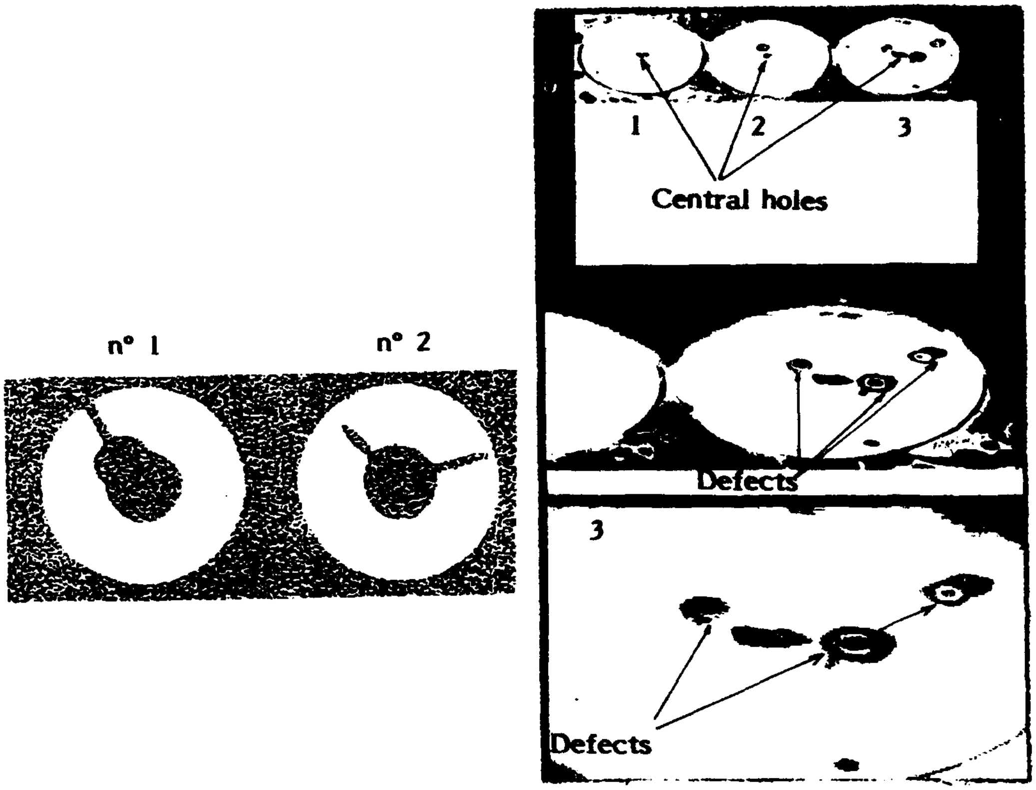

FIGURE 4a FIGURE 4b

FIGURE 4 : Ultrasonic visualization of defects

With the help of the ultrasonic apparatus, the position of a defect found with the electrical method is located, and a slice of the ceramic is sawn. Then an optical photograph of the microcrack is made as shown on Figure 5.

FIGURE 5 : Photograph of a microcrack

ORIGIN OF THE FLAWS

Two main causes can be distinguished :
- Defects due to the piezoceramics[4,5]
- Defects due to the assembly and working of the Tonpilz transducer.

1) Flaws can occur during the fabrication process. Local stresses are developed near discrete defects, such as impurities, porosity or too large grains, and these are responsible for microcracks located near these defects. Microcracks can also appear during the polarization treatment. All these flaws are distributed at random in the volume or at the surface of the ceramic. Other defects are created in the course of machining during the grinding and polishing of the surfaces and the drilling of the central hole.
2) Some systematic studies have been performed with the Tonpilz in order to test the influence of the pre-stress and to measure the maximum dynamic stress :
   - a pre-stress of approximatively 300 bars is applied on the ceramics, and after the Tonpilz has been working, it can be seen :
     - if ceramics are good ones, nothing happens
     - if ceramics are bad ones, as verified by electrical or ultrasonic method, the defects are amplified
   - the maximum dynamic stress of about 100 bars peak is weak and has no effect on the ceramic quality.

CONCLUSION

Defects on ceramic materials influence the properties of the Tonpilz transducer causing :

- a bad matching with the power supply because the characteristics have changed
- an increase of mechanical losses, hence a decrease of the transducer efficiency.

However neither the static nor the dynamic stress seem directly accountable for the flaws achieved after working. But the stress can amplify the defect if it is already present in the piezoceramics. The smallest fault on the admittance curve may be the evidence of flaws into the material which will increase during the transducer's working.

So, before utilization it is very important to test the piezoceramics by using one of the two methods described. Nevertheless with ferroelectric materials the electrical method is easier to implement.

REFERENCES

1. D. Boucher, Proc. of Int. Workshop (Springer-Verlag, Berlin, 1988) pp 100-120
2. M. M. Amadei-Guillemot, Thèse, Acoustique, INSA Lyon (1990)
3. L. Eyraud, P. Gonnard, M. Troccaz, Ferroelectrics, 93, 127 (1989)
4. R. Rice, R. Polanka, J. Am. Ceram. Soc., 62, n° 11, 559 (1979)
5. S. Chiang, R. Fulrath, J. Pask, Com. Am. Ceram. Soc., p 141 (1981)

AKNOWLEDGEMENT We are grateful to DCAN for having supported this work

Ferroelectrics, 1992, Vol. 134, pp. 175-180
Reprints available directly from the publisher
Photocopying permitted by license only

PmP118

PIEZOELECTRIC CERAMICS FOR HIGH-TEMPERATURE TRANSDUCERS

L.KORZUNOVA

Riga Technical University, Riga, Latvia

Abstract The ferroelectrics of the Aurivillius family having $T_c > 700^\circ C$ are investigated from the point of view of their application as high-temperature transducers. The value of piezoelectric modulus d_{33} and its stability are the basic parameters determining the range of application.

The bismuth-containing layered perovskite compounds of the Aurivillius family and of a general formula $Bi_2A_{n-1}B_nO_{3n+3}$ are distinguished by a high value of T_c (n is the number of BO_6 octahedra in the perovskite-like layer).[1]

There is a series of bismuth layered compounds with an even number of layers, the T_c of which is beyond $700^\circ C$. It includes familiar compounds of n=2: Bi_3TiNbO_9 (T_c=940°C), Bi_3TiTaO_9 (T=870°C) and $CaBi_4Ti_4O_{15}$ (T=790°) with n=4.[2] We have obtained 5 new bismuth layered compounds with n=2 the T_c of which is between 720 and 750°C: $Bi_2K_{1/6}Bi_{5/6}Ti_{4/3}W_{2/3}O_9$, $Bi_2K_{1/6}B_{5/6}TiNb_{2/3}W_{1/3}O_9$, $Bi_2K_{1/6}Bi_{5/6}TiTa_{2/3}W_{1/3}O_9$, $Bi_2Pb_{1/3}Bi_{2/3}Ti_{4/3}W_{2/3}O_9$ and $Bi_2Pb_{1/3}Bi_{2/3}TiNb_{2/3}W_{1/3}O_9$.[3] They have been produced by solid state reaction between two bismuth laminated compounds of different number of the perovskite layers n, and by iso- and heterovalent ion substitution in A and B sublattices of the perovskite-like layers. Besides, we have found the T_c for compounds $CaBi_2Nb_2O_9$, $CaBi_2Ta_2O_9$, $SrBi_2Nb_2O_9$, $SrBi_2Ta_2O_9$ with n=2 and $SrBi_4Ti_4O_{15}$ (n=4). Their T_c values reported by Subbarao [4] are related to the first order phase transition, the nature of which is not clear. The true

values of T_c for these ferroelectrics are considerably higher and, according to our data [5], equal to 825°C for $CaBi_2Nb_2O_9$, 810°C for $CaBi_2Ta_2O_9$, 775°C for $SrBi_2Nb_2O_9$, 730°C for $SrBi_2Nb_2O_9$, 730°C for $SrBi_2Ta_2O_9$ and 775°C for $SrBi_4Ti_4O_{15}$. The temperatures have been determined from dielectric permittivity maxima measured at 1 kHz frequency and dilatometric experiments (Figure 1).

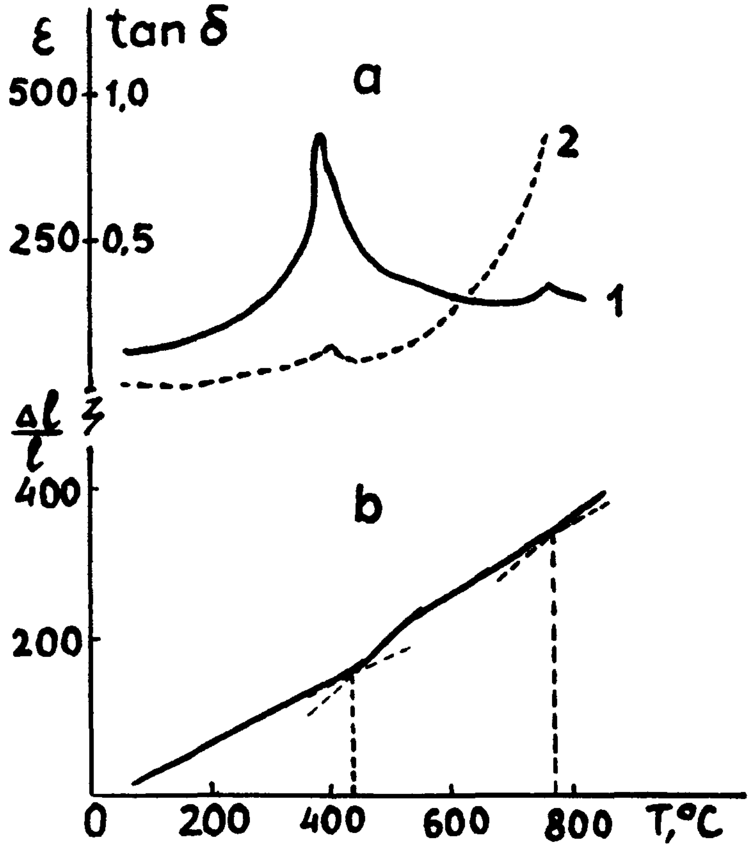

FIGURE 1 Dielectric properties (a) as function of temperature and dilatometric curve(b) of $SrBi_2Nb_2O_9$ ceramics: 1-dielectric permittivity, 2-dielectric losses.

The piezoactivity of $CaBi_2Nb_2O_9$ and $CaBi_2Ta_2O_9$ ceramics is rather low - the value of piezoelectric modulus d_{33} equals $3,3\cdot10^{-12}$ C/N and $1,5\cdot10^{-12}$ C/N, respectively. It is an order higher in the case of $SrBi_2Nb_2O_9$, $SrBi_2Ta_2O_9$ and $SrBi_4Ti_4O_{15}$ ceramics - $11\cdot10^{-12}$; $12,5\cdot10^{-12}$

and $11,2 \cdot 10^{-12}$ C/N. However, because of rather a low stability of d_{33} these compounds cannot be used to make elements for high-temperature transducers (Figure 2).

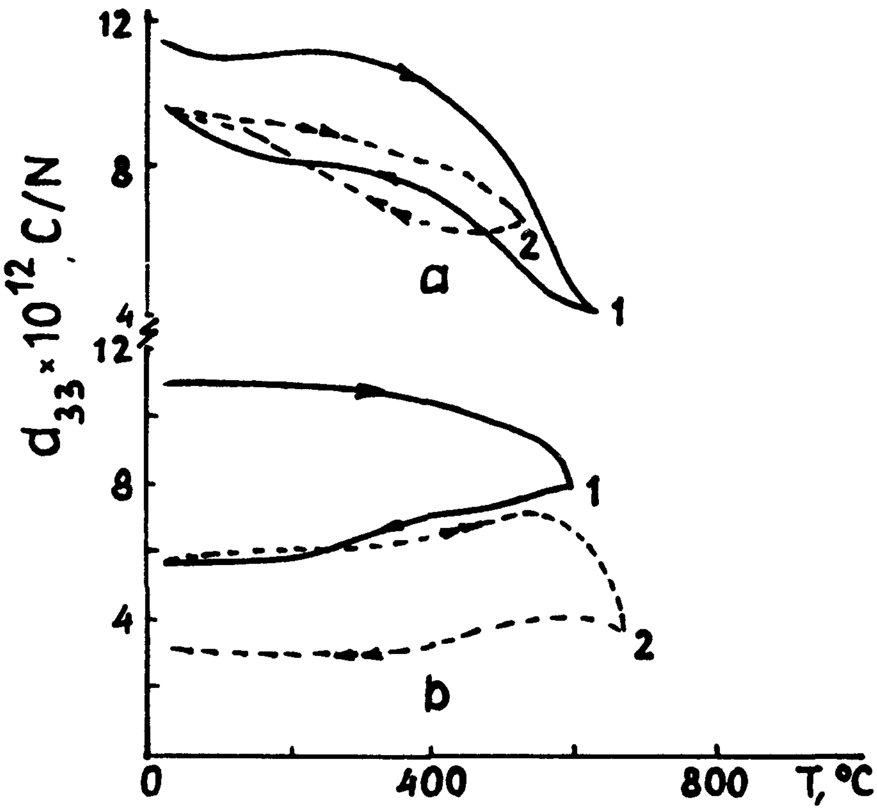

FIGURE 2 Thermal behaviour of piezoelectric modulus d_{33} of $SrBi_2Nb_2O_9$(a) and $SrBi_4Ti_4O_{15}$(b) ceramics: 1-the first cycle, 2-the second cycle

For the same reason the new layered compounds mentioned above can neither be used though amongst the known ferroelectrics of $T_c > 700^oC$ they are distinguished by the highest values of the piezoelectric modulus d_{33} ranging from $14 \cdot 10^{-12}$ to $24 \cdot 10^{-12}$ C/N.[3]

Modification of layered bismuth compounds by various oxides and substances may essentially improve the whole complex of electrophysical properties of the ceramic materials. Thus, an over-stoichiometric amount of Bi_2WO_6 of 7-10 wt % and 0,2 wt % of Cr_2O_3 in $CaBi_4Ti_4O_{15}$ has re-

duced the sintering temperature, broadened the operating range and, most important, increased the value of d_{33} from $4,4 \cdot 10^{-12}$ up to $(10-14) \cdot 10^{-12}$ C/N it's stability being improved (Figure 3). The material is stable up to 700°C.

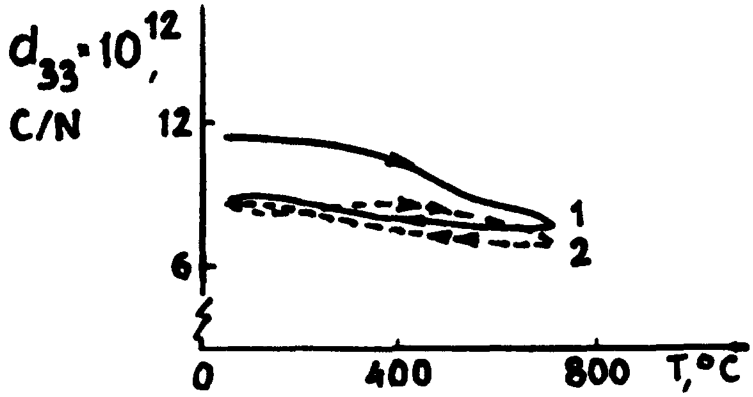

FIGURE 3 Thermal behaviour of piezoelectric modulus d_{33} of $CaBi_4Ti_4O_{15}$ ceramics modified by Bi_2WO_6 and Cr_2O_3: 1-the first cycle, 2-the second cycle.

To develop piezoelectric elements operating at the temperature of 800°C and higher, Bi_3TiNbO_9 has been used.[7,8] The value of the piezoelectric modulus of the Bi_3TiNbO_9 ceramics is $5 \cdot 10^{-12}$ C/N, reversible change of d_{33} comprising 75 %, irreversible - 25 % at 400°C.

The piezoelectric Bi_3TiNbO_9 ceramics modified by chromium, bismuth, molybdenum or antimonium oxides is more resistent to high temperature and pressure (Figure 4).

Properties of materials obtained by conventional ceramics technology at sintering temperatures 1040-1060°C are given in Table 1 and Table 2.

An increased stability of ceramic polarization at high temperature and pressure is due to lattice distortion of bismuth titanate-niobate caused by over-stoichiometric amounts of introduced ions resulting in an enhancement of the internal field of polarized ceramics and the stability of electrophysical parameters.

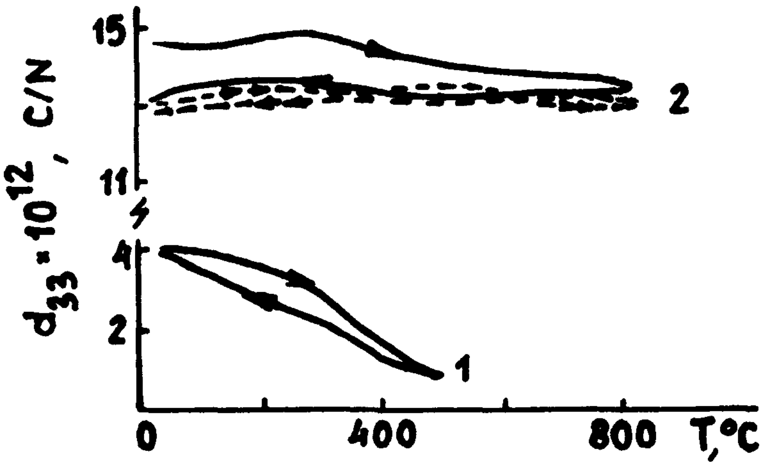

FIGURE 4 Thermal behaviour of piezoelectric modulus d_{33} of Bi_3TiNbO_9-(1) and Bi_3TiNbO_9 ceramics modified by Cr_2O_3, MoO_3, Sb_2O_2-(2)

TABLE 1 Properties of modified Bi_3TiNbO_9 ceramics

Modifier	Range of operating temperature	Piezomodulus $d_{33}.10^{12}$, C/N	Change of d_{33} at T_{max}, % reversible	Change of d_{33} at T_{max}, % irreversible
Cr_2O_3	from +20°C to +800°C	12,0	18	8
$Cr_2O_3+Bi_2O_3$	from +20°C to +800°C	14,0	6	1
$Cr_2O_3+MoO_3$	from -196°C to +850°C	15,2	7 10	4 5
$Cr_2O_3+MoO_3+Sb_2O_3$	from -196°C to +850°C	14,7	6 8	4 4

TABLE 2 Piezoelectric modulus d_{33} of Bi_3TiNbO_9 ceramics modified by Cr_2O_3 and MoO_3

T,°C	25	0	-25	-50	-100	-150	-196
$d_{33}.10^{12}$, C/N	15,2	15,3	15,4	15,5	15,7	15,9	16,0

These materials may be used for different high-temperature piezoelectric sensors of vibrations, shock, transmitters of acoustic signal and other devices.

REFERENCES

1. B.Aurivillius, Ark.Kemi, 1, 463 (1949).
2. L.Ivanova and Yu.Venevtsev, Forecast of ferroelectics science and technology (ferroelectric, antiferroelectric and related compounds), (Moscow, 1983), 99 p. (in Russian).
3. L.Korzunova and L.Shebanov, Ferroelectrics, 93, 111 (1989).
4. L.Korzunova and I.Gordijenko, Electronic ceramics - production and properties, (Riga, 1990), p.58.
5. E.C.Subbarao, J.Phys.Chem.Solids, 23, 664 (1962).
6. L.Korzunova, Z.Novikova, I.Gordijenko, Inorganic glasses, coatings and materials, (Riga, 1991), pp. 130-133 (in Russian).
7. L.V.Korzunova, Z.P.Milberg, Yu.A.Vusevker et al., Patent N 1565825, Bull. N 19 (1990) (in Russian).
8. L.Korzunova, Current problems of production and application of ferro-, piezo- and pyroelectrics and related materials, (Moscow, 1991), p.7 (in Russian).

Ferroelectrics, 1992, Vol. 134, pp. 181–187
Reprints available directly from the publisher
Photocopying permitted by license only

PmP262

THE TRANSIENT PIEZOELECTRIC RESPONSE OF IMPACT LOADED PZT CERAMICS

JULIAN A.CLOSE, R.STEVENS

Division of Ceramics, School Of Materials, University of Leeds, England.

Abstract Samples of commercially produced, poled lead zirconate titanate piezoceramics were subject to impact loading by a free falling striker. Samples were sandwiched in-between a split Hopkinson pressure bar which allowed for characterisation of the tailored, planar strain wave, 20-80μs in duration. The piezoceramic was discharged onto a relatively large capacitor ie:under short-circuit conditions. From these data, a value of the piezoelectric charge coefficient, d_{33} was derived and compared with that derived via the conventional method. Early results indicate that values obtained from the impact rig are substantially higher than those quoted in manufacturers data. It is proposed to analyse a range of materials in an effort to predict behaviour in relation to impact duration, magnitude and resulting deterioration of poling.

INTRODUCTION

A study is made of the transient electrical response of commercial lead zirconate titanate (PZT) piezoceramics, subject to rapid impact loads. The objective is to draw a distinction between these results and those derived from conventional "resonant" characterisation methods. Four PZT compositions are under test, namely: PC4, PC4A, PC5 and PC5H.*

The data derived from the study are relevant to situations in which piezoceramics are utilised as high voltage generators, in active automobile suspension systems and in impact detonation devices.

* Materials supplied by Morgan Matroc, Unilator Division, Ruabon, Wrexham, Clwyd, LL14 6HY.

EXPERIMENTAL TECHNIQUE

The "drop weight impact" testing rig comprises a free falling striker, running on an air-bearing providing an impact of approximately 20μs duration (This can be controlled within certain limits by altering the striker length, whilst the rise time can be controlled by altering the geometry of the striker facing). The piezoelectric device under test (DUT) is situated in a vertically mounted split Hopkinson pressure bar (SHPB) arrangement instrumented with miniature foil strain gauges. The strain gauges monitor the passage of the ensuing stress wave after the striker impacts the top of the "impact" bar and its subsequent passage into the "receiver" bar. The two strain gauge signals received from the SHPB are sent to a custom made high frequency (approximately 2.5MHz bandwidth) virtual-earth pulse amplifier. The amplifier output is then appropriated for analysis by a PC controlled digital storage adaptor (DSA). The two "captured" waveforms allow examination and comparison of the stress wave before and after transmission through the DUT.

A schematic diagram of the impact testing rig is illustrated in Figure 1.

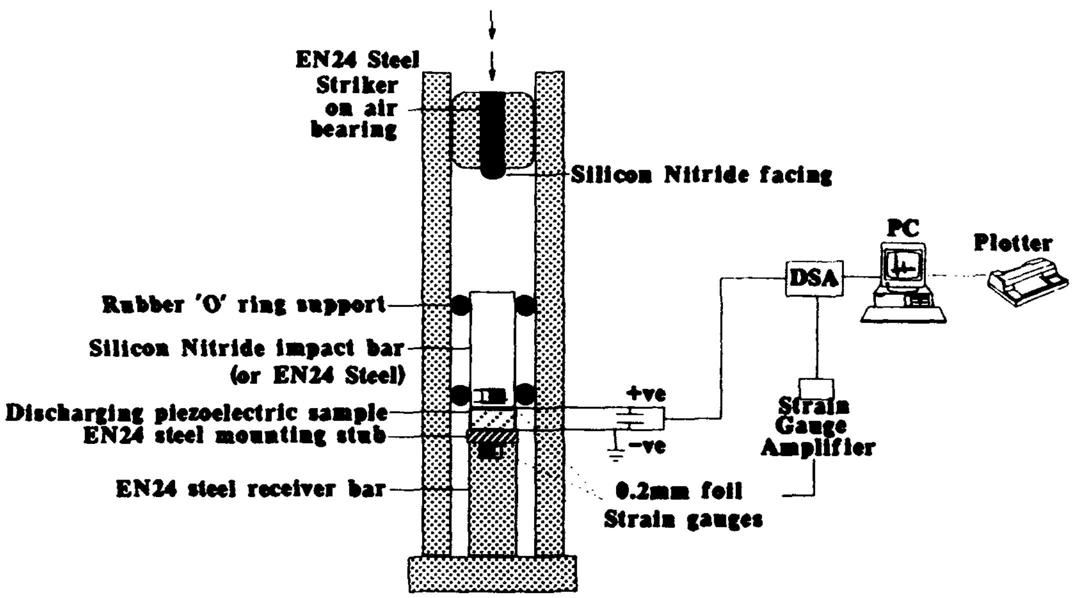

FIGURE 1. Impact testing rig setup

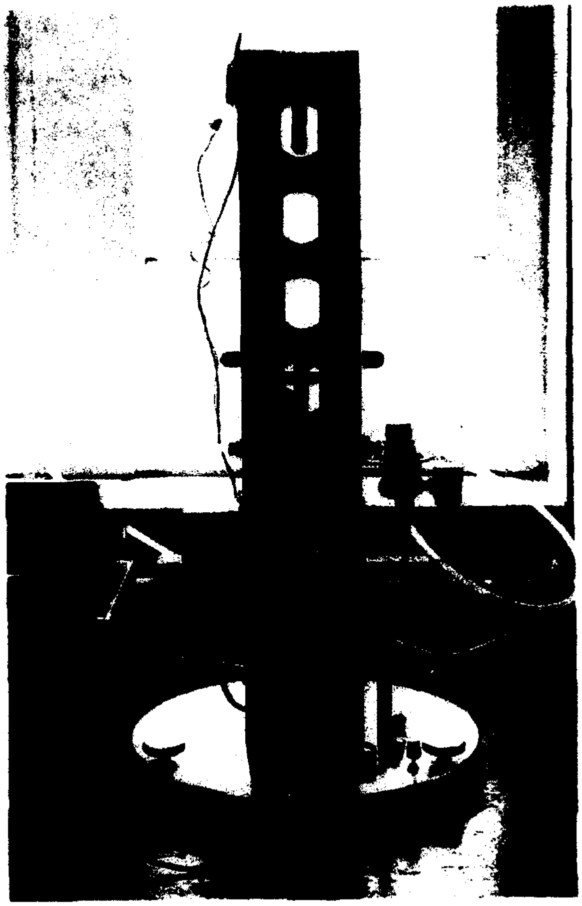

PLATE 1. The SHPB and striker

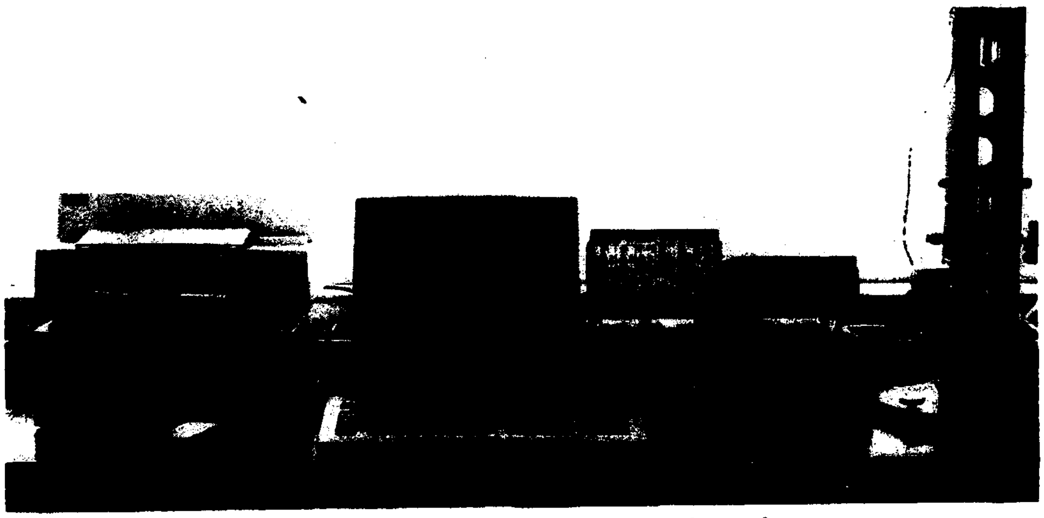

PLATE 2. The impact testing rig

The electrical discharge from the DUT (in the range of 2-3kV) is transferred to a capacitor large enough so that discharge under short-circuit conditions may be assumed, as is the convention for charge output characterisation of piezoelectric devices as it makes no assumptions about permittivity or capacitance changes in the sample during the experiment.
A high frequency 100:1 attenuating oscilloscope probe delivers the charge stored on the capacitor to the DSA for analysis.

INTERPRETATION OF RESULTS

From the "captured" data, it is possible to correlate both the amplitude and duration of the piezoelectric output from the DUT with that of the stress wave passing through it. An estimation can therefore be made of the piezoelectric charge coefficient (d_{33} CN^{-1}) and also the conversion of input mechanical energy into electrical energy ie: k_{33}, the coupling coefficient.
viz:

$$d_{33} = \left(\frac{dD}{dX}\right)_{E,T}$$

and

$$k_{33}^2 = \frac{(output\ electrical\ energy)}{(input\ mechanical\ energy)}$$

where D is the dielectric displacement, X is the stress, the subscripts E and T denoting constant field and temperature respectively, whilst "33" indicates the direction of applied stress and that of the charge flow ("3" being the polarisation direction in the ceramic device).
For each composition, two sample thicknesses (2mm and 5mm) are tested with a view to verifying suspected thickness effects arising from stress wave reflections. An aim of the study is to quantify the finite time taken for the onset of charge flow after application of stress to the DUT ie: t_r, the

"relaxation time" due to domain mobility effects.

Ageing resulting from decay of polarisation can be monitored by the influence on the piezoelectric coefficient values of repeated impacts. An examination by scanning electron microscopy might also reveal microcracking at grain boundaries leading to short-circuiting within the DUT and consequently to a drop in electrical output.

RESULTS

Results obtained from the SHPB rig are shown in Figure 2 and are typical of the responses gained; the upper curve is that of the strain "seen" in the receiver bar whilst the lower is that of the electrical output from the DUT. The evident time difference is due to the time taken for the stress wave to reach the strain gauge, remote from the DUT, on the receiver bar. It is straightforward to compensate for this lag. Preliminary calculations from these data suggest that the PC5 DUT used, (5mm thick; 10mm diameter) was subject to a stress of 54.04 MPa and developed a charge of 16.8 μC.

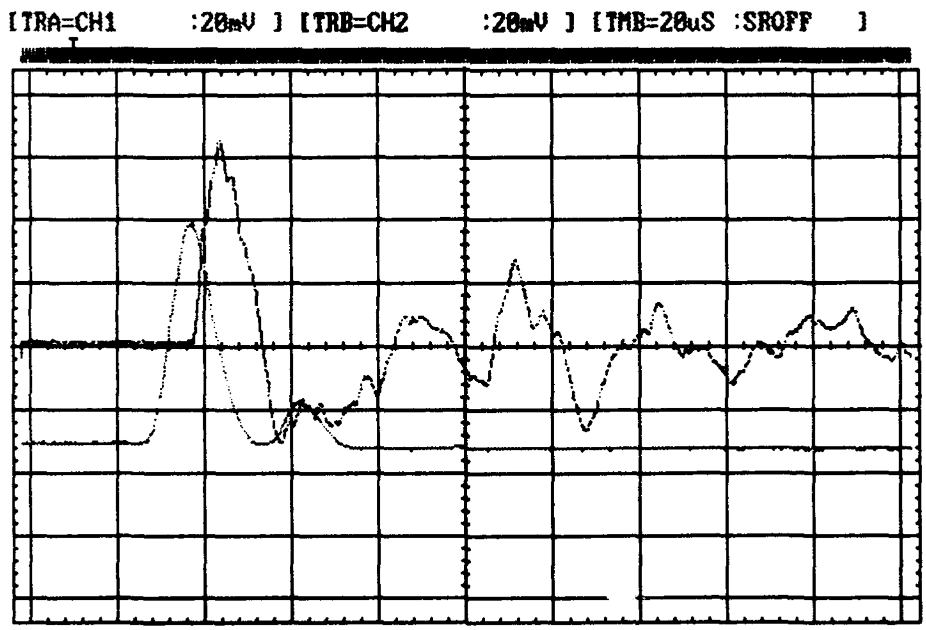

FIGURE 2. Results gained from the SHPB and PC5 sample

The upper curve is a measure of the strain in the sample, the lower, the output from the DUT.

Using these data the "33" charge coefficient for the PC5 material is estimated to be:

$$d_{33} = 3.96\ nCN^{-1}$$

Compared with 340 pCN^{-1} derived from conventional measurements.

UNDERLYING THEORIES

The theories below are based on the assumption that the system obeys the laws of linear elasticity ie: that initial and final body configurations are identical. The duration of the impact is dependent on the time taken for an (acoustic) stress wave, travelling at a speed C_0 (where C_0 is the longitudinal acoustic wave velocity in the material), to traverse the striker twice[1] and the rise time of the stress, by the geometry of the striker facing. The stress wave originates from a point source producing a radial wave, but as this propagates down an impact bar of specific aspect ratio, the axial stress wave assumes a planar, one dimensional profile[2]. The stress pulse duration as already noted is solely dependant on the striker geometry (neglecting dispersive effects, which are negligible), though the pulse length is intrinsically dependant on the value of C_0 in the SHPB. The stress wave passes through the DUT with minimal reflection at the interfaces and is passed into the receiver bar. From the signal picked up by the strain gauge on the receiver bar, a measure of the stress put on the DUT can be derived. The axial stress on the DUT, X_s is directly related to the strain, x_r measured in the receiver bar and is obtained from the balance of the total force between the sample and the receiver bar[3]. ie:

$$X_s = \left(\frac{A_r}{A_s}\right) E_r\, x_r$$

where A_s is the area of the cross section of the sample and A_r is that of the receiver bar whose Young modulus is E_r.

"In situ" calibration of the SHPB is also to be carried out by using X-cut quartz discs of known characteristics in place of the piezoceramic specimens.

The DUT itself cannot be strain gauged directly due to extremely adverse effects arising from capacitive coupling between the discharging piezoceramic and the strain gauge filament.

CONCLUSION

From this experiment the following will be examined.

1) The relationship between values of d_{33} and k_{33} derived from impact testing and those obtained from conventional methods.
2) The effect of impact duration, energy and repetition on the performance of piezoceramic devices.
3) A microstructural analysis to assess the degree of damage generated by the impacting process.

** This work is supported by the National Physical Laboratories, Teddington, Middlesex, England. TW11 OLW.

REFERENCES

1. B.Hopkinson, Phil.Trans.Royal Soc.London, A213, 437-456 (1913-1914).
2. R.M.Davies, Phil.Trans.Royal Soc.London, A240, 375-457 (1946-48).
3. S.Nemat-Nasser, J.B.Isaacs and J.E.Starrett, Proc.Royal Soc.London, A435, 371-391 (8th Nov.1991).

SECTION III
CONTRIBUTED PAPERS
IIIg. Pyroelectrics

Ferroelectrics, 1992, Vol. 134, pp. 189–194
Reprints available directly from the publisher
Photocopying permitted by license only

PcP151

THIN-FILM PYROELECTRIC INORGANIC/ORGANIC COMPOSITES

C.E. MURPHY, T. RICHARDSON[a], G.G. ROBERTS[b]
Department of Engineering Science, University of Oxford, Parks Road, Oxford, OX1 3PJ, U.K.

Abstract Current methods of pyroelectric composite production are incompatible with microelectronics fabrication techniques. Thin-film (1-5μm) inorganic/polymer composites have been produced using a spin-coating method. In the thickness range attainable a quarter-wave cavity for the enhanced absorption of infra-red radiation may be formed. Barium titanate, lead titanate, PZT and lithium tantalate have been incorporated as inorganic dispersoids. A vinylidene fluoride/trifluoroethylene copolymer acts as the host matrix. After the requisite poling procedure the thin film composite materials exhibit pyroelectric coefficients significantly greater than that of 70:30mol% vinylidene fluoride:trifluoroethylene copolymer. They also possess low values of relative permittivity due to the low volume percentages of inorganic material incorporated. As a result the dielectric noise figure of merit is greatly enhanced over conventional polymer pyroelectric materials. These materials are therefore suitable candidates for use in an integrated thermal imaging device.

1. INTRODUCTION

Pyroelectric materials have been extensively investigated recently for use in integrated thermal imaging devices. Inorganic single crystal and ceramic materials[1] possess large pyroelectric coefficients, but their overall performance is limited by high relative permittivity and thermal conductivity. It is also difficult to produce optimum film thicknesses due to the mechanical properties of the materials. Ferroelectric polymers, including polyvinylidene fluoride[2] and associated copolymers[3], possess moderate pyroelectric activity, but have low relative permittivity and thermal conductivity. It is possible to produce thin films using these polymers of the optimum thickness for infra-red radiation absorption. In order to overcome the limitations inherent in these single-phase materials, composite materials were proposed whose properties are described in terms of the connectivity concept[4]. Thick film composites consisting of a ferroelectric ceramic powder phase dispersed in a host polymer matrix (0-3 connectivity) have been produced[5-7]. These composites contain a large percentage of inorganic material and are fabricated by tape-casting or hot-pressing methods. This results in film thicknesses from 50μm to 500μm. The pyroelectric coefficients are large compared to polymers and the relative permittivity values small compared to ceramics. Therefore the figures of merit are enhanced over conventional single-phase polymer materials.

In an integrated thermal imaging device the pyroelectric material is in intimate contact with the readout and analysis electronics in the form of an integrated circuit. The processing of the pyroelectric material must therefore be compatible with microelectronics fabrication techniques. This paper describes thin-film composite materials which have been produced by a spin-coating method. This technique is regularly used to yield polymer films in the thickness range 0.1μm - 5μm. By producing pyroelectric composite films of this thickness a quarter wavelength cavity for the enhanced absorption of infra-red radiation may be realised[8]. In a staring array of pyroelectric elements the low thermal

[a] Dr. T. Richardson is now at the Department of Physics, University of Sheffield, Sheffield, U.K.
[b] Prof. G.G. Roberts is now Vice-Chancellor at the University of Sheffield, Sheffield, U.K.

conductivity of the matrix polymer phase will effectively reduce pixel crosstalk to an acceptable level.

The polymer utilised as the matrix phase is a 70:30mol% vinylidene fluoride:trifluoroethylene copolymer (Attochem, France). This polymer may be spun effectively to form highly uniform films and has been extensively studied as a ferroelectric material. Barium titanate (TAMTRON X7R422H from TAM Ceramics, Box C, Bridge Station, Niagara Falls, N.Y. 14305, U.S.A.), lead titanate (Aldrich Chemical Company, The Old Brickyard, New Road, Gillingham, Dorset, SP8 4JL, U.K.), lead zirconium titanate or PZT (Ferroperm, Stubbeled 7, DK-2950 Vedbaek, Denmark) and lithium tantalate (Johnson Matthey, 78 Hatton Garden, London EC1N 8JP, U.K.) were incorporated as the inorganic ferroelectric phase. We describe the preparation and assessment of test structures made with these new composite materials.

2. EXPERIMENTAL

2.1 Fabrication

The thin-film pyroelectric composite material is incorporated as the dielectric into a capacitor device structure. Glass microscope slides are ultrasonically cleaned in a detergent solution (Decon 90) and then in high purity deionised water (Millipore Milli-Q system). An aluminium substrate (typically 100nm thick) is thermally evaporated onto the glass slide at a pressure of $\sim 10^{-6}$mbar.

A matrix polymer solution is produced from 2.1g 70:30mol% vinylidene fluoride:trifluoroethylene copolymer [70:30 p(VDF:TrFE)] pellets dissolved in 20ml butanone (ethyl methyl ketone). This solution is magnetically stirred at room temperature for 12 hrs. A predetermined volume percentage of the selected ferroelectric inorganic powder is then added to the polymer solution. The resulting suspension is agitated vigorously for several hours to ensure homogeneous dispersion of the powder in the polymer solution.

A thin-film composite is then produced by spin-coating the composite suspension onto the Al/glass substrate using a photoresist spinner. Typically a rotation speed of 2000 RPM and duration of 100 seconds has been used. The resultant composite film thickness was measured by a scanning optical microscope (Lasertech) in comparative reflectance mode.

A pattern of gold top electrodes (typically 60nm thick) was then thermally evaporated onto the surface of the thin-film composite to produce the desired capacitor structure.

2.2 Ferroelectric Poling

In order to impart a macroscopic electrical polarisation to the composite material, it must be poled such that the dipolar entities are aligned perpendicular to the substrate plane of the film. In this work a DC thermal poling technique has been utilised.

The sample is heated to a temperature of 373K on a hotplate using heatsink compound to provide an effective thermal contact. A DC voltage (typically E=20-30 V/μm) is then applied between the device electrodes via tinned copper wires attached by air-dried conducting silver paint (Acheson Colloids Electrodag 915). The sample is held at elevated temperature for a specific period (times used were 20min and 165min), then fan-cooled to room temperature. When the sample has returned to room temperature, the applied voltage is removed.

2.3 Dielectric Measurements

The capacitance and dielectric loss tangent of the composite device structure are measured using an impedance analyser (Hewlett Packard 4192A). The frequency range scanned was 200Hz to 1MHz. The relative permittivity is then calculated using the active upper electrode area and film thickness.

2.4 Pyroelectric Measurements

The pyroelectric activity of the composite materials is determined using the quasi-static measurement method. A triangular temperature profile of amplitude 0.5°C is applied to the sample via a Peltier thermoelectric heat pump and the resultant current is measured by an electrometer (Keithley 614). The temperature of the pyroelectric material is detected by a thermocouple affixed to a dummy substrate adjacent to the device under test. Temperature and current readings are plotted as functions of time on a chart recorder.

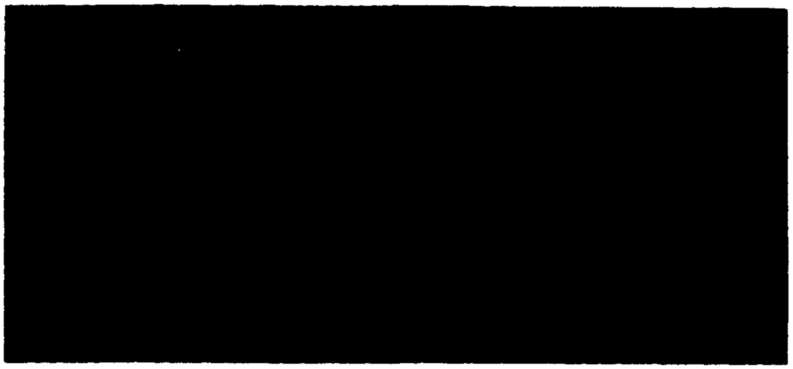

FIGURE 1 Photograph (50× magnification) of $BaTiO_3$ (8% vol)/70:30 p(VDF:TrFE) thin-film composite (thickness = 1.7 μm) with Al base electrode (at left) and Au top electrode. (See Color Plate II).

3. RESULTS

3.1 Structural Analysis

Optical microscope studies (Figure 1) showed that composites containing barium titanate powder exhibited good dispersion with a fine particle size (material specification indicates an average particle size of 1.3μm). PZT / 70:30 p(VDF:TrFE) composites showed a lesser degree of uniform dispersion. Composites incorporating lead titanate exhibited a certain amount of particle agglomeration. Those composites consisting of lithium tantalate in a 70:30 p(VDF:TrFE) matrix showed severe non-uniformity due to the broad particle size distribution of the powder (0.2μm - 30μm).

3.2 Dielectric Results

Figure 2 shows the relative permittivity and dielectric loss tangent spectra from 200Hz to 100kHz of two barium titanate/70:30mol% vinylidene fluoride:trifluoroethylene copolymer thin-film composites. A significant reduction in the relative permittivity after poling is apparent from the 8% inorganic composite data. According to these results the dielectric constant after poling appears to scale linearly with volume percentage of inorganic phase.

3.3 Pyroelectric Results

Figure 3 illustrates the effect of poling field on the pyroelectric coefficient for two thin film composites with barium titanate as the inorganic dispersoid. The composite with the greater inorganic volume fraction exhibited the higher activity. The pyroelectric coefficient increases as the electric field increases for both materials and tends to a limit at higher poling fields. The maximum field applicable is limited by electrical breakdown of the film.

All composites examined displayed a large temperature dependence of the pyroelectric coefficient. The pyroelectric coefficient rises sharply as T increases from room temperature.

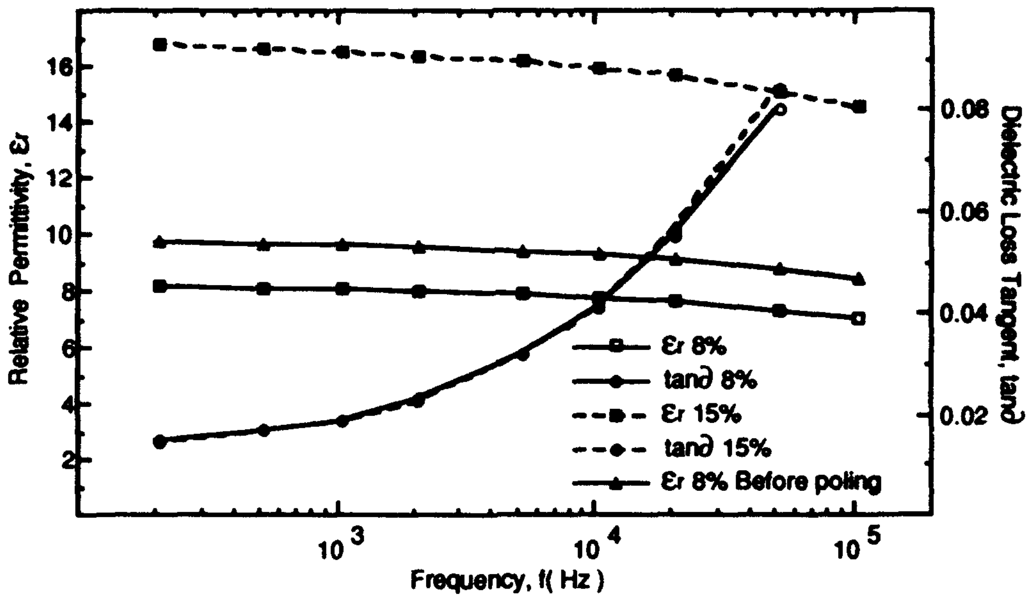

FIGURE 2. Graph of dielectric constant and dielectric loss tangent versus frequency for two (8% and 15% by volume) $BaTiO_3$ / 70:30 p(VDF:TrFE) thin-film composites at T=293K.

Table 1 displays pyroelectric performance data for various thin-film composites which have been produced. The dielectric noise figure of merit, F_D, is quoted since the greatest noise contribution is due to the dielectric loss of the material. This is given by :-

$$F_D = \frac{p}{(\varepsilon_r \tan\delta)^{1/2}} \tag{1}$$

where p is the pyroelectric coefficient, ε_r the relative permittivity and $\tan\delta$ the dielectric loss tangent of the pyroelectric material. For a pure 70:30 p(VDF:TrFE) film of thickness 1.6μm the corresponding values for the dielectric noise figure of merit are $F_D(200\text{Hz}) = 86$ and $F_D(1\text{kHz}) = 82$. The poling field for the copolymer film is 150 V/μm which is substantially greater than the fields used to pole the composite materials.

4. DISCUSSION

4.1 Poling Considerations

The poling procedure must be designed such that a large fraction of the applied field is dropped across the inorganic dispersoid and sufficient ferroelectric domains align such that a large stable, macroscopic polarisation is achieved.

At elevated temperature the matrix polymer phase exhibits increased conductivity and therefore a significant fraction of the applied electric field is dropped across the inorganic dispersoid phase. This results in more effective poling of the inorganic material than at room temperature where there is a large mismatch between the respective resistivity values. At 100°C the polymer is well above its glass transition temperature, T_g (-40°C), but is still below its melting point, T_m (~150°C). In this region the polymer is 'soft', that is its chains are free to move, and thus the orientation of sub-micron inorganic particles under the influence of the applied field is facilitated. The matrix polymer is also affected by the poling field. Orientation of chains occurs and a reduction in relative permittivity is observed due to an induced increase in crystallinity[9].

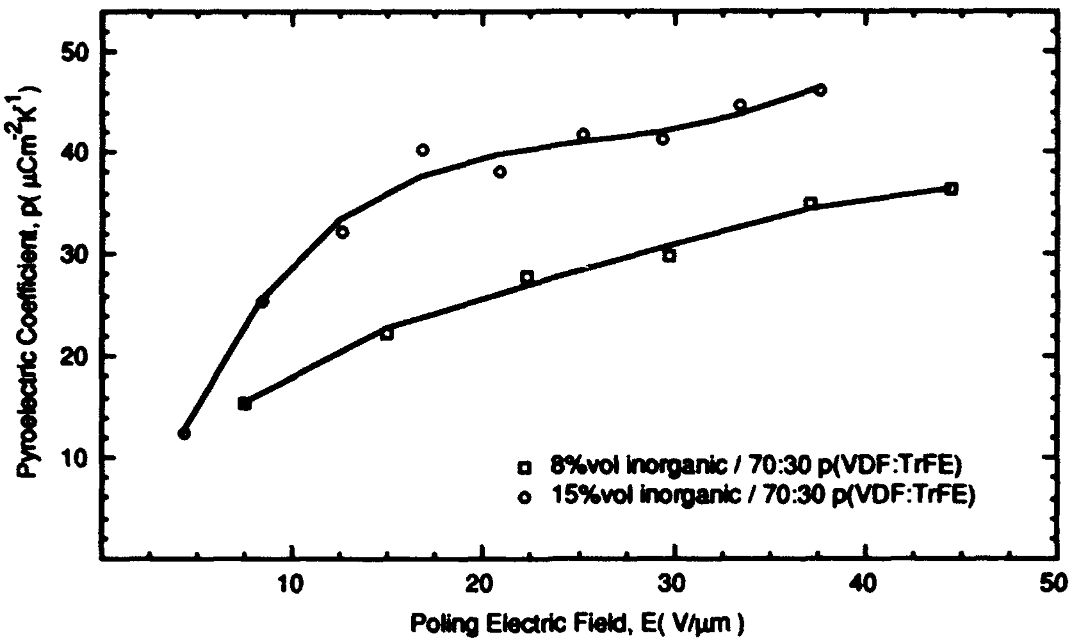

FIGURE 3. Graph of pyroelectric coefficient versus poling electric field for barium titanate / 70:30 p(VDF:TrFE) thin-film composites at T=293K.

Inorganic Material (Volume Percentage)		$BaTiO_3$ (8%vol)	$BaTiO_3$ (15% vol)	$Pb(Zr, Ti)O_3$ (7.1% vol)	$PbTiO_3$ (8% vol)	$LiTaO_3$ (6% vol)
p ($\mu Cm^{-2}K^{-1}$) at T = 293 K		42.9	43.4	51.0	50.3	59.6
Poling Field (V/μm)		25	20.8	25	62.5	22.2
Film Thickness (μm)		1.7	1.8	2.8	0.8	1.8
f = 200Hz	ε_{rel}	8.37	16.8	20.3	8.26	12.4
	tan δ	0.0150	0.0145	0.0217	0.0196	0.0180
	F_D	121	87.9	76.8	125	126
f = 1 kHz	ε_{rel}	8.23	16.5		8.10	12.2
	tan δ	0.0206	0.0186		0.0236	0.0220
	F_D	104	78.3		115	115

TABLE 1. Pyroelectric coefficient, dielectric data and pyroelectric figure of merit for inorganic / 70:30 p(VDF:TrFE) thin-film composites.

A poling duration of greater than 10^4 seconds is required in order to obtain a stable polarisation. This is due to the existence of a broad distribution of particle and domain switching times in the inorganic phase[10]. Long-term poling results in the majority of domains being preferentially oriented and stability is then maintained by co-operative alignment. In short-period poling stresses due to non-aligned domains force aligned domains to relax to their initial positions resulting in a reduction in polarisation. It may also be speculated that polymer/particle interactions lead to enhanced polarisation and stability.

The poling field applicable is limited by electrical breakdown of the thin-film composites. The inherent inhomogeneities, air trapped at interfaces, absorbed moisture and grain boundaries all represent low strength electrical pathways. Increased fractions of incorporated inorganic powder also result in a greater frequency of low field breakdown.

4.2 Dielectric Response

All of the composites display similar dielectric spectra. The general form is compatible with a Debye-type dipolar relaxation mechanism. However, since the materials are two-phase composites it is more likely that the response is due to interfacial polarisation as described by the Maxwell-Wagner effect[11].

The values of relative permittivity are smaller than expected. This may be due to errors in the thickness determination or an uncertainty in the thickness due to a high degree of surface roughness. A more likely explanation of the effect is the existence of the thin layer of native oxide on the aluminium base electrode and the presence of some trapped air within the films.

The reduction in relative permittivity on poling is probably due to an increase in the polymer crystallinity and alignment of the low permittivity inorganic polar axes.

The dielectric loss tangent of the materials is dominated by the loss mechanisms of the matrix polymer phase. For the low percentages of inorganic powder used here there is not expected to be any marked effect due to the losses in the particles.

5. CONCLUSIONS

Thin-film composite materials have been produced by a spin-coating method. This technique resulted in robust, good quality films with thicknesses from 0.5μm to 3μm. This is in the correct thickness range for optimum absorption of infra-red radiation. The composites consist of a highly active, ferroelectric inorganic powder dispersed within a 70:30mol% vinylidene fluoride:trifluoroethylene copolymer matrix. After poling the materials exhibit pyroelectric activity which is appreciably greater than that of the pure 70:30 VDF:TrFE copolymer at room temperature. As a result the dielectric noise figure of merit for the pyroelectric performance is up to 45% greater than that for the pure copolymer material. Therefore thin-film pyroelectric composites are good candidates for possible use in an integrated thermal imaging device.

ACKNOWLEDGEMENTS

We would like to acknowledge valuable comments from Dr. P.J. Dobson during the preparation of this manuscript. One of us (CEM) would like to acknowledge the receipt of a Science and Engineering Research Council (SERC) studentship. This work is supported by THORN EMI plc and the SERC.

REFERENCES

[1] R.Watton, M.A.Todd, Brit.Ceram.Proc., 41, 205-217, (1989)
[2] H.Kawai, Japan.J.Appl.Phys., 8, 975-976, (1969)
[3] T.Furukawa, G.E.Johnson, H.E.Bair, Y.Tajitsu, A.Chiba, E.Fukada, Ferroelectrics, 32, 61-67, (1981)
[4] R.E.Newnham, D.P.Skinner, L.E.Cross, Mat.Res.Bull., 13, 525-536, (1978)
[5] H.Yamazaki, T.Kitayama, Ferroelectrics, 33, 147-153, (1981)
[6] C.Muralidhar, P.K.C.Pillai, IEEE Transactions on Electrical Insulation, EI-21(3), 501-504, (1986)
[7] M.J.Abdullah, D.K.Das-Gupta, IEEE Transactions on Electrical Insulation, 25(3), 605-610, (1990)
[8] P.A.Silberg, J.Opt.Soc.Am., 47, 575-578, (1956)
[9] G.T.Davis, T.Furukawa, A.J.Lovinger, M.G.Broadhurst, Macromolecules, 15, 329-333, (1982)
[10] T.Furukawa, K.Suzuki, M.Date, Ferroelectrics, 68, 33-44, (1986)
[11] See, for instance, J.C.Anderson, Dielectrics, Chapman and Hall, London, (1964)

Ferroelectrics, 1992, Vol. 134, pp. 195–200
Reprints available directly from the publisher
Photocopying permitted by license only

PyC18

PYROELECTRIC PROPERTIES OF RAPID GROWTH ATGSP CRYSTALS

FANG CHANGSHUI, WANG QINGWU, ZHUO HONGSHENG, WANG MIN
Institute of Crystal Materials, Shandong University
Jinan 250100, P. R. China

Abstract The growth rate of modified TGS (ATGSP) crystal has been increased from 1mm/day to 5mm/day by increasing the stability and quickening the convection of the solution. The pyroelectric, dielectric and ferroelectric properties of the rapid growth ATGSP crystals have been measured. The quality of the crystal is good. The pyroelectric figure of merit of ATGSP crystal grown by rapid growth rates is the same as that of slow growth crystal. However the rapid growth crystal has more L-alanine content and lower tan δ than that of the slow growth crystal and it has very high bias field (E_b).

I. Introduction

L-alanine and phosphoric acid doped TGS Crystal (ATGSP) is the modified TGS Crystal with excellent properties. It has high pyroelectric coefficient p and internal bias field (E_b) and can lock the polarization. Its pyroelectric figure of merit is higher than that of TGS crystal[1] So ATGSP crystal is an optimal material for the fabrication of IR detectors and vidicon target surface.

This crystal is cultivated in aqueous solution. Generally, the growth rate of ATGSP crystal along the polar axis (b axis) direction is only 1mm/day. With the fast development of science and technology, there is an urgent demand for such doped TGS crystal with a large ($8\times8cm^2$) section. According to normal growth rate, it will take as long as several months to finish a

Supported by the National Natural Science Foundation of China

growth period, which is far from satisfying the demand for the quickly developing IR devices. Therefore, the research of the rapid growth of doped TGS crystals has an important practcal significance and also becomes an important research direction for water soluble crystals. [2]

This paper reports, for the first time, the results of the studies of rapid growth of ATGSP crystal. By increasing the stability and quickening the convection of the solution, the growth rate of ATGSP crystal has been increased from 1mm/day to more than 5mm/day. The pyroelectric, dielectric and ferroelectric properties of rapid growth ATGSP crystal have been determined systematically. It is found that the rapid growth ATGSP crystal has more L-alanine content than that of slow growth ATGSP crystal. Moreover the rapid growth crystal has very high internal bias field and very low dielectric loss. These all have important significance in the fabrication of high quality IR devices.

I Experiments and Results:

1. Single Crystal growth

The starting materials are made up according to the following chemical equation :

$$3[(1-x)NH_2CH_2COOH+xCH_3CH(NH_2)COOH]+(1-y)H_2SO_4+yH_3PO_4=$$
$$[(NH_2CH_2COOH)_{1-x}(CH_3CH(NH_2)COOH)_x]_3(H_2SO_4)_{1-y}(H_3PO_4)_y$$

where $x=10\%$ $y=30\%$. The PH value of the solution is 2.4. The crystal growth conditions are the same as those of pure TGS. The crystal seed was prepared by cleavage of an ATGSP crystal with good monodomain characteristics. The area of the seed section is 5×5 cm^2. The rapid growth of doped TGS family crystals has been realized preliminarily by using unidirectional growth technique under the conditions of fixing the seed without rotation and by increasing the supersaturation and convection of the solution. The growth rate along the polar axis increased from 1mm/day to 5mm/day. By adopting this technique, we can make the crystal grow by pushing forward along (010) or (010) face. The area of crystal thus grown is not decreased obviously.

2. The measurement of properties

The samples used for measurement were cleaved from the rapid growth and slow growth ATGSP crystals respectively. The section

areas of the crystal slices processed were about $40mm^2$ and thickness 0.5mm. Aluminium electrodes were evaporated on them.

The pyroelectric coefficient of ATGSP crystal were measured by charge integral method.[8] The temperature-rising rate was 1°/min. Fig.1 is the temperature (T) dependence of pyroelectric coefficient P of the crystals grown by different growth rates. From Fig.1 we can see that the pyroelectric coefficients of the

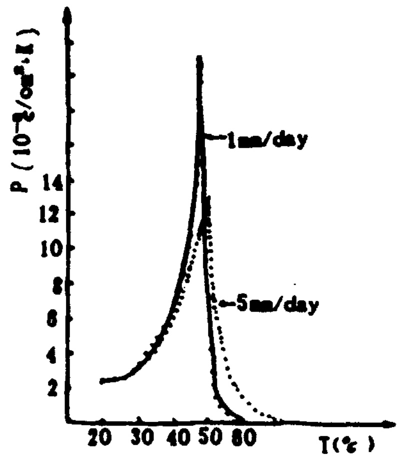

Fig.1 Temperature T dependence of pyroelectric coefficient P

crystals grown by different growth rates are identical at room temperature stage. When the temperature is higher than 30℃, the P of the rapid growth crystal is slightly smaller than that of the slow growth crystal. At Curie temperature, the peak value of the former is evidently smaller than that of the latter. When temperature is higher than Tc, the decreasing of P of the rapid growth crystal becomes slower and it decreases to zero at 70℃. Whereas the decreasing of P of the slow growth crystal is rather quick, it decreases to zero very quickly at temperature higher than 55℃. This is decided by the different bias field of these two crystals.

The electric hysteresis loop of the crystal was measured by using Model TRC-1 psudo-static electric hysteresis loop meter. This meter was designed on the basic of Sayer- Tower circuit principle and has very high measuring accuracy.[8] The electric hysteresis loops of the crystals grown from the same solution (containing 10%M L-alanine) by different growth rates are shown in Fig.2. It can be seen from this figure that the internal bias field Eb of the slow growth (1mm/day) crystal is about 1.2kv/cm while that of the rapid growth (5mm/day) crystal is as

high as 11kv/cm. This is because the magnitude of Eb is proportional to the content of L-alanine in the crytals phase. [4] From analysis, it is found that the L-alanine content in rapid growth crystal is more than 60% higher than that in the slow growth crystal.

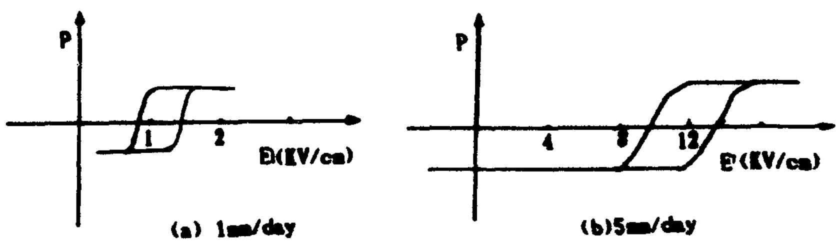

Fig. 2 Hysteresis loops of the different growth rate crystals

The dielectric constant ε and dielectric loss tan δ were measured by using HP4274A Bridge at frequency 10 KHz. The electric field exerted on the samples was less than 5V/cm. The results of measurement are shown in Fig. 3 and Fig. 4. From ε - T curve in Fig. 3, we can see that the ε's of slow growth crystal and rapid growth crystal are approximately the same at room temperature stage. When the temperature is higher than 30℃, the ε of the latter begins to decrease and its value becomes smaller than that of the former. The closer the temperature towards Tc, the more evident is the difference of ε between the two crystals. Moreover, the Tc's of the crystals grown by different growth rates are also different. The Tc of the rapid grown crystal is 50.6℃, which is slightly higher than that of the slow growth crystal (whose Tc=49.3℃). From Fig. 4, it can be seen that the dielectric loss of the rapid growth crystal is smaller than that of the slow growth crystal. In the vicinity of Tc, tan δ of the slow growth crystal has very large peak value while that of the rapid growth crystal is rather samll. These results are quite contrary to that of pure TGS crystal. [3] The ε and tan δ of rapid growth pure TGS crystal are all larger than those of slow growth pure TGS. This difference is attributed to the high internal bias field existing in the doped crystal and its being completely monodomainzed.

For the convenience of comparing the pyroelectric properties of ATGSP crystals grown by different growth rate, we summarize

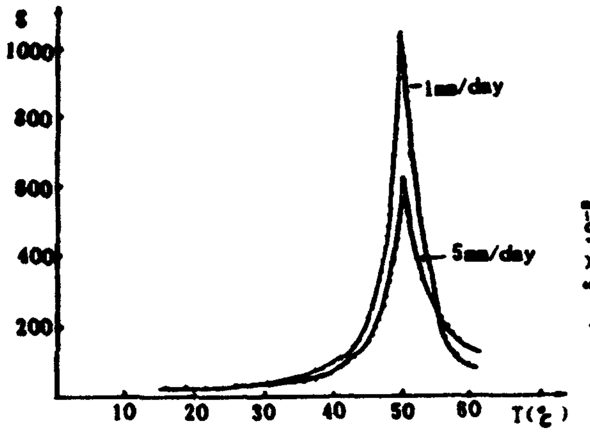

Fig. 3 Temperature T dependence of dielectaic constant ε

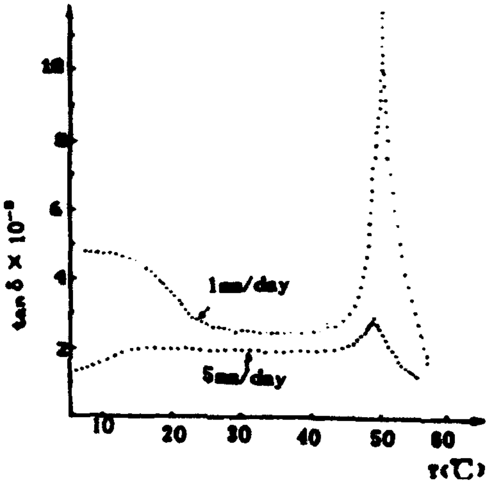

Fig. 4 Temperature T dependence of tan δ

the results of measurements in Table 1.

Table 1. Pyroelectric properties of the different growth rate ATGSP(25℃)

Growth rate	Tc (℃)	ε	tan δ	P (10^{-8}c/cm² · K)	Eb (kv/cm)	M(p/ε) (10^{-9}c/cm²K)
1mm/d	49.3	30	0.004	4.3	1.2	1. 43
5mm/d	50.6	28	0.0021	4.0	~10	1. 42

From the above table, we can see that the pyroelectric figure of merit of the rapid growth crystal is basically the same as that of the slow growth crystal , but it has a far higher internal bias field and a far smaller dielectric loss. The rapid growth crystal is completely in monodomain state. The modification of these properties plays an important role in the improvement of the quality of the IR devices.

There is evident difference between the properties of the rapid growth doped TGS and pure TGS crystals. So far as the latter is concerned, the dielectric constant ε and dielectric loss tan δ are all increased, while those of the ATGSP crystals are all decreased. This is owing to the fact that the rapid growth rate leads to the increase of L-alanine content in the crystal and increased monodomainization of the crystal.

In order to prevent depolarization of the crystal, it usually demands that the content of L-alanine in the solution should keep at about 20%M. The higher the content of L-alanine is, the more difficult is the crystal growth. However, after we adopted the rapid growth method, it is possible to grow crystal which has higher internal bias field from the solution doped with less amount (10% M) of L-alanine. This results in the prevention of depolarization. The technique of rapid growth and the comprehensive appraisal of its influence on crystals will be reported in another paper.

Acknowledgement

The authors want to express their thanks to Prof. Jiang Hui-Chu and Prof. Gao Zhang-Shou for their helps in preparing this paper and the beneficial discussions.

References

1. C. S. Fang, X. Yao, A. S. Bhalla, L. E. cross, Ferroelectrics, 51, 9-13 (1983)
2. John, F. Cooper and M. F. Singleton Lasers 84, San Fransisco. CA November, 1984
3. M, Wang, C. S. Fang, Journal of Shandong University Vol. 21, No. 94 (1986)
4. P. J. Lock, Appl. Phys. Lett. 19, 1390 (1971)

Ferroelectrics, 1992, Vol. 134, pp. 201–206
Reprints available directly from the publisher
Photocopying permitted by license only

PyP214

INFLUENCE OF SURFACE LAYERS AND ELECTROTHERMAL COUPLING ON DIELECTRIC LOSS OF THIN CHIPS MADE FROM MODIFIED TRIGLYCINE SULPHATE

NORBERT NEUMANN and GÜNTER HOFMANN
Technische Universität Dresden, Institut für Festkörperelektronik,
Dresdner Institut für angewandte Sensorik (DIAS),
O-8027 Dresden, Mommsenstraße 13, Bundesrepublik Deutschland

Abstract Dielectric loss $\tan\delta$ is an essential source of noise in pyroelectric detectors. In reflecting on the dielectric loss of thin chips made from modified triglycine sulphate (TGS), it has been found out and experimentally shown that surface effects and electrothermal coupling effects cause a considerable increase in dielectric loss. The publication gives data on temperature and frequency dependence of dielectric loss, depending on mounting, chip thickness, surface treatment regime, and electrode patterning technique.

INDRODUCTION

Modified TGS (deuterated, doped with L-α-alanin or L-α-alanin+Cr^{3+} respectively, and γ-irradiated) is applied preferably in pyroelectric sensors because of its favourable pyroelectric and dielectric properties of attaining high sensitivity and a high signal-to-noise-ratio.[1]

The dielectric loss $\tan\delta_p$ of the sensor element plays an important role as a source of noise within the frequency range from 10 cps to some 1.000 cps. With a large number of certain data available, the temperature and frequency dependences of the permittivity's real part ε' are understood, while the behaviours of the permittivity's imaginary part ε'' and the dielectric loss $\tan\delta=\varepsilon''/\varepsilon'$ are less known, particularly within the mentioned frequency range.

Of the various mechanisms contributing to the dielectric loss the influence of surface layers and electrothermal coupling effects will be considered. These mechanisms appear much stronger than for instance dc conductivity, parasitical parts of sample impedance, domain wall motions, soft mode, and piezoelectric resonances, if measuring conditions and sample preparations are chosen accordingly.[2]

SURFACE LAYER

It was found out that the dielectric loss $\tan\delta_p$ of pyroelectric elements, made from modified TGS is heavily dependent on element thickness.[3] This fact is also true for the complex permittivity of $BaTiO_3$ [4], the real part ε' of TGS [5, 6], spontaneous polarization, and coercive field strength.[7] It can be explained on

the basis of a model where the sample is considered as nonuniform and the properties of surface layers are different to the bulk values.[8]

A simple model of surface layers, consisting of ferroelectric bulk and thin nonferroelectric surface layers with low permittivity (a B-type layer [8]), is also able to reveal the thickness dependence of tanδ. Figure 1 shows the simplified model of a pyroelectric element with surface layers on both sides.

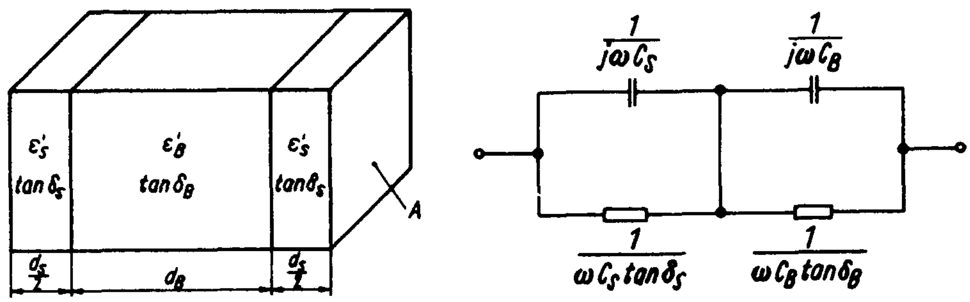

FIGURE 1 Simplified model of a pyroelectric element with surface layers and equivalent circuit

With

$$C_S = \varepsilon_0 \varepsilon'_S \frac{A}{d_S} \tag{1}$$

$$C_B = \varepsilon_0 \varepsilon'_B \frac{A}{d_B} \tag{2}$$

from the equivalent circuit, the dielectric loss is obtained

$$\tan\delta = \frac{\tan\delta_S + \dfrac{\varepsilon'_S\, d_B\,(1+\tan^2\delta_S)}{\varepsilon'_B\, d_S(1+\tan^2\delta_B)} + \tan\delta_B}{1 + \dfrac{\varepsilon'_S\, d_B\,(1+\tan^2\delta_S)}{\varepsilon'_B\, d_S\,(1+\tan^2\delta_B)}} \tag{3}$$

Provided that magnitudes ε'_S/d_S , $\tan\delta_S$, and $\tan\delta_B$ are independent of temperature, the loss dependences on temperature and thickness can be calculated. Figures 2 and 3 show the calculated temperature and thickness dependences of dielectric loss of DTGS:L-A for $\tan\delta_B = 0{,}001$, $\varepsilon'_S = 7$, $\tan\delta_S = 0{,}1$ and the parameter d_S. On the given conditions, three limitations can be deduced from Eq. (3), premised that $\tan^2\delta_S \ll 1$:

$$\text{I:}\quad \frac{\varepsilon'_S\, d_B}{\varepsilon'_B\, d_S} \gg \frac{\tan\delta_S}{\tan\delta_B(1+\tan^2\delta_S)} \qquad : \tan\delta = \tan\delta_B \tag{4}$$

$$\text{II:}\quad \frac{1}{(1+\tan^2\delta_S)} \ll \frac{\varepsilon'_S\, d_B}{\varepsilon'_B\, d_S} \ll \frac{\tan\delta_S}{\tan\delta_B(1+\tan^2\delta_S)} \qquad : \frac{1}{\tan\delta} = \left(\frac{\varepsilon'_S\, d_B}{\varepsilon'_B\, d_S} + 1\right)\frac{1}{\tan\delta_S} \tag{5}$$

$$\text{III:} \quad \frac{\varepsilon_S' d_B}{\varepsilon_B' d_S} \ll \frac{1}{(1+\tan^2\delta_S)} \qquad : \tan\delta = \tan\delta_S \tag{6}$$

These limitations are illustrated in Figs. 3 and 4. At Curie point temperature, where values of 10^5-10^6 for ε_B' are measured, or if the quotient d_B/d_S is small, surface determines total dielectric loss, whereas at low temperatures or with a large quotient d_B/d_S bulk determines loss. In some case, the temperature dependence of $1/\varepsilon_B' \sim |T_C - T|$ typical of ferroelectrics involves just such a one of $1/\tan\delta$.

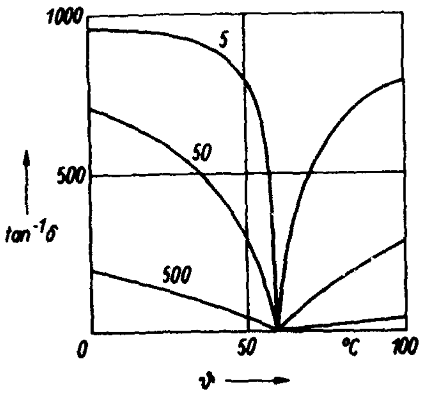

FIGURE 2 Theoretical behaviour of $\tan\delta$ as a function of temperatur (parameter d_S/nm; $d_B = 20\mu m$)

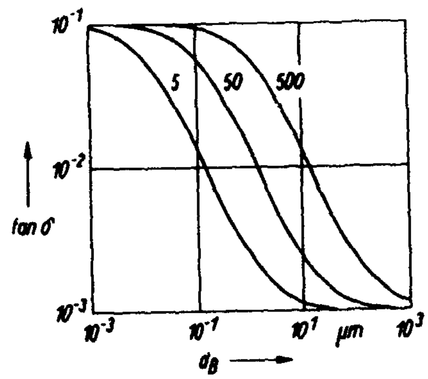

FIGURE 3 Theoretical behaviour of $\tan\delta$ as a function of thickness (parameter d_S/nm; $\theta = 25$ °C)

In Fig. 4 this is illustrated by samples of TGS prepared in various ways. Samples 1, 2, and 3 were made by cleavage and treated by glow discharge before depositing the electcrodes by high vacuum evaporation. The unfavourable effect of glow discharging on the TGS surface is clearly visible . Indeed the adhesion on untreated TGS surfaces, of metal layers deposited by high vacuum evaporation is not satisfactory. An alternative method was found by cleaning the surfaces with ion beam milling, which was used for sample 4. Interpreting the ascent, one obtains an effective thickness of surface layer d_S/ε_S' of about 6 nm for sample 4, compared with about 40 nm for the glow discharged sample 2. Applying $\varepsilon_S' = 7$,[9, 10] one arrives at a thickness of surface layer $d_S/2$ of about 20 nm, which shows the superiority of ion beam milling.

If the sample surface is treated by glow discharge before evaporating electrodes, the thickness dependence of dielectric losses of TGS:γ and DTGS:γ shown in Fig. 5 is observed in contrast to the DTGS:L-A-samples treated by ion beam milling. The thickness dependence that was measured on samples with surfaces treated by glow discharging can be clearly attributed to the influence of surface layers, wich confirms Eq. (3). With $d_p > 100$ μm, the value $\tan\delta_B$ of $1...2\cdot10^{-4}$ of bulk determines the measured loss $\tan\delta$ of ion beam milled chips.

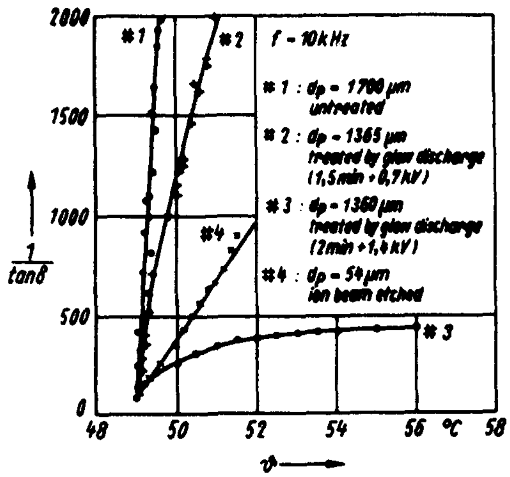

FIGURE 4 Dielectric loss vs. temperature of samples with various ways of surface treatment

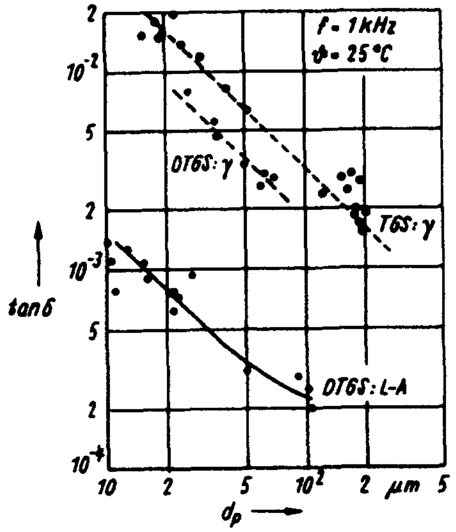

FIGURE 5 Dielectric loss vs. thickness of samples with various ways of surface treatment

ELECTROTHERMAL COUPLING

Figure 6 shows the frequency response of a freely suspended sample of TGS:L-A+Cr^{3+} for various measuring conditions. There is a typical minimum of loss between 10^3 cps and 10^4 cps; its value is determind by crystal growth and samples preparation. The increase found at lower frequencies is due to the transition from adiabatic to isothermal measuring conditions.[11]

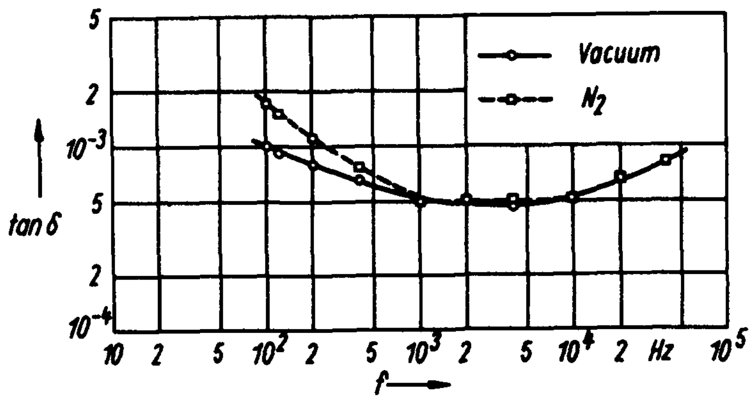

FIGURE 6 Dielectric loss vs. frequency of samples of TGS:L-A+Cr^{3+} measured in N_2 and high vacuum

In high vacuum there is no thermal conduction to surrounding gas layers and so the increase found at lower frequencies is not so pronounced. The frequency response of complex permittivity caused by

thermal conduction between sample or sensor element respectively and surrounding can be calculated, in regarding the pyroelectric as a thermodynamic system in stress-free state :

$$\varepsilon = (\varepsilon' - j\varepsilon'') = \varepsilon^T - \frac{p^2 T}{c'_P\, \varepsilon_0} T_R(j\omega) \tag{7}$$

where in contrast to Stokowski [12] the complex normalized current responsitivity $T_R(j\omega)$ [13] is used to describe the thermal conduction between chip and surrounding. Hence the dielectric loss caused by thermal conduction with the surrounding is

$$\tan\delta_T = \frac{\varepsilon''}{\varepsilon'} = k_T^2 \, \mathrm{Im}\{T_R(j\omega)\} \tag{8}$$

with the electrothermal coupling coefficient

$$k_T = \sqrt{\frac{p^2 T}{c'_P \varepsilon_0 \varepsilon'_P}} \tag{9}$$

In Fig. 7 the measured and calculated dielectric losses $\tan\delta$ are represented as a function of frequency for two different arrangements. The measurement of dielectric loss was not only taken directly by a capacitance measuring bridge HP 4275 but also indirectly by pyroelectric sensors in determining the normalized noise voltage with Eq. (10)

$$\tan\delta_T = (\tilde{u}'^2_{rn} - \tilde{u}'^2_{rnR} - \tilde{u}'^2_{rnI} - \tilde{u}'^2_{rnU}) \frac{\omega}{4kT} \frac{(C_P + C_{iP})^2}{C_P} \tag{10}$$

where $\tilde{u}'_{rn}$ is the normalized noise voltage of the sensor, $\tilde{u}'_{rnR}$, $\tilde{u}'_{rnI}$, and $\tilde{u}'_{rnU}$ are the normalized noise voltages caused by input resistance, current and voltage noises of the preamplifier integrated in the sensor, and C_P and C_{iP} are the capacitance of the pyroelectric element and the input capacitance of the preamplifier; and in measuring the phase shift φ and amount of normalized current responsitivity $|T_R|$ with Eq. (11)

$$\tan\delta_T = k_T^2 \sin\varphi \, |T_R| \tag{11}$$

The complex normalized current responsitivity $T_R(j\omega)$ is calculated on the basis of the thermal conduction equation of a sensor with layer structure. The part $\tan\delta_T$ can be determined with the help of Eqs. (8) and (9).[14] In both variants of mounting, an increase in dielectric loss $\tan\delta$ is found at lower frequencies; it is pronounced with element 3_T3. The very good coincidence of measured and calculated values of sample 3_T3 shows that Eq. (8) can be applied for calculating the part of loss $\tan\delta_T$ at frequencies $f \leq |\mu_P d_P|$ ($\mu_P = (j\omega/a_P)^{1/2}$, a_P...thermal diffussivity of the pyroelectric), where a homogenous change of the pyroelectric's temperature can be supposed. Also with the freely suspended chip 5_T4 the surrounding gas layers and the carrier made of a polymer cause the loss part $\tan\delta_T$ at $f = 10$ Hz to be dominant.

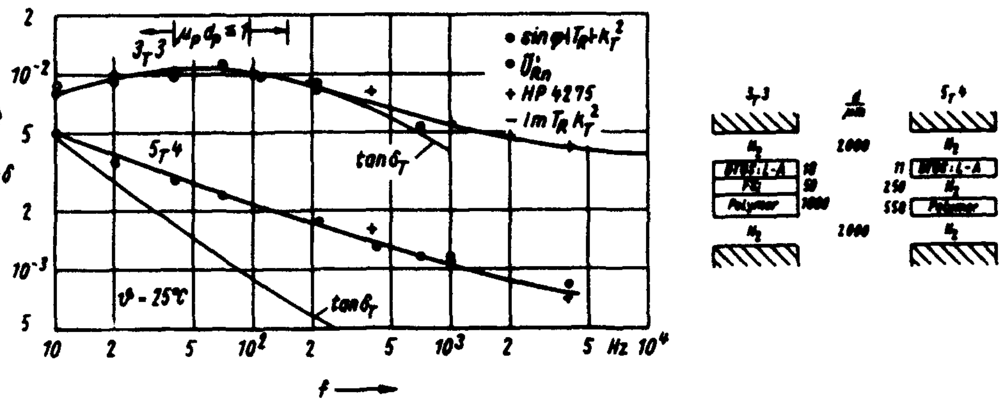

FIGURE 7 Influence of DTGS:L-A sensor element mounting on frequency response of dielectric loss

CONCLUSIONS

The experimental results are in accordance with the theoretical considerations, showing that surface layers and electrothermal coupling effects can cause an increase in dielectric loss. The thinner the pyroelectric chip is, the stronger both effects will appear. This has to be taken into account in design and production techniques, since thin pyroelectric chips with low losses are prefered for pyroelectric sensors. Dielectric loss can be influenced not only in TGS, but also in other pyroelectrics, for instance thin ferroelectric layers on substrates.

REFERENCES

1. L. Walther and D. Gerber, Infrarotmeßtechnik (Verlag Technik, Berlin, 1981)
2. V. Lhotska, J. Fousek and N. Neumann, phys. stat. sol. (a), 120, 273 (1990)
3. N. Neumann, Wissenschaftliche Beiträge (Martin-Luther-Universität Halle-Wittenberg, 1989/5), p.56
4. H. Schlosser and M. E. Drougard, J. Appl. Phys., 32, 1227 (1961).
5. T. Sekido and T. Mitsuit, J. Phys. Chem. Solids, 28, 967 (1967).
6. V. S. Chincholkar and H.-G. Unruh, phys.stat. sol., 29, 669 (1968).
7. A. Hadni, R. Thomas, S. Ungar and X.Gerbaux, Ferroelectrics, 47, 201 (1983)
8. E. Fatuzo and W. J. Merz, Ferroelectricity (North-Holland Publ. Co., Amsterdam, 1967),
9. M. S. Tsedrik, G. A. Zaborovkij and N. V. Ulasen, Dokl. AN BSSR, 19, 498 (1975)
10. A. Mansingh and E. Prasod, J. Phys. D: Appl. Phys., 9, 1379 (1979)
11. M. E. Lines and A. M. Glass, Principles and Applications of Ferroelectrics and related Materials (Clarendon Press, Oxford, 1977)
12 S. E. Stokowski, Appl. Phys. Letters, 29, 393 (1976)
13 W. R. Blevin and J. Geist, Appl. Optics, 13, 1171 (1974)
14. S. H. Wu, IEEE Trans. Electron. Dev., ED-27, 88, (1980)

Ferroelectrics, 1992, Vol. 134, pp. 207–212
Reprints available directly from the publisher
Photocopying permitted by license only

PyP216

PYROELECTRIC RESPONSE OF PIEZOELECTRICS

Yu.M. POPLAVKO, M.E. ILCHENKO, L.P. PEREVERZEVA
Kiev Polytechnical Institute, 37 Pobedi ave. Kiev
Ukraine 252056

Abstract It has been originally shown that uniform elastic or thermal perturbation may induce volume piezoeffect or pyroelectricity correspondingly in all 20 piezoelectric classes of crystals if they are partially clamped. The last of these effects may be named "thermopiezoelectric" response - TPER. It has the same value of magnitude as the usual pyroelectric response but TPER can be essentially amplified in the vicinities of SHF-electromagnetic or (and) electromechanical resonances. Piezoelectric crystals significantly extend the choice of pyroelectric materials and the possibilities of its applications. For instance, the semiconductors of GaAs type gives rise to a new generation of pyroelectric sensors being microelectronics processors in which thermal transducers, amplifiers and commutation system could be integrated in the space of the same crystal.

INTRODUCTION

The extraordinary pyroelectric responses have been observed in piezoelectrics[1-3] and even in pyroelectrics in the direction perpendicular to the unique axis[4,5]. As a rule these responses were associated with temperature gradient[1,5] and explained as tertiary pyroelectricity[2]. Linear electromechanical response (piezoeffect) may be considered as the linearization of electrostriction by intercrystal electric bias depending from polarity[6]. The intrinsic polar structure is noncompensated in 10 pyroelectric classes of crystals but is exactly compensated in the other 10 piezoelectric classes.

For instance, planar neutralization of intrinsic polarity takes place in crystals of point group 32 such as quartz. It has three polar axes of two-fold symmetry crossing at on angle of 120° and being perpendicular to the non-polar axis of three-fold symmetry. The spatial self-compensation of electric polarity can be observed in cubic crystal

classes $\bar{4}3m$ and 23 point groups. Thay have four polar axes of three-fold symmetry crossing at on angle of 109°. That is why piezoelectrics could be described as "antipyroelectrics". Prefix "anti-" acquires sense only if the components of electric polarity can be detected.

TABLE 1 Charge separation phenomena in insulators.

The type of charge response according to the crystal symmetry	Elastic constraints of samples
1. UNIFORM CHANGE OF TEMPERATURE	
1.1. Primary pyroelectricity - thermal disodering and the change of spontaneous polarization in 10 polar classes of crystals.	From completely free to totally clamped crystal
1.2. Secondary pyroelectricity - piezoelectric transduction of thermal strain in 10 pyroelectric (polar) classes.	Stress-free crystal or partially clamped one
1.3. THERMOPIEZOELECTRICITY - piezoelectric transduction of anisotropic limited thermal strains in 20 noncentrosymmetric classes of crystals	Partially clamped crystal solely
2. GRADIENT CHANGE OF TEMPERATURE	
2.1. Tertiary pyroelectricity in 20 noncentrosymmetic crystals	Spatial nongomogeneously stressed crystal
2.2. Thermopolarization in any dielectrics noticeable when $\varepsilon = 10^3$-10^4.	

But it is well known that uniform change of temperature can not generate any charge in "antipyroelectrics" because piezoelectrically transduced thermal strains are compensated totally. Nevertheless recently we have found the conditions in which scalar (uniform) thermal or elastic influences induce pyroelectricity or volume piezoeffect in all 20 pyroelectric classes of crystals[3]. It is anisotropic limitation of thermal strain that we propouse to prove the polar

motivation of piezoelectrics = "antipyroelectrics". As shown further, partially clamping may be realized.

This new THERMOPIEZOELECTRIC RESPONSE (TPER) gives "pyro-coefficient" $p = (10^{-6}-10^{-3})C\ m^{-2}\ K^{-1}$ in various piezoelectrics. The TPER has been confirmed by experiment in SiO_2, $NH_4H_2PO_4$ and $Bi_{12}GeO_{20}$ crystals[3]. The place of TPER amidst the related properties is shown in the Table 1.

The secondary pyroelectricity looks like thermopiezoelectricity but it is inherent only to 10 pyroelectric classes. It may be observed both in partially clamped condition and in stress-free crystals. Apparently, it is the spontaneous strains that plays a part of "partial clamping" in pyroelectrics. Both TPER and secondary pyroelectricity are impossible in totally clamped crystals.

The special interest is to compare TPER and tertiary pyroelectricity. Both of them are inherent to piezoelectric classes of crystals and may be excited by elastic stresses which are thermally induced. Nevertheless, the reason for the tertiary effect is the spatially nonhomogeneous temperature distribution while the source of TPER is the anisotropic boundary conditions. The last leaves the possibility of only one type of thermal strains, just in the direction of a piezoelectric axis. The other strains are forbidden.

BASIC RELATIONS

To obtain the formula of TPER coefficients we used thermodynamic equations of a short circuited piezoelectric crystal[7]:

$$\begin{aligned} dS_n &= s_{mn}^{E,T}\, dT_m + \alpha_n^{T,E}\, dT, \\ dP_i &= d_{in}^{T}\, dT_n, \quad i=1,2,3, \quad m,n=1,2,\ldots 6, \end{aligned} \tag{1}$$

where E- electric field, T- temperature, P_i- electrical polarization, S_n and T_m - the components of strain and stress tensors, $s_{mn}^{E,T}$, d_{im}^{T} and $\alpha_n^{T,E}$ the components of elastic compliance, piezoelectric strain coefficient and the thermal expansion coefficient respectively.

The solution of these equations depends on crystal symmetry and the partial elastic constraints. There were consi-

dered: tangentially clamped plate and longitudinally clamped rectangular rod. The following boundary conditions were used:

1. Very thin but "endless" plate of piezoelectric crystal, which must be cut perpendicularly to one of the crystal polar axis, then covered by electrodes and stuch to the substrate. The plate's thickness has to be much less then the thermal diffusion wave lengh so that the temperature gradient is negligible and tertiary pyroelectricity is practically absent.

No-bending comparatively thick substrate obtained from the SiO_2 glass for instance, must be characterized by very small thermal expansion coefficient to provide the tangential clamping of the plate. But the plate is free to expand in the normal direction corresponding to the polar i-axis. At such condition the TPER coefficient p_i for piezoelectrics of trigonal and hexagonal systems equals

$$p_i = \frac{dP_i}{dT} = \frac{d_{ii}(\alpha_1 s_{33} - \alpha_3 s_{13})}{s_{11}s_{33} - s_{13}^2} \qquad (2)$$

where i=1 for the 32 and $\bar{6}$ point group of symmetries and i=2 for the $\bar{6}$m2 and $\bar{6}$ groups.

The crystals of cubic system of $\bar{4}$3m and 23 point group of symmetries shows

$$p_3 = \frac{2\sqrt{3}\, d_{14}\alpha}{4s_{11} + 8s_{12} + s_{44}} \qquad (3)$$

2. Thin but very long rectangular piezoelectric rod may be clamped by the longitudinal electromechanical resonance. The piezoactive facets have been covered by the electrodes. In this case the TPER coefficients equal

$$p_1 = \frac{d_{14}(\alpha_1 + \alpha_3)}{s_{11} + s_{33} + s_{44} + 2s_{13}} \quad \text{(for 622 and 422 groups)},$$

$$p_3 = \frac{d_{36}(\alpha_1 + \alpha_2)}{s_{11} + s_{22} + 2s_{12} + s_{66}} \quad \text{(for } \bar{4}\text{2m and 222 groups)},$$

and $p_3 = d_{31}\alpha_1 s_{11}^{-1}$ (for $\bar{4}$ group of crystal symmetry).

EXPERIMENT

Partial clamping which causes the anisotropic limitation of thermal strains may be realized:

-in static experiment by fastening a thin plate of piezoelectric crystal on a stiff substrate which restricts the planar strain components but leaves free the thickness strain;

-in the dynamic case one may use the electromechanical resonance clamping in piezoelectric transducer such as a thin disk or long but thin rectangular rod.

In both cases the allowed part of elastic strains must correspond to one of the polar axes directions. It is transformed to unique polar axis. Consequently, the partially clamped piezoelectric crystal decreases the symmetry of its response and acquires pyroelectricity and volume piezoeffect.

The temperature dependence of such artificial pyroelectric response was used to obtain the components of intrinsic polarisation P_1 which is totally compensated in a free piezoelectric crystal. For example, quartz has ΔP_1 = 0.2 $\mu C\ cm^{-2}$ at 300K which linearly decreases with temperature ($P_1 \sim (\Theta - T)$ and vanishes at $\alpha - \beta$ transition (Θ = 846K)). So due to partially clamping we obtained one of three components of intrinsic polarization ΔP_1.

Above the Curie point piezoelectrics of KDP type shows another temperature change of intrinsic polarizations $\Delta P \sim (\Theta - T)^2$. Here Θ is the point of the high temperature transition (Θ = 484 K for KH_2PO_4, 428 K for RbH_2PO_4 and 398 K for KD_2PO_4). When T = Θ the dielectric permitivity ε_1 in these crystal decreases approximately two times[8]. In ADP crystal the low $\Delta P \sim (\Theta - T)^2$ is justified with Θ = 680 K.

APPLICATION

The value of TPER coefficient of piezoelectrics is the same magnitude as in usual pyroelectrics. For instance,at 300K ADP has p_3=17 10^{-6} C $m^{-2}K^{-1}$, $Bi_{12}GeO_{20}$ has 30 10^{-6}C $m^{-2}K^{-1}$. In berlinite p_1=5.3 10^{-6}, quartz 2.7 10^{-6}, gallium arsenide has 1.5 10^{-6} C $m^{-2}K^{-1}$ and so on. In the vicinity of electro-

mechanical resonance with the quality Q_m TPER can be amplified proportionally to $Q_m = 10^3 - 10^5$. We have shown that it is possible to excite SHF electromagnetic resonance in TPER elements simulteneously with the electromechanical one[9]. The result is the additional increase of detector sensitivity. In non-polar piezoelectrics microwave dielectric dispersion is absent and loss tangent $\tan\delta \sim 10^{-4}$ unlike a ferroelectric pyroelectric with microwave $\tan\delta = 0.1 - 1$. That provides the high electric quality of such piezoelements as SiO_2, GaAs, $Bi_4(SiO_4)_3$, $Bi_{12}GeO_{20}$ which are characterized $Q_{el} = (\tan\delta)^{-1} = 10^4$. It is possible to create one-crystal pyroelectric infrared sensors using piezoactive semiconductors such as GaAs. Their voltage sensitivity $S = 0.01 - 0.1$ V m^2 J^{-1} corresponds to pyroelectric one. There could be a new generation of uncooled wideband pyroelectric sensors. Their main advantage is the possibility to manufact the TPER transducers, amplifires and commutation system in a single semiconductor. Nothing but microelectronics technology can guarantee the same properties of each elementary cell of such transducers containing $10^2 - 10^6$ cells. As a result high uniformity and resolution can be obtained.

REFERENCES

1. C.D.Peltz, A.E.Karpelson, Fiz.Tverdogo Tela(Sov),13, 3104 (1971).
2. K.M.Nurieva, A.K.Tagantsev, Fiz.Tverdogo Tela(Sov),31,130 (1989).
3. L.P.Pereverzeva, Yu.M.Poplavko, S.K.Skljarenko and A.G.Chepilko, Pis'ma Zh.Eksp.Teor.Fiz., 52, 820 (1990).
4. A.M.Glass and R.L.Abrams, J.Appl.Phys., 41, 4455 (1970).
5. L.B.Schein, P.J.Cressman and L.E.Cross, Ferroelectrics, 22, 937 (1979).
6. I.S.Rez and Yu.M.Poplavko, Dielectrics.Main Properties and Electronics Applications(Radio i sviaz,Moscow,1989),p.287.
7. S.T.Liu and Donald Long, Proc. IEEE, 66, 14 (1978).
8. L.P.Pereverzeva, Yu.M.Poplavko, I.S.Rez, Fiz.Tverdogo Tela (Sov), 13, 3199 (1971).
9. J.N.Bondarenko, L.P.Pereverzeva, Yu.M.Poplavko, Izvestija V.U.Z., Radioelectronica(Sov), 33, N10, 19 (1990).

Ferroelectrics, 1992, Vol. 134, pp. 213–216
Reprints available directly from the publisher
Photocopying permitted by license only

PyP217

THE ELECTROCALORIC COEFFICIENT OF LATGS CRYSTALS

F. JIMENEZ-MORALES
Dpto. Física de la Materia Condensada. P.B. 1065
41080-Sevilla. Spain.

Abstract: The specific heat and the pyroelectric coefficient of a TGS crystal doped with L-alanine are measured. With the data the electrocaloric coefficient is obtained. The behaviour of the crystal is similar to he behaviour of TGS under an external electric field. The results are compared with the thermodynamic theory.

INTRODUCTION

Since the introduction of the ferroelectric triglycine sulphate (TGS) as a pyroelectric material a great part of the work on pyroelectric detectors has been based on it[1]. The major disadvantage of using TGS is the possibility of a single crystal becoming multidomain or depoling in use. To avoid this the crystal is grown from a solution containing L-alanine[2]. The introduction of L-alanine molecules in the lattice of TGS (LATGS crystals) causes an internal bias field which makes the crystal permanently single-domain[3].

Since the parameters involved may differ from sample to sample, it is important that all measurements are performed on the same sample. In this work we have measured the specific heat and the pyroelectric coefficient of a sample and with the data we obtain the electrocaloric coefficient.

EXPERIMENTAL

The sample, 0.8 cm^2 in section and 3 mm high along the ferroelectric axis, was cut from a single crystal of LATGS grown in water solution of TGS containing 1 mol of l-alanine per 8 mol of glycine. The experimental device is based on the rotating disc method and the growth procedure is described elsewhere[4].

Measurements of the specific heat were taken by means of a conduction calorimeter designed for the study of ferroelectric materials under applied electric field[5]. A constant power is supplied to two heaters during a period of 9 min. A stationary regime is obtained in which the sample reaches a uniform temperature. The power is then cut

off for a second period of 9 min., during which the e.m.f. of a thermopile (96 thermocouples of chromel-constantan) caused by the heat flux exchanged between the sample and the calorimeter block is measured with a HP Data adquisition system. The e.m.f. is previously amplified by a Keihtley 148 Nanovoltmeter.

The pyroelectric coefficient was measured by a dynamic method. The experimental cell for the measurements was used previously[6]. A block of aluminium holds two rectangular surfaces of brass, each containing an electric heating element. The temperature is measured by two platinum thermometers. The output of one is directed to a Stanton-Redcrof temperature programmer which enables us to work with a thermal rate of 1 K/min. The pyroelectric signal was measured with a Takeda Riken TR-8651 electrometer. The other thermometer and the electrometer were connected to a HP-Data acquisition system.

RESULTS

In figure 1 the pyroelectric coefficient $p=(dP/dT)_E$ and the specific heat (C) are shown versus the temperature. The maximum value of the pyroelectric coefficient (.7 $\mu C/cm^2K$) and the maximum specific heat jump ($\sim$.16 J/g.K) are lower than in pure TGS ($\sim$1 $\mu C/cm^2K$ and .28 J/g.K). This effect is due to the internal bias field (B=311V/cm, measured by hysteresis loop) induced by the L-alanine molecules inside the crystal[3,7].

According to the thermodynamical model of an uniaxial ferroelectric crystal the following relations can be obtained:

$$e= \frac{-T.p}{\rho.C}. \qquad (1)$$

$$1/e= \beta.\ P + C_o.\left(\beta.(T-T_o) + 3.\gamma.P^2\right)/\beta.P.T \qquad (2)$$

Where $e = (dT/dE)_S$ is the electrocaloric coefficient, p the pyroelectric coefficient, ρ the density of the crystal, T_o the critical temperature, β and γ are coefficients, C the specific heat and C_o the non singular part of the specific heat. The values of the polarization P are obtained from the state equation $E = \beta.(T_o-T).P + \gamma.P^3$. The electric field acting on the crystal is $E = E_{ex}+ B$, where $E_{ex}(=0)$ is the external applied electric field and B is the internal bias associated with the L-alanine content[3].

The magnitude of B shows a remarkable temperature dependence[6,8]

within ± 1 K of T_o. In this region B decreases in the form $B=\alpha.(T_f-T)^{1/2}$ T_f is a temperature slightly higher than T_o. In this case the electrocaloric coefficient is:

$$1/e = \beta.P + (C_o.\ \beta.(T-T_o) + 3.\gamma.P^2)/(\beta.P-dB/dT).T \qquad (3)$$

In figure 2 the electrocaloric coefficient obtained from (1), (2) and (3) are shown versus the temperature. We have used the values: $\rho= 1.69$ g/cm^3, $T_o = 322.6$ K, $T_f = 323.5$ K, $\gamma= 6.25\times10^3$ Vcm^5/ C^3, $\alpha= 220$ V/cm K$^{1/2}$, $\beta= 4.2\times10^3$ Vcm/ C.K., $C_o= 1.33$ J.g^{-1}K^{-1}

The behaviour of the electrocaloric coefficient of LATGS can be explained by the fenomenological theory of ferroelectricity using the equivalence between the internal bias and an external electric field. Near T_o the experimental values of e are higher than that predicted by equation (2). The discrepancy is solved using the fact that the internal bias decreases near the transition and then the equation (3) must be used.

REFERENCES

1. Keve E T, Philips tech. Rev. 35, (9), 247-257 (1975).
2. Lock P J, Appl. Phys. Letters, 19, 390 (1971).
3. Bye K L, Whipps P W, Keve E T, Ferroelectrics 7, 179-181 (1974).
4. Jiménez F, Dieguez E, del Cerro J, Ferroelectrics 81, 127-130 (1988).
5. del Cerro J, J. Phys.E. Sci. Instrum, 20, 609 (1987).
6. Jiménez F, Ramos S, del Cerro J, Ferroelectrics 94, 443-447 (1989).
7. del Cerro J, Ramos S., Jap. Jour. Appl. Phys. 24, 341-3 (1985).
8. Martínez J.L., Cintas A., Dieguez E. and Gonzalo J.A. Ferroelectrics Letters 44, 221-226 (1983).

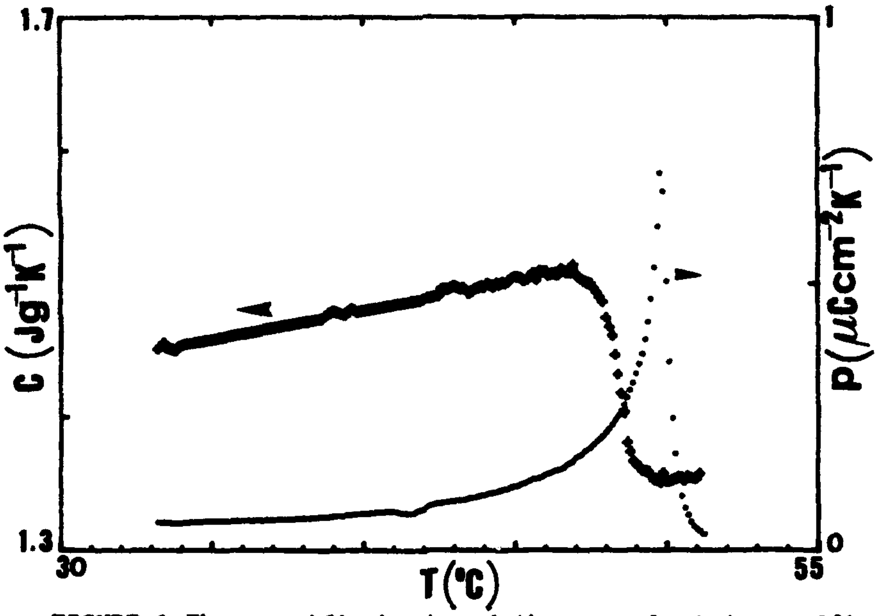

FIGURE 1 The specific heat and the pyroelectric coefficient of a LATGS crystal versus the temperature

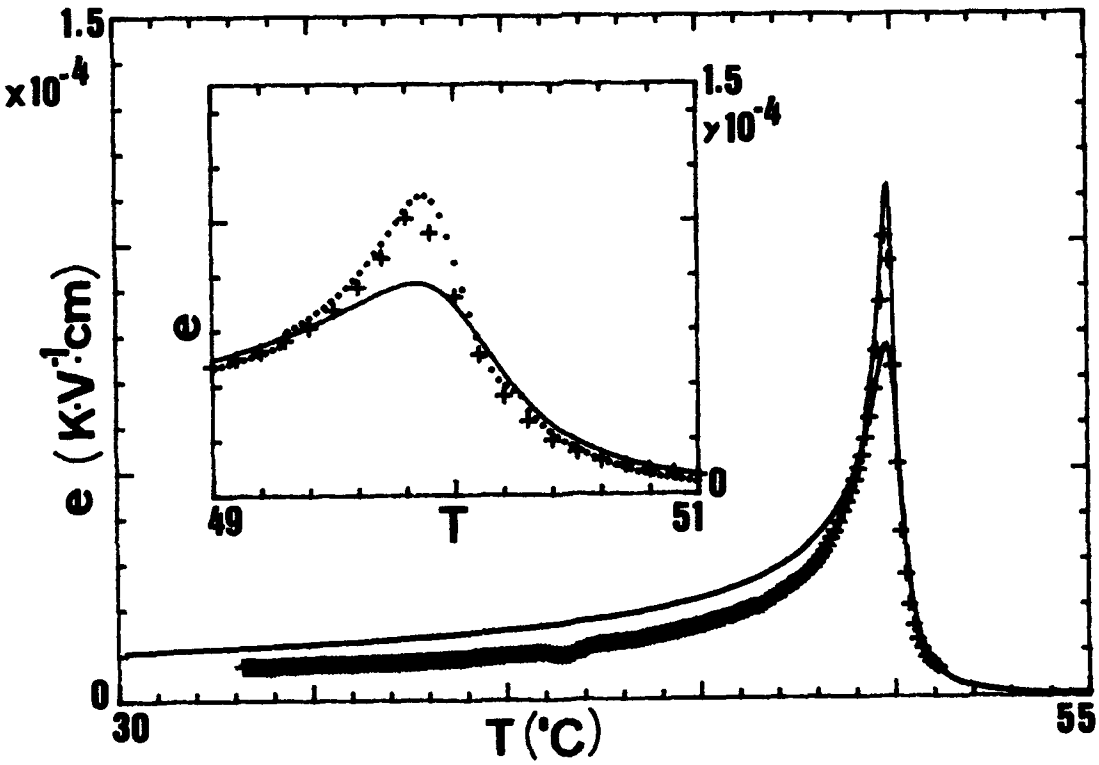

FIGURE 2 The electrocaloric coefficient of LATGS:
+) Experimental data eq. (1).
-) Theoretical results eq. (2).
.) Theoretical results eq. (3).

Ferroelectrics, 1992, Vol. 134, pp. 217–222
Reprints available directly from the publisher
Photocopying permitted by license only

PyP247

STUDIES ON THE DIELECTRIC, PIEZOELECTRIC, PYROELECTRIC AND STRUCTURAL PROPERTIES OF $(Pb_{1-x}Gd_x)(Zr_{.6}Ti_{.4})O_3$.

ANIL GOVINDAN, H.D. SHARMA, A.K. TRIPATHI,
P.K.C. PILLAI & T.C. GOEL
Department of Physics, IIT Delhi,
New Delhi - 110016, India

__Abstracts__ $(Pb_{1-x}Gd_x)(Zr_{.6}Ti_{.4})O_3$ was prepared using the solid solution technique with different Gadolinium ratios (x=0.0 & 0.5); variation of Dielectric constant of the pellets prepared from these powders was studied as a function of temperature and frequency. The results on piezo- and pyro-electric coefficients, after suitable corona poling, are encouraging. The X-ray diffraction patterns were studied and the results are included in the paper.

Introduction

A considerable amount of work is being done on Ferroelectric Ceramics both on preparation and characterisation because of their use in piezo and pyroelectric devices [1-2]. Poling is an important criterion for their device applications. Lead Titanate is a highly anisotropic material but its device application is restricted due to the difficulty in poling the ceramic. This is because of high c/a ratio [3] in $PbTiO_3$. Normally solid solutions of $PbTiO_3$ with $PbZrO_3$ are made with different amount of lanthanum doping. The lanthanum doping has a marked effect both on the dielectric constant and ferroelectric coefficients of PZT ceramic [4].

In the present work, PZT has been doped with Gadolinium. (Gd). The preparation technique, pyroelectric, dielectric and structural characteristics of Gd doped PZT, are reported. Gd is a member of the Lanthanide series and is expected to yield interesting results.

Experimental:-

The Chemical formula of the ceramic is $(Pb_{1-x}Gd_x)(Zr_{.6}Ti_{.4})O_3$ Where x = 0.0 & 0.5. This substitution is assumed to occupy vacancies in the Pb position, so that the structure would be electrically neutral. The starting materials were PbO, ZrO_2, TiO_2, Gd_2O_3 obtained from Aldrich Chem. Co. USA. These oxides were mixed in stoichiometric proportions. Extra lead oxide (4% by weight to the lead oxide required to form stochiometric ratios) was added in the mixture before calcination. This is to avoid lead losses during calcination and sintering. It was then dried and calcined at 800°C for two hours. To the calcined powder 4% by weight Polyvinyl alcohol (PVA) was

added as a binder and mixed thoroughly. The mixture was compacted to form pellets of 1cm diameter, using a die and hydraulic press, under a load of 10 tons. The pellets were then sintered at 950°C, 1150°C and 1250°C in different batches. During sintering the samples were heated upto 600°C very slowly (3°C/min) to aviod bending or cracking of the samples. The samples were then taken to final sintering temperature at a heating rate of 5°C/min and were maintained at that temperature for two hours. The sintering was done in a closed Alumina crucible in lead atmosphere. PZT samples were also prepared in the same way. The densities of different samples were:

	(950°C)	(1150°C)	(1250°C)
PZT	6.47	6.625	6.984
PGZT	5.57	5.797	5.912

As the density of samples prepared at 1250°C is maximum the data given is for these samples unless otherwise mentioned.

The X-ray diffractograms of these samples were taken using Cu K_α radiation on a Rigaku diffractometer. The voltage and current ratings used for the present experiment were 40 KV and 30 mA respectively. X-ray scan speed was 10°/minute. Dielectric measurements were done using a Hewlett-Packard impedance analyser model no. 4192A. Quick drying silver paint electrode was used for these and other electrical measurements. Samples were corona poled at a corona voltage of 7 kV and current 50 uA for pyroelectric coefficient measurements. The pyroelectric current was measured at a heating rate of 4°C/min on a Keithley 610C electrometer. The pyroelectric coefficient was calculated using the relation:

$$P = (I/A)/(d\theta/dt)$$

Where I is the pyroelectric current; A is the sample electrode area; $d\theta/dt$ is the heating rate.

d_{33} measurements on the corona poled samples were done on a Pennebaker Model 8000 Piezo d_{33} tester. The d_h measurements were done on an indegeniously designed d_h measurement assembly. It has a hydrostatic pressure vessel containing the sample holder. The charge that develops on the sample charges a standard capacitor (.1µF). The voltage on the capacitor is recorded on an Omniscribe recorder and the corresponding pressure change is monitored on a manometer.

Differential scanning calorimetric thermograms of the samples were taken on a DuPont DSC meter.

Results & Discussion:-

Representative X-ray diffractograms of PZT and PGZT are shown in Fig.1 and 2 respectively. PZT and PGZT plane giving rise to diffraction peaks are also identified in these figures. The presence of well resolved peaks due to (002) and (200) plane indicates that the material is in tetragonal form[5]. The c/a ratio for PZT and PGZT was found to be 1.02 and 1.01 respectively. No appreciable

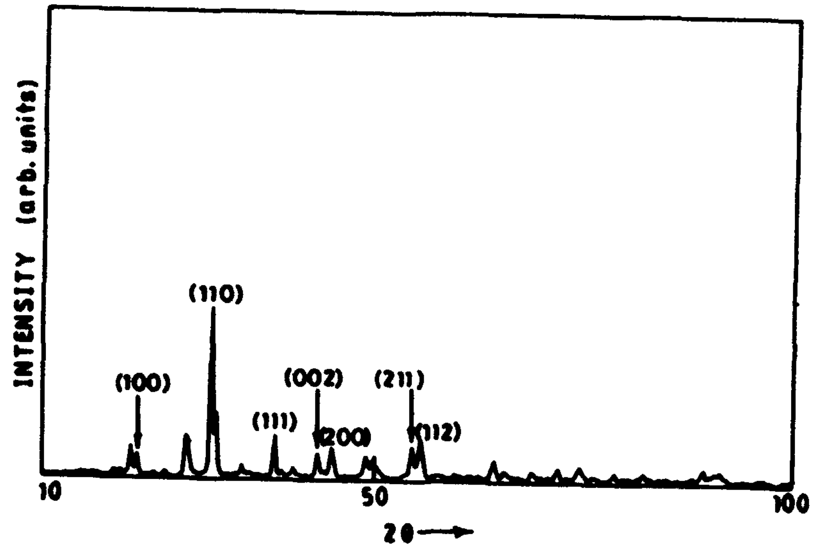

Fig 1. X-ray diffractogram of PZT ceramic.

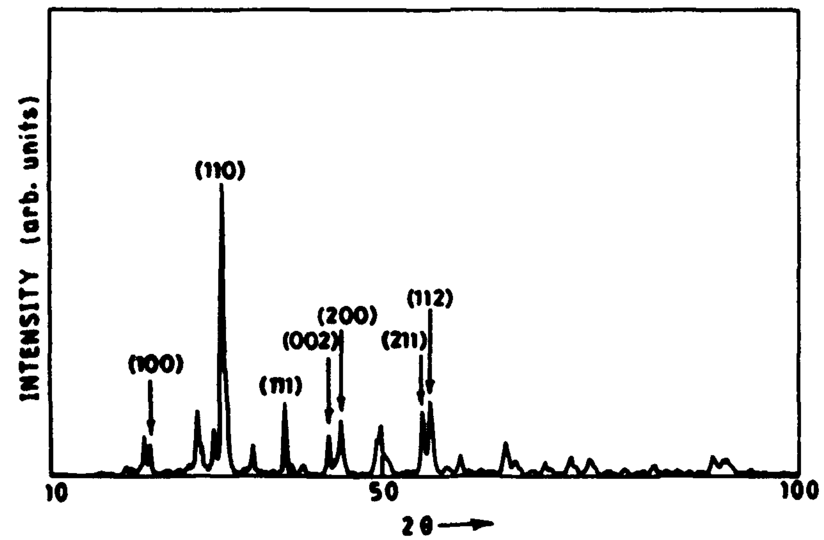

Fig 2. X-ray diffractogram of PGZT (5% Gd doped) ceramic

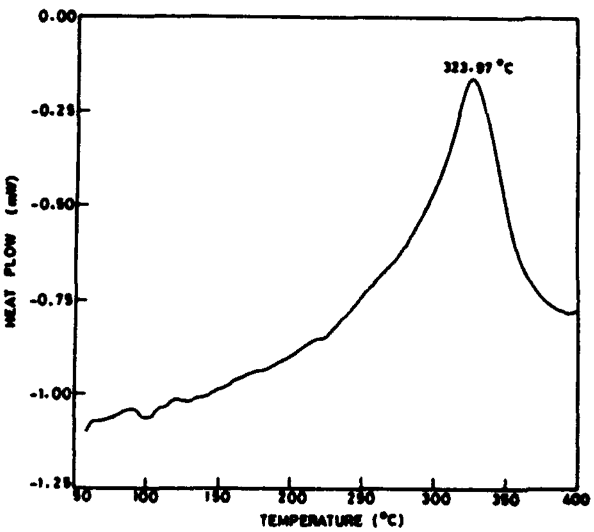

FIG 3. DSC Thermogram of PGZT ceramic

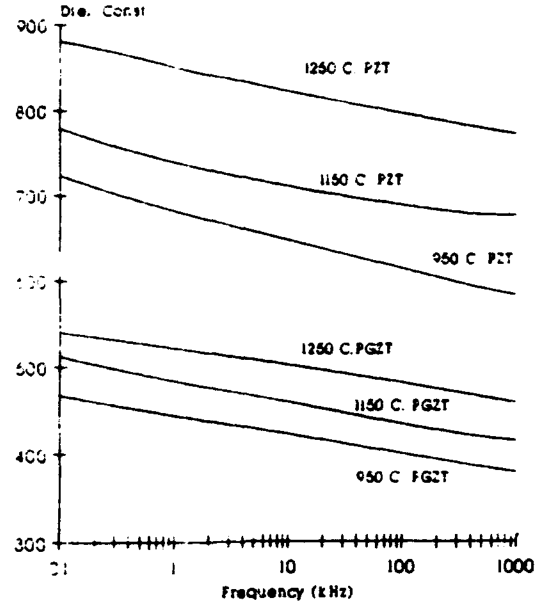

FIG 4. Dielectric constant E' vs frequency for both PZT and PGZT for samples sintered at 950°C, 1150°C & 1250°C

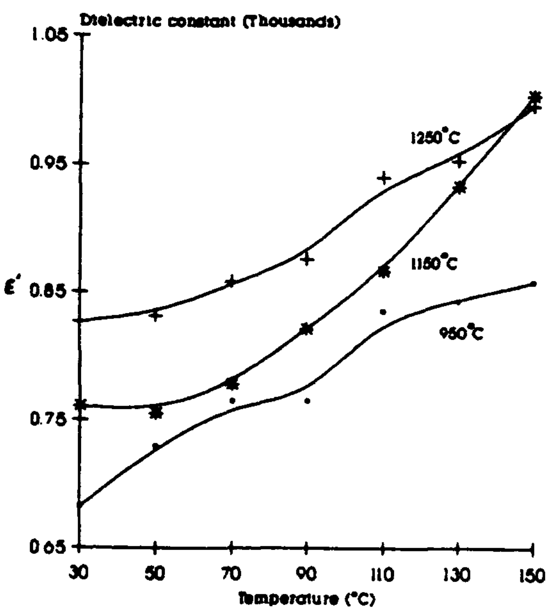

FIG 5. Dielectric constant vs Temperature for PZT samples subjected to 950°C, 1150°C and 1250°C sintering temperatures at a fixed frequency of 1 kHz.

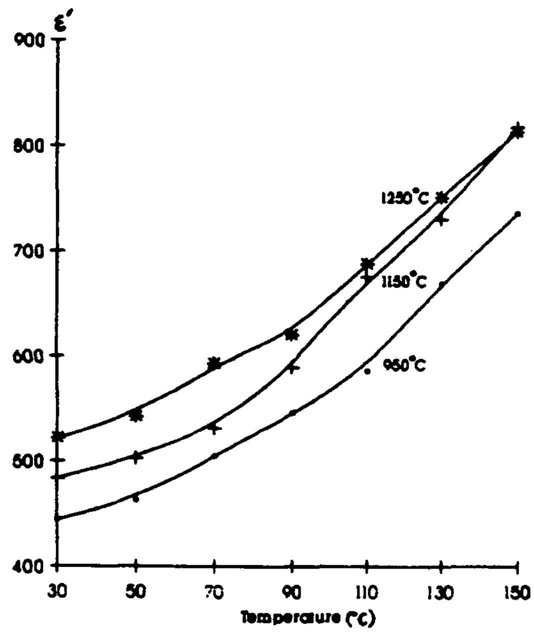

FIG 6. Dielectric constant vs Temperature for PGZT samples subjected to 950°C, 1150°C and 1250°C sintering temperatures at a fixed frequency of 1 kHz.

change in the peak positions was observed. The absence of any new peak in PGZT indicates that Gd goes into the lead vacancies without distorting the PZT lattice. Here it is pertinent to note that although 4% by weight extra lead was introduced in the sample before sintering, we cannot rule out the possibilities of lead vacancies due to the evaporation of lead.

The Differential scanning calorimetric thermogram of PGZT sample is shown in Fig.3. The curie transition temperature of the sample is as indicated by Fig.3. is around 323.97°C. The curie temperature for 60:40 $ZrTiO_3$: $PbTiO_3$ composition is above 400°C [6]. This suggests that Gd doping decreases the curie transition temperature of PZT. Similar results were also observed in La, Sm doping in PZT

The representative curves showing dielectric constant ε' versus frequency at Room temperature (30°C) for both PZT and PGZT are shown in Fig.4 , while the variation of ε' with temperature at 1 kHz is shown in figures 5 & 6. The effect of sintering temperature on E' is also shown in

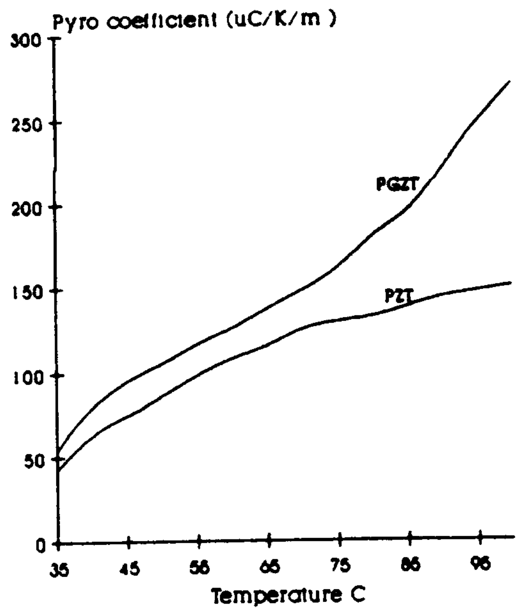

FIG 7. Variation of pyroelectric coefficient of PZT and PGZT with temperature

these figures. It can be seen from these graphs that the variation of dielectric constant with temperature and frequency shows normal behaviour of a dipolar material and is similar to PZT in this temperature and frequency range[6]. The value of dielectric constant of the Gd doped PZT is lower than that of undoped PZT. This could be due to the smaller tetragonal distortion in PGZT samples compared to PZT, which may lead to lesser dipole moment of PGZT unit cell. Moreover, the lower density of PGZT may also contribute to the observed low value of E' compared

to PZT. The effect of density on ε' is evident from the increase in E′ with the increase in sintering temperature.

The variation of pyroelectric coefficient with temperature for both PZT and PGZT is shown in Fig.7. It was found that the pyro coefficient increases with the increase in temperature. The piezoelectric d_{33} and d_h coefficients of PZT were found to be 125 and 15 pC/N, while for Gd doped PZT these values were 200 pC/N and 26 pC/N respectively. The voltage sensitivity g_h for Gd doped PZT was 12×10^{-3} Vm/N which is higher than that of undoped PZT.(5.64×10^{-3} Vm/N). This suggests that Gd doping facilitates the poling of PZT. The results are compared with Lanthanum doped PZT in table 1.

Table 1. Comparison of PGZT with PLZT*

	ε'	p_i nC/cm^2/K	$p_i/E'E_o$	d_h	g_h	$d_h \cdot g_h$
PZT	826	8.20	1.154	41	1.34	54.94
PLZT[7]	1200	17.4	1.638	40	3.76	150.49
PGZT	521	20	4.332	21	5.23	135.93

* The unit for d_h is pC/N
g_h is $\times10^{-3}$ Vm/N
$d_h \cdot g_h$ is $\times10^{-15}$ m^2/N

It can be concluded on the basis of these results that Gd doped PZT is a better material than PLZT for the development of pyroelectric devices. The above result also indicates that the piezoelectric figure of merit is comparable with that of PLZT and hence a good candidate for its use in piezoelectric devices.

References

1. Bergmman J.G., Crane G.R. & Tuner E.H. (1977) Jour.Sol.State.Chem 21 127 33.
2. R.Sekar, A.K. Tripathi, and P.K.C. Pillai, Mater.Sci.& Engg. B5 33 (1989)
3. Yokoyama K, et. al. Proc. 2nd. meeting on ferroelectric materials and application. pp 227
4. B. Jaffe, W.R. Cook and H. Jaffe Piezoelectric Ceramics (Academic press New York) (1971) Chap.5.
5. S. Naka, et al. Rep. Asahi glass foundation Indus. Technol. 22 (1973) 155
6. M.E. Lines & A.M. Glass "Principles and Applications of Ferroelectrics and related materials" Clarendon Press Oxford (1979. pp. 539 & 570.
7. Pramila. C., T.C. Goel and P.K.C. Pillai,'Paper presented during The Dielectric Society 25th Anniversary Meeting held at Imperial College'.London U.K. Paper No. DiP248. 12-15 April 1992.

Ferroelectrics, 1992, Vol. 134, pp. 223–228
Reprints available directly from the publisher
Photocopying permitted by license only

PyP261

CHARACTERIZATION OF FERROELECTRIC $LiTaO_3$ THIN FILM

A.KANDUŠER, D.MANDRINO, M.KOSEC, P.PANJAN,
and B.B.LAVRENČIČ

J.Stefan. Institute, University of Ljubljana, Ljubljana, Slovenia.

Abstract Ferroelectric $LiTaO_3$ thin films were grown using an RF sputtering method from a monocrystalline target on heated substrates of $LiTaO_3$, silicon and sapphire. The structure and composition of obtained films were checked by means of XRD, AES and RBS spectroscopies. The analysis of results showed that the films were preferentially oriented with the c-axis perpendicular to the surface of substrates and stoichiometric.

INTRODUCTION

For sensitive pyroelectric detectors, crystalline $LiTaO_3$ is a material of choice due to excellent figure of merit and other desirable fabrication characteristics.[1-2] With the advances in the methods of deposition of thin film ferroelectrics, the situation should be reconsidered. The main thrust of research in thin film and integrated ferroelectrics has been directed toward the nonvolatile ferroelectric memories, which do not require the preferentially oriented material as it is the case with pyroelectrics.[3-4] For this orientation requirement the reactive RF sputtering deposition method has been selected. Ideally, one should aim for the perfect epitaxial film growth with the figure of merit equal to the bulk crystalline material.

Excellent thin film pyroelectric detectors have been obtained by Takayama et al.[5], made from La-modified $PbTiO_3$, deposited on oriented Pt film and cleaved MgO. On the other hand, reported $LiTaO_3$ detectors have been made from polycrystalline films.[6-7] Their performance so far does not match comparable detectors made from thinned crystalline material.

While there are reports on the growth of oriented $LiNbO_3$ film, there is little on $LiTaO_3$[8-9] , which has similar properties. It may not be always the case as

far as the film formation is concerned.[10] The emphasis of this report is on the growth of $LiTaO_3$ thin films on various substrates and their structural composition.

EXPERIMENTAL

We employed the RF magnetron reactive sputtering method (see conditions in Table I). For the target we used monocrystalline $LiTaO_3$ block of 45 mm diameter and 8 mm thickness. The substrates used were (111) silicon, fused sapphire, metallic Pt, and (001) $LiTaO_3$ and deposition was made on cold and 600 °C heated surfaces.

Due to our target - substrate separation, the RF power was important parameter. Lowering the power tends to increase the quality of films[10] until reaching the range of nonstoichiometry. The structural characteristics and compositions were checked by means of XRD, AES, RBS and SEM methods. The thickness of films were checked by means of a profilometer and were measured to be 200 - 250 nm.

TABLE I. Deposition parameters.

Parameter	Value
Target dia.	45 mm
Separation	20 cm
RF power	350 W
Pressure O_2	4-4.6x10^{-4} mbar
Pressure Ar	2x10^{-3} mbar
Deposition rate	60 nm/h

RESULTS AND DISCUSSION

The degree of crystallinity and orientation was checked by XRD. Fig.1 shows the film deposited on the cold (111) silicon and then thermally treated for 1 hour at 600 °C. The film was amorphous after deposition and clearly reverted to polycrystalline form after treatment with the residual amorphous phase that is rather weak. The analysis of this spectrum shows identical peaks with the single crystal powder result. The (006) peak is much smaller that the (104) peak. We have also tried various heat treatment regimes as well as the deposition on sapphire substrate. The resulting XRD peaks were slightly shifted from the powder diffraction peak positions due to internal stresses. The treatment used in Fig.1 showed the least deviation from the single crystal powder.

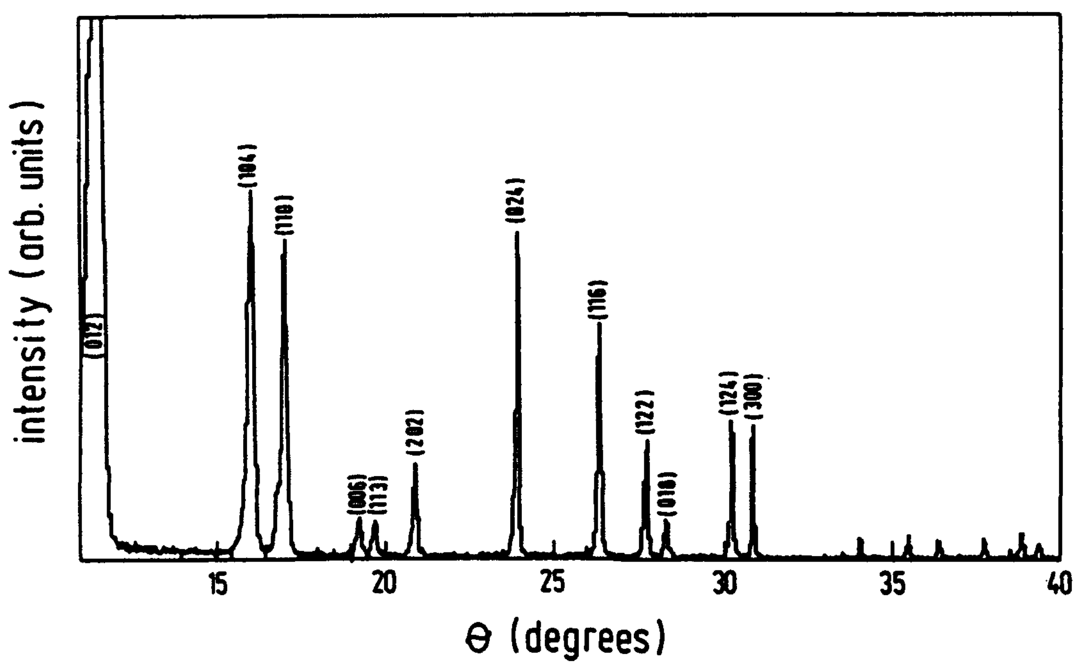

FIG.1. XRD diffraction spectrum of $LiTaO_3$ polycrystalline annealed film grown on (111) silicon.

The film obtained on the 600 °C heated (111) silicon produced XRD spectra as shown in Fig.2. Comparing this result with that of Fig.1 we find that the spectrum exhibits only prominent peaks at (104) and (006), thus indicating the preferred c-axis orientation of grown film perpendicular to the surface of the silicon. It should be noted the markedly different peak ratio as obtained in Fig.1. Now the (006) peak is very prominent. The spurious Θ = 13.5 ° peak (labeled with X) has been discussed earlier[10] and was then attributed to silicon substrate. We have found this peak in the case of both silicon and (001) $LiTaO_3$ substrates.

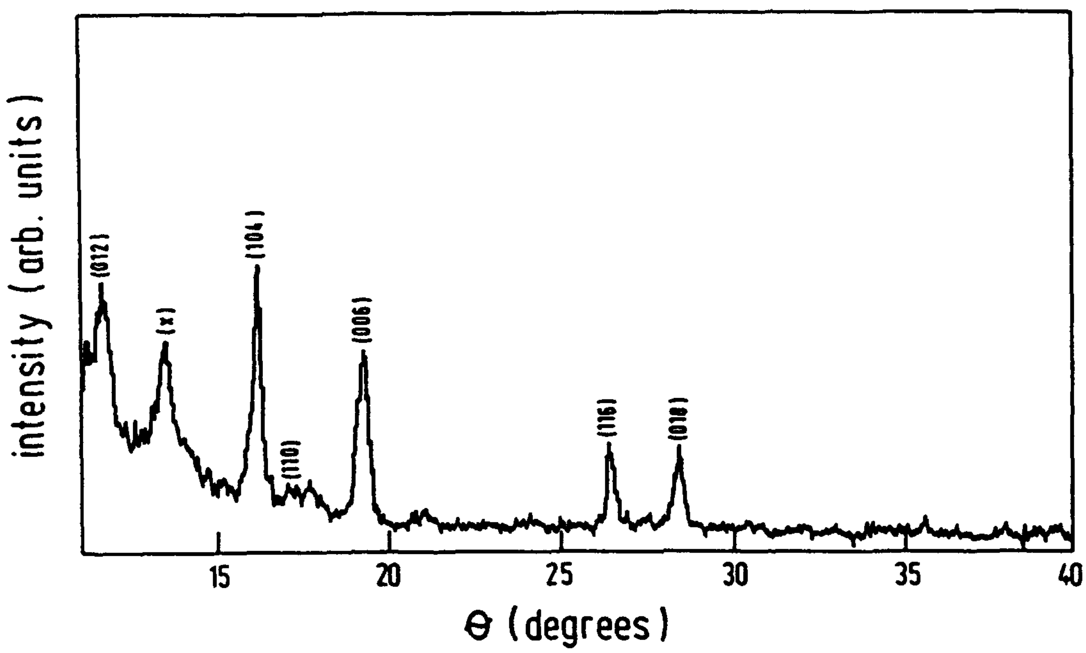

FIG. 2. XRD diffraction spectrum of $LiTaO_3$ oriented film grown on (111) silicon at 600 °C.

Due to reports on possible stoichiometric composition problems[9-10] we performed careful checks on the films deposited on cold and heated silicon surfaces. Fig.3 shows the Auger electron spectroscopy (AES) depth profile for the

latter surface. The result shows that the obtained film had the ratio for Li:Ta:O calculated to 1:1:3 by taking into account the relative Auger sensitivities of the elements.[11] The same result was obtained also for the unheated surface. The depth profile indicated homogeneous composition throughout the thin $LiTaO_3$ film as well as the residual carbon impurities.

To further determine oxygen and tantalum contents the Rutherford backscattering spectroscopy (RBS) with 1.3MeV hydrogen ions was used, Fig.4. The spectrum shows strong tantalum and much weaker oxygen peaks (lithium could not be resolved). The solid lines represents the model calculation from which we could determine that the tantalum vs. oxygen ratio should be placed between 1:2.5 and 1:3.

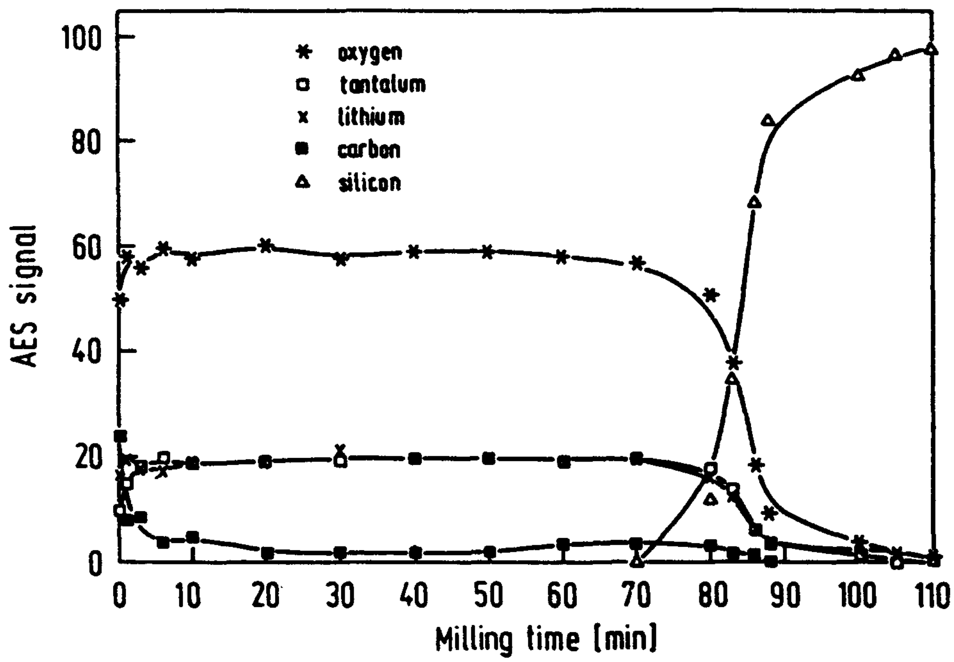

FIG. 3. AES depth profile obtained from $LiTaO_3$ thin film deposited on (111) silicon at 600 °C.

In conclusion: we have grown the polycrystalline and oriented $LiTaO_3$ thin films with a good stoichiometric composition. At presently it is not entirely clear why such composition is found with single crystal targets while in the case of usual powdered ones[10] the excess of Li_2O was required.

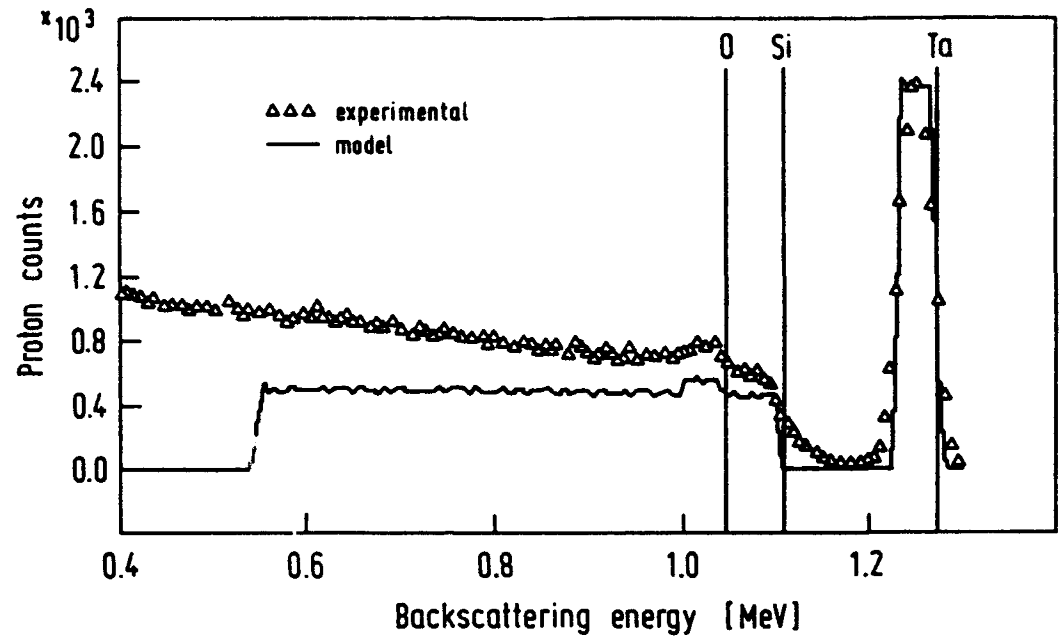

FIG. 4. RBS spectrum obtained from $LiTaO_3$ thin film deposited on (111) silicon at 600 °C. The solid line represents the model calculation.

REFERENCES

1.S.B.Lang, The Sourcebook of Pyroelectricity (Gordon & Breach, New York, 1974).
2.B.B.Lavrenčič, J.Polanec, P.Cevc, and A.Kandušer, Ferroelectrics, 91, 323 (1989).
3.J.F.Scott, C.A.Paz da Araujo, Science, 246, 1400 (1989).
4.Proc. Sec. Symp. Integrated Ferroelectrics, Ferroelectrics, Vol.116 (1991).
5.R.Takayama, Y.Tomita, K.Iijima, and I.Ueda, J.Appl.Phys., 61, 411 (1987).
6.D'Amico, G.Petrocco, A.Lucchesini, and F.Giannini, Materials Letters, 3, 33 (1984).
7.S.W. Kim, J.Y.Song, Korean Appl. Physics, 3, 229 (1990).
8.T.Kanata, Y.Kobayashi,and K.Kubota, J.Appl.Phys., 62, (1987).
9.R.C.Baumann, T.A.Rost, and T.A.Rabson, J.Appl.Phys., 68, (1990).
10.P.W.Haycock and P.D.Townsend, Appl. Phys. Lett., 48, (1986).
11.Handbook of Electron Spectroscopy, L.E. Davies et al. editors, published by Phys. Electron. Ind. 1976.

SECTION III
CONTRIBUTED PAPERS
IIIh. PVDF and Copolymers

Ferroelectrics, 1992, Vol. 134, pp. 229–234
Reprints available directly from the publisher
Photocopying permitted by license only

PvP127

EFFECT OF MOISTURE ON THE ELECTRICAL PROPERTIES OF BIAXIALLY STRETCHED POLYVINYLIDENEFLUORIDE (PVDF) FILMS

PAULO ANTÓNIO RIBEIRO, M. RAPOSO and J. N. MARAT-MENDES
Faculdade de Ciências e Tecnologia #, Universidade Nova de Lisboa.
Torre, 2825 Monte da Caparica- PORTUGAL

Abstract Films of biaxially stretched Polyvinylidenefluoride (PVDF) polymers were charged by corona discharge under humidity controlled atmospheres. The surface potential builup is observed to have a first increase followed by a plateau like region, after which a later stage the surface potential grows again reaching a maximun value and decreasing again slowly. The maximum value reached depends on the humidity content. The higher the humidity content, the lower the value of the maximum observed. This behaviour is explained in terms of protonic motion due to water absorved in the bulk of the sample.

INTRODUCTION

The effect of moisture in the electrical properties of polymer films has been reported before. It was shown, for α- PVDF samples, that the evanescent transient current in step-voltage measurements[1] and also the buildup potential in corona charging measurements for α and β PVDF[2-5] are strongly dependent of moisture. The results were partly explained by the drift of charges generated by the ionic dissociation of the absorbed water molecules in the bulk of the sample.

A sistematic study of the potential buildup curves of constant current charging biaxially stretched PVDF samples in different humidity atmospheres was first carried on[5]. The presence of a saturation voltage maximum and a subsequent slow decay was attributed to ionic conductivity due to water dissociation and the equilibrium of water molecules and its ionic species. In this work we studied further the humidity induced conductivity in PVDF samples.

EXPERIMENTAL SETUP

Figure 1 shows the corona triode we have developed in order to study the buildup of the surface potential of samples charged with a constant corona current for various degrees of humidity.

and Centro de Fisica Molecular das Universidades de Lisboa (INIC)

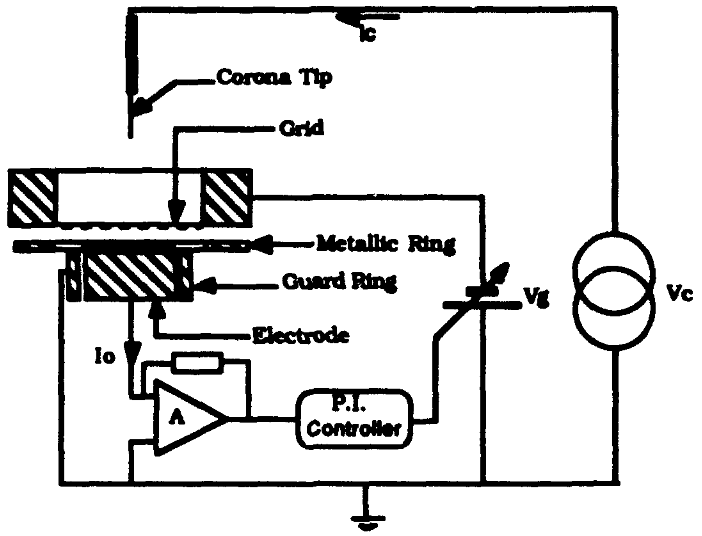

FIGURE 1 Schematic circuit of the corona triode for charging samples with constant current. Vg and Vc are high voltage power supplies.

The triode is basically formed by a corona point, a metallic plate and a grid in between. A guard ring on the plate prevents the surface currents from reaching the measuring electrode (plate). The grid is a stainless steel mesh of 750 μm spaced wire of 160 μm in diameter. The grid to point distance was 11 mm and the distance plate to grid was 2 mm. The plate current Io, was kept constant by means of a proportional integral controller driving the gird voltage V_g, and the corona current I_c, was allways kept at 4 μA by the supply V_c.

The sample potential V(t), is determined by means of the grid voltage using the equation[6]:

$$V(t) = V_g(t) - V_r \tag{1}$$

where $V_g(t)$ and V_r are the grid voltage and the potential difference across the air gap, respectively. For each set of experimental conditions - values of I_o, I_c, humidity content . V_r was determined before the charging process with a bare sample older (in this case, V_r=V_g).

The samples were 12 μm thick, circular foils of biaxially stretched PVDF film manufactured by Kureha Chemical Industries Company Ltd. The foils have a degree of crystallinity of about 50% with cristalline parts consisting of nominaly equal amounts of α and β phases. Circular aluminium electrodes of 15 mm diameter and 500 Å thick were vacuum evaporated on one side of the samples. The samples were kept stretched with the help of a metallic ring (holder) during the charging process.

EXPERIMENTAL RESULTS AND DISCUSSION

Potential Buildup Curves in Different Atmospheres

Figure 2 shows typical curves of the potential buildup versus time of positively charged samples in dry air (0 % H.R.) and in various degrees humidity atmospheres with a constant current density of $J_0 = 17 nA/cm^2$. Each sample was previously charged in a dry air and afterwards its surface charge was neutralized by exposing the sample to the corona ions of opposite polarity, then it was submited to a new charging process in the required humidity content. Similar results are obtained for negatively charged samples.

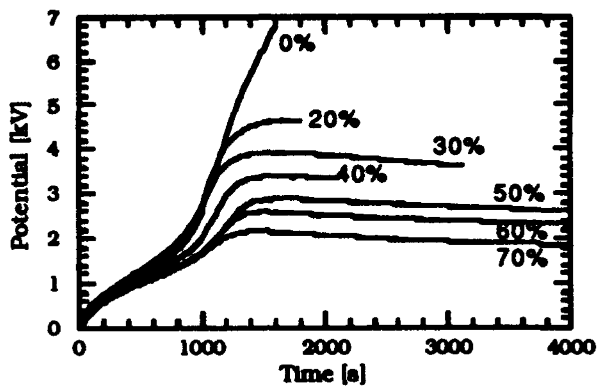

FIGURE 2 The buildup of the surface potential for samples positively charged under different humidity conditions. Prior to the measurement, each sample was previously charged under dry air with negative corona.

Dry air curve plainly shows the ferroelectric behaviour of PVDF sample . One can distinguish three distinct regions: i) a initial fast increase of the potential associated with the capacitive behaviour of the sample; ii) a plateau like region due to dipole orientation and iii) another region of fast potential increase since the dipoles had already been oriented.

By opposition curves of potential buildup in humid air present lower values of the potential for similar times and a maximum potential value V_m is attained. Also a slow decay is observed after this maximum.

Since no surface current is observed or charge injection from the corona wind species[5] it should be concluded that the effect is due to ionic conduction.

This decrease on the saturation of the surface potential with the humidity content is interpreted as an increase in the conductivity of the sample, which should be linked to the conduction due to the presence of the water in the bulk of the polymer. This can be clearly seen if one writes that the total current density J_0, which is constant during the charging process components:

$$J_0 = \varepsilon\frac{\partial E(x,t)}{\partial t} + \frac{\partial P(x,t)}{\partial t} + J_c(x,t) \qquad (2)$$

where $\varepsilon\frac{\partial E(x,t)}{\partial t}$ and $\frac{\partial P(x,t)}{\partial t}$ are the displacement current components due to free charge and dipoles and $J_c(x,t)$ is a conduction current through the sample. The displacement terms explain the continuous increase of the surface buildup potential regions and the plateau like region in dry air, where no significant conduction is taking place. On the other hand for PVDF charging in humid air a conduction current term is necessary to explain the saturation of the surface potential.

It has also been observed that a strait line is obtained if one plots the maximum surface potential values versus the chamber relative humidity content, Figure 3.

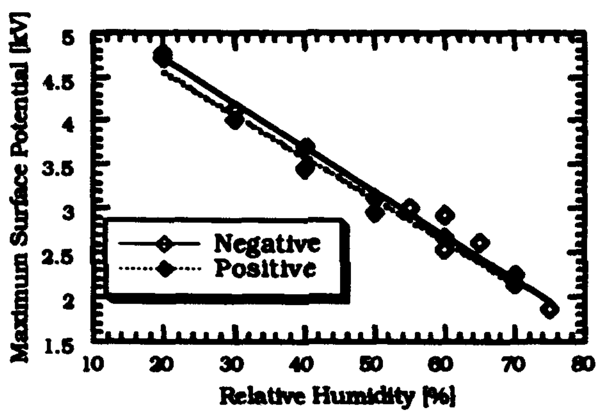

FIGURE 3 The maximum voltage, V_m, attained during the charging process as a function of the relative humidity.

This effect is similar to that occuring in porous ceramics where the electric resistivity decreases lineary with relative humidity[7,8]. As in ceramics the increase of the conductivity may be related to the water adsorbed in the walls of the pores of the material. The dissociation of the water molecules into H^+ and OH^- ion may lead to an ionic conductivity process.

In the polymer the water molecules may be adsorbed on the interfaces of the lamellar folded crystalline chains of the polymer and with increasing humidity, further layers of water are adsorbed and dissociated.

The conductivity should then be due to proton exchange according with the equation:

$$H_3O^+ + H_2O \leftrightarrow H_2O + H_3O^+ \qquad (3)$$

This process has also been suggested for ceramics[7] and is a characteristic conduction fenomena in a medium where water is present.

This one carrier transport process is compatible with the similarity of the surface potential buidup curves for positive and negative charging as reported [4,5].

Since surface buildup curves are similar for samples charged either positively or negatively, we believe that we are in the presence of one carrier conduction process associated to a proton tranfer in the sample.

Protonic conduction in PVDF has been reported before[9]. According to this reference, it has been suggested that protons generated by dissociation of adsorbed water molecules penetrate in the polymer. Since PVDF charging in a dry atmosphere of 7.5% hidrogen, 92.5% nitrogen does not show charge injection[5], the proton tranfer must be associated with the water of the sample.

Potential Buildup Curves for Differents Charging Currents

We also studied the effect of the charging current on the buildup of the polymer surface potential at constant relative humidity. Figure 4 shows results for negative charging of PVDF samples in 60% H.R.

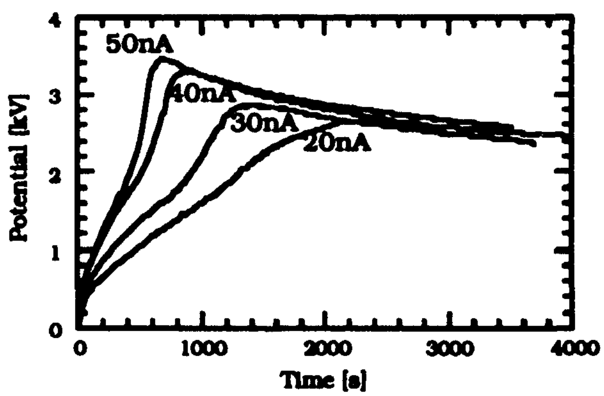

FIGURE 4 The buildup of surface potential for negatively charged samples with different charging currents under 60% R.H. atmosphere.

As usual these samples were previously charged in a dry air atmosphere. Results for positive charging are similar.

If one plots the maximum of the surface potential attained in each charging process versus current, a square root dependence is found for both positive and negative charging processes[2,6], which means a process of excess of charge carrier transport. Calculations of the carrier mobilities under 60% H.R., give values of 4.8

$\cdot 10^{-16}\ m^2/Vs$ and $3.5 \cdot 10^{-16}\ m^2/Vs$ for positive and negative charging processes respectively. The similarity of these values support the one carrier idea.

ACKNOWLEDGMENTS

The authors are grateful to Junta Nacional de Investigação Cientifica e Tecnológica (JNICT-Portugal) for the financial support.

REFERENCES

1. R. M. Faria, N. Alves and G. F. Leal Ferreira, Solid State Ionics, 28-30, pp. 1938-1041, 1988.
2. J. A. Giacometti, Neri Alves and M. M. Costa, Proc. of the Conf. on Electrical Insulation and Dielectric Phenomena, (IEEE, Piscataway, N. J., USA, 1990) pp. 77-82.
3. J. A. Giacometti, M. M. Costa and G. Minami, Proc. of the 7th International Symposium on Electrets (ISE7), (IEEE, Piscataway, N. J., USA, 1991) pp. 432-437.
4. P. A. Ribeiro, J. A. Giacometti, M. Raposo and J. N. Marat Mendes, Proc. of the 7th International Symposium on Electrets(ISE7), (IEEE, Piscataway, N. J., USA, 1991), pp. 322-327.
5. P. A. Ribeiro, J. A. Giacometti, M. Raposo and J. N. Marat Mendes, Constant Current Corona Charging of Biaxially Stretched Polyvinylidenefluoride (PVDF) films under Humidity Controlled Atmospheres,accepted for publication
6. J. A. Giacometti and J. S. Carvalho Campos, Rev. Sci. Instrum., 61, pp. 1143-1150, 1990.
7. M. J. Madou and R. Morrison, Chemical Sensing with Solid State Devices, (Academic Press, 1989), chap. 12.
8. A. J. Moulson and J. M. Hebert, Electroceramics Materials Properties Applications, (Chapman and Hall, 1990), chap. 4.
9. Akira Doi, J. Appl. Phys., 59, pp. 2068-2071, 1986.

Ferroelectrics, 1992, Vol. 134, pp. 235–240
Reprints available directly from the publisher
Photocopying permitted by license only

PvP128

INTERACTION OF CORONA DISCHARGE SPECIES WITH TEFLON-FEP (FLUOROETHYLENEPROPYLENE) FOILS

MARIA RAPOSO, P. A. RIBEIRO and J. N. MARAT-MENDES
Faculdade de Ciências e Tecnologia #, Universidade Nova de Lisboa.
Torre, 2825 Monte da Caparica, P.

Abstract Negatively corona discharge is a practical method of introducing electrical charges in dielectrics to produce electrets. Results have shown that the Teflon-FEP (fluoroethylenepropylene) electret charge stability is dependent on the corona atmospheres. We have carried out charging experiments on atmosphere of CO_2, O_2, N_2, dry air and humid air. The charge stability has been studied by surface charge and thermally stimulated discharge (TSD) measurements. The corona process produces electrons, ions and neutral species. The charged species transfer their electrical charge to polymer surface traps. The activated neutral species interact with the polymer surface creating new traps or modifying the preexisting ones, being responsible for the decrease of the electret charge stability. This effect is strongly dependent on the corona atmosphere and charging time.

INTRODUCTION

Corona charging in air is one of the most used methods for introducing electrical charges in polymers to produce electrets[1,2]. The charges are known to remain at the polymer surface or near it[3]. Studies of the electrets charge stability using thermally stimulated depolarization current measurements (TSD) of Teflon-FEP (fluoroethylenepropylene) polymers[4], show that the corona polarization time and current influence the charge stability and therefore the electret lifetime. This was attributed to the molecular species, formed the process of in corona discharge, impinging on the surface of the polymer. In order to further understanding this process it is necessary to study the effect of the interaction of the various corona molecular species with the polymer surface.

In this way we carried on corona charging experiments of Teflon-FEP samples in various controlled atmospheres (N_2, CO_2, O_2, dry air and humid air)[5]. Thermally stimulated depolarization current measurements of these samples show that different molecular species formed in the corona discharge have an effect on the polymer modification of surface states in different ways.

EXPERIMENTAL SETUP

A special corona setup was developed for discharges under controlled atmospheres. This setup is schematically represented in Figure 1. It consists essentially of a cylindrical vacuum

and Centro de Fisica Molecular das Universidades de Lisboa (INIC)

chamber 50 cm high and 30 cm in diameter. The chamber is connected to a high vacuum system, with a link-up for gas admittance. A horizontal flange, with connections for high voltage, current, a humidity sensor, heating resistances, electrical motors and feedthroughs for thermocouples, joining the lower and the upper parts of the chamber. This flange also holds the mechanical supports for a corona triode, a fan, and a shutter. The corona triode is composed of a flat, horizontal metallic plate (sample holder), 15 mm in diameter, electrically isolated from the chamber, a grid 30 mm in diameter, made of a mesh of 750 μm spaced steel wires of 160 μm, and a corona tip made of a stainless steel sewing needle (Figure 1). The distance between tip to grid and grid to sample is 6 mm and 5 mm respectively. The triode was used in the constant voltage mode as indicated in Figure 1, with a negative high voltage regulated power supply connected to the tip. A voltage of 350 V was applied to the sample holder. All the charging experiments were performed under 1 atm pressure.

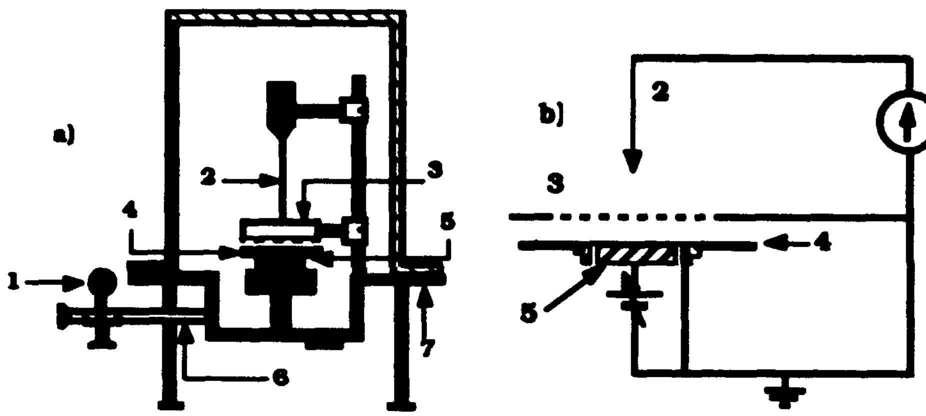

FIGURE 1 a) - The Corona Chamber: 1-manometer; 2-Corona tip (sewing needle); 3-Metallic Grid; 4- Electret ; 5-Metallic sample holder (Back electrode); 6- to vacuum pump and gas inlet; 7- Horizontal flange. b) - The Corona Triode.

A metallic shutter operated by remote controle is placed between the grid and the sample to allow the control of the charging time. A gas flux with a speed of 5 ms^{-1} could be forced between the grid and the sample, when required, by a fan conveniently placed inside the chamber. Samples were films of Teflon-FEP (Dupont), 12.7 μm of thickness, with a 15 mm diameter 500 Å vacuum evaporated aluminium electrode in one side. The films were kept slightly stretched by two concentric stainless steel rings with an internal diameter of 25 mm. The unmetallized surface was exposed to the corona discharge. Measurements of the sample surface potential were performed with a electrostatic capacitive probe, Trek Model 344-3 at a 2 mm distance from the sample. TSD current measurements were performed with an air gap, using a low noise system. This set up is enclosed in a long and heavy metallic cylinder with the connection to the electrometer far away from the heating source. An heating rate of 3.5 °C/min was used. The distance between the sample and the upper measuring electrode was 1 mm.

EXPERIMENTAL RESULTS AND DISCUSSION

Corona Charging Experiments in Various Atmospheres

Samples of Teflon-FEP were corona charged, with a surface potential of 350 V, under atmospheres of N_2, CO_2, O_2, dry air and humid air for various time periods. Negative corona currents of 20 μA were used in all experiments. Results of charge stability, obtained by the thermally stimulated depolarization technique of samples charged under different atmospheres during 10 seconds and 30 minutes are shown in Figures 2 and 3, respectively.

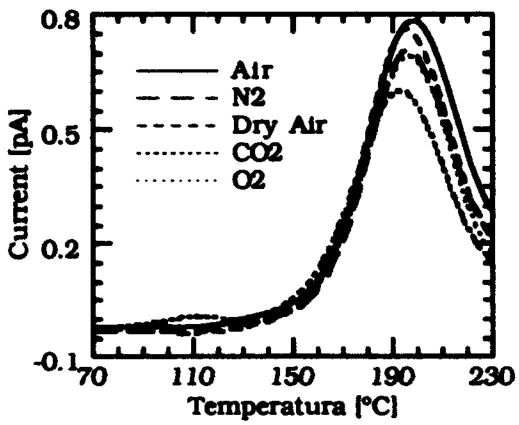

FIGURE 2 TSD results of Teflon-FEP samples charged during 10 seconds under various gas atmospheres.

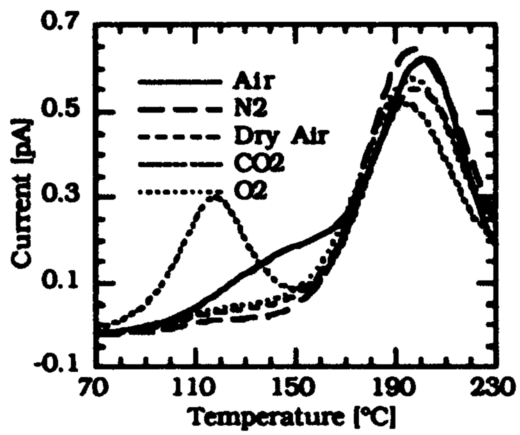

FIGURE 3 TSD results of Teflon-FEP samples charged during 30 minutes under various gas atmospheres.

These results show that for short charging time (10s), independently of the corona discharge atmospheres, all thermograms present a single current peak centered at 200°C. This current peak is interpreted by assuming the release of electrical charges from the surface traps during the heating process. The existence of a single current peak means that a single type of traps is involved. Calculation of the activation energies, using the initial current rise method[1,2,6] give a value of 1.9 eV. For longer charging times, only for polarization under N_2 atmosphere the thermogram presents the single current peak, while for the others atmospheres, the thermograms present new peaks. Therefore the atmosphere of corona charging has an influence on the charge trapping by the samples for longer exposure times. For charging in CO_2 during 30 minutes the results show a clear peak with a maximum at 120°C, to which corresponds an activation energy of 1.4 eV. For other gas atmospheres a broad band appears between 100 °C and 180 °C.

Measurement of the sample surface potential distribution taken immediately after the charging process, show that a good charge uniformity is obtained in every experiment.

The Effect of Sample Treatment

In the process of the corona discharge there is the formation of charged particles and neutral activated species[7-10]. In order to account for the effect of each we carried out experiments with a gas flux forced tangentially to the electret surface during the charging process. The charged particles follow the electric field lines. The species without charge deviated from their normal trajectories, not interacting with the polymer surface.

Figure 4 shows thermal stimulated current curves of two samples charged during 30 minutes in a CO_2 atmosphere. Curve I refers to a sample charged in the normal way i.e. as that of Figure 3. Curve II was obtained from a sample charged under the forced gas flux. The major differences between the two curves is the 120°C current peak which is absent in the thermogram of the sample charged under the forced gas flux. Therefore we associate that current peak with the neutral activated species impinging upon the polymer surface and which are believed to change the physical properties of the surface [11] by the formation of new traps. The blowing of the gas flux over the sample surface during the charging process under other corona atmospheres leads also to thermograms with a single peak as in Figure 2. This suggests that for short charging times under these atmospheres and for the corona current used, the amount of neutral species interacting with the sample surface might be small.

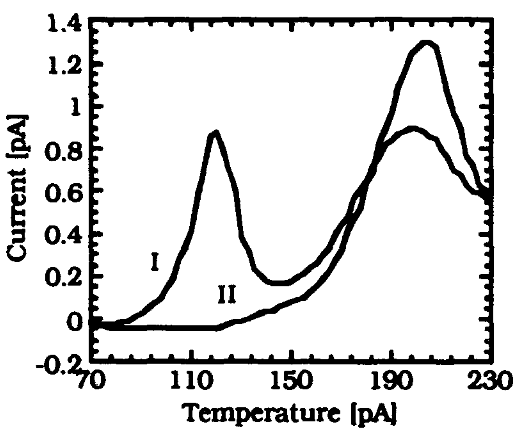

FIGURE 4 TSD results of the samples charged during 30 minutes in CO_2. Curve I - usual charging. Curve II - using a forced gas flux during the charging process.

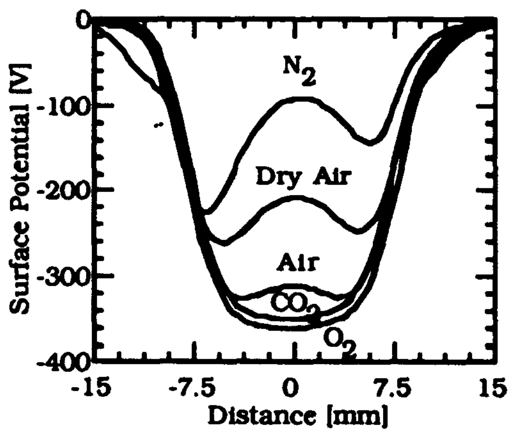

FIGURE 5 Surface Potential profiles of samples treated under various atmospheres.

We have observed that the effects of the neutral activated species in producing new traps can occur either during or before the charging process. Experiments were carried out on samples exposed to the neutral activated species produced by a 20 μA negative corona current, with the metallic sample holder connected to ground during 30 minutes, followed by a 10

seconds charging process with the sample holder connected to +350 V. TSD measurements on these samples give similar results to those obtained for samples charged during 30 minutes under the corresponding gas atmospheres (Figure 3). The surface potential measurements show also a good charge uniformity over the sample. As in these experiments the charging time was only 10 seconds one would expect to get the typical results of 10 seconds charging (Figure 2). However the results obtained are comparable to those of Figure 3. Therefore one has to assume that the exposure of the samples to the neutral activated species before charging introduced surface modifications that are responsible for the low temperature current peaks observed in Figure 3.

We also carried out experiments to study the effect of the activated species upon precharged samples. The samples were charged for 10 seconds and consecutively exposed during 30 minutes to the neutral activated species of the same gas atmosphere of the charging process. Thermograms obtained from these samples are also qualitatively similar to those presented in Figure 3. However in this case the surface potential measurements do not show the usual charge uniformity for all samples. Namely, samples treated in N_2, dry air and laboratory air atmospheres show a clear potential decay in the center of the sample surface (Figure 5). This effect is very strong for samples treated in N_2, and if the experiment proceeds for longer time than 30 minutes the potential decays to 0 V. No difference in this behaviour was observed when a forced gas flux was blown tangential to the sample surface. Furthermore, TSD measurements on theses samples show a corresponding decrease in the 200 °C current peak that becomes null when the potential is 0 V. Experiments of polymer surface potential decrease has been reported before and tentatively explained in terms of i) corona produced excited molecules and photons inducing charge from surface states to enter the bulk of the polymer (polyethylene)[12,13]; ii) excited molecules emptying of surface traps by energy transfer in low density polyethylene [10]; iii) an electronic current made of hot electrons passing through the grid of the corona triode that may create pairs when loosing their energy, the positive ions being driven to the sample surface by the electric field[4]. The possibility of such an electronic current in a corona triode has also been investigated[13]. The results presented on Figure 5 show also that for samples exposed to CO_2 and O_2 corona atmospheres there is no decay in the surface potential. However these corona atmospheres seems to be good sources of excited species, since they induce modifications on the polymer surface as can be concluded from the TSD curves of Figure 3. These results together with the above mentioned ones for N_2 and air atmospheres cannot be explained in terms of charge injection into the sample. They seem however to be compatible with an interpretation where the excited species indeed play a role in the surface modifications, but the cause of the potential decay is linked with positive ions

produced between the grid and the electret surface and being driven to the sample by the electric field.

CONCLUSIONS

The atmosphere of negative corona charging of Teflon-FEP films influence the charge stability of produced electrets.In the corona discharge process charged particles and neutral excited species are produced. The production of these excited molecules seems to be very efficient in CO_2, much less in O_2, humid air and dry air and almost null in N_2. These excited molecules interact with the polymer surface, being absorbed on it or reacting with the polymer molecules producing new traps or modifying the preexisting ones The arriving corona charges fill in both the preexisting traps and the new formed ones. Corona charges (an electronic component) passing the grid of the corona triode are thought to produce ions pairs in the gap grid-electret, the positive ions being driven to the sample and removing the negative charge from the traps decreasing the surface potential.

ACKNOWLEDGMENTS

The authors are grateful to Junta Nacional de Investigação Cientifica e Tecnológica (JNICT-Portugal) for the financial support.

REFERENCES

1. G.M.Sessler, Electrets, (Topics in Applied Physics Vol33, Springer, Berlim, 1980)
2. B. Hilczer and J. Malecki, Electrets, (Studies in Electrical and Electronic Engineering 14, Elsevier, 1986)
3. H.von Seggern,J. Appl. Phys., 50(4),2817 (1979).
4. C. J. Dias, J. N. Marat Mendes and J. A. Giacometti, J. Phys. D: Appl. Phys. 22, 663 (1989).
5. M. Raposo, P. A. Ribeiro, J. A. Giacometti, M. A. Bento and J.N. Marat-Mendes, Proc. of the 7th Int. Symp. on Electrets (ISE 7) (IEEE, Piscataway, N. J., USA, 1991) pp.687-692
6. C. Christodoulides, J. Phys. D: Appl. Phys., 18, 1501,1985.
7. M.M.Shahin, J. Chem. Phys. 43, 2600, (1965).
8. P.S. Gardiner and J.D.Cragg, J. Phys. D: Appl. Phys., 10, 1003,1977.
9. Creswell, B.A.; Gribbon, B.I.; Kabayam, M.A. and Perlmann,M.N.; Telesis 2, 21 (1971).
10. S. Haridoss and M.M. Perlman, J. Appl. Phys., 53(9),8106 (1982).
11. N. Takahashi, J. Rault, A. Goldman and M. Goldman, Proc. 2nd Int. Conf. on Conduction and Breakdown in Solid Dielectrics (Erlanger, Germany,1986)
12. E. A. Baum, T. J. Lewis and R. Toomer, J. Phys. D: Appl. Phys., 10, 487,1977.
13. E. A. Baum, T. J. Lewis and R. Toomer, J. Phys. D: Appl. Phys., 10, 2525,1977.
14. D. L. Chinaglia, G. F. Leal Ferreira, J. A. Giacometti and O. N. Oliveira,Jr., Proc. of the 7th Int. Symp. on Electrets (ISE 7) (IEEE, Piscataway, N. J., USA, 1991) pp.225-260.

Ferroelectrics, 1992, Vol. 134, pp. 241–246
Reprints available directly ııom the publisher
Photocopying permitted by license only

PvP129

STUDY OF THE POLARIZATION OF VDF-TrFE 75%-25% COPOLYMER FILMS USING THE PRESSURE WAVE PROPAGATION METHOD

Christine LABURTHE TOLRA, Claude ALQUIE, Jacques LEWINER
Laboratoire d'Electricité Générale, E.S.P.C.I, 10 rue Vauquelin, 75005 - Paris, France

Abstract The PWP method allows the non-destructive measurement of the homogeneity of the piezoelectric coefficient. The influence of the conditions of polarization (amplitude of the poling field, temperature and duration of the polarization process), associated to various thermal treatments, is investigated in the case of VDF-TrFE 75%-25% copolymer samples. From these results, we show that the thermal treatment has a large influence both on the kinetics and on the homogeneity of the polarization. This is attributed to the variation of the amount of ferroelectric phase resulting from these treatments. It has also been observed that the injection of electrons at the cathode plays an important role in the build up of the polarization.

INTRODUCTION

The pressure wave propagation method (PWP)[1-4] is well suited to study the mechanisms involved in the polarization of piezoelectric polymers such as PVDF or copolymers of vinylidene trifluoroethylene (VDF-TrFE)[3-6]. In this paper, the PWP method is used to determine the amplitude and homogeneity of the piezoelectric coefficient e_{zz} in VDF-TrFE 75%-25% copolymer samples for various conditions of polarization. First, the influence of thermal treatment before polarization, of the value of the poling field and of the duration of the polarization process is analysed for thin films poled at room temperature. Second, we analyse the build up of the polarization when the polarization is performed at 100°C.

THE PWP METHOD

We will only briefly recall the principle of this method applied ·· piezoelectric materials[3,4,7]. We consider a plane sample containing a distribution of dipoles which is supposed to be uniform in a plane parallel to the surface of the film and perpendicular to the z axis. The propagation of a short pressure pulse travelling at the

velocity of sound v along this axis produces a variation of the image charges on the electrodes which results, in short-circuit conditions, in a current I(t). Time t is related to the position of the wave front by t=z/v. For very short pressure pulses, the current measured during the penetration of the pulse in the sample or its exit is directly proportional to the piezoelectric coefficient e_{zz} at the interfaces. During its propagation in the bulk, I(t) is proportional to $de_{zz}(z)/dz$.

EXPERIMENTAL

The samples are typically 120 to 170 µm thick VDF-TrFE 75%-25% films. They have been made by mold injection.

After polarization, e_{zz} and $de_{zz}(z)/dz$ are measured using the PWP method. Short pressure pulses (1ns duration) are generated by the impact of a 35 ps laser pulse on a thin absorbing layer covering one of the electrodes. The current I(t) is measured using a fast transient recorder.

RESULTS AND DISCUSSION

Polarization at room temperature

The samples, metallized on both sides, are poled at room temperature by applying a high voltage between these electrodes. Various conditions of poling are used and in each case, the resulting polarization is determined by the PWP method.

Thermal treatment

In a first series of experiments, virgin samples are poled without previous thermal treatment. In a second series, the samples are heated during 10 mn up to 140°C, that is to say slightly above the Curie temperature (120°C) and then cooled down to 20°C before poling.

The evolution of the polarization as a function of the duration of the poling process is studied by measuring the distribution of e_{zz} at different steps.

On FIGURE 1, the results obtained for a low value of the electric field E, equal to 0,3MV/cm, are presented. For the samples with no prethermal treatment (FIGURE 1a), the polarization develops slowly near the anode, while, in annealed samples (FIGURE 1b), a uniform polarization is observed.

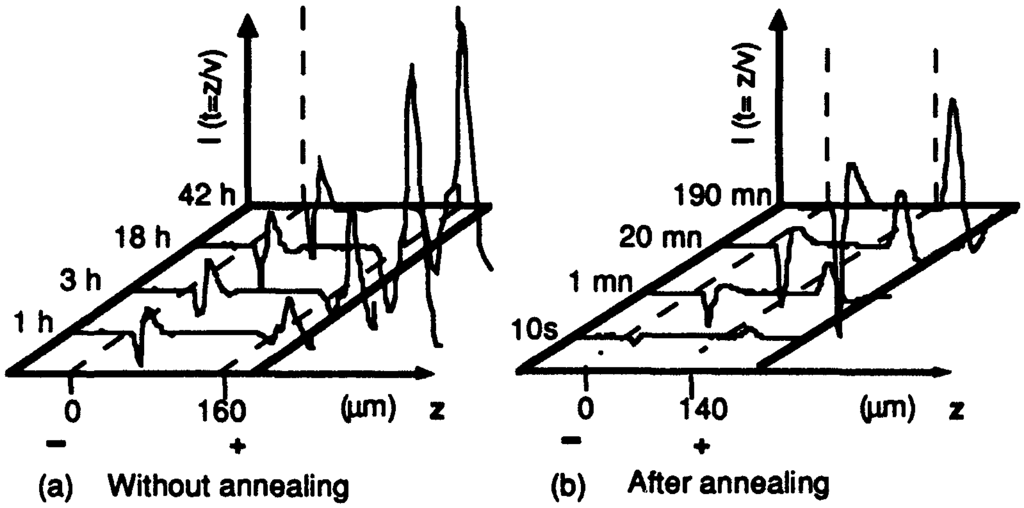

FIGURE 1 Evolution of the distribution of de_{zz}/dz with the duration of polarization (E=0,3MV/cm). The position of the electrodes during the polarization is indicated.

For larger poling fields (E = 0,7 MV/cm), the polarization is uniform in the two series of experiments but the kinetics of the build up of the polarization are different. For annealed samples (FIGURE 2b), the build up is faster than for samples without previous thermal treatment (FIGURE 2a).

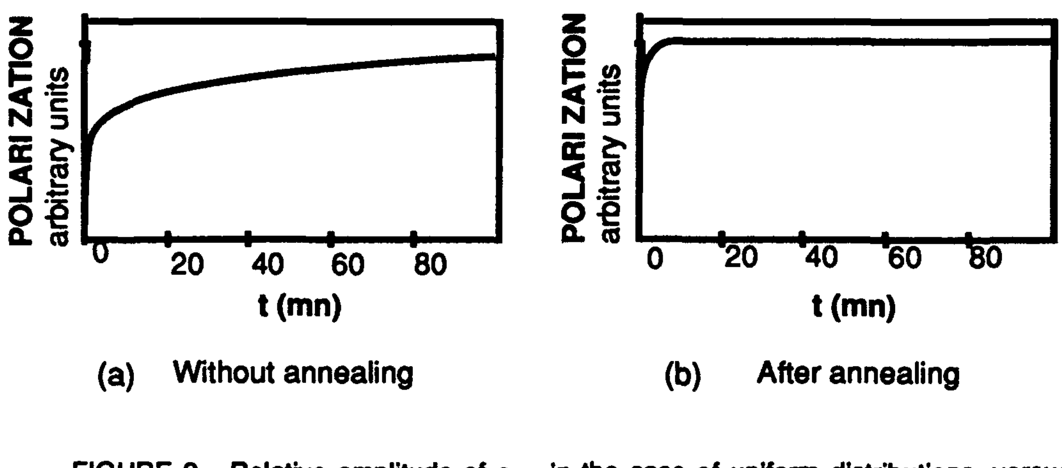

FIGURE 2 Relative amplitude of e_{zz} in the case of uniform distributions, versus duration of poling (E=0,7MV/cm)

It can be concluded that, in VDF-TrFE 75%-25% samples, annealing above the Curie transition before poling at room temperature leads to a fast response to the poling field and to a more homogeneous polarization.

Hysteresis cycle

The samples are first heated above the Curie temperature at 140°C and poled during 10s, at room temperature, with different values of E. The polarizations observed by the PWP method are uniform. Thus, it is possible to plot the piezoelectric coefficient e_{zz} versus E (FIGURE 3). The resulting curve is an hysteresis cycle which shows that e_{zz} goes to saturation for an applied field equal to 0,6 MV/cm and that the inversion of the polarization is possible with a field equal in absolute value to 0,5 MV/cm.

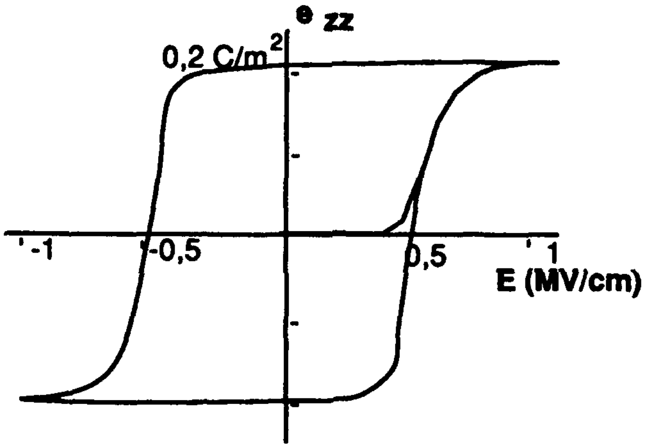

FIGURE 3 Hysteresis cycle of VDF_{75} - $TrFE_{25}$

Polarization at 100°C

The samples, non metallized, are first heated above the Curie temperature. They are polarized at 100°C and $e_{zz}(z)$ is measured at room temperature.

A typical evolution of the signal I(t) as a function of the total duration of polarization at 0.3 MV/cm is shown on FIGURE 4a, and the corresponding distributions of e_{zz} are presented on FIGURE 4b.

At 100°C, a non uniform polarization develops. After a few seconds, the polarization is localized in a thin region of width Δz, close to the anode. For longer durations of polarization, this region spreads toward the cathode, first rapidly, then slowly. We have also observed that the spread of Δz is faster for increasing poling fields. Moreover, Δz depends on the thermal history of the sample : if the polarization at 100°C occurs after a heating process, from 20°C to 100°C, Δz spreads out faster than if it is done after a cooling process, from 140°C to 100°C[8].

This difference in the kinetics of the spreading of the polarized region is due to the hysteresis of the temperatures of the ferroelectric to paraelectric and paraelectric to ferroelectric transitions : 100°C is intermediate between the exothermic and endothermic Curie temperatures of the copolymer[9]. Consequently, the amount of ferroelectric phase is larger in the first case than in the second one.

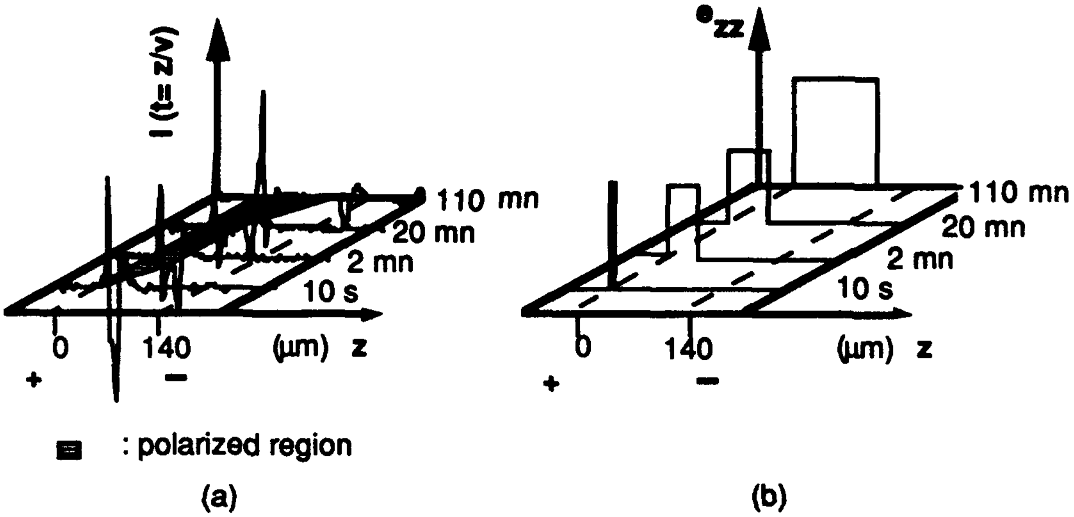

FIGURE. 4 : Evolution of the distribution of de_{zz}/dz as a function of the duration of polarization.

Discussion

According to the history of the sample, the amount of the ferroelectric phase varies. The polarization is more homogeneous when the ferroelectric phase is dominant. This also explains why the the build up of the polarization is larger at room temperature than at 100°C.

The partial polarization observed at 100°C can be attributed to the presence of a negative space charges which enhances the applied field in the region close to the anode and stabilizes the oriented dipoles. Such a space charge can originate either from the migration of internal charges due to the applied field or from injection of electrons at the cathode, also followed by a migration towards the anode. In the first case a symetric distribution of positive charges close to the cathode should also accelerate the orientation of dipoles and lead to a more symetrical build up of the polarization.

Moreover, the experiments prove that charge injection at the cathode plays a very important role in the polarization of the copolymer. The injected charges migrate

towards the anode, accelerate and stabilize the orientation of dipoles. Such a large influence of injection of electrons was previously observed[7,10] in the case of polarization at room temperature.

CONCLUSION

The pressure wave propagation method was used to measure non destructively the distribution of the piezoelectric coefficient $e_{zz}(z)$ through the thickness of VDF-TrFE copolymer films. A fast response to the poling field is observed in films previously heated above the Curie point and for applied fields equal to 0,6MV/cm. In this case, the polarization is uniform. The polarization which develops when the poling is performed at 100°C, is very inhomogeneous and originates at the anode. The kinetics of the spreading of the polarized region towards the cathode depends on the applied field and on the thermal treatment applied to the samples. According to the history of the sample, the amount of the ferroelectric phase varies. The influence of the morphology of the samples, and the role of injection of charges at the cathode explain the observed behaviours.

REFERENCES

1. P. LAURENCEAU, G. DREYFUS, J. LEWINER, Phys. Rev. Lett., 38,.46 (1977)
2. C. ALQUIE, G. DREYFUS, J. LEWINER, Phys. Rev. Lett., 47,.1483 (1981)
3. C. ALQUIE, J. LEWINER, Rev. Phys. Appl. , 20,.1395-402 (1985)
4. R. GERHARD-MULTHAUPT, G.M. SESSLER, J.E. WEST, K. HOLDIK, M. HAARDT, W. EISENMENGER, J.Appl.Phys., 55, 2769 (1984)
5. G.M. SESSLER, A. BERRAISSOUL, Ferroelectrics, 76, 489 (1987)
6. M. WOMES, E. BIHLER, W. EISENMENGER, IEEE Trans. Electric. Insulat., 24, n°3, 461-468 (1989)
7. C. LABURTHE TOLRA, C. ALQUIE, J. LEWINER, 1990 Annual report, Conference on Electrical Insulation and Dielectric Phenomena, 71-76 (1990)
8. C. LABURTHE TOLRA, C. ALQUIE, J. LEWINER, 7th International Symposium on Electrets (ISE7), 293 (1991)
9. TANAKA H., YUKAWA H., NISHI T., Macromolecules, 21, 2469-2474 (1988)
10. E. BIHLER, G. NEUMANN, G. EBERLE, W. EISENMENGER, 1990 Annual report, Conference on Electrical Insulation and Dielectric Phenomena, 140 (1990)

Ferroelectrics, 1992, Vol. 134, pp. 247-252
Reprints available directly from the publisher
Photocopying permitted by license only

PvP150

DIFFUSE PHASE TRANSITION IN FERROELECTRIC POLYMERS

R.L. MOREIRA and B.V. COSTA
Depto. de Fisica, ICEx, UFMG, C.P. 702, CEP 30161, Belo Horizonte, Brazil. E-mail: OPTIKA@BRUFMG.BITNET

Abstract The first order ferroelectric-paraelectric transitions in ferroelectric polymers are discussed in the framework of the Diffuse Phase Transition models. In order to describe these transitions, we use the classical Landau-Devonshire treatment for the sample micro-regions undergoing normal phase transition and look for a critical temperature distribution function. Thus, this model is applied to study the phase transition of a vinylidene fluoride-trifluoroethylene copolymer. We show how to obtain the correct behaviour of the spontaneous polarization and of the dielectric constant besides the Landau expansion parameters.

INTRODUCTION

Poly(vinylidene fluoride - trifluoroethylene) copolymers [P(VDF-TrFE)] present a first order ferroelectric transition, for trifluoroethylene (TrFE) contents ranging from 18 to 48 mol%.[1-3] The Phase Transition (PT) occurs over very large temperature intervals, reflecting a distribution of critical temperatures (T_c) for the different regions of the material.[4-5] Due to this diffuse character of the PT, the anomalies of the physical properties at the transition are smeared out into the phase coexistence region.

Diffuse phase transition (DPT) is a very common occurrence in solid solutions and other disordered structures.[6-10] In the systems presenting DPT, the macroscopic properties can be described as weighted sums of contributions from a large number of micro-regions undergoing normal PT at different T_c.[7,11-13]

In this work, we use the basic ideas developed to study DPT in disordered materials, in order to obtain a better understanding of the dielectric behaviour of ferroelectric polymers, near their transitions.

EXPERIMENTAL

Differential Scanning Calorimetry (DSC), Dielectric susceptibility and Thermally Stimulated Depolarization Current (TSDC) data have been used to investigate the DPT of a P(VDF-TrFE) copolymer with 30 mol% TrFE (sample reference: ATOCHEM P997). These data have been published in previous works.[14,15]

Since the transition presents a strong dependence on the thermal history,[5,14] all data correspond to the first thermal cycle. The heating/cooling rates were +- 20°C/min for DSC and + 1.9°C/min for TSDC runs. For the latest measurements, the samples (with 2.5 cm^2 of area and 50 μm thick) were previously polarized by a 500 KV/cm electric field at 65 °C for 20 min. For more experimental details, including sample handling, see the references 14 and 15.

RESULTS AND DISCUSSION

In the case where the macroscopic properties of a sample with DPT are seen as an envelope of normal PT from its micro-regions, the Landau's parameters are the same for each micro-region (only T_c varies).[11-13] Thus, this approach assumes an entropy change (per unity volume) and a polarization jump at T_c constant for all micro-regions. The macroscopic spontaneous polarization and the reciprocal dielectric susceptibility are given by

$$P(T) = \int_0^\infty P'(T,T_c)\ f(T_c)dT_c \qquad \text{and} \qquad (1)$$

$$\chi^{-1}(T) = \int_0^\infty \chi'^{-1}(T,T_c)\ f(T_c)dT_c \quad ; \qquad (2)$$

where $P'(T,T_c)$ and $\chi'^{-1}(T,T_c)$ are the classical Landau-Devonshire expressions for first order normal PT at T_c,[13,16] and $f(T_c)$ a particular critical temperature distribution function.

Let us now investigate the DPT of a 30 mol% TrFE copolymer. For this material, the DSC thermograms show an interesting profile, with the presence of two anomalies at the PT.[14,17] Assuming that the doubling of the DSC peaks is originated by sample inhomogeneities, we use these data to generate our $f(T_c)$ functions. The assumption of a constant entropy change for the different micro-regions allows us to obtain, in a first order PT, an isoentropic function by:

$$f(T_c) = N \frac{1}{T_c} \frac{dH}{dT_c} \qquad (3)$$

where N is a normalization factor, and dH/dT_c the calorimetric curve, after baseline subtraction. Figure 1 presents the obtained $f(T_c)$ functions for the 30 mol% TrFE copolymer, for heating and cooling runs.

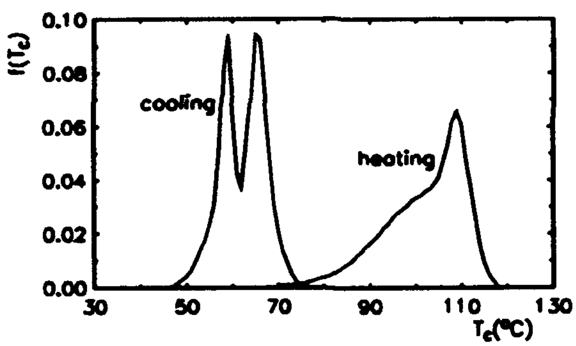

FIGURE 1 Critical temperature distribution functions for the DPT of a 30 mol% TrFE copolymer, obtained from the first DSC heating and cooling runs.

Using the $f(T_c)$ functions of Figure 1 in Eqs. (1) and (2), we have generated theoretical curves for the macroscopic sample polarization and dielectric susceptibility, shown with the corresponding experimental data in Figures 2 and 3, respectively. Note that the theoretical curves display the main features of the macroscopic behaviour of the polymer - a smooth decrease of the spontaneous polarization at the PT and a very good fitting of the dielectric response.

The higher experimental values of the polarization at

lower temperatures should be linked to the contributions of sample heterocharges. In fact, since this sample has been polarized at 65 °C, its TSDC thermogram contains a contribution of space charges (heterocharges), with a maximum around the polarization temperature, as in other PVDF copolymers, irrespectively of the PT.[18] In the present case, the high value of this contribution (about 15% of the total sample polarization) shows the important role played by other kinds of heterocharges, besides the space charges (maybe some orientation of the strained amorphous phase).

The dielectric constant curves, besides the $f(T_c)$ ones, show a large thermal hysteresis presented by this polymer. This had been taken into account on the theoretical fittings, leading us to four adjustment parameters: β, ΔT ($=T_c-T_0$), ΔT_c^+ and ΔT_c^- . These parameters come from the conventional free energy expansion

$$g = \beta\,(T-T_0)\,P^2/2 + \xi\,P^4/4 + \zeta\,P^6/6 \quad ; \tag{4}$$

T_0 being the Curie-Weiss temperature, and β, ξ and ζ the Landau coefficients. ΔT_c^+ (ΔT_c^-) represents the difference between the temperature where the transition occurs in heating (cooling) and the critical temperature (where the energy of the ferro and para phases are equal). ΔT is linked to the expansion parameters by

$$\Delta T = \frac{3\,\xi^2}{16\,\beta\zeta} \quad . \tag{5}$$

So, for the complete determination of ξ and ζ we need to use another expression, as for instance

$$\Delta S = -\frac{1}{2}\,\beta\,\frac{3\,\xi}{4\,\zeta} \quad ; \tag{6}$$

for the entropy change per unit volume at T_c. Using this equation the sample crystallinity must be taken into account. For our material, we estimate a value of 80% for it. Thus, with $\Delta S = 1.36$ cal/gK (from our DSC data, after

correction due to the diffuse nature of the PT), we can propose the expansion and adjustment parameters presented in Table I. These results are to be compared with the Furukawa[19] ones, obtained for a polarized 35 mol% TrFE sample with a small diffuse character. Note, in both cases, the high values of the expansion coefficients, which explain the high coercive fields in these materials.

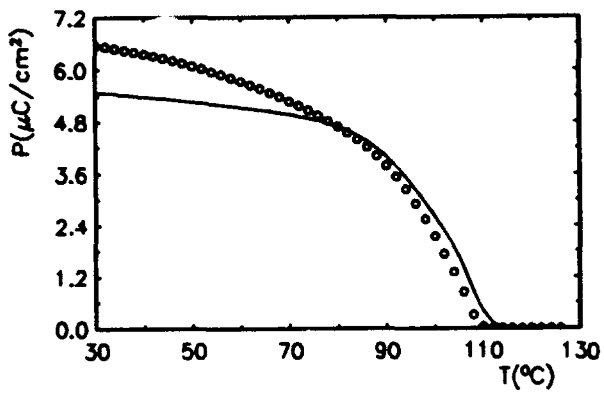

FIGURE 2 Experimental (circles) and calculated (continuous line) thermal dependence of the sample polarization.

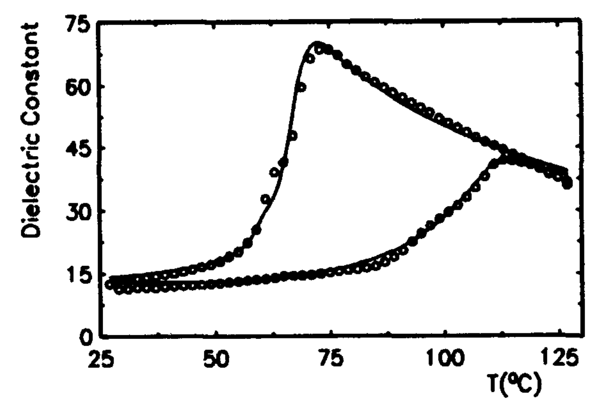

FIGURE 3 Temperature dependence of the dielectric constant measured at 10 KHz (circles) and that derived from the model (continuous line).

TABLE I Adjustment and expansion parameters for the 30 mol% TrFE copolymer (a), compared with the Furukawa ones for a 35 mol% TrFE polarized sample (b). In MKS units.

β	ΔT	ΔT_c^+	ΔT_c^-	ξ	ζ	
2.6×10^{7}	40	8	-3	-4.2×10^{11}	3.1×10^{13}	(a)
3.5×10^{7}	63	-	-	-1.5×10^{12}	1.9×10^{14}	(b)

In conclusion, the use of an extended Landau-Devonshire model to study the DPT of a ferroelectric polymer allows us to describe correctly its main dielectric properties. The critical temperature distribution function has been obtained from calorimetric measurements. The Landau coefficients have also been evaluated, besides the heterocharge contribution for the sample polarization.

This work has been partially supported by the Brazilian agencies CNPq and FAPEMIG.

REFERENCES

1. T. Furukawa, M. Date, E. Fukada, Y. Tajitsu and A. Chiba, Jpn. J. Appl. Phys., 19 (2), L109 (1980).
2. T. Yagi, M. Tatemoto and J. Sako, Polymer J., 11, 209 (1980).
3. for a recent review see: T. Furukawa, Phase Transitions, 18, 143 (1989) and K. Tashiro, ibid, 18, 213 (1989).
4. K. Tashiro and M. Kobayashi, Polymer, 29, 426 (1988).
5. R. L. Moreira, A. Almairac and M. Latour, J. Phys.: Condens. Matter, 1, 4273 (1989).
6. G. A. Smolensky and V. A. Isupov, Soviet Journ. Techn. Phys., 24, 1375 (1954).
7. V. V. Kirillov and V. A. Isupov, Ferroelectrics, 5, 3 (1973).
8. R. Clarke and J. C. Burfoot, Ferroelectrics, 8, 505 (1974).
9. N. Setter and L. E. Cross, J. Appl. Phys., 51, 4356 (1980).
10. V. A. Isupov, Ferroelectrics, 90, 113 (1989).
11. H. Diamond, J. Appl. Phys., 32, 909 (1961).
12. J. Kuwata, K. Uchino and S. Nomura, Ferroelectrics, 22, 863 (1979).
13. R. P. S. M. Lobo, R. L. Moreira, N. D. S. Mohallem and B. V. Costa, submitted to Ferroelectrics.
14. R. L. Moreira, P. Saint-Gregoire and M. Latour, Phase Transitions, 14, 243 (1989).
15. M. Latour, R. M. Faria and R. L. Moreira, Proceedings of the Sixth Intern. Symp. on Electrets (ISE6), Oxford, sept. 1988 (New York, USA: IEEE 1988), pp. 467-471.
16. J. Grindlay, An Introduction to the Phenomenological Theory of Ferroelectricity (Pergamon Press, Oxford 1970), 198-202.
17. R. L. Moreira, P. Saint-Gregoire, M. Lopez and M. Latour, J. Polym. Sci.: Polym. Phys. Ed., 27, 709 (1989).
18. R. M. Faria and M. Latour, J. Polym. Sci.: Polym. Phys. Ed., 27, 913 (1989).
19. T. Furukawa, Ferroelectrics, 57, 63 (1984).

SECTION III
CONTRIBUTED PAPERS
IIIi. Phase Transitions/General

Ferroelectrics, 1992, Vol. 134, pp. 253–258
Reprints available directly from the publisher
Photocopying permitted by license only

PtP240

PHASE TRANSITIONS IN PLZT CERAMICS

U.BÖTTGER, A.BIERMANN and G.ARLT
Institut für Werkstoffe der Elektrotechnik, Aachen University of Technology, W-5100 Aachen, Germany

Abstract A set of the complex dielectric, piezoelectric and elastic constants of lead lanthanum zirconate titanate PLZT 9/65/35 were measured under different electric d.c. bias fields in the temperature range 77K - 380K with regard to the polarization history. The polarization was determined by the piezoelectric coefficient g and by TSDC spectra. We observed field induced ferroelectric phase transitions from a probably rhomboedral structure to an orthorhombic between 150K and 220K. If an electric bias field $E \geq 3kVcm^{-1}$ is applied during cooling the rhomboedral phase is suppressed.

INTRODUCTION

Numerous investigations of ferroelectric ceramics with diffuse phase transition like PLZT 9/65/35 have been reported [e.g.1]. All these materials show in the temperature range a characteristic broadening of the maximum of the dielectric constant ε. This behaviour can be due to different local Curie temperatures caused by composition fluctuations [2]. Therefore, between the ferroelectric and the paraelectric phase an intermediate phase results consisting of stastistical orientated polar microregions or clusters in an surrounding non-polar matrix. The macroscopic parameters of this phase are generally non polar (polarization, X-ray structure[3]). By applying an electric field, the favourable orientated clusters grow until the ferroelectric phase is induced [4]. If the field is removed, the material returns into the macroscopic unpolarized state.

In this paper we report about the dielectric, piezoeletric and elastic properties of PLZT 9/65/35 in the ferroelectric and the intermediate phases under different applied electrical fields with special regard to the polarization history.

EXPERIMENTAL

The measurements were performed on non-transparent PLZT 9/65/35 ceramics prepared by mixed oxide method and conventional sintering techniques. The grain size is about 2μm. Bars with dimensions 10mm x 2mm x 0.6 mm were cut out of the ceramics and coated at the major faces with Ag/Au electrodes. The samples were deaged at 470K and following aged for one week at room temperature.

A resonance technique by Smits [5] allows to determine simultaneously the complex dielectric ε_{33}, piezoelectric d_{31} and elastic constant s_{11} in a temperature range between 77K and the depolarization temperature. The samples were cooled down under an applied electric d.c. field $E_{T-} \geq 2\,\mathrm{kVcm}^{-1}$ to ensure a sufficient remanent polarization at 77K. When the samples are heated the complex admittance was measured at typical frequencies of about 180 kHz by a HP 4192A LF-Impedance Analyzer. During heating and measuring an electric d.c. bias field E_{T+} is applied. To avoid damage of the analyzer input, a guard circuit with Z-diodes was used. The upper limit of voltage was restricted to 400 V ($\approx 7\,\mathrm{kVcm}^{-1}$).

Thermally stimulated depolarization current (TSDC) spectra were taken in order to calculate the remanent polarization as a function of temperature. The samples were cooled down to 4K under an applied electric field and heated without any field under short-circuit conditions. At a constant heating rate the current measured by an electrometer is proportional to the pyroelectric coefficient.

RESULTS AND DISCUSSION

Different cycles of measuring the constants ε_{33}, d_{31} and s_{11} in the temperature range were performed with varying electric bias fields up to 4kVcm^{-1}. Figure 1 shows the known dielectric behaviour of poled and aged PLZT 9/65/35 as a function of temperature [6]. The spectra are formed by the phase transitions of the material (ferrolectric - intermediate - paraelectric). Generally there is no influence of the electric field strength during cooling and heating on the dielectric constant. Only the transition temperatures slightly increases with increase of E_{T+} .

Quite different results compared with ε_{33} were obtained for the piezoelectric (Figure 2) and elastic constant. In the ferroelectric phase we observed two states

depending on the applied electric field E_{T-}, when the sample is cooled. If $E_{T-} \geq 3\text{kVcm}^{-1}$ the piezoelectric behaviour measured during heating corresponds to the upper branch (B) in Figure 2. We found no influence of the bias field E_{T+}. For $E_{T-} < 3\text{kVcm}^{-1}$, d_{31} starts in the lower branch (A). If the bias field during heating is high enough ($> 1\text{kVcm}^{-1}$), the material jumps from state A into B. This process is thermally activated. In the intermediate phase the piezoelectric constant is only determined by the actually applied field.

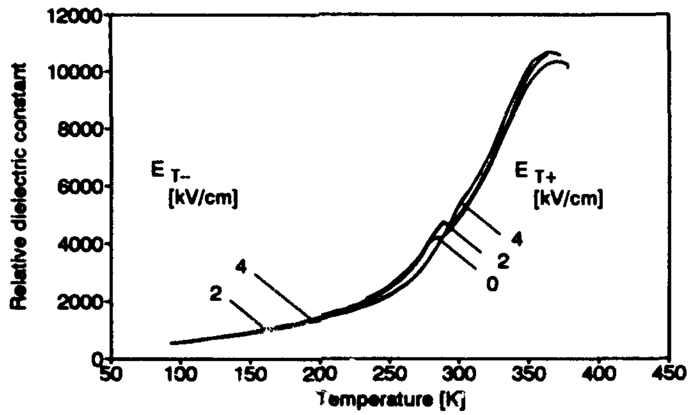

FIGURE 1 Dielectric constant ε_{33} as function of temperature under different applied electric bias fields

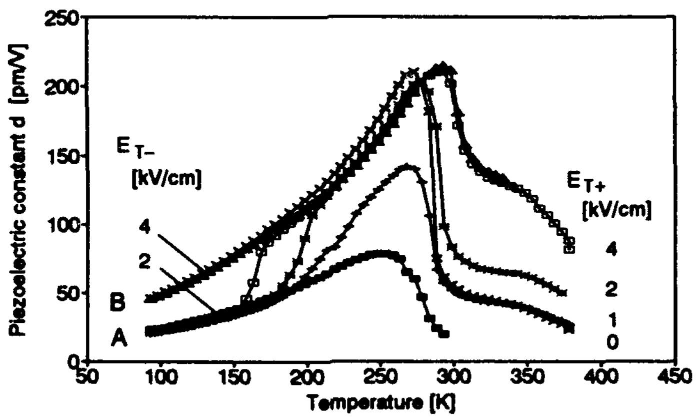

FIGURE 2 Piezoelectric constant d_{31} as function of temperature under different applied electric bias fields

A more detailed discussion is allowed considering the piezoelectric coefficient g defined as the proportional factor between the deformation and the dielectric displacement :

$$S_1 = g_{31} D_3 \qquad \text{with} \qquad g_{31} = \frac{d_{31}}{\varepsilon_{33}} = 2Q_{31} P_S$$

The g coefficient can be calculated by the dielectric and the piezoelectric constant. Furthermore it is related with the spontaneous polarization P_S by the electrostrictive coefficient Q_{31}. Assuming $Q_{31} = 0.025\ m^4C^{-2}$ and temperature independence of Q_{31}, we found a good agreement between the calculated polarization $P_S(g_{31}(T))$ and the polarization obtained by integration of the TSDC spectra (Figure 3). Because of the linear relation between g and P_S, it is reasonable to describe in the following the behaviour of the polarization by the behaviour of the g coefficient.

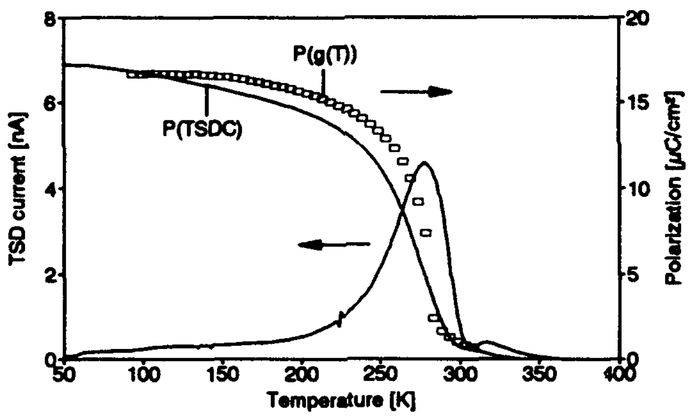

FIGURE 3 Temperature dependance of polarization calculated by g coefficient and by integration of TSD current

Two ferroelectric states are distinguished in the low temperature range (Figure 4). If the applied electric field during cooling $E_{T-} \geq 3kVcm^{-1}$, the material occupies the high polarization level B. The polarization seems to be frozen, because the g coefficient will not be influenced by changes of the temperature or the electric field E_{T+}. The phase transition (ferroelectric - intermediate) is shifted to higher temperatures with increase of E_{T+}.

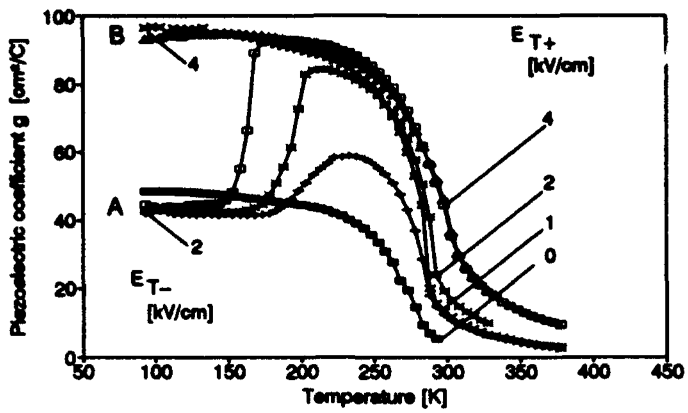

FIGURE 4 Piezoelectric coefficient g as function of temperature under different applied electric bias fields

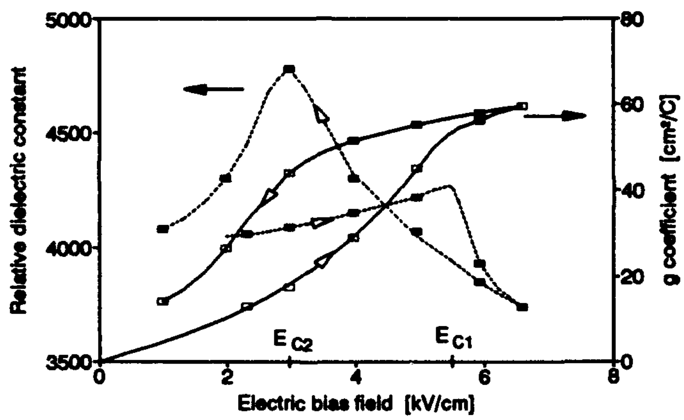

FIGURE 5 Dielectric constant and g coefficient as function of the applied bias field at room temperature

Considering the dielectric and piezoelectric behaviour at T = 300K as a function of the bias field (Figure 5), we identify the state B as a ferroelectric orthorhombic phase.We observed a field-induced phase transition at $E_{C1} = 5.5\text{kVcm}^{-1}$, when the dielectric constant has a maximum. When the field is decreased, the depolarized state is restored at $E_{C2} = 3\text{kVcm}^{-1}$. These results are in a good agreement with X-ray studies of Shebanov reporting about this field-induced ·eversible transition in PLZT 9/65/35 at $E_{C1} = 5.8\text{kVcm}^{-1}$ at room temperature [3]. Therefore, we conclude that

an electric field applied at 300K in the intermediate phase causes a certain degree of orientation of the cluster, i.e. a certain polarization (see g coefficient in Figure 5). When the temperature is decreased the material undergoes a ferroelectric phase transition. If the degree of cluster orientation is high, i.e. the applied field is not far away from induced phase transition at 300K, the orthorhombic state will be saved in the ferroelectric phase.

For $E_{T-} < 3kVcm^{-1}$ the polarization at temperatures below 150K (state A) reaches only half the value of state B. We assume that by the smaller orientation of the polar clusters their interaction is high enough to favour a reorientation of the structure, when the phase boundary is passed during cooling. It is probable that the material has a rhomboedral structure. By applied electric fields during heating E_{T+} the phase changes into the orthorhombic one. Even the transition happens for $E_{T+} < E_{T-}$. Therefore, we can exclude that the state A is an incomplete orthorhombic phase. The low temperature phase transition depends strongly on the field strength. In contrast to the transition (ferroelectric - intermediate) the transition temperature $T_{R \to O}$ diminishes with the increase of the applied bias field.

REFERENCES

1.) K.Carl, K.Geisen, Proc.IEEE, 61(6), 967 (1973)
2.) G.A.Smolenskii, J.Phys.Soc.Japan, Suppl.28, 26 (1970)
3.) L.A.Shebanov, Ferroelectrics 90, 65 (1989)
4.) G.Schmidt, H.Arndt, G.Borchhardt, J.v.Cieminski, T.Petzsche, K.Bormann, A.Zirnite, V.A.Isupov, Phays.stat.sol.(a) 63, 501 (1981)
5.) J.G.Smits, IEEE Trans. SU 23, 150 (1978)
6.) E.T.Keve, A.D.Annis, Ferroelectrics 5, 77 (1973)

Ferroelectrics, 1992, Vol. 134, pp. 259–264
Reprints available directly from the publisher
Photocopying permitted by license only

PtP242

FLUCTUATIONS OF INCOMMENSURATE WAVE NEAR PARAELECTRIC-MODULATED PHASE TRANSITION IN Rb_2ZnCl_4

M.P.TRUBITSYN, V.V.SAVCHENKO
Physical Department, State University,
Dniepropetrovsk, Ukrain

Abstract The ESR spectra of Mn^{2+} probe have been investigated in the temperature interval including paraelectric-incommensurate phase transition point T_i of Rb_2ZnCl_4. Near below T_i we have measured the temperature dependence of position of the inhomogeneously broaden ESR line. On the basis of the simple model it is shown that ESR spectrum is influenced by phase and amplitude fluctuations of modulation wave.

INTRODUCTION

Recently a great deal of attention has been paid to radiospectroscopic investigations of excitation spectra of incommensurate compounds[1-3]. These spectra are characterized by additional modes corresponding to oscillations of amplitude A and phase Φ of incommensurate atomic displacement wave $U = A\cos(\Phi)$. Particularly phase fluctuation effects were observed in a number of incommensurate materials through complete (NMR in Rb_2ZnBr_4[4], ESR in $ThBr_4$, $ThCl_4$[5,6]) or partial (NMR, NQR in Rb_2ZnCl_4 [7,8]) motional averaging of magnetic resonance lineshape.

In this paper we report the data on ESR measurements of Mn^{2+} probe in Rb_2ZnCl_4 crystals undergoing transition

from paraelectric phase (space group Pnma) to incommensurate one at T_i=302,5 K. Investigated crystals doped with manganese were grown from the melts by Czochralskii method. ESR spectra were recorded using X-band spectrometer equipped with a regulated nitrogen gas flow cell. The temperature stability was controlled to within $\pm$0.1 K.

EXPERIMENTAL RESULTS

ESR spectra observed in the paraelectric phase of $Rb_2ZnCl_4:Mn^{2+}$ are associated with two inequivalent Mn^{2+} sites and well described elsewhere[9-11]. To avoid the overlapping of the absorption lines corresponding to the different probe sites and fine structure groups we have measured the temperature dependence of the lowfield hyperfine sextuplet $M_s = -3/2 \rightarrow -5/2$ for the magnetic field orientation **H** $\parallel$ **a**. As T_i is approached from above the single sextuplet observed at $T > T_i$ splits into inhomogeneously broaden singularity spectrum restricted by the highfield H_p and the lowfield H_a singularities[1,3,12]. The experimental dependence of the singularities positions is presented on Fig.1a.

It is known that (a,b) is a mirror plane for the positions occupied by Mn^{2+} ions. Therefore for the orientation chosen the expansion of resonance fields on the powers of the order parameter $U = A\cos\{\Phi(z)\}$ consists of only even terms and the second term is the lowest one. To interpret the experimental results presented we have used the following expression given in[7,8] for the case of motional narrowing of singularity spectrum due to phase fluctuations ("floating phase" model)

$$H = H_o + \frac{1}{4}h_2A^2[1 + \cos(2\Phi)\exp(-2\sigma^2)]. \qquad (1)$$

Here H_o describes the line position in the paraelectric phase and does not depend on the temperature, h_2 denotes

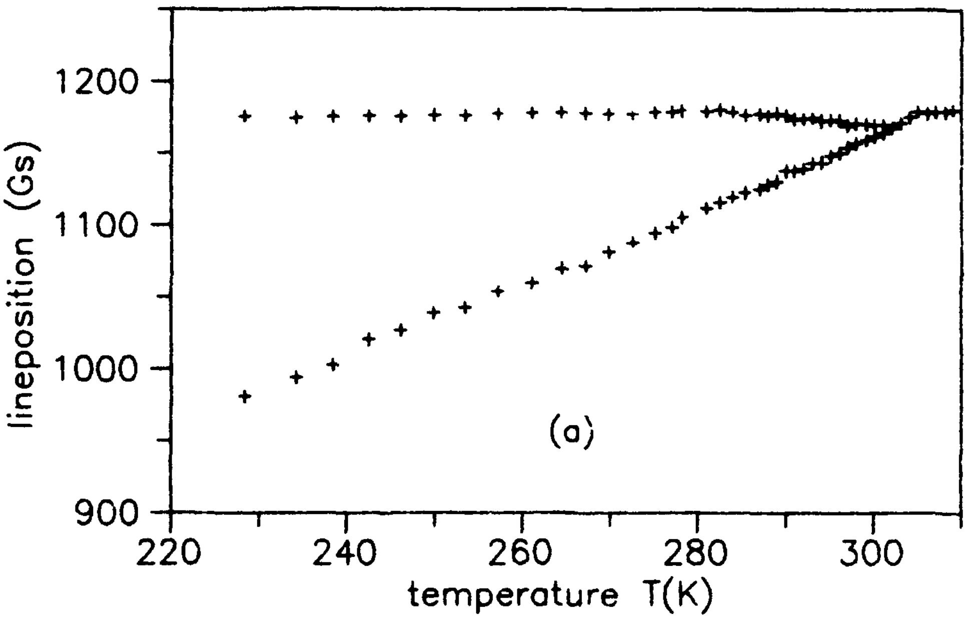

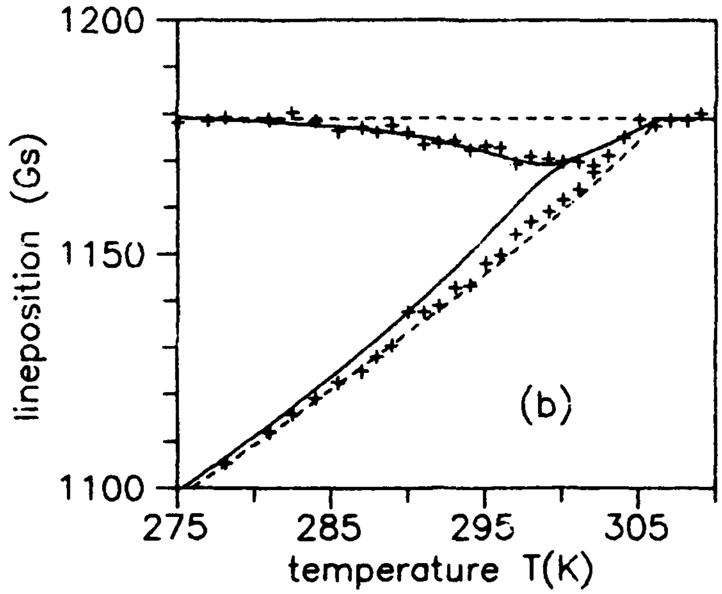

FIGURE 1. Temperature dependence of the singularities positions ($M_s = -3/2 \rightarrow -5/2$ at $H \parallel a$) :
(a) in a broad interval of incommensurate phase;
(b) near incommensurate-paraelectric transition point T_i. The pluses represent experimental data, solid line represents $H_p(T)$, $H_a(T)$ calculated on the basis of (1), dashed line corresponds to the static case (σ=0, Δ=0).

the expansion coefficient depending on the paramagnetic ions position and external field orientation, $\sigma \sim (T_i-T)^{-\beta}$ - mean square phase fluctuation, β - critical exponent for the order parameter. According to (1) well below T_i ($\sigma=0$) $H_p(\phi=\pm\pi/2) = H_o$ does not depend on the temperature while $H_a(\phi=0,\pi) = H_o + 1/2h_2A^2$ shifts in accordance with increasing of amplitude $A = a(T_i-T)^{\beta}$ on cooling. At $T \to T_i^-(\sigma \to \infty)$ the singularities tend to the center of the resonance fields distribution $H_p, H_a \to H_o + 1/4h_2A^2$.

As can be seen from Fig.1a below T_i-15 K H_p is practically independent on temperature. Hence non-local effects can be neglected [13] and "local approximation" (1) is valid. In this interval experimental behavior of singularities positions can be described by (1) with parameters H_o = 1182 Gs, a^2h_2 = -8,3 Gs/K^{β}, T_i = 302,5 K, β = 0,37, σ=0.

On approaching T_i from below the experimental position H_p significantly shifts from stationary value H_o (Fig.1b). According to the "floating phase" model this behavior can be attributed to increasing of phase fluctuations σ. The lowfield singularity curve $H_a(T)$ deviates from the solid line calculated by using mentioned model (1) and behaves itself as in the static case (Fig.1b).

DISCUSSION

The discrepancy obtained can be overcome by taking into account the amplitude fluctuations of incommensurate wave. Considering usual quadratic expansion of resonance fields

$$H = H_o + \tfrac{1}{2}h_2A^2\cos^2(\phi) \qquad (2)$$

one can express A and ϕ as a sum of static and fluctuating parts

$$A(t) = A_o + \delta A(t), \qquad \phi(t) = \phi_o + \delta\phi(t).$$

Inserting this expressions into (2) we average expansion in time and neglect all terms of orders higher then quadratic in δA and $\delta\phi$. Following ref.[7] one can assume that the fluctuations are fast comparing with frequency analogue of singularities separation $\Delta H = 1/2h_2A^2$ and substitute time average by gaussian distribution of phases and amplitudes

$$H = H_o + \tfrac{1}{2}h_2\Delta^2\cos^2(\phi_o) + \\ + \tfrac{1}{4}h_2A_o^2\{1 + \cos(2\phi_o)\exp(-2\sigma^2)\} \qquad (3)$$

where $\Delta^2 = \langle\delta A^2\rangle, \sigma^2 = \langle\delta\phi^2\rangle$. Therefore for the singularities positions one can get

$$H_p = \left[\, H_o \,\right] + \left[\, \tfrac{1}{4}h_2A_o^2\{1 - \exp(-2\sigma^2)\} \,\right], \qquad (4a)$$

$$H_a = \left[\, H_o + \tfrac{1}{2}h_2A_o^2 \,\right] + \\ + \left[\, \tfrac{1}{2}h_2\Delta^2 - \tfrac{1}{4}h_2A_o^2\{1 - \exp(-2\sigma^2)\} \,\right]. \qquad (4b)$$

Here the static and fluctuation contributions are separated and included into square brackets. Comparison of the expression obtained (3,4) with (1) shows that including of amplitude fluctuations into consideration results in appearing of the new term $1/2h_2\Delta^2$ in the expression for H_a while H_p is uneffected by Δ. For the small σ fluctuation contribution in (4b) is approximately equal to $1/2h_2(\Delta^2 - A_o^2\sigma^2)$. Thus amplitude and phase fluctuation contributions to H_a are partially compensated by each other. One may expect that $H_a(T)$ deviates from the solid line calculated using (1) and tends to the entirely static behavior (Fig.1b) due to amplitude fluctuation influence.

In Rb_2ZnCl_4 crystals ESR spectra of Mn^{2+} are sensitive to tilting of $ZnCl_4$ complexes around **b** axis and the tilt angle $\alpha = \alpha_o\cos(\phi)$ corresponds to the local order parameter U[9]. Although the above expressions (3,4) may only provide the qualitative explanation we have tried to estimate the

characteristic values of amplitude fluctuations $\langle\delta\alpha_0^2\rangle^{1/2}$. This rough estimation yields that $\langle\delta\alpha_0^2\rangle^{1/2}$ changes from 1,2^o to 0,7^o on cooling from T_i-3K to T_i-10K.

It seems important to note that in the case of linear coupling between resonance fields and order parameter $H = H_0 + h_1 A\cos(\phi)$ the amplitude fluctuations should not influence on the positions of edge singularities $H_a^{(1)}, H_a^{(2)}$. In this sense ESR experiment with orientations of magnetic field providing the quadratic connection $H \sim U^2$ may be more informative then the experiment with general orientations providing linear low $H \sim U$.

REFERENCES

1. R.Blinc, Phys.Repts., 79, 331 (1981).
2. R.Blinc, V.Rutar, J.Dolinsek, B.Topic, F.Milia, S.Žumer, Ferroelectrics, 66, 57 (1986).
3. A.Kaziba, J.C.Fayet, J.Physique, 47, 239 (1986)
4. R.Blinc, D.C.Ailion, P.Prelovsek, V.Rutar, Phys.Rev. Lett., 50, 67 (1983).
5. J.Emery, S.Hubert, J.C.Fayet, J.Phys.Lettres, 45, 693 (1984).
6. J.Emery, N.A.Yakoub, Ferroelectrics, 105, 141 (1990).
7. R.Blinc, F.Milia, B.Topic, S.Zumer, Phys.Rev.B, 29, 4173 (1984).
8. V.Rutar, F.Milia, Ferroelectrics, 66, 101 (1986).
9. M.Pezeril, J.Emery, J.C.Fayet, J.Phys.Lettres, 41, 499 (1980).
10. T.M.Bochkova, O.E.Bochkov, S.A.Flerova, Fiz.Tverd.Tela, 26, 2170 (1984).
11. J.J.L.Horikx, A.F.M.Arts, H.W.de Wijn, Phys.Rev.B, 37, 7209 (1988).
12. T.M.Bochkova, M.P.Trubitsyn, Fiz.Tverd.Tela, 31, 269 (1989).
13. R.Blinc, J.Seliger, S.Zumer, J.Phys.C:Sol.St.Phys., 18, 2313 (1985).

Ferroelectrics, 1992, Vol. 134, pp. 265–270
Reprints available directly from the publisher
Photocopying permitted by license only

PtP251

PHASE TRANSITIONS IN HIGHLY DISORDERED FERROELECTRICS

NIKOLAI K. YUSHIN and SERGEI N. DOROGOVTSEV
A.F. Ioffe Physical Technical Institute
St.Petersburg, Russia

Abstract Critical properties of disordered ferroelectrics are reviewed. The broad spectrum of the relaxation times and the nonergodicity have been observed in these materials. The proposed phase diagrams including polar glassy states are discussed.

INTRODUCTION

Highly Disordered Ferroelectrics (DF) include such materials as Ferroelectrics with Diffuse Phase Transition (FDPT) - compounds with considerable nonhomogeneity of some components (*Mg and Nb ions in such* classical FDPT as PMN = $PbMg_{1/3}Nb_{2/3}O_3$, for instance), highly polarizable crystals with impurities which induce the ferroelectric ordering in the centrosymmetric host lattice ($KTaO_3$:Li, Na, Nb), solid solutions of hydrogen-bonded ferroelectrics and antiferroelectrics (RbH_2PO_4 - $NH_4H_2PO_4$ = RADP and its deuterated analog, for instance). DF become frozen into the new inhomogeneous state below the Phase Transition (PT) temperature, which posesses different static and dynamic properties than the homogeneous ordering state.

The aim of this paper is to present some common features of the disordered ferroelectrics.

THE SPECTRA OF RELAXATION TIMES

The dielectric permittivity of DF is characterized by strong dispersion[1-10] and may be described by the distribution of relaxation times $g(\tau, T)$. For the sufficiently smooth distribution function one can calculate the spectrum as[11-12]

$$g(\tau = \omega^{-1}, T) \simeq (\pi/2) \quad \varepsilon''(\omega, T)/(\varepsilon_0 - \varepsilon_\infty), \qquad (1)$$

taking into account that actually all anomalies of $\varepsilon''(\omega,T)$ are presented in $g(\tau,T)$ in a strong smeared form.

The distribution functions for PMN and $KTaO_3$:Li crystals were calculated using Eq. (1) from the data of imaginary part of the permittivity $\varepsilon''(\omega,T)$[2, 3] and ε_0 as the lowest frequency permittivity ε (0.1 Hz,T)[4], $\varepsilon_\infty \ll \varepsilon_0$. For PMN at highest temperatures the spectrum is narrow, with the temperature reduction the distribution function broadens and becomes almost flat, τ_{min} being of the order of 10^{-12} s for all temperatures (See Figure 1)[12, 13]

The spectrum of $KTaO_3$:Li spreads with cooling and the additional bands appear. These additional relaxation regions can be connected with the ferroelectric domains existing in the low-temperature phase for 10 at.% Li concentration[5, 6]. It should be noted that for lower Li concentrations the well separated peaks were also observed.[7]

The spectrum of RADP system was also described by the homogeneous distribution of relaxation times between τ_{min} and τ_{max}. In common with other DF the spectrum of RADP spreads with the temperature reduction.[8-10]

NONERGODICITY AND LONG-TIME RELAXATION

When the maximum relaxation time τ_{max} reaches the macroscopic values compatible with the duration of the experiment, the response of the system for the equilibrium condition has to differ from one measured for an external influence which affects on the system during time less than τ_{max}. To confirm it the measurements were performed for Field-Cooling (FC) and Zero-Field-Cooling (ZFC) conditions. The results have shown that there is the specific temperature T_g below which the nonlinear electroacoustic coefficients of PMN[14] differ for FC and ZFC measurements as well as the Bragg peak intensities of neutron scattering[15]. The distinction between the FC and ZFC results can be interpreted as the manifestation of nonergodicity at DPT, what indicates an anomalously slow relaxation process in the low-temperature phase of these materials.

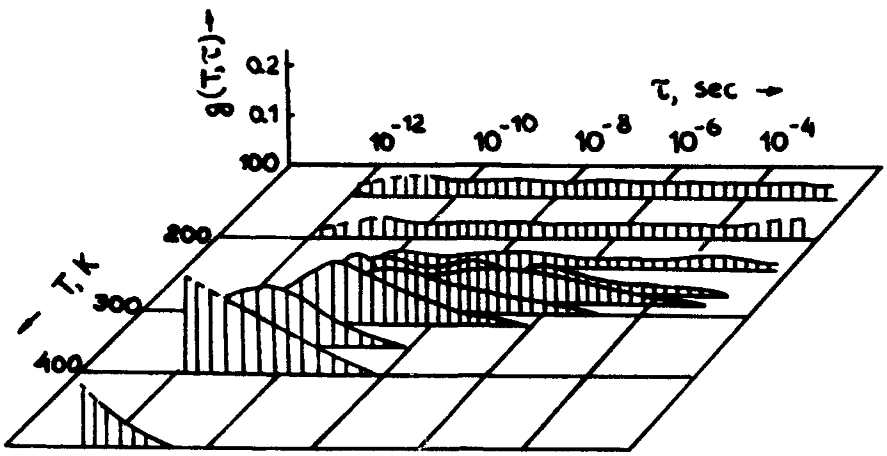

FIGURE 1 The spectrum of relaxation times for PMN crystal[12].

The existence of such broad spectrum must be revealed as the long-time relaxation. Indeed such processes were observed for PMN in the neutron scattering experiments[15] and the dielectric measurements[16].

The history dependent behavior of the static polarization was also observed for $KTaO_3$ + 1.6 at.% Li[17]. It should be noted that the maximum of nonlinear dielectric permittivity takes place in $KTaO_3$:Na at T_g[18] as well as in PMN[19].

Unfortunatelly there are no experiments which show the long-time relaxation or the nonergodicity in RADP.

PHASE DIAGRAMS

The phase diagram of $KTaO_3$:Li is rather questionable, there are two critical concentrations of Li : c_1 = 2.2 and c_2 = 4 at.% [20, 21]. The pure polar glass state is realized for concentrations less than c_1, for concentrations between c_1 and c_2 the random-field-induced domain state is achieved[20]. The crystals with Li concentrations more than c_2 become ferroelectrics with PT temperatures more than 65 K [5, 6, 21]. The alternative point of view is supported

by Hochli[7, 17] who believes that for all concentrations this system undergoes the PT into glassy state, being the polar glass for the concentration less than c_2 and the quadrupole glass for the higher concentrations.

The phase diagram of $Rb_{1-x}(NH_4)_xH_2PO_4$ includes the ferroelectric state for $x < 0.23$, the antiferroelectric state for $x > 0.74$, the polar glassy state for the intermediate concentrations ($0.23 < x < 0.74$) when there are two specific temperatures : T_M (about 100 K) connected with the onset of the local ordering and T_F consistent with the static glass transition (T_F = 10 K for RADP).[8-10]

FDPT can be characterized by three specific temperatures such as below. The mean Curie temperature T_m (or the temperature of the maximum low-frequency dielectric permittivity), T_d which markes an appearence of the local polar moments in the materials (T_d manifests the breaking of linear temperature dependences of many physical parameters[22-24]), the polar glassy PT temperature T_g which coincides with the beginning of nonergodicity[14]. For PMN these temperature are T_m = 265, T_d = 600, and T_g = 220 K (See Refs. 1, 22, 14).

Recently the microscopic experiments[25-27] have revealed in FDPT the nanometer scale domains of the ordered structure surrounded by disordered matrix. These ordered nanodomains have either another chemical composition than the disordered matrix[25-26] or regular off-center shifts of lead atoms[25, 27].

On base of these data the following phase diagram of FDPT can be proposed (See Figure 2). At highest temperatures ($T > T_d$) all the structurely ordered nanodomains are in the paraelectric state. While cooling below T_d the ferroelectric PT takes places in them with PT temperatures different for each domain. The spontaneous polarization appearing in these regions bears the polar distortion in the surrounding disorder matrix, forming the polar cluster which can include several neighboring ordered domains with correlated polarizations. These distortions will grow up

Polar cluster glassy state	Interacting clusters state	Superpara-electric state of noninteracting clusters (the model proposed by Cross[24])	Para-electric state

T_g $\qquad$ T_m $\qquad$ T_d

FIGURE 2 The phase diagram of FDPT for ZFC.

as temperature goes down, when the disturbed volume reaches a noticeable fraction of the sample the interaction of the polarized clusters suppresses their free reorientations and motions. At T_g the clusters are frozen, the glassy state may be presented as ensemble of static polar clusters, each of them having an arbitrary orientation of the polar moment so that the resulting polarization is zero. By the same reason the slowing down of the relaxations takes place in DPT, τ_{max} being of the order of the inverse measuring frequency at T_m and infinity at T_g.

It should be noted that the homogenious polar state can be created by FC below T_g if the field exceeds some threshold[28, 16].

SUMMARY

The common features such as the spread spectra of relaxation times, long-time relaxations, the nonergodicity behavior are revealed for highly disordered ferroelectrics. All of them have similar phase diagrams which include the polar glassy state. The reason of the appearence of the glassy phase is believed to be connected with the internal heterogeneity of the composition of these materials. It may be noted that acoustical properties of DF are semilar to the properties of other glassy systems.[13] However the glassy state in DF is different from the polar glass

as a simple analog of spin glasses[11].

We thank Prof. V.V. Lemanov for discussions.

REFERENCES

1. G.A. Smolensky ed., Ferroelectrics and Related Materials (Gordon and Breach, New York, 1981), 763 p.
2. V.P. Bovtun et al., Fiz.Tverd.Tela, 26, 378 (1984).
3. Yu.M. Poplavko et al., Fiz.Tverd.Tela, 27, 3161 (1985)
4. Nadolinskaya E.G. et al, Fiz.Tverd.Tela, 29, 3368 (1987).
5. V.P. Bovtun et al., Izv. AN SSSR, ser.fiz., 49, 293 (1985).
6. G.A. Smolenskii et al., Ferroelectrics, 69, 275, (1986).
7. U.T. Hochli, M. Maglione, J. Phys.-Cond.Matter, 1, 2241, (1989).
8. J. Slak et al., Phys.Rev., B30, 85, (1984).
9. E. Courtens, Phys.Rev., B33, 2975, (1986).
10. E. Courtens, H. Vogt, Z. Phys., B62, 143 (1986).
11. L.E. Wenger in Heidelberg Colloquim on Spin Glasses (Springer-Verlag, Berlin, 1983), 60.
12. N.K. Yushin in Ferroelektrizitat (Martin-Luther Universität, Halle GDR, 1988), p. 102
13. S.N. Dorogovtsev, N.K. Yushin, Ferroelectrics, 112, 27 (1990).
14. N.K. Yushin et al., Pis'ma Zh.Techn.Fiz., 13, 374 (1987).
15. S.B. Vakhrushev et al., Physica B, 156&157, 90 (1989).
16. R. Sommer et al., Ferroelectrics, in press
17. U.T. Hochli et al., Phys.Rev., B32, 4546 (1985).
18. M. Maglione et al., Phys.Rev.lett., 57, 436 (1986).
19. D. Viehland et al., J. Appl. Phys., 69, 414,(1991).
20. W. Kleeman et al., Europhys. lett., 4, 239, (1987).
21. S.R. Andrew, J. Phys., C18, 1357 (1985).
22. Burns G., F. Dacol, Sol. St. Commun., 48, 853 (1983).
23. N.K. Yushin et al., Fiz.Tverd.Tela, 29, 2947 (1987).
24. L.E. Cross, Ferroelectrics, 76, 241, (1987).
25. E. Husson et al., Mat. Res. Bull., 23, 357 (1988).
26. A.D. Hilton et al., Ferroelectrics, 93, 379 (1989).
27. P. Bunneau et al., Mat. Res. Bull., 24, 201 (1989).
28. V.A. Bokov, I.E. Mylnikova, Fiz.Tverd.Tela, 3, 841 (1961).

Ferroelectrics, 1992, Vol. 134, pp. 271–283
Reprints available directly from the publisher
Photocopying permitted by license only

FgP244

PRESSURE-ELECTRIC EFFECT IN POLAR DIELECTRICS

R.Poprawski

Institute of Physics Technical University of Wrocław,
50 -370 Wrocław Wybrzeże Wyspiańkiego 27, Poland.

Keywords: ferroelectrics, pyroelectrics, phase transitions, spontaneous polarization, pressure, pressure sensors.

ABSTRACT

A phenomenological description of physical effects occurring in polar dielectrics under hydrostatic pressure has been presented. Pressure-electric effect consisting in an electric charge generation on the dielectric surface due to pressure has been shown to be observed in polar dielectrics only.
Pressure-electric properties of linear pyroelectrics and ferroelectrics with first- and second-order phase transitions have been discussed. Conclusions coming from phenomenological solutions have been illustrated by experimental results for potasium pentaborate - a linear pyroelectric, $(CH_3NH_3)_5Bi_2Br_{11}$ crystals - a ferroelectric with a second-order phase transition, and NH_4HSeO_4 crystals - a ferroelectric with a first-order phase transition.

Possibilities of application of the pressure-electric effect to prepare a hydrostatic pressure sensor have been also discussed.

1. INTRODUCTION

Pyroelectric coefficient defined as a temperature derivative of spontaneous polarization $\gamma_i = \partial P_{Si}/\partial T$ describes a change in the vector quantity (spontaneous polarization) induced by a change of the scalar quantity (temperature). The definition shows that the pyroelectric coefficient is a

vector, therefore the pyroelectric effect can be observed in crystals belonging to one of ten polar classes of symmetry.

When investigating an impact of hydrostatic pressure on phase transitions in polar crystals either temperature changes of spontaneous polarization can be measured for a fixed pressure (isobars) or pressure changes of spontaneous polarization (isotherms). In the latter case the change in spontaneous polarization

$$dP_i = \eta_i dp, \tag{1}$$

where p denotes pressure, whereas $\eta_i = \partial P_i/\partial p$ can be treated as a pressureelectric coefficient with the pressureelectric effect definition given in Eq.(1). It should be pointed out that the pressureelectric coefficient is a vector so it transforms itself in the same way as the pyroelectric coefficient. Therefore the pressureelectric effect can be observed exclusively in crystals showing pyroelectric properties[1].

Despite a similarity between pressure- and piezo- electric phenomena there is an essential difference between the two. The piezoelectric effect consists in polarization changes due to mechanical stress so the piezoelectric coefficients form a symmetric tensor of the third order. It is sufficient that the crystal possess no symmetry cent re to be a piezoelectric. It can be stated that the pressureelectrics are a sub-group of piezoelectrics (the same as pyroelectrics).

2. THERMODYNAMIC RELATIONS

Let's consider the Gibbs function to show relations between the pressureelectric effect with other phenomena occuring in polar crystals for a constant mechanical strain:

$$G(p,t,E) = U - TS - pV - EP \tag{2}$$

where: U - internal energy, T - temperature, S - entropy, V -

volume, p - pressure, E - electric field intensity, P - polarization.
In a differential form we have

$$-dG = SdT + Vdp + PdE \tag{3}$$

and expanding the entropy, volume and polarization we get

$$dS = \frac{\partial S}{\partial T}\Big|_{p,E} dT + \frac{\partial S}{\partial p}\Big|_{T,E} dp + \frac{\partial S}{\partial E}\Big|_{T,p} dE \tag{4.1}$$

$$dV = \frac{\partial V}{\partial T}\Big|_{p,E} dT + \frac{\partial V}{\partial p}\Big|_{T,E} dp + \frac{\partial V}{\partial E}\Big|_{T,p} dE \tag{4.2}$$

$$dP = \frac{\partial P}{\partial T}\Big|_{p,E} dT + \frac{\partial P}{\partial p}\Big|_{p,E} dT + \frac{\partial P}{\partial E}\Big|_{T,\ p} dE \tag{4.3}$$

The respective terms in Eq. 4.1 are connected with the specific heat, pressurecaloric and electrocaloric effects, the ones in Eg. 4.2 are connected with the thermal volume expansion, compressibility and electric-field-inducted change of the crystal volume (reversed phenomenon to the pressureelectric effect), while in Eq. 4.3 the terms describe pyroelectric, pressureelectric effects and electric susceptibility of the crystal. Eqs. 4.1 - 4.2 give that coefficients in the pressurecaloric effect and volume thermal expansion coefficients are equal, coefficients in the electrocaloric and pyroelectric phenomena are the same, and coefficients in the straight and reverse pressureelectric effects are also equal to each other. Moreover, Eq. 4.3 shows for constant electric field E that

$$dP = \frac{\partial P}{\partial T}\Big|_{p,E} dT + \frac{\partial P}{\partial p}\Big|_{T,E} dp. \tag{5}$$

In p,T coordinates the polarization can be treated as a unique function of p,T variables so that the pressure -temperature dependence of polarization is represented by a plane which lies in p-T elevation in the case of non-polar crystals, whereas the plane is inclined both towards p as well as T in the case of polar crystals.

3. PRESSUREELECTRIC EFFECT IN LINEAR PYROELECTRIC (CASE STUDY FOR POTASSIUM PENTABORATE)

Potassium pentaborate (KPB) applied to elektrooptics[2] belong to P point group[3], therefore it should show pyroelectric properties. Unpublished studies [4] revealed that KPB is a pyroelectric with no phase transition in temperature range of 4.2 to 430 K. Pressure and temperature dependence of spontaneous polarization change in KPB crystal is presented in Fig.1 for pressure range of 0 - 250 MPa and temperature range of 203 - 233 K. As seen from the figure the crystal shows simultaneously pyro- and pressureelectric properties. Pyroelectric coefficient increases from $9*10^{-6}$ Cm^{-2} at 203 K to $9.9*10^{-6}$ Cm^{-2} at 233 K. Relation between the spontaneous polarization and pressure is non-linear. Coefficient $dP/dp|_{p=0}$ increases with temperature (cf. Fig.2). This increasing can be assumed linear in the analyzed temperature range. Moreover, it can be concluded that the spontaneous polarization is a monotonic function of both pressure and temperature. The remaining coefficients in Egs. 4.1 - 4.3 may also be expected to be monotonic functions of pressure, temperature and (or) electric field.

An unexpected result, however, is that the pressure increase causes polarization changes of the same direction as these inducted by the temperature rise. The pressure increase should have decreased the inter atomic distance, so the effect similar to that due to lowering of temperature.

4. PRESSUREELECTRIC EFFECT IN FERROELECTRIC WITH THE SECOND ORDER PHASE TRANSITION (CASE STUDY FOR $(CH_3NH_3)_5Bi_2Br_{11}$)

At 311 K methyl ammonium bismuthate (MAPCB) crystals show the second order phase transition from $Pca2_1$- symmetry phase to Pcab - symmetry one[5]. We have found[6] that the phase transition temperature increases linearly with pressure in range 0 - 170 MPa, and pressure dependence of electric permittivity satisfies a relation similar to the Curie-Weiss rule. Taking the above into a count the Gibbs function for

MAPBB crystals can be rewritten in the form similar to that used by Jona and Schirane[7] for TGS crystals

$$G(P,T,p) = G_0 + \frac{1}{2} A P^2 + \frac{1}{4} \beta P^4 + \ldots - E P \tag{6}$$

where: $A = A(T,p) = \alpha (T - T_t)$, $T_t = T_{t0} + \Omega p$, $\Omega = \partial T_t/\partial p$, T_{t0} is a normal pressure phase transition temperature. Thus we get temperature and pressure dependence of electric permittivity. For $T > T_t$

$$\frac{1}{\chi} = \frac{\partial^2 G}{\partial P^2} = \alpha(T - T_{t0} - \Omega p) \tag{7}$$

reverse electric permittivity is a linear function both pressure and temperature. From the condition of the minimum Gibbs function with respect to the polarization we get temperature and pressure dependence of spontaneous polarization in the form

$$P_s = \left[\frac{\alpha}{\beta}\left(T_{t0} + \Omega p - T\right)\right]^{-1/2} \tag{9}$$

Therefore in ferroelectrics with the second order phase transitions the second powder of the spontaneous polarization is a linear function of both temperature and pressure.

$P_s(T,p)$ relation for MAPBB crystals is shown in Fig. 3 for data taken from[6] and[8]. As seen in the figure the polarization is a continuous function of temperature and pressure in accordance with Eq. 8. The pressure derivative of Eq. 8 gives the pressure-electric coefficient in the form

$$\eta = \partial P_s/\partial p = \pm \frac{\alpha}{\beta} \Omega \left[\frac{\alpha}{\beta} \left(T_{t0} + \Omega p - T\right)\right]^{-1/2} \tag{9}$$

Fig.4 shows pressure dependence of the pressure-electric coefficient for MAPBB crystals at 317 K, six degrees above the phase transition temperature. As seen from the figure the pressure-electric effect is not observed for $p < (T_{t0} - T)/\Omega$. Relation $\eta(p)$ reminds the temperature dependence of the pyroelectric coefficient which can be expected from Eq.9. It

is worth mentioning that $\partial P_s/\partial p$ around the phase transition is four orders higher for MAPBB crystal than that for linear pyroelectric such as KPB. MAPBB crystals are a good example for preservation of pressure-electric properties during the second-order phase transition from the non-polar phase to the ferroelectric one, the phase transition temperature being increasing with pressure.

5. PRESSURE-ELECTRIC EFFECT IN FERROELECTRICS WITH THE FIRST-ORDER PHASE TRANSITIONS (CASE STUDY FOR NH_4HSeO_4)

First-order transition from the low-temperature polar phase with unknown symmetry to the ferroelectric triclinic phase was observed in NH_4HSeO_4 (AHSe) crystals at about 105K. A step-like change in the ferroelectric component (electric-field reversible) and in the pyroelectric component[9] (being the subject of the investigation) took place in the above transition. Temperature-pressure dependence of changes in pyroelectric component of the spontaneous polarization is shown in Fig.5 for AHSe crystals around the above phase-transition temperature. The spontaneous polarization changes in a step-like manner in this transition showing a temperature-pressure hysteresis characteristic for first-order transitions. This is an example of pressure-electric properties of crystals showing first-order transition between two polar phases, the phase transition temperature being decreasing with the pressure. The pressure-electric effect can be observed in both phases (Fig.6).

It should be pointed out that for the described phase transition in AHSe $dT_t/dp < 0$ which remains contrary to results of Krasikov[10]. However, taking account of calorimetric[11] and dilatometric data[12] we can obtain negative dT_t/dp from the Claussius-Clapeyron equation.

6. PRESSURE-ELECTRIC-EFFECT-BASED SENSOR FOR HYDROSTATIC PRESSURE CHANGES

The pressure-electric effect can be employed to measure pressure changes due to the direct relation between changes in hydrostatic pressure and electric energy. In the commonly used piezoelectric pressure sensors the pressure change is transformed into a mechanic strain. This is done usually by a sensing membrane pushing the piezoelectric crystal through a piston. Such a construction is complex and slow in operation due to membrane-piston inertia which is an essential drawback of the sensor.

When employing the pressure-electric effect these disadvantages will be eliminated. A schematic view of such a sensor is shown in Fig.9. This is a plane-parallel wafer cut out of the pyroelectric crystal in the way that the largest surface with electrodes is perpendicular to the polar axis of the crystal. The electrodes are connected through load resistance, R_o. When in the surrounding medium (gaseous or liquid) the prevailing pressure changes, then the current, I flowing through the load resistance is the following:

$$I = S \frac{\partial P_{*} \partial p}{\partial p \; \partial t} . \tag{10}$$

The current is proportional to the electrode area S, the pressure-electric coefficient ($\eta = \partial P_{*}/\partial p$) of the sensor material and the pressure change rate. As mentioned before the η coefficient for ferroelectrics (around the phase transition temperature) is three to four orders of magnitude greater than that for linear pyroelectrics. This is why ferroelectrics such as L-α-alanine-doped TGS crystals are more recommended for pressure-electric sensors. The electric charge flowing through the load resistance being equal to:

$$Q = \int_0^t I\,dt = S\eta \int_0^p dp \qquad (11)$$

is proportional to the pressure change. Thus measuring the charge flowing through the load resistance we directly have the pressure change.

Based on the relation between the phase transition temperature and the pressure, sensors can be prepared which detect a certain pressure limit excess, the pressure threshold being widely adjusted by the sensor temperature.

REFERENCES

1. J.F. Nye, Physical Properties of Crystals Their Representation by Tensors and Matrix, Oxford 1957, Clarendon Press pp . 88-89.
2. C.F. Dewy, W.R. Cook, R.T.Hadson, J.J. Wynne, Applied Phys. Lett, 26, 714 (1975).
3. W.R. Cook, H. Jaffe, Acta Cryst, 10, 705 (1957).
4. R. Poprawski, St. Matyjasik, unpublished work.
5. R.Jakubas, Solid State Commun, 69, 267 (1989).
6. J. Mróz, R. Poprawski, A. Kolarz and R. Jakubas, Solid State Commun., 76, 821 (1990).
7. F. Jona, G. Schirane, Phys. Rev., 117, 139 (1960).
8. J. Mróz, R. Jakubas, Solid State Commun. 72, 813 (1989).
9. R.Poprawski, J. Dziedzic, J. Phys. Chem of Solids, 45, 355 (1984).
10. V.S. Krasikov, L.I. Zherebcova and M.P. Zaitseva, Fiz. Tverd. Tella, 23, 289 (1981).
11. R. Poprawski, P.S. Smirnov, B.A. Strukov, Fiz. Tverd. Tella, 26, 1339 (1984)
12. J. Dziedzic, R. Poprawski, Ferroelectrics, 77, 1 (1988).

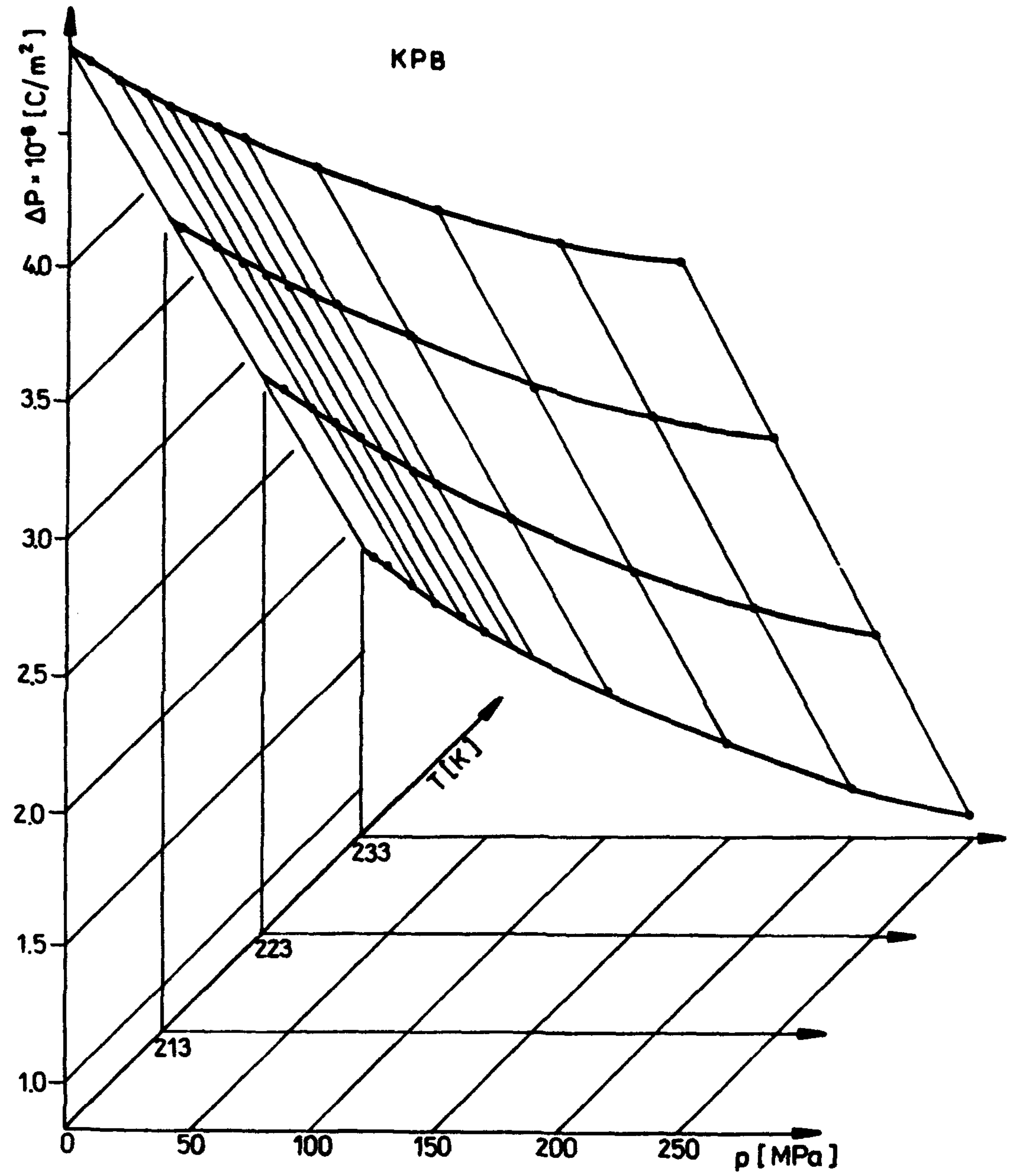

Fig.1. Pressure-temperature dependence of the spontaneous polarization changes for potassium pentaborate crystals.

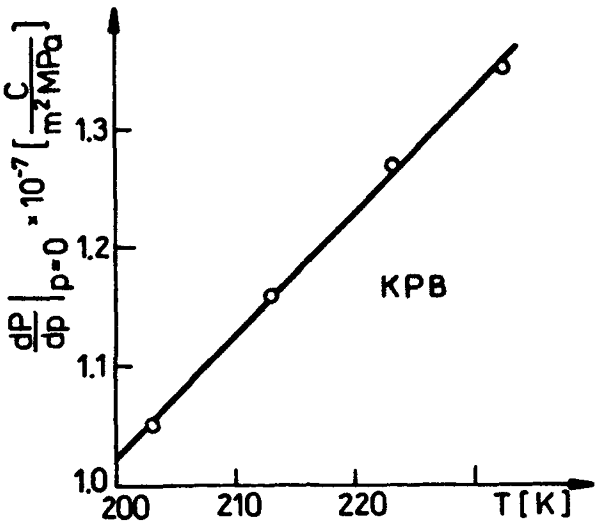

Fig.2. Temperature dependence of the pressureelectric coefficient for potassium pentaborate crystals (at p = 0).

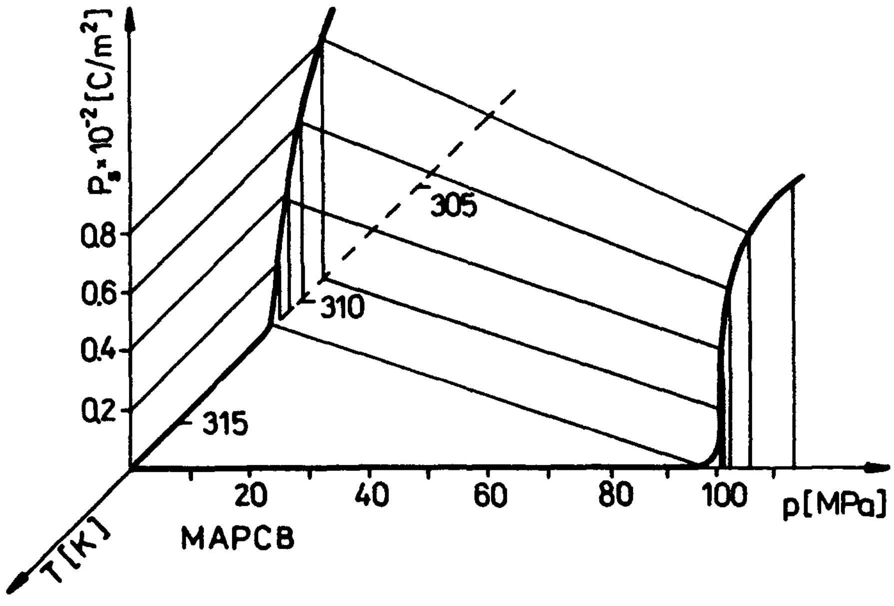

Fig.3. Pressure and temperature dependence of the spontaneous polarization for MAPBP crystals[6,8].

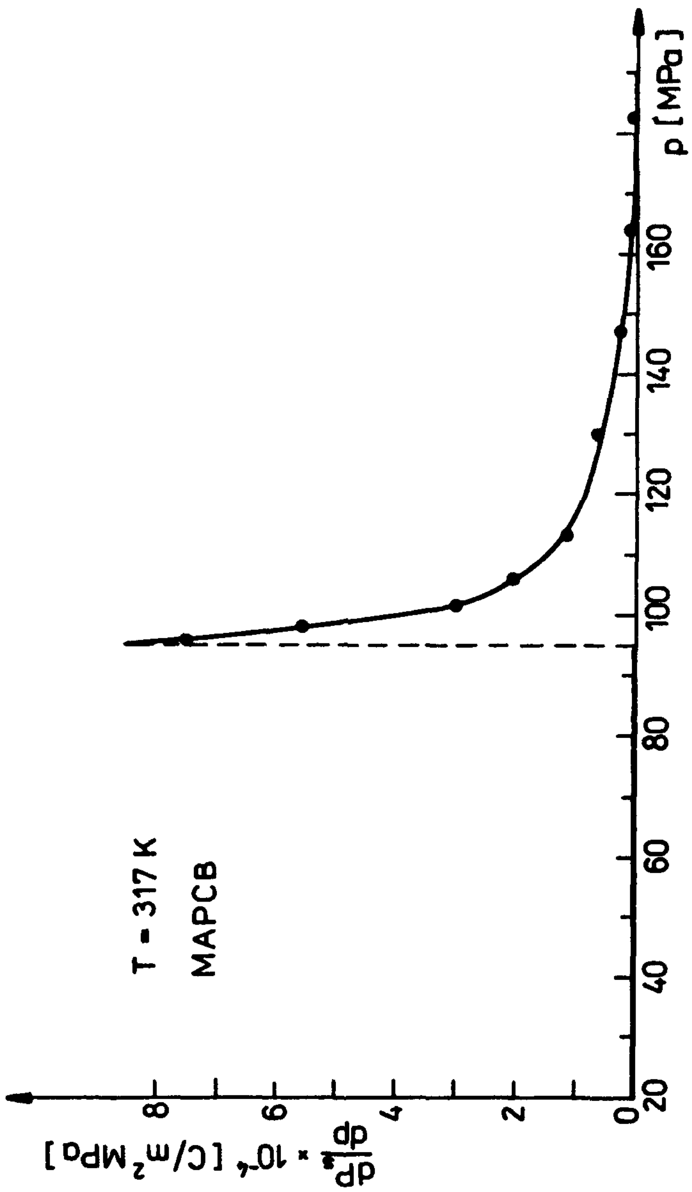

Fig.4. Pressureelectric coefficient of MAPBP crystals as a function of hydrostatic pressure at 317 K.

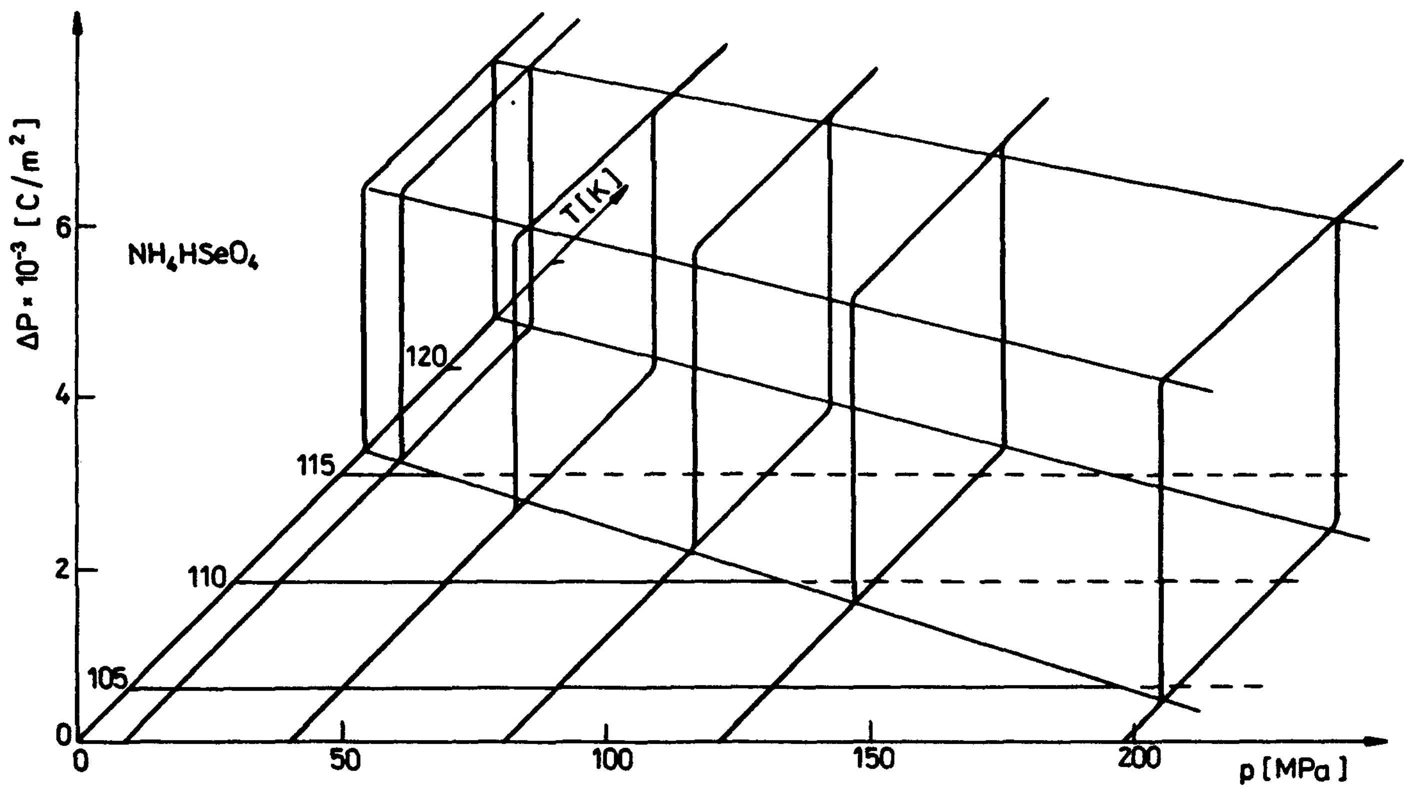

Fig.5. Pyroelectric component of the spontaneous polarization changes for NH_4HSeO_4 crystals as a function of the temperature and pressure.

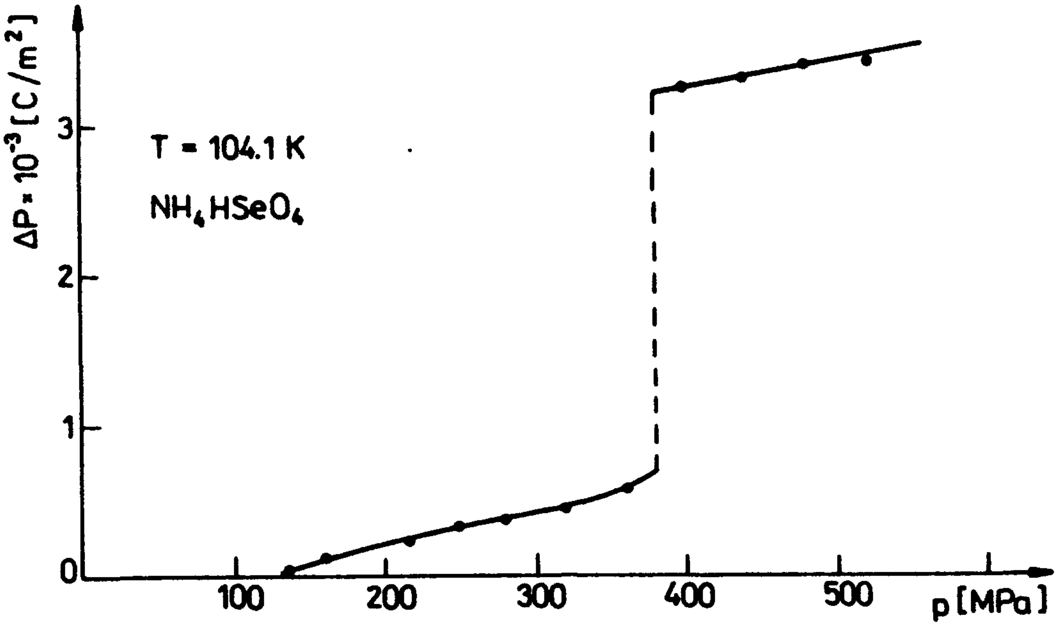

Fig.6. Pressure dependence of the spontaneous polarization changes for NH_4HSeO_4 crystals at 101.4 K.

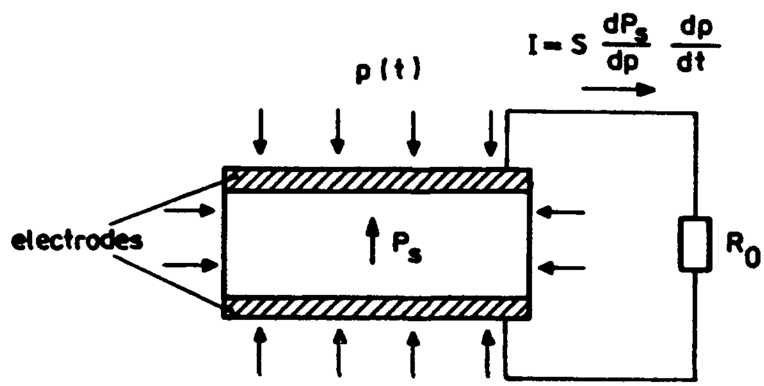

Fig.7. Schematic view of the pressureelectric sensor of hydrostatic pressure changes.

SECTION III
CONTRIBUTED PAPERS
IIIj. Ferroelectric Thin Films (Materials and Devices)

Ferroelectrics, 1992, Vol. 134, pp. 285–290
Reprints available directly from the publisher
Photocopying permitted by license only

TfC13

RAPID THERMAL PROCESSING OF PZT THIN FILMS

Y. HUANG, I.M. REANEY and A.J. BELL
Laboratoire de Céramique, EPFL, MX-C Ecublens, 1015 Lausanne, Switzerland

Abstract Thin films of $Pb(Zr_{0.53}Ti_{0.47})O_3$ on Pt-coated Si substrates were prepared by sol-gel deposition. The dielectric properties and polarization reversal characteristics were measured as a function of sintering conditions using a rapid annealing technique. The results are interpreted with respect to the phase and microstructural development of the films. Their suitability for incorporation into semiconductor devices is discussed, with particular attention given to the possibility of low temperature processing.

INTRODUCTION

Ferroelectric thin films deposited on semiconductor substrates are of interest for a number of applications, including non-volatile memories[1], pyroelectric detectors[2] and micromechanical devices[3]. Due to their favourable polarization reversal, pyroelectric and piezoelectric properties, films based upon the $Pb(Zr_xTi_{1-x})O_3$ system [PZT] have been the focus of many studies. A variety of vacuum[4] and liquid phase or solution deposition[5] techniques have proved successful in producing films which show adequate properties for the demonstration of these applications. However, the logistics of the semiconductor industry demand that for the fabrication of a device, the ferroelectric film is deposited after completion of the semiconductor processing. Annealing temperatures required for the realization of high quality PZT films are often quoted to be in the region 600 to 850°C. Exposure of a processed semiconductor wafer to temperatures in this range may result in distortion of the dopant profiles, causing damage to the semiconductor circuit. In addition this temperature range is not consistent with the use of aluminium metallisation (melting point 659°C). Present research work is therefore targeted at minimizing the thermal energy required in the preparation of PZT thin films. In this paper we report on the sol-gel deposition of $Pb(Zr_xTi_{1-x})O_3$ films in conjunction with the use of a rapid thermal annealing technique and assess the possibilities of low temperature processing.

A sol-gel technique, similar to that reported by Gurkovich and Blum[6] and later by Budd et al.[7], was selected because of its potential to form Pb-Ti-Zr-O molecular units within the gel before film deposition. Diffusion distances may therefore be minimized, consistent with the requirement for minimal thermal treatment. However, other factors such as the mass of organic groups within the gel, the crystallization temperature of the perovskite phase and the densification of the microstructure are important considerations in obtaining short, low temperature annealing cycles. "Rapid thermal annealing"[8] was selected as a means of reducing the total annealing cycle time.

EXPERIMENTAL

Precursor stock solutions were prepared by a method similar to that of Budd[9]. Lead acetate tetrahydrate was dissolved in 2-methoxy ethanol in a molar ratio of 1:8. The

solution was fractionally distilled at 110°C to remove the water of crystallization of the lead acetate. 0.47 moles of titanium iso-propoxide and 0.53 moles of zirconium n-propoxide were mixed with 8 moles of 2-methoxy ethanol. The solution was heated to temperatures up to 125°C to remove the propyl alcohol fractions which resulted from replacement of the alkoxide propyl groups with the 2-methoxy-ethyl groups. The two solutions were mixed and boiled to promote reaction between the lead acetate and the alkoxides; the resulting ester was removed by distillation together with excess solvent. The solution concentration was adjusted to 1 molar; this stock solution was then stored under anhydrous conditions.

Portions of the stock solution were hydrolyzed by the addition of equal volumes of a 1 molar solution of water in 2-methoxy ethanol and then immediately deposited upon a substrate by spin casting at 2500 min^{-1}. The substrates consisted of device quality silicon with a 1000 Å layer of SiO_2 grown by dry oxidation, upon which a 200 Å layer of titanium and a 2000 Å layer of platinum were deposited by sputter deposition. The gel films were dried on a hot-plate at 250°C for 10 mins, before further gel layers were applied. Normally, five gel layers are applied by spin casting with a drying stage between each layer.

Annealing was carried out using a rapid heating module[9] consisting of 18 x 1500 W lamps inside a gold plated reflective quartz chamber. The sample holder is such that the wafer is exposed to radiation on both sides. The sample temperature is controlled by a thermocouple in contact with one side of the wafer, in this case the side without the gel coating. The chosen temperature profile consisted of a 40 s ramp to the annealing temperature, with a dwell at temperature in the range 30 to 300 s and a 300 s forced cool to approximately 300°C. The sample was allowed to cool naturally from 300°C to room temperature. Comparisons were made with conventionally annealed samples which were subjected to a ramp of 10°C min^{-1} and a dwell of 60 min. at temperature, before cooling at a rate of approximately 1°C min^{-1}. In addition, thermogravimetric analysis of samples of dried gel was carried out.

The phase content of the films was determined using X-ray diffractometry. The volume fraction of a "parasitic" pyrochlore type phase was estimated from a comparison of the peak X-ray intensities of perovskite and pyrochlore reflections.

Thin foils were prepared in transverse section for transmission electron microscopy (TEM) using initially a Gatan 'dimpler' to reduce the thickness to 50 μm and then a Gatan ion beam thinner operated under conventional conditions to perforate the sample. A more detailed experimental method has been described previously[10]. The foils were investigated using Philips EM430 and CM20 microscopes.

For the electrical characterization, the films were sputtered with gold electrodes 0.5 mm in diameter. The complex impedance as a function of frequency from 10 Hz to 1 MHz was measured with an HP4192A impedance analyzer with a test signal of 5 mV. The polarization as a function of field was measured with a virtual Sawyer-Tower circuit at a frequency of 10 Hz and a maximum applied voltage of 15 V.

RESULTS

The X-ray diffraction of the analysis of the films reveals an interesting comparison between rapid thermal annealing and conventional annealing process. All films annealed below 400°C appear amorphous. For conventionally annealed samples, by 450°C crystallization of the films has already started, but with the presence of a large fraction of pyrochlore phase. A steady decrease in pyrochlore content is observed with increasing annealing temperature, with no pyrochlore being detected for annealing temperatures of 600°C or above. In the rapid annealed samples no pyrochlore is observed above 600°C. However, for films annealed below 600°C, the volume of pyrochlore varies considerably with the age and history of the stock solution. In certain cases no pyrochlore could be detected by X-ray diffraction in films which were rapid annealed at 450°C

Figure 1 shows the results of the thermogravimetric analysis of the gel. A large, rapid weight loss is exhibited up to 150°C, with the rate of loss slowing down between 150 and 300°C. There is no weight loss between 300°C and approximately 440°C, when again there is further loss. There are no weight changes above 600°C.

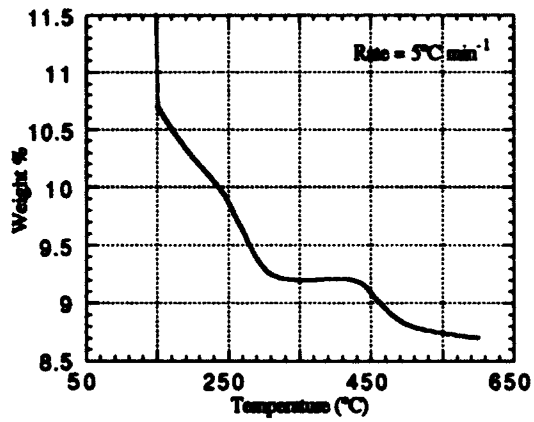

FIGURE 1. Weight loss as a function of temperature for a gel sample.

Figure 2 is a TEM image which shows part of a transverse section through a PZT thin film which has been annealed at 600°C. The PZT film shows well defined grains at the PZT/Pt interface with a grain size of 50 to 100 nm, but near the surface a layer can be observed which has only a poorly defined grain structure (verging on amorphous). Inserted in the image is a selected diffraction pattern from the film which shows rings which have arisen from the outer layer along with individual maxima from the grains near the PZT/Pt interface.

Figure 3 is a transmission electron micrograph showing part of transverse section through a PZT film that has been annealed at 700°C. In contrast to the film annealed at 600°C, the whole film has developed well defined grains. However, pores which are approximately 50 nm in size can be observed in the interior of the film. Inserted in the micrograph is zone axis diffraction pattern which can be indexed according to a primitive cubic lattice were a = 0.40 nm.

Figure 4 is a TEM image of a PZT film annealed at 850°C. The film is completely crystalline. Pores can be observed in the interior of the film as in the 700°C film, but are

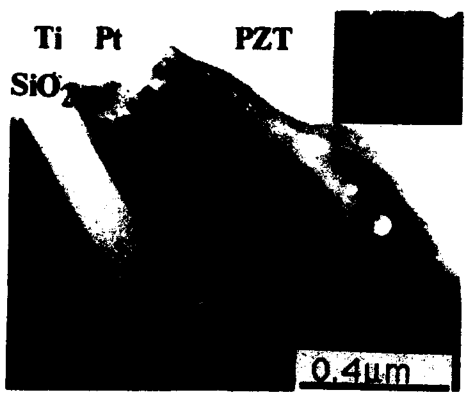

FIGURE 2. TEM image showing a transverse section through a PZT thin film annealed at 600°C. Inset is a selected area diffraction pattern from the film.

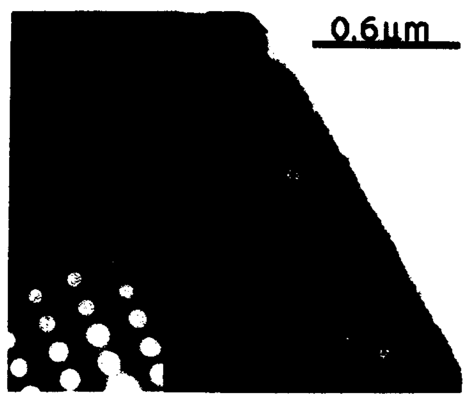

FIGURE 3. TEM image of a PZT thin film annealed at 700°C. Inset is a <110> ZADP from a perovskite grain.

also seen at the PZT/Pt interface. Deterioration of the $Pt/Ti/SiO_2$ electrode interfaces may also be observed at this temperature; this phenomenon was not seen in films annealed at 800°C. Inserted in the micrograph is a dark field image of a grain obtained using a {hk0} reflection.

FIGURE 4. TEM image of PZT film annealed at 850°C. Inset is a DF {hk0} image of a single grain.

Figure 5 shows the polarization-field hysteresis loops for two differently annealed thin films. That shown for the film annealed at 800°C is typical of films annealed at temperatures between 650°C and 800°C. The remanent polarization is approximately 0.35 C m^{-2} with a coercive field of 5 to 7 MV m^{-1}.

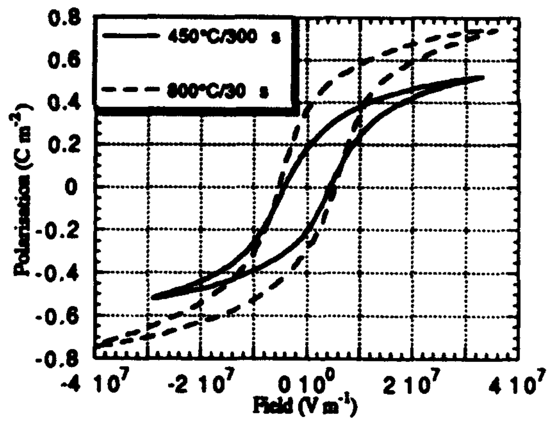

FIGURE 5. P-E hysteresis loops for two PZT thin films.

The series capacitance as a function of frequency for samples annealed at different temperatures is shown in Figure 6. The films for the lowest and highest annealing temperatures show very different behaviours; that annealed at 600°C has a low capacitance (≈ 600 pF), but a relatively flat frequency characteristic, whilst that annealed at 850°C has a capacitance at 10 kHz of almost 8000 pF which falls to less than 1000 pF at 1 MHz. The two intermediate temperature specimens show increasing capacitance with increasing temperature but without the large decrease in capacitance above 100 kHz as shown by the 850°C annealed sample.

DISCUSSION

The X-ray diffraction results seem to emphasize one of the major findings in this work, that the quality of the films is strongly dependent upon the history of the stock solution. Post-hydrolysis reproducibility for individual stock solutions was good, therefore the effects described here appear to be a function of the pre-hydrolysis chemistry. More detailed studies of the stock solution chemistry are now in progress. Variations in the pyrochlore content of the films rapid annealed at less than 600°C are thought to arise from incomplete reaction or partial distillation of the products from the alkoxide radical interchanges or the lead acetate/alkoxide reactions. In view of this, it is perhaps surprising that the thermogravimetric analyses display a far greater degree of consistency; the result

shown in Figure 1 is typical. The large weight loss up to 300°C is thought to be associated with the loss of hydroxyl and alcohol groups from the gel, whereas it is suggested that the weight loss above 400°C is due to the pyrolysis of the acetate groups. If this interpretation is correct then the presence of acetate in the gel is one of the limitations to reducing the processing temperature of the films.

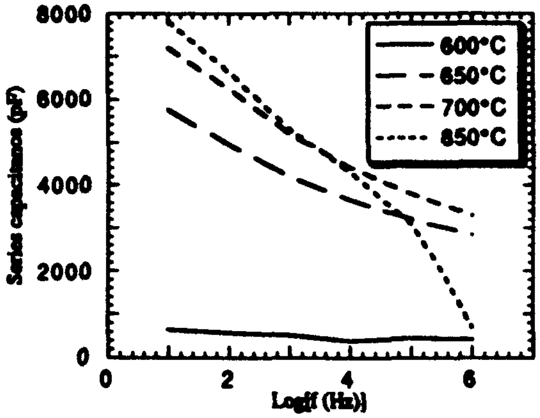

FIGURE 6. Capacitance of films as a function of frequency and annealing temperature.

The observation that hysteresis loops may be obtained for films annealed at 450°C, with remanent polarization and coercive fields approaching those of films annealed at more conventional temperatures (800°C), is encouraging and may be indicative of the formation of perovskite at relatively low temperatures. However, the complete development of the perovskite phase, together with a dense microstructure, requires higher annealing temperatures, as shown by the X-ray diffraction analysis and the TEM investigations. The low capacitance exhibited by films annealed at 600°C and below may be interpreted as due to both the presence of pyrochlore and the limited degree of crystallization in the films. Above this temperature full crystallization of the films is observed, but the capacitance is limited by the presence of porosity. At 800°C, the large value of relative permittivity of 1250 at 1 kHz, similar to that of dense bulk samples of PZT, suggests that near to the optimum density of the films has been achieved, despite the observation of some remaining porosity. The large decrease in capacitance at high frequency, for samples annealed at temperatures above 800°C, may be due to the presence of a high resistance in series with the film. The degradation of the electrode region observed in these samples is consistent with this interpretation.

Figure 2 appears to show that in the rapid annealing process, crystallization of the perovskite phase commences, or proceeds most quickly, close to the PZT/Pt interface. Conventional annealing cycles are thought to be too slow for this inhomogeneous phase development to be observed. It is not known whether the effect is due to a catalytic or epitaxial influence of the Pt electrode which promotes the growth of the perovskite phase, or whether it may be attributed to the transparency of the film. In the latter case, the radiation would initially be absorbed or reflected at the film/Pt interface, causing a thermal gradient from the electrode to the surface of the film, with the highest temperatures in the region of the electrode. Further experiments are being carried out on a variety of substrates and electrodes which may resolve this issue.

In summary, the following scheme may be proposed for the evolution of PZT films produced from the above sol-gel method by rapid annealing: pyrolysis of the film is complete by 450°C, firstly by removal of hydroxyl and alcohol groups, secondly by pyrolysis of acetate groups. Crystallization of the PZT perovskite phase has started at this temperature and proceeds from the electrode towards the film surface, however the presence of a pyrochlore phase in greater or lesser amounts is determined by the history of the stock solution reactions. Conversion to 100 % perovskite is complete by 700°C. Densification of the film progresses to 800°C, above this temperature electrode and substrate interactions degrade the contact resistance between the Pt electrode and the film.

The thermal treatment needed to produce device quality films is determined by two requirements: the pyrolysis of the acetate groups in the gel and the elimination of porosity from the films. Although the drying processes in the gel undoubtedly contribute to the porosity, it is probable that the pyrolysis of the acetate groups in the gel may itself result in the formation of micro-pores which on coalescence limit densification until higher temperatures. It would seem that to reduce processing temperatures significantly, attention should first be focused upon the possibility of the elimination of acetate groups from the gel before deposition.

Previous workers have shown that the likely reactions during formation of the stock solution are the replacement of the alkoxide propyl groups by 2-methoxy ethyl groups and then reaction of the resulting methoxy ethoxides with Pb acetate. Dekeleva et al[11] carried out analysis of the distillation products to show that in the first case the complete removal of n-propyl groups is not achieved until temperatures approaching the boiling point of the 2-methoxy ethanol. This is possibly one source of variation between batches of stock solution. Secondly they found that only half the acetate groups present could be removed from the stock solution by distillation in the form of 2-methoxy ethyl acetate. This suggests that the result of the reaction between lead acetate and the 2-methoxy ethoxides is $(OR)_3M{-}O{-}Pb(CH_3COO)$, in which M is either Zr or Ti and R is 2-methoxy ethyl, and that further reactions of this molecule, resulting in removal of the acetate, do not occur. A partial charge model, as proposed by Livage and Henry[12], has been used to estimate the relative probability of possible reactions within the stock solution. In keeping with the findings of Dekleva, the above mentioned reaction between the alkoxide and lead acetate was shown to be likely, whereas the probability of the removal of the remaining acetate group from the product by further reaction was shown to be highly dependent upon the mixture of alkoxy groups attached to the tetravalent cation.

Further partial charge calculations and experiments are in progress to determine the conditions required to remove all the acetate groups from the stock solution before hydrolysis.

REFERENCES

1. B.M. Melnick, J.D. Cuchiaro, L.D. McMillian, C.A. Paz de Araujo and J.F.Scott, Ferroelectrics, 112, 329 (1990)
2. D.L. Polla, R.S. Muller and R.M. White, IEEE Elec. Dev. Lett., EDL-7 254 (1985)
3. K.R. Udayakumar, S.F. Bart, A.M. Flynn, J. Chen, L.S. Tavrow, L.E. Cross, R.A. Brooks and D.J. Ehrlich, Proc. IEEE MEMS, 109 (1991)
4. R.A. Roy, K.F. Etzold and J.J. Cuomo, Proc. Mat. Res. Soc. Symp., 200, 141, (1990)
5. G. Yi and M. Sayer, Am. Ceram. Soc. Bull., 70, 1173 (1991)
6. S.R Gurkovich and J.B. Blum, Ferroelectrics, 62, 189 (1985)
7. K.D. Budd, S.K. Dey and D.A. Payne, Brit. Ceram. Proc. No 39, 107 (1985)
8. C.V.R. Vasant Kumar, M. Sayer, R. Pascuasl, D.T. Amm, Z. Wu and D.M. Swanston, Appl. Phys. Lett., 58, 1161 (1991)
9. Process Products Corporation, RTM 2016
10. I.M. Reaney and D.J. Barber, J. Am. Ceram. Soc., 74, 1635 (1991)
11. T.W. Dekleva, J.M. Hayes, L.E. Cross and G.L. Geoffroy, Comm. Am. Ceram. Soc., C-280, (1988)
12. J. Livage and M. Henry, in Ultrstructure Processing of Advanced Ceramics, p.183, eds. J.D. Mackenzie and D.R.Ulrich, Wiley, New York (1988)

Ferroelectrics, 1992, Vol. 134, pp. 291–296
Reprints available directly from the publisher
Photocopying permitted by license only

TfC14

GROWTH OF PARA- AND FERROELECTRIC EPITAXIAL LAYERS OF $KTa_{1-x}Nb_xO_3$ BY LIQUID PHASE EPITAXY

ROLAND GUTMANN, JÜRG HULLIGER and HERMANN WÜEST
Institute of Quantum Electronics, ETH Hönggerberg, CH-8093 Zürich

Abstract Para- and ferroelectric layers of $KTa_{1-x}Nb_xO_3$ (KTN) could be grown on pure and Sn-doped (100) $KTaO_3$ substrates by liquid phase epitaxy from KF/KTN, K_2MoO_4/KTN and KTN/K_2O solutions. Depending on the required layer thickness either dilute solutions of KTN and KF, K_2MoO_4 or a KTN melt with an excess of K_2O were used. Lattice fitting could be achieved by the growth of KTN:Na layers. The epitaxially grown samples were analysed by optical microscopy, wavelength dispersive electron probe microanalysis, scanning electron microscopy, x-ray and dielectric measurements. Ferroelectricity at room temperature was demonstrated by hysteresis loop measurements.

INTRODUCTION

The growth of homogeneous epitaxial layers of $KTa_{1-x}Nb_xO_3$ (KTN) by liquid phase epitaxy (LPE) for pyroelectrical, ferroelectrical or optical use is a challenge in regard to existing growth problems for homogeneous KTN bulk crystals. Depending on possible applications either thin (1 - 10 μm) or thick (> 50 μm) monocrystalline layers are necessary. Such thickness requirements cannot be fulfilled by only one solvent because the growth time in case of a dilute solution (necessary for thin layers) would be too long to obtain thick layers of a homogeneous thickness. In contrast, from concentrated solutions the reproducible growth of layers with thicknesses h < 10 μm seem not to be possible.

For optical investigations any kind of lattice defects related to misfit relaxation should be avoided. This implies a reduction of the lattice misfit between the cubic $KTaO_3$ substrate and the KTN(x) layers. For μm thick paraelectric and cubic KTN(x = 0.29) layers a misfit of 10^{-3} exceeds a critical value and creates dislocations

due to a lattice relaxation of the epitaxial system. Various approaches for the reduction of the lattice misfit are possible. An increase of the substrate lattice constant as well as the growth of buffer layers seems more difficult than a reduction of the layer constant achieved simply by exchanging the A-ion of the ABO_3 lattice by a smaller isovalent ion. Solid solution formation of KTN with Na was successfully performed and the replacement of a relatively small amount of K by Na ($y < 0.15$) did not change the dielectric or ferroelectric behaviour of the $K_{1-y}Na_yTa_{1-x}Nb_xO_3$ layer effectively.

GROWTH OF SUBSTRATE CRYSTALS

LPE investigations will need $KTaO_3$ crystals of a low defect density. Both, pure and doped crystals were grown from a high temperature $KTaO_3/K_2O$ solution with 5 mol% K_2O by the top seeding method. After a superheating period (~ 4 h, 1370 °C) a (100) or (110) $KTaO_3$ seed was brought in contact with the melt. Pulling rates of ~ 0.3 mm/h and a temperature decrease of ~ 0.04 °C/h lead to transparent and colourless crystals of up to 2 cm^3. To control the growth rate and crystal diameter the weight change was recorded by a digital balance. The addition of 500 to 2000 ppm SnO_2 to the solution increased the crystal quality and reduced the electrical resistivity from $\sigma = 1.2 \times 10^{11}$ Ωm for pure crystals to $\sigma = 3.6 \times 10^3$ Ωm for a crystal grown from a solution containing 1000 ppm SnO_2. The effective distribution coefficient for Sn is approximately $k_{eff(Sn)} = 0.44$. The reduction of the resistivity will facilitate the use of the substrate as a back electrode for dielectric measurements, poling experiments and for device applications, where the physical properties are controlled by electric fields.

EPITAXIAL EXPERIMENTS

Epitaxial growth from dilute solutions using KF or K_2MoO_4 as a solvent were performed in a highly temperature stabilized, 3 zone, resistor heated furnace[1]. The growth from a concentrated solution with K_2O as solvent was done in a Czochralski apparatus with temperatures of up to 1400 °C. In this case the growth was controlled by a digital balance with mg resolution. To ensure homogenization of the solution both set-ups were equipped with the accelerated crucible rotation technique (ACRT).

Growth experiments from KF solutions

Preliminary dissolution, crystallization and epitaxial experiments with KTN in a KF/KTN solution gave promising results in regard to the dissolution and crystallization

behaviour of KTN[2]. Homogeneous and heterogeneous nucleation produced blue coloured crystals or layers of μm thickness. The blue colour could be completely removed by O_2 annealing at 950 °C for 20 h. To elaborate the suitable concentration range and the width of the metastable regions the corresponding part of the KF/KTN(x = 0.68) phase diagram for $92 \leq c_{KF} \leq 99.5$ mol% was determined. The liquidus and solidus temperature, shown in Figure 1, was obtained with a heating and cooling rate of 2 °C/min.

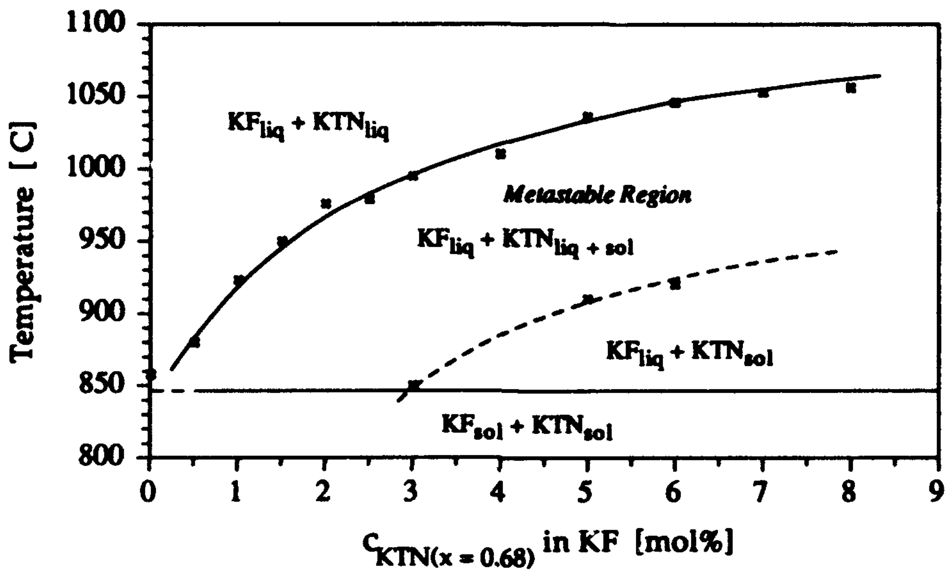

FIGURE 1 Partial phase diagram of KF/KTN(x = 0.68).

Epitaxial growth on cm^2 sized (100) $KTaO_3$ substrates gave μm thick paraelectric KTN(x = 0.29) layers from a KF/KTN(x = 0.68) solution. Ferroelectric KTN(x = 0.45) layers were obtained from a KF/KTN(x = 0.82) solution. Lattice misfit induced defects could be avoided by the incorporation of Na, which reduced the lattice constant(s) in the cubic and tetragonal phases. A misfit minimum without lattice relaxation defects could be achieved by the use of a solvent mixture of 88.5 mol% KF and 11.5 mol% NaF for cubic layers (x = 0.29), and 87.9 mol% KF and 12.1 mol% NaF for tetragonal layers (x = 0.45). For growth temperatures between 870 and 945 °C growth rates of 0.1 - 2 μm/min for pure and Na enriched layers were found. Detailed information on the growth of lattice fitted para- and ferroelectric KTN layers will be published elsewhere[3].

Growth experiments from K_2MoO_4 solutions

Epitaxial experiments growing KTN from K_2MoO_4 solution gave colourless layers of good crystal quality showing a higher distribution coefficient for Nb in comparison to KF solutions. In contrast to KF solutions, substrate orientations other than (100) e.g.

(110) could be used to obtain flat layers by post-growth polishing. The growth rates for a solute concentration of $c_{KTN} \leq 2$ mol% and growth temperatures between 910 and 960 °C varied between 0.1 and 1 µm/min. The main problem with the use of K_2MoO_4 is the low solubility of KTN ($c_{KTN} \leq 2$ mol%) and the dependence of the distribution coefficient for Nb on the growth temperature. An effective lattice fitting was not possible, because the addition of Na_2MoO_4 to the solution changed the layer composition (x) and reduced the already small solubility of KTN.

Growth experiments from K_2O solutions

The epitaxial growth behaviour of KTN from concentrated K_2O solutions with $c_{KTN} = 95$ mol% showed a different behaviour with regard to a variation of the growth rate from 2.5 to 30 µm/min. Also, the supercooling temperature was only a few degrees above the temperature where heterogeneous nucleation occured. At a growth temperature of ~ 1190 °C and growth times of 1 - 10 min layers with thicknesses between 15 - 150 µm were typically obtained. For layer thicknesses above 20 µm a slightly milky appearance was created by domains. Solutions containing 68 and 72 mol% Nb produced KTN(x) layers with x = 0.37 and x = 0.41, respectively. These samples were completely colourless and showed the known misfit induced defect pattern at the substrate/layer boundary. This defect region did not extend through the whole layer thickness but was restricted to a few µm near the interface. Therefore, lattice fitting experiments (e.g. by the addition of Na_2O or Li_2O) seem not to be necessary. In the top part of such a 50 µm thick KTN layer a 7 µm thick optical waveguiding structure was produced by He^+ implantation[4].

ANALYSIS

The investigation of the KTN layers was performed by a variety of analytical methods including optical microscopy (OM), scanning electron microscopy (SEM), wavelength dispersive electron probe microanalysis (EPMA), Rutherford backscattering (RBS), x-ray diffraction measurements, channeling experiments with electrons and α-particles, Auger electron spectroscopy (AES), x-ray photoelectron spectroscopy (XPS), dielectric and hysteresis measurements.

At first the quality of the as grown layers was investigated by OM and SEM. OM with polarized light or differential interference contrast showed defects like domains, lattice misfit relaxations at the substrate/layer interface and macrosteps at the surface. For KF/KTN solutions layers of optical quality can only be obtained for (100) substrates.

For surfaces without macrosteps the misorientation should be < 0.5° [1].

The layer thicknesses were measured either mechanically or by RBS in cases of thicknesses below 5 µm. The dependence of the thickness on the growth time and supersaturation gives information on the growth mechanism and the thermodynamical behaviour of the growth system.

Further work concentrated on the determination of the lattice quality of the layers. Extensive x-ray diffraction measurements of *00l* peaks with $l = 1$ to 8 established monocrystalline epitaxial layers. A high resolution x-ray diffractometer system allowed the determination of the lattice misfit $f < 10^{-4}$. For cubic layers the *00l* reflections were sufficient but for ferroelectric (tetragonal) layers the asymmetric Bragg diffraction technique had to be applied[3]. In addition, the crystal quality of the substrate and the layer was inspected by x-ray rocking curves and channeling experiments[3].

The chemical composition and homogeneity of the KTN layers was investigated by FPMA, AES, XPS as well as by dielectric permittivity measurements. EPMA enabled a precise quantitative determination of the main elements including F and O if appropriate reference samples were used. The chemical homogeneity was explored by AES and XPS[5]. XPS also offers the possibility of checking the chemical oxidation state of the layer forming ions. This was applied to blue layers before and after the discolouration by O_2 annealing[5]. The fact that KTN bulk crystals[6,7] and also thin layers[1] exhibit composition dependent phase transitions (Figure 2) leads to a further method to

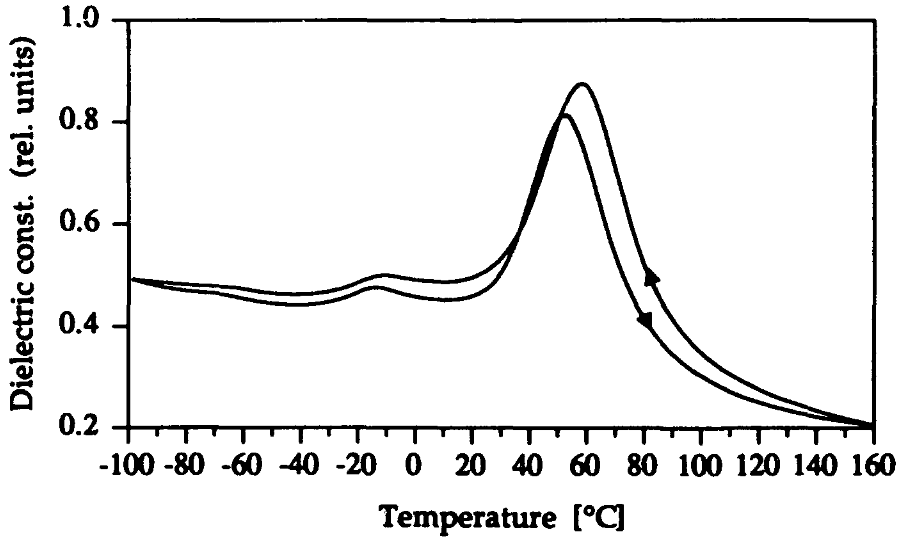

FIGURE 2 Phase transitions of a KTN(x = 0.45) layer, grown on a (100) $KTaO_3$ substrate from a KF-KTN(x = 0.82) solution with $c_{KTN} = 8$ mol%, h = 12 µm.

determine the Nb content of discoloured layers. The discolouration is necessary since

blue layers show a low resistivity of $\sigma \sim 5\ \Omega m$, while for the colourless state a value of $\sigma = 2.9 \times 10^9\ \Omega m$ was measured. The influence of Na doping on the physical properties of KTN layers was also investigated by dielectric measurements. Beside a small increase in T_C of 0.9 °C/mol% due to Na incorporation, no degradation effects were evident.

Ferroelectricity for epitaxial KTN layers was demonstrated by dielectric hysteresis measurements. With 2 parallel strip gold electrodes placed on the layer surface (separation 0.2 mm) and the application of an ac voltage of 110 V, 50 Hz a hysteresis loop as shown in Figure 3 could be recorded.

FIGURE 3
Ferroelectric hysteresis loop of a KTN ($x = 0.45$, $y = 0.125$) layer with $h = 28\ \mu m$ and $T_C = 61$ °C; $E_C \sim 2$ kV/cm at $T = 23$ °C.

Further analytical and material specific measurements such as the determination of the pyroelectric coefficient and an analysis of the domain structure are in process.

ACKNOWLEDGEMENTS
We thank Prof. P. Günter for helpful discussions. This work has been supported in part by the Swiss National Science Foundation (NFP 13 and NF).

REFERENCES

1. R. Gutmann and J. Hulliger, Cryst. Prop. Prep., 32, 117 (1991).
2. J. Hulliger and R. Gutmann, J. Cryst. Growth, 99 , 634 (1990).
3. R. Gutmann, J. Hulliger and E. Reusser, J. Cryst. Growth, (1992) (submitted).
4. D. Fluck, R. Gutmann, P. Günter and R. Irmscher, J. Appl. Phys., 70, 5147 (1991).
5. R. Gutmann, J. Hulliger, R. Hauert and E. M. Moser, J. Appl. Phys., 70, 2648 (1991).
6. S. Triebwasser, Phys. Rev., 114, 63 (1959).
7. D. Rytz and H. J. Scheel, J. Cryst. Growth, 59, 468 (1980).

Ferroelectrics, 1992, Vol. 134, pp. 297–302
Reprints available directly from the publisher
Photocopying permitted by license only

TfC16

GROWTH OF PEROVKSITE PLZT THIN FILMS BY DUAL ION BEAM SPUTTERING

D.A. TOSSELL, N.M.SHORROCKS, J.S.OBHI & R.W. WHATMORE
GEC-Marconi Materials Technology Ltd, Caswell, Towcester, Northants, NN12 8EQ, UK.

Abstract PLZT thin films have been deposited using the emerging PVD technique of dual ion-beam sputtering (DIBS). The DIBS process produces high quality orientated perovskite films of bulk refractive index, good stoichiometry and full density, i.e., few pinholes. Films have been formed at 500-600°C onto sapphire, fused silica, Mg0 and silicon substrates by sputtering from an adjustable composite PLZT ceramic/Ti and Pb metallic target. Some substrates were coated with platinum prior to deposition to allow longitudinal electrical measurements on the films. Perovskite lead titanate PLZT (0/0/100), PLZT (10/0/100) and PLZT (28/0/100) films have been grown, the former two are of interest for thin film pyroelectric detectors whereas the latter is a quadratic electro-optic suited to optical waveguide, shutter and switching applications.

INTRODUCTION

The quarternary solid solution of PLZT(x,y,z)

$$Pb_{1-3/2x}La_x(Zr_yTi_z)0_3 \qquad (1)$$

is a well known ferroelectric material that exhibits piezoelectric, pyroelectric, linear and quadratic electro-optic properties depending on the composition. In bulk form, it has been applied to a wide variety of ferroelectric devices[1]. Thin films of PLZT are of interest for enhanced pyroelectric detectors[2], optical waveguides and switches[3] and non-volatile memory applications[4]. In particular, full monolithic integration of such films with semiconducting materials would yield significant advantages in terms of increased speeds, reduced voltages and enhanced response. Due to the high temperatures required for the formation of the ferroelectric perovskite phase and the complex stoichiometry, the production of thin film PLZT has not proved easy and, at present, a wide variety of thin film synthesis techniques, such as MOCVD, sol-gel, RF magnetron and ion beam sputtering, and laser ablation are subject to intensive research[5]. In this paper, we report the use of the emerging PVD technique of dual ion beam sputtering (DIBS) for the synthesis of PLZT thin films. The compositions PLZT (0/0/100) (i.e. pure lead titanate), PLZT (10/0/100) and PLZT (28/0/100) have been selected. The former two have been reported as useful for thin film pyroelectric detectors[2] and the latter for a large quadratic electro-optic effect relevant to optical shutter and waveguide applications[3].

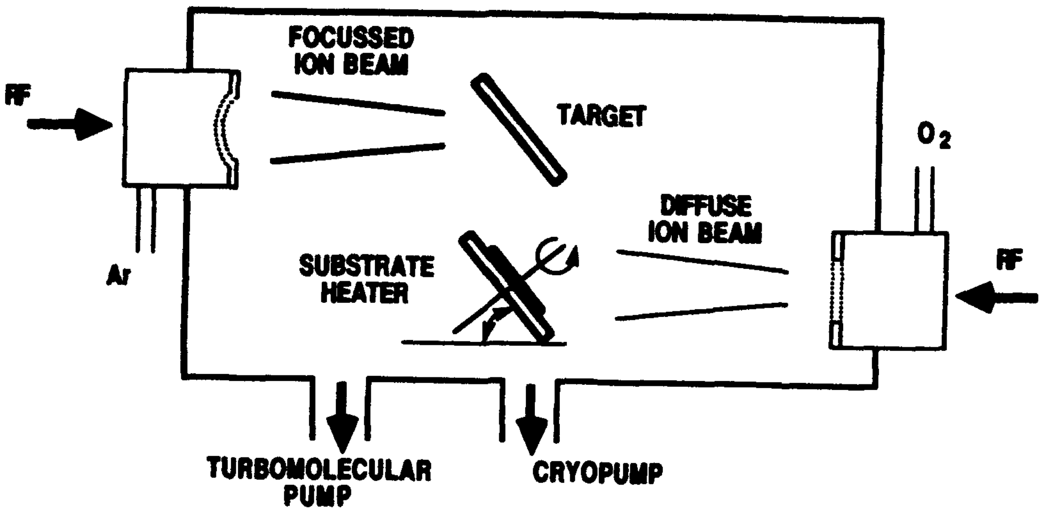

FIGURE 1 Schematic diagram of the DIBS system.

EXPERIMENTAL PROCEDURE

The Nordiko 3450 DIBS system, Figure (1), is composed of a cryo and turbo-molecular pumped chamber, base pressure 5 x 10^{-8}torr, a target turret, an 800°C rotating heater platen and two RF plasma driven ion guns capable of generating ion beams from reactive or inert gases for extended periods of time. The chamber is also fitted with two filamentless electron sources for beam neutralization and two faraday cups for measurement of beam current density. Generally, a high energy argon ion beam in the range 600-700eV, 80-100mA and beam current density (BCD) 1-5mA/cm^2 is used to sputter material from a target while the substrate is immersed in a pure oxygen ion beam of 0-100eV, 0-40mA and BCD 0-0.2mA/cm^2. More energetic oxygen or argon ion beams can be used to clean the substrate prior to film growth. A neutralisation level of 110% is used to ensure stability during the deposition of electrically insulating films. The DIBS process has a number of advantages, including: low pressure deposition (typically 10^{-4}torr); low film contamination (no filmaments); excellent film adhesion; high film density and refractive index; and full anion stoichiometry for reactive deposition.

For PLZT deposition, an adjustable composite target has been developed and is depicted in Figure (2). Pieces of titanium metal and PLZT ceramic are bolted to a copper backing plate through a lead sheet using high purity titanium bolts (>99.9% purity). By varying the configuration and utilising various PLZT ceramic compositions, films of the desired stoichiometry were obtained.

PLZT films have been grown onto (1$\bar{1}$02) sapphire, (100) Mg0, alumina capped silicon and plain silicon substrates. Films of interest as thermal detectors have been grown onto substrates previously coated with 1500Å of platinum to act as a bottom electrode. Films aimed at optical applications were deposited on double polished sapphire or fused silica to allow transmission measurements.

Film composition has been determined by microprobe EDAX using 7.5 or 10 keV electrons over a 100μm square; in combination with film of thickness in excess of 0.5μm, the signal from the substrate could be minimised. Structure was determined by X-ray diffraction (XRD) using Cu_α radiation. Optical properties have been assessed by UV/visible spectrophotometry. Electric and pyroelectric properties were determined either from surface interdigitated electrodes or top and bottom electrode

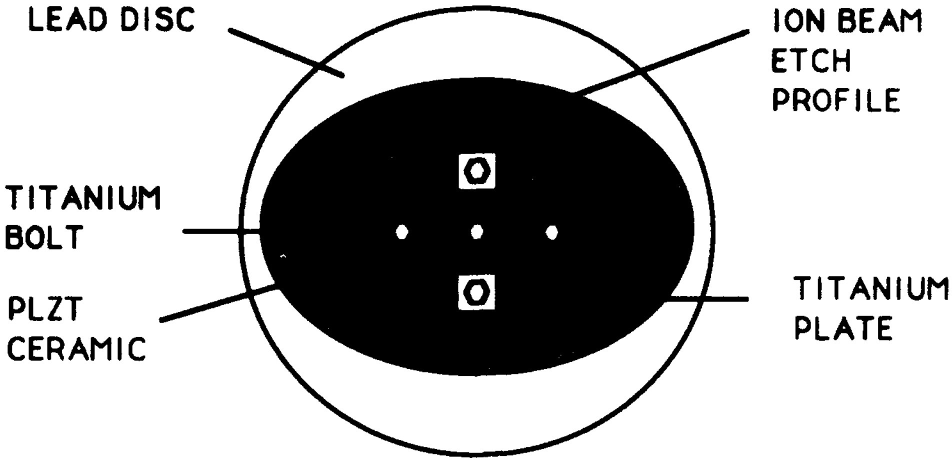

FIGURE 2 Typical Target Configuration for PLZT Sputtering.

using standard bridge techniques.

Some films were annealed after deposition in a tube furnace at 550-750°C in static air or flowing oxygen for 10 hours to induce or improve the perovskite phase. In some cases, PLZT spacer powder was placed around the film during annealing.

RESULTS

For all PLZT films it has been found that the DIBS process suppresses the formation of the pyrochlore phase. Generally, most deposition processes produce the pyrochlore phase in the 450-550°C range and perovskite between 500-650°C[5]. DIBS films are amorphous up to 400°C above which perovskite peaks begin to appear. Above 550°C, the perovskite phase becomes dominant. Trace pyrochlore peaks occasionally appeared on Si, SiO_2 and MgO substrates, but never on sapphire. It is suggested this effect is due to the oxygen ion bombardment which prevents oxygen deficiency. In flowing molecular oxygen (ie, no plasma or ion beam) films were virtually lead free (≤1.0At%) above 450°C and were amorphous. Thus, the effect of the oxygen plasma was retention of significant quantities of lead in the film even up to 650°C. Up to beam energies of 150eV, above which the film growth rate was reduced, the generation of an ion beam from the plasma had little effect on film stochiometry, phase or growth rate, although the refractive index of bombarded films tended to be higher.

In all cases, the dominant parameters controlling the lead content of a film were the target configuration and the substrate temperature. The temperature dependence is an effect common to all vacuum based PLZT thin film deposition processes and is caused by the high volatility of Pb and PbO. Since perovskite formed only above 550°C, the target configuration was adjusted to give the correct composition in this temperature regime. For example, for lead titanate at 580°C a metallic Pb/Ti target that gave a 9:1 Pb:Ti incident atomic flux on the substrate (as measured cold) was required to give 1:1 stoichiometry in the film.

For PLZT (10/0/100) an PLZT (28/0/100), it has been found that an increase in the La dopant level occurs between the target ceramic and the film. A PLZT (28/0/100) target gives PLZT (35-40/0/100) films. Extra titanium on the target or a lesser La doped target ceramic were used to correct this problem. Growth rates have been in the range 0.1-0.25μm/hour. Surprisingly, in view of their relative known sputtering rates, the faster growth rates occurred for ceramic dominated targets and the slowest

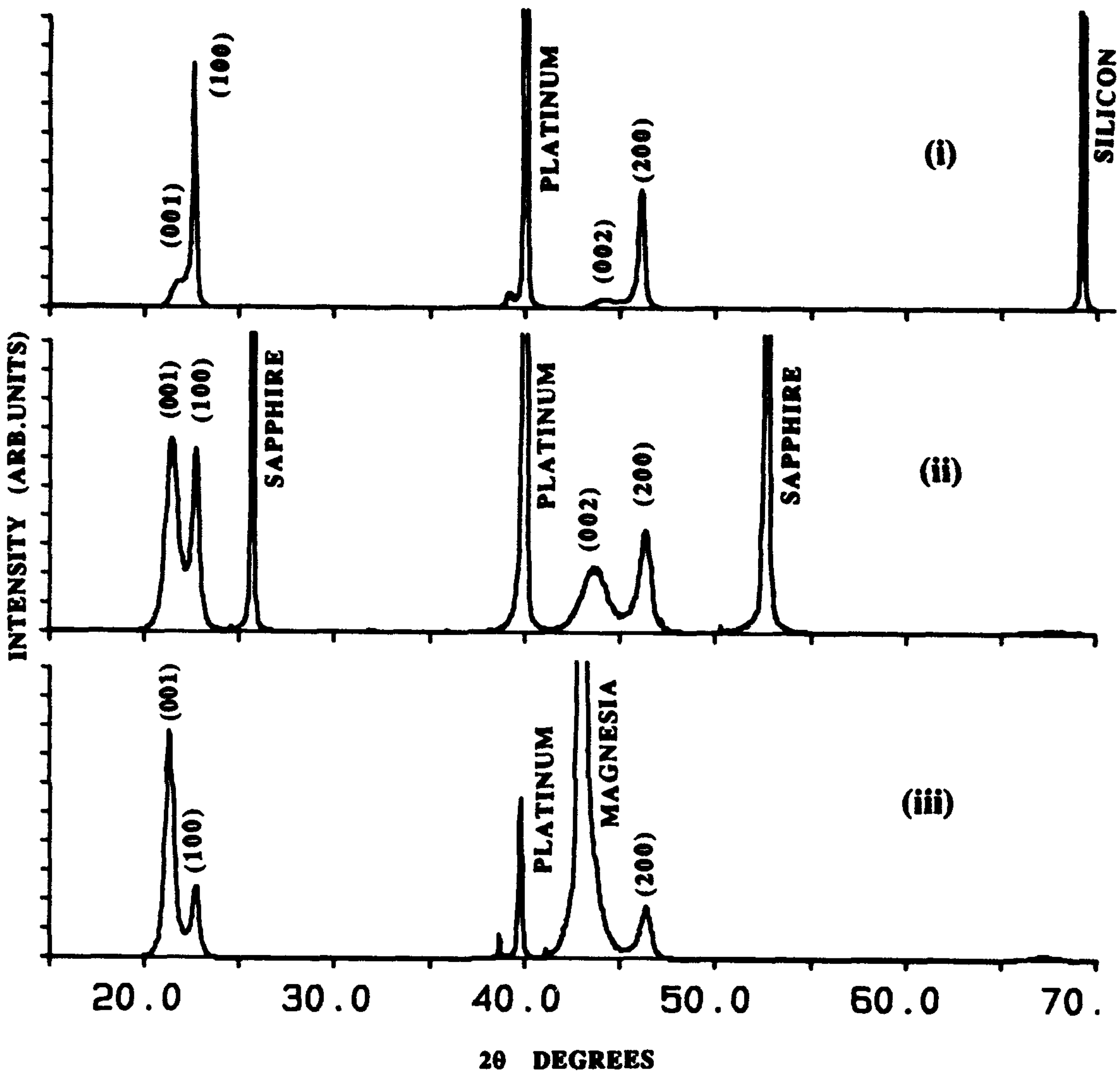

FIGURE 3 XRD traces of lead titanate films on silicon (i), sapphire (ii) and MgO (iii).

for fully metallic targets. Growth rates for films grown below 400°C were of order 0.5μm/hour, but this needs to be offset against the required annealing time.

Figure (3) shows the XRD traces for 1.0μm thick lead titanate films grown onto platinum capped (100) silicon, (1102) sapphire and (100) Mg0. A measure of film orientation has been defined[2]

$$\alpha = \frac{I(001)}{I(001)+I(100)} \tag{2}$$

For lead titanate powder $\alpha = 0.33$, for a film on platinum on silicon $\alpha = 0.10$, for sapphire or platinum on alumina capped silicon $\alpha = 0.51$ and for Mg0 $\alpha = 0.80$. The

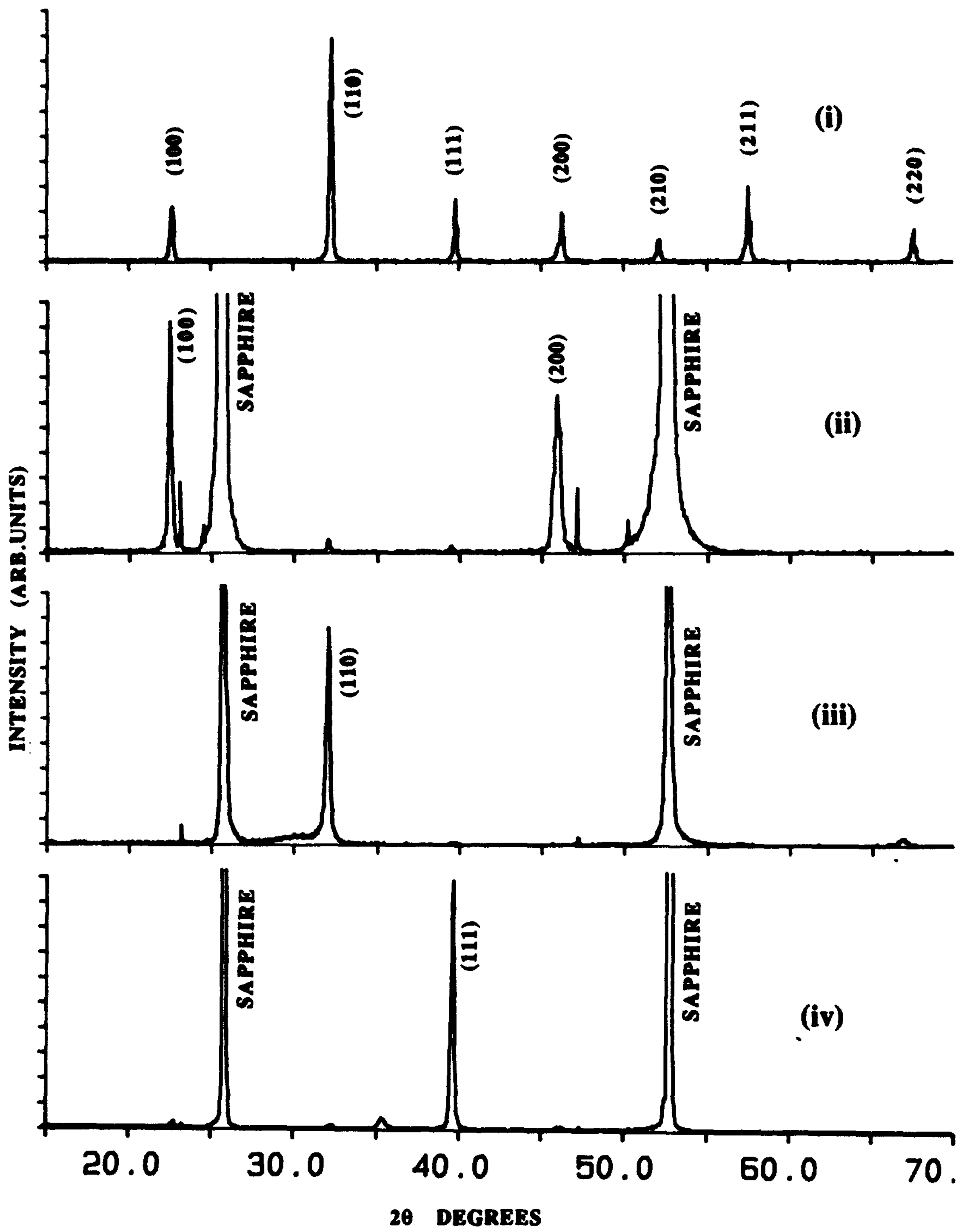

FIGURE 4 X-ray diffraction traces for (i) PLZT(28/0/100) ceramic and for PLZT films on sapphire (ii) - (iv).

orientation behaviour is attributed to thermal expansion mismatch stress between film and substrate. The high thermal expansion coefficient of MgO ($14 \times 10^{-6}K^{-1}$) places the film in compression on cooling and at the cubic-tetragonal phase change forces the longer (001) c axis out of the plane. This is beneficial to thin film pyroelectric properties, but implies that a lead titanate film on silicon for integrated devices tends towards the unwanted (100) orientation due to the small thermal expansion coefficient of silicon. However capping silicon with alumina does force the orientation towards (001) as compared with plain silicon.

To examine the electrical properties of the film 1mm diameter chrome/gold electrodes were applied to the top of the film. For thin films (<0.5 micron) most electrodes were found to have shorts to the bottom electrode but once the film thickness approached 1 micron this proved less of a problem. For the lead titanate films the room temperature dielectric constant was 300 and the loss was 0.033. For La doped films the dielectric constant was higher at 450 and a loss of 0.015. Some pyroelectric activity was observed in films as deposited but this was improved by poling with fields up to 7 kV/mm. Pyroelectric coefficients in the range $0.5\text{-}2.5 \times 10^{-4}$ $Cm^{-2}K^{-1}$ have been measured which translate into a figure of merit F_D of $2.6 \times 10^{-5}Pa^{-0.5}$ for both pure and La doped lead titanate films.

The effect of La doping on lead titanate is to reduce the tetragonality at a given temperature and for PLZT (28/0/100) the structure remains cubic at room temperature. Figure (4(i)) shows an XRD pattern for randomly orientated polycrystalline PLZT (28/0/100). For post annealed films, the XRD trace reveals an identical randomly oriented polycrystalline structure. For in-situ grown perovskite films, the crystalline quality is much higher, but the orientation behaviour is complex. Figures (4(ii), (iii) and (iv)) show XRD traces for (100), (110) and (111) orientated 1μm thick films grown under near identical conditions onto (1102) sapphire. Generally, films with two of these orientations in any combination can occur but complete random orientation never occurs. There is some critical process parameter that controls the resultant film orientation which remains to be identified.

In appearance in-situ depositied perovskite films are smooth, highly transparent with a slight yellow tinge with the PLZT (28/0/100) having a short wavelength transmission limit of 330nm and a refractive index of 2.5-2.6. The PLZT(28/0/100) films have a dielectric constant of 1500 at room temperature but as yet no electro-optic activity has been observed. The reasons for this are unclear but it is suggested that the nature of the DIBS process produces an unusual morphology that inhibits activity; the process has not yet been fully optimised in this respect. Annealed films have a much poorer morphology with a rosette-like structure, extensive cracking and a dielectric constant half that for in-situ deposited films. Uniformity of thickness and composition of the order 2% over 50mm has been achieved for both types of film.

Part of this work has been carried out with the support of the Procurement Executive Ministry of Defence.

REFERENCES

1. G.H. Haertling, Ferroelectrics, 75, 25 (1987).
2. R. Takayama, Y. Tomita, K. Iijima & I Ueda, Ferroelectrics, 118, 325 (1991).
3. H. Adachi, T. Mitsuya, O. Yamazaki & K. Wasa, J. Appl. Phys., 60, 736 (1986).
4. E.M. Griswold, M. Sayer, D.T. Amm & I.D. Calder, Can. J. Phys., 69, 260 (1991).
5. R.A. Roy, K.F. Etzold & J.J. Cuomo, Mat. Res. Soc. Symp. Proc., 200, 141 (1990).
6. H. Adachi, T. Mitsuya, O. Yamazaki & K. Wasa, Jap. J. Appl. Phys., 24, 13 (1985).

Ferroelectrics, 1992, Vol. 134, pp. 303–312
Reprints available directly from the publisher
Photocopying permitted by license only

TfC17

MICROSTRUCTURAL, COMPOSITIONAL AND ELECTRICAL CHARACTERIZATION OF FERROELECTRIC LEAD ZIRCONATE TITANATE THIN FILMS

MARIA HUFFMAN, F.D. GEALY, LEE KAMMERDINER, PETER ZURCHER
Ramtron International Corporation, Colorado Springs, Colorado, U.S.A.

JANE G. ZHU, MOWAFAK AL-JASSIM
National Renewable Energy Laboratory, Golden, Colorado, U.S.A.

CHUCK ECHER
National Center for Electron Microscopy, Berkeley, California, U.S.A.

Abstract Thin lead zirconate titanate (PZT) ferroelectric films are currently being used in a variety of applications. One of the more novel uses is in non-volatile random access memory devices. In this study, polycrystalline ferroelectric thin films were rf-sputtered on Pt-metallized Si wafers. La-doped as well as undoped PZT films were analyzed. The microstructure was examined by X-ray diffraction and TEM. The electrical characterization was carried out on discrete PZT capacitors by using switching measurements between 20 and 150° C. Nanoprobe analysis of the composition of the films has also been performed and the difficulties of obtaining reliable analytical results are explored in detail. The data obtained from these electrical and microstructural studies were correlated and modeled in order to directly relate switching to the microstructure required for improved device performance.

INTRODUCTION

Thin film PZT ferroelectrics are currently being used as elements in non-volatile memories[1]. In this application, their thickness is usually less than 0.5 micron. The most important issue in semiconductor memory fabrication is the integration of the ferroelectric films in a complete process without significant degradation. For example, in a typical semiconductor process flow, PZT will experience a variety of anneals in several ambients. Thus, stability in morphology and composition is of utmost importance.

In this study, various PZT compositions have been analyzed at both room and elevated temperatures in order to understand any degradation mechanisms that may occur in the thin films with thermal cycling. The sample compositions are described by the standard PLZT formalism (La/Zr/Ti at%). A, stands for a PZT sputtering process using an eight inch ceramic target and B stands for a PZT sputtering process using a five inch target. Both undoped and La-doped samples have been included in this analysis. Based on the bulk ceramic phase diagrams[2,3], these compositions should produce the tetragonal perovskite ferroelectric phase.

Room temperature and in-situ hot stage TEM was used to analyze the morphology of all the films and to record any structural changes with temperature. Only a La-doped sample was heated in the microscope for this study up to 500° C. Several other PZT films have been thus analyzed and results have been reported in an earlier paper[4]. Detailed nanoprobe analyses were carried out on all samples to investigate any compositional inhomogeneities. Accurately measuring the Pb content in the films is quite difficult. Only thicker areas of the samples give a more reasonable measure of Pb. The very thin, ion-milled areas are always Pb-poor, so they cannot be used for analysis.

There is quite a variability in the lead content of the samples which also affects the measured Zr/Ti ratios obtained. However, if all the potential problems are recognized, reasonable analyses can be obtained.

TEM and X-ray diffraction (XRD) show that all rf-sputtered samples are amorphous in the as-deposited state. XRD has been performed at temperatures between 400-650° C in order to document the perovskite formation. Interesting differences have been recorded on the formation temperature of the perovskite phase. In this investigation, La-doped films develop the perovskite phase at a lower temperature than the undoped samples.

Electrical characterization was performed on all films from 20° C to 150° C. Significant degradation with temperature was found on films sputtered under the same conditions using 5 inch targets. This degradation is characteristic of an increased non-ferroelectric "gap" region in series with the ferroelectric material and a decrease in the spontaneous polarization (P_S) and coercivity. This occurs only when the films are heated in a poled state and is fully recoverable when the samples are rapidly annealed at 550° C. The film sputtered under different conditions using an 8 inch target exhibited much less degradation which was characterized by only a slight reduction in the spontaneous polarization. Although the specifics of the above sputtering processes cannot be disclosed, the most significant point to be made is that the processing variables are as important as the film composition. The above mentioned degradation has also been interpreted by an electrostatic model[5] (conceptually similar to that reported earlier by Selyuk[6]) which agrees with the data reported in this study.

EXPERIMENTAL

PZT films were rf-sputtered on Pt-metallized Si wafers. The thickness of the ferroelectric films varied between 2,500 and 3,500 Å. Pt was also used to form the top electrode material for electrical characterization. TEM and AEM examinations were performed using a JEOL JEM 200CX AEM operating at 200 kV. The 200CX is equipped with a KEVEX System 8000 and two X-ray detectors: (1) a high angle EDS detector and (2) an ultra thin window EDS detector for light elements (Z = 6 and up). Further, the hot stage work was done using a Ta heated specimen holder Gatan 628-Ta. The samples used for the TEM work were first mechanically polished, and then ion milled from the substrate side. The sputtering rates of the various components in PZT differ appreciably from each other and it is possible that any kind of sample preparation process that involves sputtering will cause some degradation or artifacts. Therefore, milling was kept to a minimum whenever possible. All TEM samples were mounted on Molybdenum grids.

All PZT samples were further analyzed by in-situ hot stage XRD as a function of temperature. As-deposited samples were heated in air on a Ta strip heater with a thermocouple attached. Temperature control was better than +/- 1° C. Traces were started after about two minutes at temperature and run at a rate of 5 degrees per minute over a 2θ range of 20 to 60 degrees. The samples were then ramped up to the next temperature and the traces repeated. The total annealing time at each temperature was 10 minutes per sample.

Electrical characterization was carried out on 100 x 100 μm^2 discrete capacitors using an HP 8175A arbitrary waveform generator and a Tektronix 2430A digital oscilloscope. Hysteresis loops were measured with a 3 cycle 50 kHz triangular wave burst starting and ending at 0 V. Pulse switching measurements were made with a 5 pulse sequence consisting of one pulse at the measurement potential to set the state followed by a switching pulse, a non-switching pulse of the same polarity, a switching pulse of opposite polarity and a non-switching pulse. All pulse widths were 1 μs with a delay between pulses of 1 s. Switching kinetics were sufficiently fast to obtain saturated charge values in the requisite times. Measurement configuration was a simple Sawyer-

Tower capacitor divider with load capacitance 100x the ferroelectric capacitance, thereby ensuring that the applied potential dropped primarily across the ferroelectric capacitor. The charge was calculated from the potential across the load capacitor, 0.8 μs after the leading edge of the pulse.

RESULTS AND DISCUSSION

Microstructural Analysis

Representative XRD spectra and the corresponding TEM micrographs of all samples analyzed are included in Figure 1. The micrographs are showing the final perovskite phase after annealing at 650° C in oxygen. There is grain size variability between the samples. Sample A(0/48/52) has well formed, uniform grains with clean grain boundaries. Grain sizes vary between 3-5 kÅ. The domains are clearly seen in this sample. B(0/48/52) has smaller grains (1-2.5 kÅ) and a significantly different morphology. This is important to note since the two above-mentioned films come from targets with the same composition but different processing. Sample A(0/48/52) has better overall ferroelectric characteristics than sample B(0/48/52). The two La-doped samples, B(1/48/52) and B(3/30/70) show relatively non-uniform grain size with several grains in the range of 1-2 kÅ and then some large grains ranging between 4-5 kÅ. It is interesting to note that only in the larger grains (close to 5 kÅ) domain structure can be seen. This might indicate the existence of a critical grain size for twinning (and domain formation) to occur. Thus far, results have been quite consistent in a variety of films analyzed. Out of the B-process samples, the best morphology is exhibited by sample B(3/30/70).

Analysis of the XRD spectra in Figure 1 shows that at 400° C there are no perovskite peaks. However, there might be a hint of a peak (visible only after expanding the spectra significantly) at about 30° 2θ (for clarity, the (111) and (200) platinum bottom electrode peaks have been removed). With a subsequent increase in temperature to 500° C, the peak at 30° 2θ increases although it is still very broad. Also, very small peaks begin to appear near 22° and 45° 2θ. For the B(3/30/70) sample at this temperature, the latter two peaks are distinctly better defined than for the other samples. A further increase in temperature to 525° C produces much larger and sharper peaks at 22°, 38° and 45° 2θ, but the broad peak near 30° actually shrinks. Increasing the temperature to 550° C, produces even larger peaks at 22°, 38° and 45°, with the complete disappearance of the 30° peak. Proceeding to 650° C does not change the traces appreciably.

Although it is difficult to identify a phase from only one peak, the breadth of the 30° peak indicating high disorder and the lack of stability above 550° C strongly suggest that this peak belongs to the pyrochlore phase. The other peaks are readily identified as belonging to the perovskite phase. Since these films have a composition on the titanium rich side of the morphotropic phase boundary (MPB), one would expect to see the tetragonal phase for bulk samples . Near the MPB, a and c lattice constants differ by approximately 3%[2]. This is easily determined by pairs of peaks such as (100) and (001) near one another. However, in thin films there is only one peak. This could correspond to a cubic phase but the ferroelectric behavior seen in all these films rules this out. It would be tempting to conclude that the film is rhombohedral, in which case the resolution of XRD is incapable of seeing the pairs of peaks. It is also possible that the small grain sizes and effects of stress cause the small difference in a and c values to be indistinguishable. It is not possible to resolve this difficulty at the present time.

The formation of perovskite at slightly lower temperatures for sample B(3/30/70) could be due to either the 3% La , or the difference in Zr/Ti ratio or even to the different amounts of excess PbO in the various films which can act as a flux during grain growth. At this time, the exact cause for this lower formation temperature is not certain. In fact, it is highly likely that this would also be a function of the film deposition conditions, the machine and the technique used for sputtering, and the overall processing of the films.

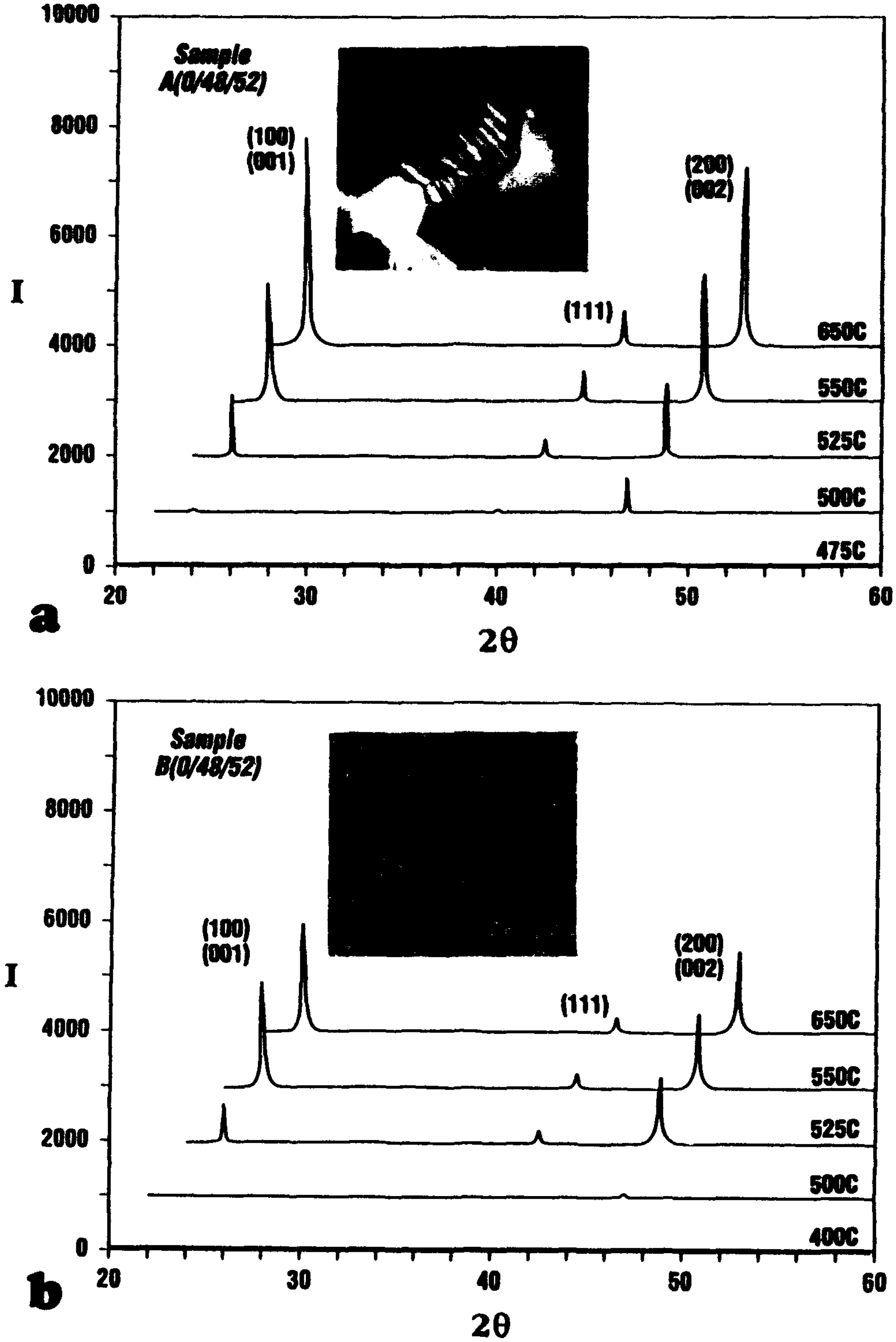

FIGURE 1 XRD spectra and correspondingTEM micrographs of samples analyzed (a,b,c,d). See text for details.

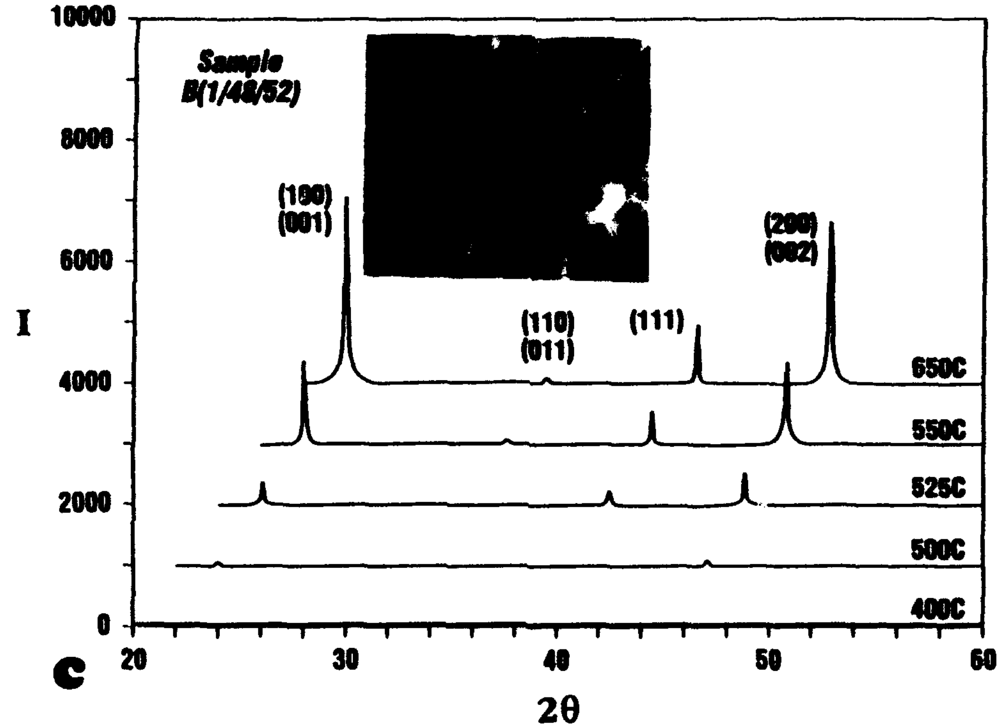

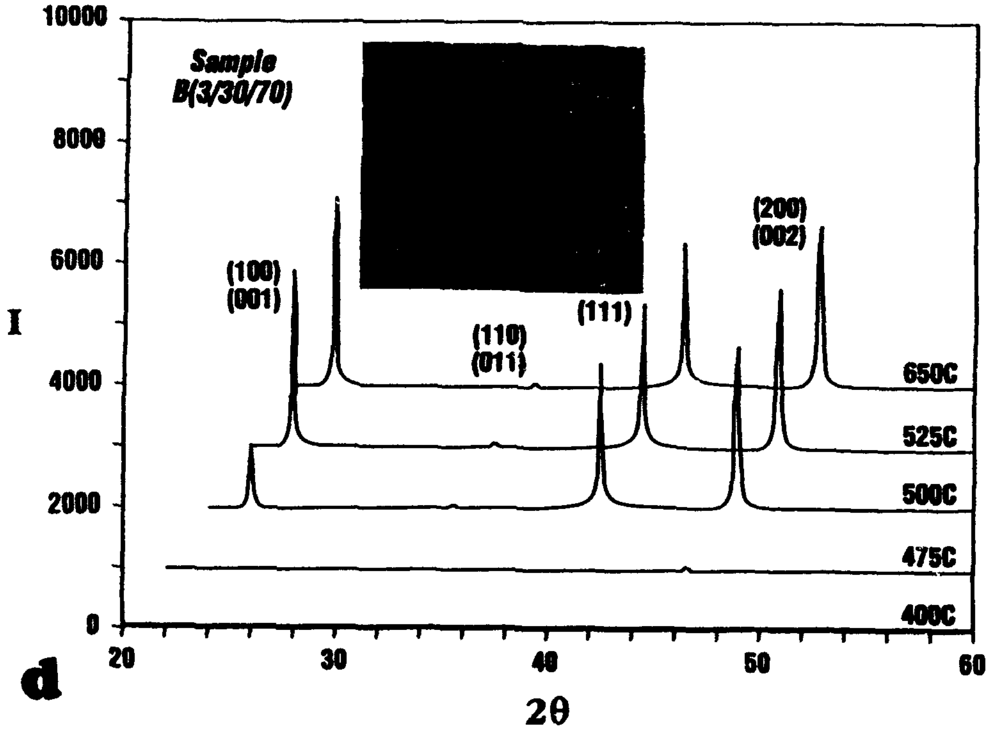

FIGURE 1 continued

<u>Compositional Analysis</u>

The compositional characterization of all films was carried out by nanoprobe EDS. All analyses were performed at room temperature. Electron beam sizes of 65, 100, 150 and 200Å were used. In this study, some hydrocarbon build-up was seen on the specimens examined at room temperature but it was not serious. The analyses were performed either with spot mode or rastered beam conditions. At least three different areas were analyzed per sample. Good counting statistics were difficult to obtain from very thin areas. Also, these areas were consistently Pb deficient and thus not reliable for analysis. Good data were obtained from relatively thicker areas of the foils. The matrix in all the PZT samples is Pb-rich and it absorbs X-rays. Thus, significant errors can be introduced in the absolute concentration of each element.

A

B

FIGURE 2 TEM micrograph of sample B(3/30/70) at 500° C. A: degraded area and B: remaining PLZT area.

Figure 2 is a plan-view of sample B(3/30/70) at 500° C. Part of it has been transformed to a Ti-Zr-O containing material and all the Pb has been completely removed from the original sample. This can be compared to Figure 1d, where the same sample is shown at room temperature and before any heating. It is obvious that the sample at 500° C and by further local heating from the beam has been irreversibly changed. This is interesting for two reasons. Firstly, when an analysis was performed on sample B(3/30/70) before the hot stage treatment, the Zr/Ti ratio was close to 40/60. La was very close to the expected 3%. The Pb concentration was a bit higher than stoichiometric as expected since all sputtering targets have excess PbO. However, after the heating run in the microscope, and since all the Pb was lost, a repeat analysis of the same sample produced Zr/Ti ratios of about 30/70, the nominal composition. The La was basically the same. Thus one can easily experience an error of 10 atom % in the Zr and Ti concentrations due to the Pb influence. In general, variability in the Pb content in the films will also cause Zr/Ti variabilities in the EDS measurements. In this study, the best results were obtained by analyzing thicker areas of the samples where milling had not significantly altered the Pb content. After all the above-mentioned problems were taken into account, all samples showed Zr/Ti ratios reasonably close to nominal for each composition with slight variability which is not totally unexpected for these films[4]. The La in the doped PZT samples was fairly uniformly distributed and no indication of segregation was found. Depending on the process and deposition conditions for each sample, the Pb content is the most variable and difficult to control and analyze reliably.

The second reason the complete Pb loss in sample B(3/30/70) is interesting is the fact that this may be associated with the amount of excess PbO in PZT thin films. PZT should not break down to its component oxides at temperatures less than at least 1200-

1300° C[2]. It is doubtful that the temperature reached locally on the sample was that high. However, local heating by the electron beam could aid the melting and evaporation of any significant excess PbO and the subsequent breakdown of the perovskite. This phenomenon is still under investigation.

Electrical Characterization

Films were characterized with pulse switching and hysteresis loops as a function of both potential and temperature. Figure 3 (Q vs. V vs. T) shows the results of these measurements for all films. The upper surface in these plots shows the switching results for a single polarity while the lower surface shows the non-switching results for the same polarity. The procedure used was to measure Q vs. V characteristics at 20° C then increase the temperature in 30° C increments to 150° C. After taking measurements at 150° C, the temperature was decreased using the same steps back to 20° C. Note that loss of switching with temperature is essentially recoverable for A(0/48/52), but is not recoverable for the other samples. B(0/48/52) has the same nominal composition as A(0/48/52). Note that the decrease in switched charge ($2P_S$) and the increase in non-switched charge for A(0/48/52) is linear with temperature as has been reported previously

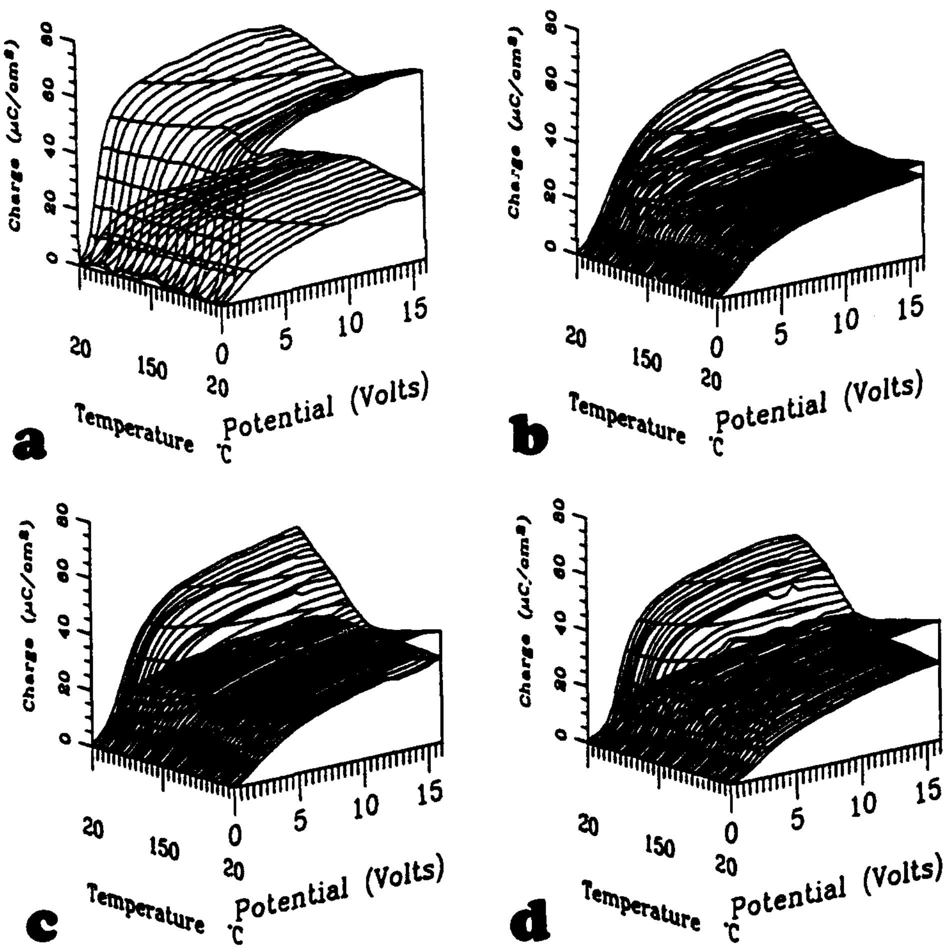

FIGURE 3 Q vs. V vs. T plots for: a) Sample A(0/48/52); b) Sample B(0/48/52); c) Sample B(1/48/52) and d) Sample B(3/30/70).

for other samples[4]. The linear Q vs. T characteristics for switched and non-switched charge intersect at the Curie point where the switched charge goes to zero. Recovery upon temperature lowering is greatly reduced for the samples sputtered from the smaller targets. Representative room temperature hysteresis loops for B(0/48/52) and B(3/30/70) are shown in Figure 4 for the same triangular pulse voltage sweep both before and after thermal cycling.

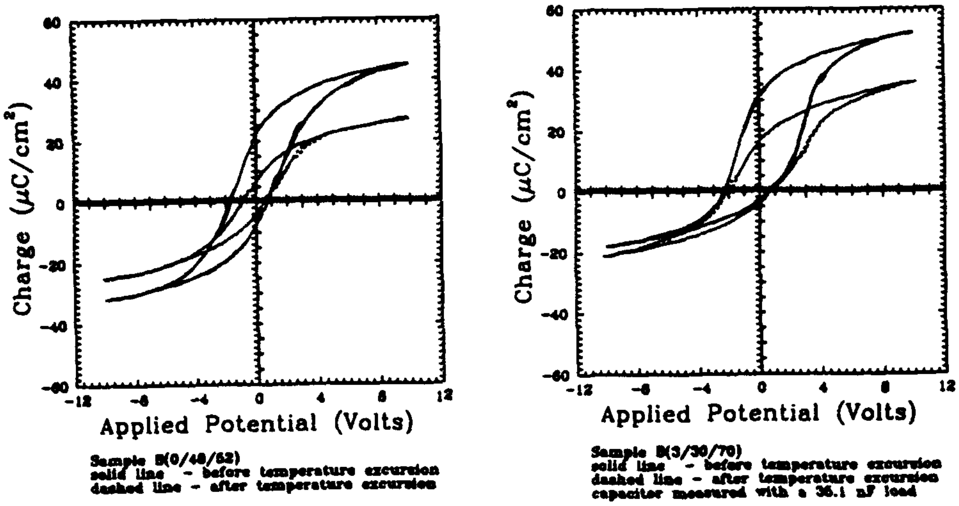

FIGURE 4 See text for details.

To first order, the dominant switching effects for the samples in this study are the ones resulting from the particular sputtering conditions and are composition independent. However, there seems to be a correlation between grain size of the films and observed switching characteristics. Sample A(0/48/52) has the best morphology and the best characteristics. Out of the B-process samples, B(3/30/70) shows the best properties. The hysteresis loops shown in Figure 4 are consistent with capacitor degradation as an increasing non-ferroelectric "gap" region (slope of the hysteresis loop) and a decrease in the spontaneous polarization and coercivity.

The working hypothesis is that the B-process samples are sputtered under conditions resulting in a highly defected perovskite. As in the case of other perovskites[7], vacancy defects are charged and migration is fast under the large fields present in these thin films. As these defects segregate to the electrode and grain interfaces, they cause more disorder and the ferroelectric lattice distortion disappears. This increases the non-ferroelectric "gap" in these regions. As the bulk is depleted of vacancies, compensating interstitials and anti-site defects form and reduce the ferroelectric distortion thereby making the material easier to switch and P_S smaller.

The changes in switching characteristics at constant temperature were simulated using a multi-grain, one-dimensional, quasi-static model by increasing the non-ferroelectric interface "gap" and decreasing the spontaneous polarization, coercivity, and bulk permittivity while maintaining constant film thickness. This simulation is shown in Figure 5. Note that both upper surface (switched charge) and lower surface (non-switched charge) are consistent with the measured data before and after the temperature excursion.

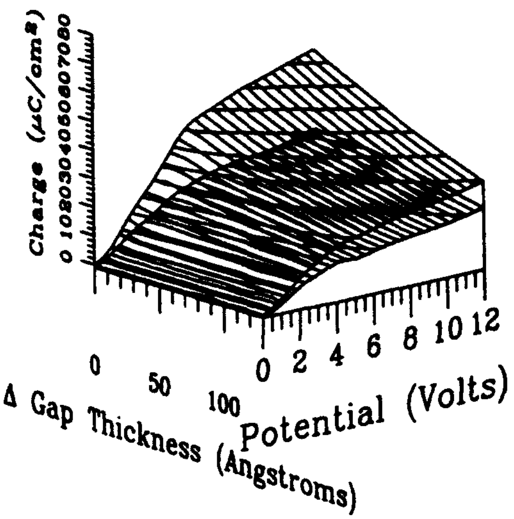

FIGURE 5 Switching surfaces simulated as a function of increasing non-ferroelectric gap and potential for a coercivity and P_S fit to the room temperature data shown in Figure 3b. See text for details.

CONCLUSIONS

1) In ferroelectric memory fabrication, processing is the major factor affecting the properties of thin PZT films.
2) Depending on the film, there is degradation with temperature characterized by both an increased "gap" region in series with the ferroelectric material and a decrease in P_S. In good quality samples, the degradation mechanism is mostly manifested as a slight reduction of P_S.
3) There are slight compositional inhomogeneities in the films analyzed and the Pb is the most variable and difficult to control and to analyze reliably. La does not segregate in the samples used in this study.
4) Hot stage XRD analysis has revealed that in the La-doped samples (especially sample B(3/30/70)) the perovskite forms at a slightly lower temperature than in the undoped samples.
5) A multi-grain, one-dimensional, quasi-static model of the observed decrease in switched charge with thermal cycling shows a good fit to experimental data.

ACKNOWLEDGEMENTS

The authors would like to thank Alice Mason of NREL for printing the TEM micrographs, Becky Weaver of Ramtron for analytical support (XRD and EDS) Tom Davenport of Ramtron for depositing the various PZT films and Teresa Mudrick of Ramtron for digitizing the XRD spectra for publication. The use of NCEM is greatly appreciated.

REFERENCES

1. D. Bondurant and F. Gnadinger, IEEE Spectrum, Vol. 18 (7), 30 (1989).
2. B. Jaffe, W.R. Cook,Jr. and H. Jaffe, Non-Metallic Solids, Vol.3 (Piezoelectric Ceramics), J.P. Roberts and P.Popper, eds., Academic Press Inc., London and New York, 1971, p. 136-137.
3. G.H.Haertling and C.E. Lang, J. Am. Ceram. Soc., Vol.54, 1 (1971).
4. M. Huffman, J.P.Goral, M.M. Al-Jassim and C. Echer, J. Vacuum Sci. and Technol. A, to be published Jul/Aug 1992.
5. To be published.
6. B.V. Selyuk, Soviet Physics-Solid State, Vol.8 (12), 2803 (1967).
7. F.D 'ealy, Photoelectrochemical Determination of the Low Temperature Redox Ki ics in $SrTiO_3$, Ph.D. Thesis, MIT, 1989.

Ferroelectrics, 1992, Vol. 134, pp. 313–318
Reprints available directly from the publisher
Photocopying permitted by license only

TfC23

PHASE TRANSITIONS IN FERROELECTRIC FILMS

D. R. TILLEY
Department of Physics, University of Essex, Colchester
CO4 3SQ, UK

B. ZEKS
Institute of Biophysics, Medical Faculty, University of
Ljubljana and J. Stefan Institute, Ljubljana, Slovenia

Abstract The system considered is a ferroelectric film between metal electrodes with polarization normal to the interfaces. The critical temperature T_c is depressed by the depolarization field, the film thickness ℓ_c for T_c to be reduced to zero being or order 10^3 times the Thomas-Fermi screening length of the electrodes. For a film with no electrodes the ferroelectric phase is completely suppressed. The variation of T_c with $\ell > \ell_c$ follows a simple hyperbolic law which should be open to experimental test.

INTRODUCTION

The experimental evidence concerning the influence of surfaces and sample size on ferroelectric phase transitions, reviewed briefly elsewhere,[1] does not exhibit any simple uniformity of results. In some materials, it appears that a surface layer orders before the bulk of the sample,[2] whilst in others[3,4] the opposite seems to occur. The influence of depolarization in reducing the critical temperature of a film was studied by Wurfel and Batra,[5] following earlier theoretical work,[6] in a study of a TGS film between one metal and one semiconducting electrode.

Two different mechanisms have been investigated theoretically. As mentioned, Batra et al[6] studied the influence of depolarization. They stressed that the phase transition is that of the

complete system of ferroelectric film plus electrodes and showed that semiconducting electrodes lead to a depression of the critical temperature and can change the nature of the phase transition from second order to first. Somewhat later, various authors[7-10] studied the implications for phase transitions within the Landau-Devonshire theory of the symmetry-allowed boundary condition

$$\mathbf{n}.\ \nabla \mathbf{P} + \delta^{-1}\mathbf{P} = 0 \tag{1}$$

The extrapolation length δ can have either sign. If it corresponds to an increase of $\mathbf{P}$ at a surface then on a semi-infinite sample a separate surface-ordered phase appears at a higher initial temperature than that of the bulk material, and in a thin film the critical temperature is enhanced above the bulk value. If $\mathbf{P}$ decreases at a surface there is no separate surface phase transition on the semi-infinite material and the critical temperature of a thin film is depressed. A fuller summary of the results has been given recently.[1]

Depolarization effects for the special case of perfectly conducting electrodes have been included previously within the Landau theory.[9,10] The free-energy expression for a ferroelectric film between metallic electrodes in which screening is described within Thomas-Fermi theory has been derived and applied to show that depolarization generally reduces the critical temperature.[1] This expression contains as a special case a description of a film in which no boundary condition like Eq.(1) is assumed. This is of interest since there is as yet no experimental evidence to support Eq.(1), whereas the influence of depolarization is obvious on general grounds and is also experimentally established.[5] Furthermore, the question has some practical significance for ferroelectric thin film devices. In this paper, therefore, we consider the effects of depolarization alone by studying the implications of the previous formalism in the limit $\delta \rightarrow \infty$.

FORMALISM

The starting point is the general expression for the free energy of a

ferroelectric film of thickness ℓ between metallic electrodes of thickness $\frac{1}{2}(L-\ell)$; this is given as Eq.(35) of ref.1. We take the special case of zero applied voltage, $V_0 = 0$, and thick electrodes, $L >> \ell$ and $L >> \ell_s$, where ℓ_s is the Thomas-Fermi screening length. This means that the quantities α and β of ref.1 are both equal to unity. As stated previously, it is also assumed that $\delta \to \infty$, so that the condition at the film-electrode interface is simply $dP/dz = 0$. Thus P is independent of z within the film and the integrals appearing within the free-energy expression become constants. The expression for the free energy per unit area of the film-electrode system reduces to

$$\frac{F}{S} = \ell\left(\frac{1}{2}AP^2 + \frac{1}{4}BP^4\right) + \frac{\ell_s \ell}{\varepsilon_0 \varepsilon_F (2\ell_s + \ell)} P^2 + \frac{\ell^2 \ell_s}{4\varepsilon_0 \varepsilon_e (2\ell_s + \ell)^2} P^2 \qquad (2)$$

Here A and B are the usual Landau-theory expansion coefficients, $A = A_0(T/T_{co} - 1)$ and $B > 0$, where T_{co} is the bulk critical temperature. It is assumed that the bulk phase transition is of second order; the potentially important extension to first-order phase transitions would require $B < 0$ and the addition of a term GP^6 with $G > 0$. ε_F and ε_e are the background dielectric constants of the film and electrodes, and ℓ and ℓ_s are the film thickness and the Thomas-Fermi screening length. The second and third terms in Eq.(2), which are both positive, result from incomplete compensation of the polarization charge.[5] They increase the coefficient of P^2 in Eq.(2) and since the critical temperature T_c is found by equating this coefficient to zero their effect is to reduce T_c below the bulk value T_{co}. This is the same effect as occurs with semiconducting electrodes.[6] The explicit equation for T_c is

$$A_0\left(\frac{T_c}{T_{co}} - 1\right) + \frac{2\ell_s}{(2\ell_s + \ell)\varepsilon_0 \varepsilon_F} + \frac{\ell \ell_s}{(2\ell_s + \ell)^2\, 2\, \varepsilon_0 \varepsilon_e} = 0 \qquad (3)$$

Two limits of Eq.(3) are immediately apparent. First, for $\ell_s \to 0$, corresponding to infinite conductivity in the electrodes and perfect charge compensation, the second and third terms vanish so

that T_c is not shifted from T_{co}. Second, for $\ell_s \rightarrow \infty$,in effect the absence of electrodes,

$$A_0\left(\frac{T_c}{T_{co}} - 1\right) + \frac{1}{\varepsilon_0 \varepsilon_F} = 0 \tag{4}$$

This can be derived in a more elementary way.[11] For a free-standing film with polarization normal to the interfaces the salient terms in the free energy are

$$F = \frac{1}{2}\ AP^2 - \frac{1}{2}EP + \frac{1}{4}BP^4 \tag{5}$$

Since $D = 0$ outside the film the boundary condition is

$$P + \varepsilon_0\, \varepsilon_F\, E = 0 \tag{6}$$

Substituting for E from Eq.(6) into Eq.(5) and equating the coefficient of P^2 to zero one recovers Eq.(4).

One further result may be derived from Eq.(3). It is clearly of interest to know the thickness ℓ_c for which T_c is reduced to zero. This follows from putting $T_c = 0$ in Eq.(3):

$$\frac{2\ell_s}{(2\ell_s + \ell_c)\varepsilon_0 \varepsilon_F} + \frac{\ell_c \ell_s}{(2\ell_s + \ell_c)^2 2\varepsilon_0\, \varepsilon_e} = A_0 \tag{7}$$

RESULTS

The susceptibility for $T > T_c$ is $\chi = A_0^{-1}\ (T - T_c)^{-1}$, so A_0 is just the Curie constant; a typical value for a displacive ferroelectric is 2×10^5 $JmK^{-1}C^{-2}$ (J.F.Scott private communication). With $\varepsilon_F = 1000$, Eq.(7) yields

$$1.771 \times 10^{-3} = \frac{2}{2 + x_c} + \frac{\varepsilon_F}{\varepsilon_e}\ \frac{x_c}{2(2 + x_c)^2} \tag{8}$$

where $x_c = \ell_c/\ell_s$. Clearly the solution is $x_c >> 1$, so it is satisfactory to retain only the leading terms in x_c; this gives

$$x_c = \frac{4 + \varepsilon_F/\varepsilon_e}{2A_0\varepsilon_0\varepsilon_F} \tag{9}$$

Here the main uncertainty is the value of ε_e. It is the long-wavelength limit of the Thomas-Fermi static dielectric function, which is formally infinite.[12] It enters Eq.(2) via the boundary

condition on normal D at the electrode-ferroelectric interface. Since this could be modified by trapped charge we take the view that $\varepsilon_F/\varepsilon_e$ should be treated as a parameter. With $\varepsilon_F/\varepsilon_e = 0$ and the values in Eq.(8), Eq.(9) gives $x_c = 1.13 \times 10^3$. For Au electrodes, for example, in which $\ell_s = 0.83$Å, this gives a critical value $\ell_c = 940$Å.

The variation of T_c with ℓ is given by Eq.(3). With the retention of only leading terms in $x = \ell/\ell_s$, Eqs.(3) and (9) lead to

$$1 - t = \frac{x_c}{x} \qquad (10)$$

where $t = T_c/T_{co}$. This simple variation is illustrated in Fig.1.

For the film without electrodes, the value of $A_0\varepsilon_0\varepsilon_F$ appearing as the left-hand side of Eq.(8) means that Eq.(4) becomes

$$\frac{T_c}{T_{co}} - 1 = -5.65 \times 10^2 \qquad (11)$$

which clearly has no solution $T_c > 0$, so the phase transition is completely suppressed in this case.

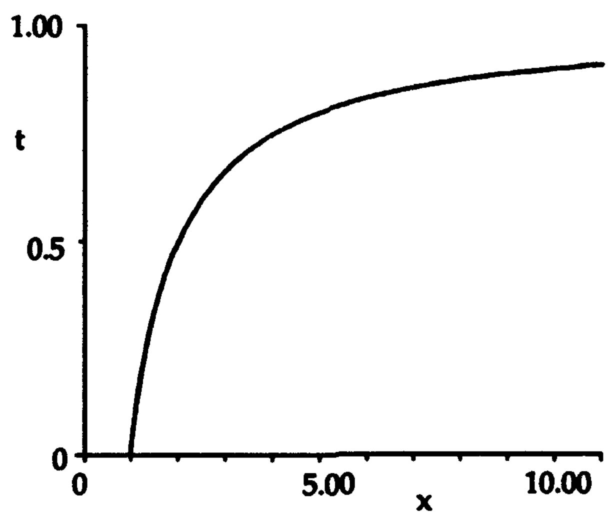

FIGURE 1 Variation of film critical temperature T_c/T_{co} with thickness ℓ/ℓ_c, where ℓ_c is the thickness for which $T_c = 0$, given by Eq.(9).

DISCUSSION

The influence of depolarization on the critical temperature of a ferroelectric film encased in metal electrodes is described by Eq.(3). The critical value of thickness ℓ_c at which the critical temperature vanishes is given by Eq.(9), in which it is suggested that $\varepsilon_F/\varepsilon_e$ may be treated as a parameter. Typical numerical values give $\ell_c \sim 10^3 \ell_s$, where ℓ_s is the Thomas-Fermi screening length in the electrodes. For a good metal ℓ_s is of order 0.5 to 1Å, giving $\ell_c \leq 1000$Å, which it is hoped might be accessible to experiment. The variation of critical temperature with thickness $\ell > \ell_c$ is given by Eq.(10) and illustrated in Fig.1. The slow approach to the bulk value arising from the x^{-1} dependence in Eq.(10) should also be capable of experimental test.

ACKNOWLEDGEMENTS

We thank Profs. J. Fousek and J.F.Scott for helpful discussions.

REFERENCES

1. D.R. Tilley, to be published in Ferroelectric Ceramics, ed.N. Setter (Birkhauser, Switzerland 1992).
2. U.T. Höchli and H. Rohrer, Phys.Rev.Lett., 48, (1982).
3. P. Marquardt and H. Gleiter, Phys.Rev.Lett., 48, 1423 (1982).
4. X. Gerbaux and A. Hadni, Phase Transitions, 14, 117 (1989).
5. P. Wurfel and I.P. Batra, Phys.Rev.B, 8, 5126 (1973).
6. I.P. Batra, P. Wurfel and B.D. Silverman, Phys.Rev.Lett., 30, 384 (1973).
7. T.C. Lubensky and M.H.. Rubin, Phys.Rev.B, 12, 3885 (1975).
8. R. Kretschmer and K. Binder, Phys.Rev.B, 29, 1065 (1979).
9. K. Binder, Ferroelectrics, 35, 99 (1981).
10. M.G. Cottam, D.R. Tilley and B. Zeks, J.Phys.C, 17, 1793 (1984).
11. J. Fousek, private communication.
12. N.W. Ashcroft and N.D. Mermin, Solid State Physics, (Holt, Reinhart and Winston, New York 1976).

Ferroelectrics, 1992, Vol. 134, pp. 319–323
Reprints available directly from the publisher
Photocopying permitted by license only

TfP205

PREPARATION OF LEAD TITANATE THIN FILMS BY REACTIVE ELECTRON BEAM COEVAPORATION USING OZONE

SHOICHI MOCHIZUKI, TOSHIYUKI MIHARA, SABURO KIMURA and TADASHI ISHIDA
Government Industrial Research Institute, Osaka,
Ikeda, Osaka 563 Japan

Abstract Lead titanate($PbTiO_3$) thin films were prepared by reactive coevaporation of lead and titanium with an electron beam gun. Each of evaporation rates of lead and titanium was independently controlled by each quartz crystal thickness monitor. To promote oxidation of deposited films, a mixed gas of oxygen and ozone was used. When the ratio of lead to titanium was controlled properly, perovskite phase $PbTiO_3$ was obtained at substrate temperature of 550°C without post thermal annealing on glass substrates. The deposition rate was 110nm/min, which was larger than that of prepared by sputtering method and that of prepared by coevaporation without ozone. The ratio of lead to titanium of the perovskite phase films was nearly equal to that of standard $PbTiO_3$ powder sample. The film prepared without post thermal annealing had a smooth surface and was transparent in the visible region.

INTRODUCTION

In recent years, ferroelectric thin films, such as lead titanate ($PbTiO_3$), PZT and PLZT, have been fabricated for the purpose of infrared sensors, electro-optic devices and so on. Usually they were deposited by sputtering method[1,2], but there were some disadvantages as follows, (1)high substrate temperature, (2)stoichiometric change, (3)low deposition rate. Several authors were engaged in other methods, such as metal-organic CVD[3], sputter assisted plasma CVD[4], laser ablation[5] and activated reactive coevaporation[6].

In previous paper[7], we reported high deposition rate(1μm/min) of $PbTiO_3$ films by coevaporation with post thermal annealing. But to obtain a transparent film, it was necessary to avoid post thermal annealing and to keep deposition rate very low(13nm/min). In this report, to promote oxidation of deposited films, a mixed gas of oxygen and ozone was used.

EXPERIMENTAL

Figure 1 is schematic diagram of the reactive coevaporation apparatus for preparation of $PbTiO_3$ films. Pb metal and Ti metal were used for evaporation sources because of their stability and their small impurities[7]. Lead and titanium were evaporated simultaneously by an electron beam gun which had triple source controller. Each of evaporation rates of lead and titanium was independently controlled by each quartz crystal thickness monitor. The substrate temperature was measured by thermocouple which was located near the substrate. Typical deposition conditions are listed in Table I.

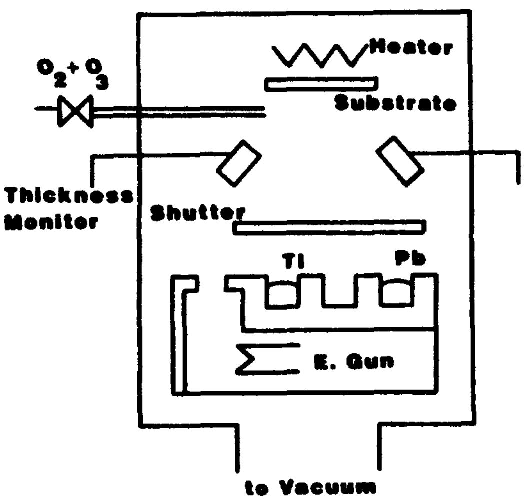

FIGURE 1 Schematic diagram of the reactive coevaporation apparatus.

TABLE I Deposition conditions of the $PbTiO_3$ films.

Vacuum chamber	520mmϕ x800mmh
Diffusion pump	1700 l/sec
Evaporation source	Ti metal(99.98%) Pb metal(99.99%)
Electron beam gun	max 10kW, triple source
Substrate	Corning 7059 glass
Oxygen pressure	max 0.1Pa
Substrate temperature	max 550^oC
Film thickness	0.2-1μm
Ozone concentration	max 5 %

RESULTS AND DISCUSSION

Crystal Structure

Crystal structure of deposited films was investigated X-ray diffraction(XRD) method. Figure 2 shows examples of XRD patterns of the films deposited on glass substrate at substrate temperature of 550^oC with various conditions. The crystal structure was sensitive to the ratio of lead to titanium. When oxygen pressure was small, the XRD pattern contained Pb metal peaks((FIGURE 2(a)). When Pb was a little excess,

the XRD pattern contained pyrochlore phase lead titanate and PbO(red) (FIGURE 2(b)). When the ratio of lead to titanium was kept moderately close, a tetragonal perovskite phase was obtained at substrate temperature of 550°C(FIGURE 2(c)). When Ti was in excess, signal intensity of XRD pattern was very small((FIGURE 2(d)).

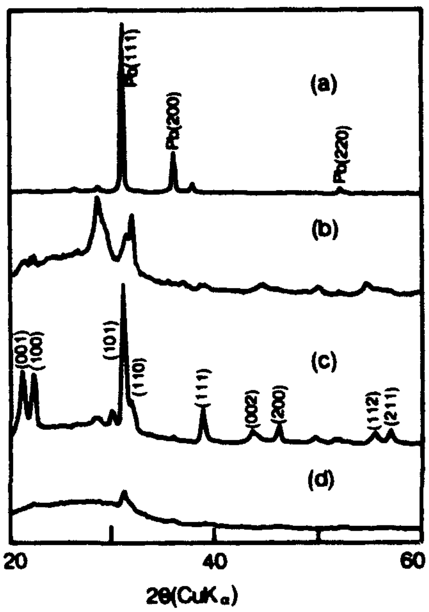

FIGURE 2 X-ray diffraction patterns of the films deposited at substrate temperature of 550°C.

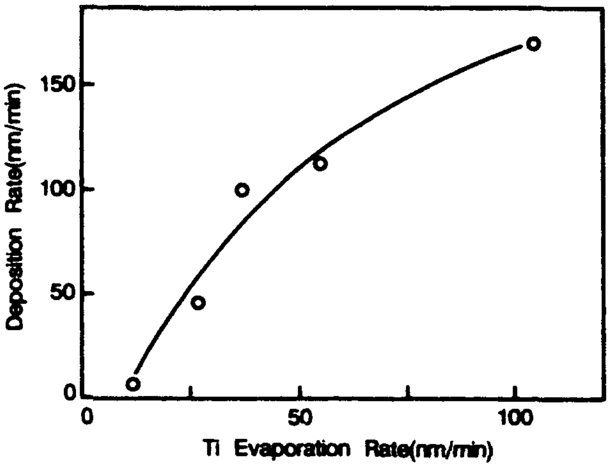

FIGURE 3 Plots of deposition rates of perovskite films vs. Ti evaporation rates.

Deposition Rate

Deposition rate of the films was changed by the various experimental conditions such as evaporation rate, oxygen pressure, substrate temperature and so on. FIGURE 3 shows the deposition rates of the perovskite phase $PbTiO_3$ films vs. titanium evaporation rates. Pb evaporation rate was controlled to obtain the perovskite phase for the respective Ti evaporation rate. Oxygen pressure and substrate temperature were 0.1Pa and 550°C, respectively. When the deposition rate was 170nm/min, diffraction peaks of other phases were present. When deposition rate was smaller than 110nm/min, perovskite phase films were obtained. This rate was much larger than that possible by sputtering

and that of coevaporation without ozone[6,7].

Chemical Composition

In order to study the chemical composition of the films, X-ray photoelectron analysis was carried out. Figure 4 shows example of the X-ray photoelectron spectrum of the perovskite phase $PbTiO_3$ film. Binding energy of Ti and Pb were similar to that of TiO_2 and PbO, respectively.

The compositions of titanium and lead were determined from Ti_{2p}(459eV) and Pb_{4f}(138eV) peak areas in X-ray photoelectron spectra. $PbTiO_3$ powder sample was used for a standard. Figure 5 shows Pb/Ti atomic ratio of deposited films vs. Pb/Ti evaporation rate. When Pb/Ti evaporation rate was greater than 2.3 and smaller than 3.1, perovskite phase films were obtained.

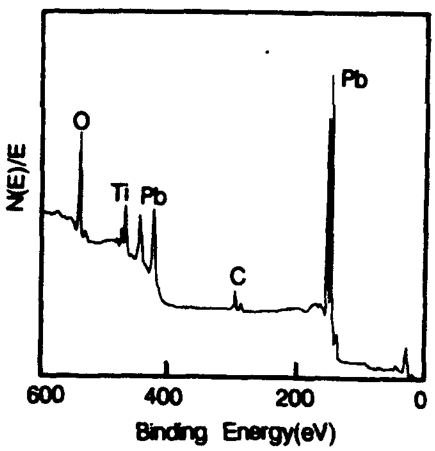

FIGURE 4 X-ray photoelectron spectrum of the perovskite phase $PbTiO_3$ film. Pb/Ti atomic ratio of the film was 0.94.

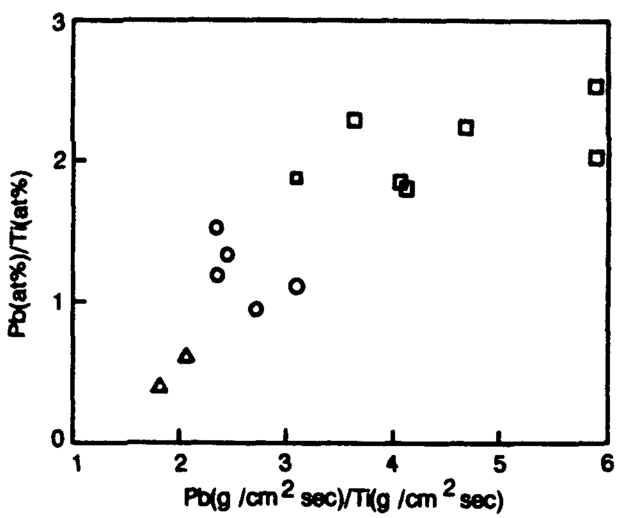

FIGURE 5 Plots of Pb/Ti atomic ratio of deposited films vs. Pb/Ti evaporation rate. o;perovskite $PbTiO_3$, □;Pb rich, △;Ti rich.

Optical Properties

The surface of the perovskite phase $PbTiO_3$ film prepared without thermal annealing was smooth and this film was transparent in visible region. FIGURE 6 shows transmission spectrum of a 200nm thick $PbTiO_3$

film.

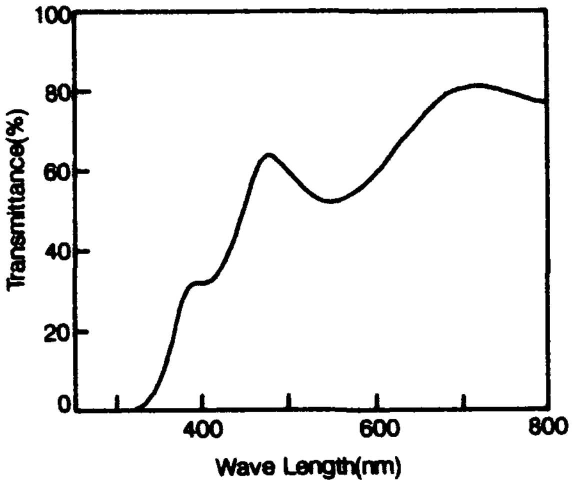

FIGURE 6 Transmission spectrum of a perovskite phase $PbTiO_3$ film of which film thickness was 200nm.

CONCLUSION

$PbTiO_3$ thin films were obtained by reactive coevaporation method. Using ozone to promote oxidation of the films, high speed formation was achieved. Maximum deposition rate of perovskite phase films was 110nm/min, which was much larger than that of prepared by sputtering method and that of prepared by coevaporation without ozone.

REFERENCES

1. M.Okuyama, Y.Matsui, H.Nakano, T.Nakagawa and Y.Hamakawa, Jpn. J. Appl. Phys., 18, 1633 (1979).
2. K.Iijima, Y.Tomita, R.Takayama and I.Ueda, J. Appl. Phys., 60, 361 (1986).
3. M.Okada, S.Takai, M.Amemiya, K.Tominaga, Jpn. J. Appl. Phys., 28, 1030 (1989).
4. S.Mochizuki, S.Kimura and R.Makabe, Jpn. J. Appl. Phys., 28, Suppl. 28-2, 15 (1989).
5. H Tabata, T.Kawai, S.Kawai, O.Murata, J.Fujioka and S.Minakata, Appl. Phys. Lett., 59, 2354 (1991).
6. T.Okamura, K.Oda, J.Takada, A.Osaka, Y.Miura, T.Terashima and Y. Bando, Nihon Seramikkusu Kyoukai Gakujutu Ronbunshi, 98, 749 (1990) [in Japanese].
7. S.Mochizuki, T.Mihara, S.Kimura and T.Ishida, J. Vac. Soc. Jpn., 35 (1992) to be published [in Japanese].

Ferroelectrics, 1992, Vol. 134, pp. 325–330
Reprints available directly from the publisher
Photocopying permitted by license only

TfP210

THIN-FILM ZnO ULTRASONIC TRANSDUCER ARRAYS FOR OPERATION AT 100 MHz

YUKIO ITO, KEIKO KUSHIDA, HIROSHI KANDA, HIROSHI TAKEUCHI, KAZUHIRO SUGAWARA* and HARUMASA ONOZATO*
Central Research Laboratory, Hitachi Ltd., P.O.Box 2, Kokubunji, Tokyo 185, JAPAN
*Technical Research Laboratory, Hitachi Construction Machinery Co., Ltd., Tsuchiura, Ibaraki 300, JAPAN

Abstract Thin-film ZnO ultrasonic transducer arrays for operation at 100 MHz were developed and evaluated. Epitaxial, high acoustic quality ZnO film layers of 10 μm thickness could be produced by sputter deposition on well (111)-oriented gold films with chromium sublayers evaporated on (0001) sapphire. Using a photoresist etching mask of the desired pattern, the upper Au/Cr electrode and subsequent ZnO film were etched to form grooves separating the multi-layered film into array elements with a 100 μm pitch. It was found that the ultrasound beam in the azimuth plane for a 32-element array could be electronically focused in the 100 MHz range to obtain a half-amplitude width of 60 μm at the focal depth in water. This value reasonably agrees with the theoretically calculated value.

INTRODUCTION

High-frequency transducers are currently being developed to obtain high image resolution in nondestructive evaluation[1] and in medical diagnosis.[2] A fast imaging time is also required for most applications and can be achieved by electronic scanning with a linear array transducer.

Although linear array transducers operating at frequencies as high as 30 MHz[3,4] were successfully produced, none operating at higher frequencies have been reported. The authors have developed thin-film ZnO linear array transducers operating in the 100 MHz range. The use of thin-film ZnO is favored because it can be easily formed into a very fine array using photolithographic techniques and has no adhesion layer to the substrate, allowing for high uniformity in response.[5]

This paper describes the preparation procedure and crystal quality of ZnO films which are well suited for fabrication of transducer arrays. It also describes the structure of the transducer and its electronic beam focusing characteristics in the azimuth plane at a frequency of 100 MHz.

EXPERIMENTAL

Figure 1 shows the schematic structure of a thin-film ZnO transducer array and an SEM micrograph of a part of a fabricated array. The array consists of thin-film ZnO sandwiched between two metal electrodes; the lower electrode is deposited on a sapphire plate whose front surface is shaped in the form of a cylindrical acoustic lens. The sapphire plate was 0.5 mm thick and had a 5.5 mm radius of curvature. As the lower electrode, a chromium layer was first formed on the (0001) sapphire surface and gold film was successively deposited over the chromium layer by vacuum evaporation at 200 to 300 °C. The thickness of the chromium film and gold film were 2 - 5 nm and 150 - 200 nm, respectively. Details on the film preparation procedure were presented previously.[6] A 10 µm thick ZnO film was then grown on the gold electrode by rf magnetron sputtering. The sputtering was done with a 100 mm diameter ZnO ceramic target under a gas (50%Ar-50%O_2) pressure of 2 Pa and at a substrate temperature of 260 °C. The rf input power was 75 W, resulting in a deposition rate of 0.7 µm/h. On top of the ZnO film, a gold/chromium film was vacuum deposited at room temperature to form the upper electrode. In addition , a 12 µm thick SiO_2 matching layer was deposited on the curved lens surface by sputtering at room temperature, giving rise to the improvement of the transmission of acoustic energy into water.

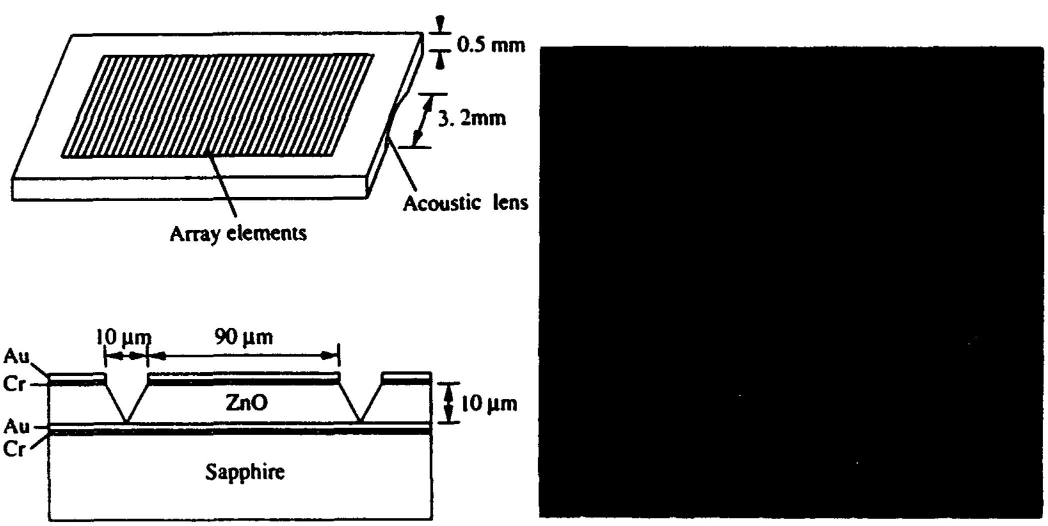

FIGURE 1 Structure of a thin-film ZnO transducer array and SEM micrograph of a part of an array

The division of the multi-layered film into array elements was performed as described in the following. Using a photoresist etching mask of the desired pattern, the upper Au/Cr electrode and subsequent ZnO film were etched to form grooves (gaps between elements). For pattern definition of ZnO, HCl and HNO_3-based solution was used at room temperature. The etching rate was about 0.15 μm/s.

After each element was wire-bonded to a focusing circuit, experiments were conducted to determine the beam focusing characteristics in the azimuth plane by applying each array element with appropriately phased, time-delayed signals at a frequency of 100 MHz. The transducer array emitting a beam was mechanically moved across a knife-edged reflector in water and the variation in signal amplitude of the reflected echo was plotted against the position of the transducer. Then, the beam width profile was obtained by differentiating the plotted curve with respect to the position. In this experiment, the elevation direction of the array was adjusted to be exactly parallel to the edge of the reflector.

RESULTS AND DISCUSSION

ZnO thin films

To obtain ZnO thin films, the most suitable growth conditions were determined. It was reported by the authors[1] and other researchers[7,8] that highly c-axis oriented ZnO films having good acoustic qualities could be produced on a well crystalline (111)-oriented gold film with chromium sublayer evaporated on a quartz or a (0001) sapphire substrate. The standard deviation, σ, in the X-ray rocking curves of the (002) plane of ZnO films is shown as a function of that in the X-ray rocking curves of the (111) plane of gold films in Figure 2. The σ of ZnO decreases almost linearly with decreasing σ of gold. Thus, well (111)-oriented gold films must be produced. It was reported previously[6] that the degree of a preferred orientation of gold films remarkably depends on the thickness of the chromium sublayers formed prior to the gold deposition. In particular, chromium sublayers with a thickness of less than 5 nm gave rise to a significant improvement in the alignment of the gold films. This could be explained in terms of the formation of the epitaxial Cr_2O_3 thin layers. In this way, gold films with σ of 0.2 to 0.5 ° were successfully produced to allow the formation of ZnO films with σ of 0.3 to 0.5 °.

Cross-sectional high resolution transmission electron microscope lattice images of the interface regions between sapphire substrate, gold/chromium and ZnO film are shown in Figure 3. It can be seen that each layer is well epitaxially grown from the sapphire substrate to ZnO. The lateral 0.26 nm periodicity present in the ZnO layer

region corresponds to the (002) lattice plane of ZnO. The 0.24 nm layer spacing in the gold region is consistent with the growth of a (111) oriented gold film. The 1.8 nm thick layer between the gold film and sapphire substrate is composed of Cr_2O_3, as reported recently.[6] In this multilayered epitaxial system, the misfit of ZnO, Au and Cr_2O_3 overgrowth arrays of atoms at the interface against the sapphire substrate are 21, 7 and 4 %, respectively. Consequently, it is concluded that both the Au layer and Cr_2O_3 layer act as buffer layers between ZnO and sapphire to induce the easy epitaxial growth of ZnO films.

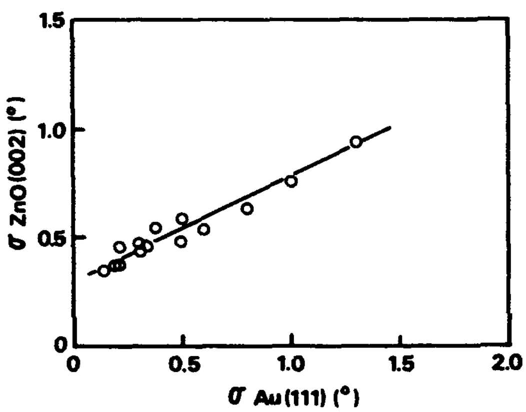

FIGURE 2 Standard deviation σ in the X-ray rocking curves of the (002) plane of ZnO films versus that of the (111) plane of gold films.

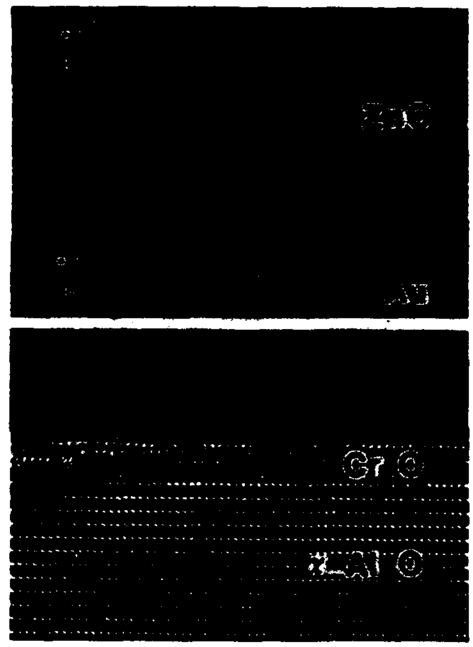

FIGURE 3 Cross-sectional transmission electron microscope lattice images of the interface between sapphire (α-Al_2O_3) substrate, gold/chromium and ZnO film.

Transducer arrays

An array was constructed using the ZnO thin film by photolithographic techniques. The dimensions of individual array elements were 90 µm wide, 100 µm pitch, 3.2 mm long and 10 µm thick, as given in Figure 1. Each element had a capacitance of 2.8 pF. A V-shaped groove bounded by the $\{1\bar{1}01\}$ or $\{11\bar{2}2\}$ planes of ZnO was formed as a gap between adjacent elements. The grooves were obtained using an anisotropic etchant, HCl and HNO_3-based solution, which preferentially etches the c-plane of ZnO. An array with well V-shaped grooves could be produced, when such highly epitaxial ZnO films as mentioned above were employed. When poor c-axis oriented ZnO films

were used, the shape of the grooves became irregular. The response of individual elements received through an echo from the back of the sapphire plate varied within ±1 dB over 160 elements. The small amount of scatter in the response is an excellent characteristic of the present thin-film ZnO array. This characteristic is very important for ultrasound beam forming of the transducer array.

Ultrasound beam focusing

We carried out ultrasound beam focusing experiments using the present thin-film ZnO transducer arrays operating in the 100 MHz range. In the azimuth plane of the array, focusing was accomplished by applying each array element with appropriately phased, time-delayed signals. The beam profiles were measured as the number of elements employed for the beam forming was varied. In this experiment, the focal length was chosen to be 2.0 mm in water. The measured half-amplitude beam widths are plotted against the number of elements in Figure 4. In the figure, the calculated widths are also given. It is clear that the beam width decreases with increasing number of elements. All experimental values agree well with the theoretical calculated values. This result indicates that the beam in the azimuth plane of the transducer array can be electronically focused. Finally, the ultrasound beam profile measured in the azimuth plane for a 32-element array at a focal depth of 6.4 mm in water is shown in Figure 5. It was found that the half-amplitude width was 60 μm. This value reasonably agrees with the theoretical value of 57 μm.

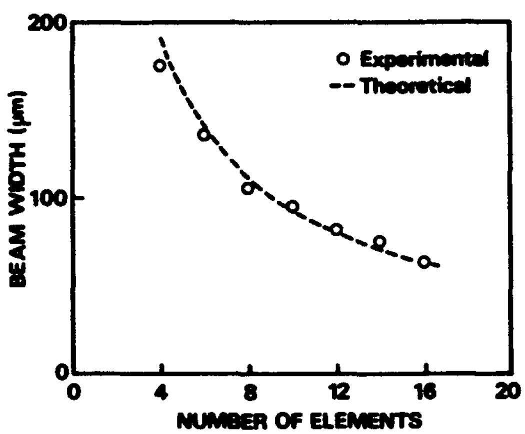

FIGURE 4 Measured and calculated half-amplitude beam width in the azimuth plane versus the number of elements employed.

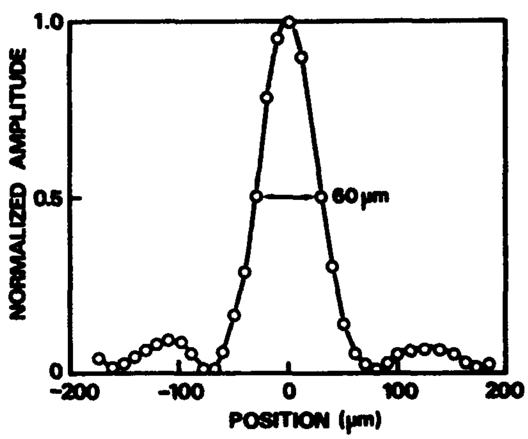

FIGURE 5 Ultrasound beam profile in the azimuth plane for a 32-element array at the focal depth.

CONCLUSION

The fabrication procedure and beam focusing characteristics of thin-film ZnO ultrasonic transducer arrays for operation at 100 MHz were shown. Epitaxial, high acoustic quality ZnO film layers with a thickness of 10 μm could be produced by sputter deposition. An array was successfully constructed using photolithographic and chemical etching techniques. It was found that the ultrasound beam in the azimuth plane for a 32-element array with a pitch of 100 μm was electronically focused to produce a half-amplitude width of 60 μm at the focal depth in water. This value reasonably agreed with the theoretical prediction. The results indicate that the present transducer arrays could possibly lead to electronic scanning in the 100 MHz range and are promising for nondestructive evaluation as well as for medical imaging.

ACKNOWLEDGEMENTS

Principal research support and encouragement from Toshio Nonaka and Yasuo Hayakawa of Hitachi Construction Machinery Co., Ltd. and Hiroyuki Miyagi of Central Research Laboratory, Hitachi Ltd. are gratefully Acknowledged.

REFERENCES

1. K. Kushida, H. Takeuchi, H. Kanda, and S. Yamaguchi, Japan. J. Appl. Phys., Suppl. 28-1, 260 (1989).
2. F.S.Foster, L. K. Ryan, and D. H. Turnbull, IEEE Trans. Sonics Ultrason., 38, 446 (1991).
3. J. Kubota, H. Okada, Y. Musha, Y. Takishita, A. Iwasaki, and S. Sasaki, 1988 IEEE Ultrason. Symp. Proc. (IEEE, New York, 1989) p. 767.
4. S. Sato and K. Tanabe, Omron Technics, 26, 395 (1986)
5. K. Kushida, Y. Ito, H. Takeuchi, H. Kanda, K. Sugawara, and H. Onozato, Ultrasonics (1992) (in press).
6. Y. Ito, K. Kushida, and H. Takeuchi, J. Crystal Growth, 112, 427 (1991).
7. R. Wagers, G. Kino, P. Galle, and D. Winslow, 1972 IEEE Ultrason. Symp. Proc. (IEEE, New York, 1973) p. 194.
8. Iran N. Court and R. N. Charke, 1977 IEEE Ultrason. Symp. Proc. (IEEE, New York, 1987) p. 305.

Ferroelectrics, 1992, Vol. 134, pp. 331–336
Reprints available directly from the publisher
Photocopying permitted by license only

TfP253

53/47 PZT FILMS BY METALLO-ORGANIC DECOMPOSITION TECHNOLOGY FOR NON-VOLATILE MEMORY APPLICATIONS

WEIGUANG ZHU
Electronic Centre, Nanyang Technological University, Singapore 2263

and

ROBERT W. VEST
School of Materials Engineering, Purdue University, West Lafayette, IN 47907, U.S.A.

Abstract Films of $PbZr_{0.53}Ti_{0.47}O_3$ (53/47 PZT) were prepared by the metallo-organic decomposition (MOD) technique on platinum coated silicon wafers. The films were nearly pin hole free with uniform composition and thickness. The crystal structure and the polarization reversal characteristics which are important for memory applications were studied. The switching characteristics with 5 V pulses both initial and after 10^{10} reversals were promising.

INTRODUCTION

The potential application of ferroelectrics for the non-volatile storage of information has long been recognized, as the polarization state can correspond to binary digital information. The most recent approach to ferroelectric memories has been using ferroelectric thin films to construct semiconductor random access memory (RAM) into a non-volatile form. The $PbZr_{1-x}Ti_xO_3$ (PZT) material is a very stable and refractory ferroelectric, and has been intensively studied for such applications[1].

The metallo-organic decomposition (MOD) process is a technique for producing inorganic films without processing in vacuum or going through a gel or powder steps. The advantages of the MOD processing of ferroelectric films include: low processing temperature, near theoretical density, easy control of stoichiometry, uniform composition, grain size control, and high volume output[2]. This paper describes the application of the MOD process to 53/47 PZT films, with the composition near the morphotropic phase boundary, on silicon substrates.

EXPERIMENTAL

The metallo-organic compounds used in this study for PZT were lead di-ethylhexanoate $Pb(C_7H_{15}COO)_2$, Titanium di-methoxy-di-neodecanoate $Ti(OCH_3)_2(C_9H_{19}COO)_2$, and zirconium tetra-neodecanoate $Zr(C_9H_{19}COO)_4$, all in xylene solution. The compounds were synthesized following the procedures given by Vest and Singaram[3]. The thermal decomposition behaviour of the compounds was studied using thermo-gravimetric analysis (TGA). Figure 1 shows the thermogram of a $Pb(Zr_{0.53}Ti_{0.47})O_3$ formulation solution at a heating rate of 2°C/min in air with a flow rate of 75 ml/min. At a temperature below 150°C, the weight loss of the sample was due to evaporation of the xylene solution. The precursor compound began to decompose at about 200°C, the decomposition being completed by 320°C.

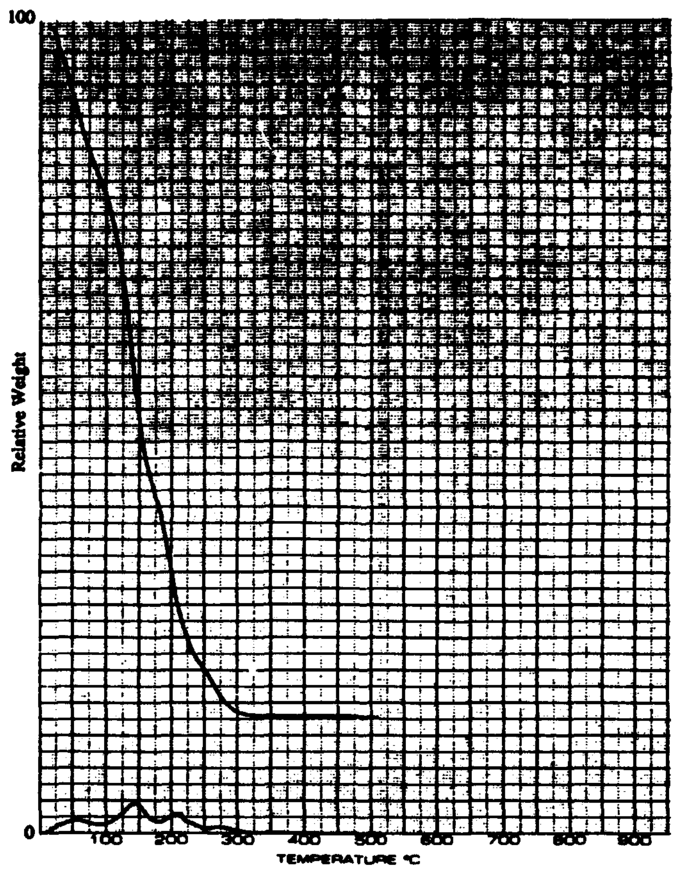

Fig. 1. Thermogram of 53/47 PZT solution heated 2°C/min in air.

A conventional spinning technique was used to form uniform wet films on (001) single-crystal silicon substrates. The substrates were coated with a titanium layer and then with a platinum layer on the top, each layer being about 100 nm thick. The wet film was then pyrolysed in a fused quartz tube furnace at 350°C for 10 minutes, which produced crack-free single-layer films. The film thickness was measured using a Tencor Alpha Step 200 surface profilometer. A Siemens D500 X-ray diffractometer was used to analyze the crystalline phases and preferred orientation in the films. The pulse polarization and fatigue were measured using a RT66 Ferroelectric Test System made by Radiant Technologies, Inc. Figure 2 shows the pulse train used to obtain pulse polarization data. As shown in Figure 2, a capacitor is first set in the negative $-P_r$ state. The first positive pulse applied (P^*) switches the polarization vector from this negative state to a positive polarization state. The second positive pulse (P^+) is then applied. The difference between P^* and P^+ equals P_r^*. This value is important for memory application since it corresponds to the total remanent polarization.

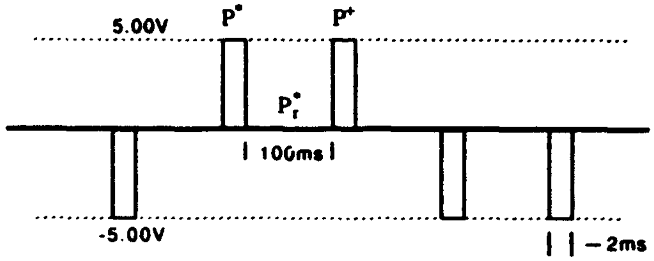

Fig. 2. Pulse train for switching tests.

RESULTS AND DISCUSSION

A 53/47 PZT film deposited on a silicon (001) substrate with a spinning speed of 1500 rpm for 15 seconds was amorphous to X-ray after pyrolysis. The film was then annealed in air at 600°C for 10 minutes. The thickness of the fired film was 210 nm. Figure 3 shows the X-ray diffraction pattern of the fired film. The intensity of the (111) peak is low as compared to the (100) and (200) peaks, indicating that the 53/47 PZT film is near the morphotropic phase boundary[4-7]. T rve also shows a good structural development of the film, even though the sample was annealed in such a short period of time.

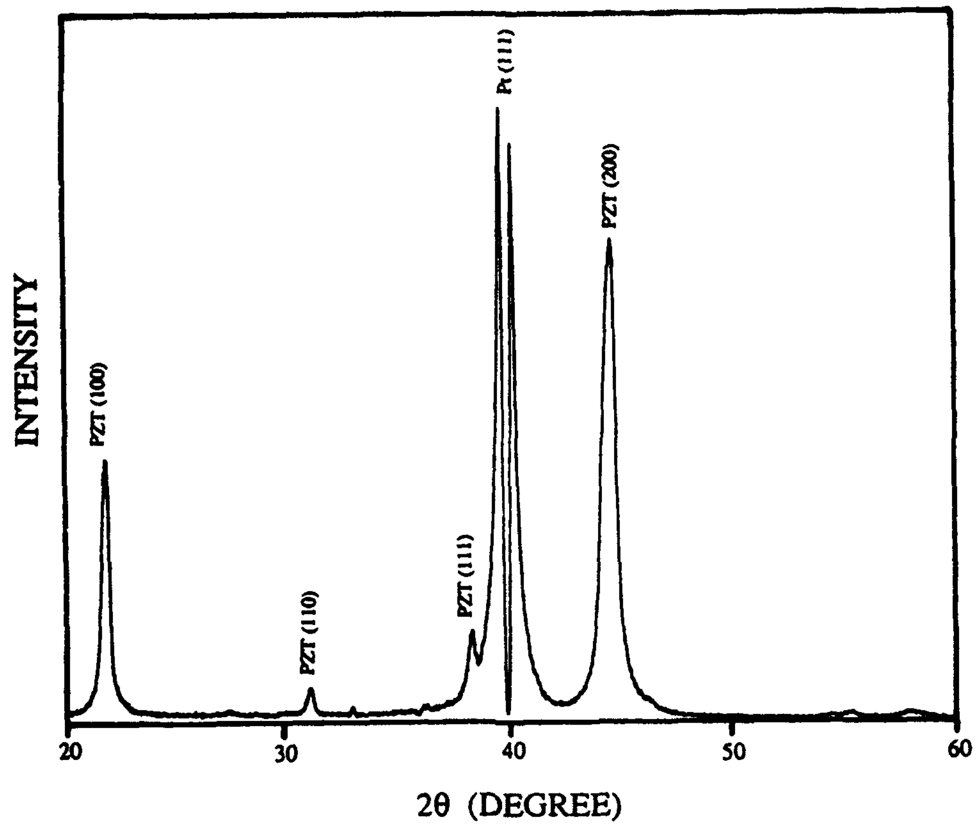

Fig. 3. X-ray diffraction pattern of the fired 53/47 PZT film.

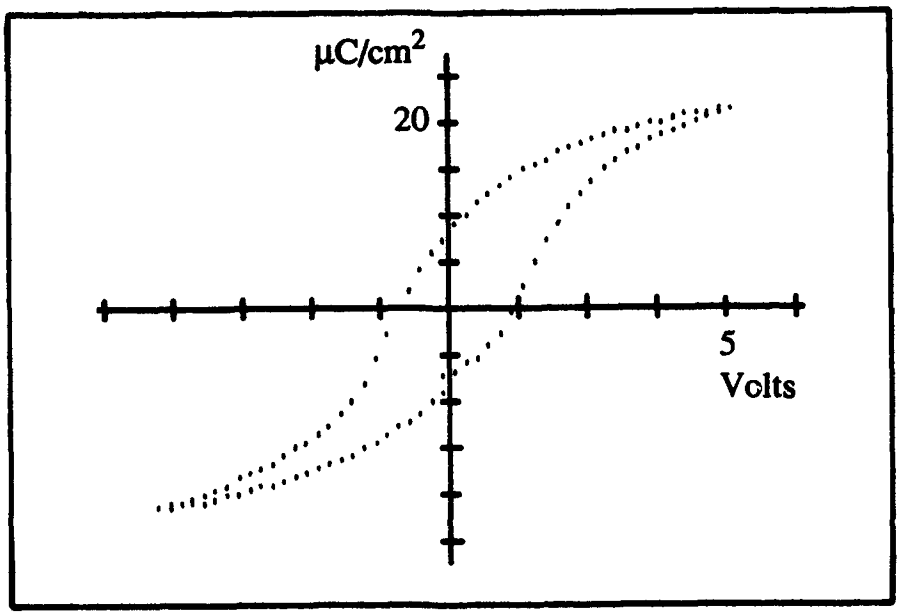

Fig. 4. Ferroelectric hysteresis loop of the fired 53/47 PZT film.

Figure 4 gives a ferroelectric hysteresis loop of the fired film before cycling. The curve shows that the 53/47 PZT film has higher initial polarizations than those of 60/40 films[8], indicating ferroelectric contribution from the tetragonal field at the morphotropic phase boundary. The value of coercive field is about 52 kV/cm calculated from the coercive voltage value of 1.1 V and the thickness of 210 nm. This E_c value is about 3 to 4 times larger than that of PZT bulk material with the same composition[4]. The value of the coercive voltage shows that 1.5 V is sufficient to switch the polarization states of the 53/47 PZT films. The lower value of the coercive voltage is compatible not only with the current Si-based semiconductor technology, but also with the GaAs.

The fatigue behaviour of the film was studied using a square wave at 5 V and 1 MHz frequency. After cycling each decade from 10^7 to 10^{10}, the film was measured using the RT66 Ferroelectric Test System. The fatigue behaviour of P^* and P_r^*, which represents the total remanent polarization, is presented in Figure 5. This figure shows a general decrease of P^* and P_r^* with a number of polarization reversals and a steeper slope than that of 60/40 PZT films[8]. It is encouraging to note that the value of P_r^* after 10^{10} cycles is of 3.2 $\mu C/cm^2$, giving the promise of the utilization of 53/47 PZT films for non-volatile memory applications.

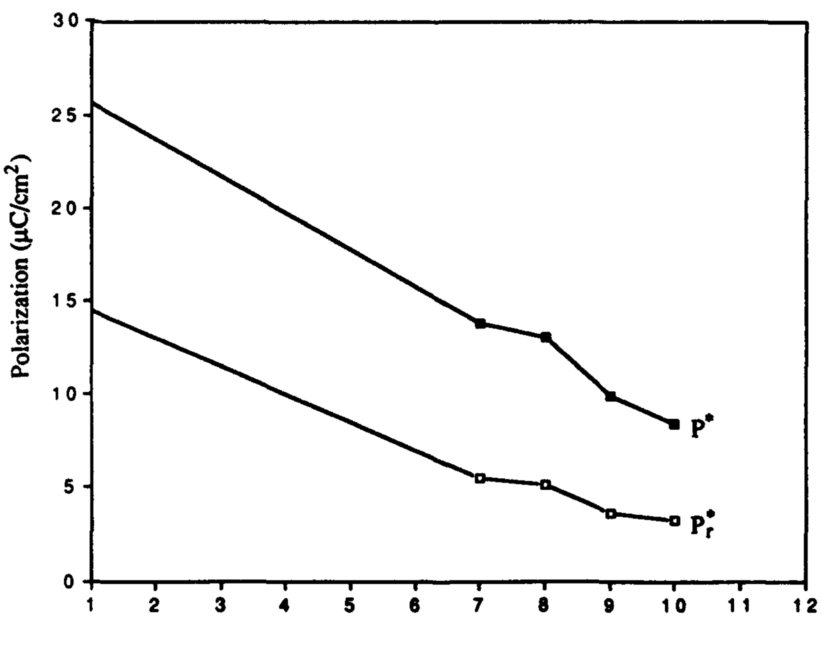

Fig. 5. Fatigue behaviour of P^* and P_r^* for the fired 53/47 PZT film.

SUMMARY

Nearly pin hole free ferroelectric 53/47 PZT films were obtained by the metallo-organic decomposition process. The films were uniform in composition and thickness. The structure of the crystalline PZT films was well developed even when annealed in a very short period of time. The value of the total remanent polarization after 10^{10} reversals was 3.2 $\mu C/cm^2$, giving the promise of the utilization of 53/47 PZT films for non-volatile memory applications.

ACKNOWLEDGEMENT

The authors thanks Mr. D. Binford for his technical assistance.

REFERENCE

1. J. F. Scott and C. A. Paz de Araijo, Science, 246, 1400 (1989).
2. R. W. Vest, Ferroelectrics, 102, 53 (1990).
3. G. M. Vest and S. Singaram, Mater. Res. Soc. Symp. Proc., 60, 35 (1986).
4. G. H. Haertling and C. E. Land, J. Am. Ceram. Soc., 54, 1 (1971).
5. C. Michel, J. M. Moreau, G. D. Achenbach, R. Gerson, and W. J. James, Solid State Comm., 7, 865 (1969).
6. B. Jaffe, R. S. Roth, and S. Marzullo, J. Res. Natl. Bur. Stand., 55, 239 (1955).
7. K. Kakegawa, J. Mohri, T. Takahashi, H. Yamamura, and S. Shirasaki, Solid State Comm., 24, 769 (1977)
8. R. W. Vest and W. Zhu, Ferroelectrics, 119, 61 (1991).

Ferroelectrics, 1992, Vol. 134, pp. 337–342
Reprints available directly from the publisher
Photocopying permitted by license only

TfP255

MAGNETOELECTRIC EFFECTS IN FERROELECTROMAGNETIC FILMS

I.E.CHUPIS
Institute for Low Temperature Physics and Engineering, Ukrainian Academy of Sciences, Kharkov, Ukraine.

Abstract Magnetoelectric susceptibility have been studied in ferromagnetic and ferroelectric-ferromagnetic films. The existence of the surface ferroelectricity and surface linear magnetoelectric effect (LMEE) is predicted in magnetics of any symmetry. The largest value of LMEE is supposed in ferroelectromagnetic films. The temperature dependence of LMEE is studied near magnetic and ferroelectric transition temperatures supposing different relations between them.

Keywords: magnetoelectric effect, polarization, surface, film.

INTRODUCTION

The linear magnetoelectric effect (LMEE) was predicted by Landay [1] for the homogeneous state of some magnetics without the centre of the symmetry. In our work it is shown that the electric polarization and LMEE exist in magnetics of any symmetry near their surface in the magnetic order state. These effects are induced by the change of the value of exchange energy and hence an effective magnetic moment near the surface. They are described by the scalar energy $\underline{P}(d\underline{M}^2/d\underline{n})$ where $\underline{P}$ -elecric polarization vector, $\underline{M}$ - magnetic moment, $\underline{n}$ -the vector of the normal to the surface. This expression is the inhomogeneous exchange magnetoelectric ME) energy. The induced surface ferroelectricity and LMEE were studied in ferromagnetic and ferroelectric-ferromagnetic films. Moreover,the contribution of the homogeneous exchange ME interaction in LMEE was calculated in a ferroelectric-ferromagnetic film in the case when the ferroelectric (FE) transition temperature θ_e and the magnetic transition temperature θ_m are close. The temperature dependence of LMEE near θ_e and θ_m was shown in the general case of different relations between θ_e and θ_m.

SURFACE FERROELECTRICITY AND LMEE IN A CENTROSYMMETRICAL FERROMAGNETIC FILM

We shall consider the centrosymmetrical monodomain ferromagnetic film

which has a thickness 2L in the normal direction Z to the surface. The direction of the magnetic moment (in the film's plane or perpendicular to it) is unimportant later on. The functional of the free energy is the following:

$$F \cdot S^{-1} = \int_{-L}^{L} \Big\{ -\frac{a_o}{2} M^2 + \frac{\beta_o}{4} M^4 + \frac{\alpha}{2}\Big(\frac{dM}{dZ}\Big)^2 - MH + \frac{\varkappa_o}{2} P_z^2 + \frac{\delta_o}{4} P_z^4 + \frac{\lambda}{2}\Big(\frac{dP_z}{dZ}\Big)^2 - P_z E + \frac{1}{2} \gamma P_z \frac{dM^2}{dZ} - \frac{1}{2} \gamma_o P_z^2 M^2 \Big\} dZ + \frac{\alpha}{2\xi}(M_+^2 + M_-^2) + \frac{\lambda}{2\Delta}(P_+^2 + P_-^2) \tag{1}$$

Here S - the film's area, coefficients $\beta_o, \delta_o, \alpha, \lambda$ are positive, $a_o = \alpha_o(\Theta_{mo} - T)$, Θ_{mo} is the magnetic transition temperature in an unlimited crystal. The terms with the coefficients ξ and Δ are the surface energies[2], $M_\pm = M\ (Z=\pm L)$, $P_\pm = P\ (Z=\pm L)$. The inhomogeneous exchange ME energy in (1) has the coefficient γ , homogeneous one has the coefficient γ_o . Here we consider $\varkappa_o > 0$ (spontaneous polarization is absent).

After the variation of the functional (1) with respect to M and $P=P_z$ we find the following differential equations and boundary conditions for the moments:

$$\begin{aligned} &\alpha M'' + a_o M - \beta_o M^3 + \gamma M P' + \gamma_o M P^2 = -H \\ &\lambda P'' - \varkappa_o P - \delta_o P^3 - \gamma M M' + \gamma_o P M^2 = -E \\ &M' = \mp \xi^{-1} M , \quad (Z=\pm L) \quad P' = \mp \Delta^{-1} P \end{aligned} \tag{2}$$

It is seen from the equation (2) that the electric polarization is induced by magnetic moment in the regions of its inhomogenety. We shall calculate the induced polarization near Θ_m in the first approximation by the ME interaction using the following expressions for M and Θ_m in the film[2] if $\xi < 0$:

$$\begin{aligned} &M = m_- ch\, qz , \quad m_- = C_-(\Theta_m^- - T)^{1/2}, \quad q = \frac{x}{L} = \sqrt{\frac{|a_o|}{\alpha}}, \\ &L|\xi|^{-1} = x\, th x , \quad \Theta_m^{\pm} = \Theta_{mo} \mp \frac{x^2}{\alpha_o L^2} \quad (\xi \gtrless 0). \end{aligned} \tag{3}$$

From (2) and (3) we find :

$$P = \frac{\gamma q m_-^2}{2\lambda(\varkappa - 4q^2)} \Big[(2q\,\mathrm{ch}\,2qL + \Delta^{-1}\mathrm{sh}\,2qL)(\sqrt{\varkappa}\,\mathrm{ch}\sqrt{\varkappa}L + \Delta^{-1}\mathrm{sh}\sqrt{\varkappa}L)^{-1}\mathrm{sh}\sqrt{\varkappa}z - \mathrm{sh}\,2qz \Big] \quad (4)$$

Here $\varkappa = \varkappa_0\lambda^{-1}$. If $\xi > 0$ it is necessary to change m_- by m_+, q by iq. We see that electric polarization (4) arising under magnetic phase transition is the odd function of the coordinate Z and has an oppositive sign on opposite sides of the film.

The other aspect of the described phenomenon is the existence of the LMEE near the surface of the magnetic (it may be ferro-, ferri- or antiferromagnetic) of any symmetry. LMEE is characterized by ME susceptibilities $\chi^{em} = dP/dH$ and $\chi^{me} = dM/dE$. The equations for these differential susceptibilities and boundary conditions to them may be obtained by the differentiation of equations (2) by E and H . We receive in the first order by ME interaction the following expressions:

$$\chi^{em} = \frac{\gamma q m_- \chi^m}{\lambda(\varkappa - 4q^2)\,\mathrm{ch}\,qL} \left[\frac{2q\,\mathrm{ch}\,2qL + \Delta^{-1}\mathrm{sh}\,2qL}{\sqrt{\varkappa}\,\mathrm{ch}\sqrt{\varkappa}L + \Delta^{-1}\mathrm{sh}\sqrt{\varkappa}L}\,\mathrm{sh}\sqrt{\varkappa}z - \mathrm{sh}\,2qz \right]$$

$$\chi^{me} = \gamma m_- \left[\alpha\varkappa_0(4q^2 - \varkappa)(\sqrt{\varkappa}\Delta\,\mathrm{sh}\sqrt{\varkappa}L + \mathrm{ch}\sqrt{\varkappa}L) \right]^{-1} \Big\{ \frac{q\,\mathrm{ch}\sqrt{\varkappa}L}{q^2\xi^2 - 1} \Big[2 + \xi^2(\varkappa - 2q^2) + 2\xi\sqrt{\varkappa}\,\mathrm{th}\sqrt{\varkappa}L \Big] \mathrm{sh}\,qz + 2q\,\mathrm{sh}\,qz\,\mathrm{ch}\sqrt{\varkappa}z - \sqrt{\varkappa}\,\mathrm{ch}\,qz\,\mathrm{sh}\sqrt{\varkappa}z \Big\} \quad (5)$$

where $\chi^m \sim (\Theta_m - T)^{-1}$ is the magnetic susceptibility.

The change of the magnetic moment near the surface occurs in the layer of the thickness $\sim |\xi| \ll L$. Hence the predicted ME effects are the surface effects. If $L \gg |\xi|, |\Delta| \gg a_c$ (a_c - the lattice constant) $\lambda \sim \varkappa_0 a_c^2$, $\varkappa_0 \sim 1$, we have from (4) the following order of the surface polarization $P \sim \gamma M^2 \xi^{-1}$. The order of the ME susceptibility will be estimated below.

LMEE IN A FERROELECTRIC-FERROMAGNETIC FILM

In a ferroelectromagnetic crystal, the FE phase transition exists, hence $\varkappa_o = k_o(T-\Theta_{eo})$ where Θ_{eo} is the temperature of the FE transition in an unlimited crystal.The expressions for Θ_e and P are similar to those in (3) if we change $M \to P$, $\Theta_m \to \Theta_e$, $\xi \to \Delta$, $q \to q_e$, $\alpha_o \to \kappa_o$, $a_o \to -\varkappa_o$, $\alpha \to \lambda$.

The existence of the spontaneous polarization in the ferroelectric-ferromagnetic state leads to the contribution of the homogeneous exchange ME interaction to LMEE in the first approximation over the ME interaction. The inhomogeneous ME interaction leads to an odd (with respect to Z) effect, and the homogeneous ME interaction induces an even effect. In the case when Θ_e and Θ_m are close and taking $\xi < 0$, $\Delta < 0$, $L \gg |\Delta|, |\xi| \gg a_c$ near the phase transition we have:

$$\chi^{em} = C_1^{em} sh q_e z + C_2^{em} ch q_e z, \quad \chi^{me} = C_1^{me} sh q z + C_2^{me} ch q z,$$

$$C_1^{me} = -\frac{\gamma L \xi^2(\xi^2+2\Delta\xi-8\Delta^2)}{3\sqrt{2}\,\alpha K_o \Delta^2(\xi^2-4\Delta^2)} e^{-\frac{L}{\xi}} \left[\alpha_o \beta_o^{-1}(\Theta_m-T)\right]^{1/2} (\Theta_e-T)^{-1} \tag{6}$$

$$C_1^{em} = -\frac{8\gamma L \Delta^2}{3\sqrt{2}\,\lambda\xi(\xi+2\Delta)} e^{-\frac{L}{\Delta}} \left[\alpha_o \beta_o (\Theta_m-T)\right]^{-1/2}$$

$$C_2^{em} = -\frac{16\gamma_o L}{9(\Delta+\xi)} e^{\frac{L}{\Delta}} \left[\alpha_o \beta_o \kappa_o \delta_o (\Theta_e-T)(\Theta_m-T)\right]^{-1/2}, \quad C_2^{me} = C_2^{em}(\Delta \leftrightarrow \xi).$$

The total susceptibilities $\bar{\chi} = (2L)^{-1}\int_{-L}^{L} \chi(z)\,dz$ are the following :

$$\bar{\chi}^{em} = \frac{8\gamma_o \Delta}{9(\Delta+\xi)} \left[\alpha_o \beta_o \kappa_o \delta_o (\Theta_e-T)(\Theta_m-T)\right]^{-1/2}, \quad \bar{\chi}^{me} = \bar{\chi}^{em}(\Delta \leftrightarrow \xi). \tag{7}$$

RESULTS AND DISCUSSION

The surface electric polarization and LMEE in a ferromagnetic film near Θ_m have the following critical behavior (see (3)-(5)) : $P \sim (\Theta_m-T)$, $\chi^{me} \sim (\Theta_m-T)^{1/2}$, $\chi^{em} \sim (\Theta_m-T)^{-1/2}$. The total values of P and ME susceptibilities are zero.

In a ferroelectromagnetic film under $T < \theta_e, \theta_m$ there are odd (surface) effects (terms with coefficients c_1 in (6) and even (volume) ME effects (terms with coefficients c_2). From (7) we see that ME susceptibilities of the volume effect have the temperature dependence $(\theta - T)^{-1/2}$ near θ .The temperature dependences of the surface LMEE near θ_m in a ferroelectromagnetic film are similar to those in a ferromagnetic film. If $\theta_e < \theta_m$, the value of the surface susceptibility χ^{em} has no anomaly near θ_e meanwhile $\chi^{me} \sim (\theta_e - T)^{-1}$ $(T \lesssim \theta_e)$. Hence, the FE order (just the large values of the dielectric susceptibility) intensifies the surface ME effect. Our analys shows that the described critical behavior of LMFF near the phase transition temperatures takes place in the general case when θ_e and θ_m are not close as well (see Table 1, where χ_s is the surface ME susceptibility, χ_v is the volume one).

TABLE I Temperature dependences of LMEE near θ_e and θ_m in a film.

Temperature	χ_s^{em}	χ_v^{em}	χ_s^{me}	χ_v^{me}
$\theta_e < T \leq \theta_m$	$(\theta_m - T)^{-1/2}$	-	$(\theta_m - T)^{1/2}$	-
$T \lesssim \theta_e < \theta_m$	without anomaly	$(\theta_e - T)^{-1/2}$	$(\theta_e - T)^{-1}$	$(\theta_e - T)^{-1/2}$
$T \lesssim \theta_m < \theta_e$	$(\theta_m - T)^{-1/2}$	$(\theta_m - T)^{-1/2}$	$(\theta_m - T)^{1/2}$	$(\theta_m - T)^{-1/2}$

Before to estimate the value of LMEE we note that the constant of the inhomogeneous exchange ME interaction $\gamma \sim \Gamma a_e$ where Γ is the coefficient in the homogeneous ME energy $\Gamma P M^2$. The last energy appears in the lower order of the perturbation theory than the energy $\gamma_0 P^2 M^2$, hence $\gamma_0 P \ll \Gamma$, $\gamma \gg \gamma_0 P a_c$.

We shall compare the value of the predicted surface ME effect with the volume ME effect in the case when these effects have similar

critical behavior near Θ_m, $\Theta_m < \Theta_e$. Using (6), (7) and considering $|\Delta| \sim |\xi|$, $P^2 \sim \varkappa_0 \delta_0^{-1}$ we have:

$$\frac{\chi_s^{em}}{\bar{\chi}^{em}} \sim \frac{\gamma}{\gamma_0 P a_c} \cdot \frac{L}{a_c} e^{-\frac{2L}{\Delta}}, \quad \xi < 0, \Delta < 0. \tag{8}$$

If $\Delta > 0$, the exponential multiplier in (8) is absent but as $L \gg a_c$, $\gamma \gg \gamma_0 P a_c$ the value of the surface ME susceptibility is significantly larger than volume ME susceptibility. This fact raises hopes in the experimental discovery and use of the predicted ME effects. For example, the change of the electric surface state under the magnetic order temperature would use for the definition of magnetic phase transition temperature.

Note that the scalar energy $\underline{P}(d\eta^2/d\underline{n})$ exists in any finite system where η is the order parameter (for example, it may be a superconductive parameter, strain etc.). Hence, any ordering in the system is accompanied by electric polarization near the surface in the direction perpendicular to it.

REFERENCES

1. L.D. Landay and E.M. Lifshitz, Electrodynamic of the Continious Media (Addison- Wesley, Reading, 1960).
2. D.R. Tilley and B. Zeks, Solid St. Commun., 49, 823 (1984).

Ferroelectrics, 1992, Vol. 134, pp. 343–348
Reprints available directly from the publisher
Photocopying permitted by license only

TfP258

PHYSICOCHEMICAL PROPERTIES OF SOL-GEL DERIVED LEAD SCANDIUM TANTALATE $Pb(Sc_{0.5}Ta_{0.5})O_3$ THIN FILMS

ANIL PATEL, NICHOLAS SHORROCKS & ROGER WHATMORE
GEC-Marconi Materials Technology Ltd, Caswell, Towcester, Northants, NN12 8EQ

Abstract Thin films of lead scandium tantalate $Pb(Sc_{0.5}Ta_{0.5})O_3$ (PST) have been prepared by a novel sol-gel process. The process involves two deposition steps. In the first, layers of $ScTaO_4$ are deposited by spin coating a solution of metallorganic compounds of scandium and tantalum. A film of lead oxide is deposited intermittently onto the surface using a solution of lead acetate, and the process repeated to obtain thicker films. After firing, the composite film, a transparent film of PST is obtained. The crystallographic and morphological properties of the films have been analysed by X-ray diffraction and SEM and elemental analyses determined using EPMA. The films' electrical properties have been measured against field and temperature, showing a strong induced pyroelectric response ($3.8 \times 10^{-3} Cm^{-2}K^{-1}$), peak permittivities of 4500 and low loss. A high material figure-of-merit ($11 \times 10^{-5} Pa^{-1/2}$) was obtained. Results are presented which illustrate the relationships between the properties and the observed structure of the films, with the processing conditions. A possible mechanism for the formation of perovskite PST is outlined.

INTRODUCTION

Ferroelectric materials have attracted considerable interest recently, due to their unique range of dielectric, pyroelectric and optical properties. Due to the need for miniaturisation and integrated processing, techniques have been developed to deposit these materials as thin films directly onto a given substrate. Conventional routes to thin film production rely on complex mixing and chemical reactionof the appropriate oxides at elevated temperatures and subsequent lapping and thinning operations. This is costly and time consuming and in cases, not particularly suited to complex specifications. Consequently, there has been renewed interest in the deposition of thin films directly by a variety of means, including physical vapour deposition (eg, sputtering), chemical vapour deposition (CVD), and solution methods (sol-gel). The method described below involves film deposition by sol-gel processing[1], which is attractive because of its simplicity. Films can be readily deposition from partially polymerised solutions by spinning or dip-coating techniques followed by pyrolysis of the film in air. In this present study, the sol-gel process has been utilised for the deposition of PST, by spin-coating a stable sol onto substrates such as sapphire, GGG ($Gd_3Ga_5O_{12}$) and magnesium oxide.

PST is a perovskite structured relaxor ferroelectric oxide, and is an important member of a class of ferroelectric compounds exhibiting diffuse ferroelectric-paraelectric phase transitions. These so-called relaxor materials are the subject of considerable interest on account of their novel dielectric behaviour, and their potential applications. PST conforms to the general formula $(A(B'_xB''_{1-x})O_3)$ with the lead atoms occupying the A-sites and the scandium and tantalum atoms located on the B-site[2] (Figure 1).

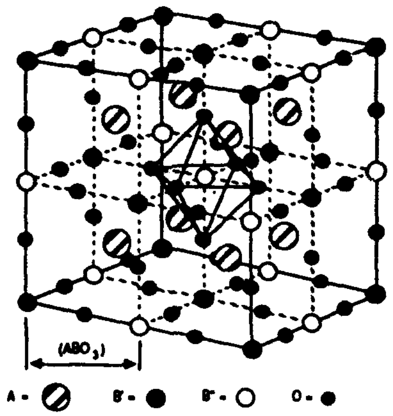

Figure 1 : Structural model of ordered PST

EXPERIMENTAL PROCEDURE

Various types of precursors have been used previously, to deposit a wide range of materials by several groups. These include organic acids, metal β-diketonates and most popularly, metal alkoxides. A combination of materials have been used here, mainly limited by the availability of a suitable scandium precursor. Previous studies by Shrout et al[3], have shown that conventional processing of $A(B_1B_2)O_3$ type ceramics invariably lead to the formation of a detrimental pyrochlore type phase. Therefore, a similar approach was used to that pertaining in bulk PST ceramic[4], whereby the two B-site elements are prereacted first to form the wolframite phase ($ScTaO_4$) before reaction with lead oxide. A flow diagram for the preparation of a typical PST film is shown in Figure 2.

Scandium acetylacetonate was prepared according to the method of Morgan & Moss[5]. Tantalum ethoxide was obtained commercially and distilled prior to use. The reaction between $Sc(acac)_3$ and $Ta(OEt)_5$ leads to the formation of a complex whose structure as yet has not been identified. The lead sol was prepared by dissolving lead acetate in 2-methoxyethanol and refluxing. The films were processed by multiple depositions with pyrolysis of 'organics' at 450°C between layers. Using this novel process, a composite film structure consisting of $ScTaO_4$ interspaced with PbO layers was sintered in a lead rich environment to attain the correct film stoichiometry.

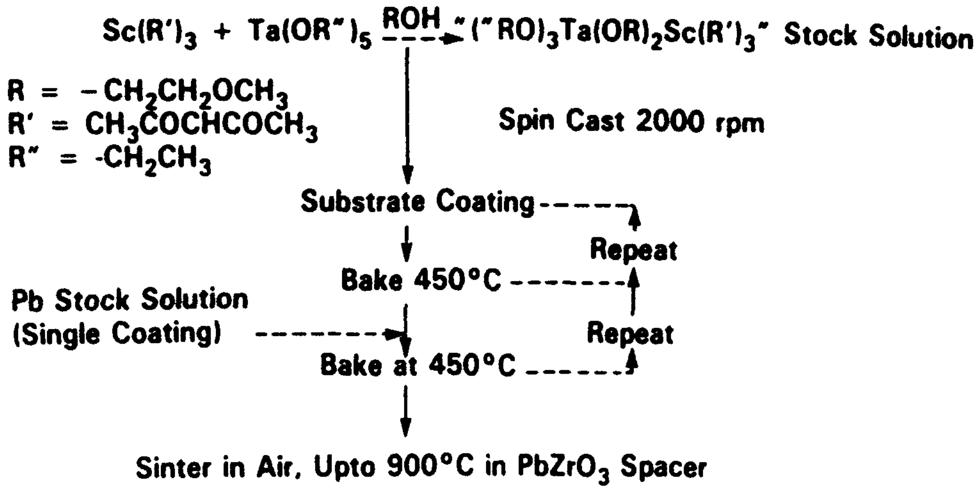

Figure 2 : Flow diagram for the preparation of PST thin films

The PST films were characterised by a number of techniques including (XRD), Scanning Electron Microscopy (SEM) and Electron Probe Microanalysis (EPMA). The films' dielectric properties were measured using Cr/Au interdigitated, and simple wire-mask patterns on the surface. Measurements were obtained using a General Radio bridge type 1615A and Wayne Kerr 6425 LCR meter.

RESULTS AND DISCUSSIONS

As shown below (Figure 3), a cubic perovskite phase was obtained for a film grown on GGG substrate. The lattice parameter value of a_0=4.075Å was obtained, which agrees with values obtained for bulk ceramic[4]. Additionally, there was evidence of superlattice reflections at (111) and (311), indicating some degree of ordering between Sc^{3+} and Ta^{5+}, ie, in a fully ordered system Sc and Ta alternate with each other in 3D, effectively doubling the lattice parameter. All the films, irrespective of substrate, show a high degree of preferred orientation along the (200) axis; this is probably related to the layering process and the film thickness, leading to different film textures. The surface and cross-sectional microstructure of a 2.7μm PST film grown on GGG are shown in Figure 4(a) and (b). The film exhibited a typical granular morphology with an average grain size of 1.5μm. The films were also fully dense and exhibited none of the fine scale porosity normally observed in sol-gel derived thin films. EPMA analysis on the deposited and fired film gave typical values of $Pb_{0.98}(Sc_{0.5}Ta_{0.49})O_3$.

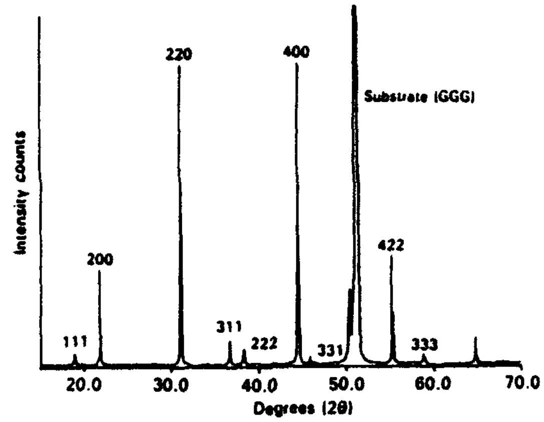

Figure 3 : X-ray diffraction pattern of 2.7μm thick PST film on GGG

The mechanism of film formation has, as yet, not been fully elucidated, but from the results obtained thus far, and from high resolution cross-sectional TEM analysis[6], the mechanism involves the formation of a weak $ScTaO_4$ phase which has some degree of inherent porosity. At the reaction temperature used (900°C), above the melting point of lead oxide, a liquid phase is formed, which diffuses through the $ScTaO_4$ layers, reacting to form PST. Any remaining PbO is lost to the surrounding atmosphere, as equilibrium is achieved.

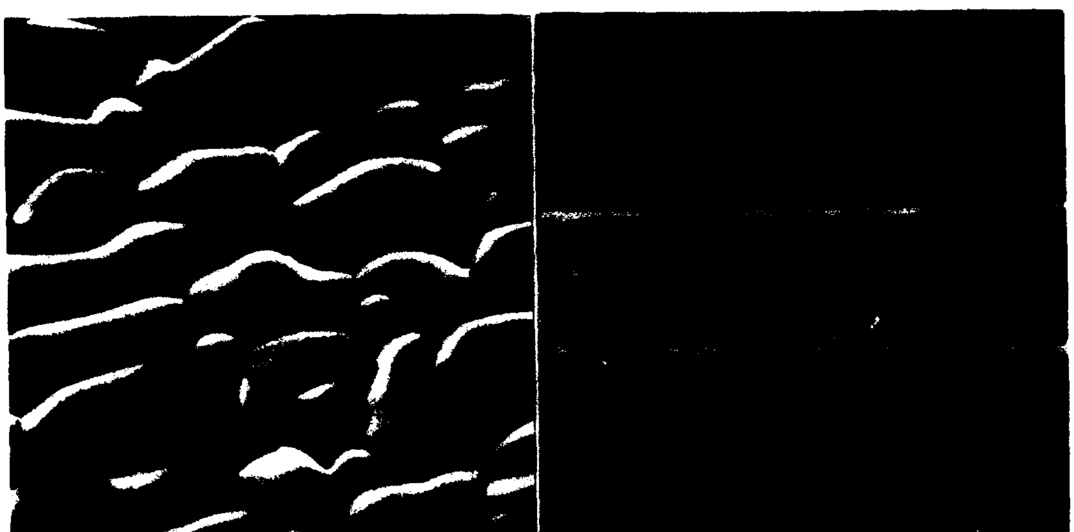

Figure 4 : SEM micrographs of (A) surface, and (B) cross-section of a PST film grown on GGG

The variation of dielectric properties of a 2.7μm thick PST film on GGG at zero bias field against temperature are shown in Figure 5. The relatively sharp characteristic in the

dielectric constant is indicative of first order type behaviour. The peak at 4500 is lower than expected, for example, average bulk ceramic values are close to 15000. Increase in the bias field shifts this peak towards higher temperatures, with a slight increase in the permittivity. The dissipation factor (tanδ) had a minimum value of ~0.2% at 70°C, which is higher than expected, and the increase with applied field is probably due to domain wall motion. The measured induced pyroelectric coefficient (P) at 30°C and 5V/μm gives a va!ue of ($3.8 \times 10^3 Cm^{-2}K^{-1}$), which compared to conventional pyroelectrics such as $PbTiO_3$[7], is over a magnitude greater. The material figure-of-merit (F_d) described as $F_d = P/(C\sqrt{(\varepsilon, \tan\delta)})$, where C = volume heat capacity ($2.7 \times 10^6 Jm^{-3}K^{-1}$) was calculated to be $11 \times 10^{-5}Pa^{-1/2}$ where equivalent bulk ceramic values can be as high as $17 \times 10^{-5}Pa^{-/12}$. A comparison of F_d value's for typical pyroelectric materials is given in Table 1. In addition, the PST films also show high dc resistivity and dielectric strength, typical values of $>10^{10}\Omega m$ and $10^6 V/m$ respectively.

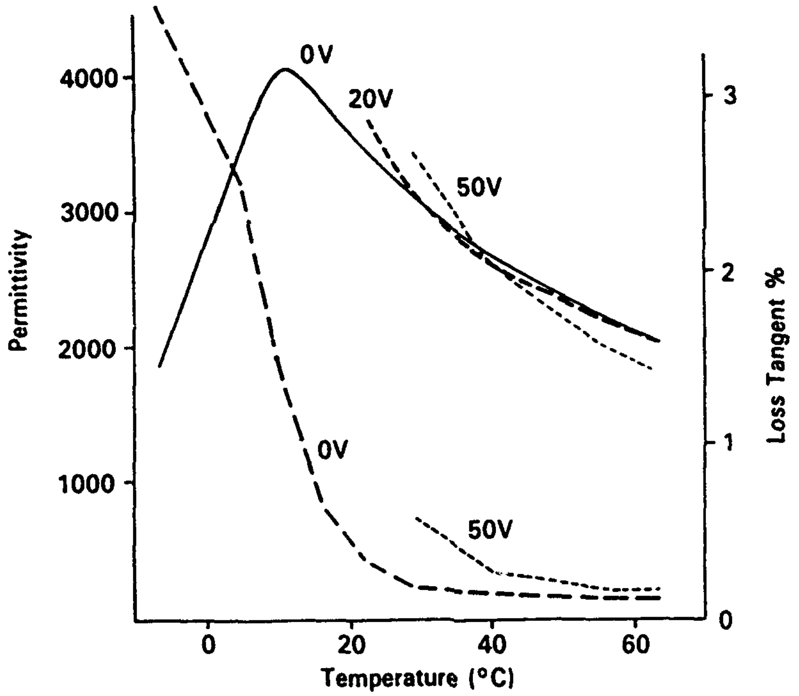

Figure 5 : Variation of permittivity and dissipation factor, under bias Vs temperature for a 2.7μm thick PST film

CONCLUSION

The preparation of suitable sols for the deposition of PST thin films has been made possible by the availability of suitable precursors. A novel 2-stage deposition process has been devised to produce good quality highly preferred orientation perovskite PST films on sapphire, and GGG substrates. The dielectric properties of the films indicate

behaviour similar to bulk ceramic, and relatively high material figure of merit's have been obtained. With further development, this is likely to come a preferred route for the fabrication of large 2-D arrays, suitable for IR applications.

TABLE 1 Comparison of Materials Merit with Conventional Pyroelectric Materials

	TGS FAMILY	SBN FAMILY	PZ CERAMICS	PST CERAMIC	SOL-DERIVED PST FILM
T_c°C	49-75	70-120	166-230	20-30	0-20
F_D ($10^{-5}Pa^{-1/2}$)	6-8.3	6-9.8	3.5-6	12-15	5-11

ACKNOWLEDGEMENT

This work has been carried out with the support of the Procurement Executive, Ministry of Defence.

REFERENCES

1. K. Okuwada, S. Nakamura, M. Imai & K. Kakunmo, Jap. J. Appl. Phys., 29(6), 1153 (1990).

2. C.G.F. Stenger & A.J. Burggraaf, Phys. Stat. Solidi., (1), 61, 653 (1980).

3. T.R. Shrout & A. Halliyal, Am. Ceram. Soc. Bull., 66(4), 704 (1987).

4. N.M. Shorrocks, R.W. Whatmore & P.C. Osbond, Ferroelectrics, 106, 387 (1990).

5. G.T. Morgan & H.W. Moss, J. Chem. Soc., 189 (1914).

6. I.M. Reaney & D.J. Barber, 'Transmission Electron Microscopy of Lead Scandium Tantalate Thin Films', submitted to the J. Microscopy.

7. N. Tohge, S. Takahashi & T. Minami, J. Am. Ceram. Soc., 74(1), 67 (1991).

Ferroelectrics, 1992, Vol. 134, pp. 349–354
Reprints available directly from the publisher
Photocopying permitted by license only

TfP259

GROWTH OF PLZT THIN FILMS USING CLUSTER MAGNETRON TECHNIQUES

K F Dexter, K L Lewis and J E Chadney
DRA Malvern, St Andrews Road, Malvern, Worcs WR14 3PS, UK

Abstract

The deposition of PLZT thin films by cluster magnetron techniques is described. X-ray photoelectron spectroscopy has been used to determine film composition over a range of substrate temperatures. As-deposited films have been studied by X-ray diffraction techniques and the role of post deposition annealing has been assessed. The morphology and growth rates have been determined.

INTRODUCTION

Thin films of PLZT have been studied extensively in order to exploit their ferroelectric and electro-optic properties [1,2]. Deposition of PLZT (x/y/z), where x, y and z are defined by:

$$Pb_{1-x/100}\,La_{x/100}\,(Zr_{y/100}\,Ti_{z/100})_{1-x/400}O_3 \qquad [3]$$

is achieved in this study using r.f. cluster magnetron sputtering. This technique offers advantages over other routes in terms of film quality, surface morphology and compositional control. In common with other methods, such as sol-gel deposition [4,5], and single target r.f. sputtering [6,7,8] control of lead stoichiometry is a key issue and using a cluster magnetron (Fig 1), we report incorporation of Pb into our PLZT films up to and in excess of the chosen stoichiometric value. This allows the exploration of two step deposition/anneal processes, where films containing an excess of Pb can be sputtered at room temperature and annealed into the perovskite phase [9]

EXPERIMENTAL

The work was carried out in a UHV system with 50mm planar magnetrons (Fig 1). The sputtering targets used in this work are PLZT (8/75/31.5) ceramic and metallic lead (99.9% purity). Polished c-plane sapphire substrates, 25mm diameter, were positioned at 110mm from the targets. A calibrated substrate heater was used to generate temperatures of up to 640°C. Sputtering was carried out in mixtures of argon and

oxygen, whose composition was controlled using Brooks 5850R series mass flow controllers. The effect of plasma thermalisation was studied by variation in deposition pressure over the range $1x10^{-3}$ to $8x10^{-2}$mbar. All experiments reported in this work were carried out at $2x10^{-3}$mbar. The composition of the films was determined after deposition by X-ray photoelectron spectroscopy (XPS). These measurements were calibrated using a PLZT 9/65/35 optical grade ceramic standard. All surfaces were etched in Ar^+ at 5000μA, 2.5kV for 30 mins to remove surface contamination before analysis. Studies of films deposited *in situ* in the UHV system used for XPS analysis confirmed the reliability of this technique, and demonstrated the absence of preferential sputtering effects. One particular advantage of using this technique is the ability to determine reliably the oxygen content of the films. The crystal structure was determined using a Siemens D5000 diffractometer, using Ni filtered CuKα radiation.

A Wyko TOPO 3 white light interferometer was used to assess the effects of a post-deposition anneal on film morphology. Growth rate data has also been determined using this technique and cross-referenced with a Dektak 2000 step meter. Annealing experiments were carried out using a fused silica resistive heater furnace with *in situ* temperatures monitored by a Pt:Pt/Rh thermocouple.

RESULTS AND DISCUSSION

The effect of power applied to the secondary lead source can be seen in Fig 2. The Pb content value required for stoichiometric 9/65/35 PLZT is 0.91 (for oxygen =3), and so an excess of lead can clearly be incorporated into the films, provided that 5% oxygen is added to the sputtering gas. The importance of oxygen in controlling the incorporation of lead into the films is clearly evident from Fig 3. This is fundamental to the achievement of the correct stoichiometry of films at growth temperatures in excess of 600°C (Fig 4). However, both the input of oxygen during deposition, and the application of power to the secondary lead target have the effect of reducing the growth rate. Films deposited at room temperature are amorphous. At intermediate temperatures (<500°C), mixed phase deposits are obtained, but even at the highest temperatures examined it has been difficult to produce 100% phase pure perovskite material. Films of highly oriented pyrochlore (Fig 5) are readily obtained at

temperatures between 500 and 640°C.

The ability to deposit films containing excess Pb allows the exploration of 2-step annealing for the production of perovskite films. This process uses a room temperature growth stage followed by post deposition anneal. Films deposited at room temperature can have lead contents in excess of 200% of the required value, and in common with the higher temperature deposition excess lead films, they are black in colour. Subsequent annealing at 600°C for 2 hours in air produced single phase 110 perovskite films (a_0 = 4.153Å). The films then have an optical transmission close to the Fresnel limit of 75% at 632.8nm.

Studies of surface morphology using white light interferometry have highlighted an increase in surface morphology produced as a result of the anneal process. This is related to the exact amount of lead present in the as-deposited films, and in the worst cases can be in excess of 5nm, with pinholes 2-3μm in diameter. These are clearly the result of grain growth phenomena and the ensuing crystallisation of the film.

SUMMARY

Cluster magnetron techniques have proved to be a very effective method for controlling the incorporation of lead in PLZT thin films. As-deposited films can be either amorphous or pyrochlore phase. Subsequent annealing of films can produce single phase perovskite layers.

REFERENCES

1. G Haertling, Ferroelectrics 75, 25 (1987)
2. S Krishnakumar, V H Ozguz, C Fan, C Cozzolino, S C Esener and S H Lee, IEEE Trans. on Ultrasonics, Ferroelectrics and Frequency Control, 38, 585 (1991)
3. H Adachi, T Mitsuyu, O Yamazaki, K Wasa, J Appl Phys 60(2), 1432? (1986)
4. G Yi, Z Wu and M Sayer, J Appl Phys 64(5), 2717 (1988)
5. S J Milne and S H Pyke, J Am Ceram Soc 74, 1407 (1991)
6. E S Ramakrishnan and W Y Yowng, J Van Sci Technol A10(1), 69 (1992)
7. K Torii, T Kaga, K Kushida, H Takeuchi and E Takeda, Jap J Appl Phys 30, 3562 (1991)
8. M Ishida, H Matsunami and T Tanaka, J Appl Phys 48(3), 951 (1977)
9. R M Hazen, Sci American, p52 (1988)

Fig. I: UHV cluster of 50mm magnetron sputter sources with shutters, gas rings and a fast atom source (courtesy of Atom Tech Ltd).

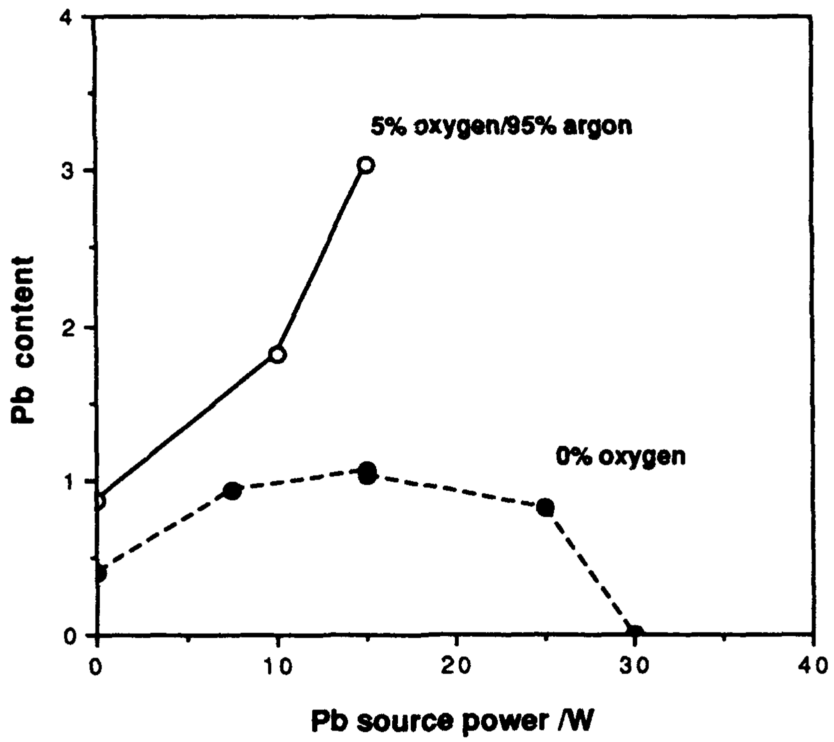

Fig.II: Variation of Pb content (normalised to oxygen = 3) with RF power applied to Pb source for films grown with and without oxygen, substrate temperature 540°C. This emphasises the role of oxygen in controlling the Pb content of PLZT films.

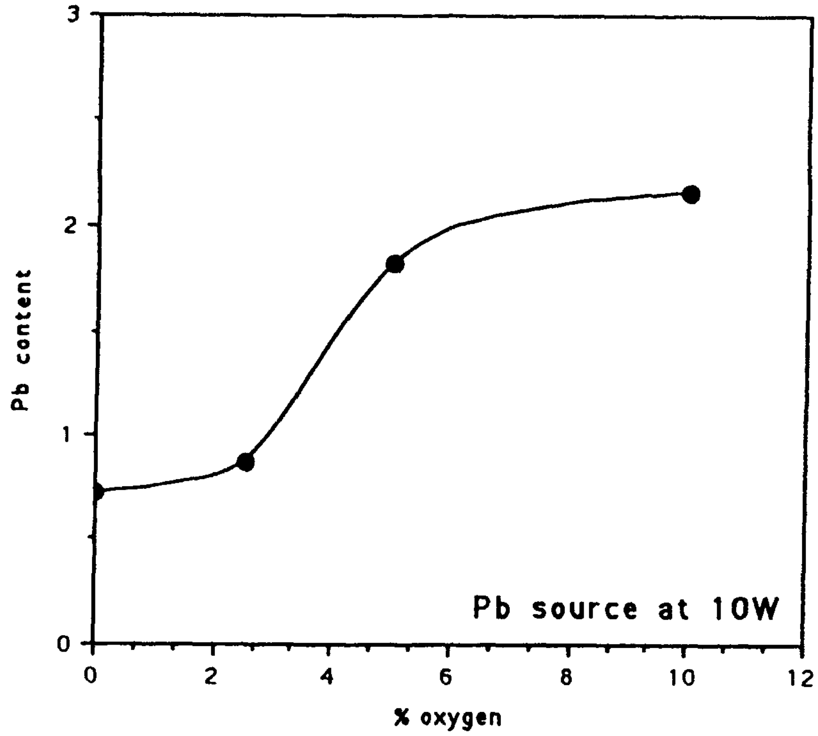

Fig. III: Variation of Pb content (normalised to oxygen = 3) with oxygen level for a fixed power level to the Pb source of 10W and substrate temperature 540°C.

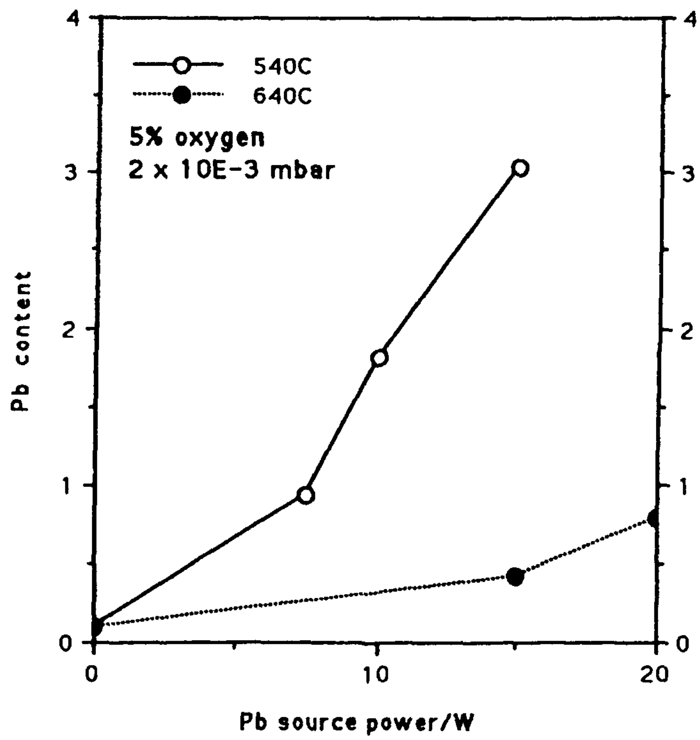

Fig. IV: Variation of Pb content with RF power applied to Pb source for films grown at two different temperatures. This shows the steep variation in Pb content with change in deposition temperature

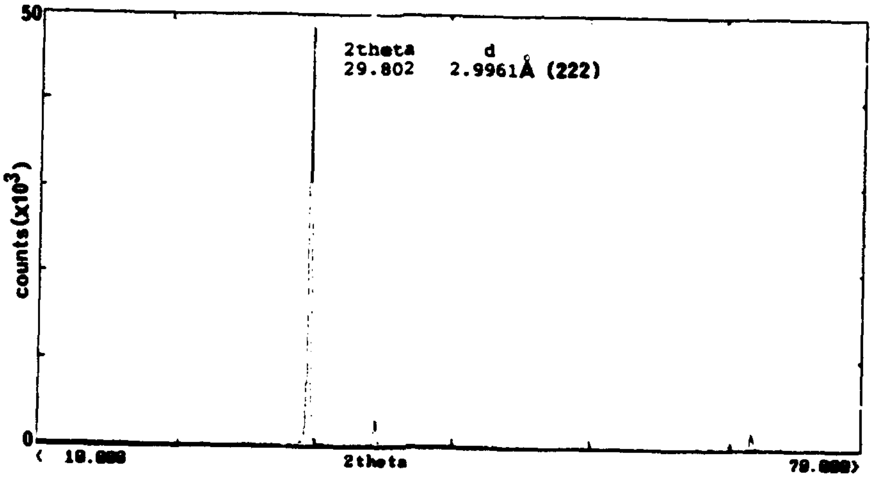

Fig. V: X-ray diffraction spectrum of a thin film of PLZT grown at 560°C, showing the high level of preferred orientation found in pyrochlore films.

Ferroelectrics, 1992, Vol. 134, pp. 355–363
Reprints available directly from the publisher
Photocopying permitted by license only

TdC20

HIGH SPEED OPTO-ELECTRONIC NON-DESTRUCTIVE READOUT FROM FERROELECTRIC THIN FILM CAPACITORS

Sarita Thakoor
Center for Space Microelectronics Technology
Jet Propulsion Laboratory
California Institute of Technology
Pasadena, California 91109

Abstract Polarization dependent photoresponse from ferroelectric lead zirconate titanate ($PbZr_{0.53}Ti_{0.47}O_3$) thin films sandwiched between metal electrodes in a capacitor configuration is reported. This phenomenon has potential application as a non-destructive readout(NDRO) of nonvolatile polarization state of thin film ferroelectric memories. High speed readout using laser pulses with full width at half maximum of ~10ns, at 532 nm wavelength is demonstrated. The polarization direction of the ferroelectric capacitor is reflected in the direction of the photocurrent response. The rise time of the photocurrent response is as fast as 25 ns and the relaxation time is fraction of a microsecond. The readout signal from individual polarized elements is repeated over a million times with no detectable degradation in the photoresponse or the remanent polarization as verified independently by the conventional destructive readout technique. In principle, both electronic as well as thermal mechanisms could be triggered by such photon exposure of ferroelectric thin films. Comparison of the photoresponses from a device with a semitransparent top electrode and an opaque top electrode respectively suggests that the observed NDRO signal is predominantly due to thermally triggered mechanisms.

INTRODUCTION

Compact on-chip, radiation hard, non-volatile memory storage with high speed interactive access is desired in a wide variety of applications that need 'power-off' memory maintenance. Such applications appear in all spheres ranging from alternatives for battery backed defense needs, power-off memory maintenance aboard space missions, and in the commercial arena for a wide variety of needs including data

storage for intelligent navigation in the automotive industry, notebook computers, solid state voice messaging systems for telephones/pagers, frame and configuration memory for high definition television. Ferroelectric non-volatile memories are promising for these applications. With the advances in technology to deposit thin films of PZT (lead zirconate titanate) and integrate them with conventional silicon technology, ferroelectric non-volatile memories are now well into their development phase[1,2,3]. The memory element consists of a thin film ferroelectric capacitor, in which the non-volatile storage is based on the remanent polarization within the ferroelectric thin film. The established readout technique relies upon the transient displacement current (or absence thereof) induced by polarization reversal under applied switching pulse. However, such a process destroys the stored information, which necessitates a rewrite operation after every read cycle and complicates the hardware.

Alternatively, a "poled" ferroelectric thin film element, when illuminated with photons, generates a small photocurrent proportional to the remanent polarization (stored memory). There are two broad classes of possible mechanisms that could be triggered by such photon exposure of ferroelectric thin films (a) photocarrier generated responses such as photovoltaic effect[4-6], or localized electronic transitions[4,7], or transient space charge currents[8-11]; and (b) effects arising due to heating of the device such as pyroelectric effect[5,12,13] (associated with temperature change) or a piezoelectric effect[13-15] (associated with propagation of an acoustic deformation wave through the ferroelectric film). If radiation-hard, nonvolatile, ferroelectric memories could be read non-destructively in terms of the photoresponse (photocurrent or photo-emf) with such contact-less optical addressing, they would clearly have a major impact on the growing need for rugged and robust solid state memory systems. Furthermore, a strong motivation for such a readout arises from the fact that the highly parallel photoresponse output from an array of memory pixels

would be ideally suited for high performance computing applications[9,16], especially those involving parallel processing and architectures such as large scale artificial neural networks. In addition, such a non-destructive readout(NDRO) may allow use of the ferroelectric capacitor as a nonvolatile analog memory. Non-destructive readout from bulk ferroelectric ceramic elements has been demonstrated[6] utilizing the remanent polarization dependent photovoltaic photo-emf. The polarity of the photo-emf depends on the direction of the remanent polarization.

This paper reports the observation of repetitive, high speed polarization dependent directional photocurrent response, generated from ferroelectric thin film capacitors of sol-gel deposited PZT at zero applied bias. The applicability of such photoresponse to non-destructive readout of the stored memory is further demonstrated.

EXPERIMENTAL DETAILS

The sol-gel lead zirconate titanate ($PbZr_{0.53}Ti_{0.47}O_3$) thin films (provided us by Raytheon Equipment Division, Sudbury, MA) were deposited by a modified Sayer's Technique[17] on oxidized silicon substrates covered with an evaporated Ti/Pt (~1000 Å/1000Å) base electrode. The lead zirconate titanate (PZT) film contained ~18% excess lead and were ~1700 Å thick. Crystallization of the as deposited PZT was accomplished by annealing the films at 550°C for 10 minutes in oxygen ambient. To complete a standard sandwich capacitor test structure[10], thin transparent films of platinum (~ 100Å - 150Å) were deposited as the top electrode. The top electrodes were patterned by conventional lift-off techniques as dots of 100μm to 250μm diameter. Optical transmission through the top electrode films (λ = 300 to 800 nm) was about 30%. The high speed photoresponse from the thin film ferroelectric capacitor (TFFC) is measured using a coherent energetic laser pulse that is capable of heating the device. A Nd-YAG pulsed laser at the wavelength of 532 nm is utilized for these experiments. The incident photon energy is lower

than the PZT bandgap (3.5 eV, as determined from optical transmission studies[11,18] on the PZT film on sapphire substrates) and is therefore weakly (< 1%) absorbed by the PZT. The laser pulse, with a full width at half maximum of 10 ns, has a winged profile and delivers ~10 μJ per pulse at 532 nm at a 10Hz repeat frequency. For the measurement of

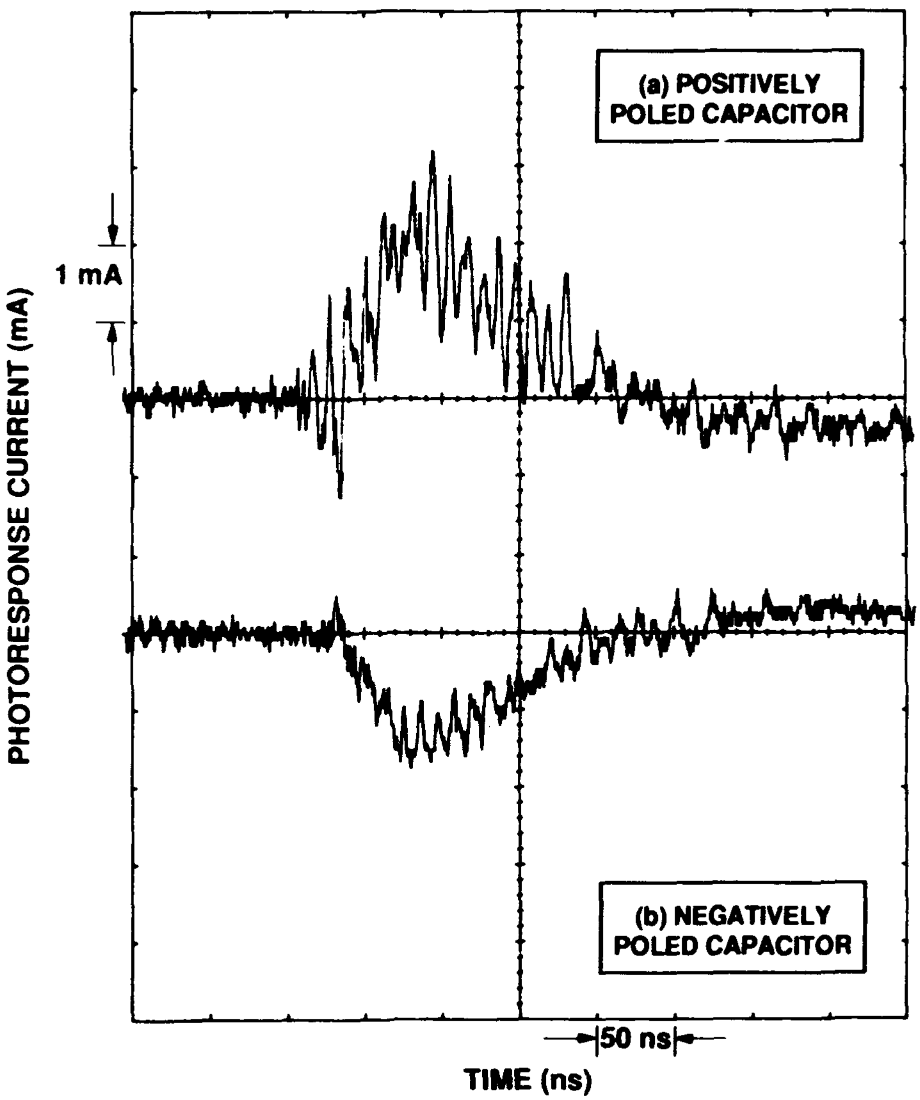

FIGURE 1 First readout of photoresponse current from thin film ferroelectric capacitor (TFFC) with semitransparent top electrode (a) positively polarized state (b) negatively polarized state

the photocurrent, the top and bottom electrodes of the TFFC are short circuited across the 50Ω internal impedance of an oscilloscope, which records the zero bias photoresponse from the TFFC on illumination with the laser pulse. The capacitor was poled positively by using a +4 V pulse for 1μsec or negatively by a -4 V pulse for the same duration.

RESULTS AND DISCUSSION

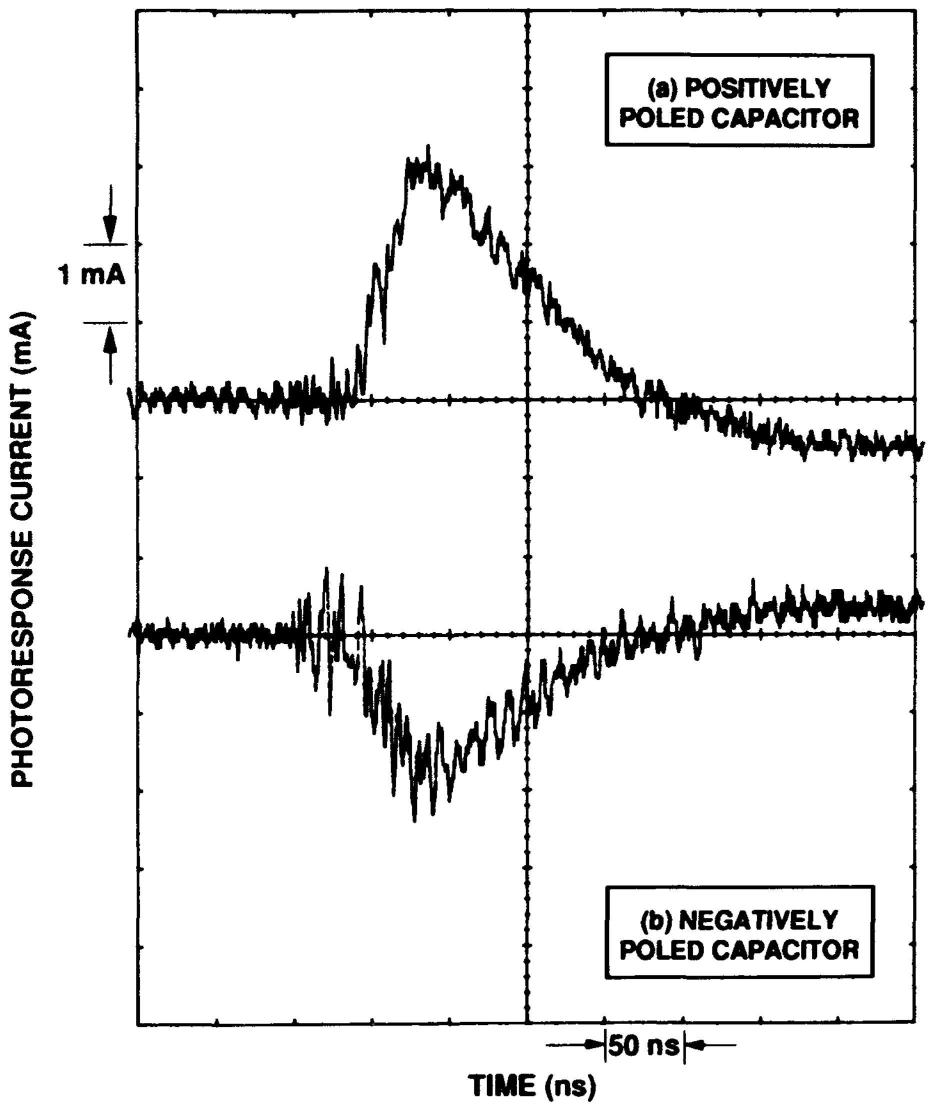

FIGURE 2 Millionth readout of photoresponse current from TFFC with a semitransparent top electrode (a) positively polarized state (b) negatively polarized state.

Figures 1(a) and 1(b) respectively show the first readout of the photoresponse current from a TFFC in its positively and negatively poled states respectively. The polarization state of the TFFC is clearly reflected in the direction of the photoresponse current. The laser pulsing was continued repetitively at a 10 Hz frequency. Even after over a million readouts from the TFFC, the photoresponse was virtually unchanged, and the polarization state (as verified by the conventional DRO technique) was unchanged. Figures 2(a) and 2(b) show the millionth readout of the photocurrent response from the TFFC in its positively and negatively poled states respectively. No degradation on the amplitude of the peak photoresponse in either direction is observed. The asymmetry in the magnitude and the shape of the photoresponse signals in the two oppositely poled cases (Figs. 1 a and 1 b and/or 2(a) and 2(b)) could be due to a photocurrent offset [9,10], a photovoltaic contribution from the pair of asymmetric (back to back) Schottky junctions at the two PZT-electrode interfaces of the TFFC. In fact, the photoresponse from a device with an opaque top electrode (Pt thickness ~ 3000 Å) shown in figure 3 (replotted for a longer duration) is observed to be almost symmetric mirror images for the positively and negatively poled cases respectively. The opaque electrode prevents light from reaching the PZT, thus avoiding any photocarrier generation and consequently the photovoltaic component is absent.

Furthermore, figure 3 shows that the charge flown in one direction giving rise to the photocurrent, when the light pulse is turned "ON", is essentially matched in magnitude (~ 0.12 ± 0.02 nC) by charge flowing in the opposite direction (current in opposite direction), following the end of the primary photoresponse signal, due to turn "OFF" of the laser. This current reversal at the end of the primary signal takes place in case of both polarization directions. The observed response profile with charge conservation confirms that the phenomenon is a thermally triggered pyroelectric[5,12,13] (associated with temperature change within the PZT) and/or piezoelectric effect[13-15] (due to propagation through PZT of

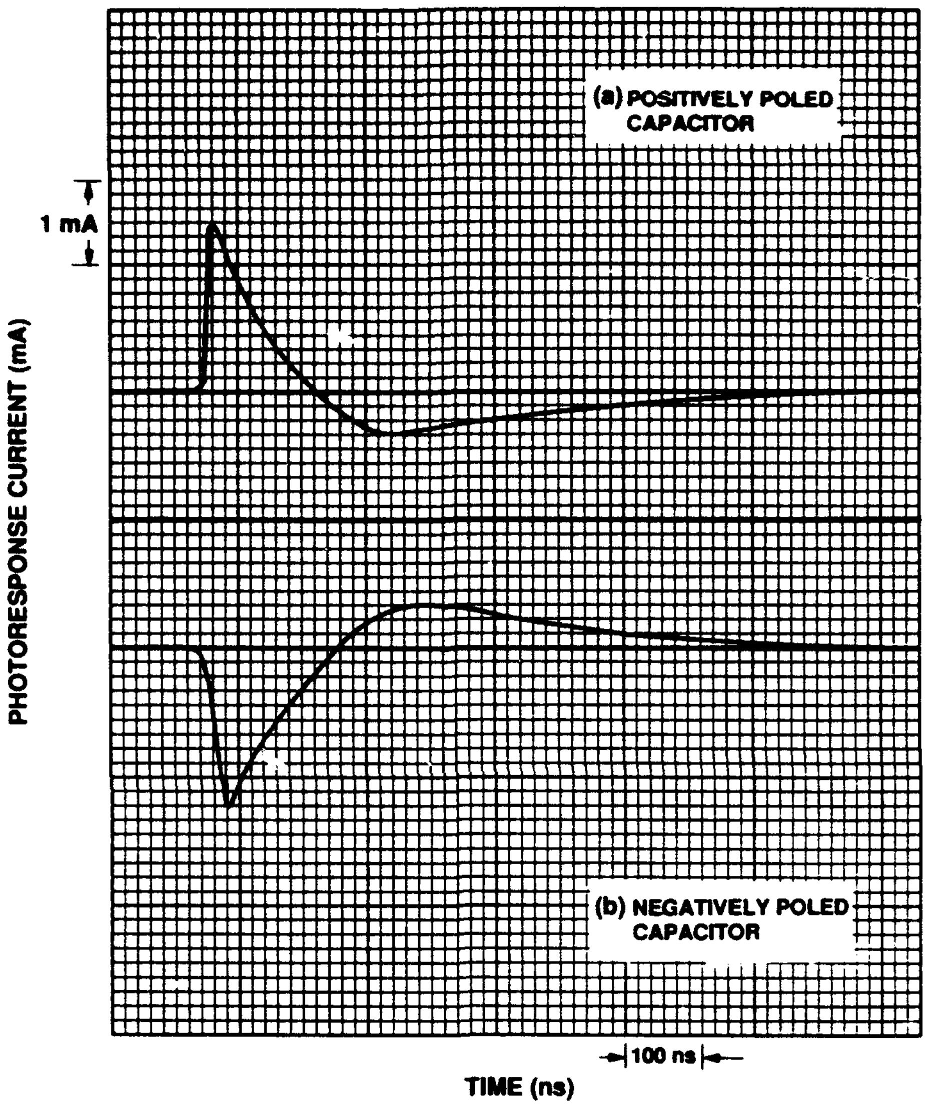

FIGURE 3 Replots on a larger time scale of the photoresponse current readout from a TFFC with an opaque top electrode (a) positively polarized state (b) negatively polarized state.

an acoustic deformation wave, initiated by sudden thermal expansion of the platinum top electrode, in response to the short energetic photon pulse: photostimulated deformation wave initiated piezoelectric response). Similar charge conservation between the total charge out within the transient photoresponse at turn on of the optical perturbation signal and the oppositely directed transient at

the turn-off of the optical signal was attributed to a pyroelectric effect by Chynoweth[12]. However, it is possible that the pyroelectric response from PZT in our experiment may be blocked by the highly reflective, opaque top electrode. On the other hand, based on the reported[19] piezoelectric coefficient of PZT, the observed ΔQ could arise due to an estimated stress of ~ 10^7 N/m^2. Assuming the Young's Modulus for Pt top electrode to be identical to the reported[20] bulk value, even a small fraction (~1%) of the incident energy being absorbed could result in stress levels as high as $9x10^7$ N/m^2.

The rise time of the photocurrent response is as short as ~25 ns, whereas the relaxation time is a fraction of a microsecond. More study of the rise time and relaxation time of the primary photoresponse as a function of the top electrode thickness and the illumination wavelength is underway to establish the exact nature of the underlying mechanism, and to differentiate between the pyroelectric effect and/or photostimulated deformation initiated piezoelectric effect.

CONCLUSION

In conclusion, this paper presents a clear observation of a high speed, repetitive, polarization dependent non-destructive-readout signal (a photocurrent), with a rise time as short as ~25 ns from thin film ferroelectric capacitor structures, when illuminated with laser (λ = 532 nm) pulses. Comparison of readout signals from devices with semitransparent and opaque top electrodes respectively suggests that the observed NDRO signal component is primarily due to thermally triggered mechanisms.

ACKNOWLEDGEMENTS

Thanks to Dr. S. E. Bernacki from Raytheon Equipment Division for providing us the sol-gel PZT films. Useful discussions

with Drs. L. E. Cross, Bill Kaiser, Joe Maserjian and Anil Thakoor are acknowledged. Thanks to Dr. J. Perry for making the high speed laser available. The work described in this paper was performed by the Center for Space Micro-electronics Technology, Jet Propulsion Laboratory, California Institute of Technology, and was sponsored by Defense Advanced Research Projects Agency through an agreement with National Aeronautics and Space Administration (NASA).

REFERENCES

1. J. T. Evans and R. Womack, IEEE Journal of Solid-State Circuits, 23, 1171 (1988).
2. D. Bondurant and F. Gnandinger, IEEE Spectrum, 30 (1989).
3. J. F. Scott and C. A. Paz De Araujo, Science, 246, 1400 (1989).
4. P.S. Brody, Appl. Phys. Lett., 38, 153 (1981).
5. M.E. Lines and A. M. Glass, Principles and Applications of Ferroelectric and Related Materials (Clarendon press, Oxford,), Chapters 5, 12, and 16.
6. V. M. Fridkin, Photoferroelectrics, Springer-Verlag (1979)
7. A. M. Glass, D. von der Linde, D. H. Auston and T. J. Negran, J. of Electronic Mat., 4, 915 (1975).
8. F. Micheron, J. M. Rouchon and M. Vergnolle, Ferroelectrics, 10, 15 (1976).
9. S. Thakoor, Ceramic Transactions: Ferroelectric Films, Edited by A. S. Bhalla and K. M. Nair, 25, 251 (1991)
10. S. Thakoor, A.P. Thakoor, and S. E. Bernacki(to be published), Proc. Third International Symp. on Integrated Ferroelectrics, April 3-5, 1991, Colorado.
11. S. Thakoor, J. Maserjian, (to be published).
12. A. G. Chynoweth, Physical Review, 102, 705 (1956).
13. A. S. De Reggi, B. Dickens, T. Ditchi, C. Alquie, J. Lewiner, I. K. Lloyd, J. Appl. Phys. 71, 854 (1992).
14. A. B. Kaufman, IEEE Transactions on Electron Devices, ED-16, 562, (1969).
15. S. Thakoor, A. W. Moopenn, and H. L. Stadler, Nasa Tech. Briefs, 15, 26 (1991).
16. S. J. Martin, M. A. Butler and C. E. Land, Electronics Letters, 24, 1486 (1989).
17. G. Yi, Z. Wu and M. Sayer, J. Appl. Phys., 64, 2717 (1988).
18. S. E. Bernacki, Proc. MRS Symposium on Ferroelectric Thin Films II, Boston, Dec(1991).
19. D. L. Polla, C. Ye, P. Schiller, T. Tamagawa, W. P. Robbins, D. Glumac, and C. C. Hsueh, Proc. MRS Symp. on Ferroelectric Thin Films II, Boston, Dec(1991).
20. R. B. Ross, Metallic Materials Specification Handbook (Halsted Press, 1972), p. 332.

Ferroelectrics, 1992, Vol. 134, pp. 365–376
Reprints available directly from the publisher
Photocopying permitted by license only

TdP213

FERROELECTRIC THIN FILMS FOR MICROELECTRONIC APPLICATIONS

E.V. ORLOVA, V.I. PETROVSKY, E.F. PEVTSOV,
A.S. SIGOV, AND K.A. VOROTILOV
Moscow Institute of Radioengineering, Electronics and Automation, 117454, Vernadsky prosp., 78, Moscow, Russia

Abstract Some microelectronic applications of ferroelectric films, such as MISFET, CCD, memory, and solid state image sensor are discussed. Certain results on preparation of thin films by sol-gel method are given as well.

INTRODUCTION

Having unique physical properties ferroelectrics are promising candidates for microelectronic applications in data processing and memory devices. However, their integration with silicon technology had been hampered, mainly, due to worse film performance compared to bulk ones. A sufficient progress in PZT film technology achieved during last few years opens new ways, and some first FeRAM are entering the market nowadays.[1] In the present paper we try to give a review of some our results concerning microelectronic application of thin ferroelectric layers in metal/ferroelectric/semiconductor devices, such as MISFET, CCD, MFeS memory, and also in solid state image sensors. Certain results on preparation of ferroelectric films by the sol-gel method are discussed as well.

HIGH DIELECTRIC CONSTANTS OF FERROELECTRICS FOR MISFET AND CCD

In this section we consider possibilities of increasing the dielectric constant ε_1 of gate dielectrics in MIS transistors and CCDs. In contrast to memory applications, it is desirable that one deals with a paraelectric phase, otherwise a semiconductor surface potential may be changed owing

to carriers motion caused by the spontaneous polarization.

For MISFET we have calculated maximum channel conductance $g(L/Z)$ (Figure 1)(or the transconductance coinciding

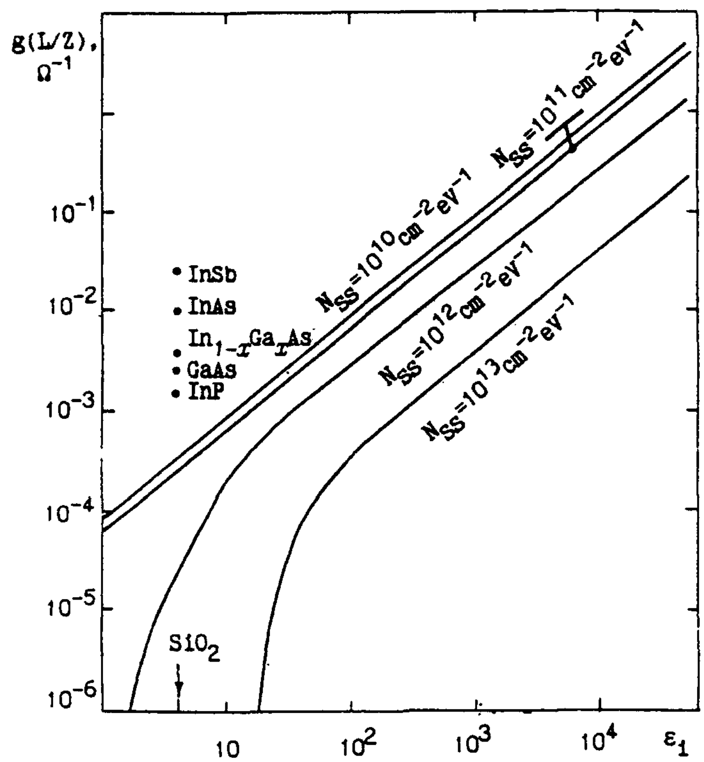

FIGURE 1 The dependencies of $g(L/Z)$ on the dielectric constant ε_i with the surface state density N_{ss} as a parameter.

with the conductance to the first approximation) normalized to the gate length L and width Z. In MOS technology low ε_i of silicon dioxide requires small ($\lesssim 10^{10}$ $cm^{-2}eV^{-1}$) values of N_{ss} to obtain acceptable transistor characteristics: $g(L/Z) \approx 3\cdot10^{-4}\ \Omega^{-1}$. Further decrease in N_{ss} doesn't improve device performance significantly. It can be seen in Figure 1 that essential increase in transistor amplification (power) characteristics can be reached if $\varepsilon_i > 100$ even for high values of N_{ss} ($N_{ss} \geqslant 10^{12}$–10^{13} $cm^{-2}eV^{-1}$). In this case one can obtain very high values of the parameters (up to $g(L/Z) \simeq 10^{-1}\ \Omega^{-1}$), which are almost inaccessible by other means (e.g., by increasing the electron mobility μ). For the sake of illustration, we expose in Figure 1 extreme va-

lues of $g(L/Z)$ of MISFET on the base of some semiconductor compounds with high μ. In calculations we have used the bulk low-field mobility, while real values of surface mobility in such structures are 2-3 times smaller.[2] Trapping has not been accounted as well. In addition, it should be only noted, but not enumerated, a great number of wellknown difficulties existing in MISFET semiconductor compounds technology.[3]

One of the most important practical applications of CCDs are readout registers of solid-state image sensors. To improve picture quality in this devices it is required to increase the amount of information transferred through the register during frame scanning (B). B is defined by the CCD cell data-storage capacity (i.e., the dynamic range γ) and data-transfer rate (i.e., the register clock frequency f):

$B = \gamma f$.

We have calculated maximum B - B_{max} as a function of ε_i for different N_{ss} as it is shown in Figure 2. It can be

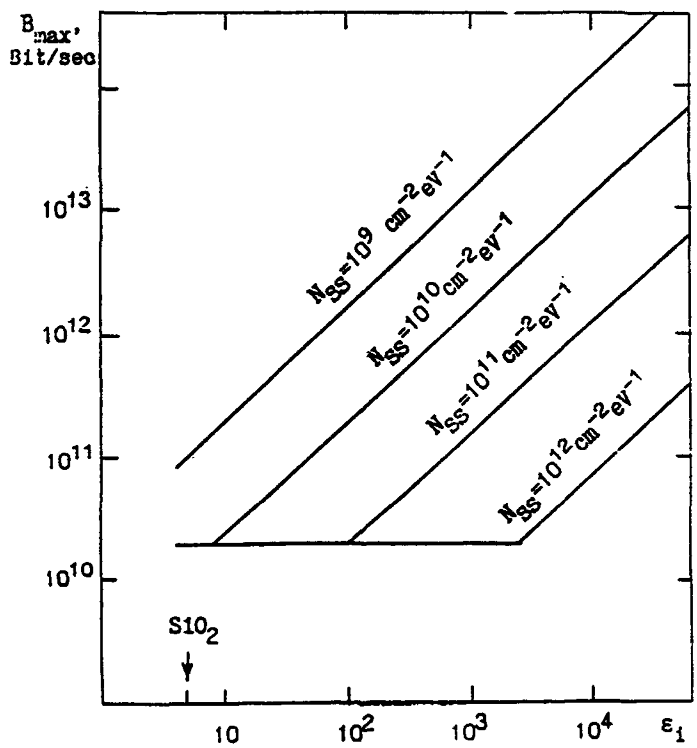

FIGURE 2 The dependencies of B_{max} on the ε_i with N_{ss} as a parameter.

seen that at $N_{ss} \simeq 10^{10}$ $cm^{-2}eV^{-1}$ and $\varepsilon_i \simeq 1000$, the amount of information transferred through the register during frame scanning may reach 10^{12}-10^{13} bits/second, what is completely inaccessible by other means.

The calculations above relate to one CCD register cell. Characteristics of the CCD matrix depend on its specific design. For example, for standard matrix 320 × 512 and $B = 10^{13}$ bits/second the contrast level number is $5 \cdot 10^3$, that essentially exceeds the up-to-date level and can be important, for instance, for increase of color picture transmission quality in high-definition television.

METAL-FERROELECTRIC-SEMICONDUCTOR MEMORY

Integrated ferroelectric memory is now a reality, but to our surprise, the main attention focuses on memory devices using ferroelectric capacitor structure, and a negligible attention is devoted to devices with ferroelectrics as gate dielectrics, such as MFeS transistor. It is connected, on the one hand, with sufficient problems of interaction between ferroelectric and semiconductor and interfacial performance, which are arisen in the last case. But on the other hand, nondestructive data reading in MFeS memory gives it obvious advantages over ferroelectric capacitor memory: more reading/writing cycles, lower time and power spending during reading, etc.

The operation of MFeS memory is based on changing semiconductor surface potential by alteration of spontaneous polarization vector direction. An example of such a device is a wellknown MFeS transistor shown in Figure 3a. Principle of reading, used in MFeS transistor, is not the unique one. Figure 3b shows MFeS memory with CCD reading. A signal charge moves under the first transfer electrode and is transferred along the interface for further processing.

Analysis of operation of MFeS memory cell will be performed in terms of characteristic fields that enables us to remove from considering its dimensions. Characteristic

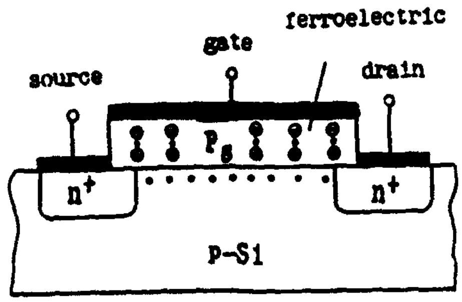

a)

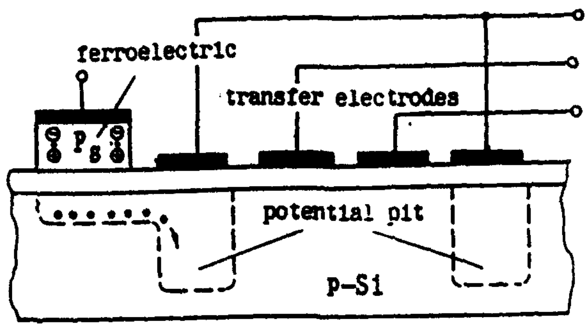

b)

FIGURE 3 Principles of data reading in MFeS memory
a) MFeS transistor
b) MFeS memory with the CCD reading

fields in MFeS memory must be tied up with the following relation:

$$E_S < P_S/(\varepsilon_0\varepsilon_1) < E_C < E_A < E_B \;, \qquad (1)$$

where $E_S=[4kTN \ \ln(N/n_i)/(\varepsilon_0\varepsilon_s)]^{1/2}$ is the field at the interface, corresponding to the change in surface potential of semiconductor by the value needed for distinct information reading (in this case, from flat band to strong inversion), k is the Boltzmann constant and N, n_i, ε_s are concentration, intrinsic concentration and dielectric constant of silicon; P_S is the spontaneous polarization; ε_0,ε_1 are dielectric constants of vacuum and ferroelectric; E_C is the coercive field; E_A is the field in ferroelectric, created by applied voltage; E_B is the breakdown field.

Thus, the figure of merit of MFeS memory is $P_S/(\varepsilon_0\varepsilon_1)$ describing the electric field at the ferroelectric/semicon-

ductor interface and, therefore, the efficiency of ferroelectric layer influence on the semiconductor. A similar figure of merit is found for pyroelectric devices. But for ferroelectric capacitor memory an appropriate figure of merit for ferroelectric material is the ratio $P_S/(\varepsilon_0\varepsilon_1 E_C)$ characterizing the ratio of nonlinear switching response to linear nonswitching response.[4] Thus, different principles of data reading in capacitor and MFeS memories lead to different requirements to ferroelectric performance.

Relation (1) is displayed in Figure 4. The upper limit

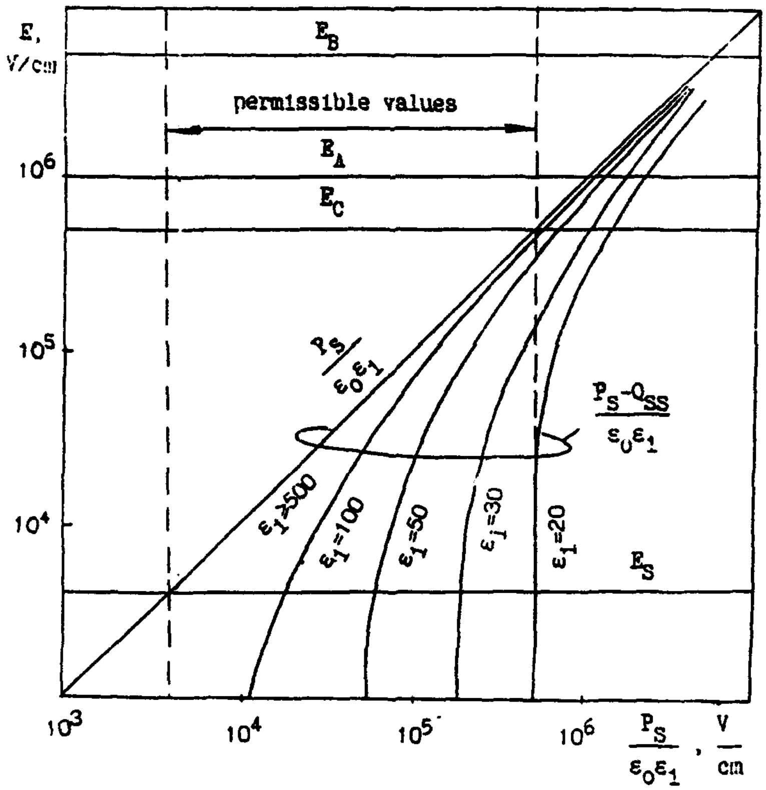

FIGURE 4 The representation requirements to MFeS memory

of permissible values of $P_S/(\varepsilon_0\varepsilon_1)$ is defined by E_C, and the lower one by E_S. The whole permissible area is shown for $E_B = 5\cdot10^6$ V/cm, $E_A = 10^6$ V/cm, $E_C = 5\cdot10^5$ V/cm, $E_S = 4\cdot10^3$ V/cm ($N = 10^{14}$ cm^{-3}), when one finds $P_S/(\varepsilon_0\varepsilon_1) = 4\cdot10^3 - 5\cdot10^5$ V/cm.

For a real MFeS structure it is necessary to take into

account the quality of interface between semiconductor and ferroelectric, and one obtains the following relation:

$$\frac{P_S - (Q_F + Q_{SS})}{\varepsilon_o \varepsilon_i} > E_S , \qquad (2)$$

where Q_F is the fixed charge, and Q_{SS} is the charge captured in surface states.

Usually, a mechanism of Q_F and Q_{SS} generation is connected with broken and weakened bonds at the dielectric/semiconductor interface strongly depending on processing conditions. For example, for films deposited by sputtering techniques it is difficult to provide appropriate quality of the dielectric/semiconductor interface due to bombardment of the substrate by high energy particles.[5]

But there may exist a generation mechanism of Q_{SS} that is directly connected to ferroelectric nature of the film. It is known that the charge in dielectric of MIS structure can generate surface states at the interface. For instance, the interface trap density increases with the number of mobile charges driven to the Si-SiO_2 interface when the capacitor is bias-temperature stressed or exposed under the ionizing radiation.[6] To interpret this fact the charge model[7] introducing the interface states by semiconductor mobile charge carriers binding to charge centers in the oxide in the immediate vicinity of the interface have been suggested. The fluctuation model of surface states,[8] developing this approach, deals with the interface three-dimensional potential pits caused by space fluctuation of fixed charge. The influence of the spontaneous polarization in ferroelectrics induces a number of surface states[9]:

$$N_{ss} = \frac{1}{\Delta} \frac{(P_S/q\pi)^{5/8}}{(4a_n a_p)^{3/8}} \exp\left[-\frac{W_g}{4\Delta}\right] \mathrm{ch}\,\frac{\Phi - \phi_o}{2\Delta} , \qquad (3)$$

where $\Delta = [q^2/(4\pi\varepsilon_o \text{æ})]\cdot(\pi P_S/q)^{1/2}$, is the characteristic energy scale of fluctuations; $\text{æ} = (\varepsilon_i + \varepsilon_S)/2$; a_n, a_p are electron and hole Bohr radii; W_g is the gap energy; Φ is

the difference between the conductivity zone and the Fermi level energies at the interface; ψ_0 is the minimum of the surface states energy distribution. It can be seen (Figure 5) that P_S can cause intensive generation of surface states

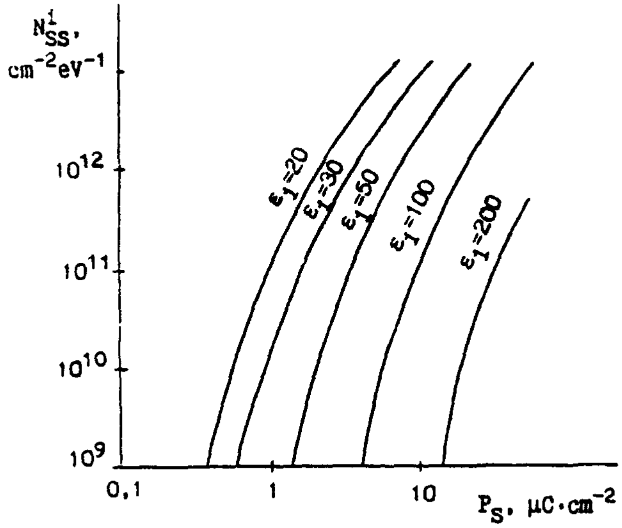

FIGURE 5 Dependencies of N_{ss} at the middle of the gap N^i_{ss} ($\Phi = \psi_0$) on P_S for different values of ε_1.

($N_{ss} \geqslant 10^{13}$ $cm^{-2}eV^{-1}$ for $\varepsilon_1 = 20$). But if ε_1 increases the influence of P_S upon N^i_{ss} diminishes.

For small fluctuations $\Delta \ll W_g$ and $\Phi = 0$, the induced charge Q_{SS} may be estimated as

$$\frac{Q_{SS}}{\varepsilon_0\varepsilon_1} = \frac{A}{\varepsilon_1^{3/8}(\varepsilon_1 + \varepsilon_S)^{3/4}} \left[\frac{P_S}{\varepsilon_0\varepsilon_1} \right]^{5/8}, \tag{4}$$

where $A = q^{3/8}/(\pi^{5/8}a_0{}^{3/4}\varepsilon_0{}^{3/8}) = 5535$ for the Bohr radius $a_0 = 5.29 \cdot 10^{-9}$ cm.

The corresponding changes of permissible values $P_S/(\varepsilon_0\varepsilon_1)$ found from Eqs.(1-4) are shown in Figure 4. The influence of surface states induced by spontaneous polarization is sufficient at $\varepsilon_1 \leqslant 500$. So if $\varepsilon_1 \leqslant 20$, the density of indu-

oed traps is so high that the most part of spontaneous polarization field is baffled and the required ohange in the surface potential is not realized. With inoreasing ε_1 the influence of induoed traps falls down. Therefore for operation of MFeS memory device it is practioally necessary to provide $\varepsilon_1 \geqslant 100$.

PYROELECTRIC IMAGE SENSORS

Pyroeleotric properties of ferroeleotrios are widely used in thermal image sensors.[10] One of the key problems is to provide a good ooupling between detectors and signal prooessing IC with keeping high thermal insulation of the sensitive layer. For this purpose, the integrated solid-state pyroelectric CCD sensor was analized and some its fabrioation teohniques based on deep ohemioal etohing were developed.[11]

Pyroeleotrio signal has a differential nature and brings a very low voltage on deteotor oells, therefore, an input signal is usually transformed before it enters CCD.[12] We proposed a simple detector input stage[13], whose oharge diagrams are shown in Figure 6. During a time period t_1, the ohopper opens inoident radiation and the deteotor (D) charge ohange is oompensated by the oharge transferred from diode V_S under the input diode V_I. During a period t_2, when the oharge on the deteotor reaches its maximum value, the voltage is applied to the diode V_S and the charges under the gates V_P, Φ1 and Φ2 are deleted. Thus the potentials of the deteotor and the nearest gate V_P become equal. During a period t_3, the diode V_S is isolated from the gate Φ2. After olosing the inoident radiation, the polarization of the deteotor ohanges and the oorresponding signal charge is generated under the gate Φ1. During the next period t_4 this oharge is olooked into the line register Φ3 and the deteotor input stage returns in its initial state.

Ferroeleotrios offer new feasibility for thermal imaging arrays. For instanoe, it is possible to carry out preliminary signal processing in the input oircuit by ohanging

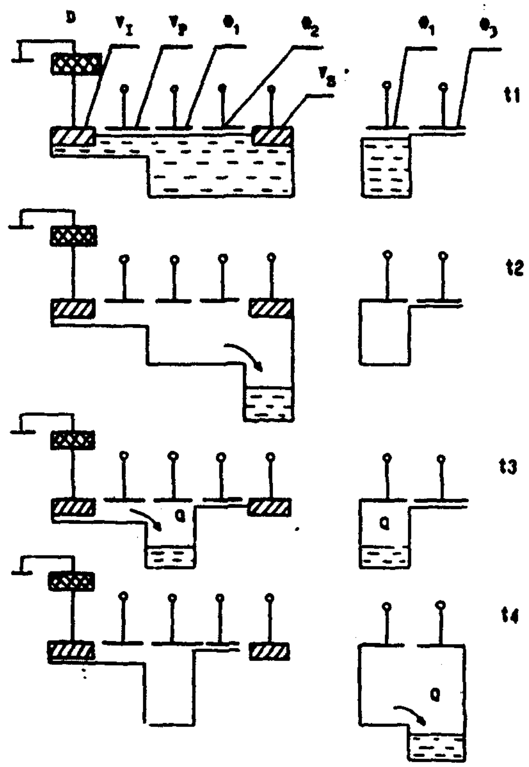

FIGURE 6 Charge diagrams the detector input stage of CCD image sensor.

spontaneous polarization of each detector due to charges from CCD registers. We have used this principle for sensitivity correction of each detector element in order to decrease signal non-uniformity at uniform illumination. Such an idea may be used also for image storage and convolution of two images.

SOL-GEL PREPARATION OF THIN FILMS

We have investigated general phenomena of film formation, including influence of initial sol composition and film formation conditions on morphology, microstructure and electric properties of different films, including some simple oxides (SiO_2, TiO_2, etc.)[14-17] as well as complex ones (e.g., ferroelectrics). It should be noted, that sol-gel SiO_2 and TiO_2 films are not only appropriate model objects, but also have practical importance in micro-

electronics technology, for instance, for planarization of interlevel dielectric of multilevel metallization of VLSI[18], for tapered etching of silicon oxide[19], and as passivation layers on GaAs.[20] At the same time TiO_2 films, having high dielectric constant from 20 up to 150, can be used as a gate dielectric in MISFET or CCD as it was mentioned earlier. We have also investigated processes of film preparation and examined electrical properties for a number of thin ferroelectric films, including lithium niobate[21], barium titanate[22] and PZT. Common problems of these films formation on silicon substrates are a growth of SiO_2 sublayer on the film/substrate interface due to silicon oxidation and chemical interaction between film and substrates. The role of these processes increases with growing temperature of annealing (the thickness of SiO_2 sublayer can reach up to near hundred nm[22]) and deterioration of MFeS structure performances takes place. To prevent this, it is necessary to form a barrier layer. For example, the protecting Si_3N_4 layer is appropriate to prevent growth of SiO_2 sublayer during $BaTiO_3$ film formation.[22] This leads also to decreasing the surface state density on ferroelectric/semiconductor interface, and, moreover, the interfacial performance of sol-gel films becomes better than that of sputtered ones.[21,22] The preparation of ferroelectric films on metallized substrates is an easier task. Thus, PZT films with the thickness 0.2-0.4 μm prepared by in cooperation with M.I. Yanovskaja (L.Ya. Karpov Institute of Physical Chemistry) on Pt and Si-SiO_2-Pt substrates have coercive voltage ≈ 1 V, spontaneous polarization ≈ 20 μC/cm^2 and dielectric constant ≈ 500.

REFERENCES

1. Proceedings 2nd Symp.on Integrated Ferroelectrics, Ferroelectrics, 116 (1991).
2. D.L. Lile, in Physics and Chem. of III-V Compound Semiconductor Interfaces (London, 1985), p. 327.
3. J.F. Wager, and C.W. Wilmsen, ibidem, p. 165.

4. J.F. Scott, L.D. Mcmillan, and C.A. Araujo, Ferroelectrics, 116, 147 (1991).
5. Y. Matsui, M. Okuyama, M. Noda, and Y. Hamakawa, J. Appl. Phys., A28, 161 (1982).
6. J.G. Hwo, C.M. Lin, and W.S. Wang, Thin Solid Films, 142, 183 (1986).
7. A. Goetzberger, V. Heine, and E.H. Nicollian, Appl. Phys. Lett., 12, 95 (1968).
8. V.A. Gergel and R.A. Suris, Soviet J. Exper. and Theor. Physics, 84, 719 (1983) (in Russian).
9. K.A. Vorotilov, V.I. Petrovsky, and Ya.A. Fedotov, Elektronnaya Tekhnika, ser.3 (Microelectronics), 1, 7 (1989) (in Russian).
10. R.W. Whatmore, Rep. Prog. Phys., 49, 1335 (1986).
11. V.K. Grigoriev, E.F. Pevtsov, V.I. Petrovsky, Ja.A. Fedotov, and V.V. Tchernokosin, U.S.S.R. Pat.N 1463084 (23.12.86).
12. P. Manning, D. Burgess, and J. Gooding, Infrared Phys., 22, 259 (1982).
13. V.I. Petrovsky, E.F. Pevtsov, and V.V. Tchernokosin, U.S.S.R. Pat.N 1665540 (08.04.87).
14. K.A. Vorotilov, E.V. Orlova, and V.I. Petrovsky, Thin Solid Films, 207 (1991), in the press.
15. idem, ibidem, in the press.
16. K.A. Vorotilov, I.P. Krikunov, E.V. Orlova, and V.I. Petrovsky, Elektronnaya Tekhnika, ser.2 (Semiconductor Devices), 1, 12 (1989) (in Russian).
17. K.A. Vorotilov, E.V. Orlova, and V.I. Petrovsky, ibidem, 1, 11 (1985) and 5, 85 (1985) (in Russian).
18. A.S. Valeev, K.A. Vorotilov, and V.I. Petrovsky, Elektronnaya Tekhnika, ser.3 (Microelectronics), 2, 54 (1991) (in Russian).
19. K.A. Vorotilov, I.P. Krikunov, E.V. Orlova, and V.I. Petrovsky, Elektronnaya Tekhnika, ser.2 (Semiconductor Devices), 1, 75 (1989) (in Russian).
20. K.A. Vorotilov, E.V. Orlova, and V.I. Petrovsky, ibidem, in the press (in Russian).
21. K.A. Vorotilov, E.V. Orlova, V.I. Petrovsky, and E.P. Turevskaya, Elektronnaya Tekhnika, ser.6 (Materials), 4, 25 (1987) (in Russian).
22. K.A. Vorotilov, E.V. Orlova, V.I. Petrovsky, M.I. Yanovskaja, S.A. Ivanov, E.P. Turevskaya, and N.Ya. Turova, Ferroelectrics, (1991), in the press.

Ferroelectrics, 1992, Vol. 134, pp. i–iii
Reprints available directly from the publisher
Photocopying permitted by license only

AUTHOR INDEX

Proceedings of the Second European Conference on the Application of Polar Dielectrics

Volumes 133–134

Special Issue on Piezoelectric and Electrostrictive Actuators

A special issue of the international journal *Ferroelectrics* is scheduled for 1992 on the subject "Piezoelectric and Electrostrictive Actuators."

Recent developments in piezoelectric and electrostrictive ceramics are remarkable, especially in the field of optics and precision machinery. Camera shutters, dot-matrix printers, and air valves have been widely commercialized. Ultrasonic motors will partially replace conventional electromagnetic motors in the future.

This special issue will cover the fundamental studies of ceramic actuators and applications:

1. Ceramic actuator materials — piezoelectrics, electrostrictors, phase transition — related ceramics
2. Fabrication processes — powders, tape casting
3. Micro/macrostructure — grain size dependence, monomorph, electrode configuration
4. Control technique — polarization control, pulse drive method
5. Applications — deformable mirrors, positioners, pulse drive motors
6. Ultrasonic motors

Invited and contributed papers are welcome. All manuscripts will be reviewed. Manuscripts should be prepared according to the instructions on the inside back cover of "Ferroelectrics."

Authors are cordially invited to submit their papers to the Guest Editors below:

Professor Kenji Uchino
Department of Physics
Sophia University
Kioi-cho 7-1, Chiyoda-ku
Tokyo 102, Japan
or
Materials Research Laboratory
The Pennsylvania State University
University Park, PA 16802, USA
(July 1-September 30)

Professor L. Eric Cross
Materials Research Laboratory
The Pennsylvania State University
University Park, PA 16802

For further information, please feel free to contact the Guest Editors.

First Announcement

The Eighth
INTERNATIONAL MEETING OF FERROELECTRICITY

8–13 August 1993
National Institute of Standards and Technology
Gaithersburg, Maryland USA

The scope of the conference will be similar to that of the preceding IMFs. Both invited and contributed papers will be presented on fundamental and applied research on ferroelectrics, including but not limited to:

Phase transitions and critical phenomena
Electronic structure, quantum effects
Lattice dynamics, lattice instabilities, and soft modes
First principles calculations
Low-temperature properties
Superconductivity in oxides
Charge density waves, polarization fluctuations
Structure and crystal growth
X-ray and neutron scattering
Acoustic and ferroelastic properties
Dielectric, piezoelectric, and pyroelectric properties
Optical properties and phase conjugation
Modulated and incommensurate systems
Disordered and glassy systems
Domains, domain boundaries, and imperfections
Raman, Brillouin, IR, and submillimeter spectroscopy
NMR, ESR, PAC, and other types of spectroscopy
Electron microscopy
High-pressure effects
Polymers and liquid crystals
Ceramics and composite materials
Sensors, actuators, and transducers
Thin films and surfaces
Ferroelectric/semiconductor integration

Wallace A. Smith
Office of Naval Research
IMF8 Chairman

L. Eric Cross
Pennsylvania State University
IMF8 Vice Chairman

George W. Taylor
Princeton Resources
IMF8 Vice Chairman

To receive future announcements, send your name and address to:

Ms. Kathy Kilmer, IMF8 Conference Manager
National Institute of Standards and Technology
Administration Building, Room A917
Gaithersburg, MD 20899
TEL (301) 975-2776; FAX (301) 926-1630

Title and Name ______________________
Institution ______________________
Department ______________________
Street ______________________
City/State/Zip ______________________
Country ______________________
Phone ______________
FAX ______________

❒ I will present a paper entitled: ______________________
❒ I will be accompanied by _____ guests.
❒ I will attend, but will not present a paper.
❒ I will not attend, but would like to be kept informed.

FLC 93 TOKYO

強誘電性液晶
国際会議

第4回強誘電性液晶国際会議
(日本学術振興会 主催)

FOURTH
INTERNATIONAL CONFERENCE
ON
FERROELECTRIC
LIQUID CRYSTALS

SEPT. 28 - OCT. 1
1993

TOKYO, JAPAN

FIRST ANNOUNCEMENT

こまばエミナース, 東京
KOMABA EMINENCE, TOKYO

FLC 93 TOKYO, to be held Sept. 28 - Oct. 1, 1993, at Komaba Eminence under the auspices of JSPS (Japan Society for the Promotion of Science), is the fourth in the series of biennial international meetings on ferroelectric liquid crystals begun in Arcachon (1987) and continued in Göteborg (1989) and Boulder (1991).

Scientists with interests in the basic and applied aspects of ferroelectric liquid crystals are welcome to participate in this meeting. The program will consist of single sessions of invited lectures, contributed oral and poster presentations.

To receive further information, please fill out and return by mail or FAX the attached preregistration form by Oct. 1, 1992. Preregistrants will be sent the second circular, including details of abstract submission and meeting arrangements, by the end of 1992.

Comments and questions on FLC 93 TOKYO are welcome and should be directed to the conference organizers:

Atsuo FUKUDA (FLC 93 TOKYO)
Tokyo Institute of Technology
Faculty of Engineering
Department of Organic & Polymeric Materials
O-okayama, Meguro-ku, Tokyo 152, JAPAN

FAX : +81-3-3748-5369
TEL : (03) 3726-1111 Ext. 2437
E-mail: ytakanis@cc.titech.ac.jp

Mail to:

Atsuo FUKUDA (FLC 93 TOKYO)
Tokyo Institute of Technology
Faculty of Engineering
Department of Organic & Polymeric Materials
O-okayama, Meguro-ku, Tokyo152, JAPAN

Preregistration Form

Name & Title:

Affiliation:

Address:

FAX:

E-Mail:

Telex:

(over)

Area of FLC Interest:

- Dynamics
- Physics
- New Materials
- Phase Behavior & Microscopy
- Device Technology
- Polymer FLC's
- Chiral Systems
- Antiferroelectrics
- Optics
- Interfaces
- Theory
- Others (

Tentative Title of Your Contribution:

ORGANIZING COMITTEE:

Atsuo Fukuda: Chair
Hideo Takezoe
Naoyuki Koide
Ichiro Tsunoda
Hirokazu Toriumi
Dietrich Demus

INTERNATIONAL ADVISORY BOARD:

L. Bata	U. Finkenzeller
R. Blinc	J. Fousek
L. M. Blinov	J. W. Goodby
E. Chiellini	G. Heppke
N. A. Clark	S. T. Lagerwall
H. Coles	R. B. Meyer
C. Destrade	J. Prost
G. Durand	M. Schadt
C. Escher	

142 COMMITEE of JSPS:

M. Takeda: Chair
K. Okano
H. Sasabe
H. Kokado

Komaba Eminence, where the scientific meeting will take place, is located within walking distance from the University of Tokyo, Komaba Campus, and is close to one of the downtown area, Shibuya. The days fixed for FLC 93 TOKYO are Sept. 28 - Oct.1, 1993; just after the Conference, Oct. 5 - 9, the 1993 Electronic Show will be held at Makuhari Messe near Tokyo. The participants will surely enjoy not only the scientific meeting of FLC 93 TOKYO but also exhibitions of devices and equipment, particularly of liquid crystal displays, in the 1993 Electronic Show.

Magnetoelectric Interaction Phenomena in Crystals

2nd International Conference
September 13–18, 1993

Centro Stefano Franscini, Monte Verità
Ascona (Ticino), Switzerland

GENERAL INFORMATION

Conference Site

The conference will be held at the Centro Stefano Franscini, Monte Verità, Ascona, on the banks of Lago Maggiore in the Italian-speaking part of Switzerland.

Accommodation

The possibilities of getting suitable accommodation are limited. Lodging facilities are available at the Centro itself for about 60 participants. For the others, hotels in nearby Ascona are foreseen, but it cannot be guaranteed that accommodation can be found for all participants. Moreover the lecture room available also limits the total number of participants.

Second Circular

A second circular with a call for papers and more detailed information will be sent in December 1992 to all those returning the attached form to:

Mme Odile Hirth/MEIPIC
Secrétariat de Chimie appliquée
Université de Genève, Sciences II
30, Quai Ernest Ansermet

CH-1211 Genève 4
Suisse/Switzerland

E-mail: MEIPIC@sc2a.unige.ch
Phone: (+41)22-702-6408(Hirth)
-6419 (Rivera)
-6418 (Ye)
-6111 (Exchange)
Fax: (+41) 22-329-6102
Telex: 421.159 SIAD

Organization

Organized by the Department of Mineral, Analytical and Applied Chemistry of the University of Geneva, in collaboration with the Laboratory for Neutron Scattering at the Paul Scherrer Institute, Würenlingen and Villigen, Switzerland and with the Institute for Theoretical Physics, University of Nijmegen, The Netherlands.

Financial support

Swiss Federal Institute of Technology, Zürich.

Motivation

The magnetoelectric effect foreseen by Landau and Lifshitz in 1956 has been predicted to occur in chromiumoxyde Cr_2O_3 by Dzyaloshinskii (1960). It is characterized by the appearance of an electric polarization on applying a magnetic field and a magnetization on applying an electric field. The experimental observation of the effect in Cr_2O_3 followed rapidly (Astrov 1960, 1961; Folen, Rado and Stalder 1961). Thereafter the effect was observed and studied in many more materials.
The status of theoretical understanding and experimental work after the first decade of research in magnetoelectricity is well reflected by the book *The Electrodynamics of Magneto-Electric Media* of O'Dell (1970) and the proceedings of the conference *Magnetoelectric Interaction Phenomena in Crystals* held in 1973 (Freeman and Schmid 1975).
During the following two decades of research more theoretical and experimental know-how has been accumulated, but many problems

still remain unsolved. It has become clear, however, that the magnetoelectric effect is an invaluable tool for studying materials, for example the magnetic symmetry and phase transitions of magnetically ordered phases. These facts are to a great extent still ignored by the scientific community working in solid state physics.

Organizing Committee

H. Schmid (chairman),
A. Janner, H. Grimmer, J.-P. Rivera,
Z.-G. Ye.

International Advisory Board

Czechoslovakia: V. Janovec.
France: F. Bertaut, M. Clin, P. Tolédano
Germany: H. G. Kahle
Great Britain: G. Gehring, D. Tilley
Israel: S. Shtrikman, R. M. Hornreich
Japan: J. Kobayashi, K. Kohn, K. Siratori
The Netherlands: T. Janssen
Poland: J. Barnas
Russia: M. I. Bichurin,
A. S. Borovik-Romanov,
R. V. Pisarev,
Yu. Venevtsev
Switzerland: E. Ascher, P. Fischer,
P. Günter
Ukraine: I. E. Chupis
USA: I. Dzyaloshinskii, G. T. Rado,
J. F. Scott

SCIENTIFIC PROGRAM

Fields and Special Topics

- Linear and higher order magnetoelectric, piezomagnetoelectric and other magnetoelectrically related effects.
- Relation between symmetry and magnetoelectric properties (tensorial, crystallographic, relativistic).
- Phenomenological and microscopic theories (Landau theory of phase transitions, exchange effects).
- Frontier fields (toroidal moments, kinetoelectric and kinetomagnetic effects, problems of magnetoelectricity and related symmetry phenomena in quantum magnets, e.g. anyonic systems and chiral phases).
- Synthesis, structural and physical properties of magnetoelectric materials (single crystals, ceramics, composites): ordinary magnetoelectrics and complex ones, such as ferromagnetic, ferrimagnetic or antiferromagnetic ferroelectrics, antiferroelectrics and ferroelastics ("Seignettomagnetics").
- Magnetoelectric effect in incommensurate crystals (modulated, intergrowth and quasicrystals).
- Magnetoelectrically monitored magnetic phases and phase transitions.
- Field induced effects. Static magnetic field induced polarization, electric field induced magnetization, quasistatic, pulsed, dynamic and high frequency.
- Optical properties (crystal optics of magnetoelectric materials in transmission and reflection; magnetoelectrically generated non-linear optical effects).
- Domains and domain walls (switching, symmetry aspects, coupling with applied fields, stress, etc.).
- Elementary excitations in magnetoelectric materials.
- Inhomogeneity and defect induced magnetoelectric effects.
- Measuring techniques.
- Applications.

Contributions and Proceedings

Plenary sessions of tutorial expositions and invited lectures selected among the contributed papers are foreseen, as well as posters. Conference proceedings are planned to be published. Invited lecturers and contributing participants are asked to have their manuscripts available at the beginning of the conference.
All papers will be refereed.

5th International Symposium on Integrated Ferroelectrics

April 19, 20, 21, 1993

Antlers Doubletree Hotel
Colorado Springs, Colorado

Chairman: Prof. C. A. Paz de Araujo
Co-chairman: Prof. R. Panholzer
General Technical Program Coordinator:
Prof. J. F. Scott

Symposium Sponsors

Office of Naval Research
Defense Advanced Research Projects Agency
Naval Postgraduate School
University of Colorado at Colorado Springs

Call for Papers

Deadline for abstracts—
September 30, 1992

This is the 5th Annual International Symposium dedicated to ferroelectric thin-film materials integrated with semiconductor circuits.

Over the past few years, interest in this field of integrated ferroelectrics has grown beyond all expectation and the 1993 symposium should attract an even larger number of participants.

Authors are invited to submit a 300-word abstract by *September 30, 1992*. Topics include but are not limited to:

- ferroelectric memories
- ferroelectric and pyroelectric CCDs
- high dielectric constant materials for integrated circuits (64 Mbit DRAM, etc.)
- ferroelectric and pyroelectric sensors
- integrated optics
- optical storage
- radiation-related subjects, such as radiation hardness
- fundamental properties
- process and substrates
- process integration
- new devices and architecture
- device modeling
- materials processing and integration
- supporting circuitry and applications
- ferroelectric ASICs
- smart tags
- RF identification
- neural networks
- bypass capacitors

Abstracts should be submitted on 8½ × 11 paper with the title centered in upper case, leaving two line spaces, then the author's name and affiliation, centered. Up to two pages of pictures or figures of supporting data may be included.

Abstracts will be juried and authors will be informed of acceptance at a later date.

Deadline for Abstracts

September 30, 1992

Registration Fee

	Before April 5	After April 5
General	$275.00	$350.00
Government	$225.00	$300.00
All students	$ 40.00	$ 60.00

One copy of the Symposium Proceedings is covered by the registration fee. Additional copies will be available at $55.00 each.

Hotel Accommodations

Antlers Doubletree Hotel

	Single	Double
General	$72.00	$82.00
Government	$51.00	$71.00

Please make hotel reservations for the Symposium *before* April 5, 1993 *directly with*:

Antlers Doubletree Hotel
4 South Cascade Avenue
Colorado Springs, Colorado 80903
(719) 473-5600

Send check or money order made payable to Antlers Doubletree Hotel or guarantee your reservation with a major credit card.

A limited number of economy accommodations are available in the proximity of the Antlers Doubletree Hotel.

Mail Abstracts to:

Alona S. Miller, Symposium Coordinator
University of Colorado at Colorado Springs
1420 Austin Bluffs Parkway
P.O. Box 7150
Colorado Springs, Colorado 80933
Phone: 719-593-3488
FAX: 719-594-4257

FERROELECTRICS
and related materials

NOTES FOR CONTRIBUTORS

Manuscripts should be typewritten with double-spacing and submitted in triplicate. Authors are requested to forward their manuscripts to either the Editor:

G. W. Taylor
Princeton Resources,
P.O. Box 211,
Princeton, New Jersey 08540, USA

or one of the Associate Editors:

Peter Günter
Institut für Quantenelektronik
ETH
CH 8093 Zürich
Switzerland

Sidney B. Lang
Department of Chemical Engineering
Ben Gurion University of the Negev
Beer Sheva 84120, Israel

Koichi Toyoda
Research Institute of Electronics
Shizuoka University
Hamamatsu 432
Japan

Submission of a paper to *Ferroelectrics* will be taken to imply that it represents original work not previously published, that it is not being considered for publication elsewhere, and that if accepted it will not be published elsewhere in the same form, in any language, without the consent of the editors.

It is a condition of the acceptance by the editor of a typescript for publication that the publishers acquire automatically the copyright in the typescript throughout the world.

Manuscript length: The maximum length preferred is 35 units, where a unit is a double-spaced typewritten page or one figure. Longer papers, or papers not following the prescribed editorial format, cannot be guaranteed prompt publication.

Abstracts and Key Words: Each manuscript should contain a leading abstract of approximately 100–150 words and be accompanied by up to six key words which characterize the contents of the paper.

Figures should be given numbers and captions, and should be referred to in the text. Captions should be collected on a separate sheet. Please label each figure with the figure number and the name of the author. Line drawings of high enough quality for reproduction should be prepared in India ink on white paper or on tracing cloth; coordinate lettering should be included. Figures should be planned so that they reduce to a 6½ cm column width. The *preferred* width of submitted figures is 12 to 15 cm, with lettering 4 mm high, for reduction by one-half. Photographs intended for halftone reproduction should be good, original glossy prints, at roughly twice the desired size. Redrawing, and author's alterations in excess of 10%, will be charged.

Color Plates: Whenever the use of color is an integral part of the research, or where the work is generated in color, the journal will publish the color illustrations without charge to authors. Reprints in color will carry a surcharge. Please write to the Editor for details.

Equations should be typewritten wherever possible, with subscripts and superscripts clearly indicated. It is helpful to identify unusual symbols in the margin.

Units: Acceptable abbreviations will be found in the *Style Manual* of the American Institute of Physics and similar manuals. Metric units are preferred.

References and Notes are indicated in the text by superior numbers; the full list should be collected and typed on a separate page at the end of the paper. Listed references are arranged as follows:

1. J. C. Slater, *J. Chem. Phys.* **9**, 16 (1941).
2. F. Jona and G. Shirane, *Ferroelectric Crystals* (Pergamon Press, Oxford, 1962), pp. 186–7.

Proofs: Page proofs, including figures, will be forwarded by air mail to authors for checking.

Reprints: Reprints may be purchased; a reprint order form will be sent with page proofs.

There are no page charges to authors or to institutions.

COLOR PLATE I.
See Hofmann *et al.*, Figure 2.
FERROELECTRICS, Volume 133(1–4).

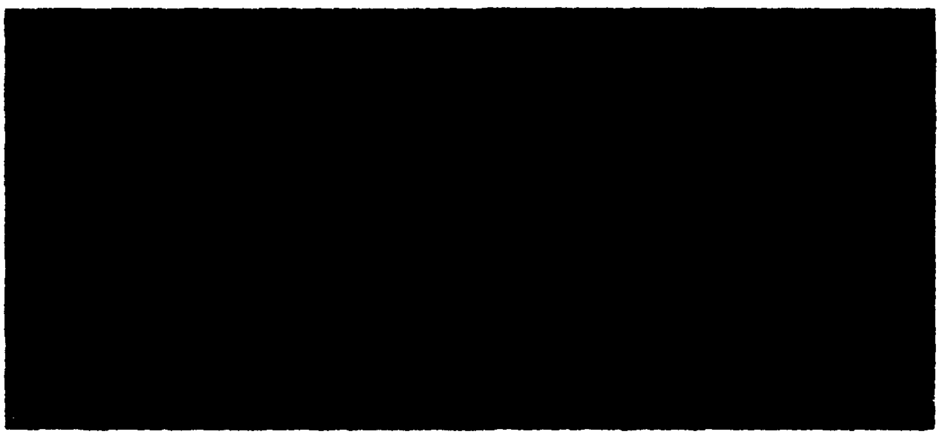

COLOR PLATE II.
See Murphy *et al.*, Figure 1.
FERROELECTRICS, Volume 134(1–4).

(continued from inside front cover)

Ordering Information Published monthly. Subscriptions are renewed on an annual basis. 1992 Volumes: 125–137.

Orders may be placed with your usual supplier or directly with Gordon and Breach Science Publishers S.A., c/o STBS Ltd., (distributor for Gordon and Breach Science Publishers S.A.), P.O. Box 90, Reading, Berkshire RG1 8JL, Great Britain or P.O. Box 786, Cooper Station, New York, NY 10276, U.S.A. Journal subscriptions are sold on a volume basis only; single issues of the current volume are not available separately. Claims for nonreceipt of issues should be made within three months of publication of the issue or they will not be honored free of charge. Subscriptions are available for microform editions. Details will be furnished upon request.

SUBSCRIPTION RATES Base list subscription price per volume: ECU 316.00 (U.S. $29); Fl 736.00).* Available only to single users whose library already subscribes to the journal OR who warrant that the journal is for their own use and provide a home address for mailing. Orders must be sent directly to STBS and payment must be made by personal check or credit card.

Separate rates exist for different users such as academic and corporate institutions. These rates may also include photocopy license and postage and handling charges. Special discounts are also available to continuing subscribers through our Subscriber Incentive Plan (SIP).

*The European Currency Unit (ECU) is the worldwide base list currency rate; payment can be made by draft drawn on ECU currency in the amount shown. Alternatively, the U.S. Dollar rate applies only to North American subscribers; the Dutch Guilder rate applies only to British and Mainland European subscribers. Subscribers from other territories should contact their agent or one of the STBS Subscription Departments:

USA
P.O. Box 786, Cooper Station, New York, NY 10276
Telephone: (212) 206-8900
Telex: 236735 (GOPUB UR)
Fax: (212) 645-2459

GREAT BRITAIN and MAINLAND EUROPE
P.O. Box 90, Reading, Berkshire RG1 8JL
Great Britain
Telephone: (0734) 560080
Telex: 849870 (SCIPUB G)
Fax: (0734) 568211

JAPAN
Yohan Western Publications Distribution Agency
3-14-9, Okubo, Shinjuku-ku, Tokyo 169
Telephone: (03) 3208 0181
Telex: 2324818 (YOHAN J)
Fax: (03) 3209 0288

All issues are dispatched by airmail throughout the world.

ASIA (Excluding Japan)
Kent Ridge, P.O. Box 1180, Singapore 9111
Telephone: 741 6933
Telex: RS 24200 TMSR QUOTE (TM 4418)
Fax: 741 6922

AUSTRALIA
Private Bag 8, Camberwell, Victoria 3124
Telephone: (03) 819-6650
Telex: 10723126 (GTET)
Fax: (03) 819-6651